Characterizing the Climate Impacts of Brown Carbon

REPORT TO THE

California Air Resources Board Research Division

Project # 13-330

Prepared by:

Dr. Lynn M. Russell[1]
Dr. Christopher D. Cappa[2]
Dr. Michael J. Kleeman[2]
Dr. Mark Z. Jacobson[3]

[1] Scripps Institution of Oceanography
University of California, San Diego
San Diego, CA 92093

[2]Department of Civil and Environmental Engineering
University of California, Davis
One Shields Avenue, Davis, CA, 95616

[3]Department of Civil and Environmental Engineering
Stanford University
473 Via Ortega, Room 397
Stanford, CA 94305-4020

February 27, 2019

DISCLAIMER

The statements and conclusions in this report are those of the contractor and not necessarily those of the California Air Resources Board. The mention of commercial products, their source, or their use in connection with material reported herein is not to be construed as actual or implied endorsement of such products.

ACKNOWLEDGEMENTS

We acknowledge California Air Resources Board (CARB) for funding this work (Agreement number: 13-330) and Dr. Nehzat Motallebi for her advice and guidance as contract manager. We thank the staff of the Fontana Fire Department and the South Coast Air Quality Management District (SCAQMD) for Fontana site logistics and the staff of UCD Extension at Fresno for their help with local logistics. The statements and conclusions in this paper are those of the researchers (contractor) and not necessarily those of CARB. The mention of commercial products, their source, or their use in connection with material reported herein is not to be construed as actual or implied endorsement of such products. The measurements used in this manuscript are available at https://doi.org/10.6075/J0VX0DF9.

TABLE OF TABLES

TABLE OF FIGURES

LIST OF ACRONYMS

3-D – three dimensional
AMS – Aerosol Mass Spectrometer
AAOD – aerosol absorption optical depth
AERONET – Aerosol Robotic Network
ANMF – ammonium nitrate mass fraction
AOD – aerosol optical depth
BB – biomass burning
BBOA – biomass burning organic aerosol
BC – black carbon
BLH – boundary layer height
BrC – brown carbon
BVOC – biogenic volatile organic compounds
BWP – beam width probe
CA – California
CAOD – cloud absorption optical depth
CAP – Cluster Analysis Panel
CARB – California Air Resources Board
CCAQS – California Ambient Air Quality Standards
CDCE – composition-dependent collection efficiency
CE – collection efficiency CI -- confidence interval
Cldfra – cloud fraction
COA – cooking organic aerosol
COD – cloud optical depth
COL – column
CRD-PAS – cavity ringdown-photoacoustic spectrometer
CS – Cosine Similarity
DDS -- dust-related detritus or SOA
DMS – dimethylsulfide
DRE – direct radiative effects
DRF – direct radiative forcing
Dm – mobility diameter
DU – dust
Dva – vacuum aerodynamic diameter
Dved – volume- equivalent diameter
E_{abs} – absorption enhancement
EC – elemental carbon
EDAS -- Eta Data Assimilation System

EI – electron impact
f43 – fraction of m/z 43 in OM
f44 – fraction of m/z 44 in OM
FFC – fossil fuel combustion
FTIR – Fourier Transform Infrared Spectroscopy
GATOR-GCMOM – Gas, Aerosol, Transport, Radiation, General-Circulation, Mesoscale, and Ocean Model
GFED – Global Fire Emissions Database
GHGs – Green House Gases
GSFC – Goddard Space Flight Center
HF – high fog
HOA – Hydrocarbon-like Organic Aerosol
HR – high-resolution
HULIS – humic-like substances
HYSPLIT -- Hybrid Single-Particle Lagrangian Integrated Trajectory
ICs – initial conditions
IE – ionization efficiency
IPCC – Intergovernmental Panel on Climate Change
IR – Incremental Reactivity
ISOP – isoprene carbon bond group
LF – low fog
LOD – level of detection
LS – light-scattering
LSI – light-scattering inorganic
LVOOA – low-volatility oxygenated organic aerosol
MAC – mass absorption coefficient
MC – mixed combustion
MEC – mass extinction coefficient
METAR -- meteorological aviation reports
MFB -- mean fractional bias
MS – mass spectrometry
MSA – methane sulfonic acid
MSC – mass scattering coefficient
N.A. – not applicable
NARR – North American Regional Reanalysis
NCEP – National Centers for Environmental Protection
NF – nonurban fossil fuel
NH_4^+ / N(-III) – ammonium
NO_3^- / N(V) – nitrate
NOx – oxides of nitrogen

NOOA – nitrate-associated oxygenated organic aerosol

NR-PM -- non-refractory particle mass

O_3 – ozone

OA – organic aerosol

OC – organic carbon

OH -– hydroxyl radical

OLE – olefin carbon bond group

OM – organic matter or mass

OOA – Oxygenated Organic Aerosol

OS – organosulfate

PAN – peroxyacetyl nitrate

PAR – paraffin carbon bond group

PAS – photoacoustic spectrometer

PAX – particle absorption extinctiometer

PET – PMF evaluation tool

PM10 – Airborne particle mass with aerodynamic diameter less than 10.0 μm.

PM2.5 – Airborne particle mass with aerodynamic diameter less than 2.5 μm.

PM1- Airborne particle mass with aerodynamic diameter less than 1 μm.

PM018- Airborne particle mass with aerodynamic diameter less than 0.18 μm.

PM -– Airborne particulate matter

PMF – positive matrix factorization

PN – particulate nitrate

POA – primary organic aerosol

POM – primary organic matter

PRD – Pearl River Delta

PSL – polystyerene latex

PToF – particle time of flight

$R_{coat\text{-}rBC}$ – ratio between coating concentration and rBC concentration for rBC-containing particles

rBC – refractory black carbon

RH – relative humidity

RIE – relative ionization efficiency

RMSE -- Root Mean Square Error

RN -- reactive nitrogen

RWB – residential wood burning

SAE – scattering Ångstrom exponent

sca -– scattering

SCAQMD -- South Coast Air Quality Management District

SCAQS – Southern California Air Quality Study

SCC – sharp-cut cyclone

SEMS – scanning electrical mobility sizer
SJV – San Joaquin Valley Air Basin
SIA – secondary inorganic aerosol
SLCF – short lived climate forcer
SMPS – scanning mobility particle sizer
SMVGEAR II – Sparse Matrix Vectorized Gear Code, 2nd Edition
SOA – secondary organic aerosol
SO_4^{2-} / S(VI) – sulfate
SoCAB – South Coast Air Basin
SOM – Statistical Oxidation Model
SOM – secondary organic matter
SOP – Standard Operating Procedure
SP-AMS – soot particle aerosol mass spectrometer
SP2 – single particle soot photometer
SSA – single scatter albedo
SV – Sacramento Valley Air Basin
SVOOA – semi-volatile oxygenated organic aerosol
TOA – top-of-atmosphere
TIR – thermal infrarred
TD – thermodenuder
TLS – timing of light-scattering signal
TMS – timing of mass spectra signal
ToF – time of flight
TOL – toluene carbon bond group
UC – University of California
UCD -- University of California at Davis
UCLA – University of California at Los Angeles
UF – urban fossil fuel
USEPA – United States Environmental Protection Agency
UV – Ultraviolet radiation
VOC – volatile organic compounds
VOOA – vehicle-associated oxygenated organic aerosol
WRF – Weather Research and Forecasting
XRF – X-ray fluorescence
XYL – xylene carbon bond group

ABSTRACT

Brown carbon (BrC) emissions from residential, agricultural, and wildfire burning activities are a highly seasonal, episodic, and poorly characterized fraction of fine particulate matter (PM2.5) in California. In addition, secondary formation of additional carbonaceous particle mass in urban areas may contribute even more light-absorbing BrC year round. These types of BrC may have substantial impacts on climate in California and worldwide. Through a multi-institution collaboration, this study identified and characterized the contribution of BrC to climate forcing in California by (1) providing PM1 and PM2.5 physical measurements and chemical analyses of fine particles that constrain the chemical concentrations and optical properties of burning emissions, (2) quantifying the BrC organic components and the multi-wavelength absorption from burning emissions and from atmospheric formation of secondary components at two California locations, and (3) examining the globally and regionally-averaged climate response of BrC. We looked at areas with significant residential burning in the San Joaquin Valley (Fresno) and with photochemical aerosol formation in the South Coast Air Basin (Fontana) to characterize their different mixes of emission sources and seasonality. The advanced cavity ring-down/photoacoustic and mass spectrometric instrumentation used for these measurements provided unprecedented chemical composition and optical property (e.g. multi-wavelength absorption and extinction) characterization of BrC. The quantitative analysis of these results separated and characterized BrC, providing important quantification of emissions-specific particle absorption properties for modeling climate forcing. These results were used to evaluate column measurements of absorption partitioning, showing good agreement when surface conditions were representative of the boundary layer and column. Global and regional models were then used with the realistic quantification of organic particles and their absorption. The combination of the source-oriented regional modeling and global plus regional modeling showed that diesel engines make a larger contribution than biomass burning to total-column absorption in California.

1 EXECUTIVE SUMMARY

Background:

Carbonaceous aerosol, including organic aerosol (OA) and black carbon, can constitute the largest fraction of fine particulate matter (PM) in many regions, but the composition and properties of carbonaceous aerosol is usually the least understood. Better understanding and characterization of organic aerosols through improved measurements are needed in order to identify their emission sources and their impacts on climate and air quality. Because the organic fraction of carbonaceous aerosol has contributions from multiple sources, there is a need for improving the linkages between sources and this fraction of ambient PM concentrations. Some organic aerosol can absorb visible radiation. Such OA is commonly referred to as brown carbon (BrC), and can have an important impact on the solar radiation budget if sufficiently abundant and strongly absorbing. Current emission inventories systematically underestimate total light absorbing carbon because they do not account for BrC, in part because the properties of BrC are not well established. Russell et al. [Russell et al., 2011] have shown that BrC from wildfires can be chemically identified by its functional group composition, for instance by using the similarities in the characteristic infrared spectra [Hawkins and Russell, 2010]. For open and contained (residential heating) biomass burning, little is known about the composition and magnitude of emissions from different fuels and burning conditions. Chemical characterization of organic particles [Liu et al., 2012; Russell et al., 2009a] can be used to identify and quantify BrC.

Brown carbon (BrC) emissions from residential, agricultural, and wildfire burning activities are a highly seasonal, episodic, and poorly characterized fraction of fine particulate matter (PM2.5) in California. Current emission control strategies are based on mass emissions and do not sufficiently consider potential effects on climate and visibility due to brown and black carbon. BrC emissions are highest during periods of strong wildfire impact and, importantly, in the winter months when air quality is worst in the San Joaquin Valley and Sierra foothill communities. Quantifying and characterizing the role of BrC in the atmosphere is essential both to improving local air quality and to understanding their impact on climate change. In addition, secondary organic aerosols (SOA) formed from urban emissions may provide another source of BrC aerosol. Due to the range of sources and chemical complexity of brown carbon, advanced measurements are needed to characterize their chemical and radiative properties and their sources in order to improve net climate forcing estimates.

The primary objectives of the original project were to identify and characterize the contribution of BrC to climate forcing in California by (1) providing physical measurements and chemical analyses of fine particles that constrain the chemical concentrations and optical properties of burning activities, (2) quantifying the BrC organic components and the multi-wavelength absorption from burning emissions and from atmospheric formation of secondary components at two California locations, and (3) examining the globally and regionally-averaged climate response of BrC. We have achieved these objectives, and report the results of our work in a series of chapters that address the abundance and compositional variability in $PM_{2.5}$, link OA composition to the

presence and associated properties of BrC using *in situ* methods, assess the comparability between estimates of BrC contributions to total absorption made from *in situ* measurements versus from remote sensing, and calculate the radiative forcing of California-specific emissions of BC and BrC.

Methods:

The methods used to accomplish these objectives are summarized below:

Tasks 1 and 2 were carried out by measurement campaigns in Fresno and Fontana with a comprehensive suite of instruments and analysis techniques.

Measurements of inorganic and organic fine particle composition and size distributions were made with sub-hourly time resolution using an Aerodyne High-Resolution Time-of-Flight Aerosol Mass Spectrometer (AMS). Detailed information on the organic component composition was obtained by FTIR, with integrated filter sampling performed for different periods of the day. Elemental concentrations were also determined from the integrated filter sampling. The collection of filter samples alongside simultaneous AMS measurements allowed for comparison of total organic mass and providing complementary information on organic composition. Black carbon concentrations and size distributions were measured using a single-particle soot photometer, important for distinguishing between black and brown carbon absorption. Multi-wavelength optical measurements were made using cavity ring-down (aerosol extinction spectrometer) and photo-acoustic absorption spectroscopy (CRDPAS), from which the optical properties of black and brown carbon were determined. Additionally, a limited set of complementary absorption measurements were made of Water-Soluble (extractable) Organic Carbon using Ultraviolet-Visible Absorption spectroscopy (WSOC/UV-VIS).

Ambient organic aerosol particles were chemically characterized and source-associated using complementary techniques: mass fragments from the AMS and functional group analysis via FTIR. All of these measurements were incorporated in statistical analyses, where we determined both simple correlations and multi-linear regression relationships to relate particle composition to the light absorption properties. Additional methods including multi-instrument inversions with positive matrix factorization (PMF) and other techniques, such as tensor decomposition, were used to identify robust relationships between particle composition characteristics from different instruments.

Task 3 was designed to compare the BrC concentrations and properties evaluated in Tasks 1 and 2 to the concentrations and properties of biomass burning and other brown carbon sources included in regional and global climate models. This task consists of three parts:

Task 3a developed a detailed BrC emissions inventory for California by combining standard emissions developed by the California Air Resources Board with wildfire emissions described by the Global Fire Emissions Database (GFED). Regional simulations for BrC effects on climate were then conducted with a Source-Oriented WRF/Chem model. The source-apportionment features within the WRF/Chem model enabled direct calculations for absorption associated with diesel engines, biomass combustion (including wildfires), high sulfur fuel combustion, and other

sources. Perturbation studies were used to disable absorption by BrC to directly quantify the effects in California.

Task 3b combined the regional emissions developed in Task 3a with global emissions of BrC to investigate the effects of global plus regional BrC on climate in California. Global through regional calculations were conducted with the GATOR-GCMOM model. Perturbation studies were used to disable absorption by BrC and to disable absorption by BC+BrC to quantify the effects in California.

Task 3c has compared the in situ chemical and physical data collected by Tasks 1 and 2 to the brown carbon optical depths and climate forcing estimated independently with the nearest available AERONET (AErosol RObotic NETwork) measurements.

Results:

Tasks 1, 2, and 3 were completed with the major results listed below.

A selection of results from the finalized Fresno and Fontana measurements that were part of Task 1 are highlighted below. Overall, our observations provide insights into the sources, abundance and properties of BrC, specifically, and organic aerosol in general for the Fresno wintertime environment. These observations provide a basis and ground-truthing for remote sensing and modeling efforts that were part of Tasks 2 and 3. These key Task 1 results include:

- FTIR OM at Fresno increased from about ~3 $\mu g/m^3$ at the beginning of the campaign to ~15$\mu g/m^3$ at the end the campaign for PM1. For PM2.5, alkane groups have the largest campaign averaged mass fraction among all functional groups (40%). Alcohol, acid and amine groups contributed to 26%, 25% and 5% of the mass fraction.
- At Fontana, the time series of particle density exhibits an average of 1.3 g/cm^3 for the campaign. For the FTIR OM at Fontana, the $PM_{2.5}$ alkane groups have the largest campaign averaged mass fraction among all functional groups (50%). Alcohol, acid and amine groups contributed 21%, 21% and 6% mass fractions, respectively. The OM mass variation and functional group fraction in PM_1 is similar to $PM_{2.5}$. On July 4th there was an unusually high concentration of OM as well as nitrate and sulfate.
- At Fresno, there is a very strong diurnal variation in black carbon (BC) concentrations and light absorption at 405, 532 and 870 nm wavelengths during non-foggy periods. Both BC and absorption were largest at night. The observed absorption enhancements generally exhibited similar diurnal variability as BC and absolute absorption during the non-foggy period. However, the diurnal variability in the 405 nm absorption enhancement measurements was much stronger than at longer wavelengths, indicative of an important contribution of brown carbon to the total absorption. The ratio between the amount of coating material (i.e. material that is internally mixed with BC) and BC exhibited a weak diurnal variability, with a peak in the afternoon that is driven by condensation of ammonium nitrate.
- At Fontana, light absorption exhibited a prominent peak around 9 am, likely due to rush-hour emissions. There was no diurnal variability in the observed absorption enhancement at any wavelength, and the observed absorption enhancements were very close to unity. However, the coating-to-BC ratio exhibited a strong diurnal variability, with a peak around 3 pm that is primarily driven by condensation of secondary organic aerosol.

For Task 2, the Russell group and Cappa groups completed optical closure calculations to separate out contributions from black carbon, coating-induced absorption enhancements and brown carbon. These calculations were made available for assessment and determination of refractive indices of brown carbon for use in Task 3. A few highlights from the chemical and optical characterization at Fresno and Fontana are:

- Aerosol particles in Fontana from primary vehicular emissions are smaller than aerosol particles in Fresno from residential wood burning.
- Black carbon containing particles are thickly coated in Fresno compared to Fontana.
- Volume-limited aqueous oxidation and condensation and surface-limited oxidation are the aerosol growth mechanisms in Fresno and Fontana, respectively.

For Task 3a, source-oriented regional simulations carried out from August 2014 – July 2015 produced ground level $PM_{2.5}$ concentrations and ground level BrC concentrations that were in reasonable agreement with measurements. The predicted top of atmosphere net downward irradiance change associated with BrC was predicted to be 0.28 W m^{-2} and the surface temperature increase was predicted to be 0.005K. The majority of the BrC that caused these effects was emitted from wildfires with much smaller contributions from residential wood combustion.

For Task 3b, global plus regional simulations carried out from July 1, 2014 – July 1, 2015 predicted top of atmosphere net downward irradiance change from BrC over California, the adjacent eastern Pacific Ocean, and parts of Nevada to be 1.07 W m^{-2} and surface warming to be 0.018K. The effects of total BC+BrC were more pronounced, with 5.1 W m^{-2} of net downward irradiance change at the top of the atmosphere and +0.17K of surface warming attributed to these combined species in the global-regional simulations.

Synthesizing the results of Task 3a and 3b, we find that, overall, the global plus regional modeling results are consistent with the source-oriented regional simulations subject to the assumptions in each calculation. The regional and global calculations bound the range of reasonable assumptions related to atmospheric BrC. Regional BrC in Chapter 10 was defined as BrC emitted in California. Global plus regional BrC in Chapter 11 was defined as BrC emitted in California plus BrC transported to California from outside the domain. The background BrC in the global simulations is significant, accounting for approximately 40% of the column-total BrC over California. The regional calculations assumed that food cooking OC and SOA was not absorbing based on measurements of fresh or 2-3 day equivalent aged aerosols. The global calculations assumed that all OC was absorbing given sufficiently long time scales in the atmosphere. In summary, global calculations assumed that all atmospheric OC was absorbing, while regional calculations assumed that only biomass combustion OC was absorbing. Despite the factor of three differences in calculated irradiance change and surface temperature change, both calculations are in agreement that BrC changes surface temperature by less than 0.02K (which is a very small perturbation). Both calculations predict that BC absorption dominates over BrC absorption in California.

For Task 3c, the AERONET optical ground based aerosol monitoring network results were retrieved and used to compare column and *in situ* absorption. The agreement was good for periods of coincident measurements and suitable boundary layer conditions.

Conclusions:

This study has addressed four ARB needs: (a) *improving emission inventories* by providing measurements that constrain the contributions of burning activities to PM2.5, (b) *improving the understanding of atmospheric processes* that contribute to the formation of secondary components of PM2.5 from urban and burning activities by quantifying the oxidized functional groups, (c) *exploring the mitigation of BrC as a greenhouse gas (equivalent) emission* reduction strategy by quantifying the multi-wavelength absorption by BrC in California, and (d) *documenting the frequency of behaviors (that are associated with BrC-producing activities) that impede the success of regulatory programs* by quantifying the daily patterns of contributions of burning sources to PM2.5 in California.

For example, as part of Task 1, the measurements from this project provide important constraints on emission inventories and modeled atmospheric processes. The detailed chemical and physical measurements provide source-specific signatures as well as tracers for air quality impacts. The results showed a large contribution of residential burning to BrC in Fresno, as expected, but also a potentially important role for fog in increasing BrC-related components.

As part of Task 2, this project found that in Fontana, the amount of light-absorbing SOA was lower than expected, showing important differences from past studies.

Independent modeling exercises carried out at the regional scale (Task 3a) and at the global plus regional scale (Task 3b) both predict that BrC has relatively minor climate impacts in California. Surface temperature increase associated with BrC is calculated to be less than +0.018K. The largest sources of BrC are predicted to be wildfires. Climate impacts from BC emitted by diesel engines are predicted to dominate over the effects of BrC.

Task 3c calculations show that the limited overlap of retrieved BrC absorption makes the comparison to observations poorly constrained.

In summary, this project has provided accurate chemical and optical characterization of particles in diverse but much polluted regions of the state. These results have shown that BrC is important for surface-level absorption in wintertime Fresno, although BC is still the largest fraction of surface-level absorption. In summertime Fontana, BC is the major surface-level absorber with relatively small contributions from BrC. These surface measurements provide an important comparison to remote sensing measurements, reflecting local surface conditions with hourly time and source type resolution. Using these measurements to constrain regional and global simulations provides an accurate simulation of BC and BrC absorption for California, showing that BrC results in very little warming (less than 0.02K) and that diesel emissions of BC are the major contributor of that aerosol warming.

The measurements from this project are archived in a curated dataset (Russell LM, Betha R, Sanchez KJ, Liu J, Price DJ, Chen C-L, Lee A. 2017. Aerosol Composition and Size Measurements at Fresno and Fontana. doi: http://dx.doi.org/10.6075/J0VX0DF9). The peer-reviewed publications that have resulted from this project to date are listed below.

Chen CL, Chen SJ, Russell LM, Liu J, Price DJ, Betha R, Sanchez KJ, Lee AKY, Williams L, Collier SC, Zhang Q, Kumar A, Kleeman MJ, Zhang XL, Cappa CD. 2018. Organic Aerosol Particle Chemical Properties Associated With Residential Burning and Fog in Wintertime San Joaquin Valley (Fresno) and With Vehicle and Firework Emissions in Summertime South Coast Air Basin (Fontana). *Journal of Geophysical Research-Atmospheres*. 123(18):10707-10731. doi: 10.1029/2018jd028374.

Betha R, Russell LM, Chen C-L, Liu J, Price DJ, Sanchez KJ, Chen S, Lee AKY, Collier SC, Zhang Q, Zhang X, Cappa CD. 2018. Larger Submicron Particles for Emissions With Residential Burning in Wintertime San Joaquin Valley (Fresno) than for Vehicle Combustion in Summertime South Coast Air Basin (Fontana). *Journal of Geophysical Research: Atmospheres*. 123(18):10,526-510,545. doi: 10.1029/2017JD026730.

Cappa CD, Zhang X, Russell LM, Collier S, Lee AKY, Chen C-L, Betha R, Chen S, Liu J, Price DJ, Sanchez KJ, McMeeking GR, Williams LR, Onasch TB, Worsnop DR, Abbatt J, Zhang Q. 2019. Light Absorption by Ambient Black and Brown Carbon and its Dependence on Black Carbon Coating State for Two California, USA, Cities in Winter and Summer. *Journal of Geophysical Research: Atmospheres*. 0(0). doi: 10.1029/2018JD029501.

Chen SJ, Russell LM, Cappa CD, Zhang XL, Kleeman MJ, Kumar A, Liu D, Ramanathana V. 2019. Comparing black and brown carbon absorption from AERONET and surface measurements at wintertime Fresno. *Atmospheric Environment*. 199:164-176. doi: 10.1016/j.atmosenv.2018.11.032.

Collier S, Williams LR, Onasch TB, Cappa CD, Zhang XL, Russell LM, Chen CL, Sanchez KJ, Worsnop DR, Zhang Q. 2018. Influence of Emissions and Aqueous Processing on Particles Containing Black Carbon in a Polluted Urban Environment: Insights From a Soot Particle-Aerosol Mass Spectrometer. *Journal of Geophysical Research-Atmospheres*. 123(12):6648-6666. doi: 10.1002/2017jd027851.

Lee AKY, Chen CL, Liu J, Price DJ, Betha R, Russell LM, Zhang XL, Cappa CD. 2017. Formation of secondary organic aerosol coating on black carbon particles near vehicular emissions. *Atmospheric Chemistry and Physics*. 17(24):15055-15067. doi: 10.5194/acp-17-15055-2017.

Zhang XL, Kim H, Parworth CL, Young DE, Zhang Q, Metcalf AR, Cappa CD. 2016. Optical Properties of Wintertime Aerosols from Residential Wood Burning in Fresno, CA: Results from DISCOVER-AQ 2013. *Environmental Science & Technology*. 50(4):1681-1690. doi: 10.1021/acs.est.5b04134.

Future Work: This project has identified new questions related to BrC contributions to air quality and climate.

Task 1: There are new questions related to the contribution of residential burning to wintertime air quality that have been made clear by the results of this project. New technologies and new regulations, as well as changing demographics, mean that the magnitude and characteristics of this important source differs year-to-year, and future studies are needed to characterize those changes. In addition, the role of fog in affecting aerosol composition and concentration needs to be better understood, as well as the implications of fog-related particle production for predicted changes in California climate.

Task 2: The results of this project show that size and chemically resolved measurements of BC and BrC provide clear evidence that the roles of lensing and BrC absorption need to be separately quantified for urban and regional air quality regimes. Future measurement studies should include these capabilities and should expand the results presented here to better chareacterize the absorbing properties of photochemical and fog-related SOA.

Task 3: To further improve the interpretation of ground-based AERONET measurements, aircraft-based measurements would be needed in order to characterize the full atmospheric column.

2 Introduction

2.1 Motivation

Aerosol particles play an important role in the radiative balance of the atmosphere, with the organic fraction representing one of the largest uncertainties in our ability to quantify climate cooling and feedback effects. Particulate organic matter constitutes a significant fraction of particles transported in the troposphere across North America and the Arctic, making important contributions to light scattering and health impacts. After sulfates, organic compounds are the most abundant component of fine aerosol globally [Heintzenberg et al., 1989] and are thought to comprise 10-70% of the mass of fine aerosol [Middlebrook et al., 1998; Turpin et al., 2000]. The Earth's radiative forcing can be directly affected by anthropogenically-produced particles [IPCC, 2007], but the quantity and composition of the man-made contribution to atmospheric organic particles are not well characterized.

Since organic aerosol is the largest contributor to both aerosol air quality and radiative forcing in many parts of the Earth, assessing their atmospheric role requires clear understanding of their composition. One key way in which organic composition can be characterized is by the number and type of organic functional groups on the molecules that make up organic aerosol. Identifying organic functional groups helps us to understand how these particles will behave in the atmosphere in terms of their thermodynamic, microphysical, and optical properties. One example is that these properties determine the underlying processes that control particle-cloud interactions. These fundamental processes control the indirect effect of particles on clouds, yet they are poorly understood [IPCC, 2007; Lohmann and Feichter, 2001; Ramanathan et al., 2001].

Particularly uncertain is the impact of absorbing organic aerosol, also known as brown carbon, on radiative forcing. Brown carbon emissions from residential, agricultural, and wildfire burning activities are a highly seasonal or episodic and very poorly characterized fraction of PM2.5 in California. The terminology "brown carbon" refers to the components of organic aerosol that are light absorbing at near-UV and visible wavelengths [Andreae and Gelencser, 2006]. The term has gained broad acceptance in the aerosol research community because of a clear set of measurement-based criteria. By its nature, brown carbon, or BrC, is operational in definition and has properties that vary with source. Like all particles, particles containing BrC can scatter radiation, but because they contain these light absorbing components they can also absorb solar radiation. This can be contrasted with, for example, sulfate and nitrate particulates, which are entirely scattering in the near-UV and visible. Because primary emissions of BrC are highest in the winter months when air quality is worst in the San Joaquin Valley and Sierra foothill communities, quantifying their role in the atmosphere is essential both to improving local air quality and to understanding climate change. In addition, secondary organic aerosols formed from urban emissions, for example during fog in the South Coast Air Basin where aqueous oxidation produces light-absorbing organic compounds, and provide another source of brown carbon aerosol. The site selection was finalized, in consultation with CARB staff, for two sites and time periods that fit within scope of the project objectives and budget. Source-specific chemical and multi-wavelength optical measurements were

made concurrently to identify and characterize brown carbon. Characterization of secondary brown carbon was used to identify sources of absorbing carbonaceous aerosol other than biomass burning. Optical and chemical properties of brown carbon have not been determined by a single standard method in measurements to date, making comparisons and quantification inexact. To improve the representation of brown carbon in climate models, this project provided both advanced observations and improved model simulations of brown carbon particles for better assessing the effects on climate.

The research objectives of this study were to identify and characterize the contribution of brown carbon (BrC) to climate forcing in California by (1) providing physical measurements and chemical analyses of fine particles that constrain the chemical concentrations and optical properties of burning activities, (2) quantifying the BrC organic components and the multi-wavelength absorption from burning emissions and from atmospheric formation of secondary components at two California locations, and (3) examining the globally and regionally-averaged climate response of BrC. We studied two types of areas that have different mixes of emission sources and seasonality: one with significant residential burning (such as in the San Joaquin Valley) and the other with high potential for secondary formation of absorbing particles (such as in the South Coast Air Basin). We used these observations to determine representative optical and chemical properties of brown carbon from primary and secondary particles. The *in situ* observations were further used to compare and assess the determination of brown carbon absorption from remote sensing methods. Finally, we carried out two complementary modeling studies, using the *in situ* observations as constraints and for testing, to assess the regional and global climate impacts of CA brown carbon emissions. These results help to clarify the extent to which controls of brown carbon emission and formation might help to mitigate climate change within CA.

2.2 Project Tasks

The following major tasks were identified:

Task 1. Characterize and differentiate sources of BC (black carbon) from BrC.

Task 2. Quantify chemical and optical characteristics of BrC sources and examine the formation of secondary BrC.

Task 3. Assess net contribution of BrC to California climate.

2.3 Report Structure

This report comprises 12 chapters, including the Executive Summary (Chapter 1), the Introduction (Chapter 2), and the Conclusions (Chapter 12).

Chapters 3, 4, 7, and 8 describe the measurements completed as part of Tasks 1 and 2. The measurements and analysis in Chapters 2 and 3 were primarily supported by Agreement Number: 13-330, and Chapters 7 and 8 were the result of measurements funded by other sources in collaboration with the principal investigators. Chapter 9 describes analyses of prior measurements in the Fresno region that were analyzed by methods similar to those of Task 1 and 2 as part of this grant.

Chapter 5 incorporated the results of Chapters 3, 4, 7, and 8 to associate the measured absorption with specific chemical traces and components in order to complete Task 2.

Chapter 6 compared the results of Chapter 5 to AERONET measurements of column absorption as part of Task 3c.

Chapter 10 and 11 describe the methods and results of Tasks 3a and 3b.

Authors note: Chapters 3 to 8 report the same results that have been published in peer-reviewed journals. The work in Chapters 3, 4, 5, and 7 has been published in the *Journal of Geophysical Research – Atmospheres*. The work in Chapter 8 has been published in *Atmospheric Chemistry and Physics*. The work in Chapter 6 has been published in *Atmospheric Environment*. The measurements are also archived in a curated dataset (Russell LM, Betha R, Sanchez KJ, Liu J, Price DJ, Chen C-L, Lee A. 2017. Aerosol Composition and Size Measurements at Fresno and Fontana. doi: http://dx.doi.org/10.6075/J0VX0DF9). The citations for the peer-reviewed publications associated with each chapter are given below.

Ch. 3: Chen CL, Chen SJ, Russell LM, Liu J, Price DJ, Betha R, Sanchez KJ, Lee AKY, Williams L, Collier SC, Zhang Q, Kumar A, Kleeman MJ, Zhang XL, Cappa CD. 2018. Organic Aerosol Particle Chemical Properties Associated With Residential Burning and Fog in Wintertime San Joaquin Valley (Fresno) and With Vehicle and Firework Emissions in Summertime South Coast Air Basin (Fontana). *Journal of Geophysical Research-Atmospheres*. 123(18):10707-10731. doi: 10.1029/2018jd028374.

Ch. 4: Betha R, Russell LM, Chen C-L, Liu J, Price DJ, Sanchez KJ, Chen S, Lee AKY, Collier SC, Zhang Q, Zhang X, Cappa CD. 2018. Larger Submicron Particles for Emissions With Residential Burning in Wintertime San Joaquin Valley (Fresno) than for Vehicle Combustion in Summertime South Coast Air Basin (Fontana). *Journal of Geophysical Research: Atmospheres*. 123(18):10,526-510,545. doi: 10.1029/2017JD026730.

Ch. 5: Cappa CD, Zhang X, Russell LM, Collier S, Lee AKY, Chen C-L, Betha R, Chen S, Liu J, Price DJ, Sanchez KJ, McMeeking GR, Williams LR, Onasch TB, Worsnop DR, Abbatt J, Zhang Q. 2019. Light Absorption by Ambient Black and Brown Carbon and its Dependence on Black Carbon Coating State for Two California, USA, Cities in Winter and Summer. *Journal of Geophysical Research: Atmospheres*. 0(0). doi: 10.1029/2018JD029501.

Ch. 6: Chen SJ, Russell LM, Cappa CD, Zhang XL, Kleeman MJ, Kumar A, Liu D, Ramanathana V. 2019. Comparing black and brown carbon absorption from AERONET and surface measurements at wintertime Fresno. *Atmospheric Environment*. 199:164-176. doi: 10.1016/j.atmosenv.2018.11.032.

Ch. 7: Collier S, Williams LR, Onasch TB, Cappa CD, Zhang XL, Russell LM, Chen CL, Sanchez KJ, Worsnop DR, Zhang Q. 2018. Influence of Emissions and Aqueous Processing on Particles Containing Black Carbon in a Polluted Urban Environment: Insights From a Soot Particle-Aerosol Mass Spectrometer. *Journal of Geophysical Research-Atmospheres*. 123(12):6648-6666. doi: 10.1002/2017jd027851.

Ch. 8: Lee AKY, Chen CL, Liu J, Price DJ, Betha R, Russell LM, Zhang XL, Cappa CD. 2017. Formation of secondary organic aerosol coating on black carbon particles near vehicular emissions. *Atmospheric Chemistry and Physics*. 17(24):15055-15067. doi: 10.5194/acp-17-15055-2017.

Ch. 9: Zhang XL, Kim H, Parworth CL, Young DE, Zhang Q, Metcalf AR, Cappa CD. 2016. Optical Properties of Wintertime Aerosols from Residential Wood Burning in Fresno, CA: Results from DISCOVER-AQ 2013. *Environmental Science & Technology*. 50(4):1681-1690. doi: 10.1021/acs.est.5b04134.

3 Organic aerosol particle chemical properties associated with residential burning and fog in wintertime San Joaquin Valley (Fresno) and with vehicle and firework emissions in summertime South Coast Air Basin (Fontana)

3.1 Abstract

Organic aerosol mass (OM) components were investigated at Fresno in winter and at Fontana in summer by Positive Matrix Factorization of high-resolution time-of-flight aerosol mass spectra (AMS) and of Fourier Transform infrared spectra, as well as by k-means clustering of light-scattering (LS) AMS single-particle spectra. The results were comparable for all three methods at both sites, showing different contributions of primary and secondary organic aerosol sources to PM1. At Fresno biomass burning organic aerosol (BBOA) contributed 27% of OM on low-fog days, and nitrate-related oxidized OA (NOOA) accounted for 47% of OM on high-fog days, whereas at Fontana very oxygenated organic aerosol (VOOA) components contributed 58-69% of OM. Amine and organosulfate fragment concentrations were between 2 and 3 times higher on high-fog days than on low-fog days at Fresno, indicating increased formation from fog-related processes. NOOA and BBOA components were largely on different particles than the VOOA components in Fresno, but in Fontana both NOOA and VOOA components were distributed on most particle types, consistent with a longer time for and a larger contribution from gas-phase photochemical SOA formation in summer Fontana than winter Fresno. Uncommon trace organic fragments, elevated inorganic, and alcohol group submicron mass concentrations persisted at Fontana for more than five days after 4 July fireworks. These unique aerosol chemical compositions at Fresno and Fontana show substantial and extended air quality impacts from residential burning and fireworks.

3.2 Introduction

Organic aerosol components contribute the largest fraction of submicron particles, which have been shown to affect human health, climate change, and visibility in both the San Joaquin Valley (SJV) and the Southern California Air Basin (SoCAB) [Herckes et al., 2015; Reid et al., 2016]. Primary organic aerosol (POA) particles are emitted from both anthropogenic and biogenic sources, and secondary organic aerosol (SOA) particles can be formed by oxidation of volatile organic compounds (VOCs) in the atmosphere. In urban areas in California, emissions from vehicle exhaust and residential burning contribute a variety of organic compounds, most of which cannot be quantified individually at atmospheric concentrations [Russell, 2013]. Two urban areas in California, Fresno and Fontana, are considered to have severe air pollution during winter and summer, respectively.

Fresno is located in the central SJV, which has winter emissions from vehicles and other fossil-fuel sources, agricultural operations (including burning of crop waste), and residential burning [Chow et al., 2007; Ge et al., 2012a; Gorin et al., 2006; Schauer and Cass, 2000]. Persistent radiation-driven fogs form in SJV during winter, often associated with stagnation of air within this mountain-ringed large valley characterized by mild meteorological conditions [Collett et al., 1999; Herckes et al., 2007]. Fontana is located in SoCAB, where gas and particle phase emissions accumulate from the extensive use of automobiles for transport and the intense sunlight in summer,

along with another mountain-ringed basin geography, light winds, and strongly-capped inversion layers [Dolislager and Motallebi, 1999; Lawson, 1990; D Y Liu et al., 2000]. Fontana is 50 km east of Los Angeles and 20 km west of Riverside in the western part of San Bernardino County, where typically some of the highest aerosol particle concentrations occur as a result of extended photochemical oxidation reaction times, high emissions from morning commute activities, and nitrogen oxide (NOx)-rich conditions [Dolislager and Motallebi, 1999].

Positive matrix factorization (PMF) has been used to identify organic aerosol contributions from different sources in numerous field studies in urban environments based on measurements of organic particle components by both Fourier Transform Infrared spectroscopy (FTIR) and Aerosol Mass Spectrometry (AMS) [Frossard et al., 2011; Hawkins et al., 2010; Russell et al., 2009a; Schwartz et al., 2010; Ulbrich et al., 2009; Zhang et al., 2011]. The major component of organic aerosol particles has often been identified as oxygenated organic aerosol (OOA), which is mostly associated with photochemical reactions [Zhang et al., 2007]. In urban areas, organic mass spectral fragments often include signatures from hydrocarbon-like organic aerosol (HOA), cooking-related organic aerosol (COA), and sometimes biomass burning-organic aerosol (BBOA).

The chemical composition of ambient aerosol in Fresno was 55% organic mass (OM) and 35% ammonium nitrate in January 2013 [Ge et al., 2012a; Young et al., 2016], with six organic aerosol sources identified by PMF analysis of AMS measurements, including HOA, two BBOA, COA, a low-volatility oxygenated organic aerosol (LVOOA), and a semi-volatile oxygenated organic aerosol (SVOOA). Ge et al. [2012a] also measured 55% OM in Fresno during January 2010 and reported (from PMF of AMS measurements) three primary organic aerosol (POA) factors from traffic, cooking and biomass burning, in addition to OOA. The CalNex study in summer 2010 included organic source apportionment by PMF of AMS measurements in both SJV at Bakersfield [Liu et al., 2013] and in SoCAB at Pasadena [Hayes et al., 2013]. The factors at both Bakersfield and Pasadena were similar in that they included some low O/C factors (HOA, nighttime organic aerosol), cooking emissions (COA), some site-specific factors (local organic aerosol, petroleum-operations related organic aerosol), and several oxygenated aerosol factors associated with secondary formation from VOCs (OOA, aromatic SOA, alkane SOA). Also both results showed that more than 60% of the organic mass was oxygenated and likely produced by oxidation of VOCs [Hayes et al., 2013; Liu et al., 2013]. Organonitrate, organosulfate, and amine fragments from anthropogenic and biogenic sources could contribute significant OM mass concentrations [Farmer et al., 2010; Ge et al., 2012b; Xu et al., 2015; Zhou et al., 2016].

This study investigates how PM1 organic sources and composition change with fog (in wintertime SJV) and with fireworks (in summertime SoCAB). In addition, comparing the results of AMS PMF analysis, FTIR PMF analysis, and clustering of AMS Light Scattering (LS) single-particle measurements show the very different roles of POA and SOA in contributing to submicron particle number and mass in wintertime SJV and summertime SoCAB. The results were used to assess the sources of organic aerosol and the degree to which OM from different sources were mixed on the same particles. In addition, high-resolution AMS measurements were used to

estimate the organonitrate (see Appendices), organosulfate, and amine fragments that contribute to aerosol submicron composition at these sites.

3.3 Aerosol Measurements at Fresno (winter) and Fontana (summer)

Aerosol measurements were collected from 19 December 2014 to 13 January 2015 at Fresno and from 4 to 28 July 2015 at Fontana.

3.3.1 Sampling Sites and Meteorological Conditions

The Fresno sampling was located behind the UC Extension Building (36.8090 N, 119.7770 W) in Fresno, California, in central SJV. The site is between residential and commercial complexes, which allowed quantification of residential burning sources during evening hours as well as of traffic sources during commuting hours. From 25 December 2014 to 5 January 2015 the average temperatures were near 6°C, the visibility was good at 11 km on average, and the air was clear or had scattered clouds from morning to afternoon. These low-fog days (25 December 2014 to 5 January 2015) had relative humidity (RH) below 90%. Some days (28 to 30 December 2014 and 2 to 5 January 2015) had slightly hazy conditions with visibility below 11 km but still considered good because they exceeded 3.2 km (**Table 3-1**). From 7 to 13 January 2015, the temperatures were slightly warmer (average temperature 12°C), the wind speed was lower (0.8 m s-1), and fog persisted from midnight through morning rush hours. During these high-fog days, the RH was persistently at or above 90% from 2200 to 0900, with RH starting to drop at dawn. The visibility was as low as 1.6 and up to 3.2 km from 2200 to 0900. The first week of measurements (19 to 24 December 2014) were similar to the low-fog days but had stronger winds (with maximum and average wind speed of 5.7 and 1.9 m s-1, respectively) associated with different synoptic conditions, so these days are not included in the averages calculated for low-fog and high-fog days.

The Fontana sampling was located at the South Coast Air Quality Management District (SCAQMD)-managed site behind the Fontana Fire Department at 14360 Arrow Highway (34.1000 N, 117.4920 W) in Fontana, California. This area is bounded by the I-15 freeway on the west (4.3 km) and by the I-10 freeway (3.9 km) and the auto speedway to the south, and lies in eastern SoCAB. Temperatures ranged from 15 to 36°C, and wind speeds varied from 0 to 10 m s-1. There were few clouds and little precipitation with the exception of a short storm with high rainfall and winds from 18 to 19 July 2015 (two-day precipitation of 3.6 cm and maximum wind speed of 10 m s-1). The temperature at Fontana exceeded 30°C from 11 to 17, on 20, and from 23 to 28 July 2015, but was below 27°C from 9 to 10 July 2015. In addition to these temperature differences, the Fontana study included two distinctly different aerosol compositions because of the 4th of July holiday activities: “firework” days from 4 to 8 July 2015 and the remaining “non-firework” days from 11 to 17 and from 20 to 28 July 2015. The cooler days (9-10 July) and the storm days (18-19 July 2015) are excluded from the averages calculated for firework days and non-firework days because the first includes a mix of emission conditions and the second is heavily scavenged aerosol due to the rainfall and strong winds.

Boundary layer heights (BLH) were estimated from the Yonsei University (YSU) boundary layer vertical diffusion scheme [Hong et al., 2006] (see Appendices). At Fresno, the average BLH was 288 m on low-fog days and 184 m on high-fog days. At Fontana, the average BLH was 493 m on firework days and 562 m on non-firework days. The surface column loading calculated from the product of BLH and organic aerosol concentration was at a maximum in the afternoon for both Fresno and Fontana, consistent with expected photochemical contributions to organic aerosol.

The Hybrid Single-Particle Lagrangian Integrated Trajectory (HYSPLIT) model with input from NOAA Air Resource Laboratory Archived Eta Data Assimilation System (https://www.arl.noaa.gov/HYSPLIT/) was used to evaluate whether particular upwind source regions affected the aerosol measured at each site. At Fresno most back trajectories were from northwestern California on low-fog days (except for 1-2 January 2015 which were from the northeast), while on high-fog days stagnation and low wind speeds showed no distinct upwind source region (**Figure 3-1**). Chemical composition was consistent during all 12 low-fog days, with this low dependence on source region likely indicating that sources were regionally homogeneous rather than from particular individual upwind sources. At Fontana back trajectories were consistently westerlies from the coast, except for the storm days, which had southerly back trajectories (**Figure 3-1**).

3.3.2 Aerosol Particle Measurements

At Fresno and Fontana, a climate-controlled van with an isokinetic inlet was used to house the aerosol measurements. The ambient aerosol particles were distributed to a suite of online and offline instrumentation, including a high-resolution time-of-flight aerosol mass spectrometer (AMS), a single-particle soot photometer (SP2), a scanning electrical mobility spectrometer (SEMS), and filters for Fourier Transform infrared spectroscopy (FTIR) and X-ray fluorescence (XRF) analysis. The operation, calibration, and results of the SP2 and SEMS measurements are described in Betha et al. (accepted to this issue) and are used in this work for collection efficiency (CE) calibration of AMS measurements (described below and in **Figure 3-2** in Appendices).

Filter samples were collected on pre-scanned Teflon filters (Teflon, Pall Inc., 37mm diameter, 1.0 μm pore size) at Fresno and Fontana behind PM1 and PM2.5 sharp-cut cyclones (SCC2.229 PM1 and SCC2.229 PM2.5, BGI Inc.), as well as a PM0.18 Berner-type impactor [Quinn et al., 2004]. Samples were then frozen and transported to the laboratory for FTIR spectroscopy analysis using a Tensor 27 spectrometer (Bruker Optics). All samples were kept at RH below 35-45% and temperature of 20°C for at least 24 hours prior to the analysis. Organic functional groups (carbonyl, amine, alcohol, alkane and carboxylic acid groups) were measured directly on all sampled filters by FTIR. Secondary Teflon filters placed in-line behind 20% of the sampled filters were used as a measure of sample contamination or artifacts and contained negligible organic mass. An automated algorithm including baseline-fitting, peak-fitting, and integration was used to interpret the FTIR spectrum from each filter [Russell et al., 2009b; Takahama et al., 2013]. The FTIR spectra are background subtracted and normalized to air volume to calculate mass concentration of each functional group, as well as OM and OC concentrations. The detection limits of each functional group from Russell et al. [2009b] were used. The micromoles of alkene, aromatic, organonitrate,

and organosulfate functional groups were below detection limit for more than 90% of samples and are excluded from this discussion. In a number of samples, the organonitrate groups measured by FTIR were detectable, but below the limit of quantification for the sampled air volumes (0.06 μg m-3).

Twenty PM_1 and five $PM_{2.5}$ filter samples for each site were selected for X-ray fluorescence (XRF) analysis at Chester Laboratories (Chester LabNet, Tigard, Oregon) for measurements of 38 elements heavier than Na. The samples were selected to be representative of a range of meteorological conditions and aerosol concentrations at each site. The elements Al, Si, S, K, Ca, Fe, Zn, and Br were above detection limit in at least 80% of the samples and their concentrations are used to quantify dust contributions (Al_2O_3, SiO_2, S, K_2O, $CaCO_3$, Fe_2O_3) and as elemental tracers of biomass burning (K).

The high-resolution time-of-flight AMS measured non-refractory particle mass (NR-PM) fragments that were ionized by electron impact after vaporizing on a ~600°C surface. The details of the AMS have been described previously [DeCarlo et al., 2006; Jayne et al., 2000; Jimenez, 2003]. The instrument was operated in two ion flight path modes: V-mode provides better sensitivity at high-resolution (HR) and W-mode provides sufficient mass spectral resolution (4300 at m/z 200) to determine empirical formulas of the ionized aerosol fragments [DeCarlo et al., 2006]. The default fragmentation table coefficients used to estimate organic H_2O^+ and CO^+ signals are those presented by Canagaratna et al. [2015]. The AMS was operated downstream of the same PM1 sharp-cut cyclones used for filters using a 5 min mode-switching cycle with V-mode for 2-min, LS-mode (UMR) for 2-min, and W-mode for 1-min, synchronized with the switching of a thermal denuder between a bypass mode and a denuded mode (similar to that described by Cappa et al. [2016]). The denuder was operated at 225°C in the first stage and 275°C in the second stage, and more than 95% of OM evaporated. Given the extensive evaporation in the thermal denuder, the results in this manuscript report only those measurements from the bypass (non-denuded) mode.

Amine fragments were estimated from the sum of 7 ions ($\Sigma CHN = CHN^+ + CH_3N^+ + CH_4N^+ + C_2H_3N^+ + C_2H_4N^+ + C_3H_8N^+ + C_2H_6N^+$). Four N-containing organic ions (CHN^+, CH_4N^+, $C_2H_3N^+$, and $C_2H_4N^+$) were previously recognized as indicators of the presence of alkyl-amine species [Setyan et al., 2014]. In this study, three resolvable fragments, CH_3N^+ (*m/z* = 29.026), $C_3H_8N^+$ (*m/z* = 58.073), and $C_2H_6N^+$ (*m/z* = 44.050), were added because of their high production from the oxidation of triethylamine, diethylamine, and butylamine by nitrate radical [Price et al., 2016].

Two methods for quantifying organonitrates [Ayres et al., 2015; Farmer et al., 2010; Fry et al., 2013; Xu et al., 2015] were evaluated and found to have NO2-related interference during some time periods at each site that precluded consistent reporting of concentrations (Appendices).

Organosulfates can be formed under highly acidic conditions by the reaction of sulfuric acid with SOA or under less acidic conditions by nucleophilic addition reactions of sulfate with epoxide [Darer et al., 2011; Surratt et al., 2008]. CH3SO2+ (m/z = 78.985) has been shown to be a marker of methanesulfonic acid (MSA) and, more generally, an indicator of other organosulfate fragments

[Farmer et al., 2010; Huang et al., 2017; Zorn et al., 2008]. Organosulfate fragments were estimated from the sum of S-containing organic fragments (CHS^+ + CH_3S^+ + CH_2SO^+ + CH_3SO^+ + $CH_2SO_2^+$ + $CH_3SO_2^+$ + $CH_4SO_3^+$) at Fresno and Fontana (**Table 3-2**).

Single-particle chemical composition was measured for 2 min of every 5 min using a light-scattering (LS) module coupled with the time-of-flight aerosol mass spectrometer [Cross et al., 2009; Freutel et al., 2013; Lee et al., 2015; Lee et al., 2016; Liu et al., 2013; Robinson et al., 2013; Willis et al., 2016]. The LS mode uses a laser before vaporization to optically measure particles larger than 180 nm vacuum aerodynamic diameter (Dva). The operating procedures and data analysis algorithms were otherwise the same as those discussed by Liu et al. [2013]. The chemical characterization and k-means cluster analysis of the single-particle measurements were carried out using the Cluster Analysis Panel (CAP) based on the algorithms described by Lee et al. [2015]. The CE of the AMS was evaluated by comparing the AMS-measured particle mass to the mass calculated from the SEMS measurements after the contributions of refractory components (i.e. BC and minerals) were subtracted [Kostenidou et al., 2007]. The refractory mineral contribution was assumed to be a mixture of metal oxides and salts, including SiO_2, Al_2O_3, Fe_2O_3, Na_2O, K_2O, TiO_2, BaO, MnO, $CaCO_3$, and $MgCO_3$ from XRF [Liu et al., 2013; Usher et al., 2003]. The first step in the CE calculation is to estimate the particle average effective density [DeCarlo et al., 2004]. The particle mass distribution as a function of Dva from the AMS was compared to the particle mass distribution of mobility diameter (Dm) from the SEMS measurement [Betha et al., accepted to this issue]. An average particle effective density of 1.3±0.2 g cm^{-3} was calculated as the best fit to match the size of the peaks in Dva with those of Dm for both Fresno and Fontana, except on firework days (4-8 July 2015) when 1.1±0.2 g cm^{-3} was a better fit. Spherical particle shapes were assumed, which is consistent with past studies for urban conditions [Ge et al., 2012a; Hayes et al., 2013; Young et al., 2016] but is poorly known for firework emissions. The AMS CE was then determined by comparison of the AMS mass with the SEMS particle mass (after subtracting refractory components), as shown in **Figure 3-2**. The CE for Fresno was 0.36 on low-fog days and 0.49 on high-fog days, and the CE for Fontana was 0.93 (9 July to 28 July 2015) except on firework days (4 to 8 July 2015) when it was 0.52. The difference in CE for high and low fog indicates a possible composition-dependence, but since the ammonium nitrate mass fraction (ANMF) was less than 0.5 for all time periods, the composition dependent collection efficiency [Middlebrook et al., 2012] did not change mass concentrations substantially. The RH and particle acidity did not significantly change the CE since RH was dried to below 40% and acidic type compositions occurred less than 3% of the time (**Table 3-3**). The apparent lack of composition dependence could result from the different particle types evident in the LS results. The CE correction is particularly uncertain for the short fireworks period given the limited sampling time, the possible shape effects, and possible refractory sulfur contributions to XRF S.

3.3.3 Comparison of Aerosol Composition Measurements

The AMS CE-corrected time series for aerosol components are shown in **Figure 3-3** for Fresno and **Figure 3-4** for Fontana, along with the fractional composition and the elemental ratios. AMS CE-corrected organic mass (OM) concentrations were compared with FTIR PM1 OM concentrations for both Fresno and Fontana. **Figure 3-5**a,b shows that the linear fits (forced to 0) have slopes of AMS to FTIR OM of 2.6 (r^2=0.67), 1.1 (r^2=0.89), 0.8 (r^2=0.52), and 1.3 (r^2=0.84)

for Fresno low-fog and high-fog and Fontana firework and non-firework days, respectively. For Fresno high-fog days and Fontana the values are near unity (1±0.3), which is well within the uncertainties of both AMS and FTIR measurements (each at ±20%); the weak correlation and non-unity slope for Fresno on low-fog days may indicate intermittent contributions from semi-volatile components in the AMS that are not measured on the filters because they desorb before FTIR analysis [El-Sayed et al., 2016; Mader and Pankow, 2001; Russell et al., 2009a]. Semi-volatile compounds on high-fog days could be oxidized to form low-volatility SOA via aqueous chemistry [Ge et al., 2012b]. The cooler (6.2°C) temperatures on low-fog days might allow semi-volatile compounds (such as amine compounds) to partition into the particle phase [Ge et al., 2011b] but be lost by desorption during filter collection at 21°C. The higher amine (8%) and alkane (53%) group concentrations on low-fog days than on high-fog days is consistent with this explanation. Furthermore, on high-fog days there were higher concentrations of carboxylic acid (20%) and alcohol (24%) groups, which are often characteristic of low-volatility aerosol (**Figure 3-6**) [Liu et al., 2012]. Another explanation of this large difference between the AMS and FTIR measurements could be a low degree of internal mixing affecting the CE uncertainty [Middlebrook et al., 2012]. Differences in FTIR mass calibrations for functional groups on different types of molecules could account for some discrepancies in OM [Chen et al., 2016; Russell et al., 2009a; Takahama et al., 2013], but several past studies have shown little evidence for these types of compounds being important in ambient concentrations [Chen et al., 2016; Russell et al., 2009a; Takahama et al., 2013]. The low-fog conditions also had a lower CE of 0.36 than the more typical 0.49 value for high-fog days, suggesting that the AMS was missing more than the standard amount of OM [Canagaratna et al., 2007]. The ammonium nitrate mass fraction for the low-fog days is 0.3, below the cutoff of composition-dependent CE behavior [Middlebrook et al., 2012]. This means that while the default CE value of 0.45 makes the slope slightly closer to 1 at 2.1, the correlation of the linear fit forced to 0 remains unchanged.

AMS CE-corrected sulfate concentrations were also correlated to XRF-measured sulfate concentrations (assuming all S is present as sulfate) with slopes (with intercept forced to 0) of 1.4 (r^2=0.97), 1.2 (r^2=0.96), 0.6 (r^2=0.73), and 0.8 (r^2=0.95), for Fresno low-fog and high-fog days and Fontana firework and non-firework days, respectively (**Figure 3-5**c,d). At Fontana AMS sulfate is lower than XRF sulfate by 20% on non-firework days and 40% on firework days (which is within the uncertainties of the two measurements), but the larger-than-typical difference is likely due to the sulfate fraction of PM1 being too low to be accurately corrected by the estimated density and hence CE. At Fresno the lower AMS sulfate concentrations relative to the XRF S-based sulfate on low-fog days could result from refractory sulfur. Shakya and Peltier [2015] found high elemental sulfur (S) to sulfate-sulfur ratios when the potassium ion (K^+) to potassium (K) ratio was associated with biomass burning emissions at Fresno. As a consequence, XRF sulfur is not expected to agree with AMS sulfate-sulfur, and refractory sulfur (estimated as XRF S mass) was subtracted from the SEMS particle mass for the CE calculation for Fresno. The default CE value of 0.45 makes the slope slightly closer to 1 at 1.1 [Middlebrook et al., 2012], but the correlation of the linear fit forced to 0 remains effectively the same.

3.4 Apportionment of Organic Aerosol Components to Emission Sources

Three approaches were used to associate measured organic components with the sources of those emissions. The most widely used approach is that of PMF of AMS submicron bulk measurements of MS mode spectra [Lanz et al., 2007; Paatero and Hopke, 2003; Paatero and Tappert, 1994; Ulbrich et al., 2009]. The second approach of PMF of FTIR spectra has been shown to be largely consistent with the first [Corrigan et al., 2013; Liu et al., 2012], but sometimes also yields source-specific signatures that are not evident after volatilization and fragmentation [Corrigan et al., 2013; Russell et al., 2010]. The third approach of clustering the mass spectra of individual particles relies on the LS mode of AMS, which has only rarely been used for atmospheric aerosol analysis but provides number-dependent characteristics and degree of mixing of particle populations [Lee et al., 2015; Lee et al., 2016; Liu et al., 2013; Willis et al., 2016]. Here we compare and evaluate these three techniques for the Fresno and Fontana measurements (**Table 3-4**, **Table 3-5, Table 3-6**, **Table 3-7, Table 3-8**, **Table 3-9**, **Table 3-10**, **Table 3-11**, and Appendices). AMS PMF factor analysis excluded *m/z* 30 (CH_2O^+, CH_4N^+, and $C_2H_6^+$) and *m/z* 46 ($CH_2O_2^+$, CH_4NO^+, and $C_2H_6O^+$) to remove interference by NO^+ at *m/z* 30 and by NO_2^+ at *m/z* 46.

The AMS PMF results for both Fresno and Fontana show one factor with high *m/z* 44 that has a mass spectra similar to a factor identified in other studies that is typically termed "low-volatility oxygenated organic aerosol" (LVOOA) (with cosine similarity, CS=0.97~1.00). There is also a second factor with high *m/z* 43 that is correlated to nitrate and has a mass spectra similar to the previously identified "semi-volatile oxygenated organic aerosol" (SVOOA) (with CS = 0.66 ~ 0.98) [Aiken et al., 2009; Chhabra et al., 2010; Crippa et al., 2013; Docherty et al., 2011; Hayes et al., 2013; Heald et al., 2010; Mohr et al., 2012; Ng et al., 2010; Setyan et al., 2012; Struckmeier et al., 2016; Young et al., 2016](**Table 3-4**, **Table 3-5**, **Figure 3-7**, and Appendices).

Here, these two factors are not identified as LVOOA and SVOOA, despite their similarities to past factors with those names, because of the lack of volatility measurements to support naming one "low volatility" (LV) and the other "semi-volatile" (SV). Instead the LVOOA-like factor was named "very oxygenated organic aerosol" (AMS-VOOA) because it had the highest m/z 44 signal, and the SVOOA-like factor was named "nitrate-related oxidized organic aerosol" (AMS-NOOA) because it was correlated to nitrate moderately at Fresno (0.62) and poorly (0.18) at Fontana. **Table 3-4** provides a comparison of the composition and tracers of these two factors to factors identified by previous work as LVOOA and SVOOA, as well as to more oxidized OOA (MOOOA) and less oxidized (LOOOA) [Aiken et al., 2009; Crippa et al., 2013; Docherty et al., 2011; Hayes et al., 2013; Mohr et al., 2012; Setyan et al., 2012; Struckmeier et al., 2016; Young et al., 2016]. All regressions in this work are calculated by least squares. The mass spectra of AMS-VOOA and AMS-NOOA are similar to each other at Fresno (CS=0.90), but they were not combined into one factor because their O/C ratios were quite different. In urban studies, sulfate has frequently been associated with LVOOA and nitrate and ammonium with SVOOA [Crippa et al., 2013; Mohr et al., 2012; Struckmeier et al., 2016; Young et al., 2016]. Since sulfate has a small concentration in this study, it is not surprising that AMS-VOOA was not correlated to sulfate even though the AMS-

VOOA mass spectrum is very similar to previous similar factors that were correlated to sulfate (**Table 3-4**).

Both AMS-VOOA and AMS-NOOA spectra are similar to the gasoline SOA and diesel SOA spectra (CS = 0.75-0.93) produced by photooxidation of VOCs from gasoline and diesel vehicle emissions in smog chamber studies [Presto et al., 2014]. Tracers of vehicle emissions (Fe and Cu) were weakly correlated to AMS- VOOA (r^2 = 0.27 and 0.30, respectively), while other vehicle emission tracers Br, Mn, and P were moderately correlated to AMS-NOOA (r^2 = 0.60, 0.34, and 0.33, respectively). In addition, vehicle emissions are known to constitute a majority of the SJV winter and SoCAB summer VOC emissions based on the CARB inventory [CARB 2012 estimated annual average emission https://www.arb.ca.gov/app/emsinv/2017/], although existing emission inventories may be missing contributions from some non-vehicle fossil fuel sources [McDonald et al., 2018]. This similarity to smog chamber SOA from oxidation of vehicle VOCs, the correlation with vehicle-related trace metals, and the large fraction of VOCs from vehicles in the emission inventory make it likely vehicles contribute a substantial part of the AMS-NOOA and AMS-VOOA organic mass, consistent with previous findings in similar regions [Cheung et al., 2010].

3.4.1 Fresno Source Apportionment by AMS PMF, FTIR PMF, and LS Clustering

Four factors of organic aerosol were identified by PMF analysis of AMS measurements at Fresno, including a hydrocarbon-like organic aerosol (AMS-HOA), a biomass burning organic aerosol (AMS-BBOA), an AMS-NOOA, and an AMS-VOOA. AMS-NOOA makes up 47% and AMS-BBOA contributes 9% of OM on high-fog days (7 to 13 January 2015), while AMS-NOOA and AMS-BBOA contribute 17% and 27% of OM on low-fog days (25 December 2014 to 5 January 2015), respectively. The HOA and BBOA factor mass spectra are similar to factors with those names reported by previous studies [Cubison et al., 2011; Ng et al., 2011; Young et al., 2016], and these two factors correlate with combustion-related tracers, including black carbon (BC), carbon monoxide (CO), nitrogen oxides (NOx), and potassium (K). **Table 3-8** provides correlation coefficients (r^2) for the time series of PMF factors and gas tracers, metal ions, and meteorological parameters at Fresno. BC and potassium (K) concentrations are correlated moderately to the BBOA factor concentrations with r^2 of 0.42 and 0.38, respectively (**Table 3-8**), consistent with residential wood burning or agricultural biomass burning activities as a substantial source of BBOA. The evening peak of the AMS-BBOA factor concentration is similar to that previously associated with evening residential burning activities [Young et al., 2016]. Since these burning activities also partially coincided with evening traffic, it is likely that HOA and BBOA could not be fully separated by the PMF analysis given the limited study duration, which may account for the correlation of HOA to K of only r^2=0.55.

AMS-NOOA correlates strongly to ammonium (r^2 = 0.79) and moderately to nitrate (r^2 = 0.62) and sulfate (r^2 = 0.57). The average NOOA concentration increased from 2.9 μg m^{-3} on low-fog days to 7.1 μg m^{-3} on high-fog days, consistent with prior findings that the increase in organic aerosol mass is produced by aqueous-phase processing in fog [Ge et al., 2012b]. The correlation of high nitrate concentrations to nitrate-related OA likely results from the emission of both VOCs and NOx from vehicles, especially during rush hour [Kelly et al., 2014; Nowak et al., 2012; Xu et

al., 2014; Young et al., 2016]. The higher concentrations of nitrate and NOOA on high-fog days could indicate that NOOA and nitrate are enhanced by aqueous processing [Blando and Turpin, 2000; Collett et al., 1999; Herckes et al., 2007; Powelson et al., 2014; Rodriguez et al., 2017], and the weaker correlation of NOOA to nitrate ($r^2 = 0.15$) on high-fog days could result from a time lag in the formation of each. For example, the maximum concentration of nitrate occurred at 1100 on 11 January 2015 and the maximum of AMS-NOOA was not until 1200, with this offset in timing reducing the correlation of the 5-min time series even though both were elevated on fog days. Since secondary aerosol formation associated with fog-processing has been attributed to high RH causing enhanced gas-to-particle partitioning of water-soluble VOCs, SO2 and NOx [Collett et al., 1999], this correlation could indicate that fog-related aqueous reactions produced sulfate, nitrate, and AMS-NOOA. The abundance of organic aerosol formation could result from the greater surface area for uptake and reaction of the oxidation products on high-fog days.

AMS-VOOA is highly oxidized with a high O/C ratio of 0.78 and a high fraction of *m/z* 44 fragments (f_{44}) at Fresno. As discussed above, AMS-VOOA could be associated with regional sources of gasoline and diesel vehicle emissions or fuel vapor VOC emissions such as aromatic and aliphatic hydrocarbons that are photochemically oxidized to produce SOA [Bahreini et al., 2012; Gentner et al., 2012]. The AMS-VOOA factor concentration decreased on high-fog days.

Three factors were determined by FTIR PM1 PMF analysis at Fresno, including a fossil fuel combustion (FTIR-FFC) factor, a mixed combustion (FTIR-MC) factor, and a biomass burning (FTIR-BB) factor (**Figure 3-8**); each has a FTIR factor spectrum consistent with factors identified in previous studies (**Table 3-6)**. The time-series of the FTIR-FFC factor and the FTIR-MC factor both correlate moderately to the AMS-NOOA factor ($r^2 = 0.45$ and 0.50, respectively) (**Table 3-7**). Even though FTIR-FFC could include both primary and secondary fossil fuel-related components, it typically does not correlate with AMS-HOA in polluted urban areas [Guzman-Morales et al., 2014; Liu et al., 2012], likely in part because HOA is only the primary fraction of vehicle emissions and is often semi-volatile [A L Robinson et al., 2007]. The filter collection used for FTIR is not expected to retain semi-volatile components efficiently. Interestingly the FTIR-BB factor correlates with AMS-HOA, as well as with AMS-BBOA, CO, NO, K, and BC (see **Table 3-7**), possibly because some residential burning emissions are primary and similar to HOA and because both HOA and BBOA were higher in the evenings. FTIR-FFC is likely a mixture of the less-oxidized FFC, more-oxidized FFC, and alkane SOA factors reported previously [Guzman-Morales et al., 2014; Liu et al., 2012]. FTIR-FFC may lack a correlation to HOA because primary vehicle emissions are more volatile than primary residential burning emissions, so they may not be retained on filters. FTIR-FFC correlates with AMS-NOOA, confirming that AMS-NOOA includes secondary products from vehicle exhaust. The FTIR-MC may be associated with multiple combustion sources (including vehicle emissions) and secondary organic aerosol formation from those same sources. The lack of VOC measurements prevents identification of specific sources, making it difficult to identify the type of combustion (gasoline, diesel, and biomass) or to rule out some contribution from other sources. The FTIR-MC factor spectrum has absorption peaks similar to those of high O/C combustion [Russell et al., 2010; Schwartz et al., 2010] and low O/C

combustion [Hawkins et al., 2010; Shaw et al., 2010]. The FTIR-BB factor shows moderate correlations to the AMS-BBOA, AMS-HOA factors and combustion-related tracers (BC and CO) and NO, indicating PMF analyses for FTIR and AMS measurements are in general agreement, even though the two techniques separate the different sources of organic composition slightly differently. This result is consistent with prior findings that AMS factors use the higher time resolution to separate primary and secondary sources (which appear at different times of day) and that FTIR factors often associate the products of secondary reactions more closely with the primary components since the spectra represent the unfragmented molecules collected over several hours [Corrigan et al., 2013; Liu et al., 2012; Russell et al., 2011].

Of more than 77,000 laser signals detected by LS-AMS, 35,857 were classified as particles and 34,738 of those contained organic ion fragments. LS clustering analysis for single-particle organic mass spectra identified four classes, including LS-HOA, LS-NOOA, LS-BBOA, and LS-VOOA, which are consistent with the AMS PMF factors (**Figure 3-9**a,b). The LS-NOOA and LS-HOA class particles are composed of major signals at *m/z* 43, *m/z* 44, *m/z* 29, and *m/z* 55. The *m/z* 44 fraction (f_{44}) is 20% for the LS-VOOA and 10% for the LS-NOOA class particles, showing that the LS-VOOA is more oxidized than LS-NOOA. LS-BBOA has relatively high signals at *m/z* 60 and *m/z* 73, which are significant markers of BBOA. The time-series of the LS-NOOA, LS-HOA and LS-VOOA classes are correlated moderately to the AMS-NOOA, AMS-HOA, and AMS-VOOA factors (r^2 = 0.51, 0.32, and 0.34, respectively (**Table 3-9**)).

The LS cluster analysis without inorganic fragments showed that four types of organic aerosol correspond one to one with the mass-based AMS-PMF. Clustering with inorganic fragments (LS-Inorganic or LSI, Appendices and **Table 3-10**) showed similar results, but including inorganic fragments did not allow identification of organic-specific classes like BBOA.

Figure 3-10 and **Table 3-11** provide comparisons of the fraction of the AMS-PMF components, LS classes, and FTIR-PMF factors for Fresno. PMF factors from both AMS and FTIR have time series that correlate moderately or strongly to each other as discussed above. On Fresno high-fog days, the highest fractions identified by the three methods were LS-NOOA (55%), AMS-NOOA (52%), and FTIR-FFC (41%). The high O/C and carboxylic acid groups indicate they are secondary organic components; the AMS-NOOA peak at morning and evening rush hours and their correlation to nitrate (which is a tracer for vehicle NOx emissions [Fraser and Cass, 1998; Nowak et al., 2010]) support vehicle emissions as one of the sources of the VOCs. Similar fractions of AMS-BBOA (33%), LS-BBOA (40%), and FTIR-BB (38%) on low-fog days also showed good agreement for the three techniques.

3.4.2 Fontana Source Apportionment by AMS PMF, FTIR PMF, and LS Clustering

Four factors were identified for the Fontana AMS measurements: AMS-HOA, AMS-COA, AMS-NOOA, and AMS-VOOA (**Figure 3-9**a). The HOA factor has the lowest O/C ratio of 0.16 along with peaks at *m/z* 41, *m/z* 43, *m/z* 55, and *m/z* 57, suggesting that HOA includes primary emissions from vehicle traffic [Lanz et al., 2007]. The AMS-VOOA factor has an intense signal at *m/z* 44 with a high O/C ratio of 0.76, indicating a highly oxidized organic aerosol likely resulting from photochemical reactions [Young et al., 2016]. The AMS-COA factor is characterized by the

fragments at *m/z* 41 and *m/z* 55 with a relatively high *m/z* 55/57 ratio compared to the AMS-HOA factor, which is consistent with cooking-related aerosol measured by previous studies [Mohr et al., 2012]. The AMS-VOOA component constitutes the single largest fraction of the OM at 66% and correlates moderately to O_3 concentration (**Table 3-7** and **Table 3-8**). PMF analysis of PM1 FTIR spectra identified three factors, including an MC factor, a dust-related detritus or SOA (DDS) factor, and an FFC factor (**Figure 3-8**). The FTIR-MC factor is moderately correlated to ammonium (r^2 = 0.33, **Table 3-7**). The FTIR-DDS has a strong correlation with wind speed (r^2 = 0.82), and moderate correlation to AMS-VOOA (r^2 = 0.31), as well as to calcium (Ca) (r^2 = 0.27) and silicon (Si) (r^2 = 0.43), which are commonly attributed to soil sources [Gilardoni et al., 2009]. The Ca and Si concentrations showed strong correlation to aluminum (Al) (r^2 = 0.85 and 0.77, respectively), but weak correlation to K (r^2 = 0.19) (**Table 3-12**). The Si/Al and Ca/Al ratios measured at Fontana (0.98 and 0.19 respectively) were slightly lower than but generally consistent with those reported by previous studies for paved and unpaved roads, soil, and asphalt [Chow and Watson, 1998; Gilardoni et al., 2009; Vega et al., 2001] (**Table 3-12**). An informal dirt track used recreationally for 3-wheel vehicles across the street from the sampling site may have contributed to this dust source. The FFC factor is composed of 43% acid and 41% alkane functional groups (**Figure 3-8**), and has a spectrum comparable to previous FTIR-Alkane SOA factors [Liu et al., 2012] and more oxidized FFC at Pasadena [Guzman-Morales et al., 2014]. Overall, the FTIR-PMF factors correspond well to the AMS PMF factors, with both types of measurements showing clearly that SOA components (VOOA and NOOA as well as DDS, MC, FFC) contribute nearly two-thirds of PM1 OM in Fontana.

More than 33,000 laser signals were detected by LS-AMS at Fontana, and 9,485 particles were identified as particles. Excluding inorganic fragments, these mass spectra were classified by k-means clustering into four particle classes: an LS-HOA class, an LS-COA class, an LS-NOOA class, and an LS-VOOA class (**Figure 3-9**b). Their mass spectra are consistent with the corresponding AMS PMF factors.

The time-series of the four organic LS classes have weak correlations to the corresponding AMS PMF factors at Fontana (**Table 3-13**). LS clusters are correlated weakly to their corresponding AMS PMF factors. Clustering with inorganic fragments (LSI, LS-Inorganic) showed similar results [Canagaratna et al., 2004], but including inorganic fragments did not allow identification of organic-specific classes like COA (see Appendices **Figure 3-9**b,c).

Figure 3-11 shows the comparisons of AMS-PMF, FTIR-PMF, and LS-organic clustering analysis. Both the AMS-VOOA factor (66%) and the LS-VOOA class (73%) constituted the highest fractions of submicron mass and particle number, respectively, on firework days. The FTIR-DDS factor had trends similar to the LS-VOOA class and correlated moderately to AMS-VOOA (r^2 = 0.31), suggesting VOOA was in part condensed on dust-containing particles. The AMS-COA factor was 0.62 ±0.39 μg m-3 on firework days and 0.57±0.46 μg m-3 on non-firework days.

3.5 Factors Affecting the Chemical Composition of Organic Aerosol

The average AMS PM_1 concentration was 25±16 μg m^{-3} for the three-week Fresno study, with the high variability resulting from both large fluctuations during the day and differences between the low-fog and high-fog days. The time series of chemical composition of non-refractory submicron particles are shown in **Figure 3-3**. The organic fraction is the largest contribution at 57% of non-refractory PM1, followed by nitrate (28%), ammonium (11%), sulfate (3%), and chloride (1%) on low-fog days. FTIR measurements indicated that the alkane group (52%) constituted the majority of the submicron OM, followed by alcohol (22%), carboxylic acid (19%), and amine (6%) groups (**Figure 3-6**). The submicron organic mass has a slightly larger mass concentration (18 μg m^{-3}) but a smaller mass fraction (44%) on high-fog days than on low-fog days, with the remaining components being nitrate (35%), ammonium (15%), sulfate (5%), and chloride (1%). The Fresno OM measurements show different diurnal patterns: low-fog days had high OM concentrations in the evenings, while high-fog days (from 7 to 13 January 2015) did not show high evening concentrations (**Figure 3-3**). The FTIR results show higher OM mass concentrations of alcohol groups (3.2 μg m^{-3}), carboxylic acid groups (3.6 μg m^{-3}), and alkane groups (7.0 μg m^{-3}) on high-fog days than on low-fog days (**Figure 3-6**).

The average AMS non-refractory PM1 concentration was 7.2 ± 5.8 μg m^{-3} at Fontana, with much higher concentrations on firework (14.7 ± 8.5 μg m^{-3}) days than on non-firework (5.9 ± 2.6 μg m^{-3}) days (**Figure 3-4** and **Table 3-11**). OM concentrations and functional group fractions in PM1 are similar to those in PM2.5 for Fontana (Betha et al., accepted to this issue), showing that most of the organic mass is submicron. The alkane group constituted the majority of the PM1 OM (49%), followed by alcohol (29%), carboxylic acid (15%), amine (7%), and non-acid carbonyl (1%) groups.

3.5.1 Increases of Amine and Organosulfate Fragment Concentrations on High-Fog Days in Fresno

The nitrogen-containing organic ions (CxHyN, i.e. CHN+, CH3N+, CH4N+, C2H3N+, C2H4N+, and C3H8N+, and C2H6N+), also known as alkyl-amine groups, are shown in **Table 3-11** for Fresno and Fontana. The average amine fragment concentration was higher on high-fog days (0.33 μg mv) than on low-fog days (0.16 μg m^{-3}). However, the fragment composition is similar on both low-fog and high-fog conditions, indicating that the amine related components are increased by the fog but are formed even when only low-fog is present. Similarly, the amine fragment concentration is correlated moderately to the AMS-NOOA factor (r^2 = 0.42), indicating that both may be associated with aqueous reactions that are enhanced during fog but also occur in low-fog conditions.

The sum of amine fragments correlates moderately on low-fog days to three markers for residential burning, namely the AMS-BBOA factor (r^2 =0.61), BC (r^2 = 0.47), and CO (r^2 = 0.36). This correlation indicates that the amine fragments are likely increased by residential burning activities, consistent with evidence that methylamine, dimethylamine, and trimethylamine are emitted from biomass burning, automobiles, and animal husbandry [Ge et al., 2011a]. The strong

correlation of amines to the AMS-NOOA factor (r^2 = 0.70) on three high-fog days (11 to 13 January 2015) could indicate that aqueous reactions contribute additional formation pathways or shift the gas-particle partitioning [Lloyd et al., 2009; Murphy et al., 2007; Tang et al., 2013]. In fact, the high signal at *m/z* 58 ($C_3H_8N^+$) reported for a chamber experiment with trimethylamine in humid conditions [Tang et al., 2013] is consistent with the higher concentration of $C_3H_8N^+$ on high-fog days than on low-fog days. Enhancement of amine concentrations in cloud residuals by uptake of HNO_3 or by oxidation of NO_2 in the aqueous phase could explain why amine fragments were enhanced on high-fog days [Roth et al., 2016].

The organosulfate concentration was higher at Fresno on high-fog days, similar to the increased concentrations of amine fragment concentrations. This result could be explained by the promotion of organosulfate production on sulfate-containing particles at high relative humidity [Shang et al., 2016]. The organosulfate was about three times higher on high-fog days than low-fog days, but it correlates weakly to NOOA on both ($r^2 < 0.2$). Organosulfate production from isoprene oxidation has been shown to increase for particle-phase and aqueous reactions [Budisulistiorini et al., 2013; Budisulistiorini et al., 2015; Lin et al., 2012] and vehicular isoprene could contribute to this pathway [Young et al., 2016]. Higher RH could also lead to higher surface partitioning effects in mixtures of water, inorganics, and organic components [Smith et al., 2012].

3.5.2 Increases of Oxidized Organic, Amine, and Organosulfate Fragment Concentrations on Firework Days in Fontana

More than 100 firework events were advertised publicly in SoCAB for 4 July 2015. These numerous events produced emissions that resulted in higher mass concentrations on firework days compared to non-firework days, by factors of almost two for OM, more than five for nitrate, and approximately three for ammonium and sulfate. These firework-related composition markers persisted in decreasing concentrations from the evening of 4 July to the afternoon of 8 July 2015. This multi-day period of unusually high concentration and chemically distinct composition is expected because of the long residence time in SoCAB caused by the persistent capping inversion and lack of rainfall to remove particles. Additional secondary particle mass from further photochemical reactions of volatile gases could also contribute to maintaining the high concentration. **Figure 3-4** shows that the organic fraction constitutes the majority of both firework days and non-firework days; however, nitrate aerosol contributes a higher fraction on firework days (21%) than on non-firework days (11%), consistent with inorganic nitrate from KNO_3 in firework emissions [Jeong et al., 2011]. The alcohol group constitutes a higher fraction (48%) of the submicron OM on firework days than on non-firework days (18%), consistent with a contribution from partially burnt paper products (**Figure 3-6**). K_2O, determined from the mass concentration of Potassium multiplied by the ratio of the molecular weight of K_2O to K, contributes 37% (4.6 μg m^{-3}) of the metal oxide concentrations on firework days but only 3% (0.07 μg m^{-3}) on non-firework days, consistent with previous measurements of firework emissions [Dickerson et al., 2017; Drewnick et al., 2006; Li et al., 2017]. Five different types of particles (fireworks-metal,

ash, dust, organic carbon-sulfate, biomass burning) with different size distributions have been identified as primary emissions from fireworks [Li et al., 2017].

Amine and organosulfate fragment concentrations were also higher on firework days than non-fireworks days. The amine fragments also have a different composition on Fontana firework days, with CHN^+ fragments being the largest mass fraction of the alkyl-amine group on firework days and $CH4N^+$ fragments on non-firework days. The enhancement of amine fragments on firework days is likely associated with the firework emissions, but the cause of amine emissions from fireworks is not known. At Fontana, the fraction of CH3SO+ fragment ion was higher on firework days (31%) than non-firework days (23%), consistent with the higher sulfate and sulfur-containing compounds associated with firework emissions in other studies [Dickerson et al., 2017; Drewnick et al., 2006; Li et al., 2017]. The MSA-specific marker fragment $CH3SO2^+$ was higher (26%) on Fontana non-firework days than on firework days, which could be consistent with transported marine aerosol or other biogenic SOA [Gaston et al., 2010; Huffman et al., 2009; Tao et al., 2014].

3.5.3 Oxidized Organic Components More Separated on Different Particle Types at Fresno than Fontana

At both Fresno and Fontana, LS-NOOA and LS-VOOA are correlated strongly or moderately to AMS ammonium and nitrate (**Table 3-9** and **Table 3-13**), likely indicating that vehicles, which produce NOx and NH_3 [Nowak et al., 2012], contribute to all four of these components.

At Fresno, least squares regressions forced to zero give moderate or stronger correlations of all the LS types to both AMS-NOOA and AMS-VOOA (**Table 3-9**). But the only unforced regressions that give at least moderate correlations are those for LS-BBOA with AMS-BBOA, LS-HOA with AMS-HOA, and LS-NOOA with AMS-NOOA, suggesting these factors have some degree of external mixing. By contrast, LS-VOOA is moderately correlated to both AMS-VOOA and AMS-NOOA (**Table 3-9**), suggesting that this type includes contributions from both nitrate-related and other photochemical oxidation pathways. In addition, LS-NOOA and LS-VOOA have only weak correlations ($r^2<0.25$) to AMS-BBOA and AMS-HOA, indicating that these particle types are more strongly driven by secondary production than by the primary vehicle and residential burning emissions.

Figure 3-12b,c shows that the LS and AMS relationships during low and high-fog days are similar on high-fog and low-fog days, although the correlations between LS types and corresponding AMS factors are stronger on high-fog days. The correlations in **Figure 3-12** indicate that on high fog days these two particle types, while similar in composition, remain externally mixed, namely that the AMS-NOOA factor is mostly on the LS-NOOA particles but that both AMS-VOOA and AMS-NOOA factors are on the LS-VOOA particles. This separation of these mass components onto different particles, despite the contributions to both of them from vehicle emissions, could result from an offset in the timing of the formation of the secondary organic components due to different formation pathways.

Interestingly this correspondence of LS types to AMS factors was not measured at Fontana: the correlations of unforced least squares regression of all LS types to corresponding and other

AMS factors were weak (r^2<0.25) (**Table 3-13**). When these regressions were forced to zero the correlations are stronger, as expected, making all moderate, but there was no preference for the LS type to the corresponding factor. **Figure 3-13** shows these correlations were similar on both firework and non-firework days. This lack of distinct external mixtures at Fontana is likely the result of the longer time for and the larger mass contribution of photochemically oxidized components in SoCAB in summer, both of which contributed to producing a more homogeneous population of particles.

At both Fresno and Fontana all of the LS types (other than LS-HOA) had f_{44} larger than 5% in more than 27% of the particles, indicating that oxidized organic components were distributed on many different types of particles (**Figure 3-14** and **Table 3-14**). All of the LS-VOOA particles at both sites have f_{44} larger than 1%. Most LS-NOOA particles also have f44, with ~90% at Fresno and 66% at Fontana having f_{44} larger than 1%. These large numbers of particles with measurable f_{44} provide substantial evidence that most of these LS particle types include a contribution from secondary organic components. This distribution of oxidized organic components on many particle types is consistent with gas-phase formation mechanisms in which particle composition plays little role [George et al., 2015; Kroll et al., 2015]. In addition, at Fresno f_{44} is low (~10%) for LS-NOOA on both low-fog days and high-fog days, but the AMS-NOOA mass concentration increased on high-fog days. The lack of change in f_{44} indicates that the degree of oxidation of the SOA components did not change but the SOA concentration increased. For LS-VOOA, f_{44} is higher on average (~20%) and is more variable than the f_{44} of LS-NOOA particles.

The mass concentration of amine fragments correlated moderately (r^2 = 0.51) to LS-BBOA on low-fog days and had correlations of r^2 <0.4 to all particle types on high-fog days (**Figure 3-12**d,e). This means that on low-fog days amine fragments are associated with residential burning emission sources and that they are likely present on the LS-BBOA particles. On high-fog days amine fragments are more associated with LS-NOOA particles, indicating that the aqueous conditions may support a different formation pathway for amines. The weaker correlation on high-fog days also indicates the amines are more evenly distributed on different particle types, consistent with a secondary (aqueous) rather than primary formation pathway being more important on high-fog days.

At Fontana, the average f_{44} on LS-VOOA particles is 0.24, which is four times higher than the LS-NOOA particle average f_{44} of 0.06. The larger fraction of oxidized components in LS-VOOA particles compared to in LS-NOOA particles is consistent with the higher O/C of AMS-VOOA (0.78) compared to AMS-NOOA (0.40).

The moderate correlation of the FTIR-DDS factor to the AMS-VOOA factor (**Table 3-7**) suggests that the dust and detritus particles may have provided surface area to accelerate condensation of secondary organic aerosol. The LS mode of the AMS did not identify a dust-type particle since it does not measure refractory particles. There is no evidence that this distribution of secondary components to dust particles is driven by specific heterogeneous reactions, so this association is likely the result of the substantial surface area of these particles.

3.6 Conclusions and Implications

PM1 components were measured using AMS-PMF analysis, LS cluster analysis, and FTIR-PMF analysis at Fresno and Fontana. The AMS-VOOA factor with oxidized organic components and the AMS-BBOA factor from residential burning activities constitute the majority of organic mass (OM) on low-fog days, while the nitrate-related AMS-NOOA component constitutes the majority of the OM during the Fresno high-fog days in winter.

The AMS-NOOA factor (47% of OM) is associated with enhanced nitrate concentration (35%) during Fresno high-fog days. SOA formation at Fresno is strongly affected by persistent fog stagnation and high humidity impacts on particles leading to enhanced organic aerosol concentration. The increased amine, and organosulfate fragments were likely related to aqueous phase reaction at Fresno on high-fog days, which provides some preliminary evidence for aqueous reactions forming nitrate-containing, nitrogen-containing, and sulfate-containing organic component particles. Similarly, a previous study in SJV found that a large number of organic nitrogen compounds (including amines, nitrate esters, peptides, and nitroso compounds) were present in fog water [Herckes et al., 2007]. The lack of association of the products to a specific type of particle suggests that the reactions did not depend on particle components other than water.

AMS-VOOA contributes 58-69% of OM and increases in the afternoon in summertime Fontana, consistent with the expectation that SOA formation from vehicle and other VOC emissions is a significant PM_1 source in summer at Fontana. Unusual trace organic fragments (*m/z* 27, 46, and 63) and increased nitrate, ammonium, sulfate, and alcohol group submicron mass at Fontana measured for more than five days after 4th of July fireworks provided a unique aerosol signature and extended air quality impacts. These results mean that firework contributions have a chemical signature that could be used to estimate their contributions in other areas. Also the persistence of these tracers in SoCAB for multiple days suggests that the contribution of fireworks to air quality degradation in stagnant conditions may be underestimated. Amine fragments (27% CHN^+) and organosulfate fragments (32% CH_3SO^+) were higher on Fontana firework days than on non-firework days. The amine (CH_4N^+) fragment was the major difference between wintertime Fresno and summertime Fontana, consistent with the expected differences in amine precursor sources, likely more from vehicle and other fossil fuel related emissions in summertime at Fontana while including more from agriculture, residential burning, and animal husbandry operations in wintertime at Fresno.

Two sets of PMF factors from AMS and FTIR as well as LS single-particle clustering with and without inorganic fragments provided comparable source-related OM contributions and single-particle types. Particularly, nitrate-related OM (NOOA) contributes 36% of particles at Fresno, while very-oxygenated OM (VOOA) makes up 60% of particles at Fontana. In addition, at Fontana there is clear evidence from the correlation of the FTIR-DDS factor to AMS-VOOA and AMS-NOOA for SOA contributing organic components to refractory dust particles.

The moderate or strong correlations of LS-BBOA with AMS-BBOA, LS-HOA with AMS-HOA, and LS-NOOA with AMS-NOOA at Fresno indicated that BBOA, HOA, and NOOA were largely on separate particle types, in contrast to Fontana where the lack of evidence for external

mixing was likely the result of the longer time for and larger mass contribution of photochemically oxidized components in SoCAB in summer. The association of amine fragments with LS-BBOA particles from residential burning emissions on low-fog days at Fresno but with LS-NOOA particles on high-fog days suggests that the formation pathway was changed in high-fog conditions, likely to one involving aqueous processes.

3.7 Acknowledgments

The authors would like to acknowledge funding and support from California Air Resources Board (Agreement number: 13-330) and contract manager Dr. Nehzat Motallebi. The authors would also like to thank Jackie First for assistance with the Fontana FTIR analysis, the Fontana Fire Department and the South Coast Air Quality Management District (SCAQMD) for Fontana site logistics, and UCD Extension for Fresno site logistics. We thank this project research team for the cooperation and contribution to this paper. The statements and conclusions in this paper are those of the researchers and not necessarily those of CARB. The mention of commercial products, their source, or their use in connection with material reported herein is not to be construed as actual or implied endorsement of such products. The data used in this manuscript are curated at the UCSD Library Digital Collections at https://doi.org/10.6075/J0VX0DF9.

3.8 Appendices

3.8.1 Boundary Layer Height (BLH)

The Weather Research and Forecasting (WRF) v3.4 model (www.wrf-model.org) was used to generate hourly meteorological fields for both the Fresno and Fontana studies. Triple-nested domains centered at 37° N, 120.5° W, were set with the coarse domain divided into 46 × 44 grid cells of 36-km horizontal resolution and the second domain divided into 70 × 76 grid cells of 12-km resolution. The inner-most domain with 4-km resolution was divided into 106 × 118 and 118 × 76 grid cells, which cover Northern and Southern California, respectively. The 31 vertical layers from the ground level to the top pressure of 100 hPa were used for all grids. The meteorological initial and boundary conditions were taken from North American Regional Reanalysis (NARR), which has a spatial resolution of 32 km and a temporal resolution of 3 h. The Yonsei University (YSU) boundary layer vertical diffusion scheme [Hong et al., 2006] was adopted in this study.

3.8.2 SEMS and AMS Measurement Comparisons

Figure 3-2a, b shows the Fresno AMS non-refractory particle mass concentration and the SEMS PM concentration before and after black carbon (BC) and mineral dust contributions were subtracted. The best fit gives average particle density of 1.3 ± 0.1 g cm^{-3} for low-fog days and 1.2 ± 0.1 g cm^{-3} for high-fog days.

The particle density for Fontana firework days is 1.1 ± 0.2 g cm^{-3} and for non-firework days is 1.3 ± 0.2 g cm^{-3}. **Figure 3-2**c, d shows the AMS particle mass concentration with the SEMS PM concentration before and after BC and mineral contributions were subtracted.

3.8.3 Source Apportionment

3.8.3.1 AMS PMF Analysis

A custom software tool (PMF Evaluation Tool, PET [Ulbrich et al., 2009]) was used to evaluate PMF factors and related statistics. Solutions were grouped by number of factors (p), rotational values (fPeak), and seed values. Mathematical criteria (Q/Qexp, fPeak, and uncentered correlation coefficient) were used to evaluate PMF model fitting and to facilitate solution selection (**Table 3-2** and **Table 3-5**).

There were no significant changes in Q/Qexp with fPeak, and both the mass spectrum distribution and time series mass concentration did not change by varying fPeak. fPeak= 0 was identified as a robust solution for the Fresno and Fontana AMS PMF. A fit parameter Q was defined as in equation (1) below, where e_{ij} is an element of the mxn matrix E of residuals not fit by the model for each experimental data point, and σ_{ij} is an element of the mxn matrix of estimated errors (standard deviations) of the points in the data matrix, X [Ulbrich et al., 2009].

$$Q = \sum_{i=1}^{m} \sum_{j=1}^{n} \left(\frac{e_{ij}}{\sigma_{ij}}\right)^2 \qquad \text{Equation (1)}$$

An increase of the Q/Qexp value was utilized as the criteria for rejecting a result. Q/Qexp decreased as the number of factors increased (**Figure 3-15**).

Table 3-5 summarizes the criteria of PMF analysis for Fresno. The 2-factor and 3-factor solutions were rejected because of high Q/Qexp value (> 8.0). The 4-factor solution (Q/Qexp= 6.7), 5-factor solution (Q/Qexp= 5.8), and 6-factor solution (Q/Qexp= 5.2) were resolved with fPeak=0 (**Table 3-5** and **Figure 3-15**). Uncentered correlation coefficients (UC) were evaluated to determine the correlation of different factors in one solution [Ulbrich et al., 2009]. The correlation between factor 1 and factor 2 is higher than 0.8 (UC=0.94) in the 6-factor solution, indicating that the 6-factor solution has too many common features in the mass spectra. The 5-factor solution was rejected because there were 3-paired factors with UC > 0.8. As a result, for Fresno, the 4-factor solution was selected.

For Fontana, the Q/Qexp is 4.4, 3.9, and 3.5 for the 4-factor, 5-factor, and 6-factor solutions, respectively (**Table 3-5** and **Figure 3-15**). The 6-factor solution was rejected because 2 pairs of factors have similar mass spectra and 1 pair of factors has a similar time series. The 4-factor solution and the 5-factor solution both have 2 pairs of factors that have similar mass spectra. The 5-factor solution was selected because of the low value of Q/Qexp = 3.9, and the pair of factors with similar mass spectra was recombined into a single factor.

Table 3-4 summarizes the criteria used in prior studies for identification of PMF factors with sources. Based on their mass spectra and tracer correlations, the five AMS PMF factors were identified as hydrocarbon-like organic aerosol (HOA), nitrate-related oxidized organic aerosol (NOOA), biomass burning organic aerosol (BBOA), cooking emission organic aerosol (COA), and much oxygenated organic aerosol (VOOA). Details of naming these factors are discussed in the following sections. **Figure 3-9**a shows the mass spectra profiles for each factor. The m/z 30 (CH2O +, CH4N+, and C2H6+) and m/z 46 (CH2O2+, CH4NO+, and C2H6O+) were removed

in AMS PMF factor analysis due to the high-resolution peak interferences by NO+ at m/z 30 and NO2+ at m/z 46.

The 4-factor solution for Fresno includes AMS-HOA, AMS-BBOA, AMS-NOOA, and AMS-VOOA. The AMS-HOA factor was identified based on the high signals at CnH2n-1 (e.g., m/z 41, 55, 69) from alkenes and cycloalkanes and the ion series at CnH2n+1 (e.g., m/z 29, 43, 57, 71) from saturated alkanes. The m/z 57 (C4H9+) is a major fragment and often used as a tracer of AMS-HOA emitted from primary combustion sources [Lanz et al., 2007; Mohr et al., 2012; Zhang et al., 2011]. The O/C ratio is low (0.11) with a relatively high H/C ratio (1.80) for the AMS-HOA (hydrocarbon-like) factor. The signals at m/z 57 (C4H9+ and C3H5O+), m/z 60 (C2H4O2+), and m/z 73 (C3H5O2+) in AMS spectra are the main markers of BBOA [Young et al., 2016]. The AMS-VOOA factor has a strong signal at m/z 44 (mostly CO2+), which is a marker of di- and poly-carboxylic acid functional groups, representing oxidized organic aerosol.

The 4-factor solution for Fontana includes AMS-HOA, AMS-COA, AMS-NOOA, and AMS-VOOA factors (**Figure 3-9**a). The AMS-VOOA factor has an intense signal at m/z 44 with a high O/C ratio of 0.78, indicating a highly oxidized oxygenated organic aerosol likely resulting from photochemical reactions [Young et al., 2016]. The COA factor is characterized by the fragments at m/z 41 and m/z 55 with a relatively high m/z 55/57 ratio compared to the HOA factor, which is consistent with previous studies [Mohr et al., 2012].

Figure 3-16a-d shows the scatter plots that have significant correlations between AMS PMF factors and tracers. Black carbon (BC), CO, and potassium (K) concentrations have moderate correlations with the BBOA factor concentrations ($r^2 > 0.25$), indicating carbonaceous aerosols were formed from residential wood burning or agricultural biomass burning activities. The AMS-NOOA factor has a strong and moderate correlation with ammonium and nitrate ($r^2 = 0.79$ and 0.62), indicating that ammonium nitrate containing particles are the largest fraction of submicron particles on high-fog days in Fresno. The secondary species formation in fog-processing is mainly due to high relative humidity with enhanced gas-to-particle partitioning [Collett et al., 1999]. The AMS-VOOA factor constitutes the single largest fraction of the OM at 66% at Fontana and correlates moderately with O_3 concentration.

Cosine Similarity (CS) is used as a measure of similarity of two factor spectra to each other. For any two non-zero vectors A and B, it is calculated from

$$\text{Cosine Similarity (CS)} = \frac{A \cdot B}{\|A\|\|B\|} = \frac{\sum_1^n A_i B_i}{\sqrt{\sum_i^n A_i^2}\sqrt{\sum_i^n B_i^2}} \quad \text{.....Equation (2)}$$

3.8.3.2 FTIR PMF Analysis

PMF analysis of mass-weighted FTIR spectra was used for 98 samples of PM1 at Fresno and 102 samples of PM1 at Fontana [Liu et al., 2012; Russell et al., 2009]. "fPEAK" rotational values of 0, ±0.5, ±1, ±1.5 and ±2 were tested, resulting in nearly identical factors. A minimum Q/Qexp [Paatero and Hopke, 2003; Paatero and Tappert, 1994], was chosen in PM1 analysis results. Seed values of 0, 10, and 100 were tested to investigate consistency of the solutions.

The 2-factor through 6-factor solutions are summarized in **Table 3-15**. The 3-factor solution for FTIR PMF at Fresno was chosen because it reduced the Q/Qexp value while minimizing

correlations between factor spectra and time series. The 3-factor solution showed a significant decrease in Q/Qexp from the 2-factor solution, and each factor had a unique source signature that was not correlated in time with each other ($r \leq 0.6$) and each contributed an important fraction to the ambient aerosols (≥ 10% OM). It also resulted in a small percentage of residual signal, which demonstrated a random pattern over the time suggesting a good and consistent fit.

The same approach was used for FTIR PMF at Fontana. Several filters that were highly influenced by firework emissions were excluded from the PMF analysis because there were too few samples to resolve this source as a separate factor. The 3-factor solution (Q/Qexp=0.8) was chosen because the solution had a low Q/Qexp, and the factors were not similar to each other. Factors with identical or unrealistic infrared spectra were found in solutions with more than 3 factors so the 3-factor solution was used. The amount of residual was higher at Fontana compared to Fresno, probably because of the influence of the firework emissions.

Fresno FTIR measurements showed that the alkane group (52%) constituted the majority of the PM1 organic aerosol mass, followed by alcohol (22%), carboxylic acid (19%), and amine (6%) groups (**Figure 3-6**a). The alkane group constituted the majority of the PM1 OM (49%), followed by alcohol (29%), carboxylic acid (15%), amine (7%), and non-acid carbonyl (1%) groups at Fontana (**Figure 3-6**b). There were higher alcohol (24%) and carboxylic acid (20%) group mass concentrations on high-fog days than low-fog days. The alcohol group also contributed a higher fraction (48%) of the PM1 OM on firework days than non-firework days (**Figure 3-6**).

Table 3-6 and **Figure 3-8** show the summary criteria for FTIR PMF factors and FTIR absorbance spectra analysis. Three factors were identified at Fresno, including a "Fossil fuel combustion (FFC)" factor, a "Mixed combustion" factor, and a "Biomass burning (BB)" factor. The FTIR-FFC factor was identified based on its similarity to a factor observed in previous studies [Liu et al., 2012], which suggested that this factor could be from the first-generation alkane oxidation products of vapors emitted by vehicles. This factor also has similar spectra distribution with "more oxidized FFC" at Pasadena [Guzman-Morales et al., 2014]. The FTIR-MC factor was identified by its strong similarities to combustion factors with high O/C and low O/C observed from previous studies [Russell et al., 2011]. The factor contains strong ammonium absorbance (3050 and 3200 cm−1) [Corrigan et al., 2013]. The FTIR-BB factor was determined due to the sharp and narrow spectra at 2900 cm-1 (alkene functional group), which agrees with previous studies [Corrigan et al., 2013; Russell et al., 2011]. Three factors were also identified at Fontana, including FTIR-FFC, FTIR-MC, and a "Dust-related Detritus or Secondary organic aerosol (FTIR-DDS)" factor. The FTIR-DDS factor was comparable to the vegetative detritus factor [Liu et al., 2012].

3.8.3.3 LS AMS Cluster Analysis

Light-scattering single-particle measurements were analyzed using an updated version of the standard AMS light scattering data processing software Sparrow 1.04F (written by D. Sueper, Aerodyne Research Inc. and University of Colorado at Boulder; available at http://cires1.colorado.edu/jimenez-group/ToFAMSResources/ToFSoftware/index.html#Sparrow), which classifies the particles by

their vaporization types, the physical particle size (as vacuum aerodynamic diameter, dva) and chemical unit-mass spectrum of single particles. The LS AMS measured single particles larger than the optical size detection limit, 180 nm dva [Liu et al., 2013]. Measurements were categorized to find prompt particles that gave a sufficiently strong LS trigger event. Particles that were classified as "noise", "early", "delayed", "coincident", and "null" (based on the time delay between the LS signal (timing of the optical signals (TLS)) and the mass spectra (timing of chemical signals, (TMS)) were excluded. The cluster analysis panel (CAP [Lee et al., 2016]) was used to investigate the composition of prompt particles based on the k-means algorithm in IGOR Pro. Ion signals with m/z 14, 15, 16, 17, 18, 28, 32 and 39 were excluded from the total number of ions due to either the strong interferences from air and instrument background or the noisy baseline of ammonium fragment ions. The background ion threshold was calculated as the average of background particle signal ions plus 3 times the standard deviation. A total of 33,812 particles at Fresno and 9,485 particles at Fontana were measured by LS AMS and classified as prompt and real particles for clustering analysis. **Table 3-16** summarizes the LS cluster comparisons. **Figure 3-15**b shows the total distance of all spectra in the cluster to the centroid for each cluster number.

The 14-cluster solution of the LS AMS k-means clustering analysis was used to group particles for Fresno. **Figure 3-15**b shows the total Euclidian distance for each cluster number, and the total Euclidian distance is the lowest for the 14-cluster solution to reduce the number of similarities computed. Classes 1-5, 8, 9, and 11-14 were recombined as a LSI-Nitrate-OA class since these classes have similar mass spectral profiles and high fractions of m/z 30 and m/z 46. Class 6 was categorized as LSI-HOA based on high signals at CnH2n±1 (e.g., m/z 27, 29, 41, 43, 55, 57, 69, 71). Class 7 was categorized as LSI-VOOA due to its high signal at m/z 44, which is the same criterion as for the AMS-VOOA factor. Class 10 was categorized as LSI-Chloride with a strong peak at m/z 36 (HCl+) but was excluded since it had less than 200 particles.

Inorganic fragments in the mass spectra of single-particles were included in the LSI clustering analysis and classified as four types of particles: an LSI-OOA class, an LSI-HOA class, a LSI-Nitrate-OA class, and a LSI-Chloride class (**Figure 3-9**c). LSI-Chloride was excluded because it had less than 200 particles. LSI-OOA is largely composed of m/z 44 (CO2+); LSI-Nitrate-OA is largely composed of m/z 30 and m/z 46 fragments; LSI-HOA is largely composed of m/z 43, m/z 55, and m/z 57 fragments, which are typical indicators of primary (vehicular) combustion sources. The LSI-Nitrate-OA class increases rapidly on high-fog days and contributes the highest fraction (76% and 89%) of particles on both low-fog and high-fog days. The AMS PMF factors have moderate correlations to the corresponding LSI classes, namely AMS-HOA with LSI-HOA (r^2 = 0.64), AMS-NOOA with LSI-Nitrate-OA (r^2 = 0.60), and AMS-VOOA with LSI-OOA (r^2 = 0.47) (**Table 3-16**). The lack of a BBOA cluster in the LSI implies that residential burning particles cannot be distinguished when inorganic fragments are included in the clustering. Most Fresno LSI clusters had contributions from both oxidized organic and nitrate components (**Figure 3-9**b,c). LSI-Nitrate class contributes 77% of single-particles with intense signals at m/z 30 and m/z 46. LS-NOOA class contributes 42% of single-particles and is characterized by m/z 29, 43, 44, 55, and m/z 81.

The inorganic aerosol fragment ions were removed from the LS single particle spectra to explore the organic aerosol in single particle clustering analysis for comparison to the AMS PMF factors. Four classes were identified at Fresno, including LS-HOA, LS-NOOA, LS-BBOA, and LS-VOOA classes (**Figure 3-9**b), which are consistent with AMS PMF factors. LS-BBOA had signals at m/z 55, 57, 60, and 73. The LS-NOOA, and LS-HOA classes have moderate correlations to the AMS-NOOA, AMS-HOA, and LS-VOOA factors (r^2 = 0.47, 0.32, 0.31, respectively).

For Fontana the 10 cluster solution of the LSI AMS k-means clustering analysis was selected because it has a relatively lower total distance between particle spectra and the cluster centroids (**Figure 3-15**b). Class 1 and class 8 were recombined as LSI-Chloride since they have higher signal at m/z 36 and m/z 35, but the total number of single particles was less than 200 particles, so this class was omitted from this study. Class 3 was categorized as LSI-HOA because the mass spectra profile showed similar fragments as the AMS-HOA factor and previous HOA class (CS=0.94) (**Table 3-16**). Class 5 was categorized as LSI-OOA due to the high signal at m/z 44. Class 7 and class 9 were recombined as the "LSI-Nitrate-OA class" because they both have strong signals at m/z 30 and m/z 46. Class 6 was categorized as LSI-Sulfate due to the sulfate fragment signals (e.g., m/z 48, 64, 80, and 81). Classes 2, 4, and 10 were recombined as a LSI-Mixed cluster based on the presence of multiple inorganic ion fragments, including nitrate, organic, and sulfate fragments.

The mass spectra of the five Fontana LSI single-particle classes (LSI-OOA, LSI-HOA, LSI-Nitrate, LSI-Mixed, and LSI-Sulfate) are shown in **Figure 3-9**c. The nitrate-type particles constitute the majority of the single particles from 6 to 8 July 2015 and are likely associated with aged firework emissions. The LSI-Mixed class of single particles accounts for 22% of the measured single particles and is correlated weakly to the AMS-NOOA factor (r^2 = 0.12). From the LSI clustering analysis, the fractions of LSI-Chloride (4%) and LSI-Nitrate-OA classes (31%) were higher on firework days than non-firework days. The LSI-Sulfate particles (high m/z 64, m/z 48, and m/z 44), which may be associated with sulfur-containing additives in vehicle fuels [Canagaratna et al., 2004]), contributed 25% of single-particles on non-firework days.

The five LSI particle types did not correlate to each other ($r^2 \leq$ 0. 10). LSI-HOA contained 90% organic fragments, LSI-nitrate contained 61% m/z 30 and m/z 46 fragments, and LSI-sulfate contains 36% sulfate fragments (m/z 48, 64, 80, 81, 96, and 98). The LSI-mixed type particles contain 36% nitrate fragments, 13% sulfate fragments, and 51% organic fragments. The LSI-OOA and LSI-sulfate is correlated moderately to the FTIR-DDS factor (r^2 = 0.35 and 0.26, see **Table 3-17**), suggesting that the LSI-OOA single-particles have dust detritus and secondary organic components on dust-related particles or sulfate-containing particles. At Fontana, both the AMS-NOOA (67%) and the LS-VOOA class (73%) constituted the highest fractions of submicron mass and particle number on non-firework days.

Four LS classes were identified at Fontana: LS-HOA, LS- NOOA, LS-COA, and LS-VOOA classes (**Figure 3-9**b). The LS-COA class had a high ratio of m/z 55 to m/z 57, similar to the AMS-COA factor. Both NOOA classes for Fresno and Fontana have similar mass spectra fragments (e.g., m/z 29, 43, 44, 55, and m/z 81). All four LS classes have weak correlations to the

corresponding AMS PMF factors (**Table 3-13**), with r^2 = 0.17, 0.17, 0.13, and 0.22 for HOA, COA, VOOA, and NOOA LS clusters and AMS factors, respectively.

3.8.4 Organonitrate, Amine, and Organosulfate Fragments

3.8.4.1 Organonitrate Fragments and Groups

We investigated two methods for quantifying organonitrate from AMS spectra, namely the NO+/NO2+ ratio method [Ayres et al., 2015; Farmer et al., 2010; Fry et al., 2013; Xu et al., 2015] (**Table 3-18**) and the organonitrate fragment ion sum (ΣCHON) method (**Table 3-19**) with CH4NO+ excluded due to reduce interference from NO2+ on firework and high-fog days. Both ON methods are dependent on the mixture of components that are present. Since there was a substantial change in nitrate concentration during the course of each study at each site (between low and high fog days and between firework and non-firework days), we found that neither method gave consistent results (**Figure 3-17**) and so were not used.

3.8.4.2 Amine Fragments and Groups

The amine fragment composition is quite different between Fresno in winter and Fontana in summer. While the average amine concentration was greater at Fresno than Fontana, the fraction of amine fragment CH4N+ was 13 times higher at Fontana than Fresno. The difference between the two sites could be due to differences in the amine precursors as well as to differences in temperature. Atmospheric sources of amine fragments include vehicle emissions, which are present at both Fresno and Fontana, as well as agricultural and dairy or animal husbandry operations, which are likely to be higher at Fresno than at Fontana. Ge et al. [2012] reported that high concentrations of amine fragments, such as CH4N+, C2H5N+, C3H8N+, and C3H9N+, were likely from regional agricultural activities in Fresno.

The colder winter temperatures at Fresno (0-14°C) also may have resulted in a larger particle-phase fraction of amines than at Fontana (25-35°C). The solid/gas dissociation constant Kp of aminium nitrate increases with temperature [Ge et al., 2011b], so that colder temperatures might lead to more aminium nitrate salts (such as methylaminium nitrate (CH5N·HNO3), dimethylaminium nitrate (C2H7N·HNO3), and trimethylaminium nitrate (C3H9N·HNO3)) and less gas-phase amine and HNO_3 at Fresno in winter than at Fontana in summer. Kp values of six aliphatic amine nitrate salts decrease with increasing relative humidity [Ge et al., 2011b], suggesting that enhanced aminium nitrate salts could have formed from acid-base reactions at Fresno on high-fog days.

The amine fragments have a different composition on Fontana firework days than on non-firework days. The CHN+ fragment constitutes the majority of the alkyl-amine group on firework days, accounting for 29% of the alkyl-amine group concentration, while the CH4N+ fragment constitutes the majority of the alkyl-amine group (25%) on non-firework days.

The FTIR amine group mass concentration was strongly correlated to AMS amine fragment mass concentration (CxHyNz+) (slope = 0.38 and r^2 = 0. 72) at Fresno (**Figure 3-5**e). The strong correlation at Fresno between the AMS and FTIR amine measurements provides a high degree of

confidence that both methods are providing useful measures of amine fractions, and the differences provide an effective quantification of the method limitations. The amine concentration is likely too small a fraction of OM for compound-specific CE to be well accounted for by the bulk-submicron CE calculation. The lower amine concentrations and higher ambient temperatures at Fontana may explain the weak correlation between AMS amine fragments and FTIR amine group mass concentrations (**Figure 3-5**f) (slope = 0.10 and r^2 = 0.17).

3.8.4.3 Organosulfate Fragments and Groups

Table 3-2 summarizes the MSA concentrations estimated from the methods of Ge et al. [2012b] and Zhou et al. [2016]. The average MSA concentration of 0.027 μg m-3 at Fresno is higher than the 0.018 μg m-3 value found for Fresno in winter 2010 [Ge et al., 2012b].

The peak associated with possible organosulfate groups in FTIR was below or near the limit of quantification for all PM1 samples due to the limited sampling volume, so the samples were not rinsed to quantify possible interference from bisulfate ions [Russell et al., 2009]. Nonetheless, the potential FTIR organosulfate mass concentration (assuming no bisulfate) on non-firework days was correlated with AMS organosulfate concentration with a linear relationship slope of 1.06 (r^2 = 0.55), showing consistency between the two methods.

3.8.5 Elemental Analysis and Oxidized Fragment Markers

The "triangle plot (f44 vs f43)" [Ng et al., 2010] (**Figure 3-7**a) shows that the AMS composition of the organic components for both Fresno and Fontana lie within the area of the triangle identified by previous work [Hayes et al., 2013; Liu et al., 2012]. AMS-BBOA has a higher f43 ($C_2H_3O^+$) to f44 (CO_2^+) ratio (0.9) and lower O/C ratio (0.5) than AMS-VOOA (f43/f44 = 0.3, O/C = 0.8)(**Table 3-20**), consistent with findings that residential burning emissions are less oxidized than AMS-VOOA [Chhabra et al., 2010; Young et al., 2016] and the O/C ratio falls in between BBOA1 (0.3) and BBOA2 (0.6) reported by Young et al. [2016].

The Van Krevelen diagram [Heald et al., 2010] shows that Fresno and Fontana organic aerosol components have different slopes (0.05 for Fresno and -0.4 for Fontana, corrected based on [Canagaratna et al., 2015], **Figure 3-7**b). The transition slope represents the inferred chemical evolution of primary and secondary components of OM. This result illustrates that Fresno OM falls on a line with slope 0 which is representative of transition from a methyl (–CH_2–) group to an alcohol (–C(–OH–) group and that Fontana OM falls on a line that is between a transition to alcohol or peroxide group (slope 0) and to a carboxylic acid group (slope -1).

These transitions are consistent with the higher concentrations of FTIR alcohol groups and with the lower f44 (CO_2^+, i.e. organic fragments that result in part from carboxylic acids) of Fresno than Fontana. The Fontana results are consistent with the organic composition measured at Pasadena during CalNex which had a slope of -0.64, but somewhat different from Riverside during SOAR1 when the slope was -1.1 [Hayes et al., 2013; Heald et al., 2010]. The O/C ratio of 0.16 for Fontana HOA is consistent with that of 0.14 for Pasadena HOA but substantially higher than that of 0.02 for Riverside HOA.

Table 3-20 summarizes the ratios of O/C, H/C, m/z 43 (C2H3O+) to m/z 44 (CO2+), and m/z 43 (C3H7+) to m/z 44 (CO2+), and f44 for the PMF factors. The ratios of m/z 43 (C2H3O+) to m/z 44 (CO2+) and of m/z 43 (C3H7+) to m/z 44 (CO2+) were higher for Fresno AMS-BBOA than AMS-VOOA, which could result from higher aldehyde or ketone group concentrations and a much higher fraction of C3H7+ fragment in AMS-BBOA than in AMS-VOOA.

3.9 References

Aiken, A. C., et al. (2009), Mexico City aerosol analysis during MILAGRO using high resolution aerosol mass spectrometry at the urban supersite (T0) - Part 1: Fine particle composition and organic source apportionment, Atmospheric Chemistry and Physics, 9(17), 6633-6653.

Ayres, B. R., et al. (2015), Organic nitrate aerosol formation via NO3 + biogenic volatile organic compounds in the southeastern United States, Atmospheric Chemistry and Physics, 15(23), 13377-13392, doi:10.5194/acp-15-13377-2015.

Bahreini, R., et al. (2012), Gasoline emissions dominate over diesel in formation of secondary organic aerosol mass, Geophysical Research Letters, 39, 6, doi:10.1029/2011gl050718.

Blando, J. D., and B. J. Turpin (2000), Secondary organic aerosol formation in cloud and fog droplets: a literature evaluation of plausibility, Atmospheric Environment, 34(10), 1623-1632, doi:10.1016/s1352-2310(99)00392-1.

Budisulistiorini, S. H., et al. (2013), Real-Time Continuous Characterization of Secondary Organic Aerosol Derived from Isoprene Epoxydiols in Downtown Atlanta, Georgia, Using the Aerodyne Aerosol Chemical Speciation Monitor, Environmental Science & Technology, 47(11), 5686-5694, doi:10.1021/es400023n.

Budisulistiorini, S. H., et al. (2015), Examining the effects of anthropogenic emissions on isoprene-derived secondary organic aerosol formation during the 2013 Southern Oxidant and Aerosol Study (SOAS) at the Look Rock, Tennessee ground site, Atmospheric Chemistry and Physics, 15(15), 8871-8888, doi:10.5194/acp-15-8871-2015.

Canagaratna, M. R., et al. (2004), Chase studies of particulate emissions from in-use New York City vehicles, Aerosol Science and Technology, 38(6), 555-573, doi:10.1080/02786820490465504.

Canagaratna, M. R., et al. (2007), Chemical and microphysical characterization of ambient aerosols with the aerodyne aerosol mass spectrometer, Mass Spectrometry Reviews, 26(2), 185-222, doi:10.1002/mas.20115.

Canagaratna, M. R., et al. (2015), Elemental ratio measurements of organic compounds using aerosol mass spectrometry: characterization, improved calibration, and implications, Atmospheric Chemistry and Physics, 15(1), 253-272, doi:10.5194/acp-15-253-2015.

Cappa, C. D., K. R. Kolesar, X. L. Zhang, D. B. Atkinson, M. S. Pekour, R. A. Zaveri, A. Zelenyuk, and Q. Zhang (2016), Understanding the optical properties of ambient sub- and supermicron particulate matter: results from the CARES 2010 field study in northern California, Atmospheric Chemistry and Physics, 16(10), 6511-6535, doi:10.5194/acp-16-6511-2016.

Chen, Q. C., F. Ikemori, H. Higo, D. Asakawa, and M. Mochida (2016), Chemical Structural Characteristics of HULIS and Other Fractionated Organic Matter in Urban Aerosols: Results from Mass Spectral and FT-IR Analysis, Environmental Science & Technology, 50(4), 1721-1730, doi:10.1021/acs.est.5b05277.

Cheung, K. L., L. Ntziachristos, T. Tzamkiozis, J. J. Schauer, Z. Samaras, K. F. Moore, and C. Sioutas (2010), Emissions of Particulate Trace Elements, Metals and Organic Species from Gasoline, Diesel, and Biodiesel Passenger Vehicles and Their Relation to Oxidative Potential, Aerosol Science and Technology, 44(7), 500-513, doi:10.1080/02786821003758294.

Chhabra, P. S., R. C. Flagan, and J. H. Seinfeld (2010), Elemental analysis of chamber organic aerosol using an aerodyne high-resolution aerosol mass spectrometer, Atmospheric Chemistry and Physics, 10(9), 4111-4131, doi:10.5194/acp-10-4111-2010.

Chow, J. C., and J. G. Watson (1998), Guideline on Speciated Particulate Monitoring; Prepared for U.S. Environmental Protection AgencyRep., Research Triangle Park, NC, by Desert Research Institute: Reno, NV.

Chow, J. C., J. G. Watson, D. H. Lowenthal, L. W. A. Chen, B. Zielinska, L. R. Mazzoleni, and K. L. Magliano (2007), Evaluation of organic markers for chemical mass balance source apportionment at the Fresno Supersite, Atmospheric Chemistry and Physics, 7(7), 1741-1754.

Collett, J. L., K. J. Hoag, D. E. Sherman, A. Bator, and L. W. Richards (1999), Spatial and temporal variations in San Joaquin Valley fog chemistry, Atmospheric Environment, 33(1), 129-140.

Corrigan, A. L., et al. (2013), Biogenic and biomass burning organic aerosol in a boreal forest at Hyytiala, Finland, during HUMPPA-COPEC 2010, Atmospheric Chemistry and Physics, 13(24), 12233-12256, doi:10.5194/acp-13-12233-2013.

Crippa, M., et al. (2013), Identification of marine and continental aerosol sources in Paris using high resolution aerosol mass spectrometry, Journal of Geophysical Research-Atmospheres, 118(4), 1950-1963, doi:10.1002/jgrd.50151.

Cross, E. S., T. B. Onasch, M. Canagaratna, J. T. Jayne, J. Kimmel, X. Y. Yu, M. L. Alexander, D. R. Worsnop, and P. Davidovits (2009), Single particle characterization using a light scattering module coupled to a time-of-flight aerosol mass spectrometer, Atmospheric Chemistry and Physics, 9(20), 7769-7793.

Cubison, M. J., et al. (2011), Effects of aging on organic aerosol from open biomass burning smoke in aircraft and laboratory studies, Atmospheric Chemistry and Physics, 11(23), 12049-12064, doi:10.5194/acp-11-12049-2011.

Darer, A. I., N. C. Cole-Filipiak, A. E. O'Connor, and M. J. Elrod (2011), Formation and Stability of Atmospherically Relevant Isoprene-Derived Organosulfates and Organonitrates, Environmental Science & Technology, 45(5), 1895-1902, doi:10.1021/es103797z.

DeCarlo, P. F., et al. (2006), Field-deployable, high-resolution, time-of-flight aerosol mass spectrometer, Analytical Chemistry, 78(24), 8281-8289, doi:10.1021/ac061249n.

DeCarlo, P. F., J. G. Slowik, D. R. Worsnop, P. Davidovits, and J. L. Jimenez (2004), Particle morphology and density characterization by combined mobility and aerodynamic diameter

measurements. Part 1: Theory, Aerosol Science and Technology, 38(12), 1185-1205, doi:10.1080/027868290903907.

Devore, J. L., and K. N. Berk (2012), Regression and Correlation, edited, pp. 613-722, Springer New York, New York, NY, doi:10.1007/978-1-4614-0391-3_12.

Dickerson, A. S., A. F. Benson, B. Buckley, and E. A. W. Chan (2017), Concentrations of individual fine particulate matter components in the USA around July 4th, Air Quality Atmosphere and Health, 10(3), 349-358, doi:10.1007/s11869-016-0433-0.

Docherty, K. S., et al. (2011), The 2005 Study of Organic Aerosols at Riverside (SOAR-1): instrumental intercomparisons and fine particle composition, Atmospheric Chemistry and Physics, 11(23), 12387-12420, doi:10.5194/acp-11-12387-2011.

Dolislager, L. J., and N. Motallebi (1999), Characterization of Particulate Matter in California, Journal of the Air & Waste Management Association, 49(9), 45-56, doi:10.1080/10473289.1999.10463898.

Drewnick, F., S. S. Hings, J. Curtius, G. Eerdekens, and J. Williams (2006), Measurement of fine particulate and gas-phase species during the New Year's fireworks 2005 in Mainz, Germany, Atmospheric Environment, 40(23), 4316-4327, doi:10.1016/j.atmosenv.2006.03.040.

El-Sayed, M. M. H., D. Amenumey, and C. J. Hennigan (2016), Drying-Induced Evaporation of Secondary Organic Aerosol during Summer, Environmental Science & Technology, 50(7), 3626-3633, doi:10.1021/acs.est.5b06002.

Farmer, D. K., A. Matsunaga, K. S. Docherty, J. D. Surratt, J. H. Seinfeld, P. J. Ziemann, and J. L. Jimenez (2010), Response of an aerosol mass spectrometer to organonitrates and organosulfates and implications for atmospheric chemistry, Proceedings of the National Academy of Sciences of the United States of America, 107(15), 6670-6675, doi:10.1073/pnas.0912340107.

Fraser, M. P., and G. R. Cass (1998), Detection of excess ammonia emissions from in-use vehicles and the implications for fine particle control, Environmental Science & Technology, 32(8), 1053-1057, doi:10.1021/es970382h.

Freutel, F., F. Drewnick, J. Schneider, T. Klimach, and S. Borrmann (2013), Quantitative single-particle analysis with the Aerodyne aerosol mass spectrometer: development of a new classification algorithm and its application to field data, Atmospheric Measurement Techniques, 6(11), 3131-3145, doi:10.5194/amt-6-3131-2013.

Frossard, A. A., P. M. Shaw, L. M. Russell, J. H. Kroll, M. R. Canagaratna, D. R. Worsnop, P. K. Quinn, and T. S. Bates (2011), Springtime Arctic haze contributions of submicron organic particles from European and Asian combustion sources, Journal of Geophysical Research-Atmospheres, 116, doi:10.1029/2010jd015178.

Fry, J. L., et al. (2013), Observations of gas- and aerosol-phase organic nitrates at BEACHON-RoMBAS 2011, Atmospheric Chemistry and Physics, 13(17), 8585-8605, doi:10.5194/acp-13-8585-2013.

Gaston, C. J., K. A. Pratt, X. Y. Qin, and K. A. Prather (2010), Real-Time Detection and Mixing State of Methanesulfonate in Single Particles at an Inland Urban Location during a

Phytoplankton Bloom, Environmental Science & Technology, 44(5), 1566-1572, doi:10.1021/es902069d.

Ge, X. L., A. Setyan, Y. L. Sun, and Q. Zhang (2012a), Primary and secondary organic aerosols in Fresno, California during wintertime: Results from high resolution aerosol mass spectrometry, Journal of Geophysical Research-Atmospheres, 117, 15, doi:10.1029/2012jd018026.

Ge, X. L., A. S. Wexler, and S. L. Clegg (2011a), Atmospheric amines - Part I. A review, Atmospheric Environment, 45(3), 524-546, doi:10.1016/j.atmosenv.2010.10.012.

Ge, X. L., A. S. Wexler, and S. L. Clegg (2011b), Atmospheric amines - Part II. Thermodynamic properties and gas/particle partitioning, Atmospheric Environment, 45(3), 561-577, doi:10.1016/j.atmosenv.2010.10.013.

Ge, X. L., Q. Zhang, Y. L. Sun, C. R. Ruehl, and A. Setyan (2012b), Effect of aqueous-phase processing on aerosol chemistry and size distributions in Fresno, California, during wintertime, Environmental Chemistry, 9(3), 221-235, doi:10.1071/en11168.

Gentner, D. R., et al. (2012), Elucidating secondary organic aerosol from diesel and gasoline vehicles through detailed characterization of organic carbon emissions, Proceedings of the National Academy of Sciences of the United States of America, 109(45), 18318-18323, doi:10.1073/pnas.1212272109.

George, C., M. Ammann, B. D'Anna, D. J. Donaldson, and S. A. Nizkorodov (2015), Heterogeneous Photochemistry in the Atmosphere, Chemical Reviews, 115(10), 4218-4258, doi:10.1021/cr500648z.

Gilardoni, S., S. Liu, S. Takahama, L. M. Russell, J. D. Allan, R. Steinbrecher, J. L. Jimenez, P. F. De Carlo, E. J. Dunlea, and D. Baumgardner (2009), Characterization of organic ambient aerosol during MIRAGE 2006 on three platforms, Atmospheric Chemistry and Physics, 9(15), 5417-5432.

Gilardoni, S., et al. (2007), Regional variation of organic functional groups in aerosol particles on four US east coast platforms during the International Consortium for Atmospheric Research on Transport and Transformation 2004 campaign, Journal of Geophysical Research-Atmospheres, 112(D10), doi:10.1029/2006jd007737.

Gorin, C. A., J. L. Collett, and P. Herckes (2006), Wood smoke contribution to winter aerosol in Fresno, CA, Journal of the Air & Waste Management Association, 56(11), 1584-1590.

Guzman-Morales, J., et al. (2014), Estimated contributions of primary and secondary organic aerosol from fossil fuel combustion during the CalNex and Cal-Mex campaigns, Atmospheric Environment, 88, 330-340, doi:10.1016/j.atmosenv.2013.08.047.

Hawkins, L. N., L. M. Russell, D. S. Covert, P. K. Quinn, and T. S. Bates (2010), Carboxylic acids, sulfates, and organosulfates in processed continental organic aerosol over the southeast Pacific Ocean during VOCALS-REx 2008, Journal of Geophysical Research-Atmospheres, 115, doi:10.1029/2009jd013276.

Hayes, P. L., et al. (2013), Organic aerosol composition and sources in Pasadena, California, during the 2010 CalNex campaign, Journal of Geophysical Research-Atmospheres, 118(16), 9233-9257, doi:10.1002/jgrd.50530.

Heald, C. L., J. H. Kroll, J. L. Jimenez, K. S. Docherty, P. F. DeCarlo, A. C. Aiken, Q. Chen, S. T. Martin, D. K. Farmer, and P. Artaxo (2010), A simplified description of the evolution of organic aerosol composition in the atmosphere, Geophysical Research Letters, 37, 5, doi:10.1029/2010gl042737.

Herckes, P., J. A. Leenheer, and J. L. Collett (2007), Comprehensive characterization of atmospheric organic matter in Fresno, California fog water, Environmental Science & Technology, 41(2), 393-399, doi:10.1021/es06076988.

Herckes, P., A. R. Marcotte, Y. Wang, and J. L. Collett (2015), Fog composition in the Central Valley of California over three decades, Atmospheric Research, 151, 20-30, doi:10.1016/j.atmosres.2014.01.025.

Hong, S. Y., Y. Noh, and J. Dudhia (2006), A new vertical diffusion package with an explicit treatment of entrainment processes, Monthly Weather Review, 134(9), 2318-2341, doi:10.1175/mwr3199.1.

Huang, S., L. Poulain, D. van Pinxteren, M. van Pinxteren, Z. J. Wu, H. Herrmann, and A. Wiedensohler (2017), Latitudinal and Seasonal Distribution of Particulate MSA over the Atlantic using a Validated Quantification Method with HR-ToF-AMS, Environmental Science & Technology, 51(1), 418-426, doi:10.1021/acs.est.6b03186.

Huffman, J. A., et al. (2009), Chemically-resolved aerosol volatility measurements from two megacity field studies, Atmospheric Chemistry and Physics, 9(18), 7161-7182.

Jayne, J. T., D. C. Leard, X. F. Zhang, P. Davidovits, K. A. Smith, C. E. Kolb, and D. R. Worsnop (2000), Development of an aerosol mass spectrometer for size and composition analysis of submicron particles, Aerosol Science and Technology, 33(1-2), 49-70, doi:10.1080/027868200410840.

Jeong, C. H., M. L. McGuire, K. J. Godri, J. G. Slowik, P. J. G. Rehbein, and G. J. Evans (2011), Quantification of aerosol chemical composition using continuous single particle measurements, Atmospheric Chemistry and Physics, 11(14), 7027-7044, doi:10.5194/acp-11-7027-2011.

Jimenez, J. L. (2003), Ambient aerosol sampling using the Aerodyne Aerosol Mass Spectrometer, Journal of Geophysical Research, 108(D7), 1-13, doi:10.1029/2001JD001213.

Kelly, J. T., et al. (2014), Fine-scale simulation of ammonium and nitrate over the South Coast Air Basin and San Joaquin Valley of California during CalNex-2010, Journal of Geophysical Research-Atmospheres, 119(6), 3600-3614, doi:10.1002/2013jd021290.

Kostenidou, E., R. K. Pathak, and S. N. Pandis (2007), An algorithm for the calculation of secondary organic aerosol density combining AMS and SMPS data, Aerosol Science and Technology, 41(11), 1002-1010, doi:10.1080/02786820701666270.

Kroll, J. H., C. Y. Lim, S. H. Kessler, and K. R. Wilson (2015), Heterogeneous Oxidation of Atmospheric Organic Aerosol: Kinetics of Changes to the Amount and Oxidation State of Particle-Phase Organic Carbon, Journal of Physical Chemistry A, 119(44), 10767-10783, doi:10.1021/acs.jpca.5b06946.

Lanz, V. A., M. R. Alfarra, U. Baltensperger, B. Buchmann, C. Hueglin, and A. S. H. Prevot (2007), Source apportionment of submicron organic aerosols at an urban site by factor analytical modelling of aerosol mass spectra, Atmospheric Chemistry and Physics, 7(6), 1503-1522.

Lawson, D. R. (1990), The Southern California Air Quality Study, Journal of the Air & Waste Management Association, 40:2, 156-165, doi:10.1080/10473289.1990.10466671.

Lee, A. K. Y., M. D. Willis, R. M. Healy, T. B. Onasch, and J. P. D. Abbatt (2015), Mixing state of carbonaceous aerosol in an urban environment: single particle characterization using the soot particle aerosol mass spectrometer (SP-AMS), Atmospheric Chemistry and Physics, 15(4), 1823-1841, doi:10.5194/acp-15-1823-2015.

Lee, A. K. Y., M. D. Willis, R. M. Healy, J. M. Wang, C. H. Jeong, J. C. Wenger, G. J. Evans, and J. P. D. Abbatt (2016), Single-particle characterization of biomass burning organic aerosol (BBOA): evidence for non-uniform mixing of high molecular weight organics and potassium, Atmospheric Chemistry and Physics, 16(9), 5561-5572, doi:10.5194/acp-16-5561-2016.

Li, J. Y., et al. (2017), Online single particle measurement of fireworks pollution during Chinese New Year in Nanning, Journal of Environmental Sciences, 53, 184-195, doi:10.1016/j.jes.2016.04.021.

Lin, Y. H., et al. (2012), Isoprene Epoxydiols as Precursors to Secondary Organic Aerosol Formation: Acid-Catalyzed Reactive Uptake Studies with Authentic Compounds, Environmental Science & Technology, 46(1), 250-258, doi:10.1021/es202554c.

Liu, D. Y., K. A. Prather, and S. V. Hering (2000), Variations in the size and chemical composition of nitrate-containing particles in Riverside, CA, Aerosol Science and Technology, 33(1-2), 71-86, doi:10.1080/027868200410859.

Liu, S., et al. (2012), Secondary organic aerosol formation from fossil fuel sources contribute majority of summertime organic mass at Bakersfield, Journal of Geophysical Research-Atmospheres, 117, 21, doi:10.1029/2012jd018170.

Liu, S., L. M. Russell, D. T. Sueper, and T. B. Onasch (2013), Organic particle types by single-particle measurements using a time-of-flight aerosol mass spectrometer coupled with a light scattering module, Atmospheric Measurement Techniques, 6(2), 187-197, doi:10.5194/amt-6-187-2013.

Lloyd, J. A., K. J. Heaton, and M. V. Johnston (2009), Reactive Uptake of Trimethylamine into Ammonium Nitrate Particles, Journal of Physical Chemistry A, 113(17), 4840-4843, doi:10.1021/jp900634d.

Mader, B. T., and J. F. Pankow (2001), Gas/solid partitioning of semivolatile organic compounds (SOCs) to air filters. 3. An analysis of gas adsorption artifacts in measurements of atmospheric SOCs and organic carbon (OC) when using Teflon membrane filters and quartz fiber filters, Environmental Science & Technology, 35(17), 3422-3432, doi:10.1021/es0015951.

McDonald, B. C., et al. (2018), Volatile chemical products emerging as largest petrochemical source of urban organic emissions, Science, 359(6377), 760-764, doi:10.1126/science.aaq0524.

Middlebrook, A. M., R. Bahreini, J. L. Jimenez, and M. R. Canagaratna (2012), Evaluation of Composition-Dependent Collection Efficiencies for the Aerodyne Aerosol Mass Spectrometer

using Field Data, Aerosol Science and Technology, 46(3), 258-271, doi:10.1080/02786826.2011.620041.

Mohr, C., et al. (2012), Identification and quantification of organic aerosol from cooking and other sources in Barcelona using aerosol mass spectrometer data, Atmospheric Chemistry and Physics, 12(4), 1649-1665, doi:10.5194/acp-12-1649-2012.

Murphy, S. M., A. Sorooshian, J. H. Kroll, N. L. Ng, P. Chhabra, C. Tong, J. D. Surratt, E. Knipping, R. C. Flagan, and J. H. Seinfeld (2007), Secondary aerosol formation from atmospheric reactions of aliphatic amines, Atmospheric Chemistry and Physics, 7(9), 2313-2337.

Ng, N. L., M. R. Canagaratna, J. L. Jimenez, Q. Zhang, I. M. Ulbrich, and D. R. Worsnop (2011), Real-Time Methods for Estimating Organic Component Mass Concentrations from Aerosol Mass Spectrometer Data, Environmental Science & Technology, 45(3), 910-916, doi:10.1021/es102951k.

Ng, N. L., et al. (2010), Organic aerosol components observed in Northern Hemispheric datasets from Aerosol Mass Spectrometry, Atmospheric Chemistry and Physics, 10(10), 4625-4641, doi:10.5194/acp-10-4625-2010.

Nowak, J. B., J. A. Neuman, R. Bahreini, C. A. Brock, A. M. Middlebrook, A. G. Wollny, J. S. Holloway, J. Peischl, T. B. Ryerson, and F. C. Fehsenfeld (2010), Airborne observations of ammonia and ammonium nitrate formation over Houston, Texas, Journal of Geophysical Research-Atmospheres, 115, doi:10.1029/2010jd014195.

Nowak, J. B., J. A. Neuman, R. Bahreini, A. M. Middlebrook, J. S. Holloway, S. A. McKeen, D. D. Parrish, T. B. Ryerson, and M. Trainer (2012), Ammonia sources in the California South Coast Air Basin and their impact on ammonium nitrate formation, Geophysical Research Letters, 39, 6, doi:10.1029/2012gl051197.

Paatero, P., and P. K. Hopke (2003), Discarding or downweighting high-noise variables in factor analytic models, Analytica Chimica Acta, 490(1-2), 277-289, doi:10.1016/S0003-2670(02)01643-4.

Paatero, P., and U. Tappert (1994), Positive Matrix Factorization : A non-negative factor model with optimal utilization of error stimates od data values, Environmetrics, 5(April 1993), 111-126.

Powelson, M. H., B. M. Espelien, L. N. Hawkins, M. M. Galloway, and D. O. De Haan (2014), Brown Carbon Formation by Aqueous-Phase Carbonyl Compound Reactions with Amines and Ammonium Sulfate, Environmental Science & Technology, 48(2), 985-993, doi:10.1021/es4038325.

Presto, A. A., T. D. Gordon, and A. L. Robinson (2014), Primary to secondary organic aerosol: evolution of organic emissions from mobile combustion sources, Atmospheric Chemistry and Physics, 14(10), 5015-5036, doi:10.5194/acp-14-5015-2014.

Price, D. J., M. Kacarab, D. R. Cocker, K. L. Purvis-Roberts, and P. J. Silva (2016), Effects of temperature on the formation of secondary organic aerosol from amine precursors, Aerosol Science and Technology, 50(11), 1216-1226, doi:10.1080/02786826.2016.1236182.

Quinn, P. K., et al. (2004), Aerosol optical properties measured on board the Ronald H. Brown during ACE-Asia as a function of aerosol chemical composition and source region, Journal of Geophysical Research-Atmospheres, 109(D19), -, doi:10.1029/2003jd004010.

Reid, C. E., M. Jerrett, I. B. Tager, M. L. Petersen, J. K. Mann, and J. R. Balmes (2016), Differential respiratory health effects from the 2008 northern California wildfires: A spatiotemporal approach, Environmental Research, 150, 227-235, doi:10.1016/j.envres.2016.06.012.

Robinson, A. L., N. M. Donahue, M. K. Shrivastava, E. A. Weitkamp, A. M. Sage, A. P. Grieshop, T. E. Lane, J. R. Pierce, and S. N. Pandis (2007), Rethinking organic aerosols: Semivolatile emissions and photochemical aging, Science, 315(5816), 1259-1262, doi:10.1126/science.1133061.

Robinson, E. S., R. Saleh, and N. M. Donahue (2013), Organic Aerosol Mixing Observed by Single-Particle Mass Spectrometry, Journal of Physical Chemistry A, 117(51), 13935-13945, doi:10.1021/jp405789t.

Rodriguez, A. A., A. de Loera, M. H. Powelson, M. M. Galloway, and D. O. Haan (2017), Formaldehyde and Acetaldehyde Increase Aqueous-Phase Production of Imidazoles in Methylglyoxal/Amine Mixtures: Quantifying a Secondary Organic Aerosol Formation Mechanism, Environmental Science & Technology Letters, 4(6), 234-239, doi:10.1021/acs.estlett.7b00129.

Roth, A., J. Schneider, T. Klimach, S. Mertes, D. van Pinxteren, H. Herrmann, and S. Borrmann (2016), Aerosol properties, source identification, and cloud processing in orographic clouds measured by single particle mass spectrometry on a central European mountain site during HCCT-2010, Atmospheric Chemistry and Physics, 16(2), 505-524, doi:10.5194/acp-16-505-2016.

Russell, L. M. (2013), Carbonaceous Particles: Source-Based Characterization of Their Formation, Composition, and Structures. Source-Based Characterization of Their Formation, Composition, and Structures, 291-316 pp., doi:10.1016/B978-0-08-095975-7.00415-0.

Russell, L. M., R. Bahadur, L. N. Hawkins, J. Allan, D. Baumgardner, P. K. Quinn, and T. S. Bates (2009a), Organic aerosol characterization by complementary measurements of chemical bonds and molecular fragments, Atmospheric Environment, 43(38), 6100-6105, doi:10.1016/j.atmosenv.2009.09.036.

Russell, L. M., R. Bahadur, and P. J. Ziemann (2011), Identifying organic aerosol sources by comparing functional group composition in chamber and atmospheric particles, Proceedings of the National Academy of Sciences of the United States of America, 108(9), 3516-3521, doi:10.1073/pnas.1006461108.

Russell, L. M., L. N. Hawkins, A. A. Frossard, P. K. Quinn, and T. S. Bates (2010), Carbohydrate-like composition of submicron atmospheric particles and their production from ocean bubble bursting, Proceedings of the National Academy of Sciences of the United States of America, 107(15), 6652-6657, doi:10.1073/pnas.0908905107.

Russell, L. M., S. Takahama, S. Liu, L. N. Hawkins, D. S. Covert, P. K. Quinn, and T. S. Bates (2009b), Oxygenated fraction and mass of organic aerosol from direct emission and atmospheric

processing measured on the R/V Ronald Brown during TEXAQS/GoMACCS 2006, Journal of Geophysical Research-Atmospheres, 114, doi:10.1029/2008jd011275.

Schauer, J. J., and G. R. Cass (2000), Source apportionment of wintertime gas-phase and particle-phase air pollutants using organic compounds as tracers, Environmental Science & Technology, 34(9), 1821-1832, doi:10.1021/es981312t.

Schwartz, R. E., et al. (2010), Biogenic oxidized organic functional groups in aerosol particles from a mountain forest site and their similarities to laboratory chamber products, Atmospheric Chemistry and Physics, 10(11), 5075-5088, doi:10.5194/acp-10-5075-2010.

Setyan, A., C. Song, M. Merkel, W. B. Knighton, T. B. Onasch, M. R. Canagaratna, D. R. Worsnop, A. Wiedensohler, J. E. Shilling, and Q. Zhang (2014), Chemistry of new particle growth in mixed urban and biogenic emissions - insights from CARES, Atmospheric Chemistry and Physics, 14(13), 6477-6494, doi:10.5194/acp-14-6477-2014.

Setyan, A., et al. (2012), Characterization of submicron particles influenced by mixed biogenic and anthropogenic emissions using high-resolution aerosol mass spectrometry: results from CARES, Atmospheric Chemistry and Physics, 12(17), 8131-8156, doi:10.5194/acp-12-8131-2012.

Shakya, K. M., and R. E. Peltier (2015), Non-sulfate sulfur in fine aerosols across the United States: Insight for organosulfate prevalence, Atmospheric Environment, 100, 159-166, doi:10.1016/j.atmosenv.2014.10.058.

Shang, J., M. Passananti, Y. Dupart, R. Ciuraru, L. Tinel, S. Rossignol, S. Perrie, T. Zhu, and C. George (2016), SO2 Uptake on Oleic Acid: A New Formation Pathway of Organosulfur Compounds in the Atmosphere, Environmental Science & Technology Letters, 3(2), 67-72, doi:10.1021/acs.estlett.6b00006.

Shaw, P. M., L. M. Russell, A. Jefferson, and P. K. Quinn (2010), Arctic organic aerosol measurements show particles from mixed combustion in spring haze and from frost flowers in winter, Geophysical Research Letters, 37, doi:10.1029/2010gl042831.

Smith, M. L., A. K. Bertram, and S. T. Martin (2012), Deliquescence, efflorescence, and phase miscibility of mixed particles of ammonium sulfate and isoprene-derived secondary organic material, Atmospheric Chemistry and Physics, 12(20), 9613-9628, doi:10.5194/acp-12-9613-2012.

Struckmeier, C., F. Drewnick, F. Fachinger, G. P. Gobbi, and S. Borrmann (2016), Atmospheric aerosols in Rome, Italy: sources, dynamics and spatial variations during two seasons, Atmospheric Chemistry and Physics, 16(23), 15277-15299, doi:10.5194/acp-16-15277-2016.

Surratt, J. D., et al. (2008), Organosulfate formation in biogenic secondary organic aerosol, Journal of Physical Chemistry A, 112(36), 8345-8378, doi:10.1021/jp802310p.

Takahama, S., A. Johnson, and L. M. Russell (2013), Quantification of Carboxylic and Carbonyl Functional Groups in Organic Aerosol Infrared Absorbance Spectra, Aerosol Science and Technology, 47(3), 310-325, doi:10.1080/02786826.2012.752065.

Tang, X. C., D. Price, E. Praske, S. A. Lee, M. A. Shattuck, K. Purvis-Roberts, P. J. Silva, A. Asa-Awuku, and D. R. Cocker (2013), NO3 radical, OH radical and O-3-initiated secondary

aerosol formation from aliphatic amines, Atmospheric Environment, 72, 105-112, doi:10.1016/j.atmosenv.2013.02.024.

Tao, S., X. Lu, N. Levac, A. P. Bateman, T. B. Nguyen, D. L. Bones, S. A. Nizkorodov, J. Laskin, A. Laskin, and X. Yang (2014), Molecular Characterization of Organosulfates in Organic Aerosols from Shanghai and Los Angeles Urban Areas by Nanospray-Desorption Electrospray Ionization High-Resolution Mass Spectrometry, Environmental Science & Technology, 48(18), 10993-11001, doi:10.1021/es5024674.

Ulbrich, I. M., M. R. Canagaratna, Q. Zhang, D. R. Worsnop, and J. L. Jimenez (2009), Interpretation of organic components from Positive Matrix Factorization of aerosol mass spectrometric data, Atmospheric Chemistry and Physics, 9(9), 2891-2918, doi:10.5194/acp-9-2891-2009.

Usher, C. R., A. E. Michel, and V. H. Grassian (2003), Reactions on Mineral Dust Reactions on Mineral Dust, New York, 103(November), 4883-4940, doi:10.1021/cr020657y.

Vega, E., V. Mugica, E. Reyes, G. Sanchez, J. C. Chow, and J. G. Watson (2001), Chemical composition of fugitive dust emitters in Mexico City, Atmospheric Environment, 35(23), 4033-4039, doi:10.1016/s1352-2310(01)00164-9.

Willis, M. D., R. M. Healy, N. Riemer, M. West, J. M. Wang, C. H. Jeong, J. C. Wenger, G. J. Evans, J. P. D. Abbatt, and A. K. Y. Lee (2016), Quantification of black carbon mixing state from traffic: implications for aerosol optical properties, Atmospheric Chemistry and Physics, 16(7), 4693-4706, doi:10.5194/acp-16-4693-2016.

Xu, L., M. S. Kollman, C. Song, J. E. Shilling, and N. L. Ng (2014), Effects of NOx on the Volatility of Secondary Organic Aerosol from Isoprene Photooxidation, Environmental Science & Technology, 48(4), 2253-2262, doi:10.1021/es404842g.

Xu, L., S. Suresh, H. Guo, R. J. Weber, and N. L. Ng (2015), Aerosol characterization over the southeastern United States using high-resolution aerosol mass spectrometry: spatial and seasonal variation of aerosol composition and sources with a focus on organic nitrates, Atmospheric Chemistry and Physics, 15(13), 7307-7336, doi:10.5194/acp-15-7307-2015.

Young, D. E., H. Kim, C. Parworth, S. Zhou, X. L. Zhang, C. D. Cappa, R. Seco, S. Kim, and Q. Zhang (2016), Influences of emission sources and meteorology on aerosol chemistry in a polluted urban environment: results from DISCOVER-AQ California, Atmospheric Chemistry and Physics, 16(8), 5427-5451, doi:10.5194/acp-16-5427-2016.

Zhang, Q., et al. (2007), Ubiquity and dominance of oxygenated species in organic aerosols in anthropogenically-influenced Northern Hemisphere midlatitudes, Geophysical Research Letters, 34(13), 6, doi:10.1029/2007gl029979.

Zhang, Q., J. L. Jimenez, M. R. Canagaratna, I. M. Ulbrich, N. L. Ng, D. R. Worsnop, and Y. L. Sun (2011), Understanding atmospheric organic aerosols via factor analysis of aerosol mass spectrometry: a review, Analytical and Bioanalytical Chemistry, 401(10), 3045-3067, doi:10.1007/s00216-011-5355-y.

Zhou, S., S. Collier, J. Z. Xu, F. Mei, J. Wang, Y. N. Lee, A. J. Sedlacek, S. R. Springston, Y. L. Sun, and Q. Zhang (2016), Influences of upwind emission sources and atmospheric processing

on aerosol chemistry and properties at a rural location in the Northeastern US, Journal of Geophysical Research-Atmospheres, 121(10), 6049-6065, doi:10.1002/2015jd024568.

Zorn, S. R., F. Drewnick, M. Schott, T. Hoffmann, and S. Borrmann (2008), Characterization of the South Atlantic marine boundary layer aerosol using an aerodyne aerosol mass spectrometer, Atmospheric Chemistry and Physics, 8(16), 4711-4728, doi:10.5194/acp-8-4711-2008.

3.10 Tables

Table 3-1. Average temperature, humidity, visibility and wind speed at Fresno and Fontana.

	Temperature	Humidity (%)			Visibility (km)			Wind Speed (m/s)	
Date	(° C)	Max	Mean	Min	Max	Mean	Min	Max	Mean
12/19/14	10.6	89	78	67	16.1	16.1	16.1	4.5	2.2
12/20/14	13.9	96	78	60	16.1	14.5	6.4	4.5	1.8
12/21/14	11.7	100	89	78	16.1	3.2	0.0	5.8	1.8
12/22/14	13.3	96	87	78	16.1	8.0	3.2	4.0	1.3
12/23/14	12.2	100	82	64	16.1	8.0	0.0	3.1	0.9
12/24/14	11.7	100	88	75	16.1	8.0	1.6	12.5	3.1
12/25/14	7.8	85	70	54	16.1	16.1	14.5	8.9	2.2
12/26/14	6.7	92	73	54	16.1	14.5	9.7	3.1	0.9
12/27/14	6.7	92	67	41	16.1	14.5	11.3	3.6	0.9
12/28/14	6.7	92	70	47	16.1	14.5	9.7	3.1	0.9
12/29/14	6.1	89	72	54	16.1	12.9	9.7	3.1	0.9
12/30/14	3.3	96	86	76	11.3	6.4 (Haze)	0.0	6.3	2.2
12/31/14	3.9	100	79	58	14.5	4.8 (Haze)	0.0	6.3	2.2
1/1/15	5.0	92	59	26	16.1	11.3	4.8	3.6	0.4
1/2/15	5.0	85	59	32	16.1	14.5	9.7	3.1	0.9
1/3/15	5.6	85	62	38	16.1	12.9	8.0	2.7	0.4
1/4/15	6.1	89	66	43	12.9	9.7	8.0	5.8	0.9
1/5/15	8.3	96	68	40	14.5	9.7	6.4	3.6	0.9
1/6/15	10.6	89	67	44	9.7	6.4(Haze)	3.2	3.6	1.3
1/7/15	11.7	93	69	45	6.4	3.2(Haze)	1.6	3.1	0.4
1/8/15	11.7	96	74	52	4.8	3.2(Haze)	1.6	3.1	0.9
1/9/15	13.3	93	73	52	6.4	3.2(Haze)	1.6	4.0	1.3
1/10/15	13.3	96	76	56	3.2	3.2(Haze)	1.6	2.7	0.4
1/11/15	13.3	93	75	56	3.2	3.2(Haze)	0.0	2.7	0.9
1/12/15	10.0	100	89	77	3.2	1.6(Haze)	0.0	3.1	0.9
1/13/15	11.1	100	81	62	8.0	3.2(Haze)	0.0	4.0	0.4
7/4/15	24.4	84	59	34	16.1	16.1	14.5	7.2	2.2
7/5/15	23.9	90	64	37	16.1	12.9	3.2	6.7	2.2
7/6/15	22.8	84	69	54	16.1	14.5	11.3	4.0	1.8
7/7/15	23.9	100	72	43	16.1	12.9	4.8	6.3	3.6
7/8/15	22.8	84	67	49	16.1	16.1	11.3	7.2	2.2
7/9/15	22.8	78	61	43	16.1	16.1	16.1	9.4	3.1
7/10/15	22.8	78	59	39	16.1	16.1	16.1	7.2	1.8
7/11/15	23.3	78	58	37	16.1	16.1	16.1	7.6	1.8
7/12/15	25.0	84	56	27	16.1	16.1	16.1	7.2	1.8
7/13/15	26.1	73	48	23	16.1	16.1	16.1	7.6	1.3
7/14/15	25.6	84	54	23	16.1	16.1	16.1	7.6	2.2
7/15/15	25.0	90	60	30	16.1	14.5	9.7	6.7	1.3
7/16/15	25.0	90	59	28	16.1	14.5	8.0	7.2	2.2
7/17/15	26.7	84	55	26	16.1	16.1	12.9	7.6	2.2
7/18/15	22.8	90	78	66	16.1	16.1	8.0	7.2	0.9
7/19/15	27.8	90	64	38	16.1	12.9	1.6	9.4	1.8
7/20/15	26.1	93	72	50	16.1	14.5	11.3	6.3	2.2
7/21/15	25.0	90	73	55	16.1	16.1	9.7	6.7	2.7
7/22/15	26.1	84	65	45	16.1	16.1	16.1	7.6	3.1
7/23/15	25.6	87	63	38	16.1	16.1	16.1	6.7	1.3
7/24/15	27.2	84	59	33	16.1	16.1	12.9	7.2	1.8
7/25/15	27.8	76	48	19	16.1	16.1	16.1	6.7	1.3
7/26/15	26.7	76	53	29	16.1	16.1	16.1	7.6	1.8
7/27/15	25.0	87	59	30	16.1	16.1	16.1	7.6	1.8
7/28/15	26.7	84	54	24	16.1	16.1	16.1	6.7	1.3

Table 3-2. Summary of organosulfate quantification methods.

References and this study	Fragment	OS quantification	Sampling site		MSA[a]	MSA[b]	OS ($\mu g/m^3$)
Farmer et al. [2010]	CH_3SO_2	Only one standard $C_5H_{11}O_7S$ (trihydroxy sulfate ester of isoprene) was estimated.			N.A.	N.A.	1.1
Ge et al. [2012]	CHS	Sulfur-containing organic ions (i.e. $C_xH_yS_nO_z^+$, in which x≥1, y≥1, n≥1, z≥0) MSA= (mCH_2SO_2 +mCH_3SO_2+mCH_4SO_3)/0.147	Fresno in winter		0.018	N.A.	N.A.
	CH_3S						
	CH_2SO						
	CH_3SO						
	CH_2SO_2						
	CH_3SO_2						
	CH_4SO_3						
Zhou et al. [2016]	CH_2SO_2						
	CH_3SO_2	MSA=mCH_3SO_2/0.087	Northeastern U.S.		N.A.	0.66 ±0.45	N.A.
	CH_4SO_3						
Huang et al. [2017]	CH_3SO_2	MSA = total of 32 different m/z ratios based on their individual ratio to $CH_3SO_2^+$	North/South Atlantic Ocean		N.A.	N.A.	N.A.
This study	CHS	Sum of 7 major ions = CHS + CHS + CH_2SO^++ CH_3SO^+ +$CH_2SO_2^+$+$CH_3SO_2^+$+CH_4SO_3	Fresno	high-fog	0.009	0.012	0.008
	CH_3S			low-fog	0.046	0.052	0.026
	CH_2SO			average	0.027	0.032	0.017
	CH_3SO		Fontana	firework	0.048	0.045	0.018
	CH_2SO_2			non-firework	0.023	0.022	0.007
	CH_3SO_2			average	0.036	0.034	0.013
	CH_4SO_3						

a. MSA estimated by *Ge et al.*[2012b] method
b. MSA estimated by Zhou et al.[2016] method

Table 3-3. Composition-dependent collection efficiency (CDCE) method for Fresno and Fontana.

Composition-dependent collection efficiency (CDCE) method [*Middlebrook et al.*, 2012]	Fresno			
	Percentage of time series data	Average CE	ANMF[1]	$NH_4/NH_{4,\ predict}$[2]
Acidic type CE[3]	1.7%	0.60	0.14	0.55
Neutral type CE, low ANMF	38.2%	0.45(Default)	0.31	1.07
Used ANMF CE[4]	59.4%	0.51	0.46	1.16
	Fontana			
CDCE method	Percentage of time series data	Average CE	ANMF	$NH_4/NH_{4,\ predict}$
Acidic type CE	2.4%	0.76	0.19	0.33
Neutral type CE, low ANMF	94.7%	0.45 (Default)	0.13	1.13
Used ANMF corrected CE	2.4%	0.52	0.48	1.34

[1]: Ammonium nitrate mass fraction (ANMF)$=\frac{\frac{86}{62}\times NO_3}{(NH_4+SO_4+NO_3+Chl+Org)}$

[2]: $NH_{4,predict}=18\times\left(\frac{SO_4}{96}\right)\times 2+\frac{NO_3}{62}+\frac{Chl}{35.45}$

[3]: If $NH_4/NH_{4,predict}<0.75$, $CE_{dry}=(0.45,\ 1.0-0.73\times\ NH_4/NH_{4,predict})$

[4]: If $NH_4/NH_{4,predict}>=0.75$, $CE_{dry}=(0.45,\ 0.0833+0.9167\times ANMF)$

Table 3-4. Comparable AMS PMF factors from other studies.

Factor (Mass)	Major MS fragments [Tracers]	Comparable Factors	CS	Tracers [Fragments]	Citation
Fresno HOA (19.5%)	*m/z* 41, 55, 27 ,43 [BC, CO, K]	HOA (Barcelona)	0.81	[*m/z* 57]	[*Mohr et al.*, 2012]
		HOA (Nevada)	0.92		[*Setyan et al.*, 2012]
		HOA (Fresno-2013)	0.86	Toluene, benzene	[*Young et al.*, 2016]
		HOA (Mexico city)	0.93	BC, CO	[*Aiken et al.*, 2009]
Fontana HOA (11.1%)	*m/z* 43, 41, 55, 57 [NO, NOx, BC, K]	HOA (Barcelona)	0.93		[*Mohr et al.*, 2012]
		HOA (Mexico city)	0.97	BC, CO	[*Aiken et al.*, 2009]
		HOA (Riverside)	0.93		[*Docherty et al.*, 2011]
		HOA (Fresno-2013)	0.95	Toluene, benzene	[Young et al., 2016]
		HOA (Pasadena)	0.96	EC , rBC	[*Hayes et al.*, 2013]
Fresno NOOA (31.0%)	*m/z* 44, 28, 43 [NO_3^-, NH_4^+, Br, P, Mn]	SVOOA (Fresno-2013)	0.92	NO_3^-, MSA	[*Young et al.*, 2016]
		SVOOA (Barcelona)	0.83	NO_3^-	[*Mohr et al.*, 2012]
		SVOOA (Pasadena)	0.94		[*Hayes et al.*, 2013]
		LOOOA (Nevada)	0.89	Methacrolein, methyl vinyl ketone, O_3	[*Setyan et al.*, 2012]
		Gasoline SOA	0.90	*m/z* 44	[*Presto et al.*, 2014]
		Diesel SOA	0.89	*m/z* 44	[*Presto et al.*, 2014]
		m-xylene SOA (HR)	0.49	*m/z* 43 ($C_2H_3O^+$) and *m/z* 44 (CO_2^+)	[*Chhabra et al.*, 2010]
		α-pinene ozonolysis SOA (HR)	0.53	*m/z* 43 ($C_2H_3O^+$) and *m/z* 44 (CO_2^+)	[*Chhabra et al.*, 2010]
Fontana NOOA (10.3%)	*m/z* 43,29,39 [NO_3^-, NH_4^+]	SVOOA (Riverside)	0.93	NO_3^-, NH_4^+, Cl	[*Docherty et al.*, 2011]
		LOOOA (Nevada)	0.94	Methacrolein, methyl vinyl ketone, O_3	[*Setyan et al.*, 2012]
		SVOOA (Paris)	0.96		[*Crippa et al.*, 2013]
		SVOOA (Barcelona)	0.66	NO_3^-	[*Mohr et al.*, 2012]
		SVOOA (Pasadena)	0.79	N/A	[*Hayes et al.*, 2013]
		Gasoline SOA	0.75	*m/z* 44	[*Presto et al.*, 2014]
		Diesel SOA	0.76	*m/z* 44	[*Presto et al.*, 2014]
		m-xylene SOA (HR)	0.18	*m/z* 43 ($C_2H_3O^+$) and *m/z* 44 (CO_2^+)	[*Chhabra et al.*, 2010]
		α-pinene ozonolysis SOA (HR)	0.22	*m/z* 43 ($C_2H_3O^+$) and *m/z* 44 (CO_2^+)	[*Chhabra et al.*, 2010]
Fresno BBOA (22.8%)	*m/z* 60, 57, 73 [Levoglucosan, BC, K]	BBOA1 (Fresno-2013)	0.91	C_3H_7N, acetonitrile	[*Young et al.*, 2016]
		BBOA2 (Fresno-2013)	0.90	$C_2H_4O_2$, K, PAH, BC	
Fontana COA (15.0%)	*m/z* 41, 55, 55/57	COA (Barcelona)	0.87		[*Mohr et al.*, 2012]
		COA (Fresno-2013)	0.93	$C_7H_{12}O$, C_5H_8O C_3H_3O	[*Young et al.*, 2016]
		CIOA (Pasadena)	0.89	CO	[*Hayes et al.*, 2013]
Fresno VOOA (26.7%)	*m/z* 44, 28 [SO_4^{2-}, Fe, Cu]	LVOOA (Fresno-2013)	0.97	SO_4^{2-}	[*Young et al.*, 2016].
		OOA (Mexico City)	0.98	NO_3^- and Ox	[*Aiken et al.*, 2009]
		MOOOA (Nevada)	0.89	Methacrolein, methyl vinyl ketone	[*Setyan et al.*, 2012]
		LVOOA (Italy)	0.97	SO_4^{2-}	[*Struckmeier et al.*,

Table 3-4, continued. Comparable AMS PMF factors from other studies.

Factor (Mass)	Major MS fragments [Tracers]	Comparable Factors	CS	Tracers [Fragments]	Citation
					2016]
		LVOOA (Paris)	0.99	SO_4^{2-}	[*Crippa et al., 2013]*
		Gasoline SOA	0.93	*m/z* 44	[*Presto et al.*, 2014]
		Diesel SOA	0.92	*m/z* 44	[*Presto et al.*, 2014]
		m-xylene SOA (HR)	0.62	*m/z* 43 ($C_2H_3O^+$) and *m/z* 44 (CO_2^+)	[*Chhabra et al.*, 2010]
		α-pinene SOA (HR)	0.65	*m/z* 43 ($C_2H_3O^+$) and *m/z* 44 (CO_2^+)	[*Chhabra et al.*, 2010]
Fontana VOOA (63.6%)	*m/z* 44, 28 [SO_4^{2-}, O_3]	LVOOA (Fresno-2013)	0.97	SO_4^{2-}	[*Young et al.*, 2016].
		LVOOA (Riverside)	1.00		[*Docherty et al.*, 2011]
		LVOOA (Italy)	0.99	SO_4^{2-}	[*Struckmeier et al.*, 2016]
		OOA (Mexico City)	0.97	NO_3^- and Ox	[*Aiken et al.*, 2009]
		LVOOA (Paris)	0.98	SO_4^{2-}	[*Crippa et al., 2013]*
		LVOOA (Barcelona)	0.98	SO_4^{2-}	[*Mohr et al.*, 2012]
		LVOOA (Pasadena)	0.98		[*Hayes et al.*, 2013]
		Gasoline SOA	0.93	*m/z* 44	[*Presto et al.*, 2014]
		Diesel SOA	0.92	*m/z* 44	[*Presto et al.*, 2014]
		m-xylene SOA (HR)	0.64	*m/z* 43 ($C_2H_3O^+$) and *m/z* 44 (CO_2^+)	[*Chhabra et al.*, 2010]
		α-pinene SOA (HR)	0.66	*m/z* 43 ($C_2H_3O^+$) and *m/z* 44 (CO_2^+)	[*Chhabra et al.*, 2010]

Table 3-5. AMS PMF analysis for non-refractory organic aerosol at Fresno and Fontana.

Criteria \ Factor number (p)		1	2	3	4	5	6	7
Fresno	Q/Q_{exp}	14.4	10.7	8.2	6.7	5.8	5.2	4.7
	Absolute residual	24.4%	19.7%	16.7%	13.1%	12.3%	11.0%	10.2%
	Temporal correlation factors strength (R > 0.8)	N/A[a]	None[b]	None	None	None	None	2 pair
	Similarity of factor spectra (R > 0.8)	N/A	None	None	1 pair	3 pair	1 pair	4 pair
	Factors with less than 10% organic mass (OM)	None	None	None	None	None	None	None
Fontana	Q/Q_{exp}	8.1	5.5	4.4	3.9	3.5	3.2	3.0
	Absolute residual	31%	25%	20%	20%	20%	17%	17%
	Temporal correlation factors strength (R >0.8)	N/A[a]	None	None	None	None	1 pairs	3 pairs
	Similarity of factor spectra (R > 0.8)	N/A	None	1 pair	2 pair	2 pair	2 pairs	3 pairs
	Factors with less than 10% organic mass (OM)	None	None	None	None	1pair	1 pair	1 pair

a: N/A: not applicable for one factor.
b: None: no paired factors have uncentered correlation coefficients (UC) higher than 0.8.

Table 3-6. Comparable FTIR PMF factors from other studies.

Factor (Mass)	Peak locations [Tracers]	Comparable Factors	CS	Tracers [Peak locations]	Citation
Fresno FTIR-Fossil Fuel Combustion (FFC) (20.4%)	3028 cm^{-1}, 3170 cm^{-1}	Alkane SOA	0.99	Long-chain (C_{11}-C_{14}) ketones [2855 cm^{-1}]	[*Liu et al.*, 2012]
		Less oxidized FFC (Tijuana)	0.83	V, S	[*Guzman-Morales et al.*, 2014]
		More oxidized FFC (R/V Atlantis)	0.98	Sulfate, oxalate	[*Guzman-Morales et al.*, 2014]
Fontana FTIR-FFC (9.3%)	3215 cm^{-1}	Alkane SOA	0.99	Long-chain (C_{11}-C_{14}) ketones [2855 cm^{-1}]	[*Liu et al.*, 2012]
		Less oxidized FFC	0.78	V, S	[*Guzman-Morales et al.*, 2014]
		More oxidized FFC	0.96	Sulfate, oxalate	[*Guzman-Morales et al.*, 2014]
Fresno FTIR Mixed Combustion (MC) (39.5%)	3203 cm^{-1}, 3059 cm^{-1}.	Petroleum operation SOA (PO SOA)	0.99	V, S	[*Liu et al.*, 2012]
		Fuel combustion [high O/C_IC (ICEALOT)]	0.98	N/A	[*Russell et al.*, 2011; *Russell et al.*, 2010]
		Fuel combustion [high O/C_WH (Whistler Forest)]	0.98	SO_4^{2-}, S	[*Russell et al.*, 2011; *Schwartz et al.*, 2010]
		Fuel combustion [low O/C_VX (VOCALS)]	0.98	S, V, Sn, K, Br, Fe	[*Hawkins et al.*, 2010; *Russell et al.*, 2011]
		Mixed combustion factor [low OC_BW (Barrow, Alaska)]	0.99	S, non-dust K, V [3215 cm^{-1}, 3057 cm^{-1}]	[*Russell et al.*, 2011; *Shaw et al.*, 2010]
Fontana FTIR MC (41.5%)	3200 cm^{-1}, 3050 cm^{-1}, 3200cm^{-1}	Petroleum operation SOA (PO SOA)	0.98	V	[*Liu et al.*, 2012]
		Fuel combustion [high O/C_IC (ICEALOT)]	0.98	N/A	Russell et al., 2010]
		Fuel combustion [high O/C_WH	0.98	SO_4^{2-}, S	[Schwartz et al., 2010]

Factor (Mass)	Peak locations [Tracers]	Comparable Factors	CS	Tracers [Peak locations]	Citation
		(Whistler Forest)]			
		Fuel combustion [low O/C_VX (VOCALS)]	0.99	S, V, Sn, K, Br, Fe	[Hawkins et al., 2010],
		Mixed combustion factor [low OC_BW (Barrow, Alaska)]	0.99	S, non-dust K, V [3215 cm^{-1}, 3057 cm^{-1}]	[Shaw et al., 2010]
Fresno FTIR-Biomass Burning (BB) (29.2%)	2900 cm^{-1} [NO, CO, BC, K]	BB_{FTIR} (Hyytiälä)	0.87	Si, Fe [2920cm^{-1}, 2850cm^{-1}]	[*Corrigan et al.*, 2013]
		Biomass burning_MC [MILAGRO 2006:SIMAT: MC (Mexico City)]	0.71	Non-soil K	[*Gilardoni et al.*, 2009]
		Biomass burning_PD [MILAGRO 2006:Altzomoni: PD (Paso de Cortez)]	0.90	Non-soil K	[*Gilardoni et al.*, 2009]
Fontana Dust-related detritus or secondary organic aerosol (DDS) (39.2%)	2850 cm^{-1}, 2920 cm^{-1}, 1720 cm^{-1}, 3200 cm^{-1} [O_3, wind speed, AMS-VOOA, Ca, Si]	BB_{FTIR} (Hyytiälä)	0.93	Si, Fe [2920cm^{-1}, 2850cm^{-1}]	[*Corrigan et al.*, 2013; *Russell et al.*, 2011]
		Biomass burning_MC [MILAGRO 2006:SIMAT: MC (Mexico City)]	0.79	Non-soil K	[*Gilardoni et al.*, 2009]
		Biomass burning_PD [MILAGRO 2006:Altzomoni: PD (Paso de Cortez)]	0.94	Non-soil K	[*Gilardoni et al.*, 2009]
		Biogenic_AI [ICARTT 2004 : AI (Appledore Island)]	0.98	N/A	[*Gilardoni et al.*, 2007]
		Biogenic_CP [ICARTT 2004 : CP(Chebogue Point)]	0.94	TAG factor 1	[*Gilardoni et al.*, 2007]
		Biogenic_RB [ICARTT 2004 : R/V Ron Brown]	0.95	N/A	[*Gilardoni et al.*, 2007]
		Biogenic_WH [Whistler Forest 2008]	0.87	Si	[Schwartz et al., 2010]
		Vegetative detritus factor	0.62	2920 cm^{-1}, 2850 cm^{-1}, 3500 cm^{-1}	[*Liu et al.*, 2012]

Table 3-7. Correlation coefficients of FTIR PMF 3-factor solution with other measurements at Fresno and Fontana.

Fresno r^2	AMS PMF				Other tracers							
	HOA	BBOA	NOOA	VOOA	NO	O_3	CO			BC	K	Br
FFC	<0.01	0.04	**0.45**#	0.01	<0.01	0.01	0.05			0.01	0.02	**0.40**#
MC	<0.01	0.03	**0.50**#	0.12	<0.01	0.02	0.09			0.01	0.04	**0.59**#
BB	**0.53**#	**0.50**#	0.00	0.14	**0.30**#	<0.01	**0.49**#			**0.59**#	**0.64***	0.00
Fontana r^2	AMS PMF						AMS			Wind speed	Metal	
	HOA	COA	NOOA	VOOA	NO	O_3	NO_3	NH_4	SO_4		Ca	Si
FFC	0.02	0.01	0.15	0.07	0.04	0.01	0.16	0.14	0.02	<0.01	<0.01	<0.01
MC	0.18	<0.01	0.13	<0.01	0.04	0.05	0.24	**0.33**#	0.21	0.08	<0.01	<0.01
DDS	<0.01	0.10	0.05	**0.31**#	0.00	**0.25**#	0.01	<0.01	0.05	**0.82***	**0.27**#	**0.43**#

*$1.0 \geq r^2 \geq 0.64$: strong correlation; # $0.64 > r^2 > 0.25$: moderate correlation; $0.25 \geq r^2 \geq 0$: weak correlation.

Table 3-8. Correlation coefficients for unforced linear fits by least squares regression between AMS-PMF factors and aerosol species, gas tracers, metal ions, and meteorological conditions at both sites.

	Time Resolution	Fresno				Fontana			
Correlation Coefficient (r^2)		VOOA	BBOA	NOOA	HOA	NOOA	VOOA	COA	HOA
AMS_sulfate	10 min	0.19	<0.01	**0.57**$^{\#}$	<0.01	0.08	0.23	0.08	0.02
AMS_nitrate	10 min	**0.30**$^{\#}$	<0.01	**0.62**$^{\#}$	<0.01	0.18	0.12	0.01	0.07
AMS_ammonium	10 min	0.15	<0.015	**0.79***	<0.01	**0.28**$^{\#}$	0.20	0.02	0.07
BC	1 min	0.08	**0.42**$^{\#}$	0.00	0.20	0.09	0.02	0.03	**0.30**$^{\#}$
CO	0.5 min	0.09	0.23	0.05	0.20				
NO_y	1 min					0.10	0.01	0.03	**0.39**$^{\#}$
NO	1 min	0.04	0.15	0.03	0.13	0.01	0.01	0.00	**0.28**$^{\#}$
NO_x	1 min	0.07	0.15	0.00	**0.17**	0.05	<0.01	0.02	**0.35**$^{\#}$
O_3	1 hr	<0.01	<0.01	<0.01	<0.01	<0.01	**0.37**$^{\#}$	<0.01	<0.01
XRF dust	6 hr	**0.27**$^{\#}$	0.02	<0.01	0.08	<0.01	0.00	<0.01	<0.01
K	6 hr	**0.27**$^{\#}$	**0.38**$^{\#}$	<0.01	**0.55**$^{\#}$	0.19	**0.54**$^{\#}$	<0.01	<0.01
Br	6 hr	0.06	<0.01	**0.60**$^{\#}$	<0.01	<0.01	0.08	<0.01	0.02
Ca	6 hr	0.24	<0.01	<0.01	<0.01	<0.01	<0.01	<0.01	<0.01
Zn	6 hr	0.05	0.07	0.01	0.13	<0.01	<0.01	<0.01	<0.01
P	6 hr	0.05	<0.01	**0.33**$^{\#}$	<0.01	<0.01	<0.01	<0.01	<0.01
Mn	6 hr	0.17	<0.01	**0.34**$^{\#}$	0.01	<0.01	<0.01	<0.01	0.02
Fe	6 hr	**0.30**$^{\#}$	<0.01	<0.01	<0.01	<0.01	<0.01	<0.01	<0.01
Cu	6 hr	**0.30**$^{\#}$	0.02	<0.01	0.06	<0.01	0.05	<0.01	<0.01
Temperature	2 min	<0.01	<0.01	0.11	<0.01	<0.01	0.19	<0.01	<0.01
Relative Humidity	2 min	<0.01	0.04	<0.01	0.01	<0.01	<0.01	<0.01	0.03
Pressure	2 min	<0.01	0.02	0.13	<0.01	<0.01	<0.01	<0.01	<0.01
Wind Speed	2 min	<0.01	0.05	0.01	0.03	<0.01	0.15	<0.01	0.07
Amine fragments	10 min	0.20	0.17	**0.45**$^{\#}$	0.15	0.28	0.23	0.05	0.12

*$1.0 \geq r^2 \geq 0.64$: strong correlation; $^{\#}$ $0.64 > r^2 > 0.25$: moderate correlation; $0.25 \geq r^2 \geq 0$: weak correlation [*Devore and Berk*, 2012].

Table 3-9. Correlation coefficients for unforced linear fits by least squares regression between LS clusters and other measured properties at Fresno. (For organic particle properties, the linear fits when forced to zero are given in parentheses.)

Correlation Coefficient (r^2)	mass ($\mu g\ m^{-3}$)	%	LS-HOA	LS-NOOA	LS-BBOA	LS-VOOA
Number of Particles			3541	14692	11956	4549
Percentage of Particles			10%	36%	16%	6%
AMS_sulfate	1.1	5%	0.04(**0.37**$^{\#}$)	**0.39**$^{\#}$(**0.67***)	0.2(**0.62**$^{\#}$)	**0.35**$^{\#}$(**0.66***)
AMS_nitrate	7.3	29%	0.09(**0.42**$^{\#}$)	**0.68***(**0.81***)	**0.32**$^{\#}$(**0.69***)	**0.59**$^{\#}$(**0.78***)
AMS_ammonium	3.0	12%	0.07(**0.40**$^{\#}$)	**0.65***(**0.80***)	**0.27**$^{\#}$(**0.66***)	**0.58**$^{\#}$(**0.78***)
AMS-VOOA	3.8	29%	0.14(**0.46**$^{\#}$)	0.24(**0.57**$^{\#}$)	**0.33**$^{\#}$(**0.69***)	**0.34**$^{\#}$(**0.64***)
AMS-BBOA	3.0	23%	0.07(**0.25**$^{\#}$)	0.013(0.08)	0.19(**0.32**$^{\#}$)	0.02(0.07)
AMS-NOOA	3.3	25%	0.03(**0.33**$^{\#}$)	**0.51**$^{\#}$(**0.71***)	0.16(**0.55**$^{\#}$)	**0.40**$^{\#}$(**0.65***)
AMS-HOA	3.0	23%	**0.32**$^{\#}$(**0.50**$^{\#}$)	<0.01(0.17)	0.21(**0.48**$^{\#}$)	0(0.16)
FTIR-FFC	2.4	37%	0.01(0.14)	0.15(**0.32**$^{\#}$)	0(0.21)	0.13(**0.30**$^{\#}$)
FTIR-MC	2.5	38%	**0.17**(**0.46**$^{\#}$)	**0.41**(**0.63**$^{\#}$)	**0.25**(**0.55**$^{\#}$)	**0.43**$^{\#}$ (**0.66***)
FTIR-BB	1.1	17%	**0.27**$^{\#}$(**0.58**$^{\#}$)	0.02(**0.30**$^{\#}$)	0.25(**0.59**$^{\#}$)	0.01(**0.30**$^{\#}$)
Amine fragments			0.15(**0.47**$^{\#}$)	**0.30**$^{\#}$(**0.61**$^{\#}$)	**0.31**$^{\#}$(**0.69***)	0.2(**0.57**$^{\#}$)
Organosulfate fragments			0.04(**0.31**$^{\#}$)	**0.50**$^{\#}$(**0.72***)	0.15(**0.52**$^{\#}$)	**0.43**$^{\#}$(**0.69***)
BC			0.21	<0.01	**0.27**$^{\#}$	<0.01
XRF dust	0.48		0.05	0.02	0.09	0.09
K	0.17		0.18	0.07	**0.40**$^{\#}$	0.1
Br	0.003		<0.01	0.18	0.06	0.15
CO			0.23	0.06	0.23	0.01
NO			0.17	0.008	0.11	<0.01
NO_x			0.24	0.04	0.19	0.01

*$1.0 \geq r^2 \geq 0.64$: strong correlation; $^{\#}$ $0.64 > r^2 > 0.25$: moderate correlation; $0.25 \geq r^2 \geq 0$: weak correlation [*Devore and Berk*, 2012].

Table 3-10. Correlation coefficients for linear relationships between LSI clusters and other measured properties at Fresno.

Correlation Coefficient (r^2)	LSI-HOA	LSI-Nitrate	LSI-OOA
Particle number	6242	27164	2288
%	17%	76%	6%
AMS_sulfate	<0.001	**0.36**#	0.16
AMS_nitrate	<0.001	**0.62**#	**0.26**#
AMS_ammonium	<0.001	**0.57**#	0.24
AMS-VOOA	0.15	**0.40**#	**0.47**#
AMS-BBOA	**0.61**#	0.007	0.04
AMS_NOOA	0.006	**0.60**#	0.19
AMS-HOA	**0.64**#	0.04	0.07
FTIR-FFC	0.02	0.01	0.01
FTIR-MC	0.00	0.22	0.01
FTIR-BB	**0.38**#	0.07	0.07
BC	**0.46**#	0.05	0.008
CO	**0.31**#	0.12	0.13
NO	0.23	0.04	0.07
NO_x	**0.28**#	0.11	0.12
O_3	-0.16	-0.02	-0.03
XRF dust	0.04	0.05	0.008
XRF_Fe_2O_3	<0.001	0.1	0.01
K	**0.33**#	0.18	0.21
Br	0.013	0.14	0.053
$MgCO_3$	<0.001	<0.001	0.012
Amine Fragments	0.19	**0.43**#	**0.29**#
Organosulfate Fragments	0.006	**0.39**#	0.15
LSI-HOA	---	0.17	0.12
LSI-Nitrate	0.17	---	**0.65***
LSI-OOA	0.12	**0.65***	---

*$1.0 \geq r^2 \geq 0.64$: strong correlation; # $0.64 > r^2 > 0.25$: moderate correlation; $0.25 \geq r^2 \geq 0$: weak correlation [*Devore and Berk*, 2012]

Table 3-11. Summary of pie charts of AMS PMF, FTIR PMF, LS analysis, and fragments. (The numbers above each pie chart are the total non-refractory mass concentration from AMS.)

Method	Legend	Fresno low-fog		Fresno high-fog		Fontana firework		Fontana non-firework	
		Average concentration (μg m^{-3}) or mass or particle number fraction (%)							
AMS	Org	15.2±13.6	24.8 ±15.7	17.9±4.6	39.7 ±9.9	7.1±3.8	14.7 ±8.5	3.9±1.8	5.9 ±2.6
	NO_3	6.0±3.4		13.8±4.3		2.9±2.9		0.6±0.7	
	NH_4	2.3±1.3		5.8±1.9		2.0±1.3		0.6±0.4	
	SO_4	1.0±0.6		1.9±0.7		2.4±2.6		0.85±0.4	
	Chl	0.3±0.2		0.3±0.2		0.3±0.7		0.04±0.09	
AMS PMF	HOA	20%±12%	15.2± 11.9	15%±10%	15.5 ±4.4	7%±5%	6.8 ±3.2	9%±8%	3.8 ±1.9
	NOOA	17%±13%		47%±16%		14%±7%		16%±7%	
	BBOA	27%±16%		9%±7%					
	VOOA	36%±16%		28%±14%		69%±13%		58%±15%	
	COA					10%±6%		16%±9%	
FTIR groups	Alkane	51%±7%	4.3 ±0.5	53%±12%	13.8 ±5.6	51%±24%	4.8 ± 5.3	57%±5%	2.9 ± 1.6
	Carbonyl	0%±3%		0%±0%		0%±0%		1%±0%	
	Amine	10%±5%		5%±2%		7%±5%		8%±4%	
	Alcohol	20%±7%		24%±7%		30%±23%		17%±3%	
	Carboxylic acid	18%±5%		20%±4%		13%±9%		16%±4%	
FTIR PMF	FFC	7%±17%	4.3 ±3.2	40%±22%	13.6 ±5.5	13%±24%	3.1 ±3.6	10%±16%	2.9 ± 1.6
	MC	44%±23%		41%±18%		42%±30%		39%±20%	
	BB	38%±22%		11%±6%					
	DDS					31%±21%		43%±24%	
	Residual	11%±6%		7%±2%		14%±16%		8%±3%	
LS	HOA	14%±16%	1598 ±1011 #/day	7%±3%	3249 ±1673 #/day	4%±6%	883 ±488 #/day	10%±12%	413 ±198 #/day
	NOOA	33%±17%		55%±11%		16%±8%		23%±17%	
	BBOA	40%±18%		26%±8%					
	VOOA	13%±12%		12%±5%		73%±10%		51%±24%	
	COA					7%±7%		16%±14%	
Amine fragments	CHN	32%±11%	0.16 ±0.11	28%±6%	0.33 ±0.09	25%±15%	0.14 ±0.11	18%±7%	0.07 ±0.05
	CH_4N	1%±3%		0%±0%		24%±8%		25%±6%	
	CH_3N	17%±15%		17%±6%		3%±3%		3%±5%	
	C_2H_3N	10%±6%		10%±6%		10%±6%		12%±7%	
	C_2H_4N	22%±6%		24%±4%		17%±5%		22%±5%	
	C_3H_8N	6%±3%		8%±3%		13%±6%		13%±5%	
	C_2H_6N	11%±4%		13%±4%		8%±5%		8%±4%	
Organo-sulfate fragments	CHS	2%±10%	0.007 ±0.009	3%±5%	0.027 ±0.012	12%±11%	0.019 ±0.018	16%±10%	0.007 ± 0.004
	CH_3S	30%±22%		29%±11%		10%±7%		9%±7%	
	CH_2SO	2%±8%		2%±2%		5%±4%		7%±6%	
	CH_3SO	50%±26%		39%±17%		31%±17%		23%±12%	
	CH_2SO_2	2%±4%		5%±3%		9%±5%		10%±4%	
	CH_3SO_2	13%±13%		19%±7%		25%±12%		26%±9%	
	CH_4SO_3	2%±7%		4%±3%		8%±10%		9%±9%	

Table 3-12. Metal ion ratio comparisons.

Ratio	Fontana		Mexico city [*Gilardoni et al.*, 2009]		$PM_{2.5}$ [*Chow and Watson*, 1998]		
					Claremont, CA	Rubidoux, CA	Azusa, CA
	Slope	r^2	Slope	r^2	Slope	Slope	Slope
Si/Al	0.98	0.77	2.3	0.95	2.38	2.15	2.58
Ca/Al	0.19	0.85	1.9	0.8			
K/Al	3.68	0.19		0.05			

Table 3-13. Correlation coefficients for unforced linear fits by least squares regression between LS clusters and other measured properties at Fontana. (For organic particle properties, the linear fits when forced to zero are given in parentheses.)

Correlation Coefficient (r^2)	mass ($\mu g\ m^{-3}$)	%	LS-HOA	LS-COA	LS-VOOA	LS-NOOA
Number of Particles			801	1343	7119	2645
Percentage of Particles			7%	11%	60%	22%
AMS_sulfate	1.1	15%	0.02(0.24)	0.02(**0.28**$^{\#}$)	0.12(**0.35**$^{\#}$)	0.08(**0.31**$^{\#}$)
AMS_nitrate	1.0	14%	0.03(0.21)	0.11(**0.32**$^{\#}$)	**0.51**$^{\#}$**(0.65*)**	**0.45**$^{\#}$**(0.60*)**
AMS_ammonium	0.8	11%	0.05(**0.33**$^{\#}$)	0.12(**0.44**$^{\#}$)	**0.59**$^{\#}$**(0.73*)**	**0.48**$^{\#}$**(0.67*)**
AMS-NOOA	0.9	15%	0.07(**0.44**$^{\#}$)	0.11(**0.52**$^{\#}$)	0.20(**0.47**$^{\#}$)	0.22(**0.49**$^{\#}$)
AMS-VOOA	3.8	64%	0(**0.30**$^{\#}$)	0(**0.33**$^{\#}$)	0.13(**0.41**$^{\#}$)	0.02(**0.30**$^{\#}$)
AMS-COA	0.8	13%	0.14(**0.47**$^{\#}$)	0.17(**0.53**$^{\#}$)	0.01(**0.27**$^{\#}$)	0.01(**0.29**$^{\#}$)
AMS-HOA	0.4	7%	0.17(**0.48**$^{\#}$)	0.12(**0.46**$^{\#}$)	0.06(**0.32**$^{\#}$)	0.13(**0.41**$^{\#}$)
FTIR-FFC	0.5	9%	0(0.12)	0.01(0.14)	0.06(0.17)	0.08(0.20)
FTIR-MC	1.2	42%	0.23(**0.61**$^{\#}$)	**0.32**$^{\#}$**(0.71*)**	0.15(**0.47**$^{\#}$)	**0.50**$^{\#}$**(0.72*)**
FTIR-DDS	1.0	39%	0(**0.43**$^{\#}$)	0(**0.40**$^{\#}$)	0(0.22)	-0.03(0.17)
Amine fragments			0.05(**0.26**$^{\#}$)	0.09(**0.29**$^{\#}$)	0.18(**0.31**$^{\#}$)	0.17(**0.29**$^{\#}$)
Organosulfate fragments			0.02(**0.32**$^{\#}$)	0.07(**0.47**$^{\#}$)	**0.30**$^{\#}$**(0.60**$^{\#}$**)**	0.21(**0.53**$^{\#}$)
XRF dust	1.4		-0.12	-0.12	-0.01	-0.03
K	0.18		0.04	0.01	**0.31**$^{\#}$	0.07
Br	0.004		0.02	0.07	0.07	0.17
V	0.001		-0.19	-0.19	-0.03	-0.08
NO			0.07	0.02	0.00	0.03
NO_x			0.11	0.08	0.00	0.03
NO_y			0.12	0.10	0.00	0.05
O_3			0.04	0.04	0.02	0.00

*$1.0 \geq r^2 \geq 0.64$: strong correlation; $^{\#}$ $0.64 > r^2 > 0.25$: moderate correlation; $0.25 \geq r^2 \geq 0$: weak correlation [*Devore and Berk*, 2012].

Table 3-14. LS class particles with f44 higher than ion thresholds at 0.01%, 1%, 5%, 10%, 25%, and 50%.

f_{44} ion threshold	LS class particles percentage (%)			
Fresno	LS-HOA	LS-BBOA	LS-NOOA	LS-VOOA
Particles with $f_{44} > 0.01\%$	62	62	90	100
Particles with $f_{44} > 1\%$	61	59	90	100
Particles with $f_{44} > 5\%$	41	27	83	100
Particles with $f_{44} > 10\%$	11	4	53	94
Particles with $f_{44} > 25\%$	0	0	0	22
Particles with $f_{44} > 50\%$	0	0	0	1
Fontana	LS-HOA	LS-COA	LS-NOOA	LS-VOOA
Particles with $f_{44} > 0.01\%$	53	69	66	100
Particles with $f_{44} > 1\%$	40	68	66	100
Particles with $f_{44} > 5\%$	5	33	57	100
Particles with $f_{44} > 10\%$	1	7	29	100
Particles with $f_{44} > 25\%$	0	0	0	36
Particles with $f_{44} > 50\%$	0	0	0	3

Table 3-15. FTIR PMF analysis for PM1 at Fresno and Fontana.

Criteria \ Factor number (p)		2	3	4	5	6
Fresno	Q/Q_{exp}	8.5	4.5	3.8	3.4	2.9
	Absolute residual	23%	12%	11%	10%	9%
	Temporal correlation factors strength ($r > 0.6$)	None[a]	1 pair	3 pairs	2 pairs	4 pairs
	Factors with less than 10% OM	None	None	None	1 pair	2 pairs
Fontana	Q/Q_{exp}	2.1	0.8	0.5	0.4	0.4
	Absolute residual	15%	10%	9%	7%	6%
	Temporal correlation factors strength ($r > 0.6$)	None	1 pair	2 pairs	3 pairs	5 pairs
	Factors with less than 10% OM	None	1 pair	1 pair	1 pair	2 pairs

a) None: no paired factor correlation coefficients (r) higher than 0.6.

Table 3-16. Comparable LS and LSI clusters from other studies.

Class (Particle number %)	Major MS fragments [Tracers]				
		Comparable Factors	CS	Tracers or fragments	Citation
Fresno LS-HOA (10.2 %)	*m/z* 43, 41, 55, 57	HOA	0.95	*m/z* 41, 43, 55, 57	[*Lee et al.*, 2015]
Fontana LS-HOA (8.9%)	*m/z* 43, 57, 55	HOA	0.94	*m/z* 41, 43, 55, 57	[*Lee et al.*, 2015]
Fresno LS-BBOA (34.4%)	*m/z* 43, 29, 55, 57, 60	Biomass burning	0.90	Glucose: *m/z* 29, 31, 43, 60, 73	[*Freutel et al.*, 2013]
Fontana LS-COA (15.0%)	*m/z* 41, 43, 55, 29, 57	Cooking HOA	0.97	*m/z* 41, 43, 55, 69, 83	[*Freutel et al.*, 2013]
		COA class	0.95	*m/z* 41, 55 and high *m/z*55/57 ratio	[*Lee et al.*, 2015]
Fresno LS-NOOA (42.3%)	*m/z* 43, 44, 29,55, 41	OOA class-1	0.95	*m/z* 43, 29	[*Lee et al.*, 2015]
Fontana LS-NOOA	*m/z* 43, 44, 29, 81, 55	OOA class-1	0.95	*m/z* 43, 29	[*Lee et al.*, 2015]
Fresno LS-VOOA	*m/z* 44	OOA class-2	0.97	*m/z* 44	[*Lee et al.*, 2015]
Fontana LS-VOOA	*m/z* 44	OOA class-2	0.99	*m/z* 44	[*Lee et al.*, 2015]
Fresno LSI-HOA (16.1%)	*m/z* 43,55, 41	HOA	0.99	*m/z* 41, 43, 55, 57	[*Lee et al.*, 2015]
Fontana LSI-HOA (27.4%)	*m/z* 43,55, 41	HOA	0.94	*m/z* 41, 43, 55, 57	[*Lee et al.*, 2015]
Fresno LSI-OOA (6.0%)	*m/z* 44,29, 43	OOA class-2	0.91	*m/z* 44	[*Lee et al.*, 2015]
Fontana LSI-OOA (14.6%)	*m/z* 44,30, 43	OOA class-2	0.97	*m/z* 44	[*Lee et al.*, 2015]
Fresno-LSI-Nitrate (77.3%)	*m/z* 30,46	NO_3^- class	0.95	*m/z* 30, 46	[*Lee et al.*, 2015]
Fontana LSI-Nitrate (11.6%)	*m/z* 30,46	NO_3^- class	0.94	*m/z* 30, 46	[*Lee et al.*, 2015]
Fontana LSI-Mixed (22.4%)	*m/z* 30, 46, 64, 48	OOA and inorganics	0.93	*m/z* 44, 55	[*Freutel et al.*, 2013]
Fontana LSI-Sulfate (22.6%)	*m/z* 64, 48, 44	SO_4^{2-} class	0.90	*m/z* 48, 64, 80,81	[*Lee et al.*, 2015]

Table 3-17. Correlation coefficients for linear relationships between LSI clusters and other measured properties at Fontana.

Correlation Coefficient (r^2)	LSI-HOA	LSI-OOA	LSI-Nitrate	LSI-Sulfate	LSI-Mixed
Particle number	1987	909	2200	1532	2680
%	21%	10%	23%	16%	28%
AMS_sulfate	0.02	0.00	0.02	0.07	0.06
AMS_nitrate	0.00	0.01	**0.40**$^{\#}$	0.02	0.13
AMS_ammonium	0.01	0.02	**0.45**$^{\#}$	0.01	0.16
AMS_NOOA	0.08	0.01	0.13	0.01	0.12
AMS-VOOA	0.01	**0.27**$^{\#}$	0.01	0.10	0.04
AMS-COA	**0.33**$^{\#}$	0.05	0.00	0.10	0.00
AMS-HOA	0.12	0.00	0.07	0.01	0.04
FTIR-FFC	-0.01	-0.01	0.03	-0.05	**0.27**$^{\#}$
FTIR-MC	0.04	-0.08	**0.34**$^{\#}$	0.00	0.13
FTIR-DDS	0.06	**0.35**$^{\#}$	-0.04	**0.26**$^{\#}$	0.00
XRF dust	0.07	0.00	0.00	0.07	0.01
TiO_2	0.08	0.01	0.00	0.07	0.01
K	0.07	0.22	0.24	0.02	0.08
Br	0.01	0.23	0.05	0.02	0.23
V	-0.15	-0.04	-0.01	-0.12	-0.02
NO	0.04	0.01	0.00	0.03	0.03
NO_x	0.12	0.02	0.00	0.02	0.02
NO_y	0.13	0.01	0.01	0.01	0.03
O_3	0.05	0.15	0.00	0.06	0.00
Wind speed	0.05	0.09	0.04	0.05	0.01
Temperature	0.01	0.11	0.03	0.14	0.00
RH	0.01	0.12	0.04	0.10	0.02
Amine Fragments	0.06	0.08	0.14	0.00	0.20
Organosulfate Fragments	0.02	0.092	0.17	0.00	0.16
LSI-HOA	---	0.03	0.00	0.06	0.02
LSI-OOA	0.03	---	0.01	0.10	0.04
LSI-Nitrate	0.00	0.01	---	0.04	0.04
LSI-Sulfate	0.06	0.10	0.04	---	0.04
LSI-Mixed	0.02	0.04	0.04	0.04	---

*$1.0 \geq r^2 \geq 0.64$: strong correlation; $^{\#}$ $0.64 > r^2 > 0.25$: moderate correlation; $0.25 \geq r^2 \geq 0$: weak correlation [*Devore and Berk*, 2012].

Table 3-18. Summary of ambient organonitrate concentration estimation by NOx+ ratio method.

References and this study	R_{AN}[a]	R_{ON}[b]	R_{obs}[c]	x[d]	$\chi = R_{ON}/R_{AN}$	ON[e] ($\mu g\ m^{-3}$)	Fraction of ON to OM (f_{ON})
[*Farmer et al.*, 2010]	1.5±0.1	3.3±0.3					
[*Fry et al.*, 2013]	3.4	7.7	7.7	1.00	2.3±0.4	0.2~0.5	6~20%
[*Xu et al.*, 2015] upper value	2.7	5			1.9	0.06	5%
[*Xu et al.*, 2015] lower value	2.2	10			4.5	0.2	25%
[*Zhou et al.*, 2016]	1.8	2–4 times higher than R_{AN}	3.9	0.67-0.95			
Fresno low-fog	2.8	6.2	3.5±2.0	0.27	2.3	1.19	7%
Fresno high-fog			2.8±0.2	0.035		0.28	3%
Fontana firework	3.3	7.5	8.2±7.5	0.99		2.3	35%
Fontana non-firework			6.9±2.0	1.03		0.43	11%

a: R_{AN} = ratio of $NO^+_{,AN}/NO_2^+_{,AN}$ from ammonium nitrate from IE calibrations.
b: R_{ON} = ratio of $NO^+_{,ON}/NO_2^+_{,ON}$ from organonitrate standard.
c: R_{obs}: observation ratio of $NO^+_{,obs}/NO_2^+_{,obs}$ from AMS measurement.
d: x: fraction of $NO_3^+_{,org}$ to NO_x^+; $x = \frac{(R_{obs}-R_{AN})(1+R_{AN})}{(R_{ON}-R_{AN})(1+R_{obs})}$
e: Organonitrate from organic compounds: $NO_3^+_{,org} = NO_2^+_{,org} + NO^+_{,org}$;

$$NO^+_{2,org} = \frac{NO^+_{2,obs} \times (R_{obs} - R_{AN})}{(R_{ON} - R_{AN})}, \quad NO^+_{,org} = R_{ON} \times NO^+_{2,org}$$

Table 3-19. Summary of ambient organonitrate concentration estimated by NOx-containing organic ions (CxHyOzN+) method.

Reference and this study	R_{CHON}[a]	ON = $\Sigma CHON_{observed}$[b] / R_{CHON}	Fraction of ON to AMS nitrate	ON^c = $\Sigma CHON_{observed}$[d] / R_{CHON}	Fraction of ON [c] to AMS nitrate
Farmer et al. [2010]	0.045		4% ± 6%		
Fresno low-fog	0.045	0.26	4%	0.22	4%
Fresno high-fog	0.045	1.27	9%	0.42	3%
Fontana firework	0.045	0.41	14%	0.22	4%
Fontana non-firework	0.045	0.13	22%	0.06	10%

a: Ratio of NO^+/NO_2^+ from ON standards, assuming that ON are the only source of these ions, and are representative of ambient mixtures of atmospheric ON [*Farmer et al.*, 2010].
b: $\Sigma CHON = CH_4NO^+ + C_2H_5NO^+ + C_3H_4NO^+ + CH_2NO_3^+ + CH_2NO_2^+$.
c: ON^c : Total ON removes the CH_4NO^+ fragment.
d: $\Sigma CHON = C_2H_5NO^+ + C_3H_4NO^+ + CH_2NO_3^+ + CH_2NO_2^+$.

Table 3-20. Ratios of O/C, H/C, fraction of m/z 43 to m/z 44 for Fresno and Fontana PMF factors.

Site	PMF factor	O/C	H/C	f_{43} ($C_2H_3O^+$)/f_{44}	f_{43} ($C_3H_7^+$)/f_{44}	f_{44}
Fresno	HOA	0.11	1.8	0.73	1.9	0.02
	NOOA	0.44	1.7	0.67	0.12	0.10
	BBOA	0.47	1.7	0.89	0.39	0.04
	VOOA	0.78	1.7	0.33	0.01	0.16
Fontana	HOA	0.15	2.0	0.34	1.6	0.04
	COA	0.12	1.8	0.94	3.8	0.01
	NOOA	0.40	1.8	4.18	0.32	0.03
	VOOA	0.78	1.4	0.25	0.04	0.18

3.11 Figures

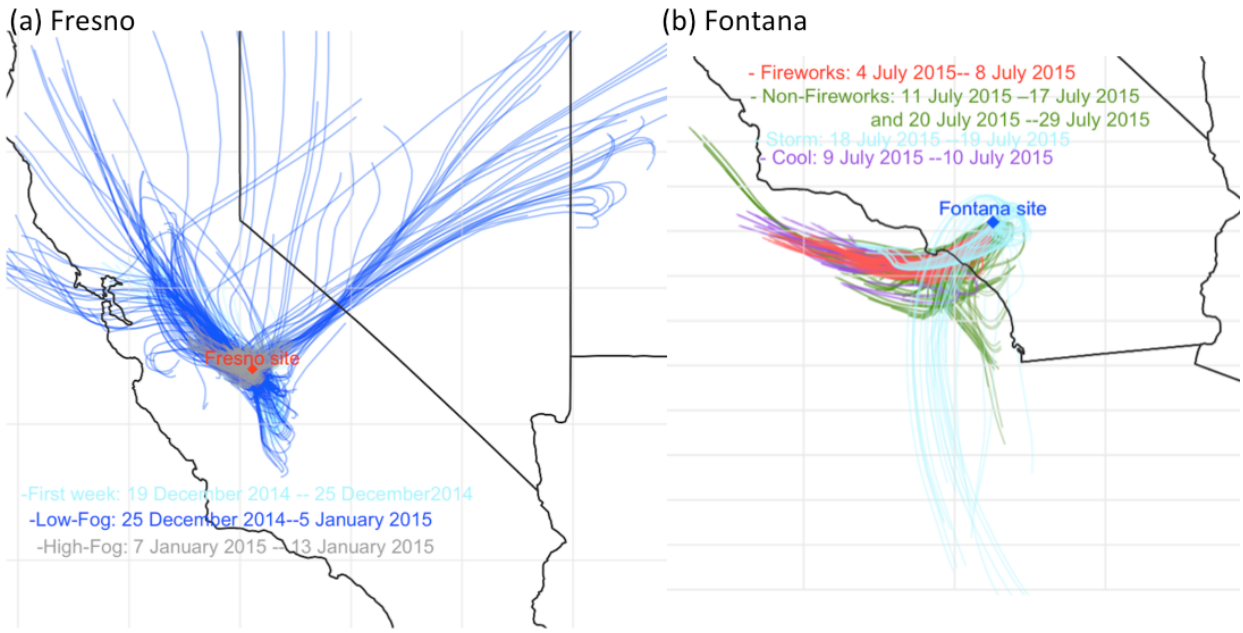

Figure 3-1. (a) 60-hour back trajectories of air masses arriving at Fresno and initialized at 50 m, 100m, and 200m above ground level were calculated every 2 hours for first-week, low-fog, and high-fog days. (b) 60-hour back trajectories of air masses arriving at Fontana and initialized at 50 m, 100m, and 200m above ground level were calculated every 2 hours for firework days, cool days, storm days, and non-firework days.

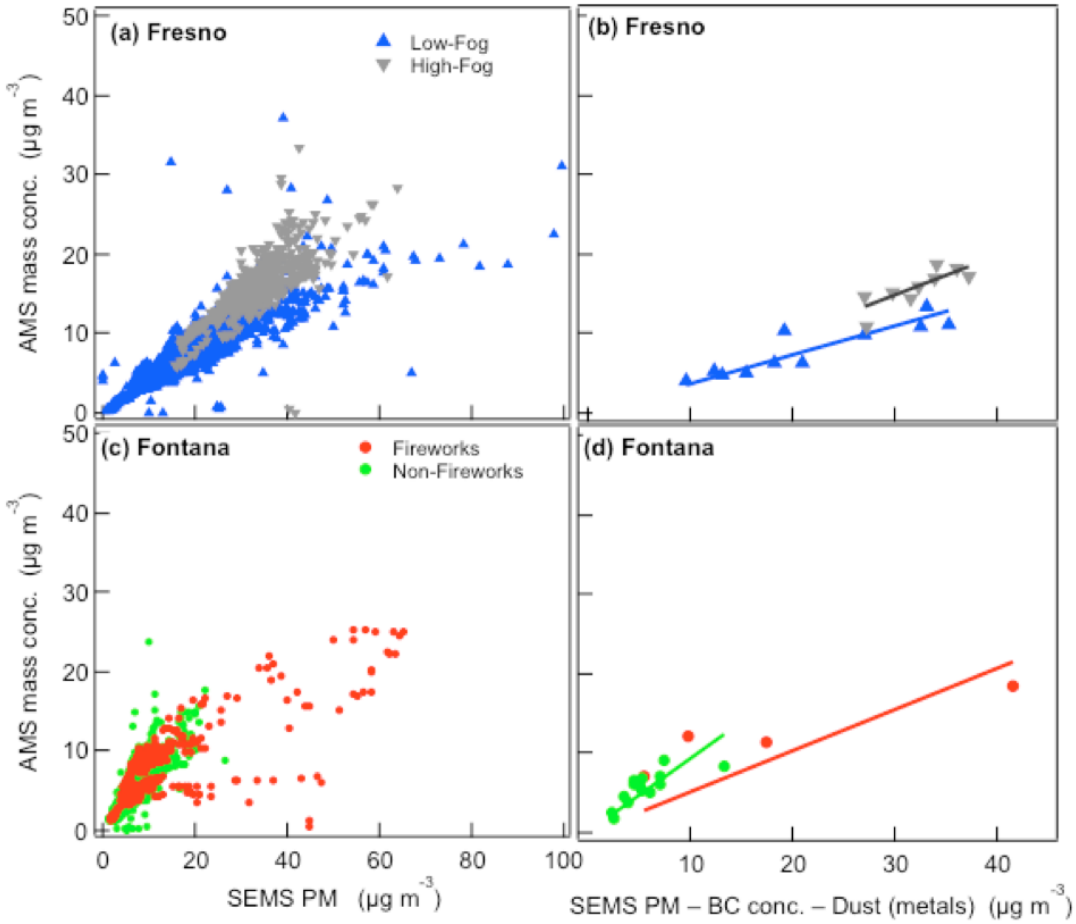

Figure 3-2. (a) Scatter plots of AMS-measured particle mass concentration and SEMS particle mass concentration measured at Fresno low-fog days, and high-fog days. (b) AMS-measured particle mass concentration and SEMS-PM after BC and mineral contribution removed. Linear correlation fit slope is 0.36+/-0.02 for low-fog days, and 0.49 +/- 0.01 for high-fog days. (c) Scatter plot of AMS-measured particle mass concentration and SEMS measurement on firework days at Fontana. The slope of the linear correlation fit is 0.45. On the non-firework days, the slope of the linear correlation fit is 0.76. (d) AMS-measured particle mass concentration and SEMS-PM after BC and mineral contribution removed on firework days at Fontana. The slope of the linear correlation fit is 0.52 ± 0.12. On non-firework days, the slope of the linear correlation fit is 0.93 ± 0.08.

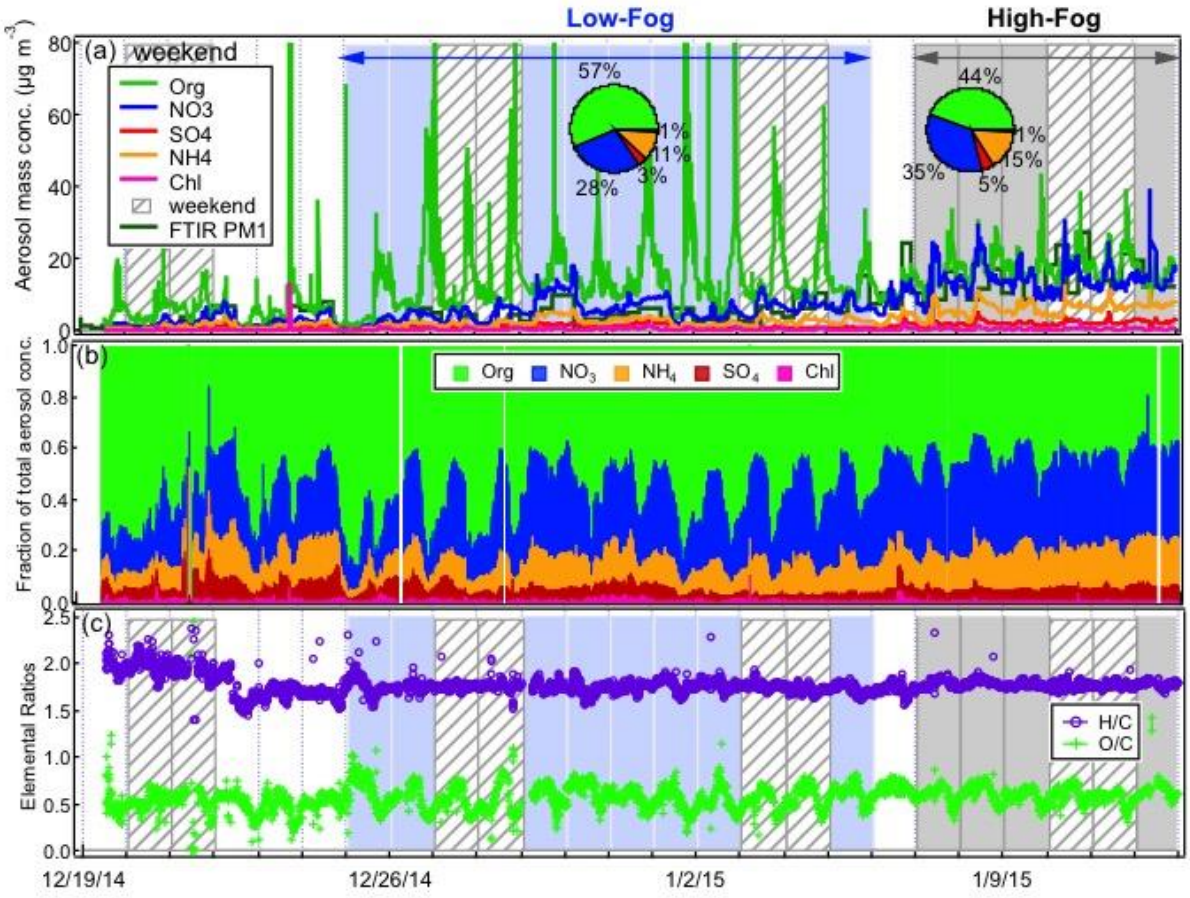

Figure 3-3. (a) Time series of non-refractory organic aerosols (Org), nitrate (NO3-), sulfate (SO42-), ammonium (NH4+), and chloride (Cl-) at Fresno. (b) Time series of fraction of PM chemical composition. (c) Elemental ratios of hydrogen-to-carbon (H/C) and oxygen-to-carbon (O/C). The low-fog days are from 25 December 2014 to 5 January 2015, and the high-fog days are from 7 January 2015 to 13 January 2015.

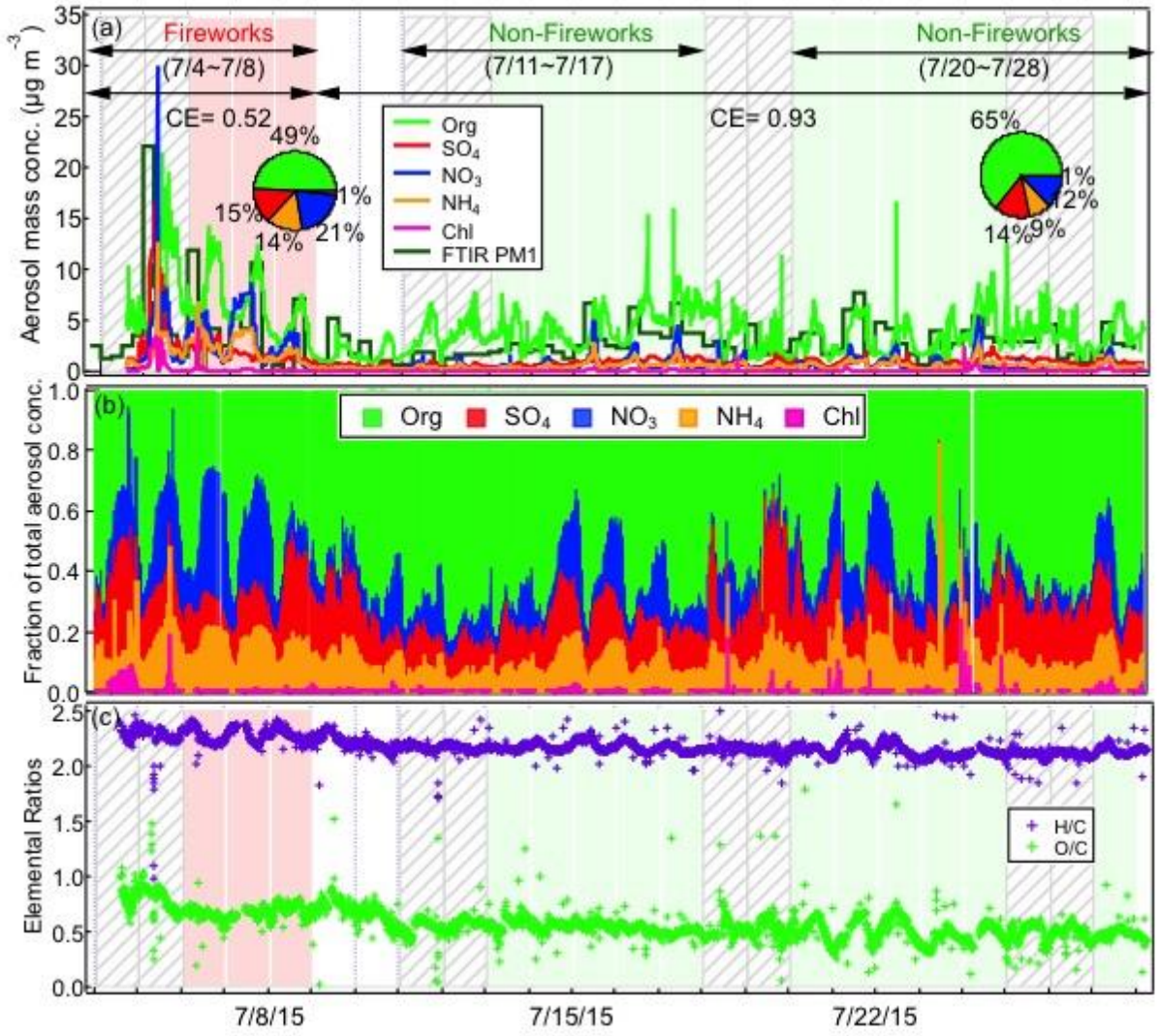

Figure 3-4. (a) Time series of non-refractory organic aerosols (Org), nitrate (NO3-), sulfate (SO42-), ammonium (NH4+), and chloride (Cl-) at Fontana. (b) Time series of fraction of PM chemical composition. (c) Elemental ratios of hydrogen-to-carbon (H/C) and oxygen-to-carbon (O/C). The firework days are from 4 July 2015 to 8 July 2015, and the non-firework days are from 11 July 2015 to 17 July 2015 and 20 July 2015 to 28 July 2015.

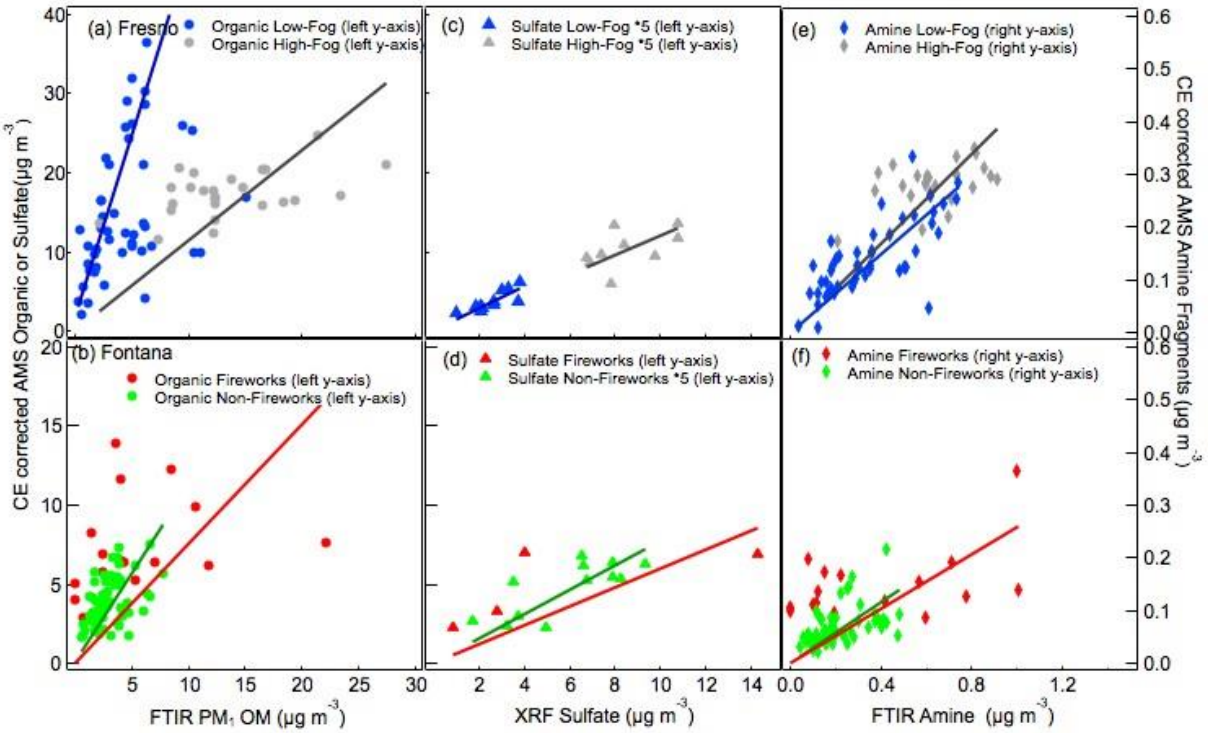

Figure 3-5. (a-b) Scatter plots of AMS organic measurements compared to FTIR-PM1-Org; the linear correlation slopes for organic on Fresno low-fog, Fresno high-fog, Fontana firework days, and Fontana non-firework days are 2.6 (r^2=0.67), 1.1 (r^2=0.89), 0.8 (r^2=0.52), and 1.3 (r^2=0.84), respectively. (c-d) Scatter plots of AMS sulfate measurements compared to XRF-sulfate analysis; the linear correlation slopes for sulfate on Fresno low-fog, Fresno high-fog, Fontana firework days, and Fontana non-firework days are 1.4 (r^2=0.97), 1.2 (r^2=0.96), 0.6 (r^2=0.73), and 0.8 (r^2=0.95), respectively. AMS organic and sulfate concentrations are CE corrected. (e-f) Scatter plots of amine fragments and FTIR amine group at Fresno and Fontana; the linear correlation slopes for amine on Fresno low-fog, Fresno high-fog, Fontana firework days, and Fontana non-firework days are 0.4 (r^2=0.89), 0.4 (r^2=0.95), 0.3 (r^2=0.64), and 0.3 (r^2=0.82), respectively. The sulfate concentrations were scaled by 5 in panel (c) and for non-firework days in panel (d).

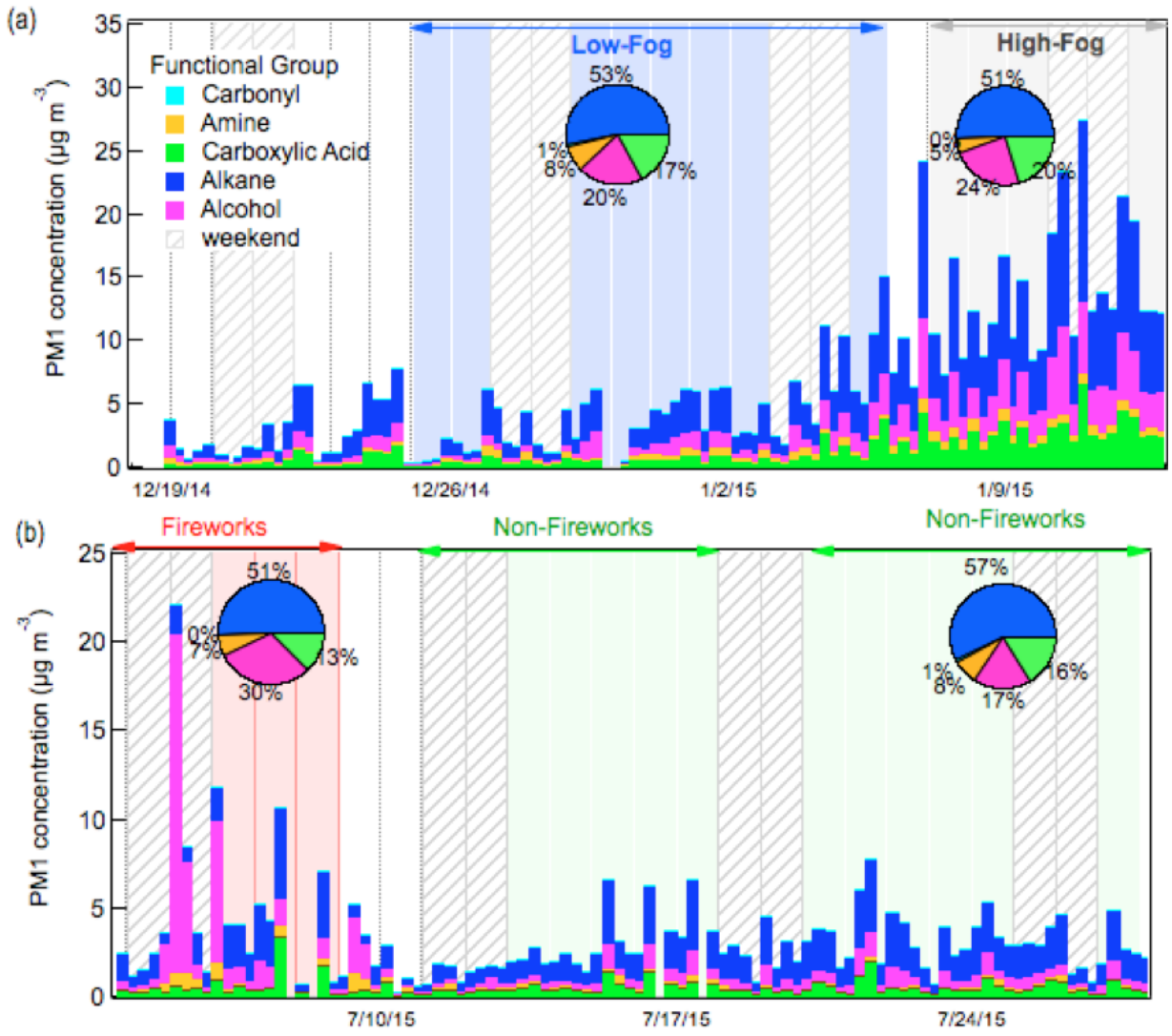

Figure 3-6. FTIR functional group measurements for PM1 at (a) Fresno and (b) Fontana.

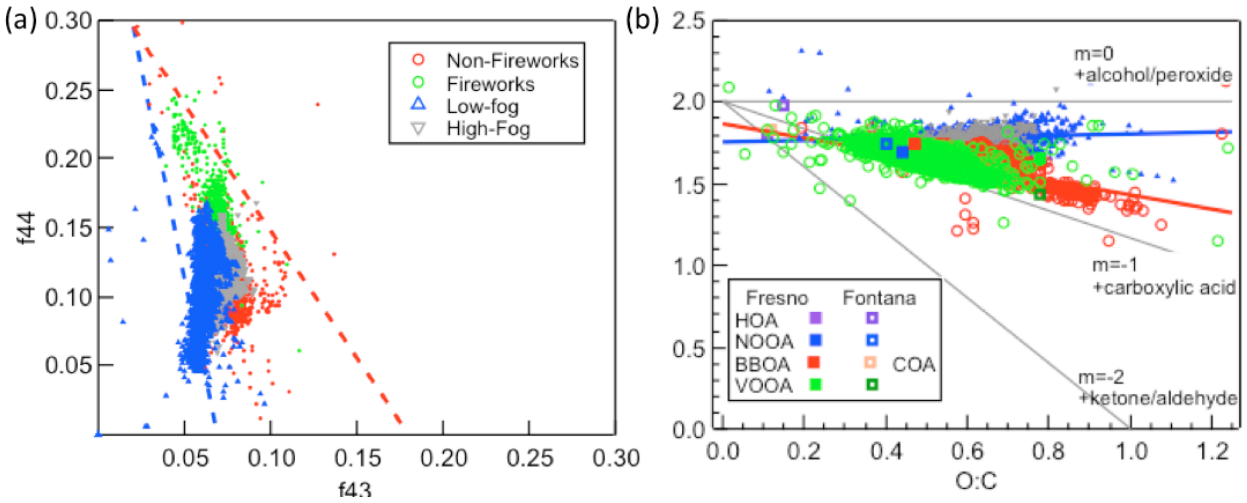

Figure 3-7. (a) Triangle plots (f43 vs. f44) for Fresno low-fog, Fresno high-fog, Fontana firework, and Fontana non-firework days. (b) Van Krevelen diagram (H:C vs. O:C) at Fresno (grey dots) and Fontana (red dots). The PMF factors identified for Fresno (squares) and for Fontana (triangles) are also shown.

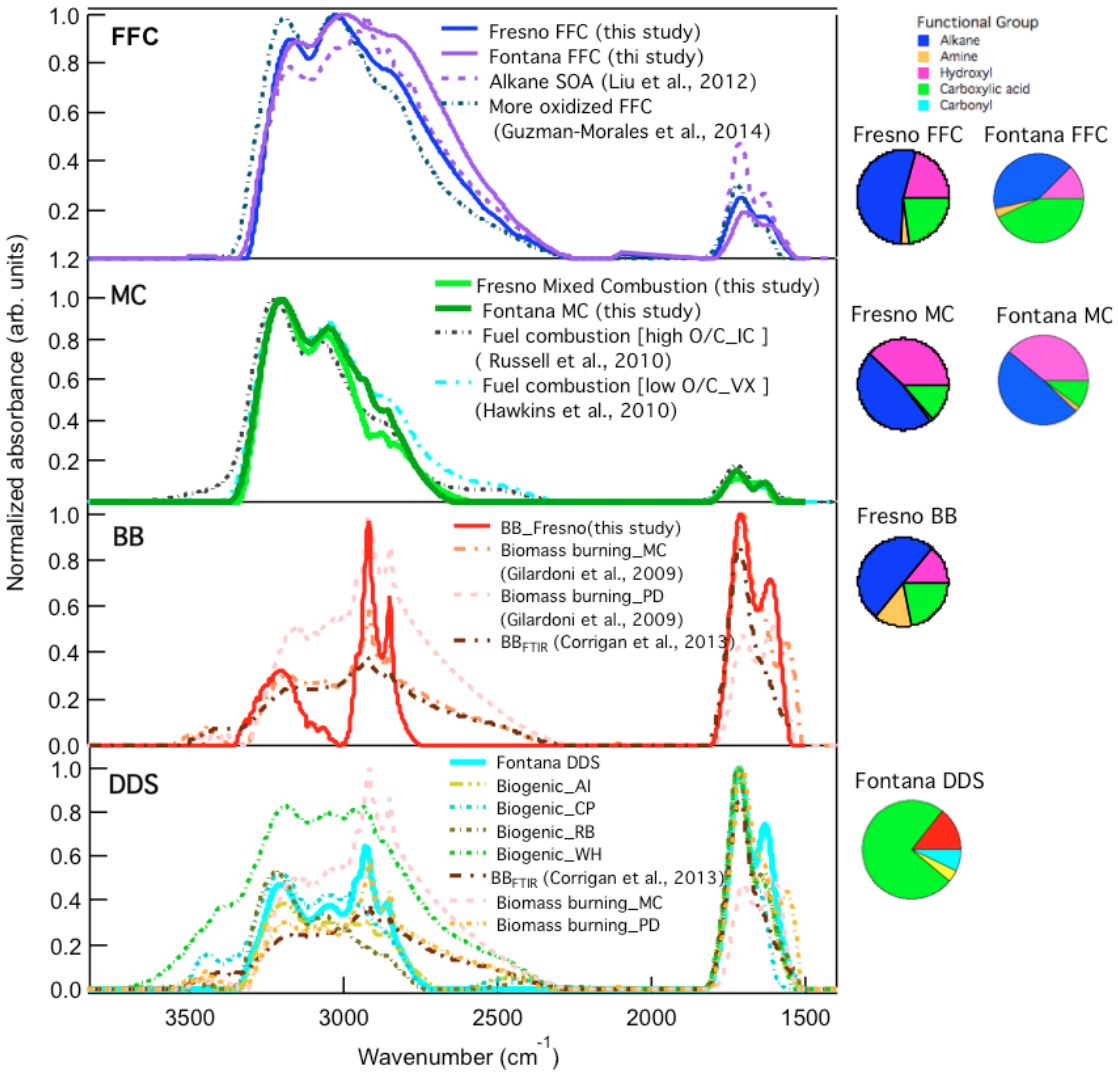

Figure 3-8. FTIR spectra of PMF factors at Fresno and Fontana.

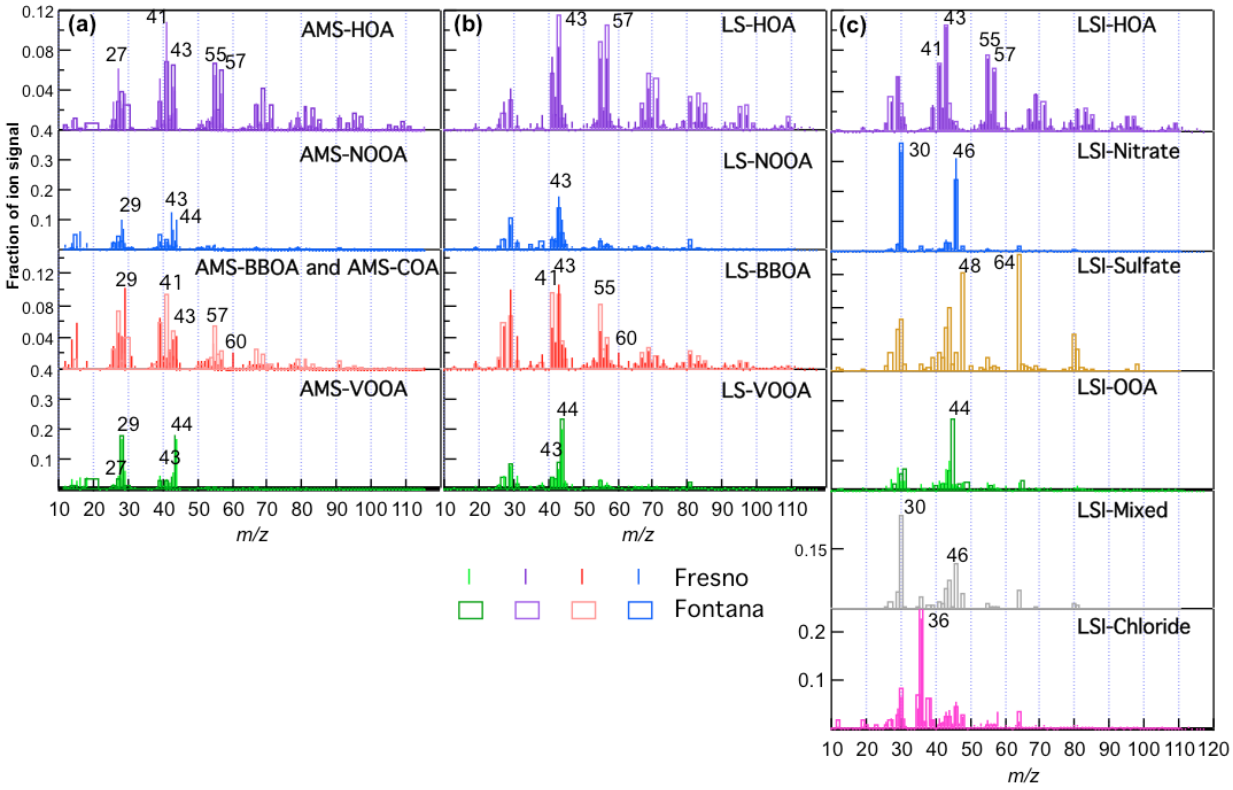

Figure 3-9. (a) High resolution mass spectra of PMF analysis results, including AMS-HOA, AMS-NOOA, AMS-BBOA, and AMS-VOOA at Fresno, and AMS-HOA, AMS-COA, AMS-NOOA, and AMS-VOOA at Fontana. (b) Single-particle cluster mass spectra at Fresno. Four classes include a hydrocarbon-like organic aerosol (HOA), a nitrate-related oxidized organic aerosol (NOOA), a biomass burning organic aerosol (BBOA), and a vehicle-related oxidized organic aerosol (VOOA) class. Single-particle cluster mass spectra at Fontana. Four classes include HOA, NOOA, a cooking emission organic aerosol (COA), and VOOA. (c) Single-particle cluster mass spectra (inorganic included) at Fresno. Four classes include a nitrate-OA, a hydrocarbon-like organic aerosol (HOA), an oxygenated organic aerosol (OOA), and a chloride class. Single-particle cluster mass spectra (inorganic included) at Fontana. Six classes include a nitrate, HOA, OOA, chloride, sulfate, and mixed class.

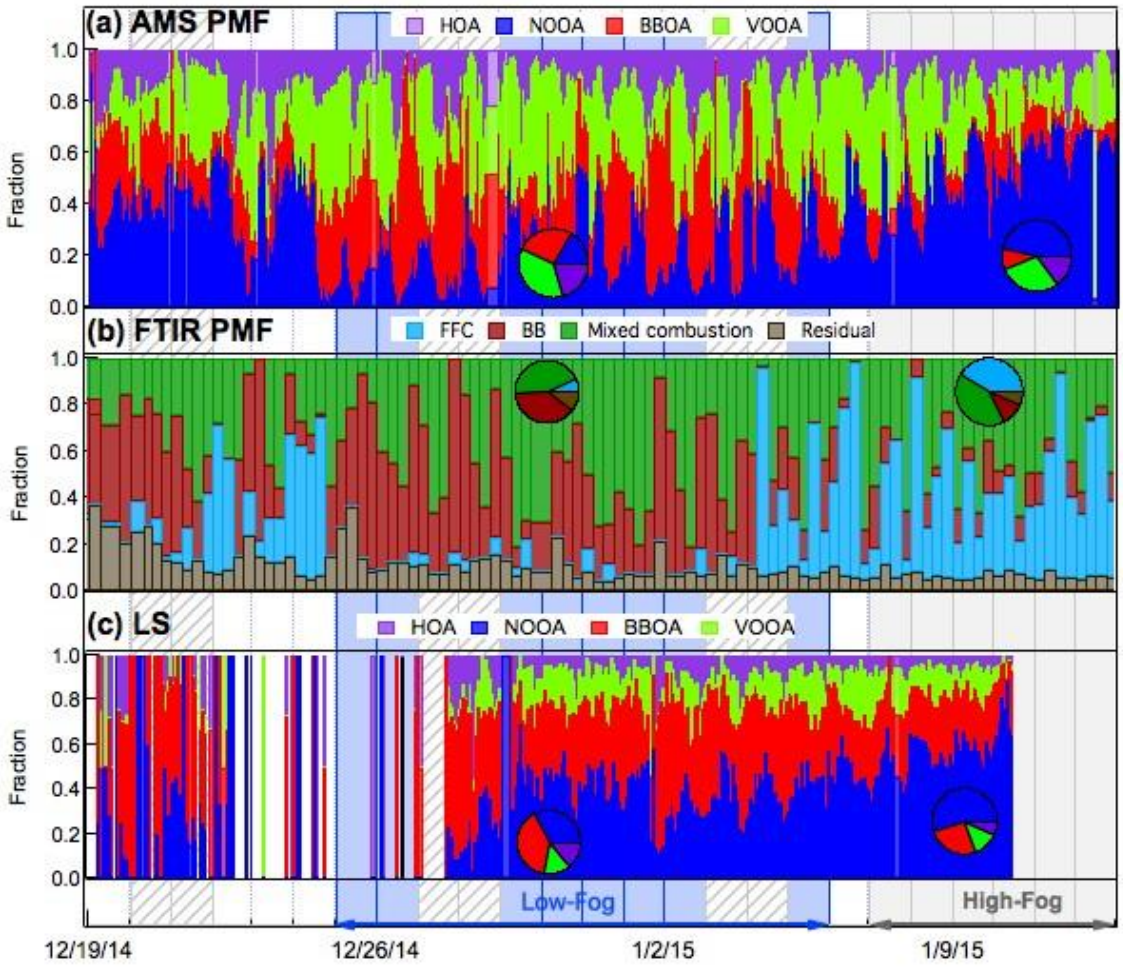

Figure 3-10. Time series of fractions of (a) AMS PMF factors, (b) FTIR PMF factors, and (c) single-particle classes by LS-AMS at Fresno. Gray area represents weekends.

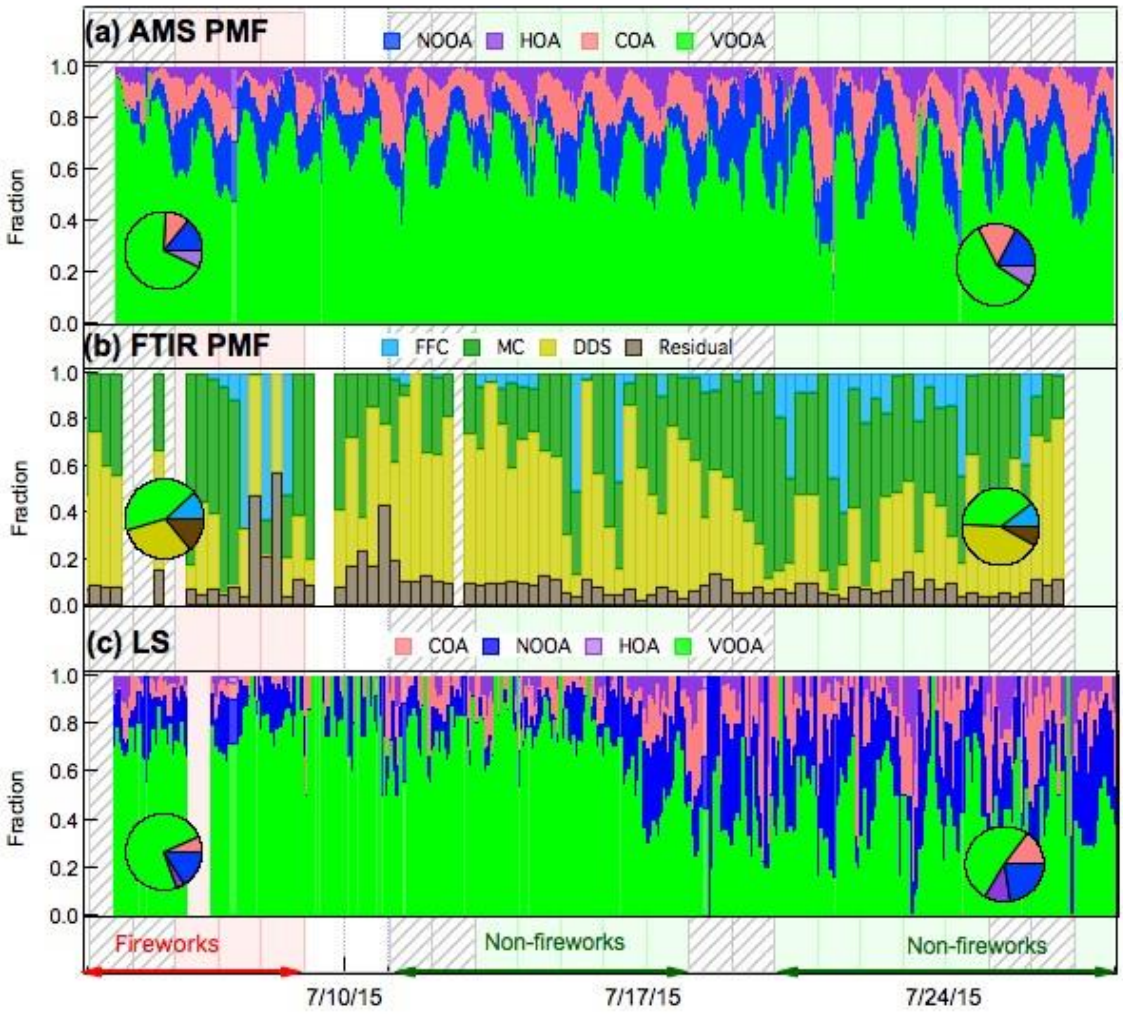

Figure 3-11. Time series of fractions of (a) AMS PMF factors, (b) FTIR PMF factors, and (c) single-particle classes by LS-AMS at Fontana.

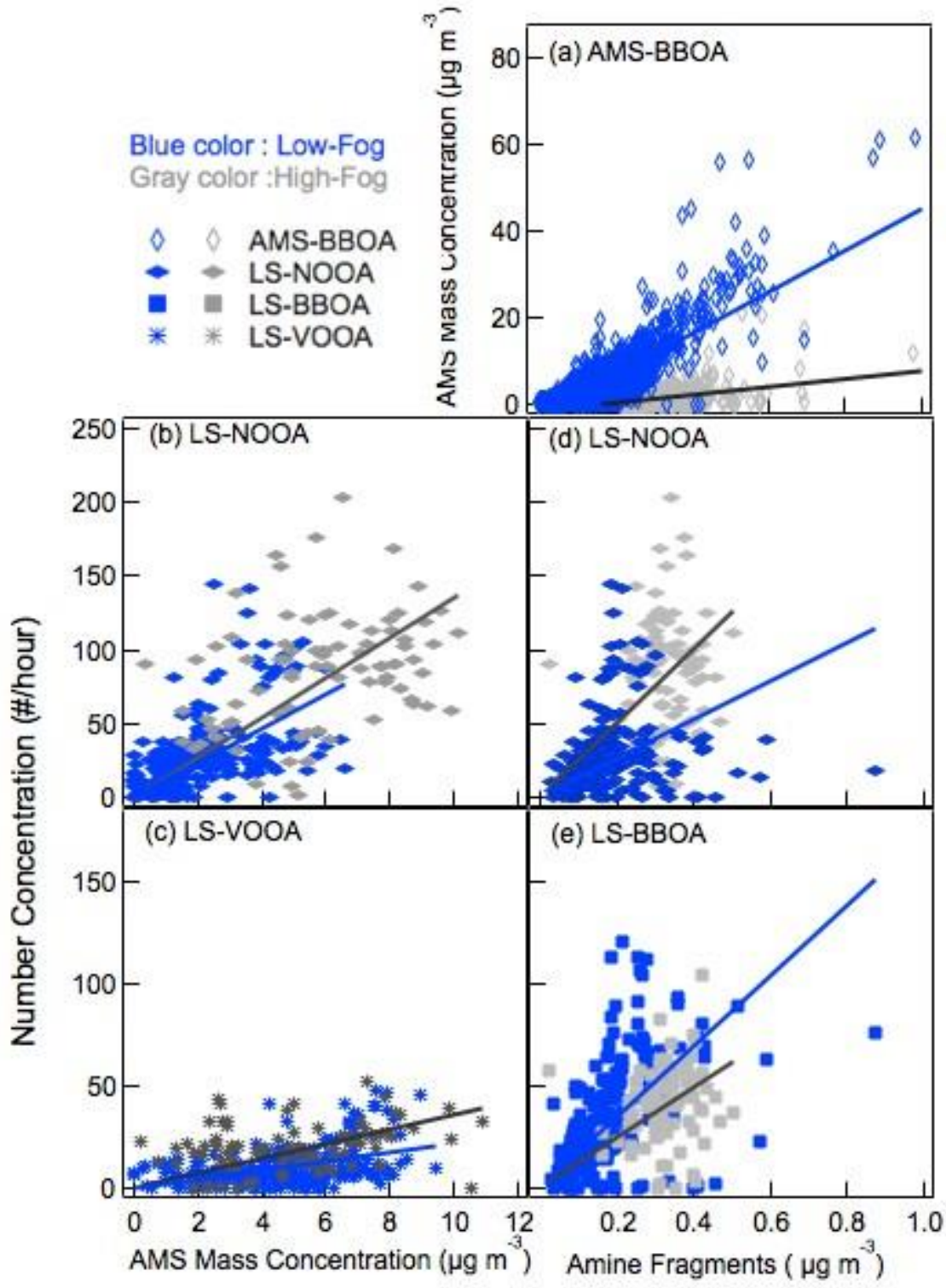

Figure 3-12. Correlations of average hourly particle numbers of LS classes compared to AMS-PMF factors and amine fragments. Correlation coefficients (r^2) for least squares regressions (forced to zero) for Fresno low-fog days and high-fog days, respectively, are (a) 0.71 and 0.56, (b) 0.64 and 0.80, (c) 0.63 and 0.72, (d) 0.49 and 0.80, (e) 0.71 and 0.81.

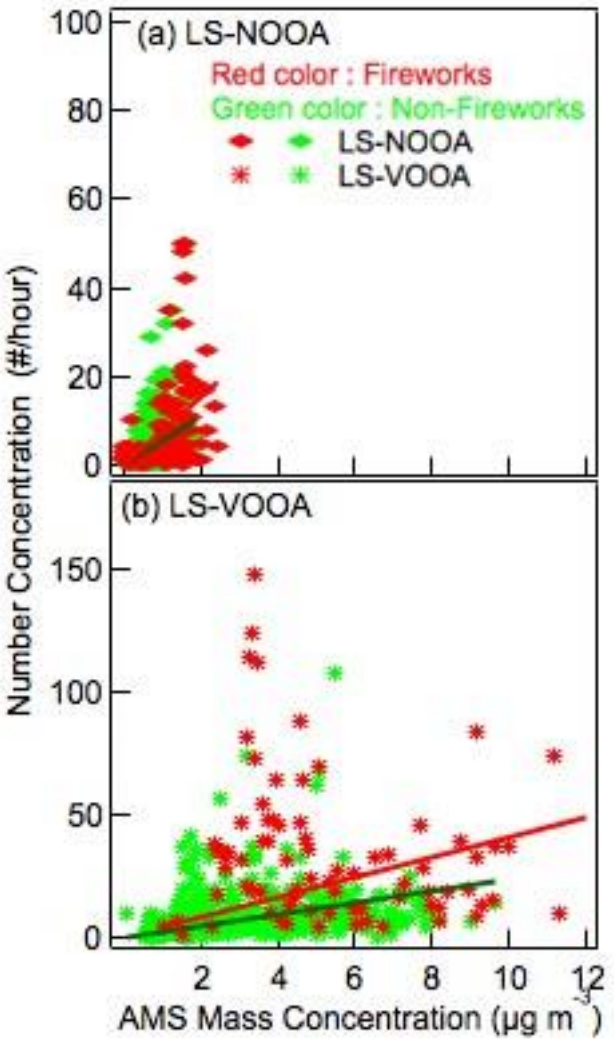

Figure 3-13. Correlations of average hourly particle numbers of LS classes compared to AMS-PMF factors. Correlation coefficients (r^2) for least squares regressions forced to zero for Fontana firework and non-firework days, respectively, are (a) 0.48 and 0.54 and (b) 0.47 and 0.42.

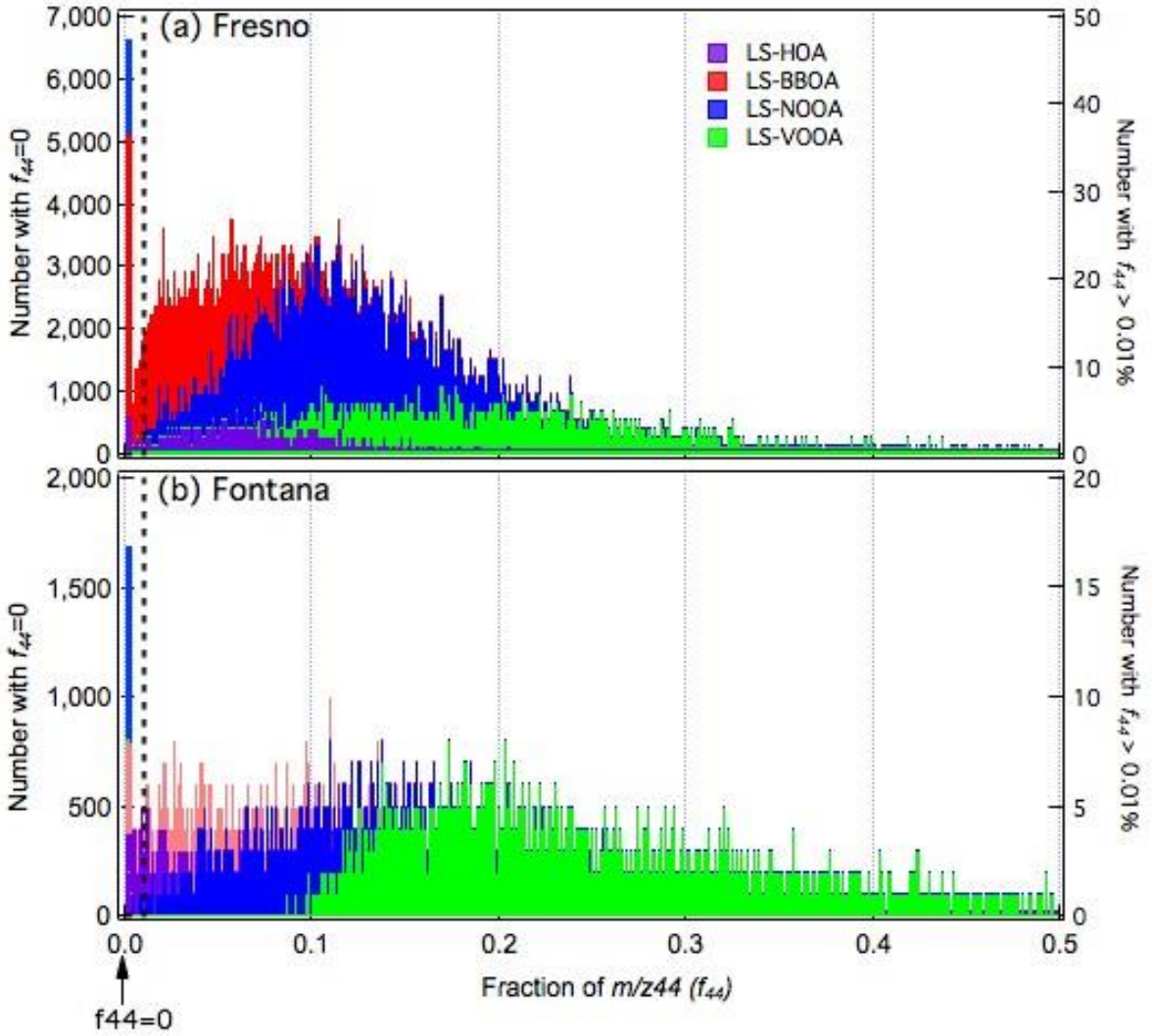

Figure 3-14. LS particle number with f44 for each particle type for (a) Fresno and (b) Fontana.

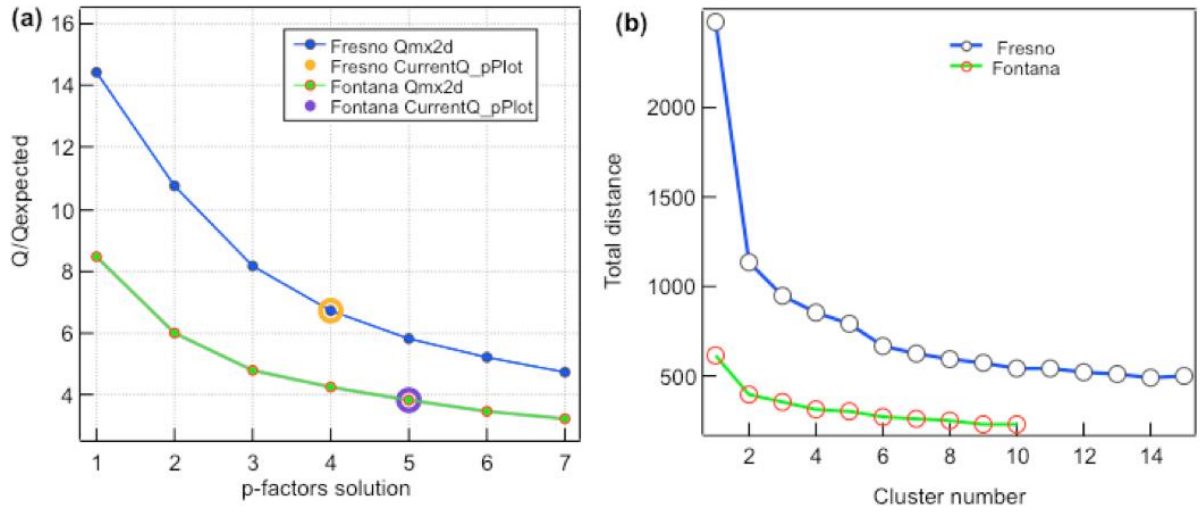

Figure 3-15. (a) Q/Qexpected for each AMS PMF factor solution for Fresno and Fontana. (b) Total Euclidean distance in CAP k-means clustering analysis for each class.

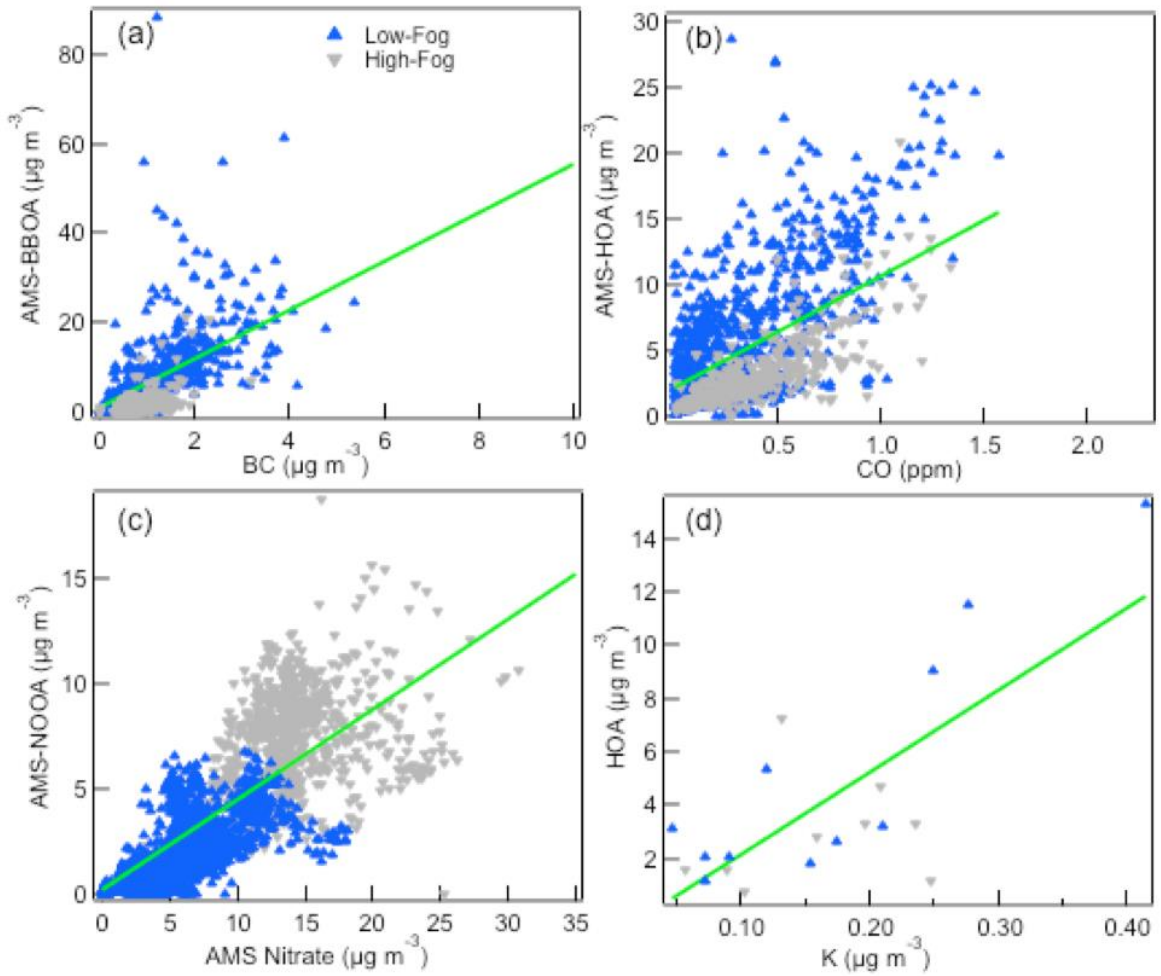

Figure 3-16. Scatter plots of PMF factors and tracers at Fresno. (a) BBOA vs BC. (b) HOA vs CO. (c) NOOA vs AMS NO3. (d) HOA vs Potassium (K).

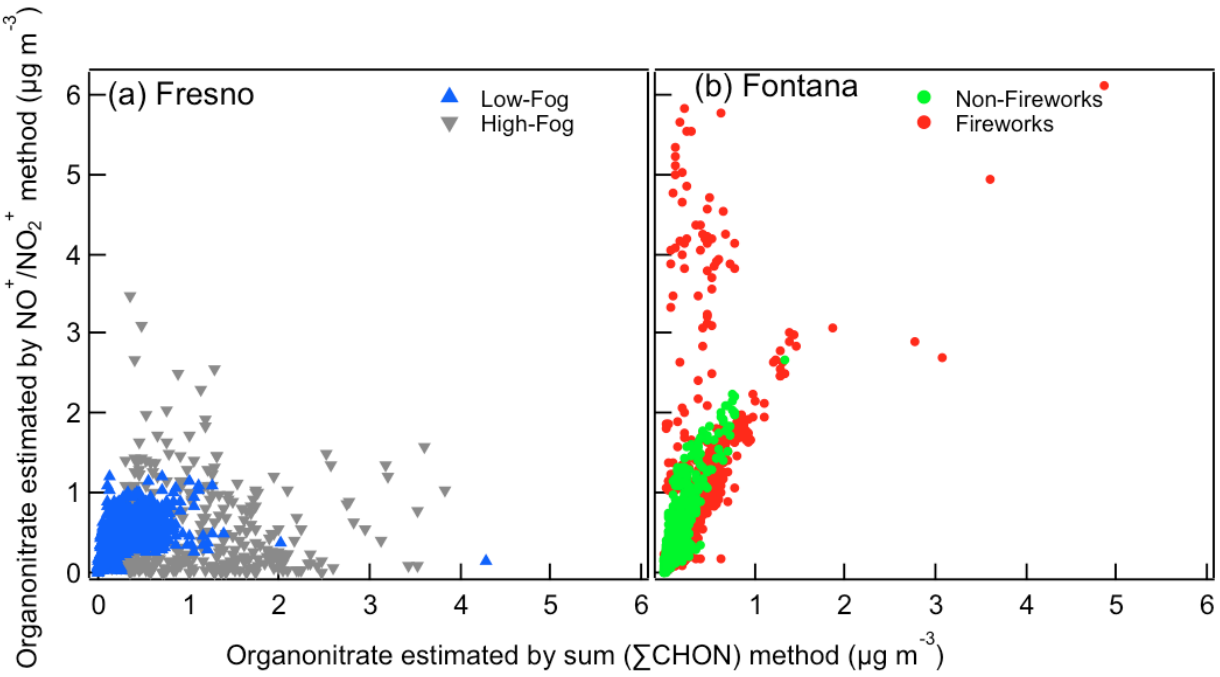

Figure 3-17. Scatter plots of organonitrate estimated by NO+/NO2+ method and ion sum (ΣCHON) method for (a) Fresno and (b) Fontana.

4 Larger submicron particles for emissions with residential burning in wintertime San Joaquin Valley than for vehicle combustion in summertime South Coast Air

4.1 Abstract

Size-resolved composition of atmospheric aerosol particles during winter (19 December 2014 to 13 January 2015) in the San Joaquin Valley at Fresno and during summer (04 to 28 July 2015) in the Southern California Air Basin at Fontana were measured by Aerosol Mass Spectrometer, Fourier Transform Infrared Spectrometer, Single Particle Soot Photometer and Scanning Electrical Mobility Sizer. The Fresno study had low-fog and high-fog winter conditions, and residential burning was a frequent contributor to evening emissions. Fireworks during 4th of July celebrations characterized the start of the Fontana study; the remaining days were categorized as non-firework days and were mostly affected by traffic emissions. Fresno had particle distributions with number mode diameters of 70-150 nm, and Fontana had 30-50 nm diameters. The non-refractory organic mass mode diameters were also larger at Fresno (250-380 nm in dry mobility diameter) than at Fontana (130-150 nm, 280 nm in dry mobility diameter) as were refractory black carbon particles (Fresno: 80-180 nm; Fontana: 80-100 nm in dry volume equivalent diameter). The size dependence of organic contributions to particle mass indicated that condensation or other surface-limited processes contributed oxidized organic fractions to aerosol mass in Fontana but that volume-limited aqueous reactions produced organic mass on both low-fog and high-fog days in Fresno. Linear regression analysis of organic aerosol sources with size-resolved particle volume at different times of day also showed that residential-burning related particles increased from 70-160 nm in the evening (18:00 to 23:59) to 150-260 nm at night (00:00 – 05:59) on low-fog days.

4.2 Introduction

Elevated concentrations of atmospheric aerosol particles in the San Joaquin Valley (SJV) and the South Coast Air Basin (SoCAB) have contributed significantly to air quality degradation for several decades [*Chen et al.*, 2014; *Hall et al.*, 2010; *Plummer et al.*, 2015]. Aerosol particle mass concentrations reach their maximum levels during winters in the SJV when boundary layers are shallower and wood burning is prevalent in the region [*Chow et al.*, 2006; *Ge et al.*, 2012a; *SJVAPCD*, 2016; *Zhang et al.*, 2016]. Frequent radiation-driven fogs associated with cool, humid and mild weather conditions, and the mountains surrounding SJV are associated with degraded air quality in the region in wintertime. SoCAB is also ringed by mountains and has large-scale subsidence inversions that frequently limit vertical ventilation to create stagnant conditions. As a result, "severe" summertime smog episodes are common in SoCAB due to accumulation of vehicle emissions and high rates of photochemical oxidation [*Kleeman et al.*, 2007; *SCAQMD*, 2016]. Several studies have been conducted to understand the sources of both primary and secondary aerosol particles so as to develop and implement regulatory plans in these regions [*Chan et al.*, 2013; *Craven et al.*, 2013; *Ge et al.*, 2012a; *Ge et al.*, 2012b; *Hasheminassab et al.*, 2014; *Hayes et al.*, 2013; *Lurmann et al.*, 2006; *Woody et al.*, 2016; *Ying and Kleeman*, 2006; *Zhang et al.*, 2016].

The diverse sources of aerosol particles in SJV and SoCAB lead to important differences in the aerosol particle composition and size distributions [*Kleeman et al.*, 2009b; *Ying and Kleeman*, 2006]. **Table 4-1** summarizes the composition and size distribution characteristics of aerosol particles from sources relevant to SJV and SoCAB. Combustion-related primary emissions from vehicles release a large fraction of hydrocarbon-like organic aerosol (HOA) mass at 120-140 nm vacuum aerodynamic diameter, refractory black carbon (rBC) mass at 100 nm and a variety of heavy metals in the accumulation mass mode (0.3-1 μm) [*Ge et al.*, 2012a; *Laborde et al.*, 2013; *Visser et al.*, 2015]. Primary biomass burning organic aerosol (BBOA) particles have been measured and found to contain a large mass fraction of oxygen-containing organic compounds at approximately 140 nm vacuum aerodynamic diameter and rBC mass in the range of 130-200 nm in volume equivalent diameter, larger than traffic-related rBC mass [*Ge et al.*, 2012a; *Kondo et al.*, 2011; *Laborde et al.*, 2013; *Zhang et al.*, 2016]. Cooking-related organic aerosol (COA) primary particles, with H/C and O/C ratios similar to vehicular emissions, have been reported to have two modes, a smaller mode of mass at 200 nm and a larger mode of mass at 450 nm vacuum aerodynamic diameter in Fresno, California, while a single mass mode at 150 nm vacuum aerodynamic diameter has been reported in Lanzhou, China [*Ge et al.*, 2012a; *J Xu et al.*, 2014].

Oxygenated organic aerosol (OOA)-containing particles in urban areas are typically secondary organic aerosol (SOA) components, which are largely formed from the oxidation of vapor emissions and transfer to the particle phase. OOA condensation depends on its volatility, with less volatile organic components contributing more to growth of smaller particles [*Pierce et al.*, 2011]. OOA are typically mixed with inorganic sulfate or nitrate salts. OOA mass has been measured to be approximately 460 nm vacuum aerodynamic diameters in Fresno, 500-600 nm in New York, and in two modes of 400-500 nm and 650 nm in Beijing China [*Ge et al.*, 2012a; *Sun et al.*, 2012; *W Q Xu et al.*, 2015]. In Bakersfield SOA particle mass from vehicle-emitted hydrocarbons were associated with aerosol particles in the size range of 200 to 500 nm dry vacuum aerodynamic diameter [*Liu et al.*, 2012].

Studies on sources and composition of aerosol particles in both SJV [*Ahlm et al.*, 2012; *Young et al.*, 2016; *Zhang et al.*, 2016] and SoCAB [*Chan et al.*, 2013; *Craven et al.*, 2013; *Hayes et al.*, 2013; *Hersey et al.*, 2013] have mostly been limited to bulk $PM_{2.5}$ or PM_1 measurements. Only a few studies have reported high-resolution size-resolved compositions of aerosol particles with on-line time resolution in these regions [*Ensberg et al.*, 2013; *Ge et al.*, 2012a; *Ge et al.*, 2012b; *Liu et al.*, 2012; *Ying and Kleeman*, 2006]. Ge et al. [2012a] estimated average daily mass size distributions of organic aerosols (HOA, BBOA, COA and OOA) in Fresno using multi-linear analysis of the size-resolved mass spectra. They found that BBOA and HOA have similar mass size distributions with mean vacuum aerodynamic diameter of 140 nm but differing chemical composition. Averaging over an entire day or multiple days can obscure the variation in the size dependence of aerosol sources during different times of day, so the source-related size dependence may only be evident for sampling frequencies higher than one day, which are not available for particle composition from most monitoring sites [*Ge et al.*, 2012b].

In this study, we use high frequency, size-resolved particle composition measurements to examine the relationships between particle composition size distributions and sources for two types of conditions at SJV and SoCAB. Measurements of size-resolved composition of organic, inorganic and refractory black carbon (rBC) aerosol particle concentrations illustrate the differences between the two regions. In addition, we use several novel approaches for investigating the dependence of different aerosol size modes on different organic sources at different times of a day. Size-resolved correlations between non-refractory components and particle volume show the explicit dependence of particle size and composition on each other as well as the effects of aerosol formation processes. These results enhance the understanding of the different organic source types in SJV and SoCAB and provide source-composition-size relationships that can be used to constrain climate and air quality modeling.

4.3 Measurement Methods

Comprehensive aerosol size and composition measurements were carried out during winter (19 December 2014 to 13 January 2015) in Fresno (in SJV) and during summer (4 to 28 July 2015) in Fontana (in SoCAB). The sampling site in Fresno was located behind the UC Extension building at 550 Shaw Ave. (36.81^0 N, 119.78^0 W) and was managed by the University of California, Davis (UCD) Extension. Residential buildings to the north, commercial complexes to the south, and the Yosemite Freeway approximately 400 m to the west of the sampling site allowed repeated daily measurements of both the residential wood burning and traffic emissions in Fresno. The sampling site in Fontana was located behind the fire station at 14360 Arrow Highway (34.10^0 N, 117.49^0 W) and was managed by South Coast Air Quality Management District (SCAQMD). The site was bounded by the I-15 freeway approximately 4000 m to the west, the I-10 freeway approximately 4000 m to the south, and an auto speedway approximately 200 m to the south, the sampling site was primarily influenced by vehicular emissions.

Chen et al. [*2017*] discuss the meteorological conditions during both campaigns. Study days at Fresno were categorized as "low-fog" days for average daily visibility of >2 miles and relative humidity (RH) < 90% (from 25 December 2014 to 05 January 2015) and "high-fog" days for average daily visibility of ≤ 2 miles and RH > 90% (from 07 to 13 January 2015). The measurements from the first week of sampling (19 to 25 December 2015) in Fresno were excluded in our calculation of averages because the mixed weather conditions (high cloud cover, precipitation, and wind speeds) caused inconsistent daily patterns. Sampling at Fontana was divided into "fireworks" days (from 04 to 08 July 2015) that were influenced by the 4^{th} of July firework celebrations and "non-fireworks" days (from 11 to 17 July and from 20 to 28 July 2015). Transition days (08 to 11, July 2015) and storm days (17 to 20 July 2015) were excluded because they included a mixture of aerosol sources and types that was not considered representative of typical conditions.

Aerosol particle instruments housed in a sampling van with a custom inlet were deployed for particle measurements at both study sites. The isokinetic inlet [*Bates et al.*, 2002] with a motorized horizontal shroud mounted on the sampling van was used to sample the ambient air. Air pulled through the inlet was dried using diffusion driers and distributed to particle instruments.

Aerosol particle sizes are typically reported as vacuum aerodynamic diameter, mobility diameter, and volume equivalent diameter depending on the instruments used, as summarized in **Table 4-2**. Submicron particles (10 – 1000 nm dry mobility diameter) and their number size distributions were measured with a Scanning Electrical Mobility Spectrometer (SEMS, Model 138 2002, Brechtel Manufacturing Inc., Hayward CA). Dried ambient aerosol particles were sampled through an impactor attached to the polydisperse inlet of SEMS at a flow rate of 0.5 lpm to remove particles greater than 1 μm. A known equilibrium charge distribution was applied to the polydisperse particles with a Po210 neutralizer [*Russell et al.*, 1996]. The condensation particle counter (Model 3086, TSI, Shoreview, MN) downstream counts the number of particles in each size bin separated by electrical mobility to provide the number size distribution in dry mobility diameter. A complete size distribution was recorded every 5 min.

A Single Particle Soot Photometer (SP2, Model SP2-C, DMT, Boulder CO) was used to measure the refractory black carbon (rBC, or soot) mass concentrations, as well as their size distributions in the range of 0.08-0.6 μm volume equivalent diameters. The incandescence signals emitted from rBC-containing particles vaporized by an Nd:YAG laser beam (λ = 1064 nm) were measured by the SP2 [*Gao et al.*, 2007; *Laborde et al.*, 2012]. Dried and size-selected particles produced from nebulization of an aqueous suspension of fullerene soot (Alfa Aeser, Tewksbury MA) were used to calibrate the broadband and narrowband incandescence detectors, allowing for accurate measurement of per-particle rBC mass. The high gain and low-gain scattering channels of SP2 were calibrated with 240 nm and 400 nm geometric diameter polystyrene latex spheres. The peak height of the incandescent signal was then converted to mass using calibration measurements made with fullerene soot at the beginning of sampling, and the volume-equivalent diameter of the rBC particle was calculated from the detected mass assuming a spherical particle with density of 1.8 g cm^{-3} [*Gao et al.*, 2007]. The reported rBC mass concentrations have not been adjusted to account for particles outside of the instrument detection range, and thus are likely lower-limits [*Cappa et al.*, 2014; *Zhang et al.*, 2016]. Temporal variability in the contribution of this missing rBC mass may influence the observed diurnal variability.

Non-refractory aerosol mass and composition were measured using a High-Resolution Time-of-Flight Aerosol Mass Spectrometer (AMS). The AMS [*DeCarlo et al.*, 2006; *Jayne et al.*, 2000] was operated in two ion flight path modes. The shorter ion flight path (V-mode) provides better sensitivity at unit mass resolution (UMR), while the longer ion flight path (W-mode) provides sufficient mass spectral resolution (4300 at *m*/*z* 200) to determine empirical formulas of the ionized aerosol fragments. The AMS was operated under a 5 min mode-switching cycle (V-mode, 2-min; LS-mode for single particle UMR spectra, 2-min; W-mode, 1-min). In V-mode, the instrument measured in both mass spectral (MS) and particle time-of-flight (PToF) modes, providing size distributions of non-refractory mass fragments as a function of dry vacuum aerodynamic diameter.

The vacuum aerodynamic diameter of the AMS PToF mode was calibrated using nebulized polystyerene latex (PSL) spheres and ammonium nitrate of known particle sizes at the beginning and end of the Fresno and Fontana studies. PSL between 240 and 400 nm geometric diameter and ammonium nitrate in the size range of 100 to 380 nm dry mobility diameter were used to calibrate

the size and ionization efficiency of the AMS. The size of particles beyond the calibration range was extrapolated from the fitted curve, making the PToF diameter (but not the mass) less accurate for particles larger than 400 nm dry mobility diameter (520 nm vacuum aerodynamic diameter). In addition, transmission of particles decreases for particle larger than 500 nm [*Jayne et al.*, 2000]. The dry vacuum aerodynamic diameter of non-refractory aerosol particles measured by AMS was converted to dry mobility diameter assuming spherical particles using equation (1) [*DeCarlo et al.*, 2004]

$$\rho = D_{va}/D_m \quad (1)$$

where ρ is density, D_{va} is dry vacuum aerodynamic diameter, and D_m is dry mobility diameter. A density of 1.3 g/cc for Fresno and non-firework days in Fontana, and a density of 1.1 g/cc were used for firework days in Fontana [*Chen et al., 2017*]. The mass concentrations and PToF size distributions were corrected for collection efficiency based on filter-based measurements (CE: Fresno low-fog 0.36, Fresno high-fog: 0.49, Fontana firework days 0.52, and Fontana non-firework days 0.93) *[Chen et al., 2017]*.

In addition, three size fractions of aerosol particles ($PM_{2.5}$ (aerodynamic diameter < 2.5 μm), PM_1 (aerodynamic diameter < 1 μm), and $PM_{0.18}$ (aerodynamic diameter < 0.18 μm)) were collected on 37mm Teflon filters (Pall Corporation, San Diego CA) for Fourier Transform Infrared (FTIR) spectroscopy. The filters were pre-conditioned to a relative humidity of 35-45% and temperature at 20^0C for at least 24 hours prior to analysis. Organic functional groups (carbonyl, amine, alcohol, alkane and carboxylic acid groups) were measured directly on all sampled filters by FTIR [*Maria et al.*, 2002].

4.4 Results

The measurements of size-resolved number distribution and composition, size dependence of organic aerosol sources, size dependence of organic contributions to particles mass, and number-to-volume relationships at different times of day (morning: 06:00 – 12:00; afternoon: 12:00 – 18:00; evening: 18:00 – 00:00; and night: 00:00 – 06:00) are described below.

4.4.1 Size-resolved aerosol particle number, mass, and composition

Time series of size-resolved submicron aerosol particle number, rBC mass, and non-refractory organic and inorganic mass concentrations in Fresno and Fontana are shown in **Figure 4-1** and **Figure 4-2** (in the supporting information). In general, Fresno had larger mode diameters of number (70-150 nm), volume (300-460 nm), and non-refractory mass (nitrate and ammonium: 320-400 nm; organic mass: 200-380 nm) than Fontana (number: 30-60 nm; volume: 120-410 nm; nitrate and ammonium: 350-400 nm; organic mass: 130-280 nm; sulfate: 330-360 nm). Measurements influenced by short-duration local emissions (identified as submicron aerosol number concentrations exceeding 50,000 cm^{-3} and rBC mass concentration exceeding 10 μg m^{-3}) were excluded; these times represented less than 2% of the sampling time at Fresno and Fontana.

4.4.1.1 Particle number distributions

Figure 4-3(a,b) shows average size distributions of submicron particle number and volume on low-fog and high-fog days in Fresno. The dry mobility diameters at the mode of number (D_{N_mode})

and volume (D_{V_mode}) distributions are provided in **Table 4-3**. A single mode number distribution with D_{N_mode} of 70 nm in the evening and 80-100 nm at night was observed on both low-fog and high-fog days. Size distributions in the morning (06:00-12:00) and afternoon (12:00-18:00) have broad peaks with D_{N_mode} in the range of 70-100 nm and 70-90 nm respectively on low-fog days and in the range of 80-150 nm on high-fog days. The shapes of the volume-weighted distributions were similar throughout the day during each period, but differed between the low- and high-fog periods, with D_{V_mode} between 300 and 320 nm on low-fog days and between 440 and 460 nm on high-fog days. As shown in **Figure 4-3**, maximum number concentrations in Fresno were highest in the evening (18:00-00:00; low-fog: 38,000 cm^{-3}; high-fog: 15,000 cm^{-3}) and at night (00:00-06:00; low-fog: 18,000 cm^{-3}; high-fog: 12,000 cm^{-3}) and lowest in the morning (low-fog: 9,000 cm^{-3}; high-fog: 8,000 cm^{-3}) and afternoon (low-fog: 8,000 cm^{-3}; high-fog: 6,000 cm^{-3}). Similar trends were observed for the volume concentrations on low-fog days (evening: 37 μm^3 cm^{-3}; night: 26 μm^3 cm^{-3}; morning: 19 μm^3 cm^{-3}; afternoon: 17 μm^3 cm^{-3}). On high-fog days, maximum volume concentrations were high in the evening (68 μm^3 cm^{-3}) and afternoon (67 μm^3 cm^{-3}) and low in the morning (58 μm^3 cm^{-3}) and at night (55 μm^3 cm^{-3}).

Mean size distributions of submicron aerosol particle number and volume on firework and non-firework days in Fontana are shown in **Figure 4-3**(c,d), and the D_{N_mode} of each mode are shown in **Table 4-3**. The number and volume distributions typically included two or more submicron modes at Fontana. On non-firework days the number and volume distributions were usually bimodal with 6 hr average D_{N_mode} at approximately 30 and 50 nm in the morning and D_{V_mode} at 125 nm and 300 nm in the afternoon. On firework days the number distributions had one to three modes (with multiple modes partially overlapping rather than being distinct) in the morning with D_{N_mode} of approximately 30 nm, 60 nm, and 180 nm but typically two modes at night with D_{N_mode} of approximately 50 and 180 nm. The large mode (D_{N_mode}: 180 nm) on firework days is consistent with emissions from pyrotechnic displays [*Zhang et al.*, 2010]. The smaller D_{N_mode} mode diameters at 30 nm and 50-60 nm on firework and non-firework days are likely associated with morning traffic emissions. The reason for two modes on some days may be emissions from different mixtures of vehicle engines and fuels [*Agarwal et al.*, 2015; *Gupta et al.*, 2016].

The wind was from the south 22% of the time in the mornings but less than 10% of the rest of the day at Fontana (**Figure 4-4**). These southerly wind times may explain the higher variability in the number distributions during the mornings at Fontana because of the arterial road located approximately 100 m to the south of the sampling site. The variability in the the smaller particle number modes may result from differences in the evolution of the size distributions from morning rush hour traffic at this road (**Table 4-4**) [*Buonanno et al.*, 2009; *Kozawa et al.*, 2012; *Zhang et al.*, 2005a; *Zhang et al.*, 2004; *Zhu et al.*, 2002a; *Zhu et al.*, 2002b].

4.4.1.2 Size-resolved non-refractory aerosol particles

Size distributions of non-refractory organic, nitrate, sulfate, ammonium, and particle mass at Fresno and Fontana are shown in **Figure 4-5**, and the dry mobility mode diameters (D_{M_mode}) are summarized in **Table 4-3**. Aerosol mass distributions were estimated from the volume size

distributions assuming all the particles in the distribution have a uniform density. **Figure 4-5** shows that in Fresno the mass distributions of all non-refractory organic, nitrate, ammonium and sulfate components on low-fog days were slightly broader than on high-fog days, consistent with the SEMS-observed size distributions. High-fog days had a large accumulation mode (with D_{M_mode} between 360 and 380 nm) of organic components throughout the day whereas low-fog days had a peak in the accumulation mode at smaller dry mobility diameter (200-280 nm) but with overlapping ranges of mass concentration (low-fog: 6-18 μg m^{-3}; high-fog: 11-15 μg m^{-3}). The D_{M_mode} of organic mass distribution was smallest in the evening (200 nm) when residential burning emissions were likely highest and increased to 260 nm at night on low-fog days. The D_{M_mode} of organic aerosol particles in the morning (250 nm) and afternoon (280 nm) were not significantly different from the D_{M_mode} at night. Nitrate, sulfate and ammonium mass distributions had similar D_{M_mode} on high-fog days (380-400 nm) and low-fog days (330-350 nm), but their mass concentrations were 2 to 4 times higher on high-fog days.

In Fontana, particle mass was nearly two times that of the non-refractory mass in the morning and at night on firework days, and the D_{M_mode} of non-refractory aerosol components were nearly the same, with the D_{M_mode} falling between 480 and 520 nm. The discrepancy between SEMS and non-refractory AMS mass on firework days is likely due to high concentrations of heavy metals in firework emissions [*Betha and Balasubramanian*, 2014]. A bimodal size distribution was observed for non-refractory organic and nitrate aerosol particles on non-firework days. The larger mode has a D_{M_mode} of approximately 280 nm for organic mass and 350-400 nm for nitrate mass (similar to Fresno), and the smaller mode has nearly the same D_{M_mode} between 130 and 150 nm for both organic and nitrate mass. In the afternoon the smaller mode organic mass concentration (peak concentration = 3.3 μg/m^3) was nearly 1.4 times higher than the concentration of larger mode (2.3 μg/m^3). Sulfate and ammonium mass distributions had a D_{M_mode} of 360-380 nm, similar to the larger mode of nitrate during non-firework days in the morning, afternoon, evening, and night.

4.4.1.3 Size resolved refractory black carbon aerosol particles

The size-resolved rBC mass distributions and the diurnal variation of the submicron rBC mass concentrations are shown in **Figure 4-6** and **Figure 4-7**, respectively. The volume equivalent diameters at the mode (D_{VED_mode}) of rBC mass distributions are summarized in **Table 4-3**. The rBC diurnal profile during winter in Fresno was characterized by high concentrations of rBC mass in the evening (18:00-00:00) and at night (00:00-06:00) when residential burning emissions were likely highest and when the boundary layer was the most shallow. The D_{VED_mode} of rBC distributions were approximately 180 nm in the evening and at night on low-fog days and approximately 140 nm on high-fog days. On high-fog days the mean temperatures (12 °C) are higher than low-fog days (6 °C), suggesting that residential wood burning activity might have been lower resulting in lower mass flux and smaller D_{VED_mode} on high-fog days because the fractional contribution of wood burning-derived rBC mass was lower [*Sakamoto et al.*, 2016]. In the morning and afternoon of low-fog days, rBC mass distributions have broader peaks and D_{VED_mode} at 140 nm, while the D_{VED_mode} of rBC mass distribution on high-fog days appears to be below the detection range of the SP2 (80 nm diameter). The D_{VED_mode} of rBC mass in Fresno are 10 to 50

nm larger than that of the rBC emissions from biomass burning (130 nm) reported by Laborde et al. [2013], but consistent with those reported by Zhang et al. [2016].

In Fontana, the rBC mass concentration was highest in the morning (especially between 09:00-10:00, as shown in **Figure 4-7**), corresponding to the rush hour traffic, and was lower during the rest of the day (**Figure 4-7**). On firework and non-firework days the rBC distribution was broad and flat with D_{VED_mode} in the range of 80-100 nm. rBC mass distributions have smaller average D_{VED_mode} in Fontana (80-100 nm) than in Fresno (80-180 nm). The volume equivalent diameters of rBC in Fontana are similar to the rBC emissions from traffic (100 nm) reported by Laborde et al. [2013]. The high concentrations at the lower diameters of the mass-weighted rBC size distributions at both Fresno and Fontana indicate that the rBC mass below the SP2 lower detectable size of 80 nm could contribute a substantial fraction to rBC mass.

4.4.1.4 Organic functional groups

The mean mass concentrations of alkane, alcohol, carbonyl, carboxylic acid, and amine functional groups for the three size fractions collected in Fresno and Fontana are shown in **Figure 4-8**, and their relative contributions are shown in **Table 4-5**. Alkane was the functional group with the highest mass concentration, contributing nearly 50% of organic mass in both Fresno and Fontana for $PM_{2.5}$, PM_1 and $PM_{0.18}$. The mass concentration and relative contributions of different groups were nearly identical for $PM_{2.5}$ and PM_1 samples, indicating that almost all of the organic mass is submicron at both sites.

On low-fog days in Fresno, contributions of alcohol and carboxylic acid groups to organic mass were nearly identical for $PM_{2.5}$ (16%) and PM_1 (19%), followed by amine groups (10% for both $PM_{2.5}$ and PM_1). The composition of $PM_{0.18}$ differs from $PM_{2.5}$ and PM_1 in that the carboxylic acid group contribution was significantly higher (23%) than the amine (14%) and alcohol (10%) groups. On high-fog days the concentration of alkane, alcohol and carboxylic acid groups were 3 to 4 times higher than on low-fog days, but the fractional contributions of alkane and carboxylic acid groups to organic mass in $PM_{2.5}$ and PM_1 are nearly the same. Alcohol groups have a slightly higher relative contribution on high-fog days compared to low-fog days, but the amine group relative contribution was lower. Back trajectories for the Fresno study show that air masses originated within the SJV region and accumulated over long periods of time with little net horizontal transport on high-fog days [Chen et al., 2017], resulting in higher concentrations of organic functional groups on high-fog days compared to low-fog days. The mass concentrations and relative contributions for all of the functional groups are nearly the same for low-fog and high-fog days for $PM_{0.18}$, indicating little influence of fog on the particles smaller than 180 nm dry diameter.

In Fontana, the fractional contribution of functional groups to organic mass was different between firework and non-firework days. On non-firework days, alkane groups contributed the largest fraction of 56-57% of organic mass, and the contribution of alcohol groups was 11-17%, which is lower than on the firework days when alkane groups contributed 45-46% of organic mass and alcohol groups contributed 25-33%. Carboxylic acid groups (12-18%) and amine groups (9-15%) were nearly the same for firework and non-firework days for $PM_{2.5}$, PM_1, and $PM_{0.18}$.

Fireworks typically consist of metals, polyalcohols, sulfur and charcoal as fuel and a large fraction of nitrates, perchlorates and chlorates as oxidizers (oxidizer/fuel ratio ~1) [*Oxley et al.*, 2015].

The high mean concentrations of PM_1 organic functional groups in Fresno were expected during peak residential wood burning activities in the evening on low-fog days and were likely associated with fog processing in the afternoon on high-fog days (**Table 4-6** and **Table 4-7**). However, the differences in mean concentrations at different times of the day are not statistically significant. In Fontana, mean concentrations of alkane, alcohol, carboxylic acid, amine and carbonyl group mass in the morning, afternoon, evening and at night are not statistically different (**Table 4-8**).

4.4.2 Correlations between Non-refractory aerosol mass distributions and volume size distributions

Figures 5 and 6 show the Pearson's correlation coefficients (R) calculated from the covariance of each size bin of the AMS size-resolved organic, nitrate, sulfate, and non-refractory mass concentrations with each size bin of the SEMS volume size distributions measured divided by the product of their standard deviations. Higher R^2 values indicate a strong correlation between the mass concentration of dry vacuum aerodynamic particles in a specific size range and the volume concentration at dry mobility diameters. Using the densities of aerosol particles in Fresno and Fontana determined by Chen et al. [2017], vacuum aerodynamic diameter was computed as a function of mobility diameter (**Figure 4-9** and **Figure 4-10**, black line). In this study, we consider R^2 between 0.64 and 1.0 ($.8 \leq |R| \leq 1$) to be a strong correlation, R^2 less than 0.25 ($0 \leq |R| \leq .5$) to be weak, and otherwise to be moderate [*Devore and Berk*, 2012].

Figure 4-9 shows moderate to strong correlations ($R^2 > 0.5$) in Fresno on both low-fog and high-fog days for non-refractory mass and organic components. Nitrate and sulfate mass have moderate to strong correlations throughout the day on high-fog days. On low-fog days, they did not show a size-resolved correlation with particle volume, except in the afternoon. The strength of the size-resolved correlation between non-refractory aerosol components and submicron particle volume depends in part on the relative contribution of each non-refractory component to submicron aerosol mass. The smaller contribution of non-refractory components to aerosol mass results in weaker correlations with particle volume because of the limited signal-to-noise for components present at low concentrations. The apparent strong to moderate correlation of nitrate and sulfate on high-fog days is likely associated with aqueous phase reactions of aerosol particles on high-fog days resulting in higher relative contributions to submicron mass.

In Fontana, non-refractory mass, organic components and nitrate were strongly correlated to particle volume distributions on non-firework days. Sulfate mass did not show a correlation to the particle volume distribution (**Figure 4-10**). The lack of correlation during firework days is likely the result of refractory components contributing a large fraction of the submicron mass.

In general, the particle vacuum aerodynamic diameters with higher R^2 are within 10% of the modeled aerodynamic diameters (diagonal black line in **Figure 4-9** and **Figure 4-10**). At diameters larger than 700 nm, the difference between the measured and computed diameter was higher than

for particles smaller than 700 nm at both Fresno and Fontana. A considerable fraction of non-refractory organic mass, nitrate, ammonium, and sulfate is in particles larger than 400 nm vacuum aerodynamic diameters where calibration uncertainties and inlet losses are higher (**Figure 4-5**). This could also result from the assumption that density is constant with size. Zhang et al. [2005b] observed that the densities are usually higher for larger particles, which appears to be the case in Fontana and Fresno, although this inference is indirect. Higher densities at larger sizes would mean that the vacuum aerodynamic diameters of these larger particles are underestimated since they are scaled by density.

4.4.3 Size Dependence of Organic Aerosol Sources

Chen et al. [2017] identified Biomass Burning Organic Aerosols (AMS-BBOA), Nitrate-related Oxygenated Organic Aerosols (AMS-NOOA), Vehicle-related Oxygenated Organic Aerosol (AMS-VOOA), Hydrocarbon-like Organic Aerosol particles (AMS-HOA), and Cooking-related Organic Aerosol (AMS-COA) submicron aerosol mass spectrometer (AMS) factors by analyzing the aerosol mass spectrometer (AMS) measurements from the same field studies in Fresno and Fontana using positive matrix factorization. To investigate the size dependence of these organic aerosol sources, the Pearson's correlation coefficient (R) was calculated as the covariance of the AMS PMF factor mass concentration with each size bin of SEMS particle volume distribution divided by the product of their standard deviations. The correlation coefficients (R) provide a measure of the linear correlation of the mass concentration of each source that can be explained by the volume of particles in that size bin. Higher R^2 values for specific particle size bins suggest that a major fraction of the mass is associated with the particles in that size range. **Figure 4-11** shows the R^2 values for organic aerosol sources in Fresno and Fontana, and **Table 4-9** summarizes the particle size range of organic sources with the highest correlations for Fresno and Fontana.

Most of the AMS-BBOA mass concentrations in the evenings in Fresno were associated with particles with dry mobility diameters between 75 and 160 nm (with maximum correlation at 120 nm) on low-fog days and between 60 and 120 nm on high-fog days (as shown in **Figure 4-11** and **Table 4-9**). At night AMS-BBOA mass concentrations were strongly correlated with larger particles between 150 and 260 nm dry mobility diameters on low-fog days and between 80 and 140 nm on high-fog days. In the afternoons, when concentrations were the lowest, AMS-BBOA mass concentrations on low-fog days were associated with particles with dry mobility diameters between 30 and 100 nm. The correlation between AMS-HOA mass and volume distributions on low-fog days is similar to that for AMS-BBOA. AMS-HOA mass concentrations were strongly correlated ($R^2 > 0.5$) with smaller particles (27-53 nm) in the afternoon and with larger particles (100 nm dry mobility diameter) in the evening and at night. On high-fog days, AMS-HOA mass concentrations are moderately correlated with particle volume distributions over a broad range of particle mobility diameters for most of the day (40 to 170 nm in the afternoon, 30 to 130 nm in the evening, and 40 to 280 nm at night). In the mornings, AMS-HOA mass appears to be mostly present in a narrow size range of 100-125 nm. In Fresno, AMS-BBOA and AMS-HOA mass have a moderate correlation with particles between 100 and 150 nm dry mobility diameter on low-fog

and high-fog days, but AMS-NOOA mass concentration has a strong correlation ($R^2 > 0.5$) for particles near 460 nm dry mobility diameter in the morning and at night, near 525 nm in the evening, and near 360 nm in the afternoons on high-fog days. On low-fog days, AMS-NOOA mass had no correlation with size-resolved particle volume throughout the day except in the afternoons, when there was a moderate correlation of particle volume distribution with AMS-NOOA mass at 300 nm dry mobility diameter. AMS-VOOA mass concentration was weakly correlated to particle volume distributions on high-fog days and moderately correlated on low-fog days. AMS-VOOA mass concentration was associated with smaller particles in the dry mobility diameter range of 220-340 nm with maximum correlations at 280 nm in the morning and the range of 200-310 nm with maximum correlations at 260 nm in the afternoon. In the evening and at night, AMS-VOOA mass concentration was associated with slightly larger particles in the size range of 240-420 nm with maximum correlations at 360 nm mobility diameter.

In Fontana, AMS-COA mass concentration and AMS-HOA mass concentration have no correlation with size-resolved particle volume ($R^2 < 0.2$) on firework days (**Figure 4-11**). AMS-VOOA mass concentration has a strong correlation with particles between 100 and 600 nm dry mobility diameter at night and a moderate correlation ($R^2 <0.5$) with particles in the size range of 40-70 nm in the evening. AMS-NOOA mass concentration has a moderate correlation with 40-60 nm particles in the afternoon and 80-260 nm particles at night. On non-firework days, AMS-VOOA mass is associated with the particle volume distribution for the size range of 60-150 nm dry mobility diameter, while AMS-NOOA mass concentration was associated with larger particles (140-456 nm) (**Table 4-9**). AMS-HOA mass concentration has a moderate ($R^2 = 0.3$-0.5) to strong ($R^2 >0.5$) correlation with particle volume distribution with maximum correlations values at 150 nm in the evening and 200 nm in the morning. AMS-COA particle mass concentration was associated with particles in the size range of 60-145, 80-116, and 80-280 nm in the morning, afternoon and evening, respectively.

4.4.4 Size Dependence of organic contributions to particle mass

The fragment ion m/z 44 is typically the highest oxygen-containing organic fragment ion measured by AMS in ambient aerosol and can include contributions from organic acids, and esters but is often a reasonable indicator of O/C [*Aiken et al.*, 2008; *Ng et al.*, 2011; *Ng et al.*, 2010; *Yatavelli et al.*, 2015]. Here the size dependence of the organic mass contribution and its oxidized fraction was investigated using the ratios of organic mass-to-particle mass, m/z 44-to-particle mass, and m/z 44-to-organic mass, similar to the approach developed by [*Maria et al.*, 2004] for size-resolved microscopy measurements. **Figure 4-12** shows these ratios at different times of day on low-fog and high-fog days in Fresno and on firework and non-firework days in Fontana.

The ratios of organic mass-to-particle mass and m/z 44-to-particle mass had little size dependence on both low and high fog days in Fresno. The m/z 44-to-organic mass ratio had a weak size dependence on both low-fog and high-fog days for particles below 200 nm, but the variability of this ratio at these small diameters was ±70%."

The ratios of organic mass to particle mass, m/z 44-to-particle mass, and m/z 44-to-organic mass were size dependent at Fontana on both firework and non-firework days. All three ratios

decreased with increasing particle diameter, although there was substantial variability in the size dependence of these ratios at various times of the day.

4.4.5 Number and volume relationship of submicron particles

Figure 4-13 shows the relationship between 1-hr averaged submicron particle number and volume in Fresno and Fontana. On low-fog days in Fresno there was a linear relationship between number and volume in the evening (R^2 = 0.71) and at night (R^2=0.75). Number and volume had moderate to strong correlations (R^2 = 0.41-0.6) with linear relationships on non-firework days in Fontana. **Figure 4-14** shows that number-to-volume ratios increase with increasing organic mass fraction. The dependence of number-to-volume ratio on organic mass fraction had a weak to moderate correlation on low-fog days in Fresno (R^2: 0.13-0.41) and on non-firework days in Fontana (R^2: 0.03-0.23) and a moderate to strong correlation on high-fog days in Fresno (R^2: 0.43-0.81) and firework days in Fontana (R^2: 0.77-0.87).

4.5 Discussion

The size-resolved number and composition of atmospheric aerosol particles and the atmospheric growth processes that produced these properties in Fresno and Fontana are discussed below.

4.5.1 Size differences of aerosol particles in Fresno and Fontana

Fontana during summertime showed a larger fraction of aerosol particles that were smaller than 200 nm, both by number and mass, compared to particles measured during wintertime in Fresno. On non-firework days in Fontana, aerosol particles smaller than 200 nm contributed 97-99% of submicron number, in contrast to 86-91% (depending on time of day) in Fresno. Fresno was also lower in fractional contributions of both organic and rBC mass below 200 nm (21-50% of organic mass; 60-69% of rBC mass) compared to Fontana (50-58% organic mass; 74-81% rBC mass). This difference was evident in the larger mode diameters and low number-to-volume ratios in Fresno compared to Fontana. D_{N_mode} on low-fog (70-85 nm) and high-fog (70-150 nm) days are larger and number-to-volume ratios on low-fog (285-2500 μm^{-3}) and high-fog days (120-1000 μm^{-3}) are lower in Fresno compared to non-firework days ($D_{N\_mode:}$ 30-60 nm; number-to-volume ratio: 800-4750 μm^{-3}) in Fontana (**Figure 4-3** and **Figure 4-14**). At Fresno, the D_{M_mode} of non-refractory organic and the D_{VED_mode} of rBC mass distributions were also larger than at Fontana (**Figure 4-5**, **Figure 4-6**, and **Table 4-3**). AMS-VOOA (vehicle-related oxidized organic aerosol) mass concentration was mainly associated with larger particles (low-fog: 260-330 nm; high-fog: 500 nm) in Fresno (**Figure 4-11**) but with smaller particles (60-150 nm) during non-firework days in Fontana.

The differences in particle sizes in Fresno and Fontana are the consequence of the different aerosol sources. **Table 4-1** shows that traffic emissions have smaller mean diameters for rBC mass (100 nm) and organic mass (120 nm) than for biomass burning particles (rBC mass: 130, 280, and 750 nm; AMS-BBOA mass: 140 nm). Fontana, surrounded by major freeways and an auto speedway, has very high traffic emissions. Also, seasonal differences between the Fresno (winter) and Fontana (summer) studies resulted in differences in biomass burning emissions between the

studies, with substantially greater biomass burning emissions in wintertime Fresno. The smaller modes of rBC mass (D_{VED_mode}: 80-100 nm) and organic aerosol mass (D_{M_mode}: 150-160 nm) are consistent with the traffic emissions, particularly during morning rush hour traffic (**Table 4-1**). The high mass fraction of smaller particles in Fontana could include contributions from secondary organic aerosols [*Craven et al.*, 2013]. Chen et al. [2017] showed that, in Fontana, AMS-VOOA mass was high in the afternoon, contributing more than 50% of organic mass. The association of VOOA mass with smaller particles in the size range of 60-150 nm (**Figure 4-11**) suggests that photo-oxidation contributes significantly to smaller particles in Fontana.

In Fresno, residential wood burning emissions are high especially in the evening and at night. Chen et al. [2017] showed that AMS-BBOA mass concentrations were higher in the evening and at night, contributing nearly 50% of organic mass on low-fog days. We also observed a very strong correlation between AMS-BBOA mass and particle number concentrations in the evening (R^2 = 0.72) and at night (R^2 = 0.61) (**Figure 4-15**), consistent with previous studies in Fresno during wintertime that showed that residential wood burning was a major source of aerosols [*Ge et al.*, 2012a; *Kleeman et al.*, 2009a; *Young et al.*, 2016]. The larger D_{VED_mode} of rBC mass (140-180 nm) and the D_{M_mode} of AMS-BBOA mass in Fresno are comparable to the mean diameter of rBC mass emitted from biomass burning (**Table 4-1**). The larger D_{N_mode} and D_{M_mode} could also be due to higher particle water content along with residential wood burning, which allows aqueous reactions to contribute more secondary inorganic and organic components (such as ammonium nitrate and AMS-NOOA) that increase particle size [*Chow et al.*, 2008; *Ge et al.*, 2012b; *Ying and Kleeman*, 2006], particularly on high-fog days. The larger D_{M_mode} and narrow, uniform size distributions of organic, ammonium, nitrate and sulfate mass on high-fog days are likely the result of aqueous processing of aerosol particle distributions. Ge et al. [2012b] measured a similar mode diameter of organic mass, nitrate, and sulfate of 500 nm in dry vacuum aerodynamic diameter (equivalent to 380 nm dry mobility diameter using a density of 1.3 g cm^{-3}), which they attributed to aqueous reactions in Fresno.

4.5.2 Volume and surface limited growth processes

The strong correlation between number and volume in Fresno during evening and at night on low-fog days and in Fontana during mornings, evenings, and at night on non-firework days is consistent with dilution of a single source of primary particles [*Hegg and Russell*, 2000]. The weak correlation between number and volume and near zero slope of the linear fit on high-fog days indicates that accumulation-mode aerosol particles likely have contributions from secondary sources that change the size distribution and prevent a linear relationship between number and volume.

The dependence of secondary organic aerosol signatures on size provides information about the processes that contribute to particle growth [*Maria et al.*, 2004]. Secondary organic aerosols preferentially condense on smaller particles resulting in higher fractional contributions to mass at smaller sizes than at larger sizes. **Figure 4-12** shows that m/z 44-to-organic mass and organic mass-to-particle mass ratios are nearly constant for submicron aerosol particles in Fresno but generally are size dependent in Fontana. These results provide evidence that, in Fresno, secondary

organic components are mainly formed by volume-limited or aqueous-phase reactions during wintertime. For particles below 200 nm, m/z 44-to-particle mass has some size dependence likely because smaller aerosol particles (below 200 nm) are not activated to fog droplets; consequently, the contributing components are from mass transfer limited processes more than aqueous processes. The strong correlations (R^2>0.5) between size-resolved non-refractory components and submicron particle volume over a narrow range of diameters (400 – 500 nm dry mobility diameter) on high-fog days are also consistent with aqueous processing (**Figure 4-9**). However, in Fontana, the size dependence of the m/z 44-to-organic mass, organic mass-to-particle mass, and m/z 44-to-particle mass ratios indicate aerosol growth resulted primarily from mass-transfer limited processes (condensation and surface-limited oxidation) rather than aqueous reactions.

4.6 Conclusions

Given that different aerosol sources have different characteristic sizes and compositions, their size and composition are not independent [*Ge et al.*, 2012a; *Laborde et al.*, 2013]. During winter in Fresno and summer in Fontana, the size-resolved number, mass, and composition of aerosol particles and organic aerosol sources showed that Fresno had single-mode distributions with D_{N_mode}, D_{V_mode}, D_{M_mode}, and D_{VED_mode} (and low number-to-volume ratio of 285-2000 μm^{-3}) that varied between 6% and 200% larger than in Fontana, which had a large fraction of smaller (<100 nm) aerosol particles (and higher number-to-volume ratios of 800-4750 μm^{-3}). In Fontana particle number distribution had a maximum number concentration between 30 and 50 nm on non-firework days but in Fresno the maximum number concentration was between 70 and 80 nm in the evening and at night. Similarly, rBC mass distributions had mode peaks at volume equivalent diameter between 100 and 120 nm in Fontana and between 130 and 180 nm in Fresno. In Fontana, organic mass distributions had D_{M_mode} between 130 and 140 nm (often with a lower-concentration mode at 275 nm) and between 260 and 370 nm in Fresno. The differences in particle mode diameters between Fresno and Fontana are consistent with the different sources in the two regions: in Fresno larger particles are at high concentrations in the evening and at night, likely due to residential wood burning activities; in Fontana smaller particles are prevalent during most of the day, likely associated with vehicular traffic emissions [*Fujita et al.*, 2007; *Ge et al.*, 2012a].

In addition to sources, different atmospheric processes in Fresno and Fontana affected particle sizes: The ratios of organic mass-to-particle mass and m/z 44-to-particle mass were nearly constant with size in Fresno and were decreasing with size in Fontana. The lack of size dependence is consistent with volume-limited growth (or aqueous phase reactions) of particles larger than 200 nm diameter in Fresno. Similarly the decrease in fraction of organic and oxidized markers with size could result from surface-limited (or mass-transfer limited) processes for aerosol particles in Fontana. In Fresno the narrowing of size distributions on high-fog days, a characteristic of aqueous processing of activated particles, increased D_{M_mode} and D_{V_mode}. In Fontana formation of organic components from mass-transfer limited processes resulted in the growth of smaller mode aerosol particles.

4.7 Acknowledgments

We acknowledge California Air Resources Board (CARB) for funding this work (Agreement number: 13-330) and Dr. Nehzat Motallebi for her advice and guidance as contract manager. We thank the staff of the Fontana Fire Department and the South Coast Air Quality Management District (SCAQMD) for Fontana site logistics and the staff of UCD Extension at Fresno for their help with local logistics. We also thank Justin Dunworth for his help in setting up the Fresno site and Jackie First for her assistance with aerosol sample analysis. The statements and conclusions in this paper are those of the researchers (contractor) and not necessarily those of CARB. The mention of commercial products, their source, or their use in connection with material reported herein is not to be construed as actual or implied endorsement of such products. The measurements used in this manuscript are available at https://doi.org/10.6075/J0VX0DF9 and https://doi.org/10.6075/J0VX0DF9.

4.8 Appendices

4.8.1 Size distributions of aerosol particles in Fresno and Fontana

Figure 4-1 and **Figure 4-2** show size distributions for aerosol particles, refractory black carbon (rBC), and non-refractory organic mass, nitrate, sulfate and ammonium mass in Fresno and Fontana. **Table 4-2** summarizes dry mobility diameter at maximum concentration of the mode of number (D_{N_mode}), volume (D_{V_mode}), and mass (D_{M_mode}) and the volume equivalent diameter at maximum concentration of the mode (D_{VED_mode}) of rBC mass distribution. In Fresno, aerosol particle volume and organic mass distributions had higher peak concentrations and smaller D_{V_mode} and D_{M_mode} in the evening and at night than during morning and afternoon on low-fog days (particle volume: 310 nm; organic mass: 200-260 nm).

In Fontana, particle number, volume, and non-refractory organic and inorganic mass distributions had large D_{N_mode}, D_{V_mode}, and D_{M_mode}, as well as higher peak concentrations during firework days, compared to non-firework days. **Figure 4-3** shows a distinct third mode (180 nm D_{N_mode}) number distribution on firework days. In **Figure 4-2**, this large aerosol particle number mode on 5 July 2015, where high particle concentrations (>10,000 cm^{-3}) associated with firework emissions persisted from the early morning hours (0200) until late in the morning (1000). Although particle number distributions returned to typical levels at noon (1200), higher organic mass, nitrate, sulfate, and ammonium mass concentrations persisted in the study region for nearly 7 days. The larger mode could be due to aging and growth of firework-emitted aerosol particles during transport from source regions to Fontana.

4.8.2 Diurnal variation of rBC concentrations in Fresno and Fontana

During winter in Fresno, high rBC concentrations were found in the evening (1800-0000) and at night (0000-0600) when residential wood burning activity was prevalent; a minor concentration peak was seen in the morning during rush hour traffic (**Figure 4-4**). At Fontana, rBC peaked in the morning between 0900 and 1000 (corresponding to rush hour traffic) and was low the rest of the day.

4.8.3 Correlation between organic aerosol factors and particle number in Fresno

Biomass Burning Organic Aerosol (AMS-BBOA) is a significant source of aerosol number in Fresno, strongly correlating with number concentrations in the evening (R^2 = 0.72) and at night (R^2 = 0.61) (**Figure 4-14**). Hydrocarbon-like organic aerosol (AMS-HOA) were also well correlated with aerosol number. AMS-HOA strongly correlated to aerosol number (R^2 = 0.89) in the afternoon when contributions from traffic were high, while AMS-BBOA strongly correlated in the evenings, when residential wood burning activities were high.

4.8.4 Size Correlation between organic mass and vehicle-related oxygenated organic aerosol (AMS-VOOA) in Fontana

Figure 4-15 shows that organic particle mass at 130-, 140- and 150-nm-size strongly correlates (R^2 > 0.7) with AMS-VOOA (secondary organic aerosol produced from vehicular emissions) in Fontana, suggesting that the secondary organic aerosols that form by photo-oxidation, especially in the afternoon, are responsible for the organic mass.

4.9 References

Agarwal, A. K., T. Gupta, P. Bothra, and P. C. Shukla (2015), Emission profiling of diesel and gasoline cars at a city traffic junction, *Particuology*, *18*, 186-193, doi:10.1016/j.partic.2014.06.008.

Ahlm, L., et al. (2012), Formation and growth of ultrafine particles from secondary sources in Bakersfield, California, *Journal of Geophysical Research-Atmospheres*, *117*, 13, doi:10.1029/2011jd017144.

Aiken, A. C., et al. (2008), O/C and OM/OC ratios of primary, secondary, and ambient organic aerosols with high-resolution time-of-flight aerosol mass spectrometry, *Environmental Science & Technology*, *42*(12), 4478-4485, doi:10.1021/es703009q.

Alfarra, M. R., et al. (2004), Characterization of urban and rural organic particulate in the lower Fraser valley using two aerodyne aerosol mass spectrometers, *Atmospheric Environment*, *38*(34), 5745-5758, doi:10.1016/j.atmosenv.2004.01.054.

Bates, T. S., D. J. Coffman, D. S. Covert, and P. K. Quinn (2002), Regional marine boundary layer aerosol size distributions in the Indian, Atlantic, and Pacific Oceans: A comparison of INDOEX measurements with ACE-1, ACE-2, and Aerosols99, *Journal of Geophysical Research-Atmospheres*, *107*(D19), 15, doi:10.1029/2001jd001174.

Betha, R., and R. Balasubramanian (2014), PM2.5 Emissions from Hand-Held Sparklers: Chemical Characterization and Health Risk Assessment, *Aerosol and Air Quality Research*, *14*(5), 1477-1486, doi:10.4209/aaqr.2013.07.0255.

Buonanno, G., A. A. Lall, and L. Stabile (2009), Temporal size distribution and concentration of particles near a major highway, *Atmospheric Environment*, *43*(5), 1100-1105, doi:10.1016/j.atmosenv.2008.11.011.

Cappa, C. D., et al. (2014), A case study into the measurement of ship emissions from plume intercepts of the NOAA ship Miller Freeman, *Atmospheric Chemistry and Physics*, *14*(3), 1337-1352, doi:10.5194/acp-14-1337-2014.

Chan, A. W. H., et al. (2013), Detailed chemical characterization of unresolved complex mixtures in atmospheric organics: Insights into emission sources, atmospheric processing, and

secondary organic aerosol formation, *Journal of Geophysical Research-Atmospheres*, *118*(12), 6783-6796, doi:10.1002/jgrd.50533.

Chen, J. J., J. Lu, J. C. Avise, J. A. DaMassa, M. J. Kleeman, and A. P. Kaduwela (2014), Seasonal modeling of PM2.5\ in California's San Joaquin Valley, *Atmospheric Environment*, *92*, 182-190, doi:10.1016/j.atmosenv.2014.04.030.

Chow, J. C., L. W. A. Chen, J. G. Watson, D. H. Lowenthal, K. A. Magliano, K. Turkiewicz, and D. E. Lehrman (2006), PM2.5 chemical composition and spatiotemporal variability during the California Regional PM10/PM2.5 Air Quality Study (CRPAQS), *Journal of Geophysical Research-Atmospheres*, *111*(D10), 17, doi:10.1029/2005jd006457.

Chow, J. C., J. G. Watson, D. H. Lowenthal, and K. L. Magliano (2008), Size-resolved aerosol chemical concentrations at rural and urban sites in Central California, USA, *Atmospheric Research*, *90*(2-4), 243-252, doi:10.1016/j.atmosres.2008.03.017.

Craven, J. S., A. R. Metcalf, R. Bahreini, A. Middlebrook, P. L. Hayes, H. T. Duong, A. Sorooshian, J. L. Jimenez, R. C. Flagan, and J. H. Seinfeld (2013), Los Angeles Basin airborne organic aerosol characterization during CalNex, *Journal of Geophysical Research-Atmospheres*, *118*(19), 11453-11467, doi:10.1002/jgrd.50853.

DeCarlo, P. F., et al. (2006), Field-deployable, high-resolution, time-of-flight aerosol mass spectrometer, *Anal Chem*, *78*(24), 8281-8289, doi:10.1021/ac061249n.

DeCarlo, P. F., J. G. Slowik, D. R. Worsnop, P. Davidovits, and J. L. Jimenez (2004), Particle morphology and density characterization by combined mobility and aerodynamic diameter measurements. Part 1: Theory, *Aerosol Science and Technology*, *38*(12), 1185-1205, doi:10.1080/027868290903907.

Devore, J. L., and K. N. Berk (2012), *Modern Mathematical Statistics with Applications*, Springer.

Elser, M., et al. (2016), New insights into PM2.5 chemical composition and sources in two major cities in China during extreme haze events using aerosol mass spectrometry, *Atmospheric Chemistry and Physics*, *16*(5), 3207-3225, doi:10.5194/acp-16-3207-2016.

Ensberg, J. J., et al. (2013), Inorganic and black carbon aerosols in the Los Angeles Basin during CalNex, *Journal of Geophysical Research-Atmospheres*, *118*(4), 1777-1803, doi:10.1029/2012jd018136.

Fujita, E. M., D. E. Campbell, W. P. Arnott, J. C. Chow, and B. Zielinska (2007), Evaluations of the chemical mass balance method for determining contributions of gasoline and diesel exhaust to ambient carbonaceous aerosols, *Journal of the Air & Waste Management Association*, *57*(6), 721-740, doi:10.3155/1047-3289.57.6.721.

Gao, R. S., et al. (2007), A novel method for estimating light-scattering properties of soot aerosols using a modified single-particle soot photometer, *Aerosol Science and Technology*, *41*(2), 125-135, doi:10.1080/02786820601118398.

Ge, X. L., A. Setyan, Y. L. Sun, and Q. Zhang (2012a), Primary and secondary organic aerosols in Fresno, California during wintertime: Results from high resolution aerosol mass spectrometry, *Journal of Geophysical Research-Atmospheres*, *117*, 15, doi:10.1029/2012jd018026.

Ge, X. L., Q. Zhang, Y. L. Sun, C. R. Ruehl, and A. Setyan (2012b), Effect of aqueous-phase processing on aerosol chemistry and size distributions in Fresno, California, during wintertime, *Environmental Chemistry*, *9*(3), 221-235, doi:10.1071/en11168.

Gupta, S., R. Agarwal, and S. K. Mittal (2016), Respiratory health concerns in children at some strategic locations from high PM levels during crop residue burning episodes, *Atmospheric Environment*, *137*, 127-134, doi:10.1016/j.atmosenv.2016.04.030.

Hall, J. V., V. Brajer, and F. W. Lurmann (2010), Air pollution, health and economic benefits-Lessons from 20 years of analysis, *Ecological Economics*, *69*(12), 2590-2597, doi:10.1016/j.ecolecon.2010.08.003.

Hasheminassab, S., N. Daher, A. Saffari, D. Wang, B. D. Ostro, and C. Sioutas (2014), Spatial and temporal variability of sources of ambient fine particulate matter (PM2.5) in California, *Atmospheric Chemistry and Physics*, *14*(22), 12085-12097, doi:10.5194/acp-14-12085-2014.

Hayes, P. L., et al. (2013), Organic aerosol composition and sources in Pasadena, California, during the 2010 CalNex campaign, *Journal of Geophysical Research-Atmospheres*, *118*(16), 9233-9257, doi:10.1002/jgrd.50530.

Healy, R. M., et al. (2012), Sources and mixing state of size-resolved elemental carbon particles in a European megacity: Paris, *Atmospheric Chemistry and Physics*, *12*(4), 1681-1700, doi:10.5194/acp-12-1681-2012.

Hegg, D. A., and L. M. Russell (2000), An analysis of processes determining the number-to-volume relationship for submicron aerosol in the eastern Atlantic, *Journal of Geophysical Research-Atmospheres*, *105*(D12), 15321-15328, doi:10.1029/2000jd900181.

Hersey, S. P., et al. (2013), Composition and hygroscopicity of the Los Angeles Aerosol: CalNex, *Journal of Geophysical Research-Atmospheres*, *118*(7), 3016-3036, doi:10.1002/jgrd.50307.

Jayne, J. T., D. C. Leard, X. F. Zhang, P. Davidovits, K. A. Smith, C. E. Kolb, and D. R. Worsnop (2000), Development of an aerosol mass spectrometer for size and composition analysis of submicron particles, *Aerosol Sci Tech*, *33*(1-2), 49-70, doi:Doi 10.1080/027868200410840.

Kleeman, M. J., S. G. Riddle, M. A. Robert, C. A. Jakober, P. M. Fine, M. D. Hays, J. J. Schauer, and M. P. Hannigan (2009a), Source Apportionment of Fine (PM1.8) and Ultrafine (PM0.1) Airborne Particulate Matter during a Severe Winter Pollution Episode, *Environmental Science & Technology*, *43*(2), 272-279, doi:10.1021/es800400m.

Kleeman, M. J., S. G. Riddle, M. A. Robert, C. A. Jakober, P. M. Fine, M. D. Hays, J. J. Schauer, and M. P. Hannigan (2009b), Source Apportionment of Fine (PM1.8) and Ultrafine (PM0.1) Airborne Particulate Matter during a Severe Winter Pollution Episode, *Environmental Science & Technology*, *43*(2), 272-279, doi:10.1021/es800400m.

Kleeman, M. J., Q. Ying, J. Lu, M. J. Mysliwiec, R. J. Griffin, J. J. Chen, and S. Clegg (2007), Source apportionment of secondary organic aerosol during a severe photochemical smog episode, *Atmospheric Environment*, *41*(3), 576-591, doi:10.1016/j.atmosenv.2006.08.042.

Kondo, Y., et al. (2011), Emissions of black carbon, organic, and inorganic aerosols from biomass burning in North America and Asia in 2008, *Journal of Geophysical Research-Atmospheres*, *116*, 25, doi:10.1029/2010jd015152.

Kozawa, K. H., A. M. Winer, and S. A. Fruin (2012), Ultrafine particle size distributions near freeways: Effects of differing wind directions on exposure, *Atmospheric Environment*, *63*, 250-260, doi:10.1016/j.atmosenv.2012.09.045.

Laborde, M., et al. (2013), Black carbon physical properties and mixing state in the European megacity Paris, *Atmospheric Chemistry and Physics*, *13*(11), 5831-5856, doi:10.5194/acp-13-5831-2013.

Laborde, M., et al. (2012), Single Particle Soot Photometer intercomparison at the AIDA chamber, *Atmospheric Measurement Techniques*, *5*(12), 3077-3097, doi:10.5194/amt-5-3077-2012.

Liu, S., et al. (2012), Secondary organic aerosol formation from fossil fuel sources contribute majority of summertime organic mass at Bakersfield, *Journal of Geophysical Research-Atmospheres*, *117*, 21, doi:10.1029/2012jd018170.

Lurmann, F. W., S. G. Brown, M. C. McCarthy, and P. T. Roberts (2006), Processes influencing secondary aerosol formation in the San Joaquin Valley during winter, *Journal of the Air & Waste Management Association*, *56*(12), 1679-1693.

Maria, S. F., L. M. Russell, M. K. Gilles, and S. C. B. Myneni (2004), Organic aerosol growth mechanisms and their climate-forcing implications, *Science*, *306*(5703), 1921-1924, doi:10.1126/science.1103491.

Maria, S. F., L. M. Russell, B. J. Turpin, and R. J. Porcja (2002), FTIR measurements of functional groups and organic mass in aerosol samples over the Caribbean, *Atmospheric Environment*, *36*(33), 5185-5196, doi:10.1016/s1352-2310(02)00654-4.

Ng, N. L., M. R. Canagaratna, J. L. Jimenez, P. S. Chhabra, J. H. Seinfeld, and D. R. Worsnop (2011), Changes in organic aerosol composition with aging inferred from aerosol mass spectra, *Atmospheric Chemistry and Physics*, *11*(13), 6465-6474, doi:10.5194/acp-11-6465-2011.

Ng, N. L., et al. (2010), Organic aerosol components observed in Northern Hemispheric datasets from Aerosol Mass Spectrometry, *Atmospheric Chemistry and Physics*, *10*(10), 4625-4641, doi:10.5194/acp-10-4625-2010.

Oxley, J. C., J. L. Smith, M. Donnelly, and M. Porter (2015), Fuel-oxidizer mixtures: their stabilities and burn characteristics, *Journal of Thermal Analysis and Calorimetry*, *121*(2), 743-763, doi:10.1007/s10973-015-4589-x.

Pierce, J. R., I. Riipinen, M. Kulmala, M. Ehn, T. Petaja, H. Junninen, D. R. Worsnop, and N. M. Donahue (2011), Quantification of the volatility of secondary organic compounds in ultrafine particles during nucleation events, *Atmospheric Chemistry and Physics*, *11*(17), 9019-9036, doi:10.5194/acp-11-9019-2011.

Plummer, L. E., C. M. Carosino, K. J. Bein, Y. J. Zhao, N. Willits, S. Smiley-Jewell, A. S. Wexler, and K. E. Pinkerton (2015), Pulmonary inflammatory effects of source-oriented particulate matter from California's San Joaquin Valley, *Atmospheric Environment*, *119*, 174-181, doi:10.1016/j.atmosenv.2015.08.043.

Russell, L. M., S. H. Zhang, R. C. Flagan, J. H. Seinfeld, M. R. Stolzenburg, and R. Caldow (1996), Radially classified aerosol detector for aircraft-based submicron aerosol measurements, *Journal of Atmospheric and Oceanic Technology*, *13*(3), 598-609, doi:10.1175/1520-0426(1996)013<0598:rcadfa>2.0.co;2.

Sakamoto, K. M., J. R. Laing, R. G. Stevens, D. A. Jaffe, and J. R. Pierce (2016), The evolution of biomass-burning aerosol size distributions due to coagulation: dependence on fire and meteorological details and parameterization, *Atmospheric Chemistry and Physics*, *16*(12), 7709-7724, doi:10.5194/acp-16-7709-2016.

SCAQMD (2016), South Coast Air Quality Management District, edited.

SJVAPCD (2016), Ambient Air Quality Standards & Valley Attainment Status, edited.

Sun, Y. L., et al. (2012), Characterization of near-highway submicron aerosols in New York City with a high-resolution aerosol mass spectrometer, *Atmospheric Chemistry and Physics*, *12*(4), 2215-2227, doi:10.5194/acp-12-2215-2012.

Visser, S., et al. (2015), Advanced source apportionment of size-resolved trace elements at multiple sites in London during winter, *Atmospheric Chemistry and Physics*, *15*(19), 11291-11309, doi:10.5194/acp-15-11291-2015.

Woody, M. C., K. R. Baker, P. L. Hayes, J. L. Jimenez, B. Koo, and H. O. T. Pye (2016), Understanding sources of organic aerosol during CalNex-2010 using the CMAQ-VBS, *Atmospheric Chemistry and Physics*, *16*(6), 4081-4100.

Xu, J., Q. Zhang, M. Chen, X. Ge, J. Ren, and D. Qin (2014), Chemical composition, sources, and processes of urban aerosols during summertime in northwest China: insights from high-resolution aerosol mass spectrometry, *Atmospheric Chemistry and Physics*, *14*(23), 12593-12611, doi:10.5194/acp-14-12593-2014.

Xu, W. Q., et al. (2015), Aerosol composition, oxidation properties, and sources in Beijing: results from the 2014 Asia-Pacific Economic Cooperation summit study, *Atmospheric Chemistry and Physics*, *15*(23), 13681-13698, doi:10.5194/acp-15-13681-2015.

Yatavelli, R. L. N., et al. (2015), Estimating the contribution of organic acids to northern hemispheric continental organic aerosol, *Geophysical Research Letters*, *42*(14), 6084-6090, doi:10.1002/2015gl064650.

Ying, Q., and M. J. Kleeman (2006), Source contributions to the regional distribution of secondary particulate matter in California, *Atmospheric Environment*, *40*(4), 736-752, doi:10.1016/j.atmosenv.2005.10.007.

Young, D. E., H. Kim, C. Parworth, S. Zhou, X. L. Zhang, C. D. Cappa, R. Seco, S. Kim, and Q. Zhang (2016), Influences of emission sources and meteorology on aerosol chemistry in a polluted urban environment: results from DISCOVER-AQ California, *Atmospheric Chemistry and Physics*, *16*(8), 5427-5451, doi:10.5194/acp-16-5427-2016.

Zhang, K. M., A. S. Wexler, D. A. Niemeier, Y. F. Zhu, W. C. Hinds, and C. Sioutas (2005a), Evolution of particle number distribution near roadways. Part III: Traffic analysis and on-road size resolved particulate emission factors, *Atmospheric Environment*, *39*(22), 4155-4166, doi:10.1016/j.atmosenv.2005.04.003.

Zhang, K. M., A. S. Wexler, Y. F. Zhu, W. C. Hinds, and C. Sioutas (2004), Evolution of particle number distribution near roadways. Part II: the 'road-to-ambient' process, *Atmospheric Environment*, *38*(38), 6655-6665, doi:10.1016/j.atmosenv.2004.06.044.

Zhang, M., X. M. Wang, J. M. Chen, T. T. Cheng, T. Wang, X. Yang, Y. G. Gong, F. H. Geng, and C. H. Chen (2010), Physical characterization of aerosol particles during the Chinese New Year's firework events, *Atmospheric Environment*, *44*(39), 5191-5198, doi:10.1016/j.atmosenv.2010.08.048.

Zhang, Q., M. R. Canagaratna, J. T. Jayne, D. R. Worsnop, and J. L. Jimenez (2005b), Time- and size-resolved chemical composition of submicron particles in Pittsburgh: Implications for aerosol sources and processes, *Journal of Geophysical Research-Atmospheres*, *110*(D7), 19, doi:10.1029/2004jd004649.

Zhang, X. L., H. Kim, C. L. Parworth, D. E. Young, Q. Zhang, A. R. Metcalf, and C. D. Cappa (2016), Optical Properties of Wintertime Aerosols from Residential Wood Burning in Fresno, CA: Results from DISCOVER-AQ 2013, *Environmental Science & Technology*, *50*(4), 1681-1690, doi:10.1021/acs.est.5b04134.

Zhu, Y. F., W. C. Hinds, S. Kim, S. Shen, and C. Sioutas (2002a), Study of ultrafine particles near a major highway with heavy-duty diesel traffic, *Atmospheric Environment*, *36*(27), 4323-4335, doi:10.1016/s1352-2310(02)00354-0.

Zhu, Y. F., W. C. Hinds, S. Kim, and C. Sioutas (2002b), Concentration and size distribution of ultrafine particles near a major highway, *Journal of the Air & Waste Management Association*, *52*(9), 1032-1042.

4.10 Tables

Table 4-1. Size and composition of ambient aerosol particles from sources.

Study	Source	Size (nm)
Elser et al. [2016] (Xian and Beijing, China)	Haze	800-1000[1]
	Non-haze	400[2]
Laborde et al. [2013] (Paris, France)	Traffic emissions (rBC)	100[2]
	Biomass burning (rBC)	130[2]
	Aged aerosols (rBC)	160[2]
	Continental (rBC)	200[2]
Ge et al. [2012a] (Fresno, California)	AMS-HOA	110[2]
	AMS-BBOA	110[2]
	AMS-COA	150 [2]and 350[2]
	OOA	350[2]
Ge et al. [2012b] (Fresno, California)	POA (Traffic, cooking, and wood burning)	120[2]
	SOA	310-380[1]
Zhang et al. [2016] (Fresno, California)	rBC	200
Kondo et al. [2011] (Canada)	rBC (biomass burning)	190
Liu et al. [2012] (Bakersfield, California)	Vehicle-emitted anthropogenic SOA	150-380[1]
	Biogenic SOA	310-540[1]
Healy et al. [2012] (Paris, France)	Biomass Burning (rBC)	280, 750[1]
	Traffic (rBC)	215[2]
	Long-range transport (rBC)	580[2]
Xu et al. [2015] (Beijing, China)	OOA	500[2]
	POA	230[2]
	SIA (Nitrate, sulfate, ammonium)	500[2]
Xu et al. [2014] (Lanzhou, China)	COA	120[2]
	Traffic related HOA	120[2]
	OOA	310-380[1]
Alfarra et al. [2004] (Urban: Slocan Park Rural: Langley, Canada)	Organics	350[2] (rural) ; 120[2], 350[2] (urban)
	Nitrate	350[2] (urban & rural)
	Sulfate	430[2] (urban & rural)
Sun et al. [2012] (New York)	Traffic related HOA	90[2]
	OOA	380-460[1]

[1]Particle size range; [2]Mode diameter; the diameter of rBC represents the core diameter of rBC particles expressed in volume equivalent diameter. Organic and inorganic aerosol particle diameters are expressed in dry mobility diameter.

Table 4-2. List of instruments used and measured aerosol properties in Fresno and Fontana.

Instrument	Measurement	Time Resolution	Diameter
Scanning Electrical Mobility Sizer (SEMS)	Number concentration and size distribution of aerosol particles (0.01 - 1 μm)	5 minute	Mobility (D_m)
Single Particle Soot Photometer (SP2)	Number concentration and size distribution of rBC particles (0.08 - 0.6 μm)	1 minute	Volume equivalent (D_{VED})[1]
Aerosol Mass Spectrometer (HR-ToF-AMS)	Mass concentrations and size distribution of non-refractory aerosol particles (0.05 - 1 μm)	2 minute	Vacuum aerodynamic (D_{va})[2,4]
Fourier Transform Infrared (FTIR) Spectroscopy	Organic functional groups (0.18 μm)	1 day	Aerodynamic (D_a)[3]
	Organic functional groups (1 μm)	6 hour	Aerodynamic (D_a)[3]
	Organic functional groups (2.5 μm)	12 hour	Aerodynamic (D_a)[3]
Vaisala Weather Station	Temperature, Relative humidity, Wind speed, Wind direction, Pressure	1 minute	

[1] $D_{VED} = D_m$

[2] $D_{va} = \frac{D_m * \rho}{\rho_0}$

[3] $D_a = D_{VED} * \sqrt{\rho / (\rho_0 * \chi)}$

where ρ is density of particles, ρ_0 is unit density (1 g cm^{-3}) and $\chi = C_c(D_{VED})/C_c(D_a)$ is shape factor, C_c is Cunningham slip correction factor.

[4] The AMS measures vacuum aerodynamic diameter (D_{va}, see DeCarlo et al. [2004]), which is proportional to particle density, and decreases with increasing dynamic shape factor for non-spherical particles. Note that D_{va} is different from the traditional definition of aerodynamic diameter (D_a), which is proportional to the square root of the particle density and also has a different dependence on particle shape factor (see DeCarlo et al. [2004] for details).

Table 4-3. Dry mobility diameters (nm) at maximum concentration of mode of number, volume, non-refractory organics, nitrate, sulfate, and ammonium aerosols, and dry volume equivalent diameters at maximum mass concentration of refractory black carbon (rBC) in Fresno and Fontana.

		Fresno		Fontana	
		Low-Fog	High-Fog	Fireworks	Non-Fireworks
Morning	Number	70-100	80-100	30, 60, 180	30, 50
(06:00-12:00)	Volume	320	440	410	410
	rBC	140	80-100	110	100
	Organics	250	380	480	155
	Nitrate	350	380	480	380
	Sulfate	350	380	500	360
	Ammonium	360	390	500	380
Afternoon	Number	70-90	150	44	57
(12:00-18:00)	Volume	320	460	320	120, 300
	rBC	140	80-100	100	80-100
	Organics	280	360	400	140, 280
	Nitrate	330	380	500	140, 350-400
	Sulfate	330	380	480	360
	Ammonium	350	400	520	
Evening	Number	70	70	40	40
(18:00-00:00)	Volume	300	440	300	280
	rBC	180	140	100	80-100
	Organics	200	360	430	130, 280
	Nitrate	350	380	500	130, 350
	Sulfate	350	380	500	330
	Ammonium	350	380	>500	
Night	Number	80	80-100	50, 180	50
(00:00-06:00)	Volume	300	440	380	310
	rBC	180	140	100	80-100
	Organics	260	360	500	280
	Nitrate	350	380	500	350
	Sulfate	330-350	380	500	350
	Ammonium	350	380-400	500	

** The ranges of particle mode diameters are determined as the minimum and maximum measured diameters with concentrations within 2% of the maximum concentration of mode*

Table 4-4. Evolution of particle number distribution near roadways.

Study	Freeway	Mode diameters in nm (distance from freeway in m)
Zhang et al.[2004] (Los Angeles, USA)	405 and 710	405: 12,22,34,60 (30); 15, 50 (60); 25, 45 (90); 60 (150) 710: 7 (17); 14, 30 (30)
Zhang et al. [2005] (Los Angeles, USA)	405 and 710	405: 12, 23 (30) 710: 7, 10 (17)
Buonanno et al. [2009] (Cassino, Italy)	A1 Freeway	7 nm (no evolution from 30 to 400 m)
Zhu et al. [2002b] (Los Angeles, USA)	405 Freeway	13, 27, 65 (30); 38.8 (90); 41(150); 75 (300)
Kozawa et al. [2012] (Los Angeles, USA)	710 Freeway	10,15,30 (10m); 10, 18, 40 (100 m)
Zhu et al. [2002a](Downey, USA)	710 Freeway	10 (17); 30 (30); 50 (90); 60 (150)

Table 4-5. Dry mobility diameters (nm) at maximum concentration of mode of number, volume, non-refractory organics, nitrate, sulfate, and ammonium aerosols, and dry volume equivalent diameters at maximum mass concentration of refractory black carbon (rBC) in Fresno and Fontana.

		Fresno		Fontana	
		Low-Fog	High-Fog	Fireworks	Non-Fireworks
Morning	Number	70-100	80-100	30, 60, 180	30, 50
(06:00-12:00)	Volume	320	440	410	410
	rBC	140	80-100	110	100
	Organics	250	380	480	155
	Nitrate	350	380	480	380
	Sulfate	350	380	500	360
	Ammonium	360	390	500	380
Afternoon	Number	70-90	150	44	57
(12:00-18:00)	Volume	320	460	320	120, 300
	rBC	140	80-100	100	80-100
	Organics	280	360	400	140, 280
	Nitrate	330	380	500	140, 350-400
	Sulfate	330	380	480	360
	Ammonium	350	400	520	
Evening	Number	70	70	40	40
(18:00-00:00)	Volume	300	440	300	280
	rBC	180	140	100	80-100
	Organics	200	360	430	130, 280
	Nitrate	350	380	500	130, 350
	Sulfate	350	380	500	330
	Ammonium	350	380	>500	
Night	Number	80	80-100	50, 180	50
(00:00-06:00)	Volume	300	440	380	310
	rBC	180	140	100	80-100
	Organics	260	360	500	280
	Nitrate	350	380	500	350
	Sulfate	330-350	380	500	350
	Ammonium	350	380-400	500	

** The ranges of particle mode diameters are determined as the minimum and maximum measured diameters with concentrations within 2% of the maximum concentration of mode*

Table 4-6. Contributions (%) of functional groups to organic mass in Fresno and Fontana.

		Alkane	Alcohol	Carboxylic Acid	Amine	Carbonyl
Fresno						
Low-Fog	$PM_{2.5}$	52	16	16	10	6
	PM1	52	19	19	10	
	PM0.18	53	10	23	14	
High-fog	$PM_{2.5}$	51	20	18	5	6
	PM1	51	23	21	5	
	PM0.18	53	13	22	12	
Fontana						
Fireworks	$PM_{2.5}$	45	27	13	10	5
	PM1	46	33	14	7	
	PM0.18	45	25	18	12	
Non-Fireworks	$PM_{2.5}$	56	16	12	10	6
	PM1	57	17	17	9	
	PM0.18	56	11	18	15	

Table 4-7. Average concentration (μg m^{-3}) of organic functional groups on low-fog and high-fog days in Fresno.

		Low-Fog			
$PM_{2.5}$		Morning	Afternoon	Evening	Night
	Alkane	1.95 ± 1.18		2.09 ± 0.93	
	Carbonyl	0		0.56 ± 0.62	
	Amine	0.25 ± 0.09		0.44 ± 0.15	
	Alcohol	0.87 ± 0.72		0.57 ± 0.41	
	Carboxylic Acid	0.76 ± 0.57		0.41 ± 0.42	
PM_1					
	Alcohol	0.72 ± 0.60	0.56 ± 0.47	0.75 ± 0.56	0.85 ± 0.82
	Alkane	1.83 ± 1.48	1.62 ± 1.15	2.6 ± 1.49	1.9 ± 1.56
	Carbonyl	0	0	0.11 ± 0.5	0
	Amine	0.19 ± 0.08	0.32 ± 0.18	0.43 ± 0.21	0.24 ± 0.17
	Carboxylic Acid	0.59 ± 0.62	0.59 ± 0.37	0.74 ± 0.42	0.65 ± 0.63

		High-Fog			
$PM_{2.5}$		Morning	Afternoon	Evening	Night
	Alkane	7.11 ± 4.4		7.3 ± 2.85	
	Carbonyl	0.69 ± 0.87		0.25 ± 0.66	
	Amine	0.47 ± 0.14		0.61 ± 0.17	
	Alcohol	2.85 ± 1.74		3.02 ± 1.39	
	Carboxylic Acid	2.14 ± 1.38		2.9 ± 1.39	
PM_1					
	Alcohol	3.28 ± 1.98	3.92 ± 1.82	2.95 ± 0.87	2.83 ± 1.17
	Alkane	6.65 ± 3.39	8.52 ± 3.97	6.6 ± 1.54	6.14 ± 1.97
	Carbonyl	0	0	0	0
	Amine	0.53 ± 0.2	0.6 ± 0.26	0.72 ± 0.13	0.7 ± 0.11
	Carboxylic Acid	2.42 ± 1.16	3.7 ± 1.78	2.49 ± 0.7	2.42 ± 0.86

Table 4-8. Average concentration (μg m^{-3}) of organic functional groups on firework and non-firework days in Fontana.

		Fireworks			
$PM_{2.5}$		Morning	Afternoon	Evening	Night
	Alcohol	2.72 ± 3.6		0.58 ± 0.42	
	Alkane	2.34 ± 1		1.54 ± 1.07	
	Carbonyl	0.63 ± 0.66		0	
	Amine	0.65 ± 0.275		0.24 ± 0.15	
	Carboxylic Acid	0.54 ± 0.55		0.59 ± 0.59	
PM_1					
	Alcohol	2.23 ± 2.69	0.92 ± 0.41	0.7 ± 0.83	5.86 ± 8.12
	Alkane	1.63 ± 0.94	2.86 ± 1.5	0.97 ± 0.5	1.48 ± 1.15
	Carbonyl	0	0	0	0
	Amine	0.35 ± 0.44	0.42 ± 0.22	0.20 ± 0.22	051 ± 0.45
	Carboxylic Acid	0.36 ± 0.12	1.32 ± 1.27	0.26 ± 0.1	0.45 ± 0.31

		Non-Fireworks			
$PM_{2.5}$		Morning	Afternoon	Evening	Night
	Alcohol	0.46 ± 0.24		0.47 ± 0.2	
	Alkane	1.7 ± 0.57		1.54 ± 0.6	
	Carbonyl	0.31 ± 0.36		0.11 ± 0.23	
	Amine	0.31 ± 0.12		0.23 ± 0.09	
	Carboxylic Acid	0.31 ± 0.27		0.37 ± 0.25	
PM_1					
	Alcohol	0.81 ± 0.5	0.49 ± 0.3	0.35 ± 0.17	0.52 ± 0.35
	Alkane	2.25 ± 1.05	1.62 ± 0.83	1.33 ± 0.62	1.65 ± 0.86
	Carbonyl	0	0.13 ± 0.35	0	0.04 ± 0.18
	Amine	0.23 ± 0.08	0.28 ± 0.12	0.17 ± 0.08	0.2 ± 0.11
	Carboxylic Acid	0.7 ± 0.39	0.53 ± 0.44	0.39 ± 0.21	0.48 ± 0.34

Table 4-9. Size range of peak dry mobility diameter (nm) of aerosol particles that showed strong ($R^2 > 0.5$) and moderate ($R^2 = 0.3$-0.5) correlation with different organic sources in Fresno and Fontana.

		AMS-BBOA	AMS-NOOA	AMS-HOA	AMS-VOOA
Fresno					
Low-Fog	Morning	80-160[2]			220-340[2]
	Afternoon	30-100[1]	220-420[1]	27-53[1], 60-134[2]	200-310[1]
	Evening	75-160[1]		30-50[2], 60-260[2]	
	Night	150-260[1]		50-130[2]	240-420[2]
High-Fog	Morning		310- 610[1]	100-125[1]	
	Afternoon		310-410	40-170[2]	
	Evening	60-120[1]	450-600[1]	30-50[2], 60-130[2]	
	Night	80-140[2]	375- 560[1]	40-100[2], 130-280[2]	450-550[2]
Fontana					
Fireworks	Morning				
	Afternoon		40-60[2]		
	Evening				35-80[2]
	Night		80-240[2]		125-550[1]
Non-Fireworks	Morning		280-410[1]	50-90[2], 100-220[1]	90-150[1]
	Afternoon		375-456[2]		75-150[2]
	Evening		140-310[2]	150-240[2]	60-150[1]
	Night		240-375[1]		100-140[1]

[1]Strong correlation $R^2 > 0.5$, [2]Moderate correlation $R^2 = 0.3$-0.5

4.11 Figures

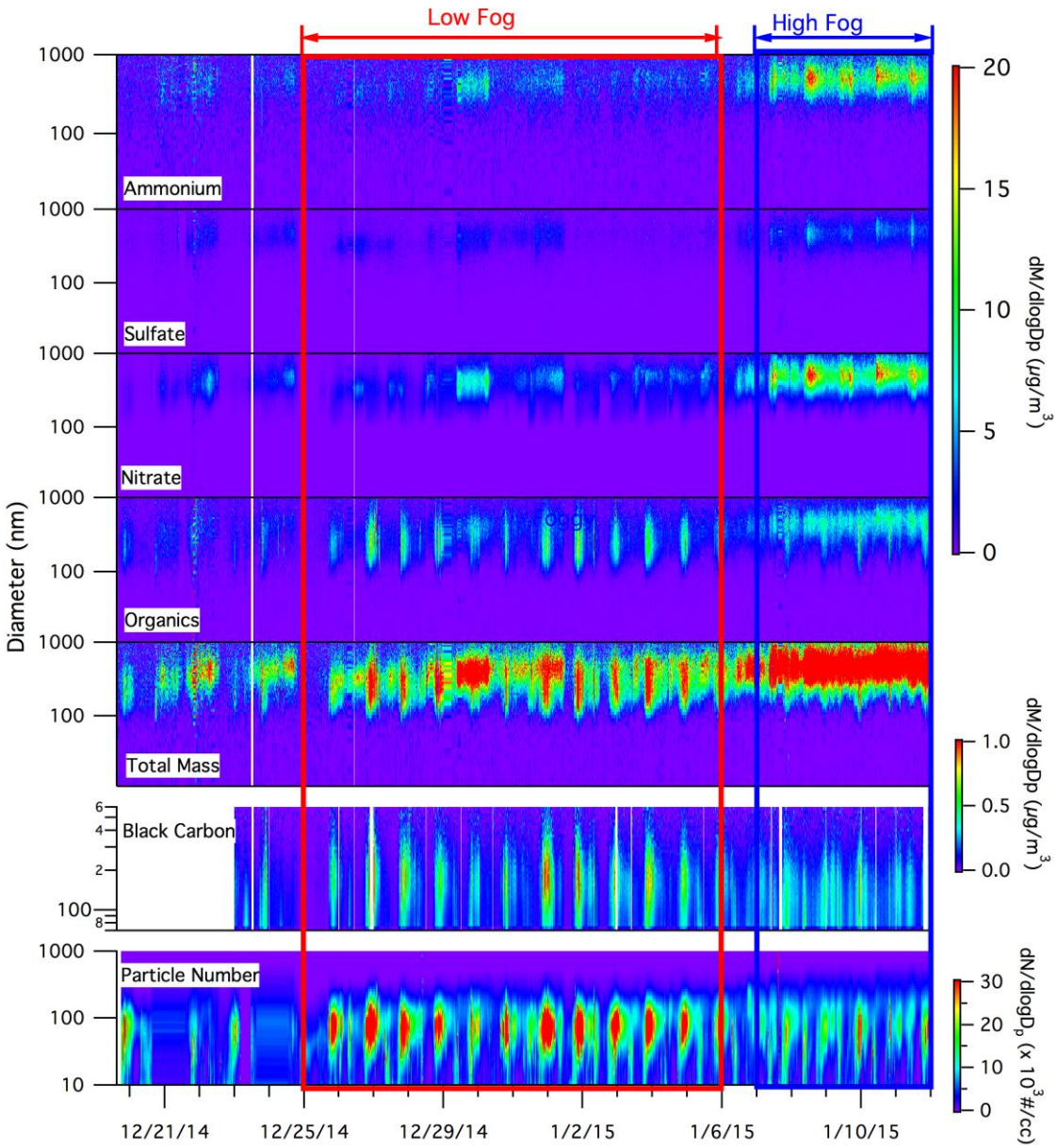

Figure 4-1. Time series of non-refractory submicron aerosols (organic, nitrate, sulfate, ammonium), refractory black carbon (rBC), and aerosol particle number size distribution in Fresno. HR-ToF-AMS was used to measure vacuum aerodynamic diameter of organic, sulfate, ammonium, nitrate, and sulfate. SP2 was used to measure volume equivalent diameter of rBC; SEMS was used to measure mobility diameter of aerosol particle number size distributions.

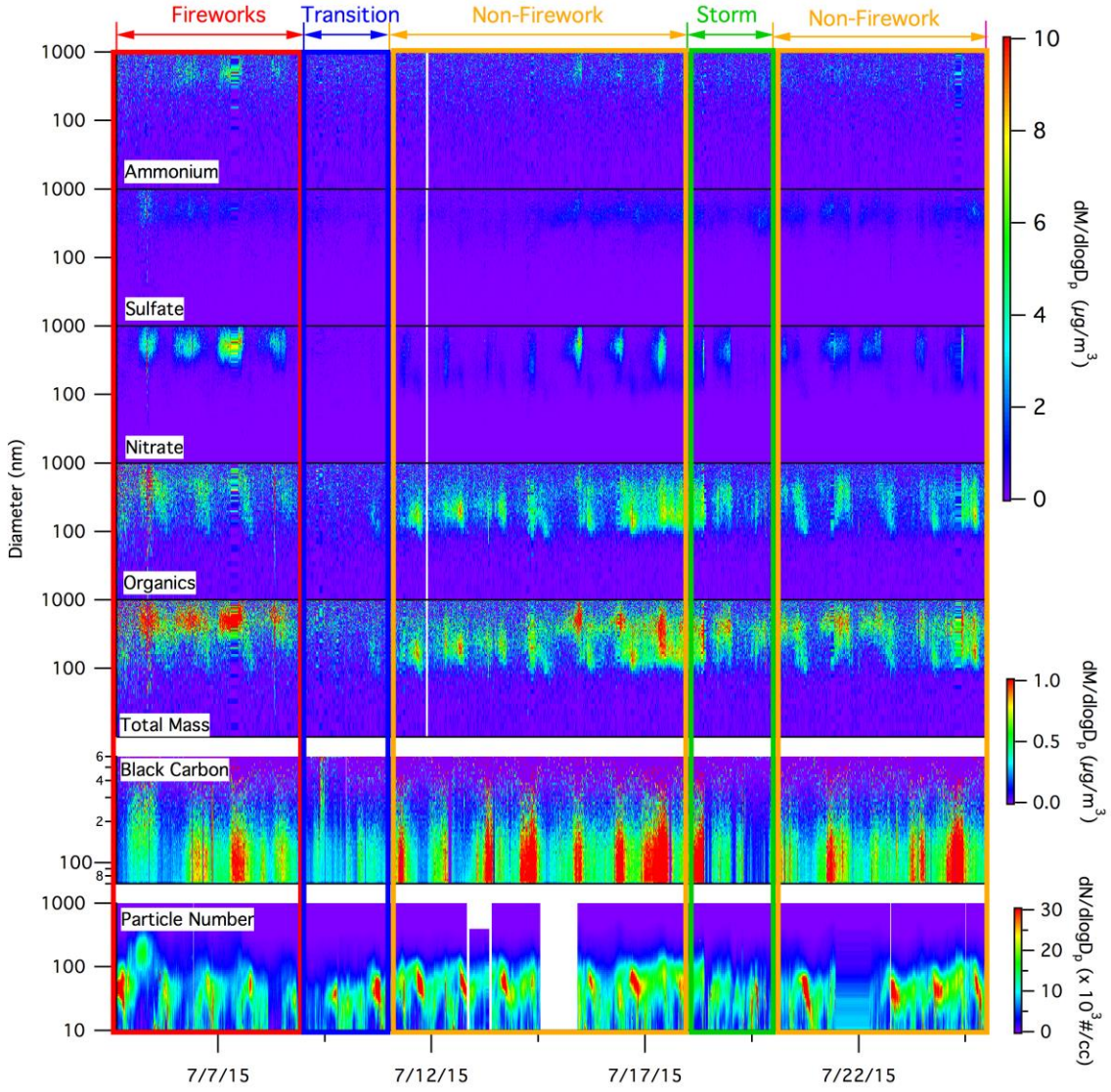

Figure 4-2. Time series of non-refractory submicron aerosols (organic, nitrate, sulfate, ammonium), refractory black carbon (rBC), and aerosol particle number size distribution in Fontana. HR-ToF-AMS was used to measure vacuum aerodynamic diameter of organic, sulfate, ammonium, nitrate, and sulfate. SP2 was used to measure volume equivalent diameter of rBC; SEMS was used to measure mobility diameter of aerosol particle number size distributions. Red arrow shows increased number concentration of 100- to 300-nm-sized particles on 5 July 2015 due to fireworks in SoCAB.

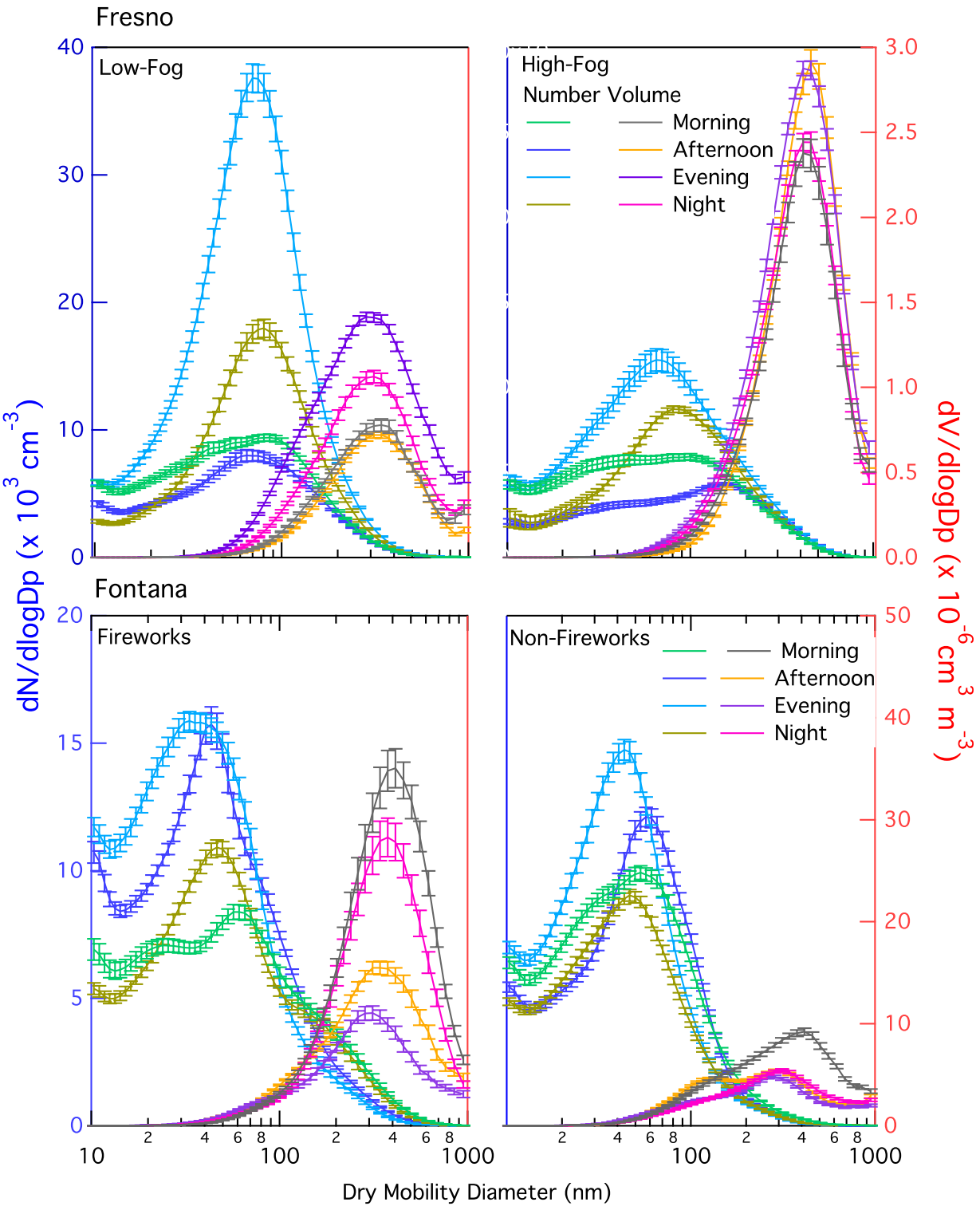

Figure 4-3. Mean size distributions of submicron aerosol particle number and volume on low-fog and high-fog days in Fresno and on firework and non-firework days in Fontana measured using SEMS. Error bars denote standard error.

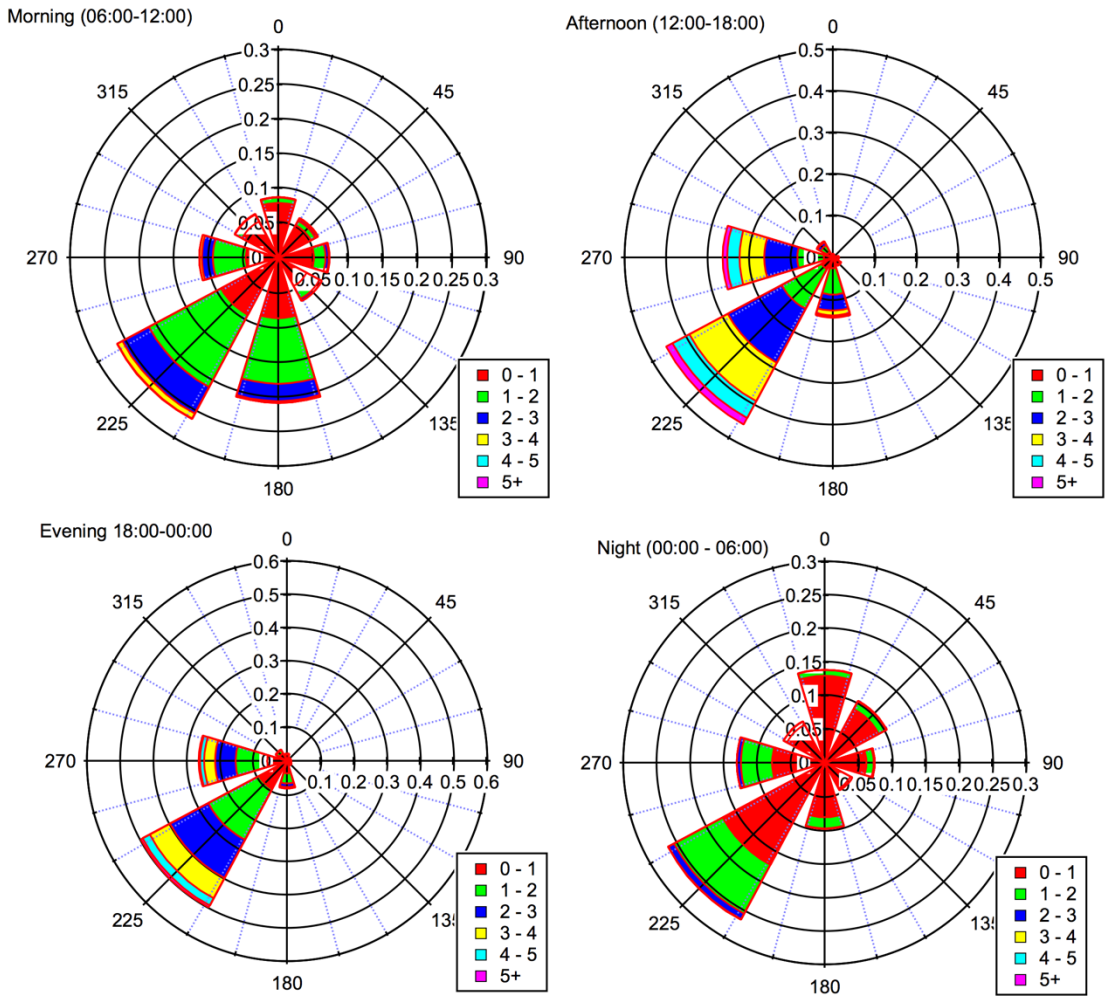

Figure 4-4. Windroses at different times of the day for Fontana.

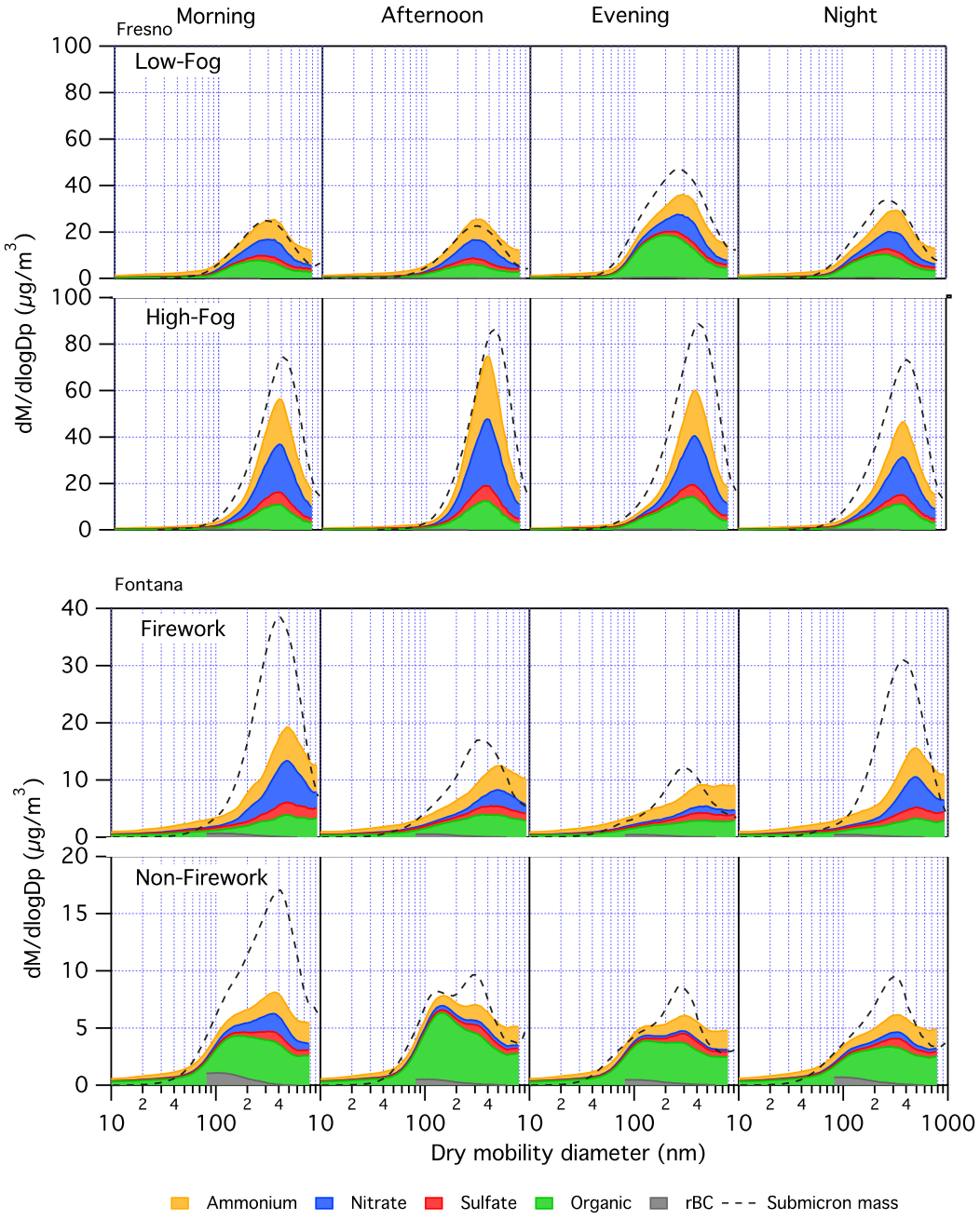

Figure 4-5. Mean size distribution of submicron particle mass non-refractory organic, nitrate, sulfate, and ammonium on low-fog and high-fog days in Fresno and on firework and non-firework days in Fontana measured using AMS. AMS provided particle size distribution in vacuum aerodynamic diameter, and the measured vacuum aerodynamic diameter were converted into mobility diameter using an aerosol particle density of 1.3 g/cc in Fresno, and 1.1 g/cc in Fontana during fireworks and 1.3 g/cc for non-firework days. The submicron mass distribution was calculated from the SEMS volume distribution and the estimated particle density. Volume equivalent diameter is the same as mobility diameter for spherical particles.

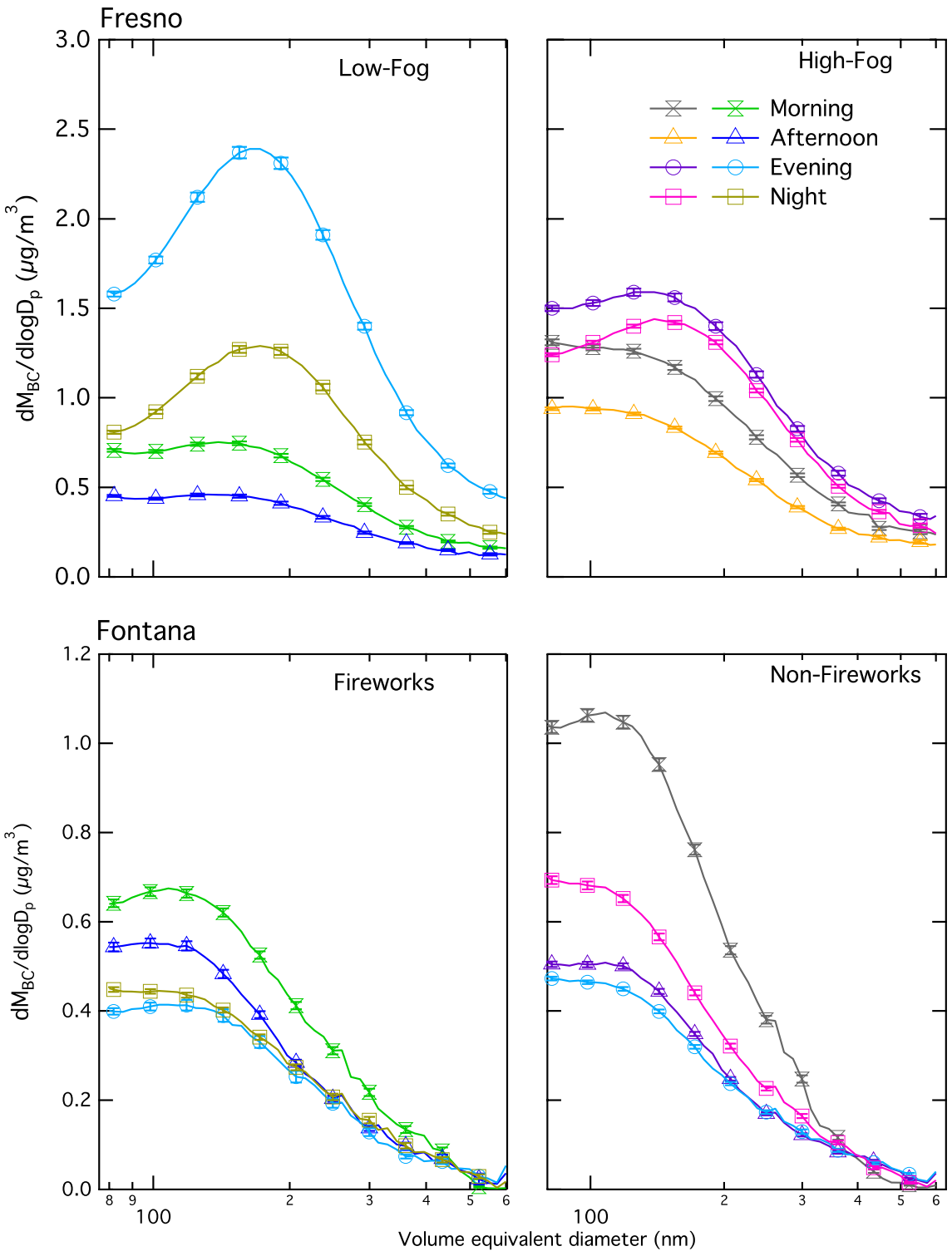

Figure 4-6. Mean size distribution of refractory black carbon on low-fog and high-fog days in Fresno and on firework and non-firework days in Fontana measured using SP2. Error bars denote standard error.

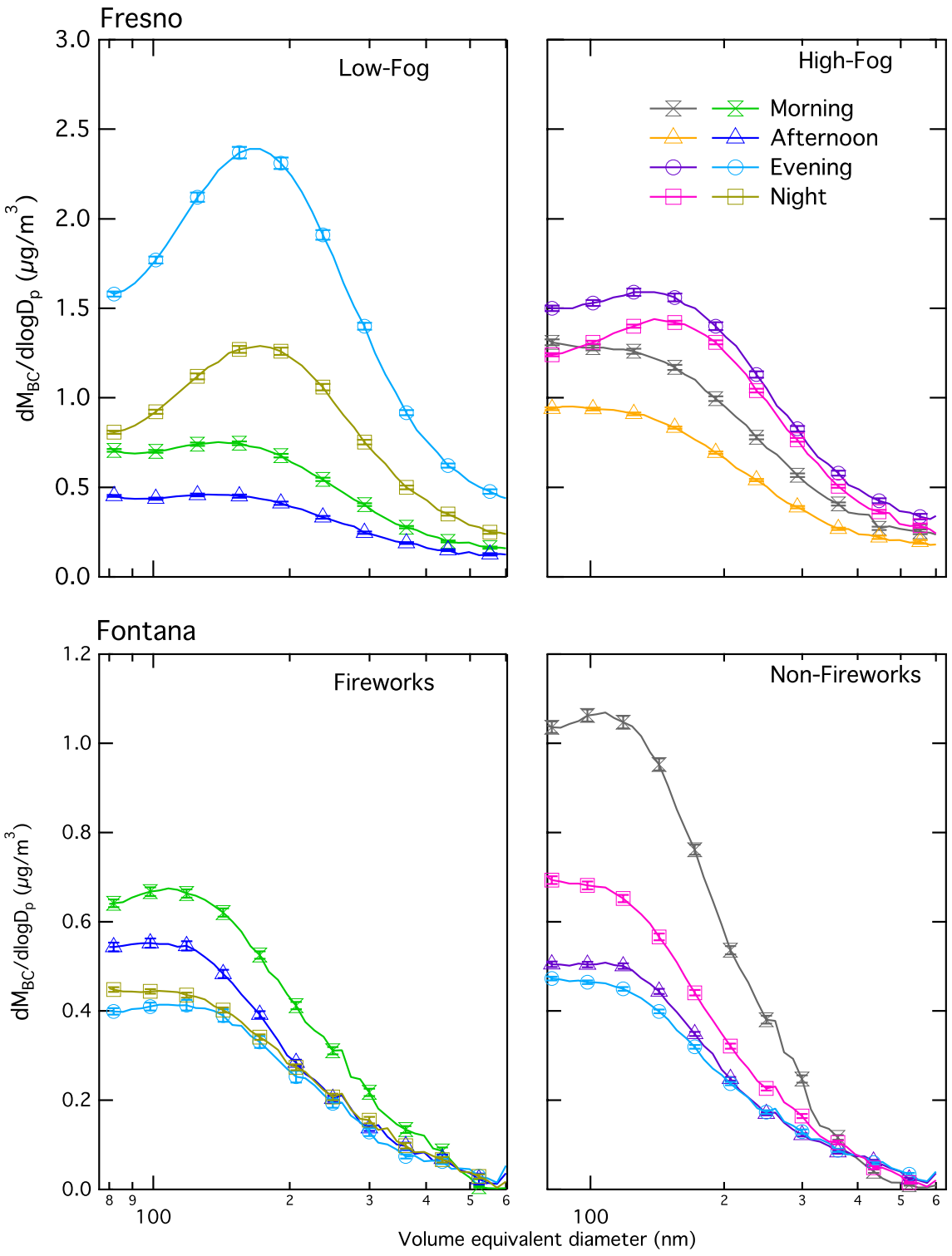

Figure 4-7. Diurnal variation of refractory black carbon in Fresno and Fontana.

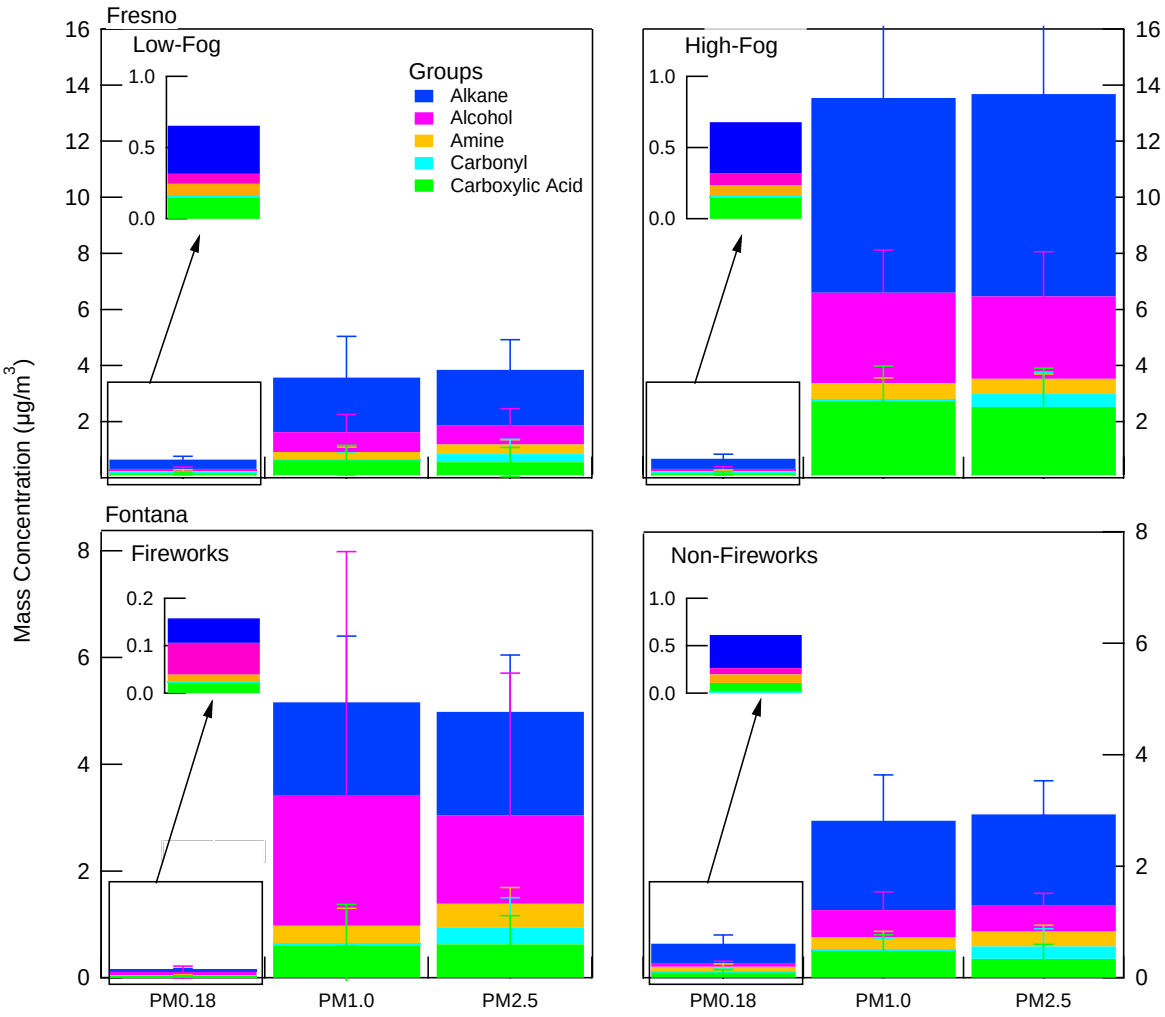

Figure 4-8. Mean concentrations of alkane (blue), alcohol (pink), amine (orange), carboxylic acid (green) and carbonyl (teal) functional groups in $PM_{2.5}$ (< 2.5 µm), PM_1 (< 1 µm), and $PM_{0.18}$ (< 0.18 µm) particle samples in Fresno and Fontana.

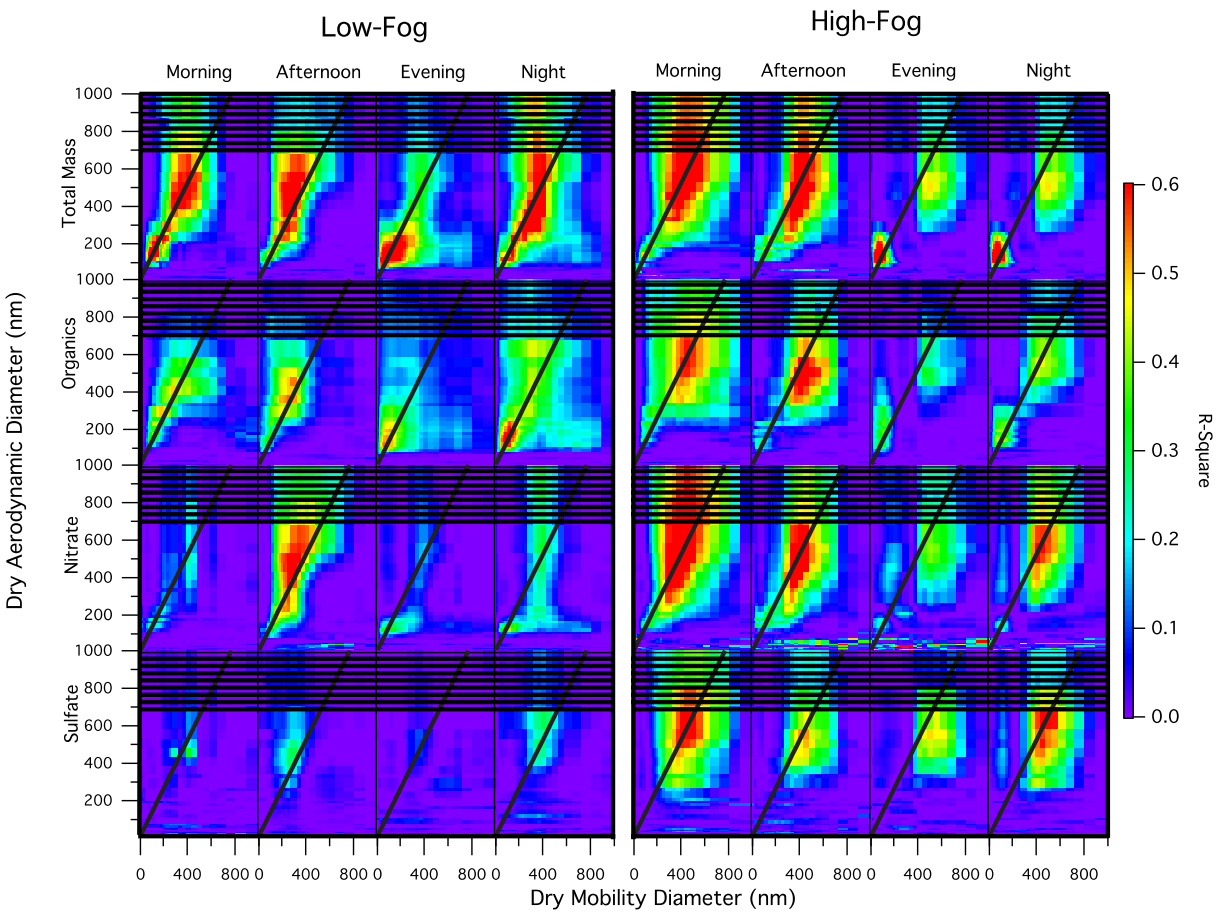

Figure 4-9. Correlation between size-resolved non-refractory organic components, nitrate, sulfate and non-refractory mass measured using AMS and particle volume derived from SEMS measurements at Fresno on (a) low-fog and (b) high-fog days. The diagonal black line shows the ideal relation between dry vacuum aerodynamic diameter and mobility diameter. The horizontal black lines show the region of higher inlet losses in AMS.

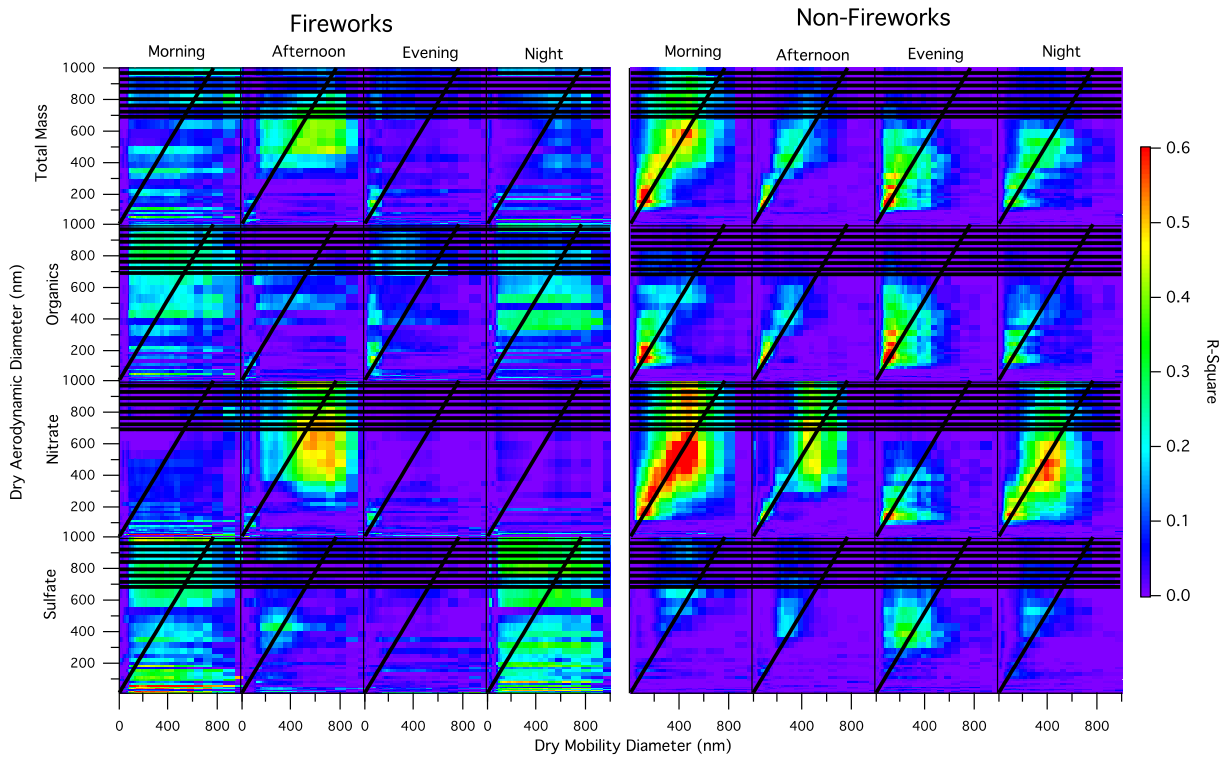

Figure 4-10. Correlation between size resolved non-refractory organic components, nitrate, sulfate and non-refractory mass measured using AMS and particle volume derived from SEMS measurements at Fontana on (a) firework and (b) non-firework days. The diagonal black line shows the ideal relation between dry vacuum aerodynamic diameter and Mobility diameter. The horizontal black lines show the region of higher inlet losses in AMS.

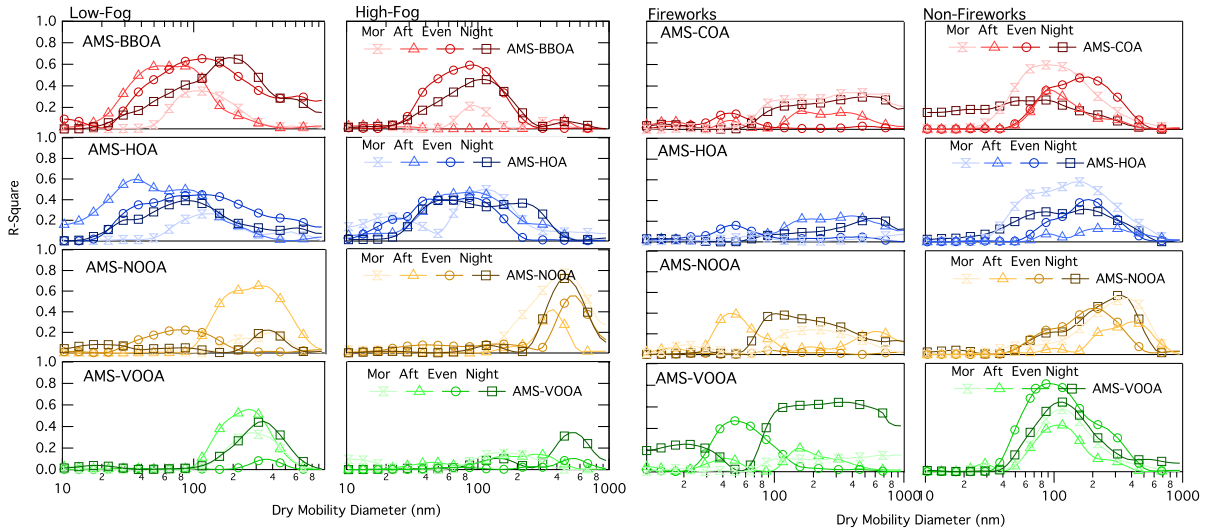

Figure 4-11. Size dependence of organic aerosol sources: biomass burning organic aerosol (AMS-BBOA), vehicle-related oxygenated organic aerosol (AMS-VOOA), nitrate-related oxygenated organic aerosol (AMS-NOOA), hydrocarbon-like organic aerosol (AMS-HOA) and cooking related organic aerosol (AMS-COA) on low-fog and high-fog days in Fresno and firework and non-firework days in Fontana.

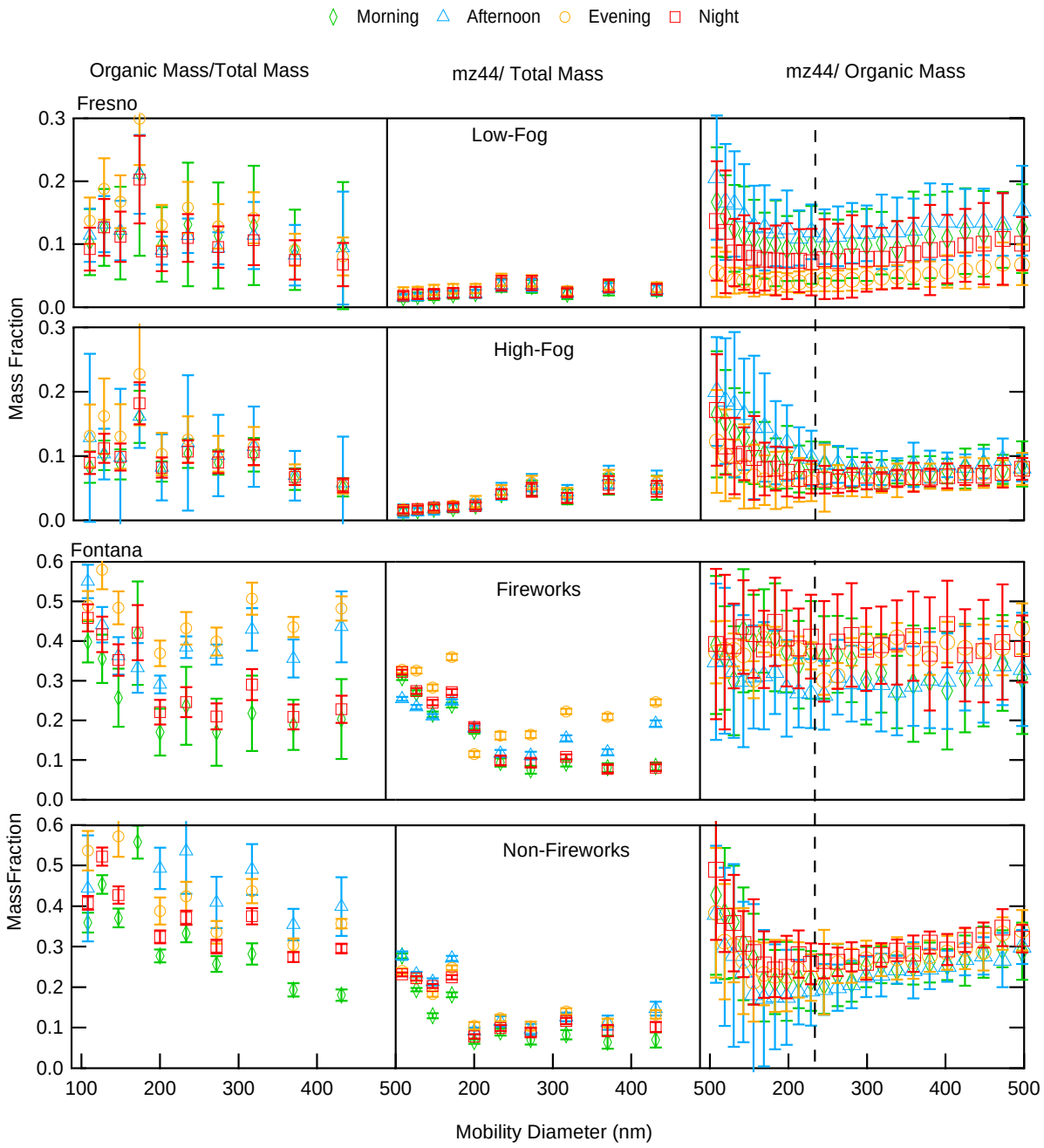

Figure 4-12. Organic mass-to-particle aerosol mass, m/z 44-to-particle aerosol mass, and m/z 44-to-organic mass ratios on low-fog and high-fog days in Fresno and firework and non-firework days in Fontana. Error bars denote standard deviation.

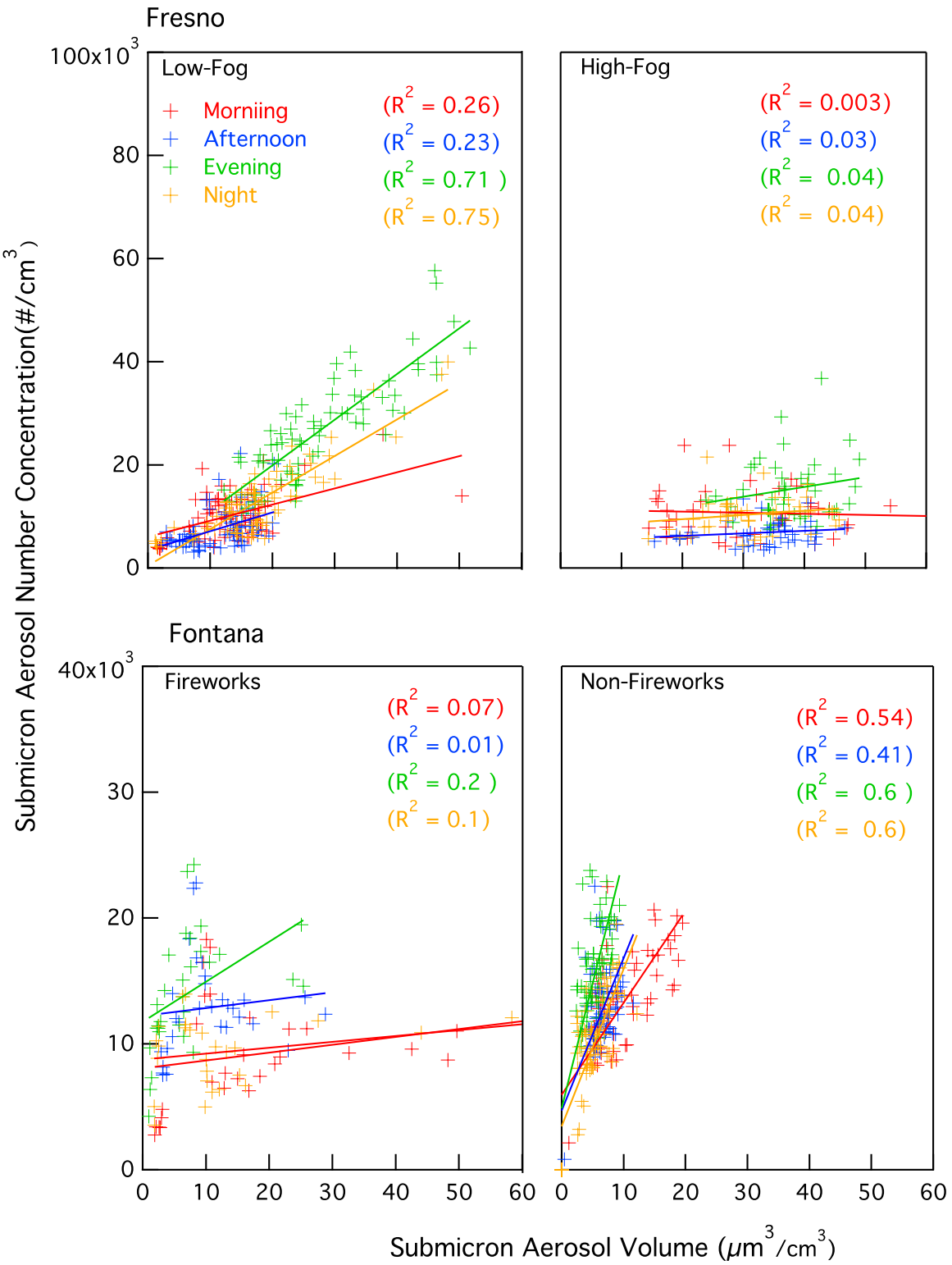

Figure 4-13. Correlation between submicron aerosol number and volume on low-fog and high-fog days in Fresno and firework and non-firework days in Fontana.

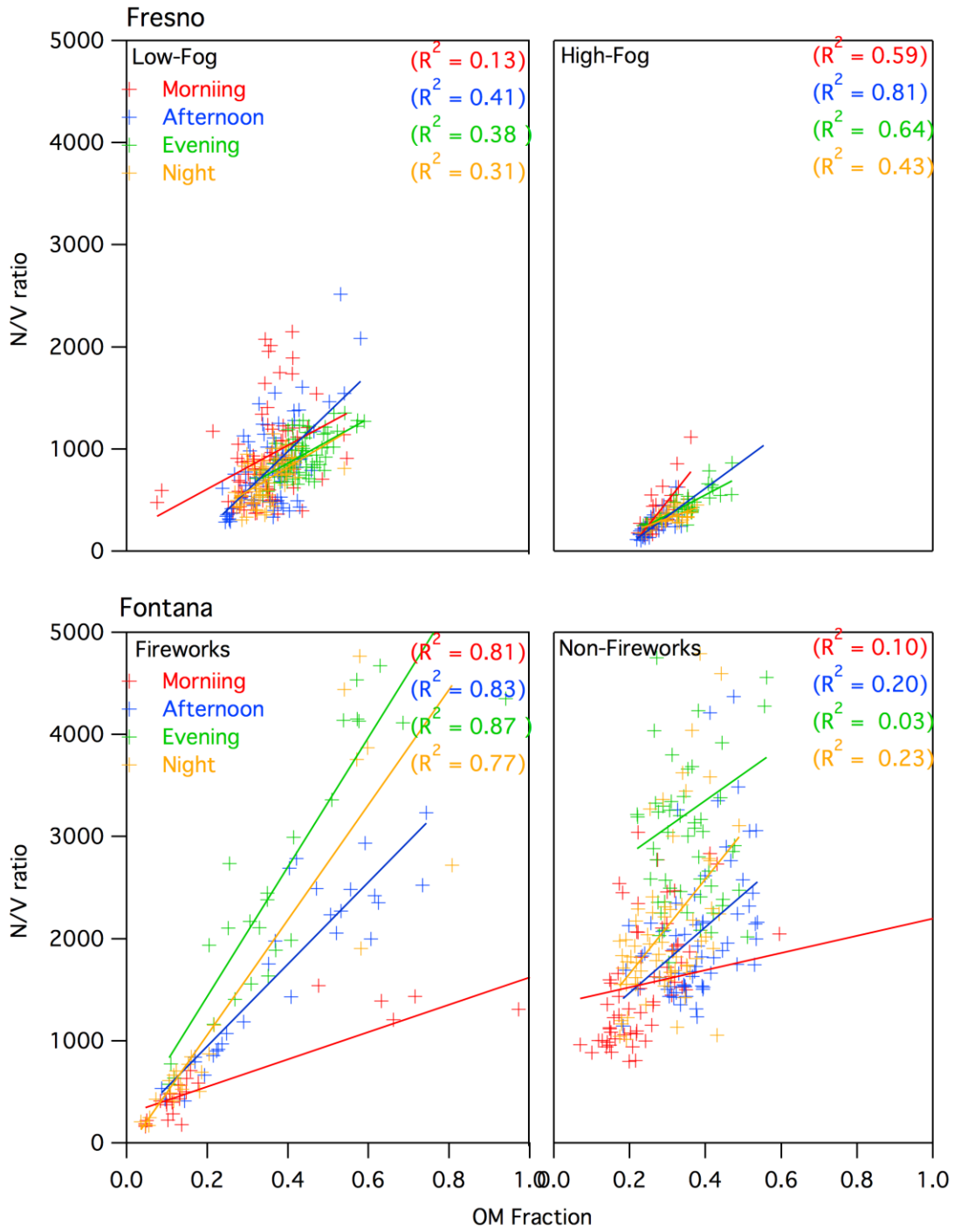

Figure 4-14. Correlation between number-to-volume ratio and organic mass fraction during low-fog and high-fog days in Fresno and firework and non-firework days in Fontana.

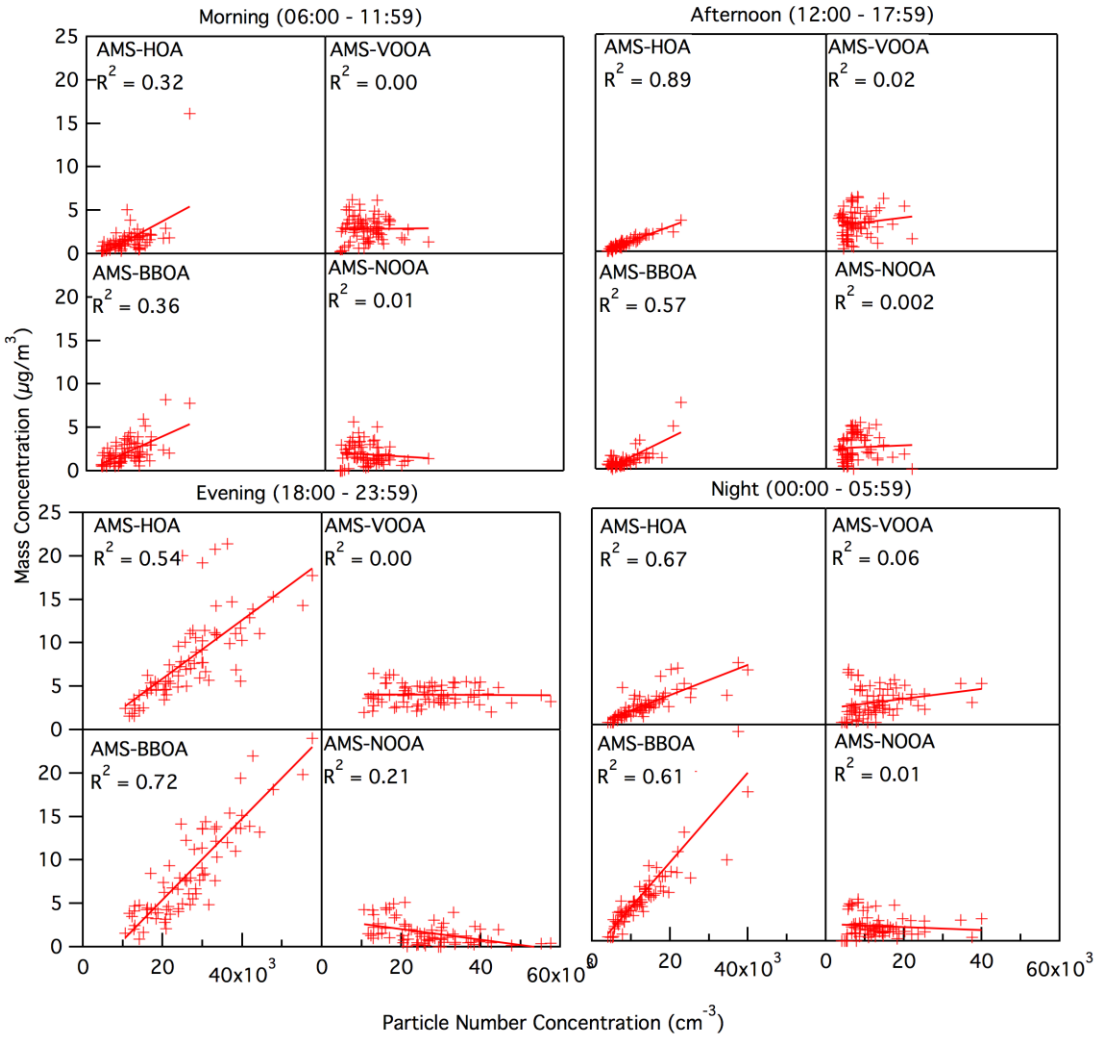

Figure 4-15. Correlations between aerosol particle number concentration and organic aerosol sources: biomass burning organic aerosols (AMS-BBOA), nitrate-related oxygenated organic aerosol (AMS-NOOA), vehicle-related oxygenated organic aerosol (AMS-VOOA), and hydrocarbon-like organic aerosol (AMS-HOA), in Fresno.

5 Light absorption by ambient black and brown carbon and black carbon coating state in winter and summer in two urban CA cities

5.1 Abstract

Observations from a wintertime and summertime field campaign are used to assess the relationship between black and brown carbon (BC and BrC, respectively) optical properties and particle composition and coating state. The wintertime campaign, in Fresno, CA, was impacted by primary emissions from residential wood burning, secondary organic and inorganic particle formation, and BC from motor vehicles. Two major types of BrC were observed in wintertime. One occurred primarily at night—the result of primary biomass burning emissions. The second was enhanced in daytime and strongly associated with particulate nitrate and the occurrence of fog. The biomass-derived BrC absorbed more strongly than the nitrate-associated BrC, but had a weaker wavelength dependence. The wintertime BC-specific mass absorption coefficient (MAC_{BC}) exhibited limited dependence on the ensemble-average coating-to-BC mass ratio ($R_{coat\text{-}rBC}$) at all wavelengths, even up to $R_{coat\text{-}rBC}$ of ~5. For the summertime campaign, in Fontana, CA, BC dominated the light absorption, with negligible BrC contribution even after substantial photochemical processing. The summertime MAC_{BC} exhibited limited dependence on $R_{coat\text{-}rBC}$, even up to ratios of >10. Based on the four classes of BC-containing particles identified by *Lee et al.* (2017) for the summertime measurements, the general lack of an absorption enhancement can be partly—although not entirely—attributed to an unequal distribution of coating materials between the BC-containing particle types. These observations demonstrate that in relatively near-source environments, even those impacted by strong secondary aerosol production, the ensemble-average, mixing-induced absorption enhancement for BC due to coatings can be quite small.

5.2 Introduction

Light absorbing aerosol particles influence climate through their ability to absorb solar and, to a lesser extent, longwave radiation. Light absorbing particles have a substantial, positive radiative forcing (*Bond et al.*, 2013; *Ramanathan and Carmichael*, 2008). However, the uncertainty in global and regional radiative forcing by light absorbing particles remains large. Two key light absorbing particle types are black carbon (BC) and light-absorbing organic carbon, commonly referred to as brown carbon (BrC). BC absorbs strongly across the solar spectrum whereas the absorptivity of BrC falls off rapidly as wavelength increases (*Andreae and Gelencser*, 2006).

Light absorption by BC depends on the particle mixing state, that is the extent to which the BC is internally mixed with other materials, including BrC. Theoretically, when BC is internally mixed with (i.e. "coated" by) non-absorbing materials, the absorption by the BC is increased (*Bond et al.*, 2006; *Fuller et al.*, 1999; *Lack and Cappa*, 2010). This mixing-induced enhancement, commonly referred to as the "lensing" based absorption enhancement, has been observed in various laboratory studies using controlled, typically mono-disperse, BC sources (*Cappa et al.*, 2012; *Cross et al.*, 2010; *Lack et al.*, 2009; *Metcalf et al.*, 2013; *Peng et al.*, 2016; *Schnaiter et al.*, 2005; *Shiraiwa et al.*, 2010). The mixing-induced absorption enhancement can be defined as $E_{abs} = b_{abs,coat}/b_{abs,BC}$,

where $b_{abs,coat}$ and $b_{abs,BC}$ are the absorption coefficients for coated and uncoated BC, respectively. This definition implies no contributions from other absorbing components (e.g. BrC), although it should be noted that the observable E_{abs} can be influenced by absorbing components that are either internally or externally mixed from BC. The observed magnitude of E_{abs} in at least some of these studies has been reasonably consistent with theoretical calculations performed using Mie theory in which the BC-containing particles are treated as having a core-shell morphology (*Cappa et al.*, 2012). However, field studies have resulted in a variety of often contradictory results. Some studies have observed relatively large E_{abs} while others have not (*Cappa et al.*, 2012; *Healy et al.*, 2015; *Knox et al.*, 2009; *Krasowsky et al.*, 2016; *Lim et al.*, 2018; *Liu et al.*, 2017; *Liu et al.*, 2015c; *Zhang et al.*, 2018). Some of this variability is probably due to methodological differences related to the measurement of E_{abs}, while some is likely due to uncharacterized differences in the particle mixing state (i.e. extent of coating) between studies as the relative amount of coating material is explicitly characterized in only a few of these studies. However, some field studies have simultaneously characterized E_{abs} (or a closely related property, the BC mass absorption coefficient, $MAC_{BC} = b_{abs,obs}/[BC]$) and the particle coating state, and we focus on these studies here as they provide stronger process-level constraints on the relationship between particle composition and absorption.

One method to characterize particle coating state uses the soot particle aerosol mass spectrometer (SP-AMS). The SP-AMS can measure the ensemble-average coating-to-core mass ratio ($R_{coat\text{-}rBC}$ = [coating]/[BC]) of BC-containing particles, as well as the composition-dependent size distribution of these internally mixed particles (*Massoli et al.*, 2015; *Onasch et al.*, 2012). Recent developments have enabled determination of particle-to-particle differences in coating amount and composition with the SP-AMS (*Lee et al.*, 2015; *Lee et al.*, 2016; *Willis et al.*, 2016). For reference, Mie theory predicts an approximately continuous increase in E_{abs} with $R_{coat\text{-}rBC}$ up to a plateau of $E_{abs} \sim 2.5$ when $R_{coat\text{-}rBC}$ is greater than ~30, with substantial enhancements, on the order of 1.5, predicted for $R_{coat\text{-}rBC}$ values as small as 3. (The exact relationship between E_{abs} and $R_{coat\text{-}rBC}$ depends on the core BC diameter and the wavelength.) *Cappa et al.* (2012) used SP-AMS measurements to relate the magnitude of the absorption enhancement to the ensemble-average $R_{coat\text{-}rBC}$, as well as to theoretical calculations based on these bulk average measurements. Their measurements were made in summertime in the coastal region around California, USA, including well downwind of a major BC source region with high photochemical activity, i.e. Los Angeles. They observed that the ensemble-averaged absorption enhancement was negligible ($E_{abs} < 1.1$, on average, at 532 nm) even when the ensemble-average coating amount was substantial (up to $R_{coat\text{-}rBC} \sim 12$), and the observed E_{abs} were much lower than that predicted from Mie theory based on the coating amount. *Healy et al.* (2015) made measurements in downtown Toronto, Canada and observed generally negligible E_{abs} at 781 nm even while $R_{coat\text{-}rBC}$ ranged from ca. 2-10, including for a period identified as being strongly impacted by wildfire emissions. *McMeeking et al.* (2014) made measurements of freshly produced particles from open biomass combustion and observed negligible enhancement at 781 nm until the $R_{coat\text{-}rBC}$ was greater than 10.

In contrast, *Liu et al.* (2015c) made measurements in a rural city near London and observed reasonably large BC absorption enhancement (up to ~1.5 at 870 nm) when the $R_{coat\text{-}rBC}$ values were only as large as ~5, and the observed E_{abs} were reasonably consistent with SP-AMS observationally constrained Mie calculations. *Peng et al.* (2016) performed an experiment that combined laboratory with field measurements, allowing for secondary material formation from ambient air (in Beijing, China or Houston, TX, USA) onto monodisperse proxy BC seeds. They observed that E_{abs} at 405 nm and 532 nm generally increased as coatings on the seed BC particles grew, although there was some evidence of an incubation period in which some minimum amount of particle growth must occur before the E_{abs} increases substantially. In a similar type of experiment, *Tasoglou et al.* (2017) observed that when BC particles derived from combustion of pine and birch were photochemically aged the observed E_{abs} increased. *Liu et al.* (2015a) made ambient measurements at a London urban site and used an alternative method to estimate the BC coating amount and relate it to E_{abs} (or more specifically, the MAC_{BC}), namely they inferred the BC coating thickness of single particles based on measurements made using a single particle soot photometer (SP2). *Liu et al.* (2015a) classified their observations into different regimes dependent upon the relative contribution of BC from solid fuel combustion versus traffic; the coating thickness was larger for BC from solid fuel combustion than from traffic. They observed a moderate increase in the MAC_{BC} at 781 nm as the average coating thickness (and solid fuel fraction) increased; the MAC_{BC} increased by a factor of 1.28 when the total particle-to-BC-only diameter ratio was ~2 (which corresponds to an $R_{coat\text{-}rBC} \sim 5$). The observations discussed above are summarized in **Figure 5-1**. Clearly, there is a great deal of variability between studies that aim to directly relate observed E_{abs} values to the particle coating state, and additional measurements in a variety of environments are needed.

In addition to BC, brown carbon can contribute substantially to regional and global radiative forcing. BrC is not one easily classifiable substance as it depends on the specific chemical nature of the organic compounds present, which in turn depends on the source and atmospheric transformations. As such, characterization of light absorbing properties of BrC in a range of environments is necessary to understand the extent to which different sources and processes are important to determining the atmospheric impacts of BrC and to allow for incorporation of BrC into climate models. One challenge in characterizing BrC properties is that the BrC absorption must be separated from BC absorption, including any coating-enhancement effect. One method to perform this separation is to extract the organic material into a solvent (e.g. water or methanol) and then to characterize the absorptivity of the extract (*Kirchstetter et al.*, 2004; *Liu et al.*, 2013; *Liu et al.*, 2015b; *Zhang et al.*, 2013). This method has demonstrated that BrC absorption typically has a very strong wavelength dependence, characterized by a large absorption Ångstrom exponent (AAE), much greater than unity. (An AAE of one is typically attributed to BC.) A large AAE indicates a very strong wavelength dependence to absorption. Other methods have relied on attribution methods, typically either via optical closure (*Cappa et al.*, 2012; *Lack et al.*, 2012a; *Liu et al.*, 2015a; *Liu et al.*, 2015c; *Zhang et al.*, 2016) or subtraction of inferred BC absorption (*Lack and Langridge*, 2013; *Saleh et al.*, 2013; *Saleh et al.*, 2014) or some combination of the two methods. Estimates of the MAC for BrC (or of the related imaginary refractive index, k) are

variable, most likely as a result of a combination of real chemical differences (*Lewis et al.*, 2008; *Saleh et al.*, 2013; *Saleh et al.*, 2014) and of imprecise understanding of which components of the total organic matter are responsible for the absorption (*Andreae and Gelencser*, 2006). One major global source of BrC is thought to be biomass combustion (*Feng et al.*, 2013; *Wang et al.*, 2014), as this is a major source of organic matter and biomass combustion-derived particles tend to be light absorbing, at least at shorter wavelengths (< ~600 nm). BrC properties from biomass combustion-produced particles can be determined from laboratory studies involving intentional burns (*Chakrabarty et al.*, 2010; *McMeeking et al.*, 2014; *Saleh et al.*, 2013; *Saleh et al.*, 2014) or from analysis of field observations (*Clarke et al.*, 2007; *Forrister et al.*, 2015; *Kirchstetter et al.*, 2004; *Lack et al.*, 2012a; *Zhang et al.*, 2016).

In the current study, we report on measurements of light absorption by ambient particles made concurrent with BC ensemble-average coating state (via SP-AMS) and ensemble-average total particle composition. We use these measurements to assess the relationship between observed light absorption coefficients and the BC mixing state along with the contribution from brown carbon. The measurements were made during two independent campaigns, within distinctly different environments. One set of measurements was made in wintertime Fresno, CA. Detailed analyses of the bulk particle composition and the BC-containing particle composition measurements from this campaign are presented in *Chen et al.* (2018) and *Collier et al.* (2018), respectively. Wintertime Fresno is strongly impacted by emissions from biomass combustion, predominantly from residential fireplaces operating at night, and from secondary nitrate and organic aerosol (*Ge et al.*, 2012; *Young et al.*, 2016; *Zhang et al.*, 2016). This gives rise to a very strong diurnal variation in the ambient concentration of biomass-derived organic aerosol (OA) compared to secondary components and in the wavelength-specific absorption enhancement. In a previous study, conducted in a different year, we used this diurnal variability to estimate the properties of BrC and the relationship between source and E_{abs} (*Zhang et al.*, 2016). However, this previous study lacked knowledge of the BC mixing state and relative coating amount. The addition of particle coating measurements and mixing state characterization here allows for a more robust assessment of the E_{abs} and BrC measurements in terms of the primary controlling factors.

The second set of measurements was made in summertime Fontana, CA. Fontana is located inland in the South Coast Air Basin (SoCAB) that includes the megacity Los Angeles. Measurements of ensemble-average particle composition are presented in *Chen et al.* (2018), and BC-containing particle composition and mixing state are discussed in *Lee et al.* (2017). The SoCAB is a highly photochemically active environment in the summertime, with much of the particulate matter being secondary in origin (*Docherty et al.*, 2008; *Hayes et al.*, 2013), especially material that is internally mixed with BC (*Cappa et al.*, 2012; *Lee et al.*, 2017). Biomass burning contributions in this region are sporadic, depending on the occurrence of wild fires. Thus, the Fontana site measurements provide a complementary assessment of the relationship between absorption enhancement and BC mixing state and coating amount.

5.3 Methods

5.3.1 Campaign overview

The measurements reported here were made from December 25, 2014 to January 12, 2015 in Fresno, CA and from July 3, 2015 to July 25, 2015 in Fontana, CA. The Fresno measurement site was located at the University of California Center (36.810, -119.778). The Fontana site was managed by South Coast Air Quality Management District (SCAQMD) and located behind the fire station at 14360 Arrow Highway (34.100, -117.490). **Figure 5-2** shows a map of CA with the locations of the two sites. In both studies all instruments were housed in a temperature-regulated modified shipping container (the "van"). Air was sampled into the van from 8 m above the ground, through a mast that extended 5 m above the ~3 m tall van. The mast had a horizontal inlet nozzle that could rotate into the relative wind so as to maintain an approximately isokinetic flow and to minimize the loss of particles. The flow through the mast was 1 m^3 min^{-1}. Twenty-one 1.6 cm outer diameter stainless steel tubes extended into the mast, and air was sampled from the mast through these tubes (not all were used). Air was sampled at 16.7 lpm through a diffusion drier packed with silica gel and then through a PM_1 cyclone. After the cyclone, the flow was split and 2.1 lpm was sampled through a custom thermodenuder with air passing alternatively through a heated channel (T = 250 °C) or a channel maintained at room temperature (i.e. the bypass) on a five-minute cycle. Part of both the heated and bypass channels were lined with charcoal cloth to scavenge NO_2. The airstream was then passed through a second diffusion drier after which the flow was split into three approximately equal streams. Air from one of these streams was sent to a single particle soot photometer (SP2, Droplet Measurement Technologies) and to a scanning electrical mobility sizer (SEMS, Brechtel Manufacturing, Inc.). The second stream went to the UC Davis dual-wavelength cavity ringdown/photoacoustic spectrometer (CRD-PAS) and a particle absorption eXtinctionometer (PAX, Droplet Measurement Technologies). The third stream went to a soot particle aerosol mass spectrometer (SP-AMS, Aerodyne Research, Inc.) and a high resolution aerosol mass spectrometer (HR-AMS, Aerodyne Research Inc.). A schematic of the instrument configuration is provided in **Figure 5-3**. Instrument details are provided in the sections that follow.

5.3.2 Refractory black carbon measurement

Refractory black carbon (rBC) concentrations and BC-specific particle size distributions were measured using the SP2 instrument at both the Fresno and Fontana sites. While the operation of the SP2 has been previously discussed for these studies (*Betha et al.*, 2018), further details are provided here and in Appendix A. The SP2 measures the concentration of rBC within individual rBC-containing particles. Sampled particles pass through a 1064 nm intracavity laser. Absorption of this light by rBC leads to rapid heating of the particles. If heating outweighs conductive cooling the particles will reach a sufficiently high temperature (i.e. their boiling point) that they will incandesce. The intensity of this incandescent light is proportional to the rBC mass of that particle (usually on the order of 0.1 – 10 fg per particle). Size distributions of only the rBC (exclusive of any other internally mixed material) are generated by converting the per particle mass to a volume equivalent diameter ($d_{p,VED}$ here, assuming ρ_{rBC} = 1.8 g cm^{-3}) and binning the particles by size.

When the number concentration of rBC-containing or non-rBC-containing particles is large, the SP2 may suffer from negative biases in the concentration measurement. This can happen when the SP2 detectors are triggered by one particle and a second passes through the viewing volume during the detection window (typically ~50 μs). Such particle coincidence effects can be minimized by decreasing the sample flowrate into the SP2 to decrease the likelihood that two particles are simultaneously in the viewing volume. Here, the SP2 was operated with a sample flowrate of only 60 cm^3 min^{-1}, or half of the typical value, to minimize the influence of particle coincidence. Inspection of individual particle detection events indicates that particle coincidence was generally avoided by operating at this reduced flowrate.

The SP2 data were processed using the SP2 Toolkit from the Paul Scherer Institute (PSI), developed by Martin Gysel. The SP2 was calibrated using size-selected fullerene particles (Lot L20W054, Alfa Aesar, Ward Hill, MA, USA). The SP2 size-dependent counting efficiency was determined by simultaneously measuring the concentration of the calibration particles with a condensation particle counter (TSI, model 3075). The particle counting efficiency was found to be unity for particles with $d_{p,VED} > 100$ nm. The SP2 used in this study measured particles over the size range 76 nm $\leq d_{p,VED} \leq$ 822 nm. Below the lower size limit, the detection efficiency falls off rapidly due, in part, to the large surface area-to-volume (SA-to-V) ratio of these particles. When the SA-to-V ratio is sufficiently large conductive cooling competes effectively with the radiative heating from the laser and the particles do not emit enough incandescent light at short enough wavelengths to trigger detection (*Schwarz et al.*, 2010). Above the upper size limit, the incandescence level is sufficient to saturate the detector, leading to an underestimate of particle mass. All SP2 mass concentration measurements were corrected for the missing mass contained in particles below the lower and above the upper size limit, using a multi-mode fitting approach (Appendix A).

5.3.3 Particle Optical Property Measurements

Particle optical properties for PM_1 were measured at 405 nm and 532 nm using the UC Davis Cavity Ringdown-Photoacoustic Spectrometer (CRD-PAS) at both the Fresno and Fontana sites. Light absorption coefficients (b_{abs}; units = Mm^{-1}) for dry particles were determined using photoacoustic spectroscopy (*Lack et al.*, 2012b). Light extinction coefficients (b_{ext}; units = Mm^{-1}) for dry (<20% relative humidity) particles were measured at 405 nm and 532 nm via cavity ringdown spectroscopy (*Langridge et al.*, 2011). Humidified light extinction measurements (RH ~85%) were also measured at 532 nm by cavity ringdown spectroscopy. The absorption measurements from the PAS were calibrated relative to the extinction measurement from the CRD using gas-phase O_3 and NO_2 with an estimated accuracy of 5% at 532 nm and 8% at 405 nm.

At the Fresno site optical properties were also measured at 870 nm using a photoacoustic eXtinctiometer (PAX; DMT, Inc.). In the PAX, light absorption coefficients were measured by photoacoustic spectroscopy. Light scattering coefficients (b_{sca}; units = Mm^{-1}) were determined for dry particles with the PAX using reciprocal nephelometry. The absorption measured by the PAX was calibrated relative to the UC Davis PAS using polydisperse fullerene soot and assuming that the absorption Ångstrom exponent was 1.4 (*Metcalf et al.*, 2013).

5.3.4 Particle Composition Measurements

5.3.4.1 Composition and concentration of NR-PM

The concentration of non-refractory particulate matter (NR-PM) species in PM_1 were measured using a high-resolution time-of-flight aerosol mass spectrometer (HR-ToF-AMS, henceforth HR-AMS) (*Canagaratna et al.*, 2007) during both the Fresno and Fontana studies, as discussed in detail by *Chen et al.* (2018). The NR-PM components are functionally defined as those materials that evaporate rapidly after impaction onto a heated surface *in vacuo* at ~600 °C. The NR-PM components characterized include particulate sulfate, nitrate, ammonium, chloride and organic matter. The data were processed using the PIKA toolkit in IGOR (Wavemetrics, Inc.). The organic aerosol composition data were further analyzed using positive matrix factorization (PMF) (*Zhang et al.*, 2011a). Four OA factors were determined during the Fresno campaign, identified as: biomass burning OA (BBOA); hydrocarbon-like OA (HOA); and two types of oxygenated OA identified as a very oxygenated OA type (VOOA) and a nitrate-associated type (NOOA) (*Chen et al.*, 2018). For Fontana, four OA factors were also determined and identified as: hydrocarbon-like OA (HOA); cooking-related OA (COA); and two oxygenated OA factors, referred to here as a more-oxidized very oxidized OA (VOOA) and a less-oxidized, nitrate-associated type (NOOA) (*Chen et al.*, 2018). (The particular terminology used here for the OA factors is discussed in *Chen et al.* (2018).)

5.3.4.2 Composition and concentration of BC-containing particles

The concentrations and composition of only BC-containing particles were determined using a soot particle aerosol mass spectrometer (SP-AMS) (*Onasch et al.*, 2012), for both the Fresno site (*Collier et al.*, 2018) and the Fontana site (*Lee et al.*, 2017). In the SP-AMS, a focused particle beam is intersected with an intra-cavity Nd:YAG laser operating at 1064 nm. Particles containing BC are rapidly heated by the laser, leading to evaporation of both the NR-PM materials and the refractory BC. In these studies, the standard HR-AMS tungsten vaporizer was removed so that particles that do not contain BC are not vaporized and are therefore not detected. Thus, the SP-AMS is specific to BC-containing particles, as operated here. In addition to BC, the SP-AMS measures the internally mixed particulate inorganic (sulfate, nitrate, ammonium, and chloride) and organic mass loading. The NR-PM species that are associated with BC will be distinguished from the bulk average NR-PM species (from the HR-AMS) using the subscript BC (i.e. NR-PM_{BC}). The SP-AMS particle detection efficiency is determined in large part by the extent of overlap between the particle and laser beam. Particles were sampled through a PM_1 aerodynamic lens, with particles measured down to ~40 nm vacuum aerodynamic diameter. For the Fresno dataset, the detection efficiency was determined by referencing the BC concentration measured by the SP-AMS to that measured by the SP2 (*Collier et al.*, 2018). The SP-AMS/SP2 ratio was observed to depend on the ratio between the NR-PM_{BC} and BC, with the NR-PM/BC ratio increasing as the SP-AMS/SP2 ratio increases, similar to previous observations (*Willis et al.*, 2014). This is likely a result of the BC-containing particles becoming more spherical as NR-PM coatings accumulate. This leads to greater collimation of the particle beam, better overlap with the laser, and ultimately an increased

detection efficiency. The dependence of the detection efficiency on the NR-PM/BC ratio was empirically determined for the Fresno study and has a functional form similar to that previously reported for laboratory studies (*Willis et al.*, 2014). For the Fontana data set, the SP-AMS collection efficiency was estimated based on measurements of the particle beam width, and a single, average value was used (*Lee et al.*, 2017). At the Fontana site, the SP-AMS was operated alternating between ensemble mode (i.e. bulk composition) and event-trigger mode (single-particle composition), and the observations were analyzed using PMF (*Lee et al.*, 2017). The coating-to-core mass ratio for both campaigns is calculated directly from the SP-AMS measurements as $R_{coat\text{-}rBC} = [\text{NR-PM}]_{BC}/[BC]$.

5.3.5 Other instrumentation

Number-weighted particle size distribution measurements for ambient and thermodenuded particles were made using a scanning electrical mobility sizer (SEMS; Brechtel Manufacturing, Inc.), operating over the mobility diameter size range 10 – 950 nm. The SEMS consisted of a differential mobility analyzer and a mixing condensation particle counter.

5.3.6 Determination of Intensive Particle Properties

The light absorption coefficient and BC concentration measurements are used to determine the observed mass absorption coefficient, referenced to BC, as:

$$MAC_{BC} = \frac{b_{abs}}{[BC]}; \quad (1.)$$

The observed MAC_{BC} may include contributions to absorption from non-BC components (e.g. BrC), whether internally or externally mixed, or from non-absorbing coatings via the "lensing" effect. The observable absorption enhancement can be determined from the MAC_{BC} values by normalizing MAC_{BC} by a reference value for pure, uncoated BC, with

$$E_{abs} = \frac{MAC_{BC}}{MAC_{BC,ref}}; \quad (2.)$$

The reference $MAC_{BC,ref}$ can be established from the literature (*Bond and Bergstrom*, 2006) or from the observations by extrapolating MAC_{BC} to the limit of $R_{coat\text{-}rBC} = 0$; the latter approach is taken here (discussed further in Section 5.4.3), although both methods give similar results for the current campaigns. The absorption enhancement can also be determined from simultaneous or sequential measurements of b_{abs} for ambient particles and thermodenuded particles (*Cappa et al.*, 2012; *Healy et al.*, 2015; *Liu et al.*, 2015c). As noted above, sequential b_{abs} measurements of ambient and thermodenuded particles were made on a 5 minute cycle. In the current study, we focus on E_{abs} as determined from Eqn. 2 above. The E_{abs} from Eqn. 2 (i.e. from the "MAC-method") are compared to E_{abs} determined from the "thermodenuder-method" in Appendix B.

The wavelength dependence of absorption is characterized by the Ångstrom absorption exponent (AAE), as:

$$AAE = -\log(\frac{b_{abs,\lambda_1}}{b_{abs,\lambda_2}}) / \log\left(\frac{\lambda_1}{\lambda_2}\right); \quad (3.)$$

where λ_1 and λ_2 indicate two different measurement wavelengths. The wavelength dependence of the imaginary refractive index, *k*, can alternatively be characterized by the parameter *w*, where:

$$w = -\log\left(\frac{k_{\lambda 1}}{k_{\lambda 2}}\right) / \log(\frac{\lambda 1}{\lambda 2}) \quad (4.)$$

The AAE and *w* can be determined from wavelength pairs or from fitting multi-wavelength data.

5.4 Results and Discussion

5.4.1 General Overview

Chen et al. (2018) provide a broad overview of the campaigns, and *Lee et al.* (2017) and *Collier et al.* (2018) provide details on the SP-AMS measurements specifically. Here, we highlight a few details from each campaign that are relevant to the current study. Time series of light extinction and light absorption for the two campaigns are shown in Figure 5-4 for reference.

The wintertime Fresno campaign is separated into two distinct time periods based on the local meteorology. In particular, after about 6 January, 2015, the morning was impacted by a persistent, relatively thick fog that would slowly dissipate as the day progressed. Prior to this date, the atmosphere is classified as being substantially less foggy. The heavy fog period will be referred to as "high" fog and the less foggy period as "low" fog. The low-fog period was colder and drier than the high-fog period (T_{avg} = 7.6 °C and RH_{avg} = 80.7% versus T_{avg} = 12.0 °C and RH_{avg} = 83.5%). The diurnal variability and average particle composition and concentrations were distinct between the low-fog and high-fog periods (*Chen et al.*, 2018), and a clear increase in extinction was observed in the high-fog period; the average $b_{ext,532nm}$ during the low-fog period was 73 Mm^1 and 226 Mm^{-1} during the high-fog period. The average BC coating amount was also larger during the high-fog period than the low-fog period, with $R_{coat\text{-}rBC}$(low fog) = 2.1 ± 0.8 versus $R_{coat\text{-}rBC}$(high fog) = 2.8 ± 0.4 (*Collier et al.*, 2018). The diurnal variation in $R_{coat\text{-}rBC}$ was more pronounced during the low-fog period than the high-fog period, with the daytime values being slightly elevated over nighttime values (*Collier et al.*, 2018). The daytime $R_{coat\text{-}rBC}$ values during the low- and high-fog periods were similar. Thus, much of this increase was attributable to a substantial increase in the particulate NO_3^- during the high-fog period, although the OA was also larger during the high-fog period (*Chen et al.*, 2018). Of particular relevance to the current study, the fraction of organics classified as BBOA was larger during the low-fog period, while the NOOA contribution increased substantially during the high-fog period. There was substantially greater diurnal variability in the absorption and extinction during the low-fog period than during the high-fog period.

The Fontana campaign was characterized by generally high temperatures (T_{avg} = 23.6 °C; range 14.9 °C to 35.9 °C) and relatively low relative humidity (RH_{avg} = 55%), with strong diurnal variability in both (*Chen et al.*, 2018). Early in the campaign, the atmosphere was strongly impacted by fireworks associated with 4th of July (U.S. Independence Day) activities; the impact of the 4th of July activities persisted through 8 July. This fireworks-impacted period is separated for analysis from the remaining non-fireworks days. The average $b_{ext,532nm}$ = 30 Mm^{-1} for the non-fireworks impacted period. The diurnal profile of NR-PM has two peaks, one at 10:00 and another at 17:00 (local times) (*Chen et al.*, 2018). The mean $R_{coat\text{-}rBC}$ was much larger than in Fresno, with $R_{coat\text{-}rBC,avg}$ = 5.2, and the diurnal variation in $R_{coat\text{-}rBC}$ is large, with a single maximum at 16:00 (*Lee et al.*, 2017).

5.4.2 BC concentrations and size distribution

The average mass-weighted BC-only size distributions, determined from multi-modal fitting of the observed SP2 measurements for each campaign, are shown in **Figure 5-5**. For each campaign, the BC-only size distributions exhibit multimodal character. For example, Fresno exhibited dominant mode maxima between $d_{p,VED}$ ~ 45-60 nm and at 115-160 nm (**Figure 5-5**), consistent with previous measurements in this region (*Zhang et al.*, 2016). **Figure 5-5** shows mass-weighted size distributions determined from multi-modal fitting of the observed size distributions. Details of the fitting procedure used to determine the mass-weighted BC size distribution over the entire size range are discussed in Appendix A.

Fresno: The multi-mode fits indicate that on average 33% of the BC mass is outside of the detection range of the SP2 used here, with a larger amount of missing mass during daytime than at nighttime. The relative contribution of the larger mode is greater at night, with the smaller mode more pronounced during the day. The greater contribution of particles with larger volume equivalent BC core diameters during nighttime reflects an increased concentration of biomass-combustion derived BC particles, as biomass-derived BC particles have larger diameters than fossil fuel-derived particles (in particular, those from vehicular emissions) (*Kondo et al.*, 2011). Consideration of the diurnal variability of the BC concentrations in each of the four fit modes (Appendix A) demonstrates that the smallest two modes (at 57 nm and 118 nm) exhibit a sharp increase starting at 6 am (**Figure 5-5**b), reflecting substantial BC emissions during the morning rush hour coupled with the still relatively low boundary layer height. The larger two modes (at 182 nm and 420 nm) increase primarily at night, when residential wood combustion is largest and the nocturnal boundary layer is shallow. The BC concentration in the two small modes also increases at night, primarily a reflection of the decreased boundary layer height relative to daytime along with continued emissions, although their fractional contribution is decreased. However, the peak concentration in these modes occurs ~1 h earlier in the night than of the larger two modes, reflecting the different sources. The campaign-average fractional contribution of the vehicle-related modes (the two smallest) was 0.5, meaning half the BC came from vehicles and half from biomass burning, with the limitation that the modes may not be purely reflective of one source or the other (i.e. there may be some small particles contributed by biomass combustion and some larger particles from vehicles). These observations demonstrate that there are two distinct sources

of BC in the wintertime Fresno atmosphere, one from motor vehicles (likely, diesel vehicles) and one from biomass combustion.

Fontana: For Fontana, the BC-only mass-weighted size distributions also had multiple modes. However, at this site the smallest two modes (at 47 nm and 116 nm) contributed the majority of the BC mass, with their campaign-average fractional contribution being 0.78. This indicates that vehicle emissions dominate the BC burden in the region. The small contribution from the two larger modes (at 182 nm and 420 nm) could indicate some contribution from regional biomass burning. Alternatively, these larger particles could result from near-source coagulation and could also be contributed by motor vehicle emissions. The contribution from the larger modes was enhanced from the night of July 4th through the following night, indicating that fireworks (from 4th of July celebrations) produced BC having larger diameters. Overall, 49% of the BC mass was contained in particles outside of the SP2 detection range, with minimal diurnal variability (and most of the variability in the campaign-average resulting from the enhanced large particle contribution on July 4th).

5.4.3 Variability in MAC_{BC} and E_{abs}

The total observed absorption, and the associated MAC_{BC}, results from a combination of absorption by BC, including mixing-induced enhancements, and absorption by BrC. The diurnal variation in the observed MAC_{BC} values for both campaigns and histograms of MAC_{BC} are shown in **Figure 5-6**. For Fresno, the MAC_{BC} distribution at 405 nm is quite broad and exhibits a clear increase at night and again during the day, with minima at 09:00 and 17:00 (local time). The MAC_{BC} values at 532 nm and 870 nm exhibit similar, but much less pronounced, diurnal variability, and the spread of the MAC_{BC} distributions decreases substantially with wavelength. The diurnal variability of MAC_{BC} attributable to mixing-induced enhancements alone should exhibit a negligible wavelength dependence. Thus, the observed wavelength-dependent behavior indicates that diurnal-varying BrC contributes substantially to the observed MAC_{BC}. In Fresno, the diurnal variability differed substantially between the low fog and high-fog periods at 405 nm in particular, but also at 532 nm. During the low-fog period, the daytime MAC_{BC} increase was suppressed while during the high-fog period it was enhanced (relative to the campaign average).

In Fontana, the MAC_{BC} values at 405 nm and 532 nm, excluding the fireworks-impacted period, increased during the early morning and stayed elevated through the afternoon (**Figure 5-6**). But, the overall day-night difference was much smaller compared to that observed in Fresno, and the MAC_{BC} distributions were also narrower than in Fresno. (When periods impacted by fireworks are included, the MAC_{BC} in the early morning (~6 am) is increased because the MAC_{BC} during the fireworks-impacted period was particularly large at this time.)

The observed MAC_{BC} values can be converted to equivalent absorption enhancement values by dividing by a reference MAC for pure, uncoated BC (referred to here as $MAC_{BC,ref}$). While values of the $MAC_{BC,ref}$ are reported in the literature, quantitative comparison to the ambient observations can be challenged by the uncertainty in the BC concentration measurement, in particular. This is especially the case here, given the large, time-varying "missing mass" correction required. Thus, a wavelength-specific reference $MAC_{BC,ref}$ for uncoated BC has been determined

for each campaign from the observations. Estimation of campaign-specific $MAC_{BC,ref}$ in this manner allows for more robust determination of E_{abs} than if the literature values were used, accounting for any campaign-specific sampling biases. However, this method does not account for potential changes in the $MAC_{BC,ref}$ that result from changes in morphology that can result from coating of materials onto BC.

Ideally, the reference $MAC_{BC,ref}$ can be determined be extrapolating the observed MAC_{BC} measured for either ambient particles or particles passed through the thermodenuder to the limit of no coating material (i.e. as $R_{coat\text{-}rBC} \rightarrow 0$). For Fresno this method is complicated by the co-occurrence of BrC that is likely externally mixed from the BC and of, likely, charring of the NOOA (see Appendix B). There is, however, a reasonable relationship between $R_{coat\text{-}rBC}$ and both the overall [OA]/[rBC] and [NR-PM_1]/[rBC] ratios (**Figure 5-7**). Thus, it is reasonable to extrapolate the observed ambient particle MAC_{BC} to the limit of [OA]/[rBC] = 0, as this reflects a condition where there is concurrently little coating material and little externally mixed absorbing OA. The Fresno observations at all three wavelengths are consistent with a sigmoidal relationship between MAC_{BC} and [OA]/[rBC] for Fresno (**Figure 5-8**). The resulting campaign-specific $MAC_{BC,ref}$ values for Fresno are 4.4 ± 0.2 m^2 g^{-1} (870 nm), 7.5 ± 0.5 m^2 g^{-1} (532 nm) and 10.7 ± 0.6 m^2 g^{-1} (405 nm), where the reported uncertainties correspond to the 99% confidence interval from the fit. The distributions of observed MAC_{BC} values are compared to the derived $MAC_{BC,ref}$ values in **Figure 5-9**. For Fontana, this method of estimation is complicated by the particles sampled during the fireworks period, which were particularly non-volatile and, likely, subject to charring. Therefore, only observations of MAC_{BC} and $R_{coat\text{-}rBC}$ outside of the fireworks-impacted period are used to determine the $MAC_{BC,ref}$ (**Figure 5-10**). The campaign-specific values for Fontana are 7.2 ± 0.1 m^2 g^{-1} (532 nm) and 9.6 ± 0.2 m^2 g^{-1} (405 nm) where the reported uncertainties correspond to the 99% confidence interval from the fit. The distributions of observed MAC_{BC} values are compared to the derived $MAC_{BC,ref}$ values in **Figure 5-11**. The absolute uncertainty on these $MAC_{BC,ref}$ values is large given the relatively large uncertainty on the SP2 measurements, and the fit-based uncertainties for the Fontana measurements is smaller than is reasonable. We suggest a reasonable precision-limited uncertainty on the $MAC_{BC,ref}$ values for both campaigns is 10%. It is noteworthy that the derived campaign-specific $MAC_{BC,ref}$ values are in reasonable agreement with laboratory measurements (*Cross et al.*, 2010; *Forestieri et al.*, *Accepted*) and literature assessments (*Bond and Bergstrom*, 2006).

The E_{abs} values derived from the MAC_{BC} observations are shown as a function of the BC coating amount ($R_{coat\text{-}rBC}$) in **Figure 5-12**. In Fresno, the E_{abs} values at 405 nm and 532 nm are notably greater than unity for all $R_{coat\text{-}rBC}$ (from 1 to 4). The mean values are 1.37 ± 0.22 (405 nm), 1.22 ± 0.15 (532 nm) and 1.10 ± 0.13 (870 nm). In contrast, the E_{abs} in Fontana are very close to one when $R_{coat\text{-}rBC}$ is in this same range, with E_{abs} = 1.10 ± 0.27 (405 nm) and 1.07 ± 0.22 (532 nm), excluding the fireworks-impacted period. There is, however, a small, increase in E_{abs} with $R_{coat\text{-}rBC}$ in Fontana.

The differences in the dependence of E_{abs} on $R_{coat\text{-}rBC}$ between Fresno and Fontana result primarily from differences in the contribution of BrC to the total absorption between the two

locations. *Chen et al.* (2018) determined four general types of OA based on PMF analysis of the HR-AMS data for both sites. In Fresno, there is a substantial contribution of BrC from biomass burning that enhances the E_{abs} above unity even at low $R_{coat\text{-}rBC}$. The fractional contribution from the biomass-burning associated factor (BBOA) is largest when $R_{coat\text{-}rBC}$ is smallest (**Figure 5-13**). Consistent with this, the fractional contribution of the $C_2H_4O_2^+$ ion (an AMS marker for biomass burning) in the BC coating material is higher when $R_{coat\text{-}rBC}$ is smallest (*Collier et al.*, 2018). This suggests that absorption by BBOA, whether internally or externally mixed from BC, contributes importantly to the $E_{abs} > 1$ at low $R_{coat\text{-}rBC}$ for Fresno. The fractional contribution of the nitrate-associated OA (NOOA) increases as $R_{coat\text{-}rBC}$ increases. This suggests that the NOOA might be somewhat absorbing and contributes to the $E_{abs} > 1$ at larger $R_{coat\text{-}rBC}$, especially at 405 nm. For Fontana, four OA factors were also identified. There, the OA mass is dominated by the very oxygenated OA factor (VOOA), and the fractional contribution of VOOA increases with $R_{coat\text{-}rBC}$ (**Figure 5-13**). Some of the increase in E_{abs} with $R_{coat\text{-}rBC}$ for Fontana might therefore result from photochemical production of coatings on BC. Further discussion of absorption by OA follows below. Regardless of the exact reason for the increase in E_{abs} with $R_{coat\text{-}rBC}$ at Fontana, comparison with the theoretical calculations in *Cappa et al.* (2012) or *Liu et al.* (2015c) demonstrates that the magnitude of the E_{abs} observed in Fontana is much lower than might be expected from simple application of core-shell Mie theory.

The small E_{abs} values in Fontana at both 405 nm and 532 nm, even at high $R_{coat\text{-}rBC}$ (~ 10), are consistent with the observations of *Cappa et al.* (2012), who similarly observed small E_{abs} values (<1.1) at high $R_{coat\text{-}rBC}$. A large fraction of the *Cappa et al.* (2012) measurements were made in the coastal waters around Los Angeles, while the Fontana measurements here were made in the inland greater LA area. In contrast, *Liu et al.* (2015c), using similar methods, observed mean E_{abs} values at 781 nm of ~1.5 at moderate $R_{coat\text{-}rBC}$ (~ 4) in a somewhat rural area located near London, UK. The assumption for the core-shell Mie theory calculations in those studies was that the coating material is equally distributed across the particle population. Under this assumption, there is an expectation that the ensemble-average E_{abs} from mixing effects (i.e. "lensing") should increase with the ensemble-average $R_{coat\text{-}rBC}$, just as it does for individual particles (*Bond et al.*, 2006; *Fuller et al.*, 1999). It is evident that the observed dependence of E_{abs} on $R_{coat\text{-}rBC}$ does not consistently follow this model and certainly does not for the CA observations. This likely results from there being different populations of BC-containing particles having varying coating amounts, with some particles having "thick" coatings and others having "thin" coatings as indicated from PMF analysis of the Fontana SP-AMS observations (*Lee et al.*, 2017). *Fierce et al.* (2016) argue from a model perspective that accounting for particle diversity and the actual distribution of coating material can have a strong impact on the population-averaged absorption, typically leading to a decrease in absorption compared to the equivalent uniformly coated population and, therefore, a smaller E_{abs}. *Liu et al.* (2017) provide experimental evidence in line with this conclusion. This suggests that the observation of small E_{abs} values here and in *Cappa et al.* (2012) at relatively high $R_{coat\text{-}rBC}$ is likely a result of mixing state (and coating amount) diversity within the BC particle population. However, we cannot rule out the possibility that morphological deviations (i.e. the distribution of coatings

and BC within individual particles) from the ideal core-shell morphology also contribute to a reduced ensemble-average E_{abs}.

The SP-AMS PMF results from *Lee et al.* (2017) for Fontana specifically indicated four BC-containing types of particles having different BC weight percentages. These were identified by PMF as an HOA-rich factor (14.2%), a BC-rich factor (44.4%), and two oxygenated factors, termed OOA-1 (13.4%) and OOA-2 (0.5%), where the numbers in parentheses are the factor-specific BC wt%. The fractional contribution of the OOA-1 factor increased with $R_{coat\text{-}rBC}$ while the BC-rich and, to a lesser extent, the HOA-rich factor contributions decreased (c.f. Figure 4 in *Lee et al.* (2017)). The OOA-2 factor contributed a large proportion of the overall coating material mass, but contained little of the BC. Assuming core-shell morphologies for each factor, the factor-specific E_{abs} can be calculated from Mie theory. The calculated factor-specific E_{abs} are 1.45 (BC-rich), 2.05 (HOA-rich), 1.99 (OOA-1) and 2.43 (OOA-2) at 532 nm, assuming a core BC diameter of 120 nm (one of the mode diameters for Fontana) and accounting for density differences between BC and the coating material. The ensemble-average E_{abs} can be calculated using a linear combination of these four factors with the fraction types from *Lee et al.* (2017). The calculated ensemble-average E_{abs} is greater than the observed E_{abs} at all $R_{coat\text{-}rBC}$ (**Figure 5-14**). This is not surprising given that the smallest factor specific E_{abs} (for the BC-rich type) was larger than the observed ensemble-average even at large $R_{coat\text{-}rBC}$. However, the dependence of the observed and calculated ensemble-average E_{abs} and $R_{coat\text{-}rBC}$ are similar if the calculated ensemble-average E_{abs} is multiplied by 0.65 (**Figure 5-14**). This, perhaps, indicates that changes in the fractional contribution of the different BC-containing particle factors with $R_{coat\text{-}rBC}$ are responsible for the slow increase in E_{abs} with $R_{coat\text{-}rBC}$, but that the calculated E_{abs} based on the average properties of each BC-containing factor are nonetheless overestimated when core-shell Mie theory is used. This could indicate additional particle-to-particle (or size-dependent) diversity in the coating amount even within each identified factor (*Fierce et al.*, 2016), or could result from particles having non-core-shell morphologies that limit the extent of the absorption enhancement (*Adachi et al.*, 2010; *Scarnato et al.*, 2013). Most likely, both phenomena contribute.

Regardless, the question persists as to the reason why the E_{abs}- $R_{coat\text{-}rBC}$ relationship seemingly differs between the urban and near-urban CA atmosphere and the UK atmosphere. We hypothesize that this difference is linked to the sources and age of the air masses sampled. In *Liu et al.* (2015c) the largest $R_{coat\text{-}rBC}$ values were observed to have particularly large BC core diameters, suggesting a biomass-burning source. However, these same particles also had the largest fraction of oxygenated OA, suggestive of photochemical or even cloud processing, and backtrajectory analysis indicated that when $R_{coat\text{-}rBC}$ was large the sampled air masses tended to come from the European continent while air masses tended to come from within the UK when $R_{coat\text{-}rBC}$ was small. It may be that longer-range transport serves to decrease the differences in coating amounts between the different BC-containing particle types observed in nearer-source regions and periods (*Lee et al.*, 2017; *Lee et al.*, 2015) and thus increases the consistency between simple core-shell calculations and observations of ensemble-average absorption. However, in Toronto, Canada, *Healy et al.* (2015) did not observe an increase in E_{abs} for periods identified as being impacted by

transboundary (i.e. long-range) pollution, even though the $R_{coat\text{-}rBC}$ was ~3.5 during this period. It is possible that their observations were confounded by inputs from local BC sources that served to maintain the particle-to-particle diversity (with respect to coating amount) and limit the overall observed E_{abs}. The results presented here indicate that measurements in remote locations that are reasonably free from local inputs (whether anthropogenic, such as from vehicles, or from fresh biomass burning) would be helpful in understanding the extent to which E_{abs} changes as a result of atmospheric processing. However, such measurements will be challenged by the low signals and BC concentrations that are typically observed in remote regions. It is suggested that a minimum of one month of measurements will be required to build sufficient statistics in low-concentration locations.

5.4.4 Brown Carbon Absorption

5.4.4.1 Methodology

To assess the contribution of BrC to the total observed absorption requires removal of the contribution from the mixing-induced enhancement, i.e. the "lensing" effect. Here, we take two approaches. In the first, an upper-limit for the contribution of BrC to total absorption is determined by assuming that the mixing-induced enhancement is zero. In the second, we estimate the $R_{coat\text{-}rBC}$ -dependent magnitude of the mixing-induced enhancement for each site based on the longest wavelength measurement available (870 nm for Fresno and 532 nm for Fontana), assuming that BrC contributes negligibly at this wavelength. The absorption from BrC is then calculated as the difference between the observed absorption and the estimated absorption by coated BC (i.e. inclusive of the mixing-induced enhancement). More specifically:

$$b_{abs,BrC} = b_{abs,obs} - b_{abs,BC,coated} = b_{abs,obs} - MAC_{BC,uncoated} \cdot E_{abs,mixing}(R_{coat-rBC}) \cdot [BC] \quad (5.)$$

where $b_{abs,BrC}$, $b_{abs,obs}$ and $b_{abs,BC,coated}$ are the absorption by BrC, the observed absorption and the estimated absorption for coated BC particles, respectively. The $MAC_{BC,ref}$ values are those determined above. For the first (upper-limit) approach, $E_{abs,mixing} = 1$. For the second approach the $E_{abs,mixing}$ values are a function of $R_{coat\text{-}rBC}$ and estimated from the longest-wavelength measurements. Note that Eqn. 5 provides for internal consistency because the $MAC_{BC,ref}$ values are determined directly from the observations and are not from the literature, i.e. they are campaign-appropriate and account for uncertainties in [BC].

As discussed above, the observed E_{abs}- $R_{coat\text{-}rBC}$ relationship does not follow core-shell Mie theory predictions. Thus, there is no *a priori* functional form that can be assumed to relate the ensemble average E_{abs} to $R_{coat\text{-}rBC}$ for the second method. We therefore adopt the approach of assuming that the E_{abs} from mixing increases linearly with $R_{coat\text{-}rBC}$, a functional form that is generally consistent with the longest-wavelength observations at each site (870 nm at Fresno and 532 nm at Fontana in **Figure 5-12**). However, for the 870 nm measurements in Fresno the observed E_{abs} actually decreases slightly as the $R_{coat\text{-}rBC}$ increases from 1 to ~2.5. We hypothesize that this

is indicative of some small absorption by BBOA at 870 nm because the concentration of BBOA decreases as $R_{coat\text{-}rBC}$ increases (discussed later) and is relatively small above $R_{coat\text{-}rBC}$ ~2.5. Therefore, for Fresno, the relationship between E_{abs} (from mixing effects) and $R_{coat\text{-}rBC}$ is determined from fitting the binned observations only for $R_{coat\text{-}rBC} > 2.5$. Thus, for Fresno it is assumed that there is no BrC absorption at 870 nm when $R_{coat\text{-}rBC} > 2.5$, but that there may be some BrC absorption at lower $R_{coat\text{-}rBC}$. For Fontana, the E_{abs}- $R_{coat\text{-}rBC}$ relationship is determined from fitting the 532 nm observations over all $R_{coat\text{-}rBC}$ because 870 nm measurements are not available. Thus, for Fontana it is inherently assumed that BrC absorption at 532 nm does not result directly in the increase in E_{abs} with $R_{coat\text{-}rBC}$. Unless otherwise specified, results reported below refer to the $b_{abs,BrC}$ determined from the second method, but results from both methods are reported in **Table 5-1**.

5.4.4.2 Fresno Brown Carbon

For Fresno, absorption by BrC is unambiguous at 405 nm and 532 nm, with large $b_{abs,BrC}$ values obtained both at night and during the day. For 870 nm, the situation is less clear although there appears to be some absorption by BrC. Comparison of the diurnal profiles of $b_{abs,BrC}$ and the various OA factors (as well as the inorganic species and BC) qualitatively suggests that BBOA and NOOA are somewhat absorbing (**Figure 5-15**). A multilinear regression of $b_{abs,BrC}$ against the OA factors confirms that BBOA and NOOA are, indeed, the major absorbing OA types, with regression coefficients (i.e. slopes) of 0.84 $m^2\ g^{-1}$ and 0.52 $m^2\ g^{-1}$, respectively, and a total $r^2 = 0.78$. The observed and reconstructed absorption are shown in **Figure 5-16**. These correspond to the individual mass absorption coefficients for BBOA and NOOA at 405 nm. Similar multilinear fits for the 532 nm $b_{abs,BrC}$ yield regression coefficients corresponding to $MAC_{BBOA} = 0.45\ m^2\ g^{-1}$ and $MAC_{NOOA} = 0.14\ m^2\ g^{-1}$ (combined $r^2 = 0.71$) and for the 870 nm $b_{abs,BrC}$ yield $MAC_{BBOA} = 0.085\ m^2\ g^{-1}$ and $MAC_{NOOA} = 0.044\ m^2\ g^{-1}$ (combined $r^2 = 0.24$). There was no evidence for appreciable light absorption by the two other OA factors, HOA and VOOA. (Although BBOA and HOA have similar diurnal profiles, there is actually only a moderate correlation between the two, with $r^2 = 0.43$. Thus, they are separable in the multilinear fit.) The appropriateness of the multilinear regression and the conclusion that BBOA and NOOA are both BrC (i.e. are absorbing) is visually demonstrated when (i) $b_{abs,BrC}$ is plotted against [BBOA] during periods when the NOOA fractional contribution is small (**Figure 5-17**a), or (ii) $b_{abs,BrC}$ is plotted versus [NOOA] when the BBOA fractional contribution is small (**Figure 5-17**b). Visual inspection of graphs of HOA and VOOA versus $b_{abs,BrC}$ (not shown) also confirms that neither of these factors are BrC. The OA-factor specific MAC values are shown as a function of wavelength in **Figure 5-18**. For the upper-limit (no mixing-induced enhancement) approach the derived OA factor-specific *MAC* values are only slightly larger than those reported above when the mixing-induced enhancement is accounted for for NOOA and are the same for BBOA. This indicates a general robustness of the results (**Table 5-1**).

The small r^2 from the multilinear regression for 870 nm is expected given that when subtracting the mixing-induced enhancement it was assumed that the OA was non-absorbing at 870 nm. However, the BBOA is largest when the $R_{coat\text{-}rBC}$ is smallest (where the mixing-induced

enhancement is smallest), and thus there is reason to think that the MAC for BBOA is substantially more reliable than the MAC for NOOA at 870 nm and that the NOOA values at 870 nm might be discounted entirely. This has been tested by performing the multi-linear fit for only the low-fog period, when the NOOA concentration was relatively small and the $R_{coat\text{-}rBC}$ was typically <2.5 (the threshold identified above). The retrieved 870 nm MAC_{BBOA} = 0.088 m^2 g^{-1} for the low-fog period, similar to that obtained for the entire dataset, and the r^2 was larger (r^2 = 0.36).

The uncertainty in these estimates comes from uncertainty in the measurement of [BC], $b_{abs,obs}$, [BBOA], [NOOA], and the accounting for the mixing-induced enhancement. Since an internally consistent $MAC_{BC,ref}$ is used (meaning that this was determined from the observations using the $b_{abs,obs}$ and [BC]) uncertainty in this value does not contribute substantially to the total uncertainty and it also leads to a substantially reduced sensitivity to uncertainty in [BC]. Assuming 30% uncertainty in the BBOA and NOOA concentrations, 10% in the $b_{abs,obs}$, and 10% in the mixing-induced enhancement, the estimated absolute average uncertainty is 35% at 405 nm and 50% at 532 nm. At 870 nm the uncertainty is more difficult to estimate given the initial assumption that BrC is nonabsorbing. It is likely at least as large as the uncertainty at 532 nm, and 50% uncertainty is assumed in **Figure 5-18** for MAC_{BBOA} at 870 nm and 100% for MAC_{NOOA}.

The MAC_{BBOA} values determined here are slightly larger than the average determined by *Zhang et al.* (2016) for measurements made in wintertime Fresno in 2013, two years earlier than the current study (0.6 m^2 g^{-1} in that study for the total BBOA compared to 0.84 m^2 g^{-1} here at 405 nm). Some of this difference is likely attributable to different analysis methods. *Zhang et al.* (2016) relied on Mie theory to extract the absorption by BrC whereas the current approach is more directly observational. Thus, we suggest that *Zhang et al.* (2016) likely underestimated the absorptivity of BBOA. In contrast to the current study, two BBOA factors were retrieved in 2013. Two OOA factors were also obtained, identified as a semi-volatile OA (SV-OOA) and a low-volatility OA (LV-OOA) (*Young et al.*, 2016). However, *Zhang et al.* (2016) did not note any evidence for absorption by these other, non-BBOA factors. Thus, the finding that the NOOA is absorbing is new to this study. Reanalysis of the *Zhang et al.* (2016) data via multilinear regression using the "upper-limit" approach (since there were no measurements of $R_{coat\text{-}rBC}$ available to allow estimation of the mixing-induced enhancement) indicates that one of the non-BBOA factors, the SV-OOA factor in that study, was likely somewhat absorbing, in addition to the BBOA factors. Consistent with *Zhang et al.* (2016), the multi-linear regression indicates that one of their BBOA factors was more absorbing than the other, with MAC_{BBOA1} = 0.79 m^2 g^{-1} and MAC_{BBOA2} = 1.22 m^2 g^{-1} at 405 nm. The derived MAC_{BBOA1} is quite similar to that obtained for the single BBOA factor from the current measurements. Their SV-OOA factor was much less absorbing than NOOA, with $MAC_{SV\text{-}OOA}$ = 0.14 m^2 g^{-1} at 405 nm. Most likely, the difference between the current study and *Zhang et al.* (2016) results from differences in environmental conditions, although we cannot rule out the possibility that there are differences in how the PMF analysis is splitting out the factors. In the current study, early morning fog was experienced during much of the study, especially in the latter half when NOOA concentrations were elevated. The ambient conditions were much colder and drier in *Zhang et al.* (2016), with little to no fog observed. This difference

in behavior between these two studies strongly implicates fog, or at least wet aerosols, in the production of the light absorbing chromophores that make NOOA brown carbon.

Given the preponderance of BBOA in the Fresno atmosphere it is tempting to implicate aqueous phase processing of biomass burning emissions as the source of absorbing NOOA (and SV-OOA). *Gilardoni et al.* (2016) suggested such a pathway as a major source of absorbing SOA in the Po Valley, Italy. However, the mass spectrum of NOOA (*Chen et al.*, 2018) lacks a substantial peak at *m/z* = 29 that *Gilardoni et al.* (2016) indicated was a key signature of SOA produced from aqueous processing of biomass burning emissions. (The *m/z* = 29 peak is slightly larger for the SV-OOA from 2013 (*Young et al.*, 2016), but still much smaller than in *Gilardoni et al.* (2016).) Additionally, the NOOA factor is strongly correlated with particulate NO_3^- ($r^2 = 0.76$), and the diurnal profile of particulate nitrate, especially during the high-fog period, is strongly suggestive of substantial production of nitrate via nocturnal processing within the residual layer (*Prabhakar et al.*, 2017). Since most biomass burning emissions (from residential wood combustion) occur at night there is little that ends up in the residual layer, the composition of which is determined primarily by what is in the atmosphere just prior to sunset. Thus, our results do not support aqueous oxidation of biomass burning emissions as the predominant source of absorbing NOOA (and by extension, SV-OOA). Instead, we hypothesize that the absorptivity of NOOA here is a result of nitrate radical-related oxidation of organic compounds to produce organic nitrates that occurs in the residual layer at night; these organic nitrates may undergo further aqueous-phase processing that could contribute to brown carbon formation. While the exact production mechanism of the secondary BrC cannot be pinpointed, it seems likely that there is some role for aqueous phase processing coupled with nitrate-radical chemistry.

For BBOA at Fresno, the AAE values depend somewhat on the specific wavelength pair considered, with $AAE_{\text{BBOA,405-532nm}} < AAE_{\text{BBOA,405-870nm}} < AAE_{\text{532-870nm}}$ (**Table 5-1**), and a fit to the three wavelengths giving $AAE_{\text{BBOA}} = 3.04$. The $w_{\text{BBOA}} = 1.20$ for the 405-532 nm pair, but is 1.79 from the fit over all three wavelengths. For NOOA at Fresno, there are only reliable results at two wavelengths (405 and 532 nm) available, with $AAE_{\text{NOOA}} = 4.81$ and $w = 3.67$ using these wavelength pairs. The NOOA exhibits a steeper wavelength dependence than the BBOA.

5.4.4.3 Fontana Brown Carbon

For Fontana, it is much less clear whether any of the OA factors are absorbing in nature at the wavelengths considered. The diurnal profiles of the derived $b_{\text{abs,BrC}}$ at 405 nm and 532 nm, excluding the fireworks impacted period, indicate a peak in $b_{\text{abs,BrC}}$ around 08:00 (local time) (**Figure 5-15**). The $b_{\text{abs,BrC}}$ at 405 nm remains elevated throughout the afternoon, while the $b_{\text{abs,BrC}}$ at 532 nm falls to zero. Given that the $R_{coat\text{-}rBC}$ for this campaign shows a clear peak in the mid-afternoon (*Lee et al.*, 2017), and since it has been assumed that all of the increase in the MAC_{BC} (and E_{abs}) with $R_{coat\text{-}rBC}$ at 532 nm results from mixing-induced enhancements, it is to be expected that the $b_{\text{abs,BrC}}$ at 532 nm is close to zero in the afternoon. The slightly elevated $b_{\text{abs,BrC}}$ at 405 nm in the afternoon could indicate some photochemical production of BrC occurs, although it could be a limitation of the assumption that E_{abs} from mixing is wavelength independent. The afternoon organic composition is dominated by VOOA. A linear fit between $b_{\text{abs,BrC}}$ at 405 nm and VOOA

has a slope of 0.04 m^2 g^{-1}, although with a very low $r^2 < 0.01$, suggesting that VOOA is effectively non-absorbing. This is further supported by considering that the $b_{abs,BrC}$ falls to near zero at night while the VOOA concentration, which peaks in the afternoon, is still elevated. Even if the upper-limit approach is taken, such that all increases in E_{abs} are assumed to result from BrC, the correlation between $b_{abs,BrC}$ and VOOA remains low ($r^2 = 0.07$). Thus, it seems reasonable to conclude that VOOA is primarily non-absorbing.

Considering the morning peak, comparison with the diurnal profiles of the OA factors (and the inorganic species and BC) provides some evidence that this peak in BrC absorption at Fontana is due to either NOOA or HOA. However, a multi-linear fit against these species results in a very small combined r^2 value (≤ 0.16 for 405 nm, depending on what combination of OA factors is considered together). Further, the concentrations of NOOA and HOA are only slightly smaller at night than they are during the day, and thus the lack of BrC absorption at night is inconsistent with these OA factors being absorbing. It may be that the time-dependent "missing mass" correction for [BC] did not sufficiently capture the diurnal variability in the correction to a level of precision required to assess the very small absorption over BC. Consequently, the observed noticeable, but ultimately small morning increase in $b_{abs,BrC}$ may simply be an analysis artifact. Regardless, the overall measurements suggest that the OA in Fontana is very weakly, if at all, absorbing, and thus the contribution to the total absorption is small; the estimated fractional contribution of BrC to total absorption, excluding the fireworks-impacted period, is 0.03 at 405 nm and even smaller at 532 nm. Even at the peak $b_{abs,BrC}$ the BrC fractional contribution is only 10% of the total absorption.

The observations for Fontana differ from previous measurements of absorption by water soluble organic carbon (WSOC) made in 2010 in both Pasadena, CA and Riverside, CA, which are located in the same air basin as Fontana (*Zhang et al.*, 2013; *Zhang et al.*, 2011b). *Zhang et al.* (2011b) found that both $b_{abs,WSOC}$ and [WSOC] peaked in midafternoon and that they were correlated with a slope of ~0.73 m^2 g^{-1} at 365 nm (for the Pasadena site), corresponding to 0.33 m^2 g^{-1} at 405 nm, based on the reported AAE. The measured absorption increased when samples were extracted from filters into methanol rather than water, and substantial absorption persisted to >600 nm for the methanol extracts (*Zhang et al.*, 2013). If the VOOA here (which peaks in the afternoon) were as absorbing as the WSOC in the Zhang et al. studies, then the total absorption observed in Fontana should have been much larger and with a very different diurnal profile. Given the close proximity of Fontana and Riverside (20 km), it is difficult to reconcile the current observations, which suggest minimal absorption by the photochemically produced OA (specifically, VOOA), with the observations of Zhang et al. (2013; 2011b). A key difference between the measurement methods is that the current measurements were made *in situ* on dried particles whereas the Zhang et al. measurements were made after extraction of particles into either water or methanol. It is possible that either the process of drying (here) or wetting (in *Zhang et al.* (2013; 2011b)) led to changes in the OA absorptivity. Some laboratory results indicate that drying can lead to rapid browning of OA (*Nguyen et al.*, 2012). However, if this impacted the current measurements then we would expect the OA to have appeared more absorbing than the extracted samples. In addition, the ambient RH was generally quite low, and thus drying should have had minimal impact on

particle water. It might be that extraction into water allowed reactions to occur that otherwise would not in the dry atmosphere. It is possible that there are distinct chemical differences between the OA during 2010 (when the Zhang measurements were made) and 2014 (when our measurements were made), although this seems unlikely as the sources are unlikely to have changed substantially during that time period and both sets of measurements were made in June.

Another possibility is that the BrC contribution to total absorption is simply too small to be readily quantified from our measurements. Although Zhang et al. (2013, 2011b) observed a strong correlation between WSOC and absorption by WSOC, the total absorption was relatively small, compared to that expected by BC. The WSOC and BC absorption at 405 nm and 532 nm are estimated from the $MAC_{WSOC,365nm}$, *AAE*, [WSOC] and [BC] reported in Zhang et al. (2013). The fractional absorption by WSOC is estimated to be only 5% at 405 nm and 1% at 532 nm, with little diurnal variability. It may be that non-water soluble organic components further contribute to the BrC absorption, so these estimates are likely lower limits. Zhang et al. (2013) note that WSOC comprises only 25% of the total organic carbon, but that absorption after methanol extraction leads to an increase in absorption at 365 nm by a factor of 3.2. Assuming methanol extraction captures all OC (i.e. BrC), this implies an *MAC* at 365 nm for the OC of 0.73 $m^2\ g^{-1} \cdot 3.2 \cdot 0.25 = 0.58\ m^2\ g^{-1}$, corresponding to 0.36 $m^2\ g^{-1}$ at 405 nm. The fractional contribution at 405 nm for the estimated BrC is then 15% in this case. This level of contribution by BrC is actually relatively similar to what we observed, suggesting that, perhaps, the two studies are not as different as they might seem, despite the very different *MAC* values that are suggested for the BrC.

5.4.4.4 Brown Carbon Refractive Indices

The determined MAC values can be used to calculate the imaginary refractive index via Mie theory for the absorbing OA types identified here. We limit this analysis to only the BBOA and NOOA factors identified in Fresno. In brief, the absorption coefficient is calculated using spherical particle Mie theory for a given size distribution and assumed imaginary refractive index (k) for the total particle. The theoretical MAC for a particle distribution can be calculated by dividing the calculated b_{abs} by the mass concentration of the distribution. Here, BBOA- and NOOA-specific particle size distributions are used as input to the Mie model. There is a relationship between MAC and particle size for a given k. Thus, it is important to use a representative size distribution when inverting MAC values to k values. Factor-specific size distributions were determined as follows. Average number-weighted size distributions are determined from the SEMS over the period when the BBOA fraction was large (>0.15) and for when the NOOA fraction was large (>0.1). These distributions are then scaled by multiplying by the average BBOA or NOOA fraction during the appropriate period to produce BBOA- and NOOA-specific distributions. The factor-specific distributions are used as input to the Mie model. The density of the particles in the distribution are assumed size-independent and estimated from *Kuwata et al.* (2012) based on the AMS-measured O:C and H:C ratios (*Chen et al.*, 2018). The assumed k is varied until the calculated MAC matches the observed component-specific MAC, resulting in the component-specific k (i.e. k_{BBOA} or k_{NOOA}). As the real refractive index (n) of the BrC components is not known *a priori*, a value of $n = 1.5$ is used. This is similar to that found for laboratory generated secondary organic aerosol and to

ammonium sulfate and ammonium nitrate. The resulting derived k_{BBOA} are 0.050 (405 nm), 0.036 (532 nm) and 0.013 (870 nm). The k_{NOOA} are 0.030 (405 nm) and 0.011 (532 nm) (see also **Table 5-1**). The comparable k values under the "upper-limit" assumption are also provided in **Table 5-1**. The wavelength dependence of the k_{BBOA} and k_{NOOA} are calculated from Eqn. 4. The $w_{BBOA} = 1.20$ for the 405-532 nm pair, but is 1.65 from the fit over all three wavelengths. For NOOA at Fresno, there are only reliable results at two wavelengths (405 and 532 nm) available, giving $w = 3.67$. As already indicated by the wavelength dependence of the OA-type MAC values, the NOOA exhibits a steeper wavelength dependence than the BBOA.

5.5 Conclusions and Implications

The observations for two field campaigns in distinctly different urban environments (wintertime Fresno, CA versus summertime Fontana, CA) here demonstrate that the magnitude of the mixing-induced absorption enhancement for BC (i.e. the "lensing" effect) is small for the ensemble-average absorption. Additionally, the absorption enhancement shows limited dependence on the ensemble-average coating-to-BC core ratio. These observations, considered with others (*Cappa et al.*, 2012; *Healy et al.*, 2015; *Liu et al.*, 2015c; *McMeeking et al.*, 2014), demonstrate that spherical core-shell Mie theory calculations will not reliably give good agreement with observations when ensemble-average properties are considered, which is what is done in most climate models. This is the case because most models that consider internal mixing of BC assume that all components are internally mixed, and do not account for only a small fraction of the NR-PM material being internally mixed with BC. For these two studies, only around 10-20% of NR-PM is internally mixed with BC. Thus, the amount of "coating" material is likely to be overestimated by models, and the mixing-induced absorption enhancement would be overestimated to an even greater extent. Instead, it is suggested that accounting for BC mixing-state diversity (i.e. differences in the composition between BC-containing particles, beyond whether a particle simply contains BC or not), such as has been done by *Fierce et al.* (2016), will be necessary to allow for accurate simulation of absorption by BC. While an empirical relationship between the mixing-induced E_{abs} for BC and $R_{coat\text{-}rBC}$ could be determined from the current observations, such a relationship is unlikely to be robust or generalizable, given differences observed around the world (*Cappa et al.*, 2012; *Healy et al.*, 2015; *Liu et al.*, 2015c; *McMeeking et al.*, 2014).

For the Fresno observations, two types of brown carbon were identified and characterized: BBOA and NOOA. The BBOA, derived from residential wood combustion, was highly absorbing at 405 nm ($MAC_{BBOA} = 0.84$ m^2 g^{-1}) and the absorptivity persisted out to 870 nm ($MAC_{BBOA} = 0.085$ m^2 g^{-1}). The NOOA was less absorbing, with $MAC_{NOOA} = 0.52$ m^2 g^{-1} at 405 nm and absorption that was indistinguishable from zero at 870 nm. The NOOA was associated with the occurrence of heavy, early-morning fog and with an increased prevalence of particulate nitrate. The NOOA likely results from nitrate radical oxidation, coupled with aqueous processing. In the Fresno wintertime environment, the BBOA contribution (and associated absorption) was limited primarily to the nighttime, when surface emissions were high and the nocturnal boundary layer was low. Consequently, the local and regional radiative impacts of BBOA from residential wood

combustion (and the co-emitted BC) are likely small because these are highly diluted into the daytime mixed boundary layer. In contrast, the NOOA concentration (and associated absorption) is greatest during the day. Thus, the NOOA may impact local and regional radiative forcing by increasing the daytime absorption of solar radiation. Also, since it seems likely that the NOOA is formed to a large extent by nocturnal chemical processing in the residual layer, the NOOA might exist above the ground-level fogs and could contribute to stabilization of the atmosphere and to fog persistence. In contrast to Fresno, there was little evidence of a notable contribution from brown carbon in summertime Fontana.

5.6 Acknowledgement

The authors would like to acknowledge funding and support from California Air Resources Board (Agreement number: 13-330) and contract manager Nehzat Motallebi. The authors would also like to thank the Fontana Fire Department and the South Coast Air Quality Management District (SCAQMD) for Fontana site logistics, and UCD Extension for Fresno site logistics. Support for the Fontana SP-AMS measurements was provided by the Natural Sciences and Engineering Research Council of Canada (NSERC). Droplet Measurement Technologies provided the PAX for use during the Fresno campaign. The statements and conclusions in this paper are those of the researchers and not necessarily those of CARB. The mention of commercial products, their source, or their use in connection with material reported herein is not to be construed as actual or implied endorsement of such products.

Measurement data from both campaigns are archived at the University of California, San Diego Library Digital Collections at https://doi.org/10.6075/J0VX0DF9.

5.7 Appendix A: rBC size distribution processing

The campaign-average mass-weighted BC size distributions derived from the SP2 for Fresno and Fontana are shown in **Figure 5-5**, along with the average size distribution for nighttime hours (7 pm – 7 am) and daytime hours (7 am – 7 pm). For Fresno, the observed campaign average distribution mode peak is around 150 nm. The size distribution mode is somewhat larger than this at nighttime, around 160 nm, and smaller during the daytime, around 130 nm. The size distribution can be seen to continuously shift from being dominated by the larger mode to being dominated by a smaller mode with time of day, as previously reported by *Zhang et al.* (2016) for this region. In addition, the observed size distributions all show evidence of an increase in concentration at diameters less than 100 nm. This upturn in concentration is especially apparent in the daytime size distributions, although is evident at all times of day. This strongly suggests that there is an additional mode that is located at a size below the SP2 detection window (< 80 nm). Although the presence of such a mode is not commonly noted in the literature, *Liggio et al.* (2012) reported measurements that also suggested a substantial small diameter mode, as did *Zhang et al.* (2016). Because these small-mode particles are below the SP2 detection window, the SP2 BC concentration measurements will be biased low. In addition, the concentration of particles at the upper limit of the SP2 (here, ~800 nm) is greater than zero, indicating that particles at even larger sizes are contributing to the actual BC mass concentration. Accounting for such "missing mass"

(i.e. mass contributed by particles outside the detection window) is important if the actual BC concentration is to be reasonably determined.

For Fontana, the mass-weighted size distribution mode occurs at a smaller diameter than in Fresno. Also, while there is still substantial diurnal variability in the BC concentration, the shape of the size distribution is quite constant throughout the day. As noted already, this difference between Fresno and Fontana is likely because in Fresno there are two major BC sources (vehicles and biomass burning) while in Fontana one source dominates (vehicles). As with Fresno, there is clear evidence of an increase in BC concentrations at diameters less than 100 nm, again suggesting the presence of a small mode that contributes substantially to the overall BC mass but that was not detected by the SP2.

One approach that has been taken to correct for the missing mass is to fit the campaign average size distribution with a log-normal distribution, and then to use this fit to extrapolate to larger and smaller sizes to estimate the fractional amount of missing mass (e.g. *Schwarz et al.*, 2006). A constant scaling factor is then applied to the data set. However, such an approach is not appropriate here, since it is clear that, at least for Fresno, the distribution shape is changing with time of day. This suggests, instead, that a temporally varying correction is required. Therefore, the approach taken here is to perform fits on 10 min average size distributions to determine a time-dependent missing mass correction. Also, instead of fitting the observations with a single log-normal distribution, the observations have been fit using the sum of 4 individual log-normal modes. Robust results were not obtained when fewer than four modes were used for either data set, although the use of 4 (rather than 3 or 2) was more important for Fresno than for Fontana.

Given that one of the modes peaks at a diameter below the measurement range, neither the exact position nor width of this mode is well constrained. To introduce consistency in the measurement method, the exact position and width of each mode is set as a constant for each campaign. As the positions of these modes is not known a priori, the following approach is taken to determine an optimal value to use for each of the mode diameters. First, initial fits are performed wherein the position and width of each mode is constrained to fall within a range, but allowed to vary within this range. The ranges considered were: Mode 1, 30 nm $< d_{p,VED} <$ 70 nm and $1.2 < \sigma_g < 1.9$; Mode 2, $90 < d_{p,VED} <$ 140 nm and $1.2 < \sigma_g < 1.9$; Mode 3, $150 < d_{p,VED} <$ 250 nm and $1.3 < \sigma_g < 1.9$; and, Mode 4, $350 < d_{p,VED} <$ 500 nm and $1.6 < \sigma_g < 3$. The average mode diameter and σ_g are then determined for each of the four modes based on initial fits to the campaign average size distributions. The optimal values used in the final, constrained fitting (where both the mode diameter, d_m, and σ_g are held constant) for both campaigns are given in **Table 5-2**, along with the fractional contribution to the total mass of each mode. An attempt was made to maintain the mode positions and widths as campaign-independent constants, but it was determined that slight shifts in the position and width of the first two modes was necessary for optimal fitting.

Each of the 10 min average mass-weighted size distributions was fit with the constrained four-mode log-normal distribution, where the amplitude (i.e. concentration) of each peak is allowed to vary but the diameter and width are held constant. The results from this fitting are shown in **Figure**

5-5, where the fit results are compared with the observed size distributions and the diurnal variation in the mode-specific BC concentration is shown for each campaign.

5.8 Appendix B: Comparison between *MAC*-based and thermodenuder-based results for absorption enhancement

The absorption enhancement from the thermodenuder (TD) method is calculated as:

$$E_{abs,TD} = \frac{2 \cdot MAC_{BC,t,amb}}{MAC_{BC,t-1,TD} + MAC_{BC,t+1,TD}} \quad (6.)$$

where the subscript *amb* and *TD* refer to the ambient or thermodenuded measurements, respectively, and the t-1 and t+1 refer to the (5 min average) measurements made just before and after the measurement made at time t. The use of MAC_{BC}, as opposed to b_{abs}, corrects for transmission losses of BC through the thermodenuder. The $E_{abs,TD}$ values can be compared to the E_{abs} values determined from the MAC method (Eqn. 2) that were used in the primary analysis above, referred to now as $E_{abs,MAC}$. Ideally, the $E_{abs,TD}$ and $E_{abs,MAC}$ values would give equivalent results. However, potential biases in either can impact their comparability, and ultimately any conclusions regarding the actual magnitude of the absorption enhancement. For the MAC-derived E_{abs}, biases in the estimated $MAC_{BC,ref}$ would cause the absolute value of $E_{abs,MAC}$ to be either too high or low. Given the need for the "missing-mass" correction for [BC], uncertainties or temporal or coating-dependent biases in this correction would potentially lead to an inaccurate assessment of the diurnal variability or the dependence of $E_{abs,MAC}$ on properties such as $R_{coat\text{-}rBC}$. For the TD-derived E_{abs}, incomplete evaporation of coatings could lead to a low bias in the measured E_{abs}. Inaccurate correction for transmission losses could lead to biases in the absolute $E_{abs,TD}$ or in the temporal variation. And there is a potential for charring of organics to occur in the TD, leading to the production of (non-ambient) BrC, that would decrease $E_{abs,TD}$.

The diurnal variability in $E_{abs,TD}$ and $E_{abs,MAC}$ are shown for both Fresno and Fontana in Figure 5-19. For Fresno, there is generally good agreement between the two methods in terms of the absolute values obtained, thus providing confidence in the overall conclusions. However, it is apparent that there is a more pronounced daytime bump in $E_{abs,MAC}$ than there is in $E_{abs,TD}$, in particular at 405 nm and 532 nm. If the low fog and high-fog periods are considered separately (not shown), it becomes evident that the disagreement between the two methods is predominately limited to the high-fog period, especially at 405 nm and 532 nm, thus implicating the NOOA as a source of the difference. We hypothesize that the difference between methods for Fresno results from charring of the BrC from NOOA. Charring of NOOA and formation of absorbing material would lead to a suppression in the daytime $E_{abs,TD}$. However, the good agreement between methods during the low-fog period suggests that BBOA is not especially susceptible to charring, and also that the missing-mass correction reasonably accounted for the diurnal variation in [BC]. Regardless, whether the $E_{abs,MAC}$ or $E_{abs,TD}$ is considered, it is apparent that the magnitude of E_{abs} at long wavelengths (here, 870 nm), where BrC contributions are relatively small, remains small

throughout the campaign, supporting the conclusion that the mixing-induced enhancement is small.

For Fontana, there is a more distinct difference between the two methods. While the diurnal variation in $E_{abs,MAC}$ shows a clear daytime maximum for both 405 nm and 532 nm, the $E_{abs,TD}$ is flat throughout the day and centered at 1 (indicating no enhancement; Figure 5-19). Correspondingly, the $E_{abs,TD}$ shows negligible dependence on $R_{coat\text{-}rBC}$, while the $E_{abs,MAC}$ increased to a small extent with $R_{coat\text{-}rBC}$ (**Figure 5-12**). Thus, it could be that residual coating material when $R_{coat\text{-}rBC}$ is high has biased the $E_{abs,TD}$ low. The ratio of the thermodenuded to ambient SP-AMS measurements can give an indication of the mass fraction of coating (MFR_{coat}) that remains after heating. The average MFR_{coat} for Fontana was 0.14. There was a distinct diurnal variation in MFR_{coat}, with the residual coating actually being smallest in the daytime when the $R_{coat\text{-}rBC}$ and $E_{abs,MAC}$ both peak. This observation indicates that evaporation of coating material was most efficient when the relative coating amount was greatest, and thus suggests that residual coating material is not primarily responsible for the difference between methods. It is possible that charring of VOOA led to suppression of the $E_{abs,TD}$. However, the MFR for the total OA was only 0.06 with a negligible diurnal dependence, indicating that very little OA remained after heating. Thus, charring does not seem likely to be the primary reason for the difference between methods. Notably, the BC missing-mass fraction exhibits a diurnal variation that is similar to the observed $E_{abs,MAC}$ dependence (**Figure 5-5** versus Figure 5-19). It is possible that the missing mass correction underestimated the amount of BC during the daytime thus leading to an overestimate of the $E_{abs,MAC}$ and introducing an apparent dependence on $R_{coat\text{-}rBC}$ since $R_{coat\text{-}rBC}$ peaks during the daytime. If true, this would imply an even smaller-to-negligible dependence of E_{abs} on $R_{coat\text{-}rBC}$. Ultimately, the specific reason for the $E_{abs,MAC}$ and $E_{abs,TD}$ measurements cannot be discerned from the Fontana observations. However, both methods indicate that the E_{abs} in this region is small and that the dependence on $R_{coat\text{-}rBC}$ is very weak, and thus the general conclusions reached are independent of which method is used. Based on the above discussion, it is strongly recommended that future experiments to measure E_{abs} in ambient employ multiple methods.

5.9 References

Adachi, K., S. H. Chung, and P. R. Buseck (2010), Shapes of soot aerosol particles and implications for their effects on climate, *J. Geophys. Res.*, *115*(D15), D15206, doi:10.1029/2009jd012868.

Andreae, M. O., and A. Gelencser (2006), Black carbon or brown carbon? The nature of light-absorbing carbonaceous aerosols, *Atmospheric Chemistry and Physics*, *6*, 3131-3148, doi:10.5194/acp-6-3131-2006.

Betha, R., L. M. Russell, C.-L. Chen, J. Liu, D. J. Price, K. J. Sanchez, S. Chen, A. K. Y. Lee, X. Zhang, and C. D. Cappa (2018), Larger submicron particles for emissions with residential burning in wintertime San Joaquin Valley (Fresno) than for vehicle combustion in summertime South Coast Air Basin (Fontana), *Journal of Geophysical Research-Atmospheres*, *In Press*, doi:10.1029/2017JD026730.

Bond, T. C., and R. W. Bergstrom (2006), Light absorption by carbonaceous particles: An investigative review, *Aerosol Science and Technology*, *40*(1), 27-67, doi:10.1080/02786820500421521.

Bond, T. C., et al. (2013), Bounding the role of black carbon in the climate system: A scientific assessment, *Journal of Geophysical Research: Atmospheres*, *118*, 1-173, doi:10.1002/jgrd.50171.

Bond, T. C., G. Habib, and R. W. Bergstrom (2006), Limitations in the enhancement of visible light absorption due to mixing state, *J. Geophys. Res.-Atmos.*, *111*(D20), doi:10.1029/2006JD007315.

Canagaratna, M. R., et al. (2007), Chemical and microphysical characterization of ambient aerosols with the Aerodyne aerosol mass spectrometer, *Mass Spectrometry Reviews*, *26*(2), 185-222, doi:10.1002/mas.20115.

Cappa, C. D., et al. (2012), Radiative absorption enhancements due to the mixing state of atmospheric black carbon, *Science*, *337*, 1078-1081, doi:10.1126/science.1223447.

Chakrabarty, R. K., H. Moosmüller, L. W. A. Chen, K. Lewis, W. P. Arnott, C. Mazzoleni, M. K. Dubey, C. E. Wold, W. M. Hao, and S. M. Kreidenweis (2010), Brown carbon in tar balls from smoldering biomass combustion, *Atmospheric Chemistry and Physics*, *10*(13), 6363-6370, doi:10.5194/acp-10-6363-2010.

Chen, C.-L., et al. (2018), Organic aerosol particle chemical properties associated with residential burning and fog in wintertime San Joaquin Valley (Fresno) and with vehicle and firework emissions in summertime South Coast Air Basin (Fontana), *Journal of Geophysical Research: Atmospheres*, *In Press*, doi:10.1029/2018JD028374.

Clarke, A., et al. (2007), Biomass burning and pollution aerosol over North America: Organic components and their influence on spectral optical properties and humidification response, *Journal of Geophysical Research-Atmospheres*, *112*(D12), doi:10.1029/2006jd007777.

Collier, S., L. R. Williams, T. B. Onasch, C. D. Cappa, X. Zhang, L. M. Russell, C.-L. Chen, K. J. Sanchez, D. R. Worsnop, and Q. Zhang (2018), Influence of emissions and aqueous processing on particles containing black carbon in a polluted urban environment: Insights from a soot particle – aerosol mass spectrometer, *Journal of Geophysical Research-Atmospheres*, *123*, 6648-6666, doi:10.1002/2017JD027851.

Cross, E. S., et al. (2010), Soot Particle Studies—Instrument Inter-Comparison—Project Overview, *Aerosol Science and Technology*, *44*(8), 592 - 611, doi:10.1080/02786826.2010.482113.

Docherty, K. S., et al. (2008), Apportionment of Primary and Secondary Organic Aerosols in Southern California during the 2005 Study of Organic Aerosols in Riverside (SOAR-1), *Environmental Science & Technology*, *42*(20), 7655-7662, doi:10.1021/es8008166.

Feng, Y., V. Ramanathan, and V. R. Kotamarthi (2013), Brown carbon: a significant atmospheric absorber of solar radiation?, *Atmos. Chem. Phys.*, *13*(17), 8607-8621, doi:10.5194/acp-13-8607-2013.

Fierce, L., T. C. Bond, S. E. Bauer, F. Mena, and N. Riemer (2016), Black carbon absorption at the global scale is affected by particle-scale diversity in composition, *Nat. Comm.*, *7*, doi:10.1038/ncomms12361.

Forestieri, S. D., et al. (*Accepted*), Measurement and modeling of the multi-wavelength optical properties of uncoated flame-generated soot, *Atmos. Chem. Phys.*

Forrister, H., et al. (2015), Evolution of brown carbon in wildfire plumes, *Geophysical Research Letters*, *42*(11), 4623-4630, doi:10.1002/2015GL063897.

Fuller, K. A., W. C. Malm, and S. M. Kreidenweis (1999), Effects of mixing on extinction by carbonaceous particles, *J. Geophys. Res.-Atmos.*, *104*(D13), 15941-15954, doi:10.1029/1998jd100069.

Ge, X., A. Setyan, Y. Sun, and Q. Zhang (2012), Primary and secondary organic aerosols in Fresno, California during wintertime: Results from high resolution aerosol mass spectrometry, *Journal of Geophysical Research: Atmospheres*, *117*(D19), D19301, doi:10.1029/2012JD018026.

Gilardoni, S., et al. (2016), Direct observation of aqueous secondary organic aerosol from biomass-burning emissions, *Proc. Natl. Acad. Sci. U. S. A.*, *113*(36), 10013-10018, doi:10.1073/pnas.1602212113.

Hayes, P. L., et al. (2013), Organic aerosol composition and sources in Pasadena, California, during the 2010 CalNex campaign, *Journal of Geophysical Research: Atmospheres*, *118*(16), 9233-9257, doi:10.1002/jgrd.50530.

Healy, R., J. Wang, C. H. Jeong, A. Lee, M. Willis, E. Jaroudi, N. Zimmerman, N. Hilker, M. Murphy, and S. Eckhardt (2015), Light‐absorbing properties of ambient black carbon and brown carbon from fossil fuel and biomass burning sources, *Journal of Geophysical Research: Atmospheres*, *120*(13), 6619-6633.

Kirchstetter, T. W., T. Novakov, and P. V. Hobbs (2004), Evidence that the spectral dependence of light absorption by aerosols is affected by organic carbon, *Journal of Geophysical Research-Atmospheres*, *109*(D21).

Knox, A., G. J. Evans, J. R. Brook, X. Yao, C. H. Jeong, K. J. Godri, K. Sabaliauskas, and J. G. Slowik (2009), Mass Absorption Cross-Section of Ambient Black Carbon Aerosol in Relation to Chemical Age, *Aerosol Science and Technology*, *43*(6), 522-532, doi:10.1080/02786820902777207.

Kondo, Y., et al. (2011), Emissions of black carbon, organic, and inorganic aerosols from biomass burning in North America and Asia in 2008, *J. Geophys. Res.*, *116*(D8), D08204, doi:10.1029/2010jd015152.

Krasowsky, T. S., G. R. McMeeking, D. B. Wang, C. Sioutas, and G. A. Ban-Weiss (2016), Measurements of the impact of atmospheric aging on physical and optical properties of ambient black carbon particles in Los Angeles, *Atmospheric Environment*, *142*, 496-504, doi:10.1016/j.atmosenv.2016.08.010.

Kuwata, M., S. R. Zorn, and S. T. Martin (2012), Using Elemental Ratios to Predict the Density of Organic Material Composed of Carbon, Hydrogen, and Oxygen, *Environmental Science & Technology*, *46*(2), 787-794, doi:10.1021/es202525q.

Lack, D. A., and C. D. Cappa (2010), Impact of brown and clear carbon on light absorption enhancement, single scatter albedo and absorption wavelength dependence of black carbon, *Atmospheric Chemistry and Physics*, *10*(9), 4207-4220, doi:10.5194/acp-10-4207-2010.

Lack, D. A., C. D. Cappa, E. S. Cross, P. Massoli, A. T. Ahern, P. Davidovits, and T. B. Onasch (2009), Absorption Enhancement of Coated Absorbing Aerosols: Validation of the Photo-Acoustic Technique for Measuring the Enhancement, *Aerosol Science and Technology*, *43*(10), 1006-1012, doi:10.1080/02786820903117932.

Lack, D. A., J. Langridge, R. Bahreni, C. D. Cappa, A. Middlebrook, and J. P. Schwarz (2012a), Brown Carbon and Internal Mixing in Biomass Burning Particles, *PNAS*, *10*(37), 14802-14807, doi:10.1073/pnas.1206575109.

Lack, D. A., and J. M. Langridge (2013), On the attribution of black and brown carbon light absorption using the Angstrom exponent, *Atmospheric Chemistry and Physics*, *13*(20), 10535-10543, doi:10.5194/acp-13-10535-2013.

Lack, D. A., M. S. Richardson, D. Law, J. M. Langridge, C. D. Cappa, R. J. McLaughlin, and D. M. Murphy (2012b), Aircraft Instrument for Comprehensive Characterization of Aerosol Optical Properties, Part 2: Black and Brown Carbon Absorption and Absorption Enhancement Measured with Photo Acoustic Spectroscopy, *Aerosol Science and Technology*, *46*(5), 555-568, doi:10.1080/02786826.2011.645955.

Langridge, J. M., M. S. Richardson, D. Lack, D. Law, and D. M. Murphy (2011), Aircraft Instrument for Comprehensive Characterization of Aerosol Optical Properties, Part I: Wavelength-Dependent Optical Extinction and Its Relative Humidity Dependence Measured Using Cavity Ringdown Spectroscopy, *Aerosol Science and Technology*, *45*(11), 1305-1318, doi:10.1080/02786826.2011.592745.

Lee, A. K. Y., C. L. Chen, J. Liu, D. J. Price, R. Betha, L. M. Russell, X. Zhang, and C. D. Cappa (2017), Formation of secondary organic aerosol coating on black carbon particles near vehicular emissions, *Atmospheric Chemistry and Physics*, *2017*(17), 15055-15067, doi:10.5194/acp-17-15055-2017.

Lee, A. K. Y., M. D. Willis, R. M. Healy, T. B. Onasch, and J. P. D. Abbatt (2015), Mixing state of carbonaceous aerosol in an urban environment: single particle characterization using the soot particle aerosol mass spectrometer (SP-AMS), *Atmospheric Chemistry and Physics*, *15*(4), 1823-1841, doi:10.5194/acp-15-1823-2015.

Lee, A. K. Y., M. D. Willis, R. M. Healy, J. M. Wang, C. H. Jeong, J. C. Wenger, G. J. Evans, and J. P. D. Abbatt (2016), Single-particle characterization of biomass burning organic aerosol (BBOA): evidence for non-uniform mixing of high molecular weight organics and potassium, *Atmospheric Chemistry and Physics*, *16*(9), 5561-5572, doi:10.5194/acp-16-5561-2016.

Lewis, K., W. P. Arnott, H. Moosmüller, and C. E. Wold (2008), Strong spectral variation of biomass smoke light absorption and single scattering albedo observed with a novel dual-wavelength photoacoustic instrument, *Journal of Geophysical Research: Atmospheres*, *113*(D16), D16203, doi:10.1029/2007JD009699.

Liggio, J., M. Gordon, G. Smallwood, S. M. Li, C. Stroud, R. Staebler, G. Lu, P. Lee, B. Taylor, and J. R. Brook (2012), Are Emissions of Black Carbon from Gasoline Vehicles Underestimated? Insights from Near and On-Road Measurements, *Environmental Science & Technology*, *46*(9), 4819-4828, doi:10.1021/es2033845.

Lim, S., M. Lee, S. W. Kim, and P. Laj (2018), Sulfate alters aerosol absorption properties in East Asian outflow, *Scientific Reports*, *8*, 7, doi:10.1038/s41598-018-23021-1.

Liu, D. T., J. W. Taylor, D. E. Young, M. J. Flynn, H. Coe, and J. D. Allan (2015a), The effect of complex black carbon microphysics on the determination of the optical properties of brown carbon, *Geophysical Research Letters*, *42*(2), 613-619, doi:10.1002/2014gl062443.

Liu, D. T., et al. (2017), Black-carbon absorption enhancement in the atmosphere determined by particle mixing state, *Nat. Geosci.*, *10*(3), 184-U132, doi:10.1038/ngeo2901.

Liu, J., M. Bergin, H. Guo, L. King, N. Kotra, E. Edgerton, and R. J. Weber (2013), Size-resolved measurements of brown carbon in water and methanol extracts and estimates of their contribution to ambient fine-particle light absorption, *Atmospheric Chemistry and Physics*, *13*(24), 12389-12404, doi:10.5194/acp-13-12389-2013.

Liu, J., et al. (2015b), Brown carbon aerosol in the North American continental troposphere: sources, abundance, and radiative forcing, *Atmospheric Chemistry and Physics*, *15*(14), 7841-7858, doi:10.5194/acp-15-7841-2015.

Liu, S., et al. (2015c), Enhanced light absorption by mixed source black and brown carbon particles in UK winter, *Nat. Comm.*, *6*, 8435, doi:10.1038/ncomms9435.

Massoli, P., et al. (2015), Characterization of black carbon-containing particles from soot particle aerosol mass spectrometer measurements on the R/V Atlantis during CalNex 2010, *Journal of Geophysical Research: Atmospheres*, *120*(6), 2575-2593, doi:10.1002/2014JD022834.

McMeeking, G. R., E. Fortner, T. B. Onasch, J. W. Taylor, M. Flynn, H. Coe, and S. M. Kreidenweis (2014), Impacts of nonrefractory material on light absorption by aerosols emitted from biomass burning, *Journal of Geophysical Research-Atmospheres*, *119*(21), 12272-12286, doi:10.1002/2014jd021750.

Metcalf, A. R., C. L. Loza, M. M. Coggon, J. S. Craven, H. H. Jonsson, R. C. Flagan, and J. H. Seinfeld (2013), Secondary Organic Aerosol Coating Formation and Evaporation: Chamber Studies Using Black Carbon Seed Aerosol and the Single-Particle Soot Photometer, *Aerosol Sci. Technol.*, *47*(3), 326-347, doi:10.1080/02786826.2012.750712.

Nguyen, T. B., P. B. Lee, K. M. Updyke, D. L. Bones, J. Laskin, A. Laskin, and S. A. Nizkorodov (2012), Formation of nitrogen- and sulfur-containing light-absorbing compounds accelerated by evaporation of water from secondary organic aerosols, *Journal of Geophysical Research-Atmospheres*, *117*, 14, doi:10.1029/2011jd016944.

Onasch, T. B., A. M. Trimborn, E. C. Fortner, J. T. Jayne, G. L. Kok, L. R. Williams, P. Davidovits, and D. R. Worsnop (2012), Soot Particle Aerosol Mass Spectrometer: Development, Validation and Initial Application, *Aerosol Science and Technology*, *46*(7), 804-817, doi:10.1080/02786826.2012.663948.

Peng, J., et al. (2016), Markedly enhanced absorption and direct radiative forcing of black carbon under polluted urban environments, *Proc. Natl. Acad. Sci. U. S. A.*, *113*(16), 4266-4271, doi:10.1073/pnas.1602310113.

Prabhakar, G., et al. (2017), Observational assessment of the role of nocturnal residual-layer chemistry in determining daytime surface particulate nitrate concentrations, *Atmos. Chem. Phys.*, *17*(23), 14747-14770, doi:10.5194/acp-17-14747-2017.

Ramanathan, V., and G. Carmichael (2008), Global and regional climate changes due to black carbon, *Nat. Geosci.*, *1*(4), 221-227, doi:10.1038/ngeo156.

Saleh, R., C. J. Hennigan, G. R. McMeeking, W. K. Chuang, E. S. Robinson, H. Coe, N. M. Donahue, and A. L. Robinson (2013), Absorptivity of brown carbon in fresh and photo-chemically aged biomass-burning emissions, *Atmospheric Chemistry and Physics*, *13*(15), 7683-7693, doi:10.5194/acp-13-7683-2013.

Saleh, R., et al. (2014), Brownness of organics in aerosols from biomass burning linked to their black carbon content, *Nature Geosci*, *7*, 647-650, doi:10.1038/ngeo2220.

Scarnato, B. V., S. Vahidinia, D. T. Richard, and T. W. Kirchstetter (2013), Effects of internal mixing and aggregate morphology on optical properties of black carbon using a discrete dipole approximation model, *Atmospheric Chemistry and Physics*, *13*(10), 5089-5101, doi:10.5194/acp-13-5089-2013.

Schnaiter, M., C. Linke, O. Mohler, K. H. Naumann, H. Saathoff, R. Wagner, U. Schurath, and B. Wehner (2005), Absorption amplification of black carbon internally mixed with secondary organic aerosol, *Journal of Geophysical Research-Atmospheres*, *110*(D19), D019204, doi:10.1029/2005JD006046.

Schwarz, J. P., et al. (2006), Single-particle measurements of midlatitude black carbon and light-scattering aerosols from the boundary layer to the lower stratosphere, *Journal of Geophysical Research-Atmospheres*, *111*, D16207, doi:10.1029/2006jd007076.

Schwarz, J. P., et al. (2010), The Detection Efficiency of the Single Particle Soot Photometer, *Aerosol Sci. Technol.*, *44*(8), 612-628, doi:10.1080/02786826.2010.481298.

Shiraiwa, M., Y. Kondo, T. Iwamoto, and K. Kita (2010), Amplification of Light Absorption of Black Carbon by Organic Coating, *Aerosol Sci. Technol.*, *44*(1), 46-54, doi:10.1080/02786820903357686.

Tasoglou, A., G. Saliba, R. Subramanian, and S. N. Pandis (2017), Absorption of chemically aged biomass burning carbonaceous aerosol, *J Aerosol Sci*, *113*, 141-152, doi:10.1016/j.jaerosci.2017.07.011.

Wang, X., C. L. Heald, D. A. Ridley, J. P. Schwarz, J. R. Spackman, A. E. Perring, H. Coe, D. Liu, and A. D. Clarke (2014), Exploiting simultaneous observational constraints on mass and absorption to estimate the global direct radiative forcing of black carbon and brown carbon, *Atmospheric Chemistry and Physics*, *14*(20), 10989-11010, doi:10.5194/acp-14-10989-2014.

Willis, M. D., R. M. Healy, N. Riemer, M. West, J. M. Wang, C.-H. Jeong, J. C. Wenger, G. J. Evans, J. P. D. Abbatt, and A. K. Y. Lee (2016), Quantification of black carbon mixing state from traffic: implications for aerosol optical properties, *Atmospheric Chemistry and Physics*, *16*(7), 4693-4706, doi:10.5194/acp-16-4693-2016.

Willis, M. D., A. K. Y. Lee, T. B. Onasch, E. C. Fortner, L. R. Williams, A. T. Lambe, D. R. Worsnop, and J. P. D. Abbatt (2014), Collection efficiency of the soot-particle aerosol mass spectrometer (SP-AMS) for internally mixed particulate black carbon, *Atmospheric Measurement Techniques*, *7*(12), 4507-4516, doi:10.5194/amt-7-4507-2014.

Young, D. E., H. Kim, C. Parworth, S. Zhou, X. Zhang, C. D. Cappa, R. Seco, S. Kim, and Q. Zhang (2016), Influences of emission sources and meteorology on aerosol chemistry in a polluted urban environment: results from DISCOVER-AQ California, *Atmospheric Chemistry and Physics*, *16*(8), 5427-5451, doi:10.5194/acp-16-5427-2016.

Zhang, Q., J. L. Jimenez, M. R. Canagaratna, I. M. Ulbrich, N. L. Ng, D. R. Worsnop, and Y. L. Sun (2011a), Understanding atmospheric organic aerosols via factor analysis of aerosol mass spectrometry: a review, *Anal. Bioanal. Chem.*, *401*(10), 3045-3067, doi:10.1007/s00216-011-5355-y.

Zhang, X., H. Kim, C. Parworth, D. E. Young, Q. Zhang, A. R. Metcalf, and C. D. Cappa (2016), Optical Properties of Wintertime Aerosols from Residential Wood Burning in Fresno, CA: Results from DISCOVER-AQ 2013, *Environmental Science & Technology*, *50*(4), 1681-1690, doi:10.1021/acs.est.5b04134.

Zhang, X., Y.-H. Lin, J. D. Surratt, and R. J. Weber (2013), Sources, Composition and Absorption Ångström Exponent of Light-absorbing Organic Components in Aerosol Extracts from the Los Angeles Basin, *Environmental Science & Technology*, *47*(8), 3685-3693, doi:10.1021/es305047b.

Zhang, X. L., Y. H. Lin, J. D. Surratt, P. Zotter, A. S. H. Prevot, and R. J. Weber (2011b), Light-absorbing soluble organic aerosol in Los Angeles and Atlanta: A contrast in secondary organic aerosol, *Geophysical Research Letters*, *38*, doi:10.1029/2011gl049385.

Zhang, Y. X., Q. Zhang, Y. F. Cheng, H. Su, H. Y. Li, M. Li, X. Zhang, A. J. Ding, and K. B. He (2018), Amplification of light absorption of black carbon associated with air pollution, *Atmospheric Chemistry and Physics*, *18*(13), 9879-9896, doi:10.5194/acp-18-9879-2018.

5.10 Tables

Table 5-1. The determined mass absorption coefficients, imaginary refractive indices, absorption Ångstrom exponents and wavelength dependencies for the BBOA and NOOA factors determined for Fresno.

Wavelength (nm)		Lensing Corrected[a]			Upper Limit[b]		
		BBOA	NOOA	R^2	BBOA	NOOA	R^2
405	MAC	0.84	0.52	0.78	0.84	0.59	0.73
	k	0.050	0.030		0.050	0.034	
532	MAC	0.45	0.14	0.71	0.45	0.21	0.69
	k	0.036	0.011		0.036	0.016	
870	MAC	0.085	0.044[c]	0.24	0.093	0.092[c]	0.35
	k	0.013	0.007[c]		0.013	0.014[c]	
405-532	AAE	2.28	4.81		2.28	3.79	
	w	1.20	3.67		1.20	2.76	
405-870	AAE	2.99			2.88	--	
	w	1.76			1.76	--	
532-870	AAE	3.39			3.21	--	
	w	2.07			2.07	--	

[a]The influence of internal mixing (i.e. lensing) on absorption by BC was removed based on the observed dependence of $MAC_{BC}(870)$ nm on $R_{coat\text{-}rBC}$.
[b]Includes potential influence from internal mixing (i.e. lensing)
[c]Uncertainty on this value makes it indistinguishable from zero.

Table 5-2. The mode diameter, width and average mass fraction characterizing the four log-normal modes fit to the observed BC mass-weighted size distributions.

	Fresno $d_{p,VED}$ (nm)	σ_g	Average Mass Fraction	Fontana $d_{p,VED}$ (nm)	σ_g	Average Mass Fraction
Mode 1	57	1.47	0.37	47	1.63	0.52
Mode 2	118	1.43	0.23	116	1.43	0.26
Mode 3	182	1.53	0.21	182	1.53	0.12
Mode 4	420	2.83	0.19	420	2.83	0.10

5.11 Figures

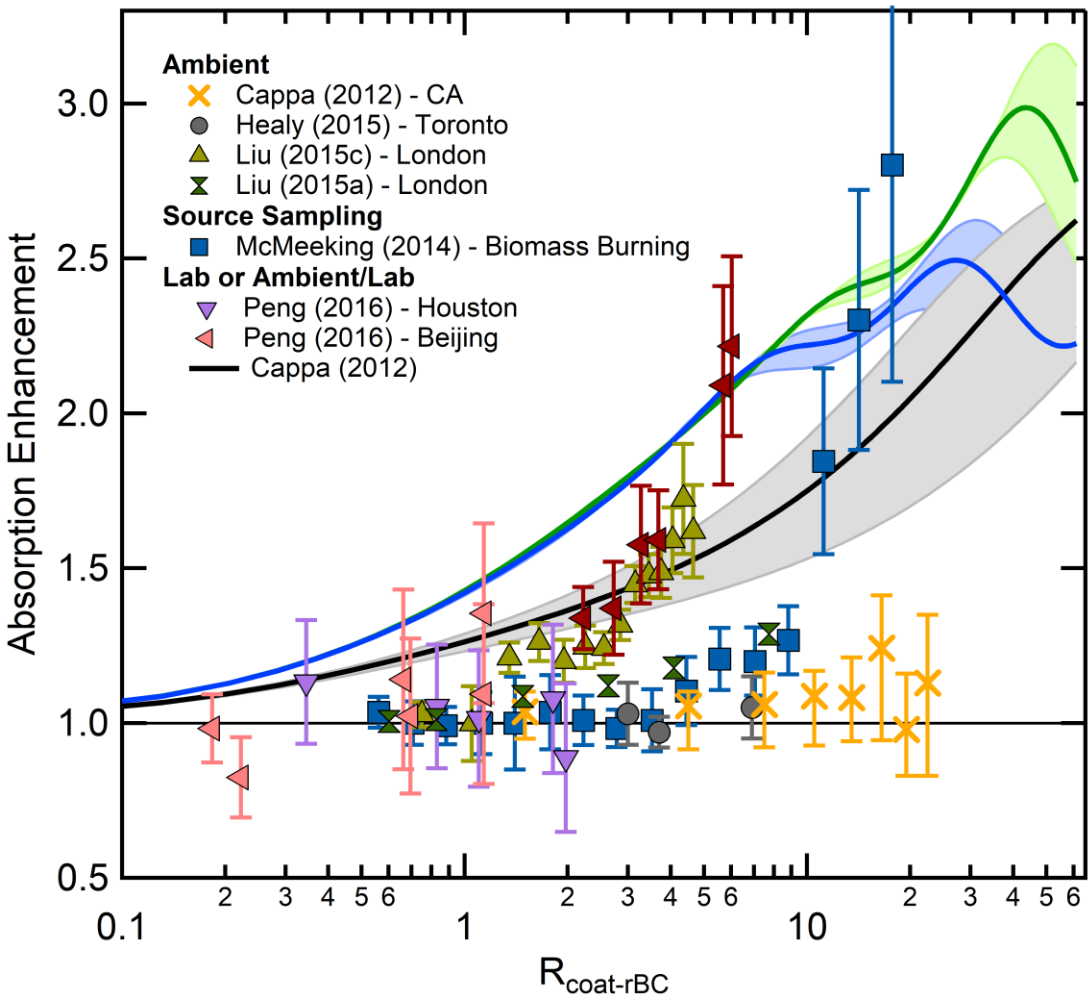

Figure 5-1. Compilation of various absorption enhancement measurements from ambient studies (*Cappa et al.*, 2012; *Healy et al.*, 2015; *Liu et al.*, 2015a; *Liu et al.*, 2015c), from source sampling of biomass burning particles (*McMeeking et al.*, 2014), and from lab (*Cappa et al.*, 2012) or combined ambient/lab measurements (*Peng et al.*, 2016). For all studies, the enhancements observed at the longest reported wavelength are used. For *Liu et al.* (2015a), the reported overall coating thickness ratio was used to calculate an equivalent $R_{coat\text{-}rBC}$, and the reported *MAC* values at 781 nm were converted to absorption enhancement values by dividing by the lowest observed value (4 m^2 g^{-1}). For *Peng et al.* (2016), the reported change in coating thickness was used to calculate an equivalent $R_{coat\text{-}rBC}$. For the lab experiments of (*Cappa et al.*, 2012), only the fit lines are shown. The error bars correspond to either a propagated uncertainty (*Peng et al.*, 2016) or a standard deviation of the observations (all other studies).

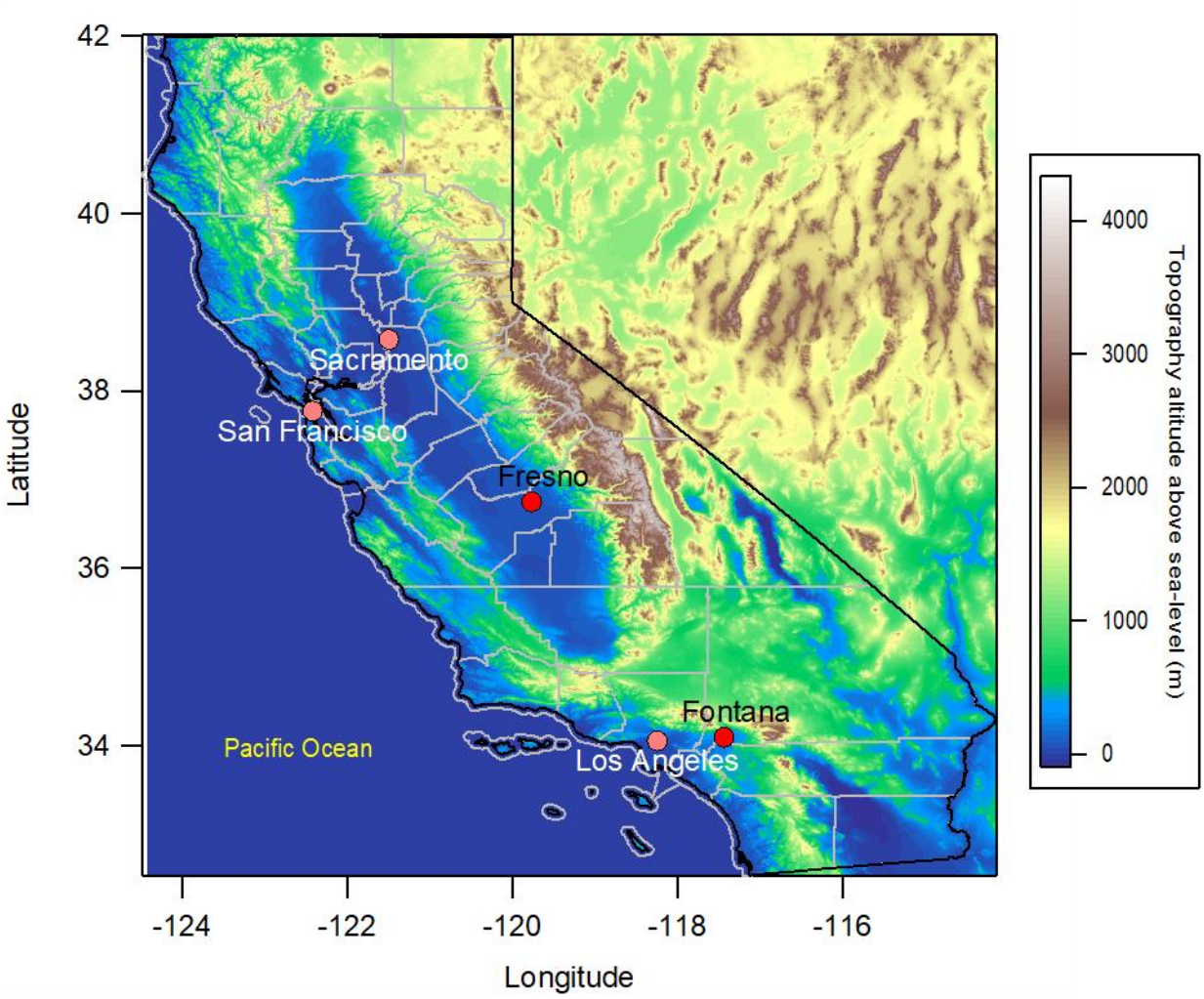

Figure 5-2. Map of California, showing the location of Fresno in the San Joaquin Valley and Fontana in the South Coast Air Basin. For reference, the locations of the cities of Los Angeles, San Francisco and Sacramento are also shown. The coloration indicates the topography.

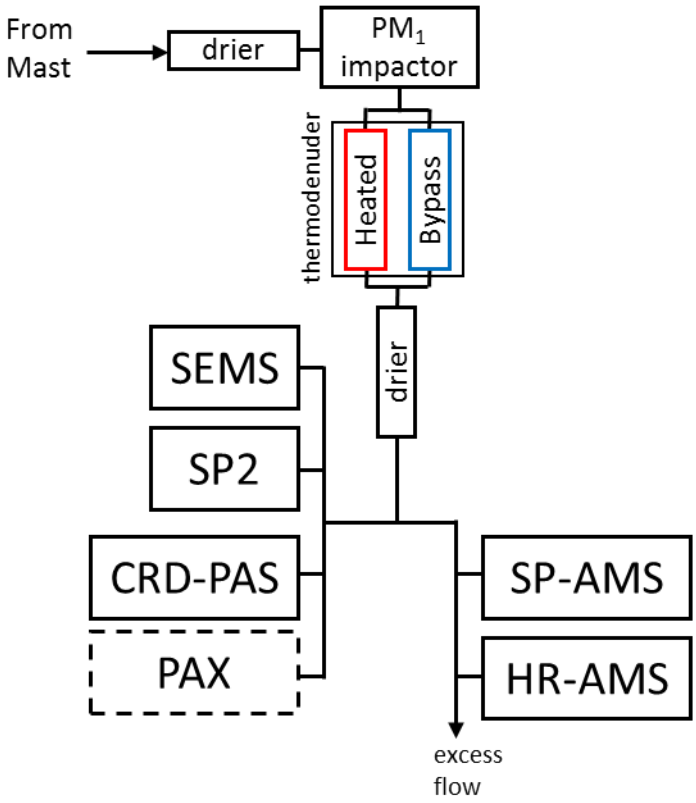

Figure 5-3. Schematic of the instrument configuration during both campaigns. The dashed box around the PAX indicates that this instrument was only deployed during the Fresno study.

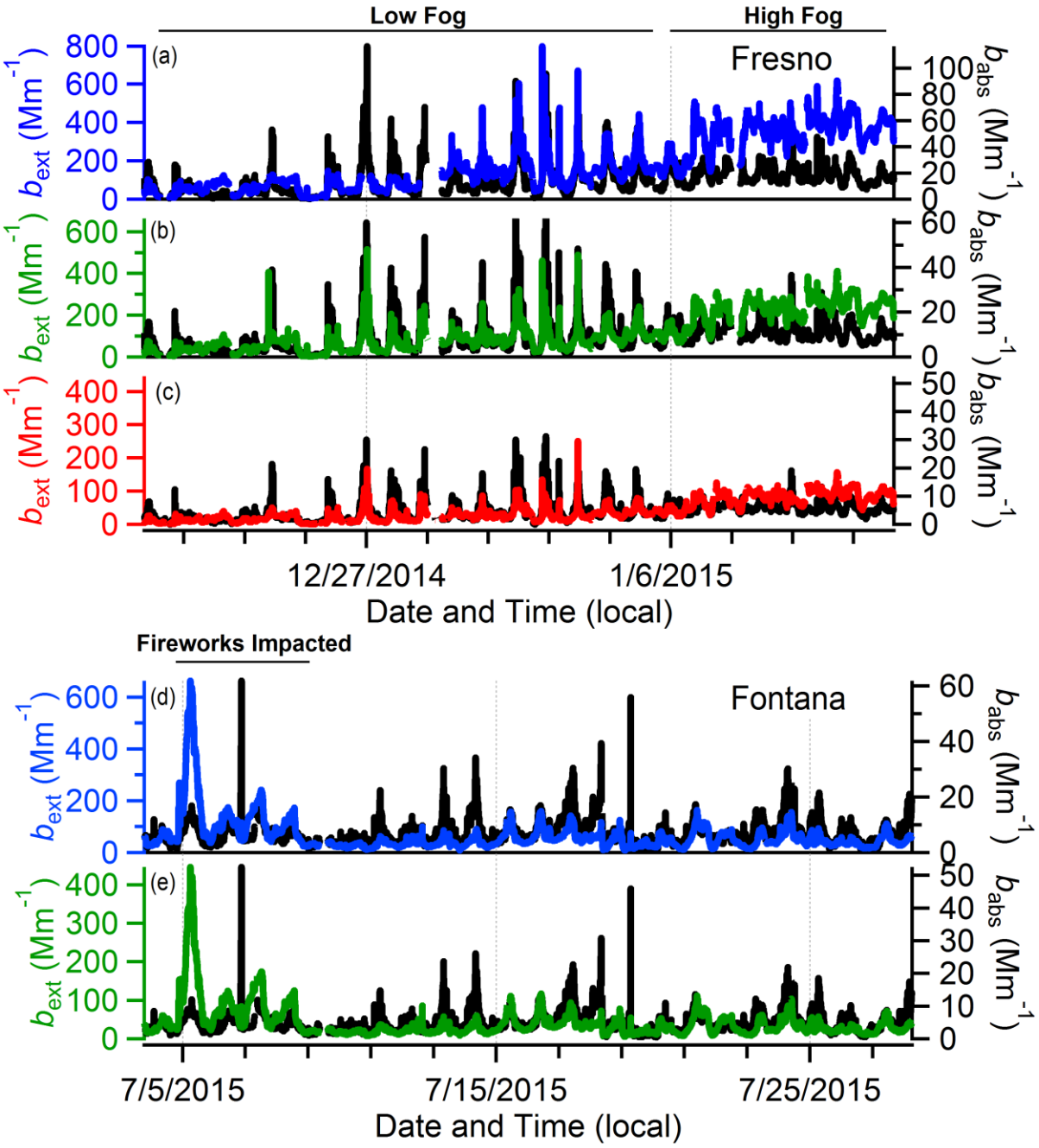

Figure 5-4. Time series of particle light extinction (left axes, color) or absorption (right axes, black) for (a-c) Fresno and (d-e) Fontana at (a,d) 405 nm, (b,e) 532 nm and (c) 870 nm.

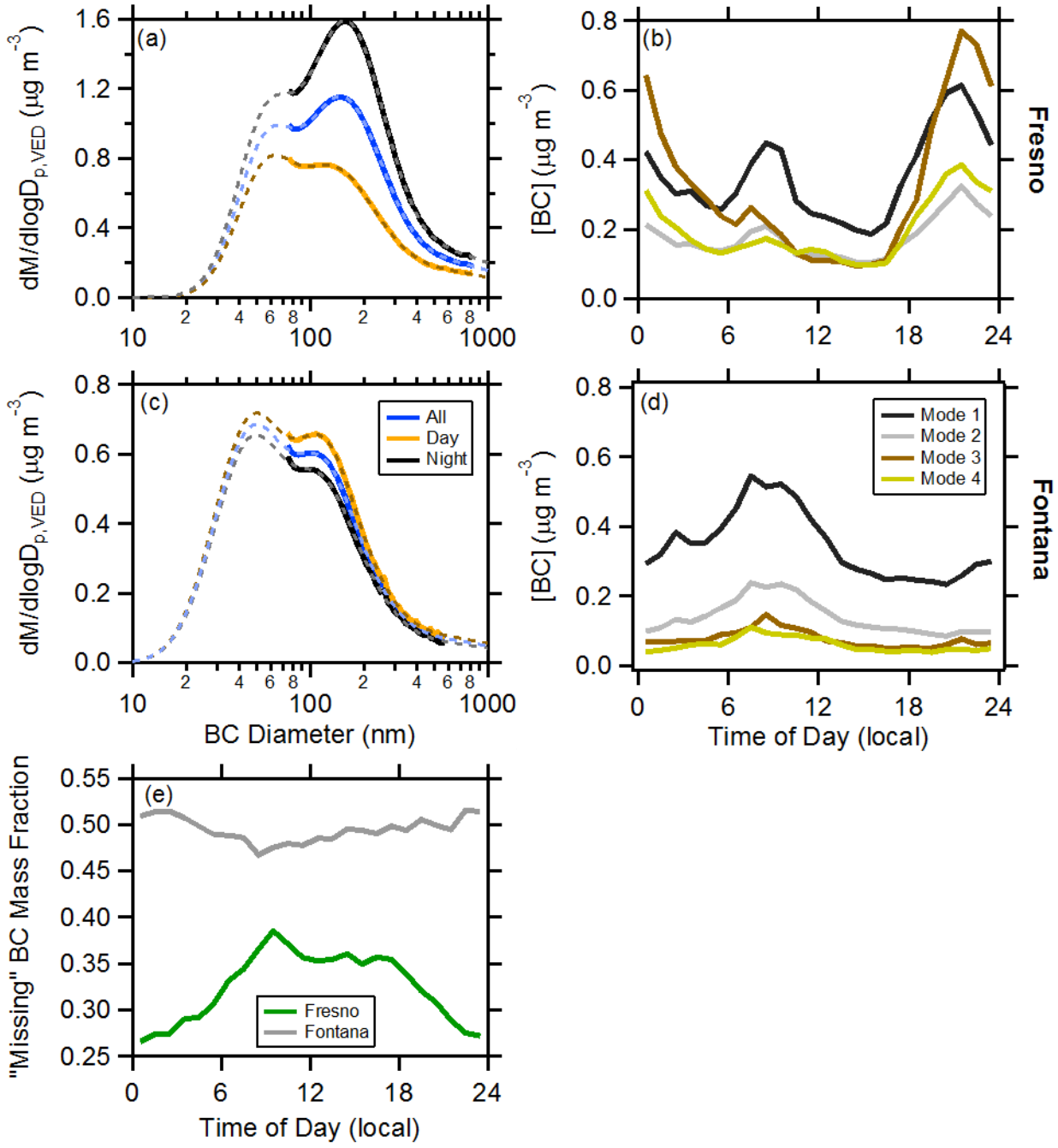

Figure 5-5. (a,c) Observed mass-weighted BC-specific size distributions (solid lines) and multi-mode fits (dashed lines) for (a) Fresno and (c) Fontana. Blue lines are for all periods, orange for daytime and black for nighttime. (b,d) The diurnal variation in the BC mass concentration of each of the four modes fit to the mass-weighted distributions. The mode diameter increases with the mode number. Mode diameters are reported in Section 5.4.2. (e) The diurnal variability in the estimated BC missing-mass fraction, calculated from the difference between the fit distributions and observed distributions, for Fresno (green) and Fontana (gray).

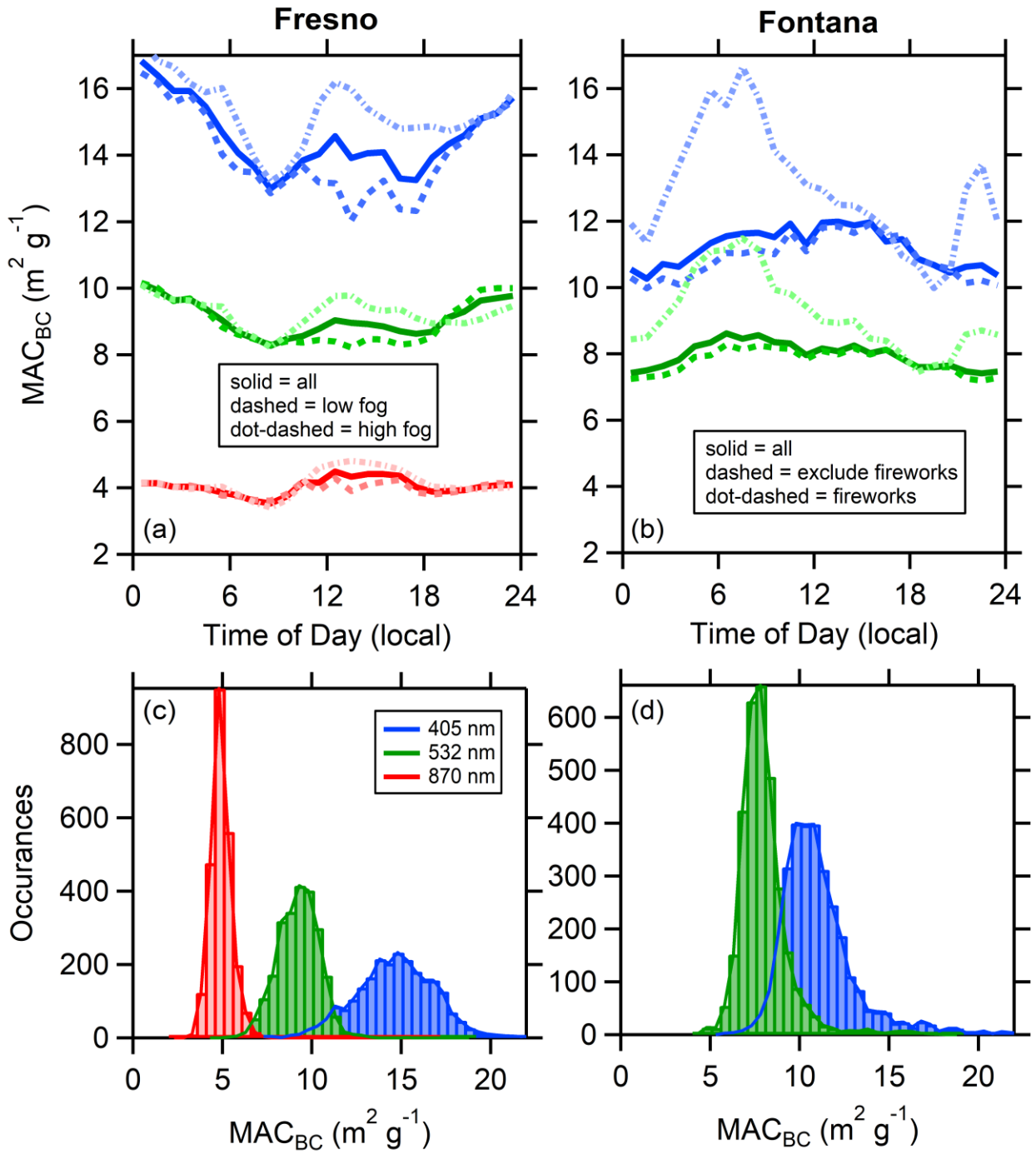

Figure 5-6. (Top Panels) Observed diurnal variation in the BC mass absorption coefficients (MAC_{BC}) in (a) wintertime Fresno and (b) summertime Fontana. For both campaigns the solid lines are the all-campaign averages. For Fresno, the dashed line is for the low-fog period and dot-dashed is for the high-fog period. For Fontana, the dashed line excludes the period impacted by fireworks (i.e. around the 4th of July) and the dot-dashed line is for the fireworks-impacted period. (Bottom Panels) Histograms of the observed MAC_{BC} values for (c) Fresno and (d) Fontana.

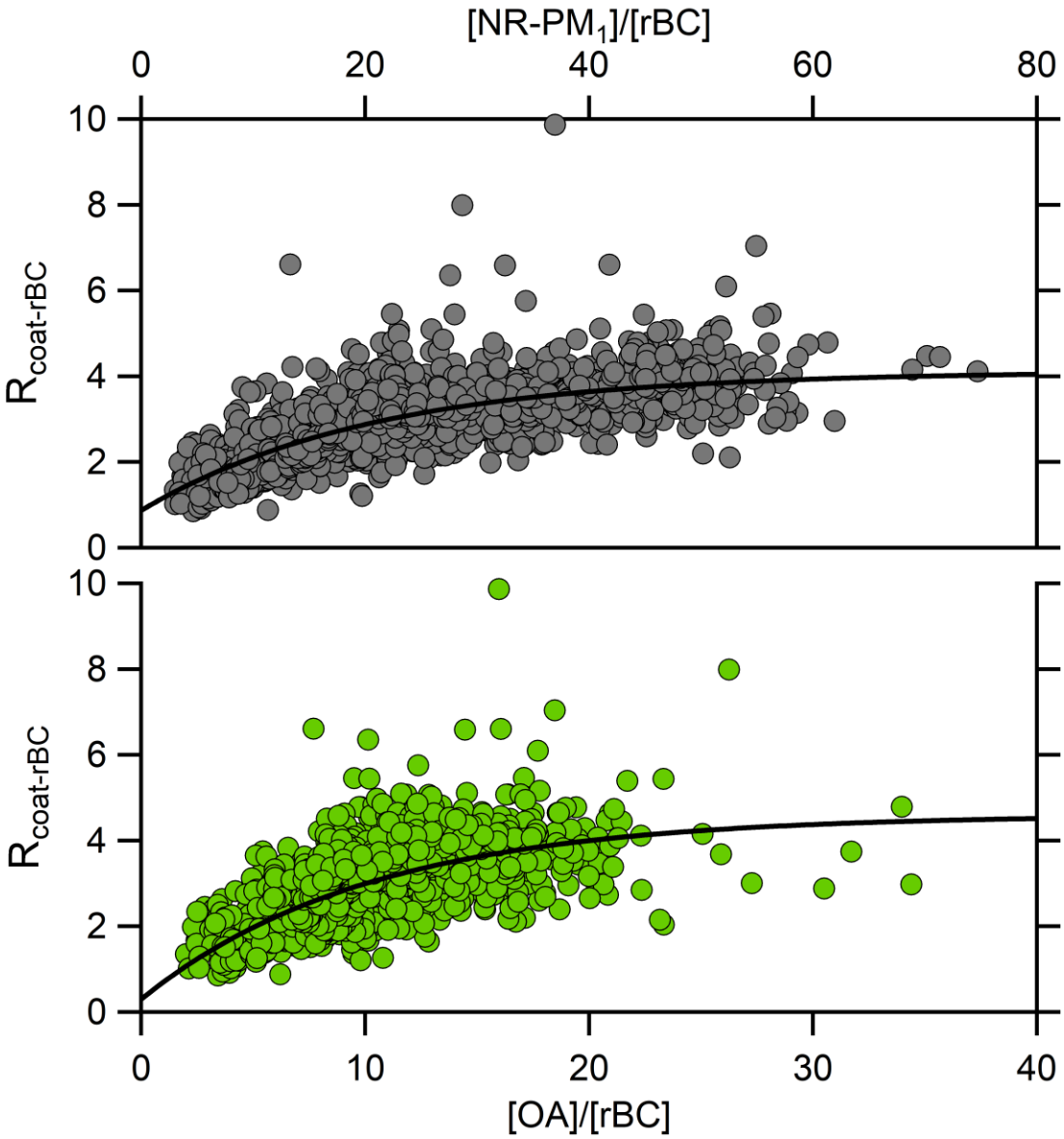

Figure 5-7. (top) Relationship between $R_{coat\text{-}rBC}$ (i.e. the OA-to-rBC ratio for only rBC-containing particles) and the total NR-PM_1-to-rBC ratio. The black line is an exponential fit to the observations, with $R_{BC} = 4.12 - 3.25 \cdot \exp(-0.04813 \cdot ([NR - PM_1]/[rBC]))$ and a reduced chi-square value of 0.38. **(bottom)** Relationship between $R_{coat\text{-}rBC}$ (i.e. the OA-to-rBC ratio for only rBC-containing particles) and the total OA-to-rBC ratio. The black line is an exponential fit to the observations, with $R_{BC} = 4.6 - 4.3 \cdot \exp(-0.09862 \cdot ([OA]/[rBC]))$ and a reduced chi-square value of 0.38.

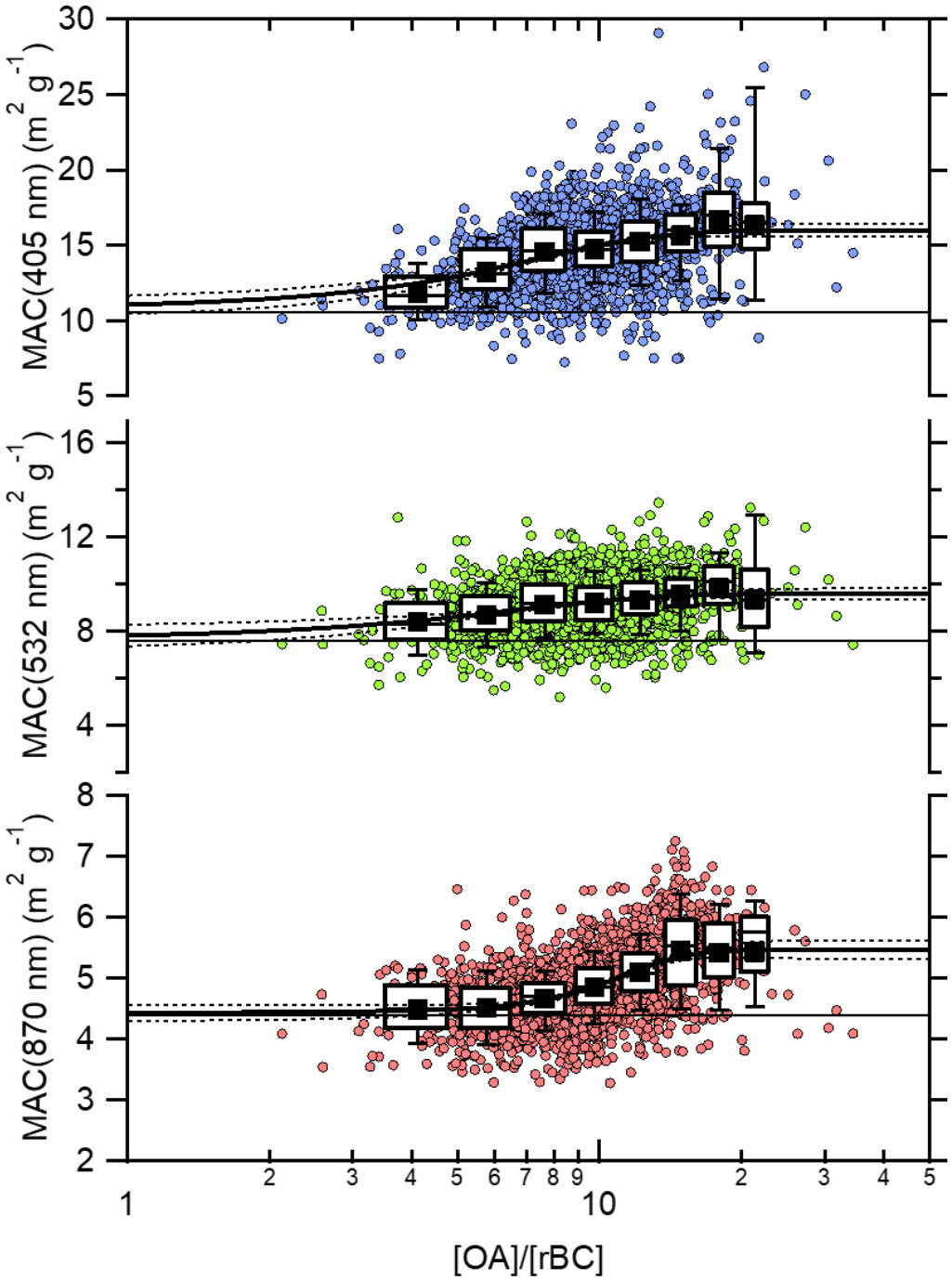

Figure 5-8. Relationship between MAC_{BC} and [OA]/[rBC] for (top; blue points) 405 nm, (middle; green points) 532 nm and (bottom; red points) 870 nm for Fresno, CA. Sigmoidal fits are shown, along with the 99% confidence intervals on the fits. The extrapolated values at [OA]/[rBC] = 0 are 4.4 ± 0.2 m^2 g^{-1} (870 nm), 7.5 ± 0.5 m^2 g^{-1} (532 nm) and 10.7 ± 0.6 m^2 g^{-1} (405 nm), and where the uncertainties correspond to the 99% confidence interval. (The absolute uncertainties are substantially larger.) The box and whisker plots show the mean (■), median (–), lower and upper quartile (boxes), and 9th and 91st percentile (whisker).

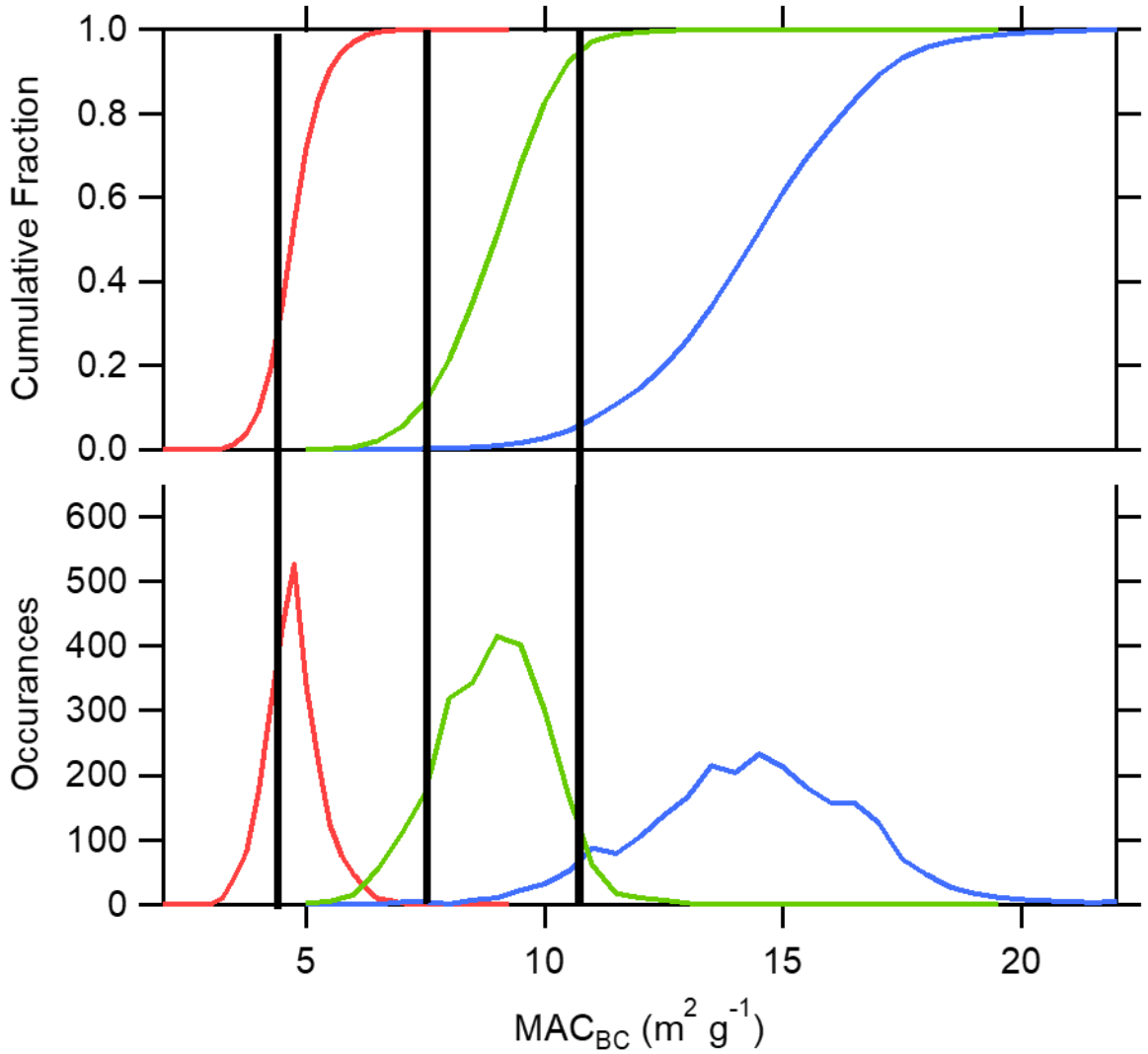

Figure 5-9. (bottom) Histograms of the observed MAC_{BC} values for ambient particles at 405 nm (blue), 532 nm (green), and 870 nm (red) for Fresno, CA. **(top)** The cumulative fraction of the observations, corresponding to the histograms. The vertical black lines indicate the derived campaign-specific $MAC_{BC,ref}$ (see Section 5.4.3). The cumulative fraction of observations below the $MAC_{BC,ref}$ value is 0.055 at 405 nm, 0.11 at 532 nm, and 0.30 at 870 nm.

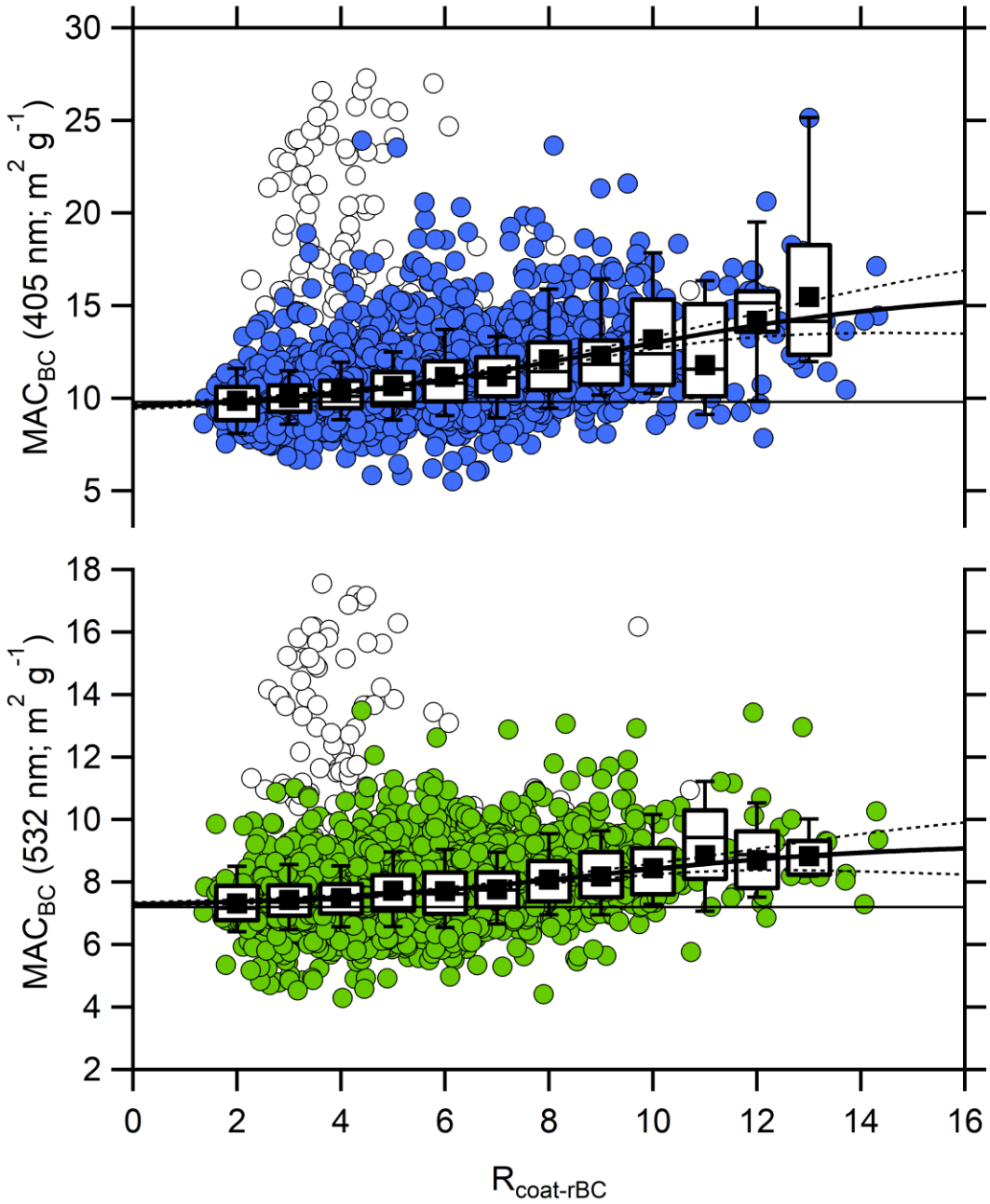

Figure 5-10. Relationship between MAC_{BC} and $R_{coat\text{-}rBC}$ for (top; blue points) 405 nm and (bottom; blue points) 532 nm for Fontana, CA. Sigmoidal fits are shown, along with the 99% confidence intervals on the fits. The extrapolated values at $R_{coat\text{-}rBC} = 0$ are 7.3 ± 0.1 $m^2\ g^{-1}$ (532 nm) and 9.6 ± 0.2 $m^2\ g^{-1}$ (405 nm), and where the uncertainties correspond to the 99% confidence interval. (The absolute uncertainties are substantially larger.) The colored points show the observations outside of the fireworks-impacted period, and the white points during the fireworks-impacted period. The box and whisker plots show the mean (■), median (–), lower and upper quartile (boxes), and 9th and 91st percentile (whisker).

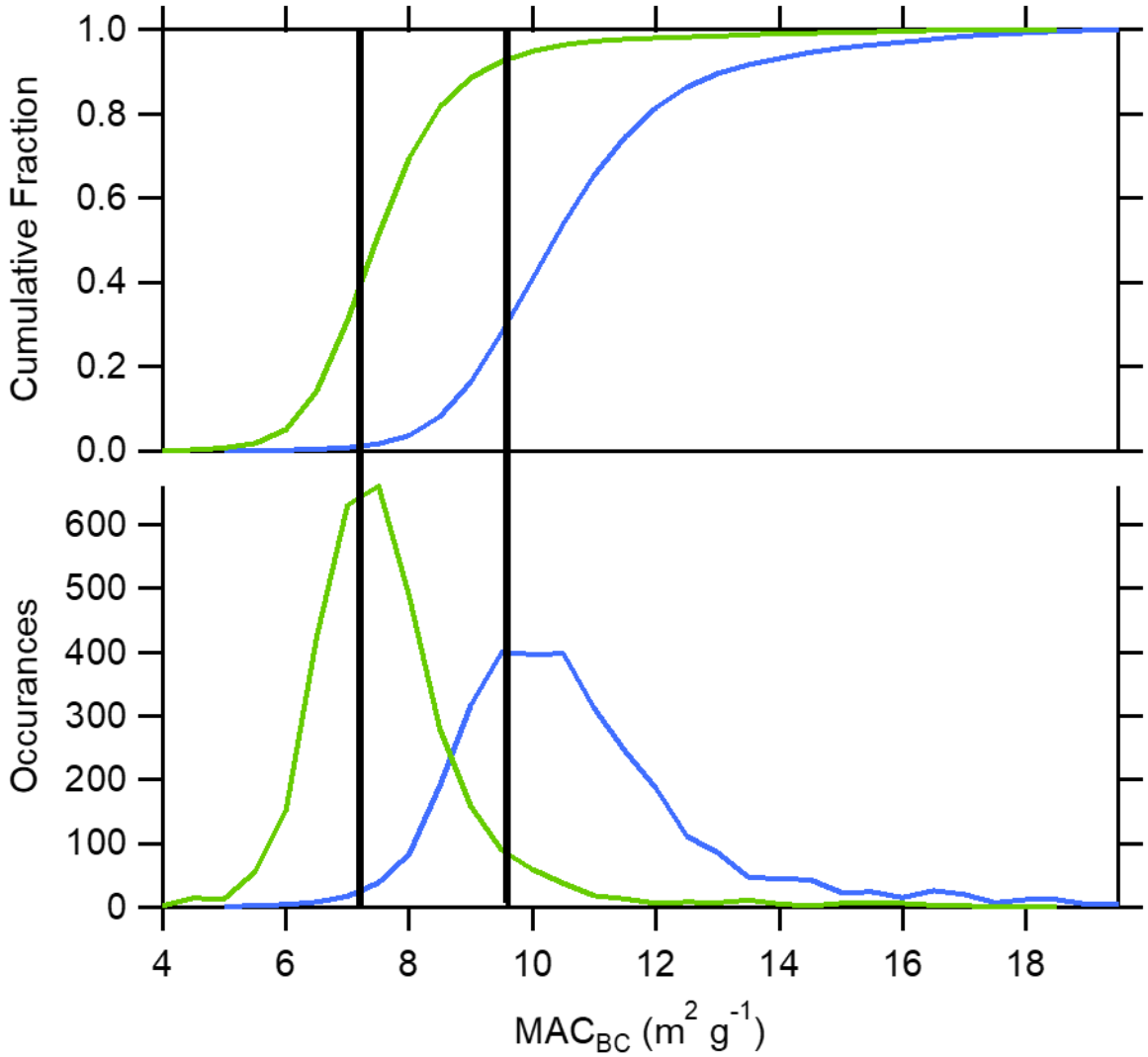

Figure 5-11. (bottom) Histograms of the observed MAC_{BC} values for ambient particles at 405 nm (blue) and 532 nm (green) for Fontana, CA. **(top)** The cumulative fraction of the observations, corresponding to the histograms. The vertical black lines indicate the derived campaign-specific $MAC_{BC,ref}$ (see Section 5.4.3). The cumulative fraction of observations below the $MAC_{BC,ref}$ value is 0.30 at 405 nm and 0.37 at 532 nm.

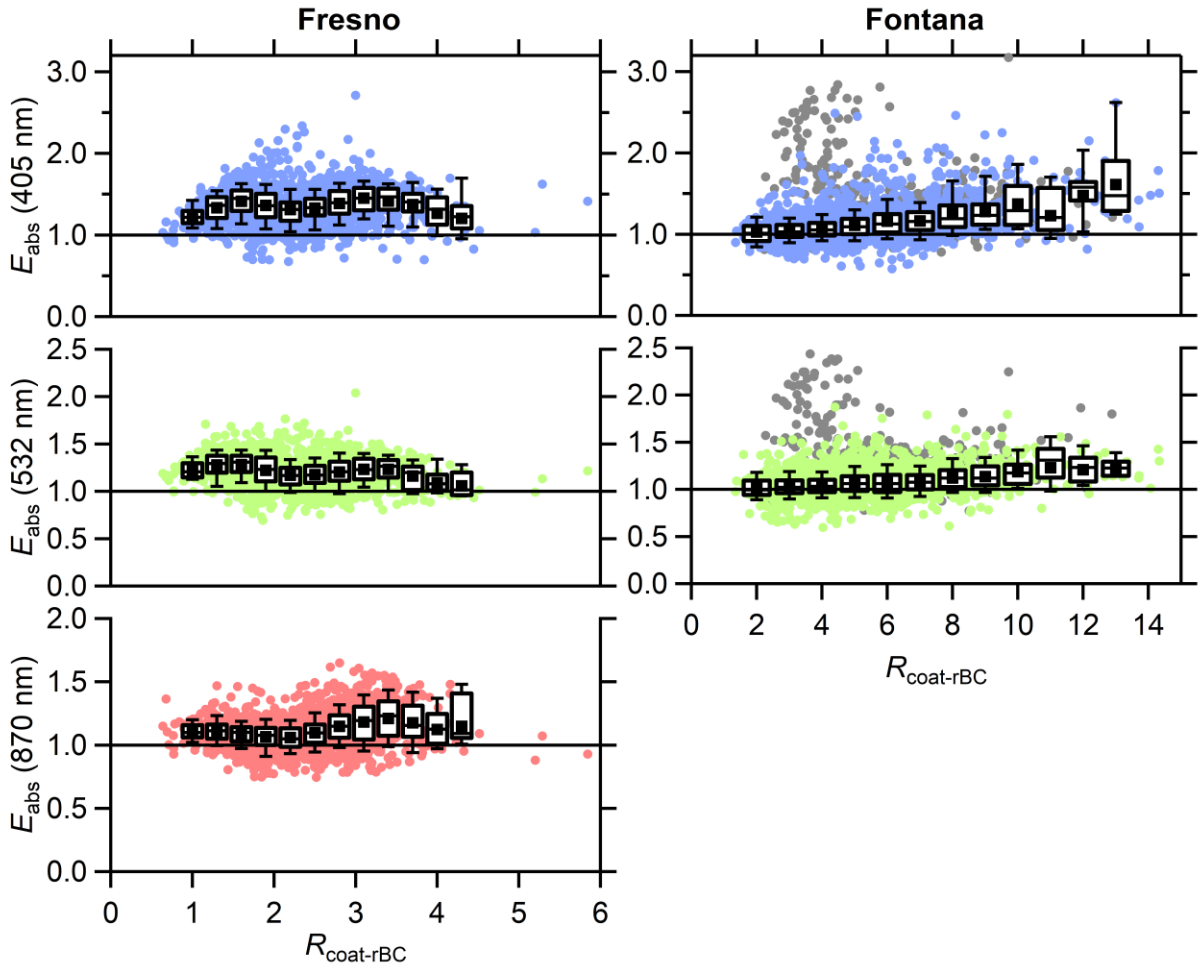

Figure 5-12. The dependence of the absorption enhancement (E_{abs}) on the BC coating-to-core mass ratio ($R_{coat\text{-}rBC}$) for 405 nm (blue, top), 532 nm (green, middle), and 870 nm (red, bottom). Results are shown separately for (left) Fresno and (right) Fontana. The points are the individual 10 min averages, colored according to wavelength. The box and whisker plots show the mean (■), median (–), lower and upper quartile (boxes), and 9th and 91st percentile (whisker). For Fontana, the gray points indicate the fireworks-impacted period which are not included in the box and whisker plots.

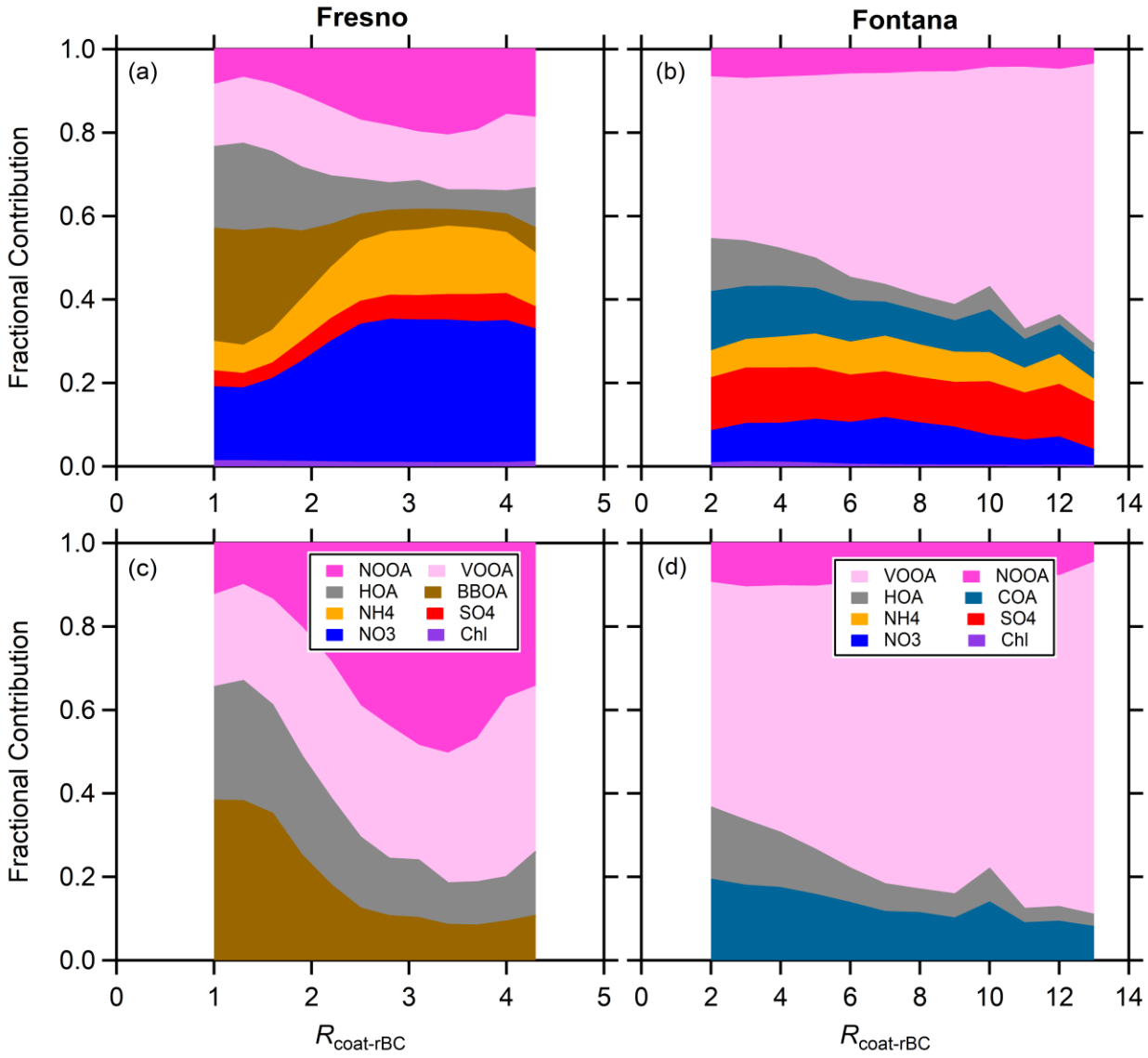

Figure 5-13. The variation of the fractional contribution of all NR-PM species (both internally and externally mixed with BC) versus $R_{coat\text{-}rBC}$ for (a) Fresno and (b) Fontana. The variation in only the OA-factors with $R_{coat\text{-}rBC}$ for (c) Fresno and (d) Fontana.

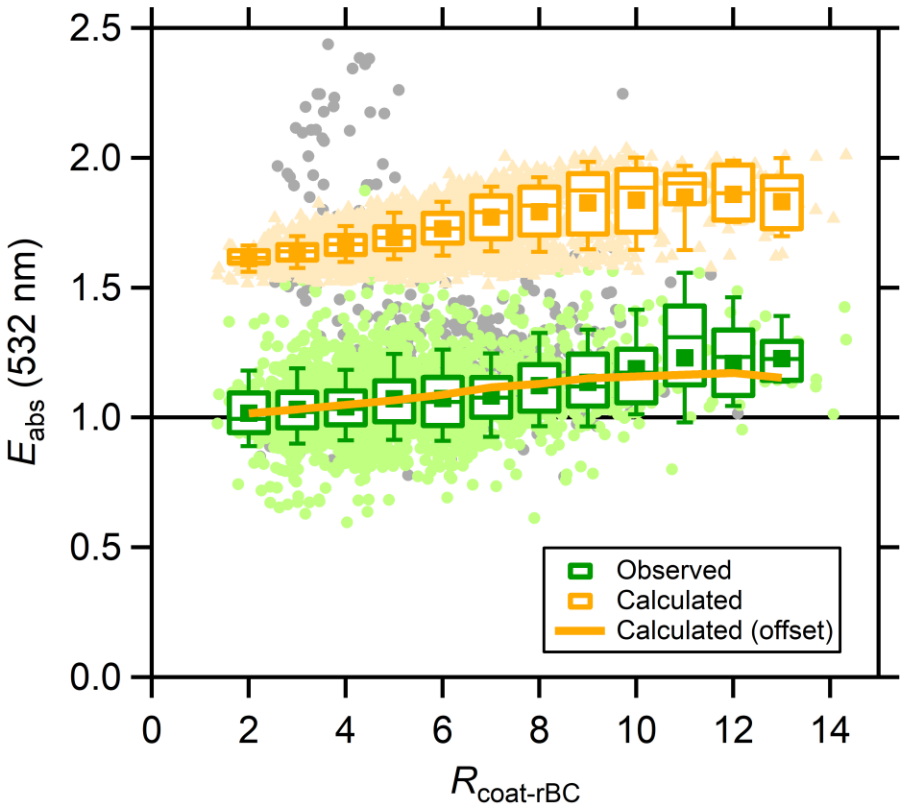

Figure 5-14. Comparison between the observed (green) and calculated (orange) E_{abs} versus $R_{coat\text{-}rBC}$ relationship for 532 nm at Fontana. The solid orange line is the mean calculated value, multiplied by 0.65. The points are the individual 10 min averages; the gray points show the fireworks-impacted period. The box and whisker plots show the mean (■), median (–), lower and upper quartile (boxes), and 9th and 91st percentile (whisker) for the non-fireworks impacted data.

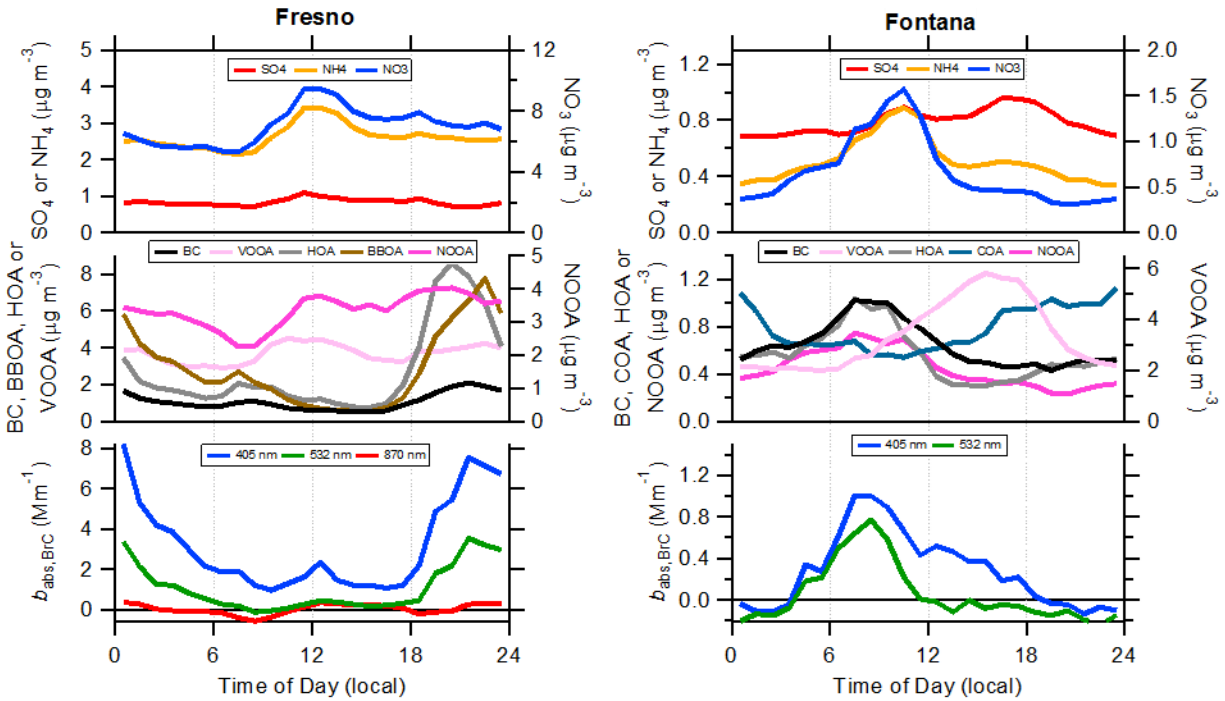

Figure 5-15. Diurnal variation in the (top panels) inorganic species, (middle panels) BC and the various OA factors, and (bottom panels) the absorption attributed to brown carbon, for (left) Fresno and (right) Fontana.

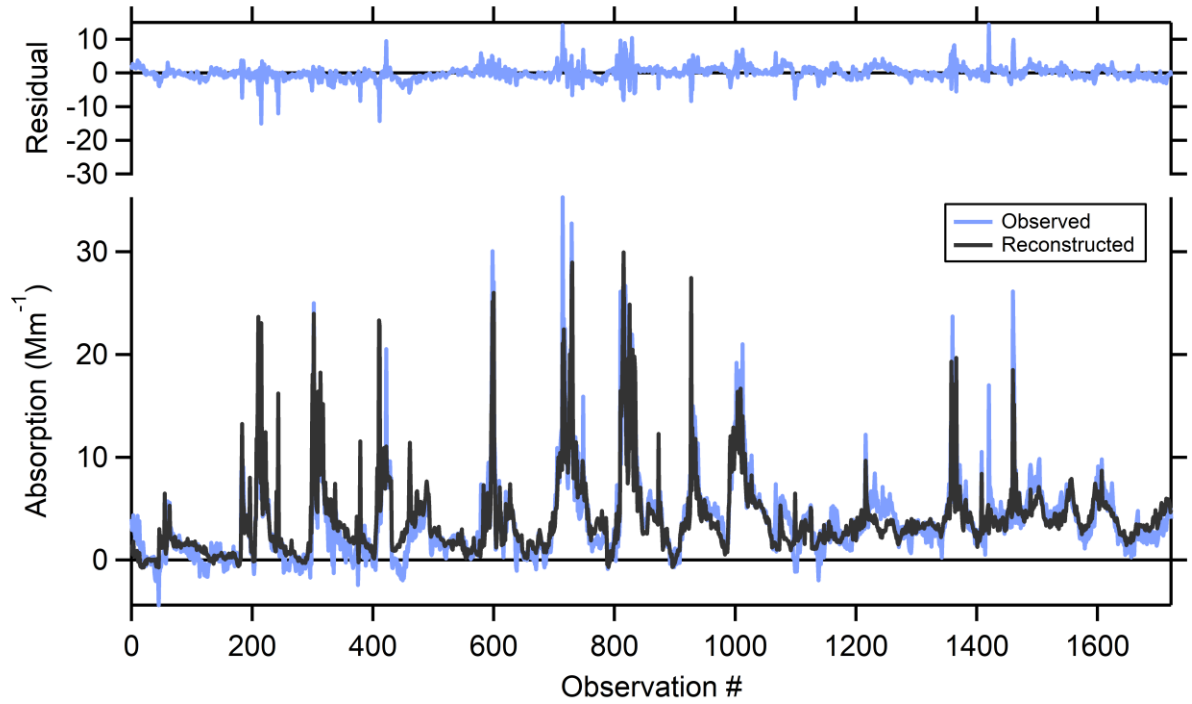

Figure 5-16. (bottom) Observed (blue) and reconstructed (gray) absorption at 405 nm from the multilinear regression for the Fresno campaign. (top) Residual, calculated as observed minus reconstructed.

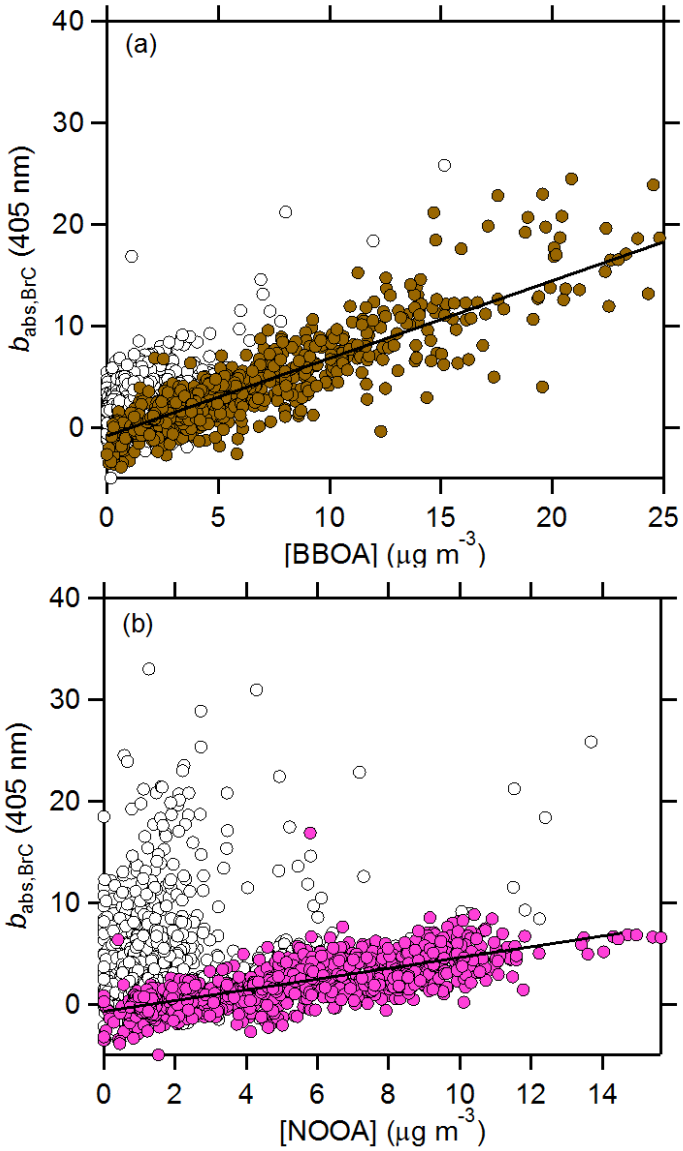

Figure 5-17. The relationship between absorption attributed to brown carbon at 405 nm and (a) the BBOA factor and (b) the NOOA factor for Fresno. In both panels the points are colored when the fraction of the factor was >20% and are white when the fraction of that factor was small. The black lines are linear fits, shown for reference.

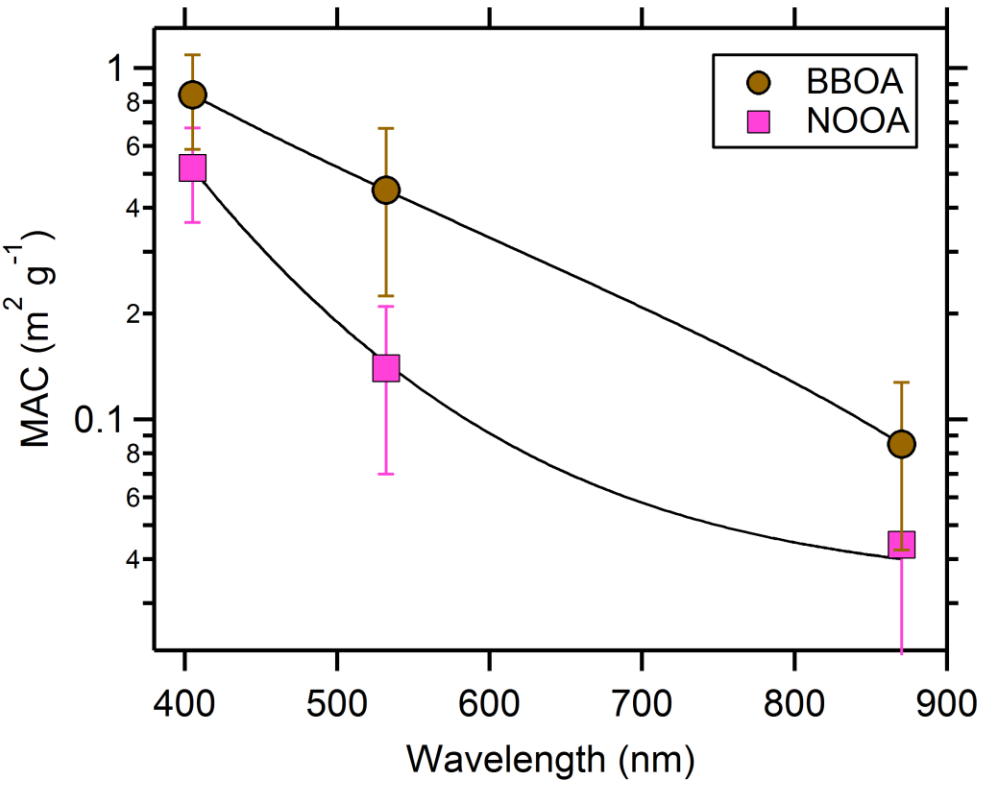

Figure 5-18. Variation of the OA factor-specific MAC values for BBOA (brown circles) and NOOA (pink squares) with wavelength for Fresno. The lines are power-law fits.

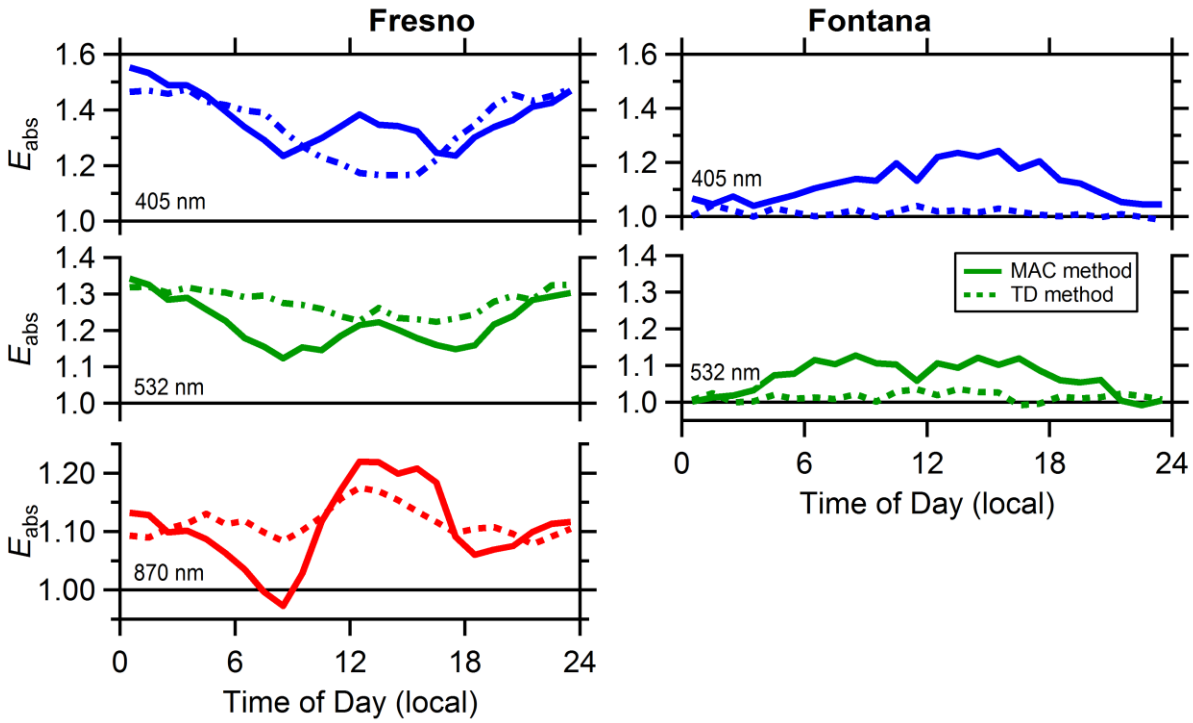

Figure 5-19. Campaign average diurnal variation in E_{abs} as calculated from the MAC-method (solid lines) and the TD-method (dashed lines). Fresno results are on the left, Fontana on the right for (top-to-bottom) 405 nm, 532 nm and 870 nm.

6 Comparing black and brown carbon absorption from AERONET and Surface Measurements at Wintertime Fresno

6.1 Abstract

The radiative impacts of black carbon (BC) and brown carbon (BrC) are widely recognized but remain highly uncertain. The Aerosol Robotic Network (AERONET) provides measurements of aerosol optical depth (AOD), aerosol absorption optical depth (AAOD), and other parameters. AERONET AAOD measurements have been used to estimate the relative contributions of BC and BrC to the total absorption at select sites and have the potential to be used across the global network, but the accuracy of the partitioning method has not been established and the uncertainties not characterized. We made surface-level measurements of aerosol optical properties from January 13 to February 10, 2013, and from December 25, 2014, to January 13, 2015, at Fresno, California. The contribution of BrC and BC to the absorption at 405 nm was estimated from the surface-level measurements using a combined mass absorption coefficient and thermodenuder method. The surface-level measurements were compared with BC and BrC absorption at 440 nm estimated from AERONET measurements of the absolute AAOD and the absorption Ångstrom exponent (AERONET-AAE method). In 2013, AERONET results showed that BC and BrC contributed 67% and 33%, respectively, of absorption at 440 nm while the surface-level measurements showed that BC and BrC contributed 89% and 11%, respectively, of absorption at 405 nm. In 2014, AERONET results showed BC and BrC absorption were 72% and 28%, respectively, and the BC and BrC surface measurements were 68% and 32%, respectively. The boundary layer conditions showed that the comparison between AERONET measurements and surface-based estimates was more appropriate in 2014 than in 2013. As a result, AERONET measurements and surface-based estimates had strong or moderate correlations and slopes near unity in 2014. Thus, surface measurements were more representative of column BC and BrC absorption in 2014.

6.2 Introduction

Black carbon (BC) and light-absorbing organic carbon (OC), known as brown carbon (BrC), represent one of the largest sources of uncertainty in predicting future climate change because of their substantial positive radiative forcing and our limited understanding of their properties and interactions (Myhre et al. 2013, Bond et al. 2013, Wang et al. 2014b). BC, BrC, and dust are known as light-absorbing aerosols because they absorb light at visible wavelengths (Moosmuller, Chakrabarty and Arnott 2009). While dust is mainly of crustal origin (Patterson 1981), BC and BrC are mainly anthropogenic from combustion processes (Bond et al. 2013, Bond et al. 2004). Since BC and BrC are often co-emitted, their mixing properties are unknown, which adds to the difficulty of characterizing their radiative effects (Andreae and Gelencser 2006).

BC is characterized by its blackness, combustion origin, and thermally refractory nature, as well as the ability to strongly absorb solar radiation across the visible spectrum (Andreae and Gelencser 2006). Direct radiative forcing (DRF) of BC is estimated to range from 0.17 to 1.48 Wm^{-2}, which indicates that BC has the potential to become the second largest anthropogenic warming agent, less than only carbon dioxide (Bond et al. 2013).

Historically, BC was the only known light-absorbing carbonaceous component. However, in the past 15 years, it has been recognized that certain types of organic aerosols are not purely scattering but absorb as well, with the mass absorptivity potentially comparable to BC absorption at short visible wavelengths (Kirchstetter, Novakov and Hobbs 2004, Hoffer et al. 2006, Andreae and Gelencser 2006). BrC is mainly produced by biomass burning and is usually accompanied with BC, depending on the combustion type. BrC is also produced from fossil fuel combustion, biogenic aerosols, soil humic matter, and as secondary formation from anthropogenic or biogenic precursors (Laskin, Laskin and Nizkorodov 2015). Global estimates of BrC radiative forcing are limited by knowing its sources, optical properties, and chemical transformations. Modeling studies estimate that the BrC fractional contribution to total carbonaceous aerosol absorption ranges from 20% to 40% and could dominate over major areas of biomass burning and biofuel combustion (Chung, Ramanathan and Decremer 2012, Feng, Ramanathan and Kotamarthi 2013, Lin et al. 2014, Wang et al. 2014a, Jo et al. 2016, Saleh et al. 2015).

Currently, several in situ techniques are used to estimate the contributions of BC and BrC to total absorption in the atmosphere (Moosmuller et al. 2009). The thermodenuder (TD) method uses a device that heats to a high temperature to (ideally) remove internally and externally mixed non-refractory components by evaporation, then measures the remaining absorption, which should be predominately from BC (Cappa et al. 2012, Lack et al. 2012, Saleh et al. 2013, Nakayama et al. 2014). This method is limited in that it assumes that the TD completely removes BrC in addition to completely removing other "coating" material, as non-absorbing coatings on BC can potentially increase BC absorptivity (Cappa et al. 2012).

Alternatively, the mass absorption coefficient (MAC) method compares observed mass absorption coefficients (calculated as the ratio between observed absorption and the observed BC mass concentration) to the MAC for theoretically "freshly" emitted, uncoated BC. Observations of the ratio between the observed MAC and that for uncoated BC greater than unity indicates contributions from either BrC or from coating material. The MAC method is limited by a reliance on high accuracy of both the absorption and BC concentration measurements, good knowledge of the reference uncoated-BC MAC, and incomplete separation of the coating contribution. For both methods BrC absorption is calculated as the difference between total absorption and BC absorption (perhaps including the coating contribution), which can have large uncertainty since it requires calculating what is often a small value from the difference between two large values that are each uncertain (Koch et al. 2009, Bond et al. 2013, Wang et al. 2014b). For both methods, BrC and coating contributions are often separated by comparing between wavelengths; BrC absorptivity increases strongly as wavelength decreases, while the potential coating contribution is nominally wavelength independent, the wavelength dependence of the ratio can be used to, at least approximately, distinguish between the two (Zhang et al. 2013, Knox et al. 2009). Alternatively, if the coating contribution is not accounted for, then the BrC contribution is an upper-limit estimate.

In situ techniques lack the temporal and spatial coverage to measure BC and BrC globally. Field campaigns are typically conducted for weeks to months, meaning that long-term BC and BrC

patterns are not measured. In addition, most field studies are located in regions with high emissions from industrialized urban areas or biomass burning events (Kirchstetter et al. 2004, Lack et al. 2012, Andrews et al. 2017). While such studies show major BC and BrC characteristics, they are biased towards high pollution conditions, which are not necessarily representitive of global or year-round conditions. Long-term measurement networks, such as the Global Atmosphere Watch, are limited to surface measurements and spatial coverage.

Remote sensing techniques have shown enormous potential for our understanding of the global absorption of aerosols using long-term measurements of aerosol optical properties. Broad spatial coverage is achieved through remote sensing networks, like the ground-based Aerosol Robotic Network (AERONET) (Holben et al. 1998, Holben et al. 2001). AERONET provides products for absorption-related column properties, such as aerosol optical depth (AOD) and column single-scattering albedo (SSA). AOD characterizes the total light extinction in the air column; the portion due to absorption (AAOD) is calculated as

$$\mathrm{AAOD}=\mathrm{AOD}\cdot(1\text{-}\mathrm{SSA}) \tag{1}$$

AERONET is commonly used as a first constraint on modeled aerosol properties. The validity of AERONET measurements has been compared with column SSA values calculated from airborne in situ measurements (Schafer et al. 2014, Leahy et al. 2007, Magi et al. 2005, Mallet et al. 2005, Corrigan et al. 2008, Osborne et al. 2008, Esteve et al. 2012, Johnson et al. 2009, Andrews et al. 2017). These studies used Version 2 AERONET level 2.0 values or level 1.5 values with additional constraints (Andrews et al. 2017); most in situ profiles are matched within 4 hours and 100 km of AERONET measurements. The results show that, while there is a generally good agreement between AERONET and in situ AOD (about 10% discrepancy), AERONET SSA is consistently lower than in situ SSA, even at higher AOD conditions (AOD > 0.5 at 440 nm), with few exceptions (Leahy et al. 2007). This is consistent with results from several comparisons between AERONET AAOD and airborne in situ measurements, which show that AERONET AAOD values are greater than those obtained from in situ measurements (Corrigan et al. 2008, Andrews et al. 2017). Schafer et al. (2014) find that for their measurements over Maryland, USA, much of the observed difference between AERONET SSA and in situ SSA may fall within the uncertainty of the SSA values.

An empirical approach to determining the relative contributions of BC and BrC to the AAOD has been developed based on AERONET observations and BC and BrC having different absorption Ångstrom exponents (AAE) (Bahadur et al. 2012). Here, we refer to this approach as the AERONET-AAE method. The AAE characterizes the wavelength dependence of light absorption:

$$\mathrm{AAE}=-\frac{\ln\left(\frac{\mathrm{abs}(\lambda_1)}{\mathrm{abs}(\lambda_2)}\right)}{\ln\left(\frac{\lambda_1}{\lambda_2}\right)} \tag{2}$$

λ_1 and λ_2 represent two reference wavelengths, and abs(λ) represents absorption-related parameters (either AAOD or absorption coefficients) at the corresponding wavelengths.

The reported AAE of BC is typically close to 1 but the AAE of BrC is often substantially larger (**Table 6-1**), which indicates BC absorption is less dependent on wavelength than BrC absorption. For a long time, BC has been thought to have AAE =1, which in many studies is still assumed to be true (Clarke et al. 2007, Herich, Hueglin and Buchmann 2011, Sandradewi et al. 2008, Yang et al. 2009, Olson et al. 2015). Studies show the AAE of BC ranged from 0.8 to 1.4 (Lack and Langridge 2013, Fuller et al. 2014, Gyawali et al. 2009, Schnaiter et al. 2003). The AAE of BrC is more varied, as deduced from measurements of particulate organic matter (POM) observed from Asian pollution outflow, biomass burning aerosols from savanna or canyon fires, extracted humic-like substances (HULIS) with water from the fine fraction of biomass burning aerosols, and anthropogenic sources from urban pollution measurements (Yang et al. 2009, Kirchstetter et al. 2004, Lack et al. 2012, Hoffer et al. 2006, Olson et al. 2015, Yuan et al. 2016). With AAE-based methods, absorption at long wavelengths (typically > 700 nm) is assumed to be entirely due to BC. At shorter wavelengths, BC absorption is then estimated from Eqn. 2, which assumes that the BC AAE is unity (or some other constant value). BrC absorption at shorter wavelengths is calculated as the difference between the observed absorption and estimated BC absorption (Section 2.2 for further discussion). The AAE-based method is commonly used to calculate BC and BrC absorption (Russell et al. 2010, Chung et al. 2012, Bahadur et al. 2012).

Here, we compare AERONET measurements of estimated BC and BrC absorption in appropriate conditions to in situ surface measurements. This work helps to assess the robustness of the AERONET estimates, which is important since AERONET measures these parameters long-term and globally. Two sets of measurements collected in winter 2013 and 2014 at Fresno were analyzed to better understand the relationship between AERONET column retrievals and surface-based estimates of column properties and identify discrepancies. In Section 2, we present an overview of AERONET data availability and of the AERONET-AAE method used to partition AAOD into absorbing components, as proposed by Bahadur et al. (2012); we then summarize the surface measurements and column estimates for studies in 2013 and 2014. Estimates were based on surface measurements of extinction and absorption multiplied by simulated planetary boundary layer height (BLH) from the Weather Research and Forecasting (WRF) model. In Section 3, we compare AERONET and surface-based column estimates for AOD, AAOD, and BC and BrC fractions of AAOD, with a discussion of uncertainties in the calculations and measurements in Section 3.4. In Section 4, we conclude by discussing the implications of AERONET and surface absorption comparisons.

6.3 Materials and Methods

6.3.1 AERONET Measurements

AERONET is a globally-distributed network of automated sun and sky radiometers that measure AOD and AAOD at four wavelengths (440, 675, 870, and 1020 nm) as well as other properties (Dubovik and King 2000, Holben et al. 2001). Version 2 AERONET products include two levels of data: level 1.5 data have automatic cloud screening; level 2.0 data have pre-field and post-field calibrations, manual inspection, and quality assurance (Smirnov et al. 2000). Though there is now a newer version of AERONET (Version 3), we used Version 2 because the key parameters and constraints used for the AERONET-AAE method of Bahadur et al. (2012) are based on Version 2 AERONET products. Within Version 2, we used level 1.5 data with additional quality criteria described below, because level 2.0 data are biased toward high aerosol loadings.

One major limitation of level 2.0 data is that SSA retrievals are only available when AOD exceeds 0.4 at 440 nm (AOD > 0.4) (Dubovik and King 2000, Dubovik et al. 2002). However, AeroCom models show that only 5% of days at locations around the world have a daily-average AOD that exceeds this threshold (Myhre et al. 2013, Andrews et al. 2017). Consequently, level 2.0 data represent only a small fraction of days, those only with high aerosol loadings, which is the reason that many analyses incorporate level 1.5 SSA (Wang et al. 2016, Andrews et al. 2017).

The drawback of using level 1.5 data is measurement uncertainty of SSA retrievals, which is higher when AOD is below 0.4. Specifically, this uncertainty is ± 0.03 when AOD exceeds 0.4 but could be as large as ± 0.07 when AOD is less than 0.2 due to increasing errors in the retrievals from the combination of sun or sky channel calibration uncertainties, inaccurate azimuth angle during sky radiance measurements, and inaccuracy in accounting for surface reflectance (Dubovik et al. 2000). In this study, we set the threshold at AOD > 0.1 at 440 nm. Given that emission sources were relatively constant during the times measured (Chen et al. 2018), the value of SSAs should be relatively consistent (i.e., within the range of confidence interval of the mean value). Therefore, a lognormal distribution was used to obtain a 95% confidence interval of all retrieved level 1.5 SSA, which helps to minimize the impact of larger uncertainties for SSA retrievals at low AOD conditions. Note that since AERONET SSA has a maximum of 1, it is converted into single scatter co-albedo (SSCA = 1 - SSA) to provide the confidence interval. We use the term “level 1.5M” for AERONET measurements with AOD > 0.1 at 440 nm and single-point SSA within the confidence interval for this analysis (**Table 6-2**). Note that at level 1.5M, AERONET measurements covered only 4.2% of the total measurement time in 2013 and 2.0% in 2014. An average of at most 3 to 5 measurements for 15-min each per day cannot represent a daily average and cannot represent the trend during each investigation.

6.3.2 The AERONET-AAE Method

The method of partitioning AERONET AAOD to BC and BrC we used in this work is based on the AERONET-AAE method, which analyzes the observed absorption in visible and near-UV spectra from the AERONET global network (Bahadur et al. 2012). It improves on previous AAE-based methods because the AAEs used are derived from actual AERONET spectral measurements

rather than relying on laboratory measurements or theoretical values (Russell et al. 2010, Chung et al. 2012, Bahadur et al. 2012). The detailed procedure for determining AAE values from selected sites is provided in the supporting information. The overall AAOD at a given wavelength is assumed to be the sum of the contributions from BC, BrC, and dust, and each absorbing component is assumed to have a known and constant AAE value. The resulting partitioning scheme of the AERONET-AAE method is expressed as

$$\mathrm{AAOD}(\lambda_i)=\mathrm{AAOD}_{\mathrm{ref,BC}}\left(\frac{\lambda_i}{\lambda_{\mathrm{ref}}}\right)^{-\mathrm{AAE}_{\mathrm{BC,i}}}+\mathrm{AAOD}_{\mathrm{ref,BrC}}\left(\frac{\lambda_i}{\lambda_{\mathrm{ref}}}\right)^{-\mathrm{AAE}_{\mathrm{BrC,i}}} +\mathrm{AAOD}_{\mathrm{ref,dust}}\left(\frac{\lambda_i}{\lambda_{\mathrm{ref}}}\right)^{-\mathrm{AAE}_{\mathrm{dust,i}}}. \quad (3)$$

Two assumptions are inherent in equation 3: 1) AAE values of each absorbing component are intrinsic properties that do not depend on the mixing state; and 2) measured AAOD values represent a well-mixed sample of these components. With these assumptions, the contribution to AAOD from the three absorbing components at wavelength (λi) can be calculated from AAOD measurements at three wavelengths (440 nm, 675 nm, and 870 nm), since equation (3) provides three equations and three unknowns. AAE values for λ1 = 440 nm and λ2 = 675 nm are denoted as AAE1, and AAE values for λ1 = 675 nm and λ2 = 870 nm are denoted as AAE2 [similar notation is used for scattering Ångstrom exponent (SAE)]. Bahadur et al. (2012) showed that the AAE1 of BC, BrC, and dust are calculated to be 0.55 ± 0.24, 4.55 ± 2.01, and 2.20 ± 0.50, respectively, and the AAE2 of BC and dust are calculated to be 0.83 ± 0.40 and 1.15 ± 0.50, respectively. Further discussion is included in the supporting information.

6.3.3 Surface Measurements

In 2013 and 2014, two sets of measurements were collected at Fresno, CA, to obtain a comprehensive and detailed understanding of the chemical, microphysical, and optical properties of wintertime aerosols within the San Joaquin Valley (SJV). As one of the most polluted regions with the highest rates of cardiorespiratory diseases in the USA, the SJV's persistent air-quality problems have been associated with high particulate matter (PM) concentrations due to anthropogenic emissions, topography, and meteorological conditions (Chow et al. 2006). Studies have shown that the major components of local PM are organic components and nitrate, particularly from residential burning in winter, which contributes up to two-thirds of the mass (Chu, Paisie and Jang 2004, Chow et al. 2006, Turkiewicz, Magliano and Najita 2006, Ge et al. 2012, Young et al. 2016). The region's surrounding mountains trap pollutants, leading to air quality deterioration (Gorin, Collett and Herckes 2006, Lurmann et al. 2006, Ngo et al. 2010).

From January 13, 2013, to February 10, 2013, surface measurements, including chemical compositions and optical properties, were collected at the California Air Resources Board (CARB) Fresno-Garland air monitoring facility (36.7854°, -119.7732°). The site, approximately 1500 m to the east of Yosemite Freeway (CA 41), is surrounded by residential and commercial areas and monitors a mix of rural and urban pollutants. We used the following: a cavity ringdown spectrometer (CRD) to measure PM2.5 dry particle (RH <30%) light extinction at 405 ($b_{ext}405$) and 532 ($b_{ext}532$) nm; a photoacoustic spectrometer (PAS) to measure PM2.5 dry particle light

absorption at 405 ($b_{abs}405$) and 532 ($b_{abs}532$) nm; and a photoacoustic extinctiometer (PAX) to measure light extinction and absorption at 870 nm ($b_{ext}870$ and $b_{abs}870$, respectively). Other instruments included a single particle soot photometer (SP2), a scanning mobility particle sizer (SMPS), a thermodenuder (TD), and a high-resolution time-of-flight aerosol mass spectrometer (HR-ToF-AMS). Zhang et al. (2016) and Young et al. (2016) have detailed the operation, calibration, and results of these instruments.

From December 25, 2014, to January 13, 2015, we collected another set of measurements at the University of California Center in Fresno (36.8101°, -119.7782°). Similar measurements were made with CRD-PAS, PAX, SP2, SMPS, TD, and HR-ToF-AMS but with PM1 size cut instead of the PM2.5 size cut used in 2013. The composition and concentrations of water-soluble gases and ionic aerosol components were measured from January to February 2013 in Fresno (Parworth et al. 2017). The observations demonstrate that there is only a small amount of particle mass (~10%) contained between PM1 and PM2.5, and there is a strong correlation ($R^2 \sim 0.9$) between the major soluble ion species (e.g. nitrate) measured in PM1 and PM2.5. This small amount of supermicron soluble mass means that the difference in size cuts is not likely to introduce substantial biases. While Parworth et al. (2017) focused on soluble inorganic ions, most BC mass is contained in PM1 (Cappa et al. (2012), Healy et al. (2015), Collier et al. (2018)). Details are provided in Betha et al. (2018), Chen et al. (2018), and Cappa et al (Submitted). Samples were also collected on pre-scanned Teflon filters (37-mm diameter, 1.0-μm pore size). We selected twenty PM1 and five PM2.5 filter samples for X-ray fluorescence (XRF) analysis at Chester Laboratories (Chester LabNet, Tigard, Oregon) to measure 38 elements heavier than Na. The elements Al, Si, S, K, Ca, Fe, Zn, and Br were above detection limit in at least 80% of the samples so their concentrations were used to quantify dust contributions (Al_2O_3, SiO_2, S, K_2O, $CaCO_3$, Fe_2O_3) and employed as elemental tracers of biomass burning (K) (Chen et al. 2018).

Since 2002, an AERONET-affiliated sun photometer mounted atop the CARB building near downtown Fresno has been maintained by the California Air Resources Board (CARB). The site, which provides column measurements at the same location where we collected surface-level measurements in 2013, is about 3000 m south of where we collected measurements in 2014. At Fresno Yosemite International Airport (FAT), important parameters for meteorological conditions (e.g., temperature, relative humidity (RH), visibility) were recorded as part of meteorological aviation reports (METAR).

The two sets of Fresno measurements allowed us to compare surface measurements of absorption properties with AERONET measurements closely matched in time and space, as well as letting us test different BC and BrC partition methods. Although AERONET measurements covered a small fraction of time, the values generally fall in the same range with surface measurements made within 15 min (multiplied by boundary layer height, BLH) in both 2013 and 2014 (**Figure 6-1**). Assuming emission sources have not changed significantly within 2 years, comparing results obtained from AERONET and surface measurements also provides valuable information on how local meteorological conditions affect the comparability of surface and column absorption measurements. Because BrC absorption produces a measurable contribution

only at short wavelengths (< 700 nm), we compared the shortest wavelength available from AERONET measurements (440 nm) against surface measurements (405 nm), unless otherwise specified.

6.3.4 Partitioning of Surface Absorption

Light absorption coefficients for BC ($b_{abs,BC}$) and BrC ($b_{abs,BrC}$) were measured at the surface using a combination of MAC and TD methods. The MAC for particles containing BC is dependent on the BC mixing state (Saathoff et al. 2003, Schnaiter et al. 2003, Schnaiter et al. 2005, Shiraiwa et al. 2010, Lack et al. 2009, Cappa et al. 2012). The presence of materials—even non-absorbing materials—internally mixed with BC can enhance BC absorption. This light absorption (E_{abs}) enhancement, which in turn increases the MAC of BC, is known as the "lensing" effect. The MAC method evaluates the E_{abs} by comparing observations of the MAC to the reference value of uncoated BC ($E_{abs} = MAC_{BC}/MAC_{BC,uncoated}$). Instead of using a reference value from the literature, we estimated a campaign-specific value of the MAC of uncoated BC from measurements of thermodenuded particles (i.e., using the TD method). Absorption was measured before and after heating in the TD, which was then used to calculate coated and uncoated BC properties (Cappa et al. 2012, Lack et al. 2012, Saleh et al. 2013, Nakayama et al. 2014). The absorption due to pure, uncoated BC is

$$b_{abs,BC} = MAC_{BC,uncoated} \cdot [BC] \quad (4)$$

BC concentration ([BC]) was determined from SP2 measurements, including a correction for the "missing mass," which accounts for the loss of particles below the lower size limit.

An upper-limit for BrC absorption was estimated as the difference between the observed absorption and the calculated uncoated BC absorption:

$$b_{abs,BrC,UL} = b_{abs,obs} - b_{abs,BC,uncoated} = b_{abs,obs} - MAC_{BC,uncoated} \cdot [BC] \quad (5)$$

Equation 5 gives an upper limit for BrC absorption because it is assumed that coatings on BC do not lead to enhancement of the absorption. For the 2014 measurements, the relative amount of coating material on refractory BC was measured. A relationship between the relative coating amount ($R_{coat,rBC}$ = [coating]/[rBC]) and the very small mixing-induced enhancement was established based on measurements at 880 nm, where BrC should contribute negligibly (Cappa et al. Submitted, Zhang et al. 2016). The theoretical mixing-induced enhancement, calculated from Mie theory, depends on both wavelength and the assumed core particle size. Ratios between the theoretical mixing-induced enhancement at 405 nm and 880 nm averaged $1 < R_{coat,rBC} < 5$, the range observed by Collier et al. (2018), and are 1.06 and 0.96 for core diameters of 100 nm and 150 nm, corresponding to typical mass-weighted sizes of the observed BC particles (Zhang et al. (2016) and Betha et al. (2018)). As such, use of the empirical relationship determined at 405 nm and at 880 nm contributes a negligible amount to the overall uncertainty. Based on this empirical relationship, the coated particle absorption at 405 nm is estimated as

$$b_{abs,BC,coated} = b_{abs,BC,uncoated} \cdot E_{abs,mixing}(R_{coat,rBC}) \quad (7)$$

The absorption by BrC is then

$$b_{\mathrm{abs,BrC}} = b_{\mathrm{abs,obs}} - b_{\mathrm{abs,BC,coated}} = \mathrm{MAC}_{\mathrm{BC,uncoated}} \cdot [\mathrm{BC}] \cdot E_{\mathrm{abs,mixing}}\left(R_{coat,rBC}\right) \quad (8)$$

In this study, the difference between BrC absorption from Eqn. 5 and Eqn. 8 is small owing to the relatively minor contribution of the mixing-induced enhancement. Throughout, we used the upper-limit BrC absorption, unless otherwise noted.

The contribution of the mixing-induced enhancement highlights an important difference between the partitioning of surface absorption and AERONET absorption. Most AAE-based methods (including the AERONET-AAE method) cannot evaluate the absorption due to mixing separately because they assume AAE values for the absorbing component to be intrinsic properties that are not dependent on the mixing state. There are studies suggesting that the mixing-induced enhancement varies geographically, and that mixing-induced absorption enhancements up to a factor of 2.4 may be observed in polluted urban environments (Peng et al. 2016). However, other measurements in urban regions, and where measurements were made for ambient particles directly (unlike in Peng et al., 2016), indicate that the mixing-induced enhancement may be very small (Zhang et al. 2016). Regardless, the impact of lensing is included in spectral observations and, correspondingly, in BC and BrC absorption calculated by the AERONET-AAE method but without being able to separate out its contribution. These methodological differences could contribute to differences observed between the partitioning methods.

6.3.5 Scaling Surface Measurements to Column Properties

For comparison to AERONET, column AOD and AAOD were estimated by multiplying the surface measurements with the BLH. The planetary boundary layer, which is the lowest part of the atmosphere, has strong vertical mixing that distributes aerosol mass from surface emissions throughout the layer, especially in daytime (Gobbi, Barnaba and Ammannato 2004). The top of the boundary layer is typically marked by a temperature inversion that traps the air within the boundary layer, separating it from the cleaner atmosphere above (Galchen, Xu and Eberhard 1992, Cooper and Eichinger 1994). The aerosol vertical distribution has frequently been found to be generally uniform within the boundary layer, indicating that the aerosols are well-mixed by surface-driven turbulence (Liu et al. 2009, Pringle et al. 2010, Winker et al. 2013, Li et al. 2017). For the surface-based estimates, we made two assumptions about the column properties: 1) the aerosol is well-mixed throughout the boundary layer, and 2) AOD and AAOD values in the boundary layer account for most of the air column (i.e., there are no absorbing aerosol layers above the boundary layer). If these assumptions are met, the comparison between AERONET measurements and surface-based estimates in the boundary layer is appropriate. Vertical profiles over Fresno in wintertime 2013 suggest that these assumptions are generally valid for the late

morning and afternoon, when vertical mixing is strongest, and the boundary layer is highest (Prabhakar et al., 2017). The column properties such as the absorption at 405 nm are calculated from the following:

$$\mathrm{AAOD}_{\mathrm{BLH,405nm}} = b_{\mathrm{abs,405nm}} \cdot \mathrm{BLH} \quad (9)$$

Analogous equations apply for surface-based estimates of column extinction ($\mathrm{AOD}_{\mathrm{BLH}}$) and the BC ($\mathrm{AAOD}_{\mathrm{BLH,BC}}$) and BrC ($\mathrm{AAOD}_{\mathrm{BLH,BrC}}$) absorption.

The BLH values were provided by simulations with the Weather Research and Forecasting (WRF) Model (Chen et al. 2018). The reliability of the WRF model was assessed by comparing the model simulated surface temperature and wind speed, both of which are related to BLH, to 7 years of surface observations in the SJV area. The mean fractional bias (MFB) of temperature and wind were generally within ± 15% (Molders and Kramm 2010, Coniglio et al. 2010, Hu et al. 2014). In 2013, the WRF model simulating the BLH was generally within ± 200 m of NARR model simulations, and within ± 160 m of simulations from the Eta Data Assimilation System (EDAS) model. In 2014, the WRF model simulating the BLH was generally within ± 180 m of NARR model simulations, and within ± 150 m of the simulations from EDAS model (see **Figure 6-2** and Appendices). The daytime hourly average BLH (220 - 840 m from 9:00 AM to 3:00 PM) generally agrees with the BLH observed (300 - 700 m) from flights circling Fresno and Bakersfield during DISCOVER-AQ (Pusede et al. 2016). Because scaling is applied to surface measurements of both BC and BrC absorptions, BLH uncertainty does not impact relative BC and BrC amounts; however, it does impact correlations between AERONET measurements and surface-based column estimates.

6.3.6 Local Conditions

Surface XRF analysis and AERONET parameters indicated that the dust contribution to absorption was low in both years at Fresno. Specifically, the 20 PM1 and 5 PM2.5 filter samples from 2014 showed that dust contributed only 3% of PM1 and 5% of PM2.5 based on XRF analysis (Chester Laboratories). For the AERONET measurements, SAE1 was 1.56 ± 0.31 and the average AAE2/AAE1 was 1.03 ± 0.85 in 2014, indicating that most of the measurements fit the dust-free conditions of the AERONET-AAE method (i.e., SAE1 > 1.2 or AAE2/AAE1 > 0.8). Here, we evaluated the conditions from average properties during the measured period rather than for each individual measurement because the level 1.5M measurements had a larger uncertainty compared to the level 2.0 measurements used by Bahadur et al. (2012). In 2013, the average SAE1 was 1.58 ± 0.30 and the average AAE2/AAE1 was 1.04 ± 0.51, which also fits the dust-free conditions. Therefore, the 2013 measurements are also assumed to have low dust influence based on AERONET parameters, although filter measurements of dust are not available for that year. Besides the low-dust conditions, a combination of different local meteorological patterns and the timing of clear-sky conditions could have contributed to the difference between the AERONET measurements and surface measurements (**Figure 6-3**).

Equation (3) yielded non-negative values for absorption by BC, BrC, and dust for 57% of level 1.5M AERONET measurements in 2013 and 49% in 2014. some small negative BC, BrC, or dust values can result from the uncertainty in the measurements and AAE parameters, but the larger negative values resulted from unreasonable values for dust. For this reason, we modified Equation (3) as follows to remove the dust contribution:

$$AAOD(\lambda_i)=AAOD_{ref,BC}\left(\frac{\lambda_i}{\lambda_{ref}}\right)^{-AAE_{BC,i}}+AAOD_{ref,BrC}\left(\frac{\lambda_i}{\lambda_{ref}}\right)^{-AAE_{BrC,i}} \quad (10)$$

Since this equation has only two unknowns, only AAOD at 440 nm and 675 nm and AAE1 between these two wavelengths were needed to calculate BC and BrC contributions to AAOD at wavelength (λ_i). Equation (7) had non-negative values for BrC and BC for 98% of AERONET 1.5M measurements in 2013 and all measurements in 2014. We checked our results by comparing the AAOD at 870 nm reconstructed from Equation (7) and AAE2 between 675 and 870 nm with the AERONET measured value. The average reconstructed AAOD was 95% of AERONET AAOD at 870 nm (see **Figure 6-4**), which is consistent with 4% error estimates at this wavelength (Bahadur et al. (2012).

6.4 Results and Discussion

6.4.1 Results

In 2013, the partitioning of AERONET measurements indicated that BC contributed 67% and BrC 33% of the absorption at 440 nm. The partitioning of surface measurements showed that BC contributed 89% and BrC contributed 11% of absorption at 405 nm. In 2014, AERONET measurements indicated that BC contributed 72% and BrC 28% to the measured AAOD. The fraction was 68% BC and 32% BrC from the surface measurements.

The BC and BrC absorption partitioned from AERONET measurements in both years were in the general range given by values reported in previous AERONET observationally constrained studies (**Table 6-3**). Using concepts similar to those of the AERONET-AAE methods, studies showed BrC contributes on average 6% to 40% of the global absorption at 440 nm and, on average, 28% at 10 AERONET sites around California (Bahadur et al. 2012, Wang et al. 2016). The BrC absorption from AERONET at Fresno in both 2013 and 2014 (28%-33%) was close to this reported range.

The BC and BrC absorption partitioned from surface measurements in 2014 were in the general range given by previous surface absorption studies that focused on areas with similar biomass burning aerosols or biomass burning-influenced aerosols (50%-88% for BC, 12%-50% for BrC at wavelengths shorter than 500 nm). BC and BrC absorption in 2013 were at the high end of BC and low end of BrC. For locations with significant residential burning, like Fresno, daytime BrC absorption was lower than during nighttime (Zhang et al. 2016). Therefore, the low BrC absorption and complementary high BC absorption in 2013 could be explained by the selection of daytime measurements (to compare with AERONET measurements made only during daytime).

The 2013 BC and BrC fractional contributions to absorption from surface measurements were most similar (within 4%) to the particulate organic fraction observed from the Asian pollution

outflow (Yang et al. 2009) and winter biomass burning from rural environments in the Pearl River Delta (PRD) region of China (Yuan et al. 2016). The BC and BrC fractional absorption from surface measurements in 2014 were close to those from the open biomass and trash burning measured in the urban Indian city of Kanpur and its surrounding regions, for which 71.5% was BC and 28.5% was BrC at 405 nm from in situ atmospheric and denuded absorption measurements (Shamjad et al. 2016). The 2013 and 2014 BrC fractional absorption partitioned from surface measurements was lower than the BrC measured during extensive wild-burning events at the Four-Mile Canyon fire in 2010, which had 54% BC, 27% BrC, and an additional 19% from lensing at 404 nm (Lack et al. 2012). Fresno BrC was also lower than the relative amount calculated from extracted HULIS from biomass burning aerosols in Hoffer et al. (2006), which was 35% to 50% BrC at 300 nm.

6.4.2 Comparison of AERONET and Surface-Based AOD and AAOD

AERONET retrievals and surface-based estimates between AOD and AAOD were more strongly correlated to each other in 2014 than in 2013 (**Figure 6-5**). In total, during the 2013 and 2014 studies, 163 AERONET measurements met the level 1.5M criteria (**Table 6-2**) for daytime, clear sky, and high AOD (AOD > 0.1). Of these, 147 measurements corresponded in time with surface measurements, which covered 4.2% of time in 2013 and 2.0% of time in 2014. Analysis of the diurnal cycle shown in the surface measurements is provided by Zhang et al. (2016) and Cappa et al. (Submitted). In the following discussion, AERONET measurements of AOD, AAOD, and BC and BrC absorption in the column are shown with the subscript "COL" as AOD_{COL}, $AAOD_{COL}$, $AAOD_{COL,BC}$, and $AAOD_{COL,BrC}$, respectively. Surface measurements of extinction, absorption, and BC and BrC absorption scaled to BLH are shown with the subscript "BLH" as AOD_{BLH}, $AAOD_{BLH}$, $AAOD_{BLH,BC}$, and $AAOD_{BLH,BrC}$, respectively. We used the square of the correlation coefficient (R^2) from one-sided linear regression by least-squares, with $R^2 \geq 0.64$ considered strong, $0.64 > R^2 > 0.25$ considered moderate, and $0.25 \geq R^2$ considered weak (Devore and Berk 2012).

In 2014, AOD_{COL} strongly correlated ($R^2 = 0.81$) to AOD_{BLH}, and $AAOD_{COL}$ moderately correlated ($R^2 = 0.60$) to $AAOD_{BLH}$ (**Table 6-4**; **Figure 6-5**b,d). The fitted slope of AOD_{COL} to AOD_{BLH} was 1.06, with a y-intercept of 0.078; the fitted slope of $AAOD_{COL}$ to $AAOD_{BLH}$ was 1.23, with a y-intercept of 0.0054. The slopes near 1 with a positive y-intercept indicated that AERONET measurements of AOD and AAOD varied similarly but were systematically higher than the surface measurements scaled to BLH. This offset was consistent with results from previous column-column AAOD comparisons between AERONET and in situ measurements (Andrews et al. 2017, Corrigan et al. 2008).

In contrast, in 2013, there were very weak correlations (**Figure 6-5**a,c) between AOD_{COL} and AOD_{BLH}, with $R^2 = 0.08$, while $AAOD_{COL}$ and $AAOD_{BLH}$ had $R^2 = 0.10$. Thus, the slopes and intercepts are not meaningful. **Figure 6-6** shows that the AOD_{COL}/AOD_{BLH} and $AAOD_{COL}/AAOD_{BLH}$ ratios increased notably when the BLH was lower than 200 m. Above 200 m these ratios were greater than 1 during both years and nominally independent of altitude. The color scale shows that measurements with low BLH occurred mainly in the morning hours (red to

orange) between 8:00AM and 10:00AM. In 2013, 41 out of 113 (36%) level 1.5M AERONET measurements were made when the BLH was lower than 200 m, and 92% of these measurements were made between 8:00AM and 10:00AM. In 2014, 3 out of 34 (9%) measurements corresponded to a low BLH, and 67% of them were made between 8:00AM and 10:00AM. There were four times more measurements with lower than 200 m BLH in 2013 than in 2014. During this period, there can be substantial amounts of aerosol in the residual layer above the boundary layer (Prabhakar et al. 2017). This residual layer contributed to the AOD_{COL} and $AAOD_{COL}$ but not to AOD_{BLH} and $AAOD_{BLH}$. Therefore, the BLH patterns and timing of AERONET measurements might be an important reason why the correlations of AERONET column retrievals and surface-based estimates of column properties were higher in 2014 than in 2013. Typically, the BLH increased as each day progressed, entraining the residual layer and reducing the amount of aerosol above the BLH, which made higher BLH measurements that occurred later in the day more likely to include all of the absorption in the boundary layer.

When we excluded measurements with BLH lower than 200 m, correlations of AOD and AAOD in 2013 increased significantly, especially for AOD (**Table 6-4**). The correlation between AOD_{COL} and AOD_{BLH} increased from $R^2 = 0.08$ to $R^2 = 0.55$ and between $AAOD_{COL}$ and $AAOD_{BLH}$ increased from $R^2 = 0.10$ to $R^2 = 0.25$. Removing low BLH measurements also increased the fitted slope of AOD_{COL} to AOD_{BLH} (0.21-0.93, y-intercept 0.093), as well as the fitted slope of $AAOD_{COL}$ to $AAOD_{BLH}$ (0.60-0.85, y-intercept 0.0055). In 2014, correlations also increased by removing measurements with low BLH, but less significantly.

Comparisons between AERONET column measurements and surface measurements multiplied by BLH were appropriate only when the boundary layer conditions met the conditions that the boundary layer accounted for most of the column absorption and that the WRF BLH was accurate (**Table 6-4**). In 2014, the AOD_{COL} correlated with $b_{ext}405$ moderately ($R^2 = 0.56$) but weakly ($R^2 = 0.07$) in 2013. Similarly, in 2014, the $AAOD_{COL}$ correlated with $b_{abs}405$ moderately ($R^2 = 0.31$), but weakly ($R^2 = 0.03$) in 2013. After removing measurements with BLH less than 200 m, correlations in 2013 increased to moderate-weak correlations but were still lower than 2014 correlations. However, in terms of the ratio, the 2013 measurements with BLH higher than 200 m were closer to unity than those in 2014. Additional information and vertical profiles are provided in the supporting information.

In general, AOD and AAOD AERONET measurements strongly or moderately correlated with surface-based estimates but they were biased high with a nearly constant offset. The lower AAOD correlations compared to AOD were likely due to the higher uncertainty contributed by AERONET SSA retrievals used in AAOD calculations. The AERONET-retrieved SSA average was 0.93 ± 0.02 in both years, while the surface-measured SSA was 0.94 ± 0.02 in 2013 and 0.95 ± 0.02 in 2014. The AERONET SSA was on average lower than in situ SSA, which might cause the AERONET AAOD values to be greater than those obtained from in situ measurements. However, the observed difference between AERONET SSA and in situ SSA falls within the uncertainty of the AERONET SSA retrievals under low AOD (AOD < 0.2 at 440 nm) conditions. Note that surface measurements were made in dry conditions (RH < 30%), while AERONET measurements

were made at ambient RH, which was 57% on average in 2013 and 61% on average in 2014. Liu et al. (2014) found that both BC and BrC are present throughout the tropospheric column (<13 km) and the fraction of BrC relative to BC increased with altitude due to contributions from secondary sources. Other studies showed that long-range transported dust from Asia and the Sahara was present in cloud layers over California, especially in winter and spring (Fan et al. 2014, Pratt et al. 2009). Therefore, it is possible that aerosols may contribute to layers above the boundary layer, which might contribute to the differences between AERONET and surface-based estimates.

6.4.3 Comparison of BC and BrC Contributions

BC and BrC absorption partitioned from AERONET retrievals and surface measurements were more strongly correlated to each other in 2014 than in 2013, which is consistent with the stronger correlation found in the overall AAOD in 2014. BC correlations were stronger than that of BrC (**Figure 6-7**).

In 2014, AERONET $AAOD_{COL,BC}$ moderately correlates with the surface-based $AAOD_{BLH,BC}$ ($R^2 = 0.49$) (**Figure 6-7**b). The fitted slope of $AAOD_{COL,BC}$ to $AAOD_{BLH,BC}$ is 1.18 with y-intercept of 0.0040. The $AAOD_{COL,BrC}$ moderately correlates with the $AAOD_{BLH,BrC}$ ($R^2 = 0.29$); the fitted slope is 0.62 with a y-intercept of 0.0019 (**Figure 6-7**d). However, stronger correlations ($R^2 > 0.5$) are found between $AAOD_{COL,BrC}$ and AOD_{COL} (**Table 6-4**). In fact, AERONET AOD strongly correlated with all surface-based AAOD estimates, that is for both AAOD and partitioned results of BC and BrC. This suggests that the correlation might be propagated from the strong correlation of AERONET and surface-based AOD compared to AAOD, then to the partitioned BC and BrC, since the BC and BrC fractions are relatively invariant. There is also a weak-to-moderate correlation between surface-based estimates and BLH simulated by the WRF model, especially for the smallest factor $AAOD_{COL,BrC}$ ($R^2 = 0.33$), which suggests the correlation could also be caused by the scaling factor (**Figure 6-8**).

In 2013, the correlation between $AAOD_{COL,BC}$ and $AAOD_{BLH,BC}$ was $R^2 = 0.08$, and the correlation between $AAOD_{COL,BrC}$ and $AAOD_{BLH,BrC}$ was $R^2 = 0.13$. The low correlations are consistent with expectations since the correlation between AERONET measurements and surface-based estimates of AAOD was already low ($R^2 = 0.10$).

6.4.4 Sensitivity Analysis

BC contributed more to absorption in both 2013 and 2014. Results from AERONET and surface measurements show that BC absorbed generally two times higher than BrC (**Figure 6-9**). In 2014, AERONET measurements showed that BC contributed 72% of absorption at 440 nm—slightly higher than that from surface measurements (68%); in 2013, AERONET measurements showed BC contributed 67%—much lower than estimated from surface measurements (89%).

AERONET and surface measurements were made at slightly different wavelengths. Since BrC has an AAE higher than 1, the BrC contribution at 405 nm is likely higher than at 440 nm. The AERONET BrC absorption at 405 nm can be calculated as follows:

$$\mathrm{AAOD405_{COL,BrC}} = \mathrm{AAOD675_{COL,BrC}}\left(\frac{405}{675}\right)^{-\mathrm{AAE1_{BrC}}} = 1.46 \cdot \mathrm{AAOD440_{COL,BrC}} \qquad (11)$$

Here, the factor of 1.46 comes from assuming BrC AAE between 405 and 675 nm to be the same as the AAE between 440 and 675 nm (AAE1 = 4.55). This shows that at 405 nm, BrC absorption would be 46% higher than at 440 nm. For BC, the AAE is less than that of BrC and would increase 5% from 440 nm to 405 nm. However, because BC contributes at least 67% of absorption at 440 nm, the resulting change in BC or BrC contribution to absorption would be only 7%. The effect of BrC AAE changing rapidly between different wavelength pairs (Laskin et al. 2015), such that BrC AAE between 405 nm and 675 nm is substantially different from the AAE between 440 and 675 nm, was determined by setting the range of BrC AAE from 3 to 6 based on literature models (Arola et al. 2011; Sun, Biedermann and Bond 2007). The resulting change in BrC contribution to absorption was 4.6% to 10.6%, which we did not consider significant given the other uncertainties in the comparison. Therefore, the impact of the difference in the AERONET (405 nm) and surface (440 nm) wavelengths on the relative BC and BrC contributions was small.

The measurement uncertainty of AERONET AAOD depends on the corresponding AOD and SSA values. We used the sum-of-squares propagation of errors to calculate the uncertainty in AAOD from AERONET measurement uncertainties. The average AOD_{COL} at 440 nm = 0.16, uncertainty of AOD = 0.01, average SSA = 0.93, uncertainty of SSA = 0.07, and average AAOD = 0.011, the AAOD uncertainty value is therefore ±0.015, which means that for $AAOD_{COL}$ less than 0.015, uncertainty is larger than 100%. Although this uncertainty is large, the AERONET-AAE method is sensitive to AAE rather than AAOD. For 2013, the average of level 1.5M $AAOD_{COL}$ was 0.011 ± 0.0039. For 2014, the average $AAOD_{COL}$ was 0.011 ± 0.0044. If we replace the $AAOD_{COL}$ measurements below 0.015 with 0.0075 (mean of 0 and 0.015), the average AAOD would be 0.009 ± 0.0038 in 2013 and 0.010 ± 0.0045 in 2014. The difference between the average AAOD, with and without replacing measurements below the detection limit with half the detection limit value, was 18% in 2013 and 9% in 2014, showing that the values below detection had a greater effect on the average in 2013 than in 2014. The small difference between the average AAOD with and without replacing measurements below the detection limit suggests that the large AAOD uncertainty has a small impact on the estimated partitioning of BC and BrC absorption. However, uncertainty in the AAE values used in the AERONET-AAE method was substantial since the method depends on AAE exponentially. Sensitivity of the AERONET-AAE method to AAE values was examined by considering alternate values for the AAE of BC and BrC (**Table 6-5**). Using 2014 as an example, the sensitivity test showed that the BC contribution to absorption determined from AERONET could be as small as 51% or as large as 87%, with the AAE range for BC at 0.55 ± 0.24 and for BrC at 4.55 ± 2.01 (Bahadur et al. (2012). Using an even wider range of AAE values, and in particular an AAE of BC closer to unity (**Table 6-1**), the BC contribution could be as large as 100%. The relatively wide AAE range in **Table 6-2** did not impact the choice of AAE in our study, because the difference between AAE values derived from global AERONET spectral measurements and values reported by those experiments with different events, sources,

wavelengths and methods was expected. However, the sensitivity test in **Table 6-5** did illustrate the extent to which the AERONET-AAE method relies on accurate AAE measurements.

6.5 Conclusions

After comparing BC and BrC absorption from AERONET and surface measurements at wintertime Fresno, California, we found greater similarities in 2014 than in 2013, although both years had more BC (67% to 89%) than BrC (11% to 33%). In 2014, BC and BrC absorption calculated from AERONET (72% BC and 28% BrC) were quite similar to those of surface measurements (68% BC and 32% BrC). Surface absorption scaled to BLH moderately correlated (R^2 = 0.60) to column AERONET AAOD. Similarly, surface BC absorption scaled to BLH moderately correlated (R^2 = 0.49) to the BC fraction of AERONET AAOD. In contrast, in 2013, the AERONET AAOD from BC (67%) and BrC (33%) weakly correlated, showing a greater difference from surface-based BC (89%) and BrC (11%).

However, the comparisons between AERONET and surface measurements are only appropriate under limited conditions. Limitations included assuming that 1) the aerosol is well-mixed throughout the boundary layer, and 2) AOD and AAOD values in the boundary layer account for most of extinction and absorption in the air column. For example, in 2013, 36% of the clear-sky measurements were made when the BLH was lower than 200 m but in 2014, only 9% of measurements were made when the BLH was below 200 m. This combination of local meteorological patterns and timing of clear-sky conditions was largely the reason that surface measurements scaled by BLH correlate strongly or moderately with AERONET measurements at wintertime Fresno in 2014 but not in 2013. By removing measurements with BLH lower than 200 m, the average ratio of AERONET measurements to the surface-based estimates was actually closer to unity in 2013 than in 2014, even though the correlations in 2013 remained only moderate.

This work demonstrates that additional research using both AERONET and surface-based measurements is needed to assess the extent to which the AERONET-AAE method could be used to provide estimates of BC and BrC absorption across the nearly global AERONET network. Because AERONET retrievals are necessarily biased toward high aerosol loadings in current AERONET products, the fraction of overlapping AERONET times and surface measurements during almost 60 days of measurements is less than 5%. The small number of overlapping AERONET and surface measurements limit the representativeness of the comparisons of surface and column measurements. This limitation might be addressed by employing retrieval algorithms that are more accurate for low aerosol absorption measurements or not limited by clear-sky conditions.

6.6 Acknowledgments

The authors would like to acknowledge funding and support from California Air Resources Board (Agreement number: 13-330) and contract manager Dr. Nehzat Motallebi. The authors would also like to thank the Fontana Fire Department and the South Coast Air Quality Management District (SCAQMD) for Fontana site logistics, and UCD Extension for Fresno site logistics. The statements and conclusions in this paper are those of the researchers and not necessarily those of CARB. The authors also thank the team of WunderGround for providing open

resource METAR information. Surface data used in this manuscript for 2013 (from DISCOVER-AQ, California) are available at https://www-air.larc.nasa.gov/cgi-bin/ArcView/discover-aq.ca-2013 and for 2014 are available at https://doi.org/10.6075/J0VX0DF9.

6.7 Appendices

6.7.1 The AERONET-AAE Method

In this work, the term black carbon (BC) is used for what Bahadur et al. (2012) termed elemental carbon (EC); the term brown carbon (BrC) is used for what the Bahadur et al. (2012) termed organic carbon (OC). The AAE of BC was parameterized from 30 global AERONET sites where a majority of emissions come from urban fossil fuel (UF) or nonurban fossil fuel (NF). Similarly, the AAE of BrC was parameterized from 8 sites where a majority of emissions come from biomass-burning (BB). The AAE of dust was parameterized from 4 sites where a majority of emissions come from dust (DU). The name and location of AERONET sites used to obtain AOD and AAOD measurements are listed in **Table 6-1** (Bahadur et al. 2012).

Bahadur et al. (2012) selects dust-dominated measurements from DU sites based on the scattering angstrom exponent (SAE) and the ratio of AAEs at separate wavelengths found to be distinct with UF, NF, or BB sites (**Figure 6-1** and Appendices). The SAE is calculated from the same equation as AAE but uses scattering parameters [sca(λ1) and sca(λ2)] instead of absorption parameters:

$$\mathrm{SAE} = -\frac{\ln\left(\frac{\mathrm{sca}(\lambda 1)}{\mathrm{sca}(\lambda 2)}\right)}{\ln\left(\frac{\lambda 1}{\lambda 2}\right)} \quad (1)$$

SAE and AAE values for λ1 = 440 nm and λ2 = 675 nm are denoted as SAE1 and AAE1, respectively. The SAE and AAE values for λ1 = 675 nm and λ2 = 870 nm are denoted as SAE2 and AAE2. Russell et al. (2010) found that the SAE and AAE values associated with aerosols of crustal origin were different from those associated with combustion sources. Measurements with SAE1 < 0.5 are considered to be dust dominated. Pure dust AAE is calculated as the average of all dust-dominated measurements to give 2.20 ± 0.50 for AAE1 and 1.15 ± 0.50 for AAE2. Measurements with SAE1 > 1.2 or AAE2/AAE1 > 0.8 are considered to be dust free.

For dust-free measurements (i.e., carbon-dominated measurements), the average AAE1 ranged from 1.06 (NF) to 1.28 (BB), agreeing well with each other despite their global distribution. There are small variations, which can be explained by the relative amounts of BrC to BC. This result supports the assumption that the AAE of BC and BrC are inherent intrinsic properties (Bahadur et al. 2012). After averaging different percentiles of the total distribution frequency at different AERONET sites, the mean AAE1 value asymptotically converges to 0.55 ± 0.24, and the mean AAE2 value converges to 0.83 ± 0.40. Since BC has a lower AAE than both BrC and dust, the average low-end baseline for the AAE is related to pure BC. The BrC AAE is calculated from the remaining dust-free measurements, which are assumed to have measurable BrC absorption. The average AAE1 of BrC is calculated to be 4.55 ± 2.01. The AAE2 of BrC is not relevant since it is assumed to not absorb at 870 nm. These values are considered constant worldwide for each

absorbing component because they were independent of location, source, and aerosol concentration.

The AERONET-AAE method has been applied to a 2008 case study of 10 AERONET sites in California: 5 in the north (> 35° N) and 5 in the south (< 35° N) (**Table 6-6**). These sites provided 342 daily average quality-assured (level 2.0) measurements. The general agreement between resolved BC and BrC absorption and regional emission trends of BC, BrC, and dust recorded by CARB emission inventory indicates that the method provides a reasonable partition of each component.

The extent that the AERONET results (using the AERONET-AAE method) agreed with the surface measurements (using the combined MAC and TD method) may also be driven by the relatively small contributions from lensing (~10%), which were estimated from surface measurements during both years. A larger impact of lensing of up to a factor of two has been estimated by models and measured in lab experiments (Chung and Seinfeld 2005, Slowik et al. 2007, Jacobson 2001, Schnaiter et al. 2005, Cappa et al. 2012).

6.7.2 Overview of Local Meteorological Conditions

Figure 6-1 provides an overview of the comparison between AERONET measurements of AOD at 440 nm (AOD_{COL}) and surface measurements of extinction at 405 nm scaled to BLH (AOD_{BLH}). **Figure 6-1** shows that after scaling the surface measurements to BLH, AERONET AOD_{COL} and surface-based AOD_{BLH} are relatively similar. The assumptions of this calculation are discussed in Section 3.3. A high-fog period in 2014 from 7 to 13 January 2015 had a slightly warmer temperature (average 12°C), lower wind speed (0.8 m/s), and persistent fog (indicated by low visibility and high RH) from midnight through morning rush hours (Chen et al., 2018). This type of high-fog period was not seen in 2013.

More than 3000 surface measurements were collected for each year at 10-min intervals; the AERONET method collects measurements at 15-min intervals but most measurements are removed by cloud screening and quality control processes (Holben et al. 1998). There were two times more AERONET measurements in 2013 than in 2014 because more AOD measurements met the $AOD_{COL} > 0.1$ threshold. This reflects that the aerosol loadings were generally higher in 2013, which is consistent with higher absorption measured at surface. The surface absorption at 405 nm ($b_{abs}405$) was on average 22.3 ± 9.7 Mm^{-1} in 2013, which was substantially higher than the 2014 average of 14.7 ± 6.7 Mm^{-1}. In 2013, the surface measurements showed that for AERONET measurements from 8:00 to 16:00 BC contributed 81% and BrC contributed 19% of absorption at 405 nm; from 16:00 to 8:00, BC contributed 70% and BrC contributed 30% of absorption. In 2014, the surface measurements showed that from 8:00 to 16:00, BC contributed 73% and BrC contributed 27% of absorption at 405 nm; from 16:00 to 8:00, BC contributed 67% and BrC contributed 33% of absorption. The details can be found in Zhang et al. (2016) and Cappa et al. (Submitted).Young et al. (2016) suggest that 2013 high surface absorption was primarily driven by enhanced emissions of residential wood burning for domestic heating due to unusually cold temperatures (compared to a previous study at Fresno in 2010). This theory could help explain the observed difference in surface absorption in this work. The average temperature is similar for

both years (9.0 °C in 2013 and 9.1 °C in 2014) but the difference between daily maximum and minimum was 11.0 ± 3.8 °C in 2013, which is about 2 °C larger than that in 2014 (8.9 ± 3.1 °C). The lower minimum temperature during the nighttime in 2013 was consistent with the higher surface absorption peak related to residential burning.

Changes in temperature also influence changes in BLH. The most rapid change in temperature occurs from 9:00 AM to 11:00 AM, while the decrease in the afternoon is relatively slower. The most rapid change of BLH occurred from 10:00 AM to 12:00 PM for both years, about 1 hour later than that for temperature. Before the rapid increase, early morning BLH was less than 200 m; solar heating was weak during this period as the temperature was less than 10°C. Since there was less rising of warm air, convective mixing was weak before 11:00 AM, which means the aerosol distribution might be less uniform throughout the layer. From 11:00 AM to 3:00 PM, BLH were high and relatively constant (594 ± 330 m in 2013 and 616 ± 230 m in 2014), indicating surface measurements were quickly diluted through convective mixing in the boundary layer.

High RH (> 80%) increases the particle light scattering due to water uptake by a factor of 2 (Kotchenruther, Hobbs and Hegg 1999, Skupin et al. 2016). However, impact of high RH on particle absorption was variable. Fresno typically had high RH during winter: the period average RH was 72% in 2013 and 78% in 2014. However, because AERONET measures only during daytime, humidity impacts were reduced. The average RH during AERONET measurement times was lower (60% in 2013 and 68% in 2014), suggesting that the influence of relative humidity might be small except during the high-fog period (7 to 13 January 2015) of 2014. The high-fog period shows significantly lower visibility (3.0 ± 0.9) than the average in 2014 (9.1 ± 1.4 km) and 2013 (10.5 ± 1.7 km). Surface absorption during the high-fog period was higher (18.9 ± 4.4 Mm−1) than the average in 2014 (14.7 ± 6.7 Mm−1) but still lower than that in 2013 (22.3 ± 9.7 Mm−1). The high (> 80%) RH that persisted until 11:00 AM during the high-fog period indicates that the morning measurements could have been affected by the difference between ambient conditions in which AERONET measurements were made and the dry conditions (RH < 30%) in which surface measurements were collected. Using vertical profiles of sounding simulations from the EDAS model at 13:00 each day, we found that the average RH at the surface level (80 m above ground) was 45.76 ± 7.34% in 2013 and 50.51 ± 11.25% in 2014; and the average RH at average BLH (669.68 ± 358.81 m in 2013, 653.42 ± 229.40 m in 2014), RH measured 38.19 ± 17.80% in 2013 and 44.78 ± 20.30% in 2014. These observations indicate that the RH change in the boundary layer is small relative to the variability and is assumed to be constant.

Another set of measurements was collected from July 3, 2015, to July 25, 2015, in Fontana, CA, to understand the aerosol chemical and optical properties in the South Coast Air Basin (SoCAB) (Lee et al. 2017, Chen et al. 2018, Cappa et al. Submitted). The SoCAB has a highly photochemically active environment in the summertime with extensive internal SOA mixing (Docherty et al. 2008, Hayes et al. 2013). Unfortunately, the AERONET measurements near Fontana were not available due to an operation problem at the Rogers Dry Lake site and the large elevation difference (~1000 m) at Table Mountain site. The sites at CalTech and Santa Monica College, which are both more than 80 km away, are impacted by local emissions at Los Angeles

and by coastal influences that may not be representative of the Fontana conditions. In addition, measurements at those two sites during the study period mostly occurred between 5:00 PM and 7:00 PM (67% of total measurements) with no measurements collected between 10:00 AM and 2:00 PM. Measurements near sunset hours have a low angle of incidence, making them more uncertain. Therefore, comparing AERONET to surface measurements was not possible at Fontana.

6.7.3 WRF Model

The WRF model used in this study incorporated North American Regional Reanalysis (NARR) data with 32-km horizontal resolution and 3-h time resolution for initial and boundary conditions to simulate hourly meteorological fields with horizontal resolutions of 12 km and 4 km (Hu et al. 2014). For the operational definition of BLH, the model used the Yonsei University (YSU) scheme (Hong, Noh and Dudhia 2006, Banks et al. 2016). For eta levels, the model used 50 eta vertical levels up to the top pressure of 100 hPa from the surface; these eta levels were as follows: (1.000, 0.994, 0.987, 0.979, 0.97,0.96, 0.949, 0.937, 0.924, 0.909, 0.892, 0.873, 0.851, 0.826, 0.798, 0.768, 0.736, 0.702, 0.666, 0.629, 0.5915, 0.5536, 0.5153, 0.4773, 0.44, 0.404, 0.3695, 0.3375, 0.3085, 0.2845, 0.2645, 0.2465, 0.2305, 0.2165, 0.2035, 0.1915, 0.1792, 0.1667, 0.1539, 0.1407, 0.1272, 0.1134, 0.0995, 0.0855, 0.0713, 0.0571, 0.0429, 0.0287, 0.0145, 0.000).

6.7.4 Modeled Vertical Profile in 2013

The correlations suggest that, especially in 2013, surface measurements did not represent the average boundary layer properties or that the boundary layer does not account for most of the air column. An hourly averaged vertical profile of PM10 mass was predicted by the UCD/CIT airshed model from January 16 to 21, 2013 (**Figure 6-10**). The 9:00 AM profile reflects a more stable boundary layer that favors aerosol accumulation near the surface during the night as the ground cooled from below. Later in the day (9:00 AM to 3:00 PM), the BLH grows due to thermal convection by solar heating at surface which dilutes aerosols and mixes them higher in the atmosphere. When BLH starts to decrease (3:00 PM), PM10 mass once again starts to increase near the surface while the profile in the upper atmosphere becomes isolated from emissions and remains largely unchanged. At all times, some PM10 is mixed into the free troposphere above the BLH, which indicates that some extinction and absorption in the column were not included in the surface-based estimates by scaling surface measurements to BLH. The relative fraction of PM10 above BLH is larger in the morning, when BLH is low and the boundary layer accounts for a small fraction of the air column. This is consistent with the poorer agreement between AERONET and surface measurements scaled to BLH in the morning and the improved agreement for other portions of the day.

The profile of aerosols above the mixing height is largely driven by the presence of a second capping inversion related to the stagnation of a high-pressure system over the region during the study period. The fact that PM10 decreases slowly above the mixing height suggests this region is not well mixed. However, there is no evidence of a strong rising plume during January 16 to 21, 2013. The aerosols above the mixing height originate from upward mixing of aerosols in the boundary layer from the previous day or result from a weak capping inversion due to a low

temperature difference across the thin inversion layer during winter (Tavousi and Hussein 2016). Although well-mixed aerosols confined below BLH are supported by several studies and are frequently used as basic assumptions in models, this condition may not be universal (Reid et al. 2008, Liu et al. 2009, Zhang et al. 2015). Tan et al (2013) identified 7 outliers out of 118 predictions from their AOD model, which were over or under-predicted owing to non-uniformly loaded aerosols in the atmosphere at different altitude levels. Other studies at winter urban sites identified aerosol extinction at altitudes above the BLH with a similar profile as we find in this work (Satheesh, Vinoj and Moorthy 2006, He et al. 2008). The question of when, where, and how frequently the aerosol is lofted above the boundary layer requires additional research that is beyond the scope of this work.

6.7.5 Reconstructed AAOD at 870 nm

Figure 6-4 illustrates the comparison between reconstructed AAOD with AERONET retrievals at 870 nm. AAOD at 870 nm is reconstructed from BC absorption calculated using Equation (7) and AAE2 = 0.83 ± 0.40 between 675 and 870 nm from Bahadur et al. (2012). BrC is not considered here since it has been assumed to not absorb at long wavelengths. The average value of reconstructed AAOD is 95% of AERONET AAOD at 870 nm for 2 years This closely matches the 4% error underestimation at this wavelength shown in Bahadur et al. (2012).

6.7.6 Correlations in 2014

Although our results showed that AERONET retrievals and surface-based estimates correlated strongly or moderately to each other in 2014 but this correlation did not translate to accurate measurements or accurate partition methods. **Figure 6-4** illustrates strong correlations between AERONET AOD and all surface-based estimates ($R^2 > 0.64$, see **Table 6-4**), including AAOD and partitioned results of BC and BrC. Through the 2014 investigation, the BC fraction varied between 53% and 83%, the average being 72% (BrC fraction is complementary). Since the fractions of BC and BrC were relative constant, their correlation might be propagated from the strong correlation seen in the AOD comparison. In addition, the surface-based estimates also moderately correlated with BLH simulated by the WRF model. The correlation ranged from $R^2 = 0.26$ to $R^2 = 0.45$ after removing BLH measurements below 200 m. BLH simulations also have a weak to moderate correlation with AERONET measurements ($R^2 = 0.05$ to $R^2 = 0.27$), implying that multiplying surface measurements by BLH may have contributed to the correlations. **Figure 6-5**b showed that the high correlation observed in 2014 may have been largely governed by the few, high AOD measurements (~0.5 from AERONET and surface-based estimates); thus, the high dynamic range in AOD was likely responsible for the correlation. If the three high AOD measurements were removed, the correlation between AOD_{COL} and AOD_{BLH} dropped to $R^2 = 0.31$. However, when AOD_{COL} and AOD_{BLH} were correlated with BLH above 200 m, the correlation remained strong ($R^2 = 0.81$). The high dynamic range in AOD in 2014 might be part of the reason for its correlation and, consequently, its impact could have been emphasized by the small sample number.

6.8 References

Andreae, M. O. & A. Gelencser (2006) Black carbon or brown carbon? The nature of light-absorbing carbonaceous aerosols. *Atmospheric Chemistry and Physics,* 6**,** 3131-3148.

Andrews, E., J. A. Ogren, S. Kinne & B. Samset (2017) Comparison of AOD, AAOD and column single scattering albedo from AERONET retrievals and in situ profiling measurements. *Atmospheric Chemistry and Physics,* 17**,** 6041-6072.

Bahadur, R., P. S. Praveen, Y. Y. Xu & V. Ramanathan (2012) Solar absorption by elemental and brown carbon determined from spectral observations. *Proceedings of the National Academy of Sciences of the United States of America,* 109**,** 17366-17371.

Betha, R., L. M. Russell, C.-L. Chen, J. Liu, D. J. Price, Sanchez, K. J., S. Chen, L. A. K. Y., S. C. Collier, Q. Zhang, X. Zhang & C. D. Cappa. 2018. Larger submicron particles for emissions with residential burning in wintertime San Joaquin Valley (Fresno) than for vehicle combustion in summertime South Coast Air Basin (Fontana). Journal of Geophysical Research: Atmospheres.

Bond, T. C., S. J. Doherty, D. W. Fahey, P. M. Forster, T. Berntsen, B. J. DeAngelo, M. G. Flanner, S. Ghan, B. Karcher, D. Koch, S. Kinne, Y. Kondo, P. K. Quinn, M. C. Sarofim, M. G. Schultz, M. Schulz, C. Venkataraman, H. Zhang, S. Zhang, N. Bellouin, S. K. Guttikunda, P. K. Hopke, M. Z. Jacobson, J. W. Kaiser, Z. Klimont, U. Lohmann, J. P. Schwarz, D. Shindell, T. Storelvmo, S. G. Warren & C. S. Zender (2013) Bounding the role of black carbon in the climate system: A scientific assessment. *Journal of Geophysical Research-Atmospheres,* 118**,** 5380-5552.

Bond, T. C., D. G. Streets, K. F. Yarber, S. M. Nelson, J. H. Woo & Z. Klimont (2004) A technology-based global inventory of black and organic carbon emissions from combustion. *Journal of Geophysical Research-Atmospheres,* 109.

Cappa, C. D., T. B. Onasch, P. Massoli, D. R. Worsnop, T. S. Bates, E. S. Cross, P. Davidovits, J. Hakala, K. L. Hayden, B. T. Jobson, K. R. Kolesar, D. A. Lack, B. M. Lerner, S. M. Li, D. Mellon, I. Nuaaman, J. S. Olfert, T. Petaja, P. K. Quinn, C. Song, R. Subramanian, E. J. Williams & R. A. Zaveri (2012) Radiative Absorption Enhancements Due to the Mixing State of Atmospheric Black Carbon. *Science,* 337**,** 1078-1081.

Cappa, C. D., X. Zhang, L. M. Russell, S. Collier, A. K. Y. Lee, C.-L. Chen, R. Betha, S. Chen, J. Liu, D. J. Price, K. J. Sanchez, G. McMeeking, D. Worsnop, L. Williams, T. Onasch, J. P. D. Abbatt & Q. Zhang. Submitted. Black carbon mixing state and absorption by ambient black and brown carbon.

Chen, C.-L., S. Chen, L. M. Russell, J. Liu, D. J. Price, R. Betha, K. J. Sanchez, A. K. Y. Lee, L. Williams, S. C. Collier, Q. Zhang, A. Kumar, M. J. Kleeman, X. Zhang & C. D. Cappa. 2018. Organic aerosol particle chemical properties associated with residential burning and fog in wintertime San Joaquin Valley (Fresno) and with vehicle and firework emissions in summertime South Coast Air Basin (Fontana). Journal of Geophysical Research: Atmospheres.

Chow, J. C., L. W. A. Chen, J. G. Watson, D. H. Lowenthal, K. A. Magliano, K. Turkiewicz & D. E. Lehrman (2006) PM2.5 chemical composition and spatiotemporal variability during the California Regional PM10/PM2.5 Air Quality Study (CRPAQS). *Journal of Geophysical Research-Atmospheres,* 111.

Chu, S. H., J. W. Paisie & B. W. L. Jang (2004) PM data analysis - a comparison of two urban areas: Fresno and Atlanta. *Atmospheric Environment,* 38**,** 3155-3164.

Chung, C. E., V. Ramanathan & D. Decremer (2012) Observationally constrained estimates of carbonaceous aerosol radiative forcing. *Proceedings of the National Academy of Sciences of the United States of America,* 109**,** 11624-11629.

Clarke, A., C. McNaughton, V. Kapustin, Y. Shinozuka, S. Howell, J. Dibb, J. Zhou, B. Anderson, V. Brekhovskikh, H. Turner & M. Pinkerton (2007) Biomass burning and pollution aerosol over North America: Organic components and their influence on spectral optical properties and humidification response. *Journal of Geophysical Research-Atmospheres,* 112.

Coniglio, M. C., K. L. Elmore, J. S. Kain, S. J. Weiss, M. Xue & M. L. Weisman (2010) Evaluation of WRF Model Output for Severe Weather Forecasting from the 2008 NOAA Hazardous Weather Testbed Spring Experiment. *Weather and Forecasting,* 25**,** 408-427.

Cooper, D. I. & W. E. Eichinger (1994) STRUCTURE OF THE ATMOSPHERE IN AN URBAN PLANETARY BOUNDARY-LAYER FROM LIDAR AND RADIOSONDE OBSERVATIONS. *Journal of Geophysical Research-Atmospheres,* 99**,** 22937-22948.

Corrigan, C. E., G. C. Roberts, M. V. Ramana, D. Kim & V. Ramanathan (2008) Capturing vertical profiles of aerosols and black carbon over the Indian Ocean using autonomous unmanned aerial vehicles. *Atmospheric Chemistry and Physics,* 8**,** 737-747.

Devore, J. L. & K. N. Berk. 2012. *Modern mathematical statistics with applications*. New York ; London: Springer.

Dubovik, O., B. Holben, T. F. Eck, A. Smirnov, Y. J. Kaufman, M. D. King, D. Tanre & I. Slutsker (2002) Variability of absorption and optical properties of key aerosol types observed in worldwide locations. *Journal of the Atmospheric Sciences,* 59**,** 590-608.

Dubovik, O. & M. D. King (2000) A flexible inversion algorithm for retrieval of aerosol optical properties from Sun and sky radiance measurements. *Journal of Geophysical Research-Atmospheres,* 105**,** 20673-20696.

Dubovik, O., A. Smirnov, B. N. Holben, M. D. King, Y. J. Kaufman, T. F. Eck & I. Slutsker (2000) Accuracy assessments of aerosol optical properties retrieved from Aerosol Robotic Network (AERONET) Sun and sky radiance measurements. *Journal of Geophysical Research-Atmospheres,* 105**,** 9791-9806.

Esteve, A. R., J. A. Ogren, P. J. Sheridan, E. Andrews, B. N. Holben & M. P. Utrillas (2012) Sources of discrepancy between aerosol optical depth obtained from AERONET and in-situ aircraft profiles. *Atmospheric Chemistry and Physics,* 12**,** 2987-3003.

Fan, J., L. R. Leung, P. J. DeMott, J. M. Comstock, B. Singh, D. Rosenfeld, J. M. Tomlinson, A. White, K. A. Prather, P. Minnis, J. K. Ayers & Q. Min (2014) Aerosol impacts on California winter clouds and precipitation during CalWater 2011: local pollution versus long-range transported dust. *Atmospheric Chemistry and Physics,* 14**,** 81-101.

Feng, Y., V. Ramanathan & V. R. Kotamarthi (2013) Brown carbon: a significant atmospheric absorber of solar radiation? *Atmospheric Chemistry and Physics,* 13**,** 8607-8621.

Fuller, G. W., A. H. Tremper, T. D. Baker, K. E. Yttri & D. Butterfield (2014) Contribution of wood burning to PM10 in London. *Atmospheric Environment,* 87**,** 87-94.

Galchen, T., M. Xu & W. L. Eberhard (1992) ESTIMATIONS OF ATMOSPHERIC BOUNDARY-LAYER FLUXES AND OTHER TURBULENCE PARAMETERS FROM DOPPLER LIDAR DATA. *Journal of Geophysical Research-Atmospheres,* 97**,** 18409-18423.

Ge, X., A. Setyan, Y. Sun & Q. Zhang (2012) Primary and secondary organic aerosols in Fresno, California during wintertime: Results from high resolution aerosol mass spectrometry. *Journal of Geophysical Research-Atmospheres,* 117.

Gobbi, G. P., F. Barnaba & L. Ammannato (2004) The vertical distribution of aerosols, Saharan dust and cirrus clouds in Rome (Italy) in the year 2001. *Atmospheric Chemistry and Physics,* 4**,** 351-359.

Gorin, C. A., J. L. Collett, Jr. & P. Herckes (2006) Wood smoke contribution to winter aerosol in Fresno, CA. *Journal of the Air & Waste Management Association,* 56**,** 1584-1590.

Gyawali, M., W. P. Arnott, K. Lewis & H. Moosmüller (2009) In situ aerosol optics in Reno, NV, USA during and after the summer 2008 California wildfires and the influence of absorbing and non-absorbing organic coatings on spectral light absorption. *Atmospheric Chemistry and Physics,* 9**,** 8007-8015.

Herich, H., C. Hueglin & B. Buchmann (2011) A 2.5 year's source apportionment study of black carbon from wood burning and fossil fuel combustion at urban and rural sites in Switzerland. *Atmospheric Measurement Techniques,* 4**,** 1409-1420.

Hoffer, A., A. Gelencser, P. Guyon, G. Kiss, O. Schmid, G. P. Frank, P. Artaxo & M. O. Andreae (2006) Optical properties of humic-like substances (HULIS) in biomass-burning aerosols. *Atmospheric Chemistry and Physics,* 6**,** 3563-3570.

Holben, B. N., T. F. Eck, I. Slutsker, D. Tanre, J. P. Buis, A. Setzer, E. Vermote, J. A. Reagan, Y. J. Kaufman, T. Nakajima, F. Lavenu, I. Jankowiak & A. Smirnov (1998) AERONET - A federated instrument network and data archive for aerosol characterization. *Remote Sensing of Environment,* 66**,** 1-16.

Holben, B. N., D. Tanre, A. Smirnov, T. F. Eck, I. Slutsker, N. Abuhassan, W. W. Newcomb, J. S. Schafer, B. Chatenet, F. Lavenu, Y. J. Kaufman, J. V. Castle, A. Setzer, B. Markham, D. Clark, R. Frouin, R. Halthore, A. Karneli, N. T. O'Neill, C. Pietras, R. T. Pinker, K. Voss & G. Zibordi (2001) An emerging ground-based aerosol climatology: Aerosol optical depth from AERONET. *Journal of Geophysical Research-Atmospheres,* 106**,** 12067-12097.

Hu, J. L., H. L. Zhang, S. H. Chen, C. Wiedinmyer, F. Vandenberghe, Q. Ying & M. J. Kleeman (2014) Predicting Primary PM2.5 and PM0.1 Trace Composition for Epidemiological Studies in California. *Environmental Science & Technology,* 48**,** 4971-4979.

Jo, D. S., R. J. Park, S. Lee, S.-W. Kim & X. Zhang (2016) A global simulation of brown carbon: implications for photochemistry and direct radiative effect. *Atmospheric Chemistry and Physics,* 16**,** 3413-3432.

Johnson, B. T., S. Christopher, J. M. Haywood, S. R. Osborne, S. McFarlane, C. Hsu, C. Salustro & R. Kahn (2009) Measurements of aerosol properties from aircraft, satellite and ground-based remote sensing: A case-study from the Dust and Biomass-burning Experiment (DABEX). *Quarterly Journal of the Royal Meteorological Society,* 135**,** 922-934.

Kirchstetter, T. W., T. Novakov & P. V. Hobbs (2004) Evidence that the spectral dependence of light absorption by aerosols is affected by organic carbon. *Journal of Geophysical Research-Atmospheres,* 109.

Knox, A., G. J. Evans, J. R. Brook, X. Yao, C. H. Jeong, K. J. Godri, K. Sabaliauskas & J. G. Slowik (2009) Mass Absorption Cross-Section of Ambient Black Carbon Aerosol in Relation to Chemical Age. *Aerosol Science and Technology,* 43**,** 522-532.

Koch, D., M. Schulz, S. Kinne, C. McNaughton, J. R. Spackman, Y. Balkanski, S. Bauer, T. Berntsen, T. C. Bond, O. Boucher, M. Chin, A. Clarke, N. De Luca, F. Dentener, T. Diehl, O. Dubovik, R. Easter, D. W. Fahey, J. Feichter, D. Fillmore, S. Freitag, S. Ghan, P. Ginoux, S. Gong, L. Horowitz, T. Iversen, A. Kirkevag, Z. Klimont, Y. Kondo, M. Krol, X. Liu, R. Miller, V. Montanaro, N. Moteki, G. Myhre, J. E. Penner, J. Perlwitz, G. Pitari, S. Reddy, L. Sahu, H. Sakamoto, G. Schuster, J. P. Schwarz, O. Seland, P. Stier, N. Takegawa, T. Takemura, C. Textor, J. A. van Aardenne & Y. Zhao (2009) Evaluation of black carbon estimations in global aerosol models. *Atmospheric Chemistry and Physics,* 9**,** 9001-9026.

Lack, D. A. & J. M. Langridge (2013) On the attribution of black and brown carbon light absorption using the Angstrom exponent. *Atmospheric Chemistry and Physics,* 13**,** 10535-10543.

Lack, D. A., J. M. Langridge, R. Bahreini, C. D. Cappa, A. M. Middlebrook & J. P. Schwarz (2012) Brown carbon and internal mixing in biomass burning particles. *Proceedings of the National Academy of Sciences of the United States of America,* 109**,** 14802-14807.

Lack, D. A., P. K. Quinn, P. Massoli, T. S. Bates, D. Coffman, D. S. Covert, B. Sierau, S. Tucker, T. Baynard, E. Lovejoy, D. M. Murphy & A. R. Ravishankara (2009) Relative humidity dependence of light absorption by mineral dust after long-range atmospheric transport from the Sahara. *Geophysical Research Letters,* 36.

Laskin, A., J. Laskin & S. A. Nizkorodov (2015) Chemistry of Atmospheric Brown Carbon. *Chemical Reviews,* 115**,** 4335-4382.

Leahy, L. V., T. L. Anderson, T. F. Eck & R. W. Bergstrom (2007) A synthesis of single scattering albedo of biomass burning aerosol over southern Africa during SAFARI 2000. *Geophysical Research Letters,* 34.

Li, Z. Q., J. P. Guo, A. J. Ding, H. Liao, J. J. Liu, Y. L. Sun, T. J. Wang, H. W. Xue, H. S. Zhang & B. Zhu (2017) Aerosol and boundary-layer interactions and impact on air quality. *National Science Review,* 4**,** 810-833.

Lin, G. X., J. E. Penner, M. G. Flanner, S. Sillman, L. Xu & C. Zhou (2014) Radiative forcing of organic aerosol in the atmosphere and on snow: Effects of SOA and brown carbon. *Journal of Geophysical Research-Atmospheres,* 119**,** 7453-7476.

Liu, J. M., E. Scheuer, J. Dibb, L. D. Ziemba, K. L. Thornhill, B. E. Anderson, A. Wisthaler, T. Mikoviny, J. J. Devi, M. Bergin & R. J. Weber (2014) Brown carbon in the continental troposphere. *Geophysical Research Letters,* 41**,** 2191-2195.

Liu, P. F., C. S. Zhao, Q. Zhang, Z. Z. Deng, M. Y. Huang, X. C. Ma & X. X. Tie (2009) Aircraft study of aerosol vertical distributions over Beijing and their optical properties. *Tellus Series B-Chemical and Physical Meteorology,* 61**,** 756-767.

Lurmann, F. W., S. G. Brown, M. C. McCarthy & P. T. Roberts (2006) Processes Influencing Secondary Aerosol Formation in the San Joaquin Valley during Winter. *Journal of the Air & Waste Management Association,* 56**,** 1679-1693.

Magi, B. I., P. V. Hobbs, T. W. Kirchstetter, T. Novakov, D. A. Hegg, S. Gao, J. Redemann & B. Schmid (2005) Aerosol properties and chemical apportionment of aerosol optical depth at locations off the US east coast in July and August 2001. *Journal of the Atmospheric Sciences,* 62**,** 919-933.

Mallet, M., R. Van Dingenen, J. C. Roger, S. Despiau & H. Cachier (2005) In situ airborne measurements of aerosol optical properties during photochemical pollution events. *Journal of Geophysical Research-Atmospheres,* 110.

Molders, N. & G. Kramm (2010) A case study on wintertime inversions in Interior Alaska with WRF. *Atmospheric Research,* 95**,** 314-332.

Moosmuller, H., R. K. Chakrabarty & W. P. Arnott (2009) Aerosol light absorption and its measurement: A review. *Journal of Quantitative Spectroscopy & Radiative Transfer,* 110**,** 844-878.

Myhre, G., B. H. Samset, M. Schulz, Y. Balkanski, S. Bauer, T. K. Berntsen, H. Bian, N. Bellouin, M. Chin, T. Diehl, R. C. Easter, J. Feichter, S. J. Ghan, D. Hauglustaine, T. Iversen, S. Kinne, A. Kirkevag, J. F. Lamarque, G. Lin, X. Liu, M. T. Lund, G. Luo, X. Ma, T. van Noije, J. E. Penner, P. J. Rasch, A. Ruiz, O. Seland, R. B. Skeie, P. Stier, T. Takemura, K. Tsigaridis, P. Wang, Z. Wang, L. Xu, H. Yu, F. Yu, J. H. Yoon, K. Zhang, H. Zhang & C. Zhou (2013) Radiative

forcing of the direct aerosol effect from AeroCom Phase II simulations. *Atmospheric Chemistry and Physics,* 13**,** 1853-1877.

Nakayama, T., Y. Ikeda, Y. Sawada, Y. Setoguchi, S. Ogawa, K. Kawana, M. Mochida, F. Ikemori, K. Matsumoto & Y. Matsumi (2014) Properties of light-absorbing aerosols in the Nagoya urban area, Japan, in August 2011 and January 2012: Contributions of brown carbon and lensing effect. *Journal of Geophysical Research-Atmospheres,* 119**,** 12721-12739.

Ngo, M. A., K. E. Pinkerton, S. Freeland, M. Geller, W. Ham, S. Cliff, L. E. Hopkins, M. J. Kleeman, U. P. Kodavanti, E. Meharg, L. Plummer, J. J. Recendez, M. B. Schenker, C. Sioutas, S. Smiley-Jewell, C. Haas, J. Gutstein & A. S. Wexler (2010) Airborne particles in the San Joaquin Valley may affect human health. *California Agriculture,* 64**,** 12-16.

Olson, M. R., M. V. Garcia, M. A. Robinson, P. Van Rooy, M. A. Dietenberger, M. Bergin & J. J. Schauer (2015) Investigation of black and brown carbon multiple-wavelength-dependent light absorption from biomass and fossil fuel combustion source emissions. *Journal of Geophysical Research-Atmospheres,* 120**,** 6682-6697.

Osborne, S. R., B. T. Johnson, J. M. Haywood, A. J. Baran, M. A. J. Harrison & C. L. McConnell (2008) Physical and optical properties of mineral dust aerosol during the Dust and Biomass-burning Experiment. *Journal of Geophysical Research-Atmospheres,* 113.

Parworth, C. L., D. E. Young, H. Kim, X. L. Zhang, C. D. Cappa, S. Collier & Q. Zhang (2017) Wintertime water-soluble aerosol composition and particle water content in Fresno, California. *Journal of Geophysical Research-Atmospheres,* 122**,** 3155-3170.

Patterson, E. M. (1981) OPTICAL-PROPERTIES OF THE CRUSTAL AEROSOL - RELATION TO CHEMICAL AND PHYSICAL CHARACTERISTICS. *Journal of Geophysical Research-Oceans,* 86**,** 3236-3246.

Peng, J. F., M. Hu, S. Guo, Z. F. Du, J. Zheng, D. J. Shang, M. L. Zamora, L. M. Zeng, M. Shao, Y. S. Wu, Y. Wang, C. R. Glen, D. R. Collins, M. J. Molina & R. Y. Zhang (2016) Markedly enhanced absorption and direct radiative forcing of black carbon under polluted urban environments. *Proceedings of the National Academy of Sciences of the United States of America,* 113**,** 4266-4271.

Prabhakar, G., C. L. Parworth, X. L. Zhang, H. Kim, D. E. Young, A. J. Beyersdorf, L. D. Ziemba, J. B. Nowak, T. H. Bertram, I. C. Faloona, Q. Zhang & C. D. Cappa (2017) Observational assessment of the role of nocturnal residual-layer chemistry in determining daytime surface particulate nitrate concentrations. *Atmospheric Chemistry and Physics,* 17**,** 14747-14770.

Pratt, K. A., P. J. DeMott, J. R. French, Z. Wang, D. L. Westphal, A. J. Heymsfield, C. H. Twohy, A. J. Prenni & K. A. Prather (2009) In situ detection of biological particles in cloud ice-crystals. *Nature Geoscience,* 2**,** 397-400.

Pringle, K. J., H. Tost, A. Pozzer, U. Poschl & J. Lelieveld (2010) Global distribution of the effective aerosol hygroscopicity parameter for CCN activation. *Atmospheric Chemistry and Physics,* 10**,** 5241-5255.

Pusede, S. E., K. C. Duffey, A. A. Shusterman, A. Saleh, J. L. Laughner, P. J. Wooldridge, Q. Zhang, C. L. Parworth, H. Kim, S. L. Capps, L. C. Valin, C. D. Cappa, A. Fried, J. Walega, J. B. Nowak, A. J. Weinheimer, R. M. Hoff, T. A. Berkoff, A. J. Beyersdorf, J. Olson, J. H. Crawford & R. C. Cohen (2016) On the effectiveness of nitrogen oxide reductions as a control over ammonium nitrate aerosol. *Atmospheric Chemistry and Physics,* 16**,** 2575-2596.

Russell, P. B., R. W. Bergstrom, Y. Shinozuka, A. D. Clarke, P. F. DeCarlo, J. L. Jimenez, J. M. Livingston, J. Redemann, O. Dubovik & A. Strawa (2010) Absorption Angstrom Exponent in

AERONET and related data as an indicator of aerosol composition. *Atmospheric Chemistry and Physics,* 10**,** 1155-1169.

Saathoff, H., O. Mohler, U. Schurath, S. Kamm, B. Dippel & D. Mihelcic (2003) The AIDA soot aerosol characterisation campaign 1999. *Journal of Aerosol Science,* 34**,** 1277-1296.

Saleh, R., C. J. Hennigan, G. R. McMeeking, W. K. Chuang, E. S. Robinson, H. Coe, N. M. Donahue & A. L. Robinson (2013) Absorptivity of brown carbon in fresh and photo-chemically aged biomass-burning emissions. *Atmospheric Chemistry and Physics,* 13**,** 7683-7693.

Saleh, R., M. Marks, J. Heo, P. J. Adams, N. M. Donahue & A. L. Robinson (2015) Contribution of brown carbon and lensing to the direct radiative effect of carbonaceous aerosols from biomass and biofuel burning emissions. *Journal of Geophysical Research-Atmospheres,* 120**,** 10285-10296.

Sandradewi, J., A. S. H. Prévôt, E. Weingartner, R. Schmidhauser, M. Gysel & U. Baltensperger (2008) A study of wood burning and traffic aerosols in an Alpine valley using a multi-wavelength Aethalometer. *Atmospheric Environment,* 42**,** 101-112.

Schafer, J. S., T. F. Eck, B. N. Holben, K. L. Thornhill, B. E. Anderson, A. Sinyuk, D. M. Giles, E. L. Winstead, L. D. Ziemba, A. J. Beyersdorf, P. R. Kenny, A. Smirnov & I. Slutsker (2014) Intercomparison of aerosol single-scattering albedo derived from AERONET surface radiometers and LARGE in situ aircraft profiles during the 2011 DRAGON-MD and DISCOVER-AQ experiments. *Journal of Geophysical Research-Atmospheres,* 119**,** 7439-7452.

Schnaiter, M., H. Horvath, O. Mohler, K. H. Naumann, H. Saathoff & O. W. Schock (2003) UV-VIS-NIR spectral optical properties of soot and soot-containing aerosols. *Journal of Aerosol Science,* 34**,** 1421-1444.

Schnaiter, M., C. Linke, O. Mohler, K. H. Naumann, H. Saathoff, R. Wagner, U. Schurath & B. Wehner (2005) Absorption amplification of black carbon internally mixed with secondary organic aerosol. *Journal of Geophysical Research-Atmospheres,* 110.

Shamjad, P. M., S. N. Tripathi, N. M. Thamban & H. Vreeland (2016) Refractive Index and Absorption Attribution of Highly Absorbing Brown Carbon Aerosols from an Urban Indian City-Kanpur. *Scientific Reports,* 6.

Shiraiwa, M., Y. Kondo, T. Iwamoto & K. Kita (2010) Amplification of Light Absorption of Black Carbon by Organic Coating. *Aerosol Science and Technology,* 44**,** 46-54.

Smirnov, A., B. N. Holben, T. F. Eck, O. Dubovik & I. Slutsker (2000) Cloud-screening and quality control algorithms for the AERONET database. *Remote Sensing of Environment,* 73**,** 337-349.

Turkiewicz, K., K. Magliano & T. Najita (2006) Comparison of two winter air quality episodes during the California Regional Particulate Air Quality Study. *Journal of the Air & Waste Management Association,* 56**,** 467-473.

Wang, Q. Q., D. J. Jacob, J. R. Spackman, A. E. Perring, J. P. Schwarz, N. Moteki, E. A. Marais, C. Ge, J. Wang & S. R. H. Barrett (2014a) Global budget and radiative forcing of black carbon aerosol: Constraints from pole-to-pole (HIPPO) observations across the Pacific. *Journal of Geophysical Research-Atmospheres,* 119**,** 195-206.

Wang, X., C. L. Heald, D. A. Ridley, J. P. Schwarz, J. R. Spackman, A. E. Perring, H. Coe, D. Liu & A. D. Clarke (2014b) Exploiting simultaneous observational constraints on mass and absorption to estimate the global direct radiative forcing of black carbon and brown carbon. *Atmospheric Chemistry and Physics,* 14**,** 10989-11010.

Wang, X., C. L. Heald, A. J. Sedlacek, S. S. de Sa, S. T. Martin, M. L. Alexander, T. B. Watson, A. C. Aiken, S. R. Springston & P. Artaxo (2016) Deriving brown carbon from multiwavelength

absorption measurements: method and application to AERONET and Aethalometer observations. *Atmospheric Chemistry and Physics,* 16**,** 12733-12752.

Winker, D. M., J. L. Tackett, B. J. Getzewich, Z. Liu, M. A. Vaughan & R. R. Rogers (2013) The global 3-D distribution of tropospheric aerosols as characterized by CALIOP. *Atmospheric Chemistry and Physics,* 13**,** 3345-3361.

Yang, M., S. G. Howell, J. Zhuang & B. J. Huebert (2009) Attribution of aerosol light absorption to black carbon, brown carbon, and dust in China - interpretations of atmospheric measurements during EAST-AIRE. *Atmospheric Chemistry and Physics,* 9**,** 2035-2050.

Young, D. E., H. Kim, C. Parworth, S. Zhou, X. L. Zhang, C. D. Cappa, R. Seco, S. Kim & Q. Zhang (2016) Influences of emission sources and meteorology on aerosol chemistry in a polluted urban environment: results from DISCOVER-AQ California. *Atmospheric Chemistry and Physics,* 16**,** 5427-5451.

Yuan, J. F., X. F. Huang, L. M. Cao, J. Cui, Q. Zhu, C. N. Huang, Z. J. Lan & L. Y. He (2016) Light absorption of brown carbon aerosol in the PRD region of China. *Atmospheric Chemistry and Physics,* 16**,** 1433-1443.

Zhang, X. L., H. Kim, C. L. Parworth, D. E. Young, Q. Zhang, A. R. Metcalf & C. D. Cappa (2016) Optical Properties of Wintertime Aerosols from Residential Wood Burning in Fresno, CA: Results from DISCOVER-AQ 2013. *Environmental Science & Technology,* 50**,** 1681-1690.

Zhang, X. L., Y. H. Lin, J. D. Surratt & R. J. Weber (2013) Sources, Composition and Absorption Angstrom Exponent of Light-absorbing Organic Components in Aerosol Extracts from the Los Angeles Basin. *Environmental Science & Technology,* 47**,** 3685-3693.

6.9 Tables

Table 6-1. Literature review comparing AAE values to BC and BrC from previous studies.

	Comparable to BC		Comparable to BrC	
Citation	Measured Constituents	AAE (λ in nm)	Measured Constituents	AAE (λ in nm)
(Cappa et al., Submitted)	BC Fresno 2014	0.89 (405 – 532)	BBOA Fresno 2014	2.37 (405 – 532)
(Yuan et al. 2016)	BC PRD, China	0.82 – 1.02 (405 – 781)	BrC PRD, China	1.7 – 6.2 (405 – 781)
(Olson et al. 2015)	BC (assumption)	1.0 (370 – 880)	BrC Multiple sources	6.9 – <1.0 (370 – 880)
(Fuller et al. 2014)	BC London	0.96 (370 – 880)		
(Lack and Langridge 2013)	BC Varied	0.8 - 1.4 (467 – 660)		
(Bahadur et al. 2012)	BC/soot/EC AERONET Sites	0.55 ± 0.24 (440 – 675)	OC AERONET Sites	4.55 ± 2.01 (440 – 675)
(Lack et al. 2012)	BC Canyon fire	1.1 - 1.4 (404 – 658)	POM Canyon fire	1.25 - 2.3 (404 – 658)
(Gyawali et al. 2009)	BC Reno, USA	1.0 - 1.1 (405 – 870)		
(Yang et al. 2009)	BC (assumption)	1.0 (470 – 660)	BrC Biomass burning	1.53 ± 0.10 (470 – 660)
(Sandradewi et al. 2008)	BC (assumption)	1.0 (470 – 950)	OC Switzerland	1.8 - 1.9 (470 – 950)
(Hoffer et al. 2006)	Diesel Soot LBA-SMOCC	1.056 (300 – 700)	HULIS LBA-SMOCC	6 - 7 (300 – 700)
(Kirchstetter, Novakov and Hobbs 2004)	BC SAFARI, LBNL	0.6 - 1.3 Varied	OC Urban Vehicle	4.69 (350 – 550)
(Schnaiter et al. 2003)	Diesel Soot AIDA	1.1 (450 – 700)		

Table 6-2. AERONET quality assurance criteria at each level with corresponding data availability in 2013 and 2014.

	Major Criteria*	Measurements in 2013 (Time%)	Measurements in 2014 (Time%)
Level 1.5	Automatic cloud screening	125 (4.7%)	69 (2.9%)
Level 1.5M	Automatic cloud screening AOD > 0.1 SSA440 within 95% confidence intervals for the mean of a log-normal distribution	115 (4.2%)	48 (2.0%)
Level 2.0	Criteria for level 1.5 AOD > 0.4	0 (0%)	3 (0.12%)

*: The complete quality assurance criteria for level 1.5 and level 2.0 can be found in Holben et al. [2006]

Table 6-3. Literature review of BC and BrC absorption contributions from previous studies.

	Citation	BC Absorption (λ nm)	BrC Absorption (λ nm)	Notes
Column (AERONET) Measurements	This work Fresno 2014	72% (440)	28% (440)	
	This work Fresno 2013	67% (440)	33% (440)	
	(Wang et al. 2016) Global AERONET sites	60 – 94% (440)	6 – 40% (440)	Dust not included in analysis
	(Bahadur et al. 2012) California AERONET sites	56% (440)	28% (440)	Additional 16% contribution from dust
Surface Measurements	This work Fresno 2014	68% (405)	32% (405)	BrC absorption includes contribution from lensing
	This work Fresno 2013	89% (405)	11% (405)	BrC absorption includes contribution from lensing
	(Shamjad et al. 2016) Kanpur, India Dec-2014 to Feb-2015	71.5% (405)	28.5% (405)	BrC absorption includes contribution from lensing
	(Yuan et al. 2016) PRD, China 2014	88.3 ± 5% (405)	11.7 ± 5% (405)	BrC absorption includes contribution from lensing
	(Lack et al. 2012) Four-Mile Canyon fire 2010	54% ± 16% (404)	27 ± 15% (404)	Additional 19 ± 8% from lensing
	(Yang et al. 2009) EAST-AIRE	85% (470)	15% (470)	
	(Hoffer et al. 2006) LBA-SMOCC 2002	50% - 65% (300)	35% - 50% (300)	

Table 6-4. Correlation coefficients for linear relationships between AERONET measurements, surface measurements, BLH, and surface-based column estimates. Values were calculated using measurements or estimates corresponding to time resolution. Values in parentheses were calculated using measurements with BLH above 200 m.

2013 Fresno		AERONET Measurements and Partitioned Results				Model
Correlation Coefficient R^2		AOD_{COL}	$AAOD_{COL}$	$AAOD_{COL,BC}$	$AAOD_{COL,BrC}$	BLH
Model	BLH	0.00(0.02)	0.01(0.11)	0.04(0.00)	0.00(-0.03)	--
Surface Measure-ments	$b_{ext}405$	**0.07(0.26)**	0.00(0.19)	0.05(0.05)	0.09(0.35)	-0.13 (0.01)
	$b_{abs}405$	0.03(0.11)	**0.03(0.19)**	0.00(0.05)	0.07(0.35)	-0.46 (0.00)
	$b_{abs}405_{BC}$	0.04(0.14)	0.00(0.24)	**0.03(0.10)**	0.07(0.35)	-0.36 (0.00)
	$b_{abs}405_{BrC}$	0.01(0.02)	0.00(0.04)	-0.01(0.00)	**0.04(0.19)**	-0.29 (-0.03)
Column Estimates	AOD_{BLH}	**0.08(0.55)**	0.12(0.34)	0.05(0.20)	0.18(0.39)	0.05 (0.01)
	$AAOD_{BLH}$	0.13(0.24)	**0.10(0.25)**	0.02(0.15)	0.17(0.29)	0.12 (0.00)
	$AAOD_{BLH,BC}$	0.12(0.22)	0.07(0.22)	**0.08(0.20)**	0.07(0.17)	0.29 (0.00)
	$AAOD_{BLH,BrC}$	0.02(0.04)	0.01(0.04)	0.00(0.00)	**0.13 (0.18)**	-0.07 (-0.03)
2014 Fresno		AERONET Measurements and Partitioned Results				Model
Correlation Coefficient R^2		AOD_{COL}	$AAOD_{COL}$	$AAOD_{COL,BC}$	$AAOD_{COL,BrC}$	BLH
Model	BLH	0.21(0.27)	0.10(0.13)	0.13(0.16)	0.03(0.05)	--
Surface Measure-ments	$b_{ext}405$	**0.56(0.56)**	0.42(0.24)	0.34(0.13)	0.67(0.40)	-0.00 (0.17)
	$b_{abs}405$	0.16(0.14)	**0.31(0.27)**	0.17(0.07)	0.50(0.35)	-0.18 (-0.13)
	$b_{abs}405_{BC}$	0.12(0.11)	0.23(0.13)	**0.11(0.05)**	0.42(0.30)	-0.25 (-0.18)
	$b_{abs}405_{BrC}$	0.64(0.65)	0.54(0.40)	0.40(0.28)	**0.59(0.49)**	0.02 (0.06)
Column Estimates	AOD_{BLH}	**0.81(0.89)**	0.38(0.42)	0.40(0.38)	0.22(0.35)	0.18 (0.36)
	$AAOD_{BLH}$	0.64(0.84)	**0.60(0.60)**	0.42(0.45)	0.25(0.47)	0.23 (0.26)
	$AAOD_{BLH,BC}$	0.64(0.82)	0.39(0.51)	**0.49(0.49)**	0.25(0.46)	0.28 (0.32)
	$AAOD_{BLH,BrC}$	0.70(0.84)	0.35(0.41)	0.42(0.40)	**0.29(0.28)**	**0.33 (0.45)**

Table 6-5. Uncertainty (% Change) in BC absorption (%) calculated using the AERONET-AAE method with a variation of AAE values.

	AAE BC (440-675 nm)	AAE BrC (440-675 nm)	BC contribution at 440 nm	BC% Change
Reference AAE	0.55	4.55	72%	0
Sensitivity Test of BC Values	**0.67**	4.55	76%	6%
	0.79	4.55	81%	13%
Sensitivity Test of BrC Values	0.55	**2.55**	51%	-29%
	0.55	**3.55**	60%	-17%
	0.55	**5.55**	80%	11%
	0.55	**6.55**	87%	21%
Sensitivity Test of Both Values	**0.89**	**2.37**	102%	42%
	1.0	**4.4**	91%	26%
	1.4	**7**	104%	44%

*: BC% change is defined as percentage change of BC absorption relative to that derived from the reference AAE used in this work.

Table 6-6. AERONET sites used in Bahadur's California case study.

California Case Study in 2008	AERONET Sites	Valid SSA retrievals
North California (>35 N)	Fresno Monterey Moss Landing Trinidad Head UCSB	342 in total
South Carlifornia (<35 N)	La Jolla UCLA San Nicholas Table Mountain Jet Propulsion Laboratory	

6.10 Figures

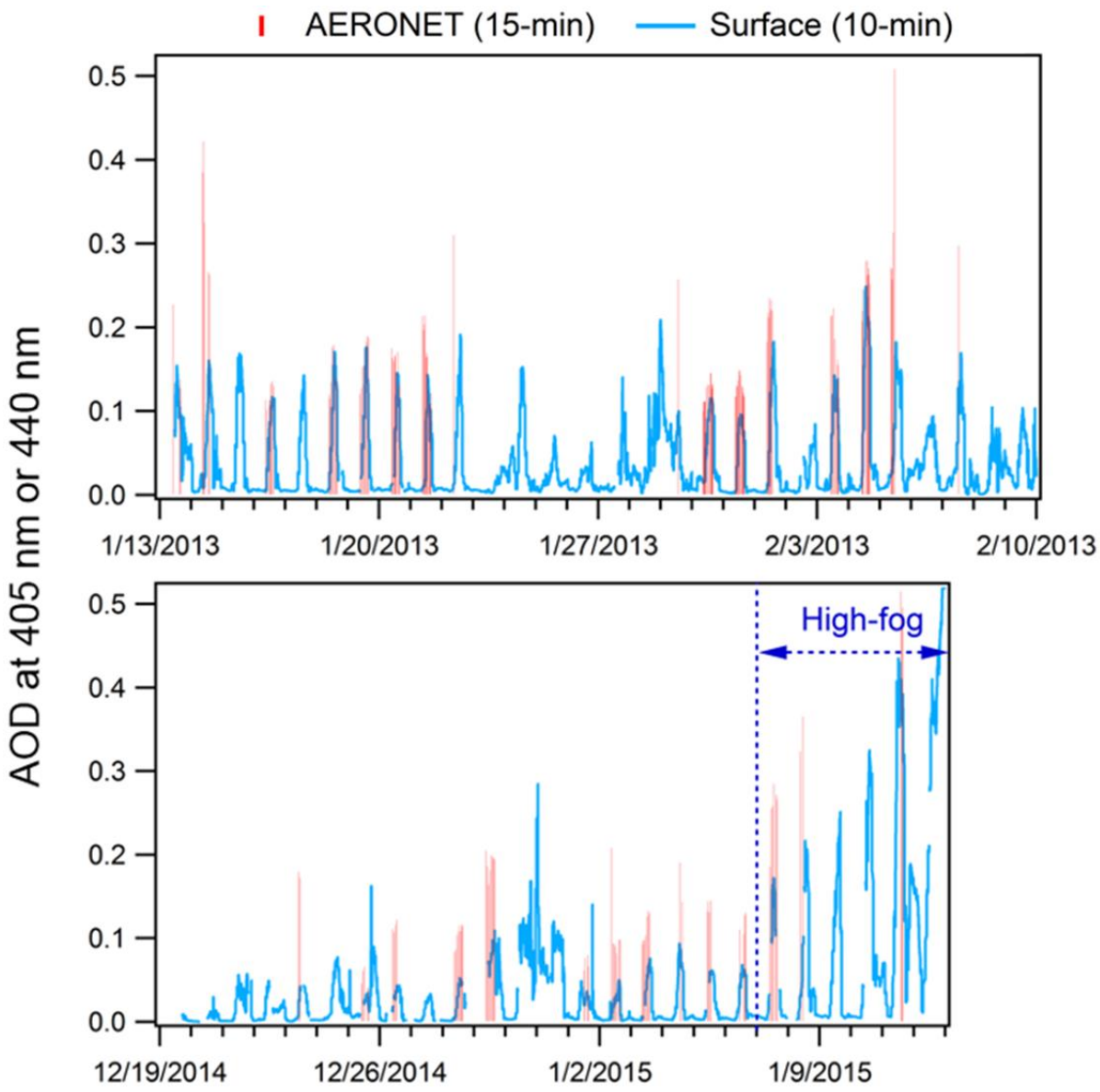

Figure 6-1. Time series of AERONET AOD measurements at 440 nm and surface-based estimates of extinction within the BLH at 405 nm (b_{abs}405 x BLH) in 2013 (above) and 2014 (below). The period from 7 to 13 January 2015 is labeled high-fog days for high RH (persistently at or above 90% from 22:00 to 9:00) and low visibility (1.6 - 3.2 km from 22:00 to 9:00).

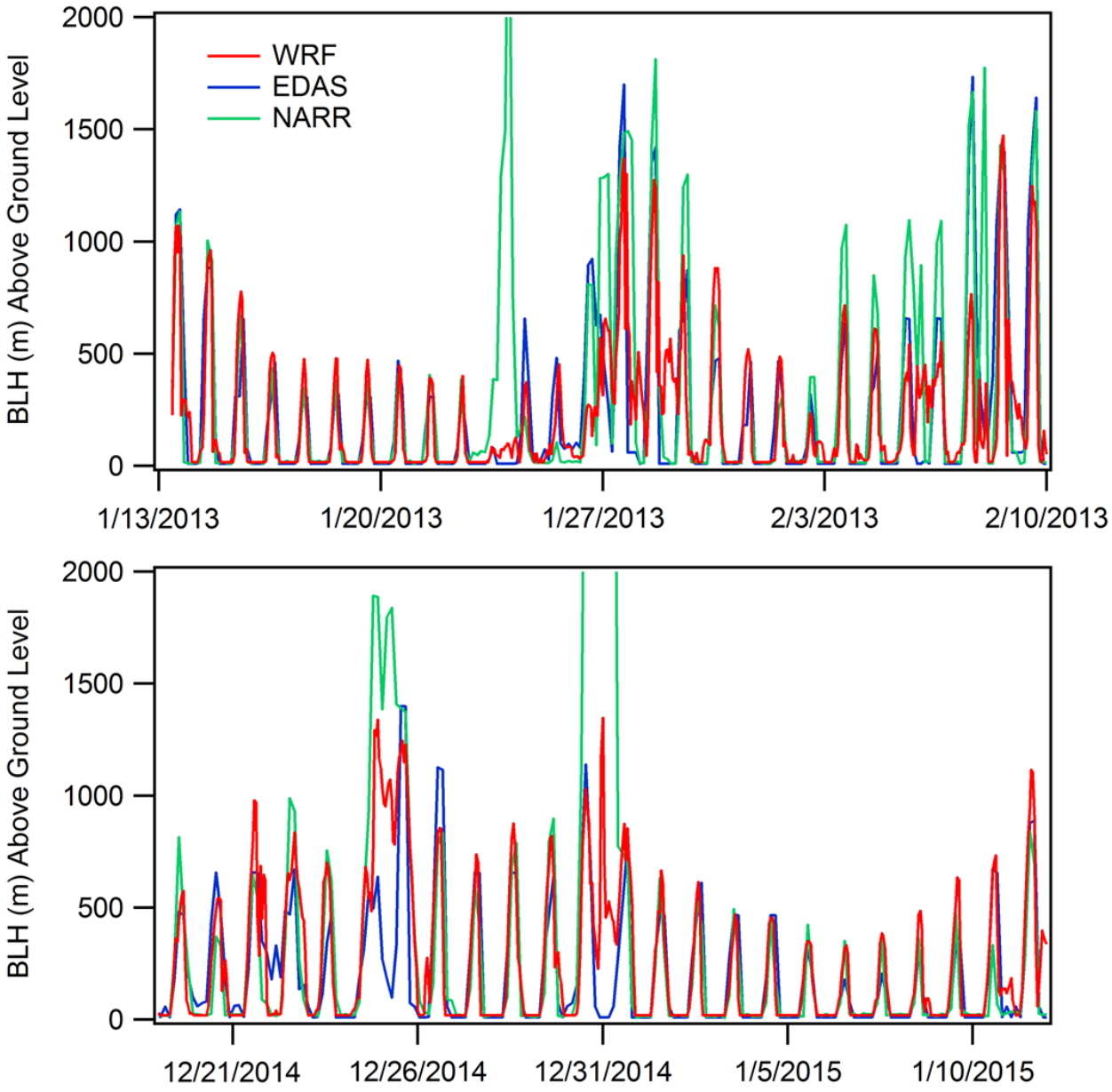

Figure 6-2. BLH (m) simulations compared among the WRF model, EDAS model, and NARR model at Fresno in 2013 and 2014.

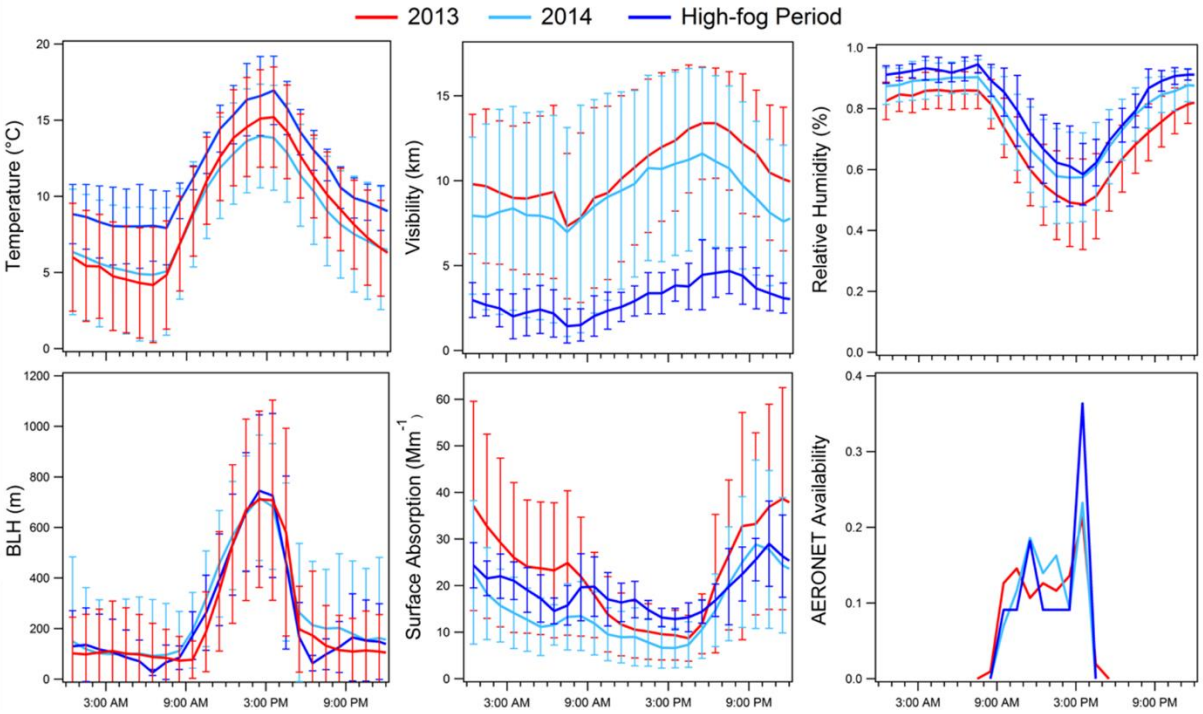

Figure 6-3. Hourly average of meteorological conditions (temperature, relative humidity, visibility, and BLH), surface absorption ($b_{abs}405$) and AERONET measurements availability observed in 2013 and 2014. AERONET measurements availability is defined as a fraction of the total account of measurements. Error bars show the standard deviation of the hourly average.

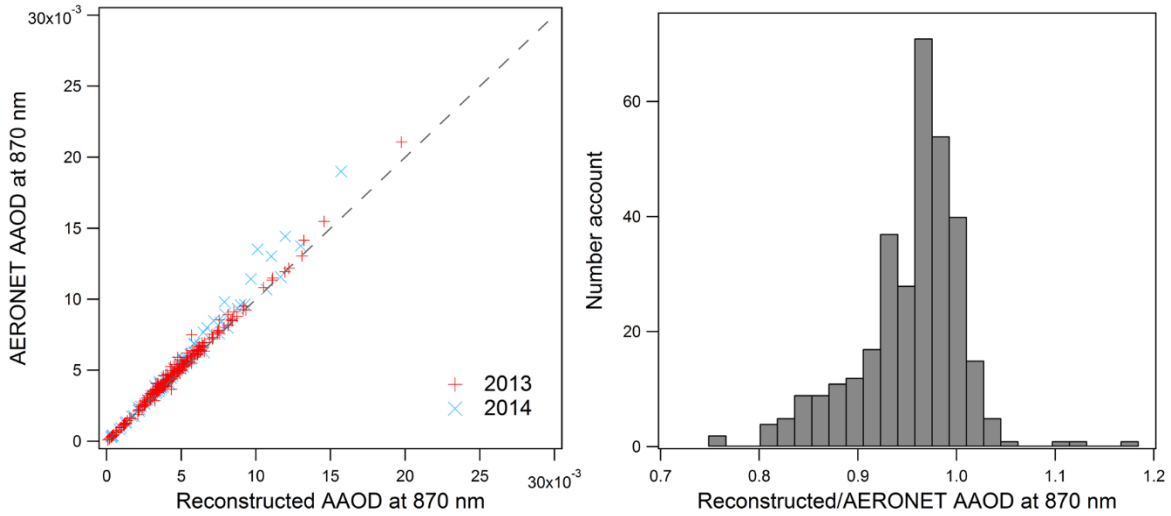

Figure 6-4. Comparison of AERONET AAOD at 870 nm with AAOD reconstructed from partitioned BC and BrC using AERONET AAOD at 440 nm and 675 nm, and AAE from Bahadur et al. (2012). Left plot shows a scatter plot of AERONET vs. reconstructed AAOD in 2013 and 2014. Right plot shows a histogram of the ratio.

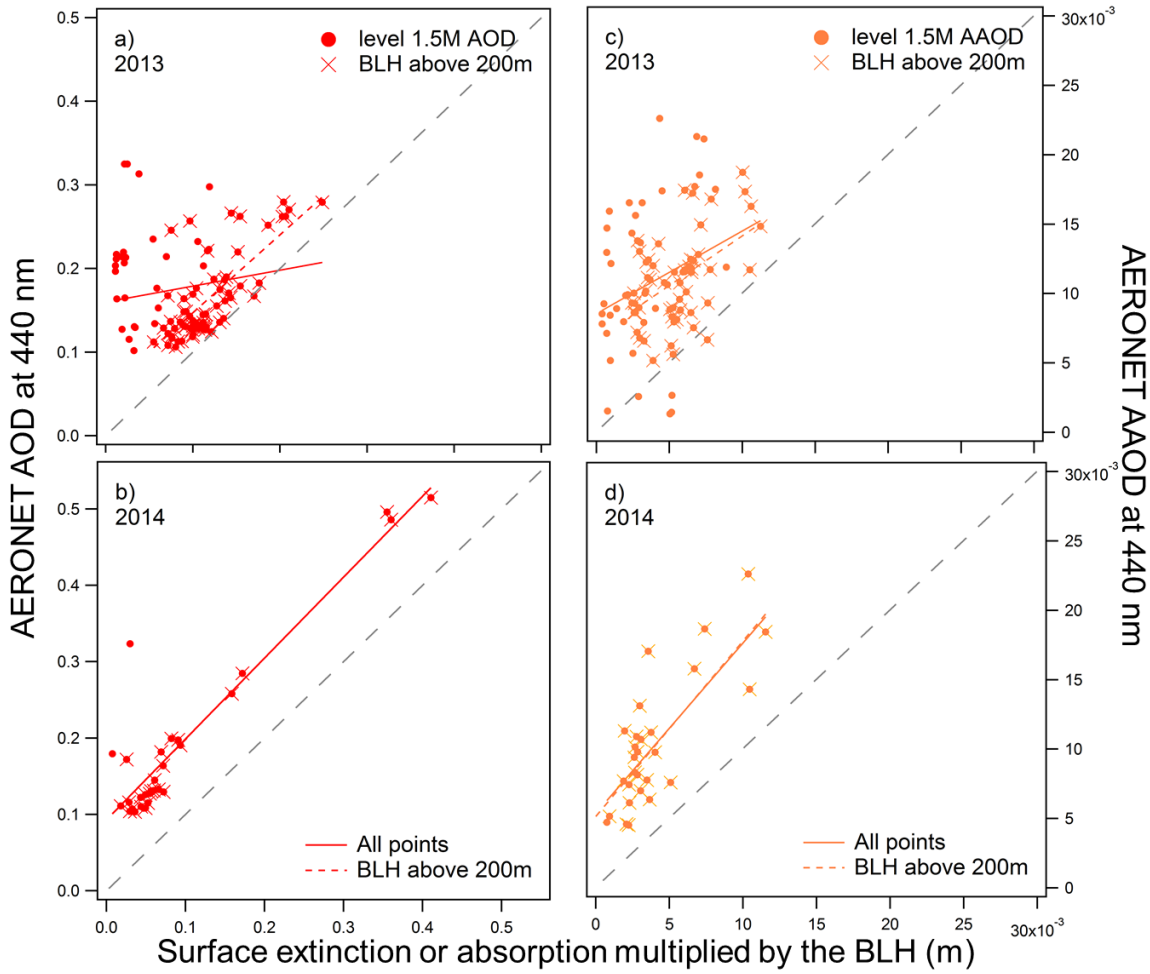

Figure 6-5. AOD and AAOD comparisons in 2013 (above) and 2014 (below). Solid circles (red for AOD, orange for AAOD) show results using level 1.5M AERONET measurements; cross mark shows results using measurements with BLH above 200 m. Left plots (a,b) compare column AERONET AOD with dry surface extinction scaled to BLH; right plots (c,d) compare column AERONET AAOD with surface absorption scaled to BLH. BLH is simulated from WRF model. Gray line is 1-to-1 ratio line. Regression lines show the correlation coefficient R^2 from one-sided linear regression (see **Table 6-4**).

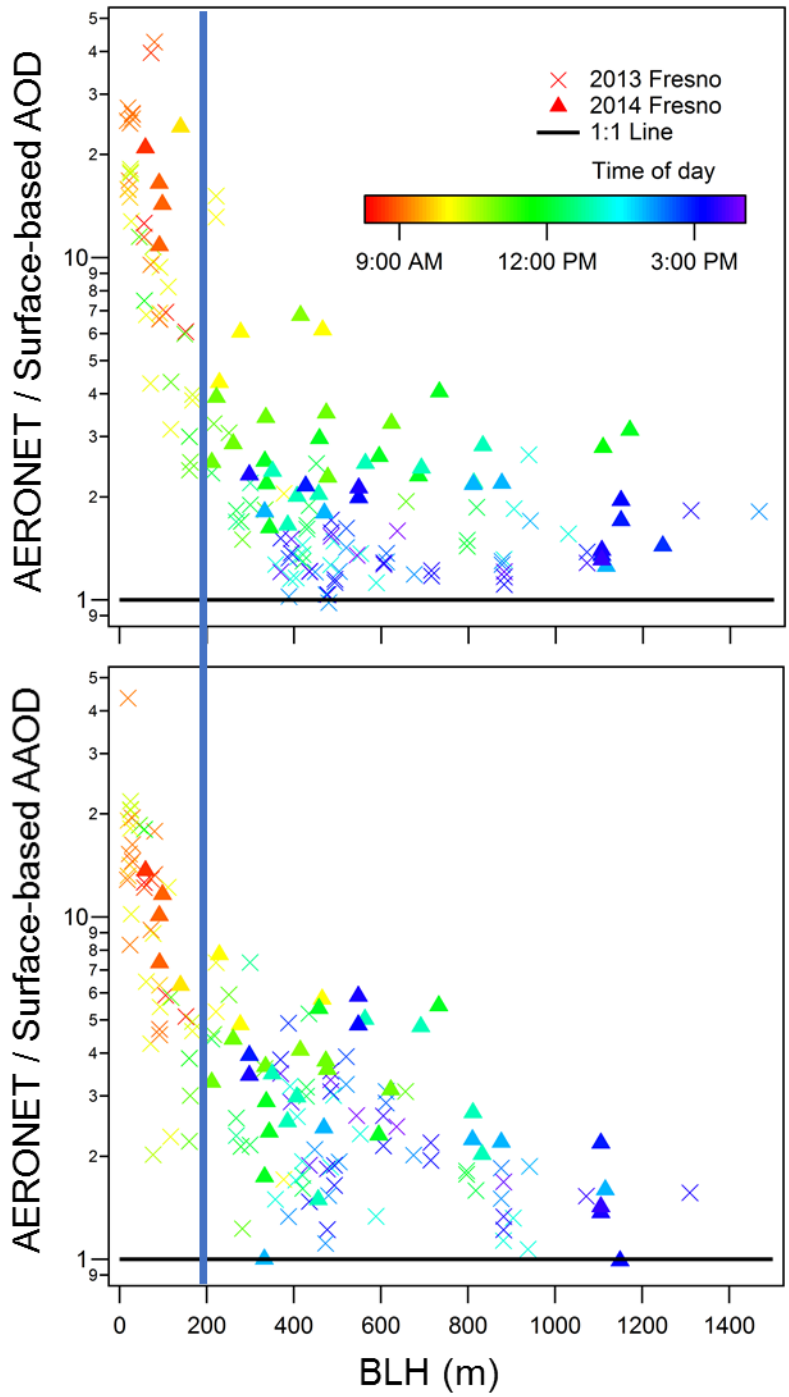

Figure 6-6. Ratio of AERONET measurements to surface-based estimates vs. BLH. AERONET measurements of AOD and AAOD are from level 1.5M data at 440 nm. Surface-based estimates of AOD and AAOD are from surface measurements of extinction and absorption at 405 nm, scaled to BLH. BLH are simulated by WRF model. Black line is the 1:1 ratio line. Blue line is the 200 m BLH line.

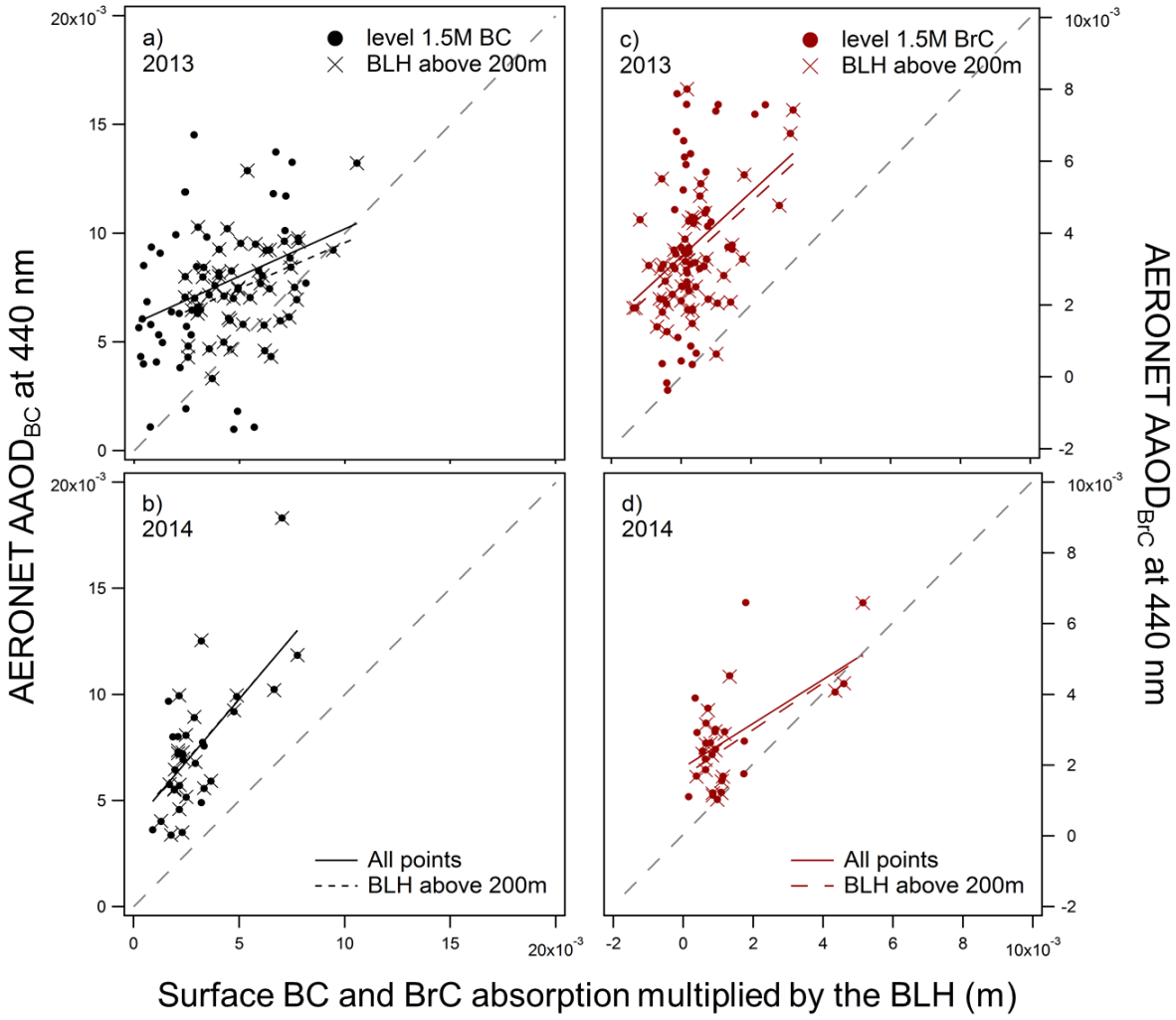

Figure 6-7. BC and BrC comparisons in 2013 (above) and 2014 (below). Solid circles (black for BC, brown for BrC) show the results using level 1.5M AERONET measurements; cross mark shows results using measurements with BLH above 200 m. Left plots (a,b) compare the BC fraction of AERONET AAOD with the surface BC absorption scaled to BLH; right plots (c,d) compare the BrC fraction of AERONET AAOD with the surface BrC absorption scaled to BLH. BLH is simulated from WRF model. Gray line is 1-to-1 ratio line. Regression lines give the correlation coefficient R^2 from one-sided linear regression, see **Table 6-4**.

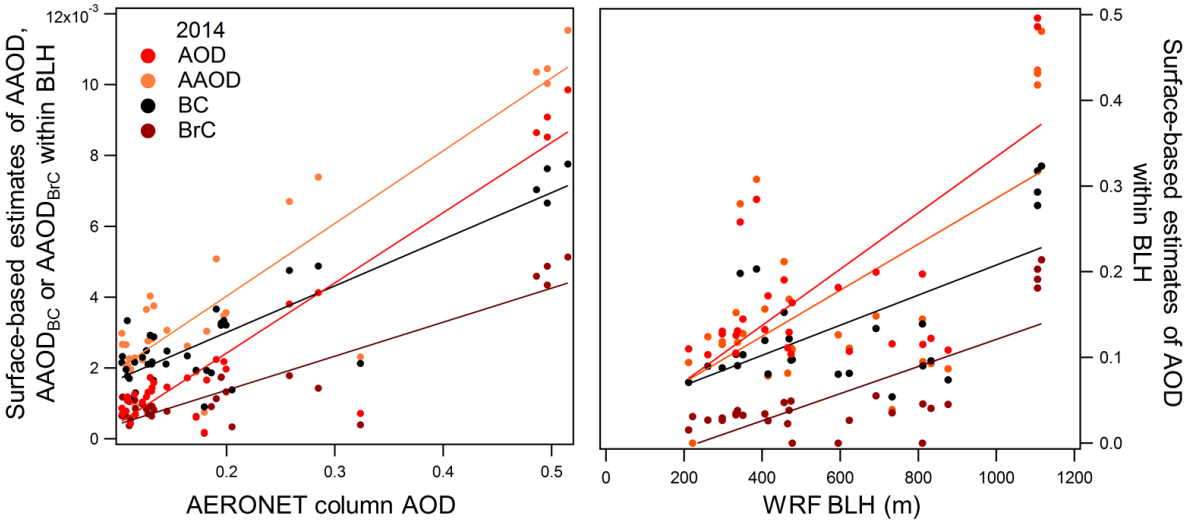

Figure 6-8. Comparison of surface-based estimates of extinction, total absorption and partitioned BC and BrC absorption at 405 nm with AERONET column AOD at 870 nm, as well as WRF BLH in 2014. See **Table 6-4** for values of R^2.

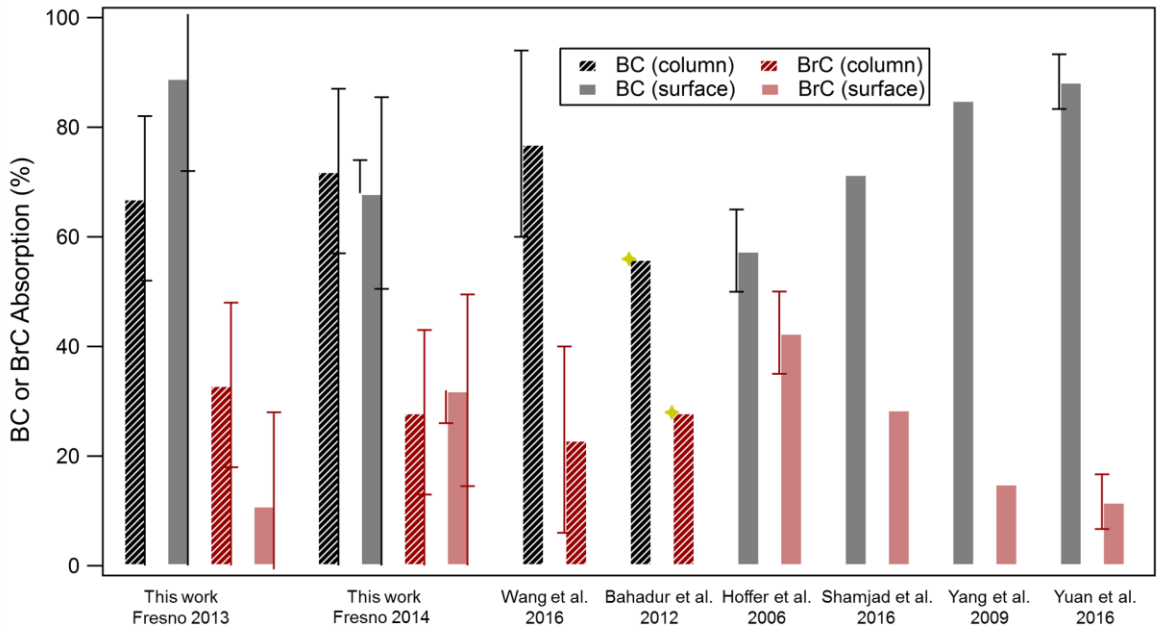

Figure 6-9. Relative amount of absorption from BC and BrC to the total absorption in this work and literature review. The wavelength ranged from 300 nm to 470 nm. For specific wavelength measured and other information, see **Table 6-3**. For this work, the error bars on the right edge indicate uncertainty of results from the AERONET-AAE method based on the sensitivity to the AAE values, and uncertainty of results from surface measurement and combined MAC and TD method from instruments and propagate through calculations. The error bars on the left edge representing surface measurements in 2014 indicate that if the coating contribution was not counted as part of BrC absorption, the BC absorption would be higher and BrC absorption would be lower. This is also true for 2013 but cannot be quantified due to lack of observation. Error bars for other work is the given range of BC and BrC absorption in that work. Star mark means the work also include evaluation of dust contribution.

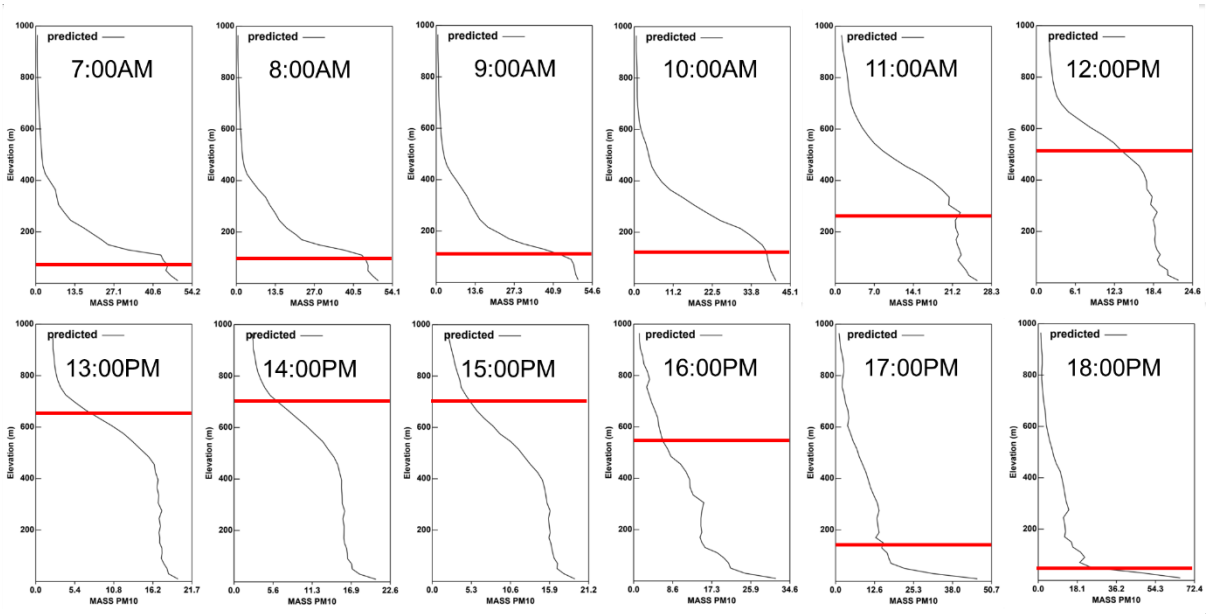

Figure 6-10. Hourly averaged vertical profile of PM10 mass using the airshed model from January 16 to 21, 2013, at Fresno. Red bars mark the hourly averaged BLH during the same period from the WRF model.

7 Influence of emissions and aqueous processing on particles containing black carbon in a polluted urban environment: Insights from a soot particle – aerosol mass spectrometer

7.1 Abstract

Inorganic and organic coatings on black carbon (BC) particles can enhance light absorption and affect atmospheric lifetimes of BC-containing particles and thus have significant implications for climate. To study the physical and chemical characteristics of atmospheric BC and BC-associated coatings, a soot-particle aerosol mass spectrometer (SP-AMS) was deployed during the winter of 2014-2015 in Fresno, a city located in the San Joaquin Valley of California, to selectively analyze BC-containing particles. Comparing SP-AMS measurements to those from the collocated single particle soot photometer (SP2) and high resolution aerosol mass spectrometer (HR-AMS), we found that 17% of total submicrometer aerosol mass was associated with BC-containing particles, suggesting that a majority of the fine particles in Fresno contained no BC. Most BC-containing particles appeared to be associated with residential wood burning and vehicular traffic. These particles typically had a bulk-average mass ratio of coating-to-BC ($R_{coat/rBC}$) less than 2. However, during periods of persistent fog larger $R_{coat/rBC}$ values were observed, with the coatings primarily composed of secondary inorganic and organic components that likely resulted from aqueous-phase processing. Specifically, compared to periods with less fog, the BC coating increased in concentration and contained a larger fraction of nitrate and oxidized organic matter. The size distributions of BC and associated organic coating were generally centered around 300 nm in vacuum aerodynamic diameter. However, during foggy periods BC had an additional peak at ~ 400 nm and organics and nitrate displayed a prominent mode in the accumulation size range.

7.2 Introduction

Black carbon (BC) is defined approximately as the fraction of carbonaceous aerosol that strongly absorbs visible radiation (Petzold et al., 2013). Positive radiative forcing due to direct absorption of sunlight by BC is estimated to be second only to the positive forcing by carbon dioxide (Bond et al., 2013) and light absorption by BC has been shown to increase the frequency of haze in heavily polluted regions by impacting local meteorology (Ding et al., 2016). BC particles, such as soot, are the product of incomplete combustion of biomass and fossil fuels, and freshly emitted BC tends to have a fractal morphology (Tumolva et al., 2010) and to be hydrophobic (Bond et al., 2013; Dusek et al., 2006; Martin et al., 2013). The concentrations and properties of BC particles tend to be spatially inhomogeneous with high concentrations occurring near sources such as urban centers and wildland fires (Schwarz et al., 2008), while atmospheric transport disperses them to distant locations (China et al., 2015). During transport, the microphysical and optical properties of BC-containing particles can change greatly due to condensation of secondary species.

The extent to which the BC component is internally mixed with organic and/or inorganic species can significantly affect the BC radiative properties, which according to theoretical calculations tend to be highly sensitive to mixing state and particle size (Bond et al., 2006; Fuller

et al., 1999). It has been demonstrated that the materials coated on BC can have an effect on BC radiative properties via optical lensing, which can induce an absorption enhancement (Cappa et al., 2012; Cross et al., 2010; Liu et al., 2017; Nakayama et al., 2014; Shiraiwa et al., 2010). Additionally, the composition and amount of material internally mixed with BC affect particle hygroscopicity (Lambe et al., 2015; Liu et al., 2013) and overall size, which have a large effect on BC particle removal rates and hence atmospheric lifetime (Taylor et al., 2014). It is thus critical to characterize the properties of BC-containing particles and their atmospheric processing to reach a better understanding of their effects on climate and air quality.

Characteristics of freshly emitted BC can be influenced by combustion source (Gong et al., 2016; Schwarz et al., 2008) and emission conditions (China et al., 2014). The mixing state, composition, and size of BC-containing particles are also influenced by physical and chemical processes occurring in the atmosphere (Cappa et al., 2012; Healy et al., 2015; Lee et al., 2015). BC-containing particles have been observed in the accumulation size mode coated by inorganic and organic species suggesting that secondary processing affected the BC size distribution (Massoli et al., 2015). Both fresh and aged BC particles can also co-exist, leading to externally mixed behavior (Adachi et al., 2014; Decesari et al., 2014). This wide variety of conditions complicate the development of parameterizations of BC properties for climate modeling and air quality forecasting. Additionally, though models treat mixing state simplistically, they are sensitive to mixing state inputs (Liu et al., 2017; Matsui et al., 2013; Willis et al., 2016). Thus, it is critical to provide detailed characterizations of BC, including its coating, composition, and size, in various environments for refinement of regional air quality and climate models.

Measurement techniques that can provide in-situ information on mixing state, composition, particle size, and optical properties of BC-containing particles are crucial for improving our understanding of the atmospheric behavior of these particles. The Aerodyne soot particle aerosol mass spectrometer (SP-AMS) (Onasch et al., 2012) allows for measurement of BC-containing particulate matter (PM), including refractory BC (rBC) and its associated coating material, i.e., inorganic and/or organic components internally mixed with BC. It has also been used in a variety of environments to measure specific rBC sources (e.g. Buffaloe et al. (2014); Corbin et al. (2015); Dallmann et al. (2014)) as well as atmospheric rBC (e.g. Hayes et al. (2013); Lee et al. (2015); Wang et al. (2016a); Wang et al. (2016b)). Also, the SP-AMS can be used to distinguish BC particle types in the lab (Corbin et al., 2014; Onasch et al., 2015) and in the field (Wang et al., 2016b) by examining the distribution of C_x^+ ($x \geq 1$) ions.

In this study, we use an SP-AMS to examine the composition, size distribution, and mixing state of BC-containing particles during wintertime in Fresno, CA. Fresno and surrounding areas within the San Joaquin Valley (SJV) have been the focus of various air quality studies due to high pollutant levels, particularly in winter. The wintertime SJV is characterized by increased PM emissions from primary sources such as residential wood burning (RWB) coupled with unfavorable meteorological conditions (e.g., Chow et al., 2008; Ge et al., 2012a; Parworth et al., 2017; Young et al., 2016). The SJV frequently experiences wintertime radiation fogs, which have led to elevated particulate nitrate, sulfate, and secondary organic aerosol (SOA) due to aqueous-

phase processing (Collett et al., 2008; Ge et al., 2012b; Herckes et al., 2007; Herckes et al., 2002). Although boundary layer dynamics combined with transport have led to elevated concentrations of secondary inorganic aerosol components across the valley (Brown et al., 2006; Chow et al., 2008; Pusede et al., 2016), primary particulates, such as BC, tend to be concentrated in urban locations like Fresno (Chow et al., 2008). Due to this mixture of sources and processes, Fresno is an ideal location to study the mixing state and atmospheric behavior of BC-containing particles. During this study, two markedly different meteorological conditions, clear and colder versus foggy and warmer, led to contrasting BC particle characteristics. Here, we report the chemical and physical properties of BC-containing particles in Fresno, CA, including concentrations, composition and size distributions, and how these characteristics changed under different meteorological regimes.

7.3 Materials and Methods

7.3.1 Campaign Location and Overview

The campaign took place from December 19th 2014 to January 13th 2015, during which instruments were housed in a modified shipping container parked at the University of California Merced Cooperative Extension (36°48'35.26"N, 119°46'42.00"W), north of a large commercial center and surrounded by residential neighborhoods with a busy freeway directly to the west (**Figure 7-1**). Ambient air was sampled from 20 feet above ground level and then subsampled at 10 L/min through a diffusion drier followed by a $PM_{2.5}$ cyclone and subsequently sampled through a thermodenuder which switched alternately between ambient (bypass) and heated lines every 5 minutes. The thermodenuder consisted of two equal-length heated stages (set at 200 °C and 280 °C to minimize charring), and a third stage containing activated carbon cloth to scavenge evaporated gases and had an approximate residence time of 10 seconds. Ambient or thermally conditioned air was then sampled by a suite of real-time instruments including an SP-AMS, a high resolution aerosol mass spectrometer (HR-AMS), a single particle soot photometer (SP2), a cavity ring-down photoacoustic spectrometer (CRD-PAS), a photoacoustic extinctiometer (PAX) and a scanning electrical mobility sizer (SEMS) (**Figure 7-2**). Further information on the operation and results from the HR-AMS and SP2 can be found in Chen et al. (2018) and Betha et al. (2018), respectively. In this study we focus on results obtained by the SP-AMS, which measured the size and composition of BC-containing particles. The measurements of the rBC portion were directly compared to results from the SP2, which also measures rBC mass, and from the CRD-PAS, which provides real-time measurements of particulate absorption.

Additional information on meteorology (temperature, relative humidity (RH), wind speed and direction from a Vaisala WXT520) and gas-phase species concentrations (CO from a T300 Teledyne API, and NO, NO_2 from a T200M, Teledyne API) were also measured on site. Water vapor concentration (g/m^3) was calculated from RH and temperature by calculating the saturation pressure using the Antoine approximation (Antoine, 1888) and converting to water vapor.

7.3.2 SP-AMS operation, data analysis, and quantification

The SP-AMS instrument has been described in detail elsewhere (Onasch et al., 2012). Briefly, particles in the submicrometer mode (PM_1) are sampled and concentrated using an aerodynamic lens. The focused particle beam is modulated by a chopper wheel to probe the bulk chemical properties of aerosols (MS mode) or the size-resolved chemical composition (particle time-of-flight, PToF). The particle beam intersects an intracavity infrared laser (1064 nm) where absorbing particles are heated to their boiling point (> 1000°C) and incandesce and vaporize, enabling the detection of rBC and internally mixed non-absorbing refractory components including metals and metal salts. The more volatile non-refractory components are volatilized at lower temperatures as the BC-containing particles heat up (<1000 °C). Since the SP-AMS and SP2 use the same laser and vaporization technique, they both measure rBC, and we use this term henceforth to denote the absorbing carbonaceous fraction of BC-containing particles (Petzold et al., 2013).

Traditionally, AMS instruments vaporize particles using a porous tungsten surface (600°C) and some SP-AMS instruments use both the laser and the tungsten vaporizer simultaneously to enable the detection of particles both with and without an absorbing fraction. During this campaign, the tungsten vaporizer was removed; hence, only rBC-containing particles were detected. This enables us to unambiguously analyze the composition, concentration and size distribution of inorganic and organic material internally mixed with rBC. Thermally vaporized materials are then ionized via 70 eV electron impact (EI) and the gaseous ions are subsequently sampled into a high resolution time-of-flight mass spectrometer.

The SP-AMS mass spectrometer was operated in ion optical V mode (average $m/\Delta m \sim 2300$) for higher sensitivity for ions with mass-to-charge ratios up to m/z=1000. Before removal of the tungsten vaporizer, an ionization efficiency calibration was performed using pure ammonium nitrate particles. Filtered air was sampled once at the beginning of the campaign and a second time near the middle of the campaign (for 30 and 10 minutes respectively) in order to determine the limit of detection (LOD, 3x the standard deviation) for the various aerosol components and to make adjustments to air-influenced mass spectral signals (Allan et al., 2004; Allan et al., 2003; Canagaratna et al., 2007; Zhang et al., 2005b). The LODs for 5-minute averaging were 98, 13, 11, 10, 9 and 120 ng/m^3 for organics, nitrate, sulfate, ammonium, chloride and rBC, respectively.

At the beginning and the end of the campaign, atomized and size-selected regal black (Cabot Corporation R400) was introduced into the SP-AMS to determine the ionization efficiency of rBC relative to nitrate. The instrument measured 152 ions per pg of carbon, which corresponded to a relative ionization efficiency (RIE) of 0.05. This is a relatively low value, which suggests the overlap between the particle beam from the aerodynamic lens inlet and the laser beam may have been misaligned slightly. However, more than 98% of rBC signals reported here were above the LOD. The ion signals corresponding to rBC are composed of C_x^+ fragments with C_3^+ having the largest signal. Since organics contribute significantly to C_1^+, the ratio of C_1^+/ C_3^+ determined for regal black is used to constrain the C_1^+ contribution to rBC for ambient data. All C_x^+ signals ($x=1\rightarrow9$) are attributed to rBC, where the largest peak is C_3^+ (45%), followed by C_1^+ (25%), C_2^+

(17%), C_5^+ (5.5%) and C_4^+ (4.7%) and where $C_{x>6}^+$ and isotopes of $C_{x\leq6}^+$ make up a small percentage of rBC mass (**Figure 7-3**a).

7.4 Data treatment

All data were analyzed using SQ: ToF-AMS Analysis Toolkit 1.57 and PIKA: ToF-AMS HR Analysis 1.16 (downloaded from http://cires.colorado.edu/jimenez-group/ToFAMSResources/ToFSoftware/index.html), open source data analysis toolkits programmed in Igor Pro 6.37 (Wavemetrics, Inc.). High resolution ion peak fitting was performed for ion fragments up to *m/z*=150 enabling the quantification of isobaric ions and the calculation of atomic ratios: oxygen-to-carbon (O/C), hydrogen-to-carbon (H/C), organic matter-to-organic carbon (OM/OC) and nitrogen-to-carbon (N/C). Elemental ratios were calculated using the Improved Ambient (IA) method (Canagaratna et al., 2015a) with an adjustment to the O/C and H/C by factors defined in Canagaratna et al. (2015b) and recommended for SP-AMS data. Collection efficiency (CE) of rBC in the SP-AMS has been found to be dependent on particle morphology (Massoli et al., 2015; Willis et al., 2014). During this campaign a noticeable shift in CE, determined by comparison with the SP2 measurements, was observed when rBC-containing particles had higher amounts of internally mixed organic and inorganic material. The mass ratio of total non-refractory material to rBC ($R_{coat/rBC}$) was used to parametrize changes in CE following the methods used by Willis et al. (2014) and Massoli et al. (2015). Detailed discussions on this correction are provided in the Appendix. Bulk mass concentrations discussed in sections 4 and 5 have been corrected using this method. This method was not applied in a size-dependent way. Thus, vacuum aerodynamic particle sizes are correct but the relative mass concentrations at a given size may be over or underestimated due to differences in collection efficiency. Note that $R_{coat/rBC}$ indicates the amount of non-rBC material associated with rBC and is used to estimate the average coating thickness. The SP-AMS measures ensemble particle-weighted mass rather than the mixing state of individual particles. Thus, the average $R_{coat/rBC}$ detected at any given time could result from a range of coating thicknesses. When we refer to the ensemble of particles as being "thickly" coated or "thinly" coated, this is in reference to the overall ensemble-average coating-to-core mass ratio and in the context of previous SP-AMS measurements (e.g. Cappa et al. (2012), Liu et al. (2015)). Further work to understand the distribution of coatings across the rBC population will be important in future studies.

The default values of RIE for chloride, nitrate and organics are assumed (1.1, 1.05, and 1.4, respectively) (Jimenez et al., 2003). The RIEs of ammonium and sulfate, derived from pure standard tests prior to removal of the oven, were 4 and 1.1 respectively. However, the quantification of absolute mass of coating components using the laser in the SP-AMS is still uncertain and requires further investigation (Onasch et al., 2012). For instance, an RIE_{NH4+}=5.2 was required to achieve neutralization of measured BC-containing particles when comparing the measured ammonium to predicted ammonium based on the anions (nitrate, sulfate and chloride) (**Figure 7-3**b). This suggests that removing the oven may result in a different RIE for these coating components, likely due to differences in evaporation processes occurring to coating materials heated by rBC incandescence versus heating on the tungsten oven, respectively, although we

cannot rule out the possibility that the inorganic coatings on the BC-containing particles were not fully neutralized. Note that previous campaigns in Fresno using AMS instruments have observed bulk neutralized particles (Ge et al., 2012b; Young et al., 2016). Furthermore, differences in particle vaporization between the SP-AMS and HR-AMS might result in somewhat different RIE for organics (Jimenez et al., 2016; Murphy, 2016), which may impact the comparison of results derived between these two instruments.

The HR-AMS and SP-AMS instruments are capable of detecting trace metals, but the RIE of metals can vary significantly by compound (Carbone et al., 2015; Salcedo et al., 2012). Potassium (K^+) was unambiguously detected in BC-containing particles during this study. However, quantification of K^+ is challenging since potassium is known to undergo surface ionization, in addition to electron ionization (EI), inside both the HR-AMS and SP-AMS. For the HR-AMS instrument, where surface ionization is likely important on the hot surface of the vaporizer, an RIE_{K+}=2.9 was previously determined (Drewnick et al., 2006) but the true RIE_{K+} of the SP-AMS is as yet unknown. Thus K^+ is reported in ion signal strength (Hz) in this study and when reporting the ratio of K^+-to-rBC, both species are in Hz.

The material density of BC-containing particles was calculated based on the mass fractional contributions of organics, rBC, and each of the non-refractory inorganic species (ammonium nitrate, ammonium sulfate and ammonium chloride) measured by the SP-AMS using the following equation:

$$\rho = 1/\sum_{i=0}^{n} \frac{MF_i}{\rho_i} \qquad \text{Eq. 1}$$

where i denotes species and MF_i and ρ_i are the species specific mass fraction and density, respectively. The time-dependent density of the organic fraction in BC-containing particles was calculated by applying the equation reported in Kuwata et al. (2011), which accounts for variability in the chemical nature of the organic components. Note that the elemental ratios used for calculation of organic density were derived using the Aiken method for consistency with the Kuwata et al. (2011) equations (Aiken et al., 2007). The densities for rBC, ammonium nitrate, ammonium sulfate and ammonium chloride were assumed to be 1.8, 1.72, 1.77 and 1.53 g/cm^3, respectively. Potassium was not included in the calculation.

PToF information is typically derived using unit mass resolution but major C_x^+ ions can be influenced by isobaric ions. For example, both C_3^+ and HCl^+ influence the size distribution at *m/z*=36 and C_1^+ at *m/z*=12 can have a large contribution from organics. Therefore, the rBC mass-based size distributions were calculated using only *m/z*=24 (C_2^+) which is less likely to have significant organic or inorganic influences. A correction factor was derived using the area under the curve (40 nm < vacuum aerodynamic diameter (D_{va}) < 1000) of each *m/z*=24 size distribution and comparing that to the corresponding rBC mass derived using high resolution MS data.

Quality assurance and control was performed on this data set by removing problematic periods. In addition, HR-AMS data was used here to compare to the BC-containing fraction. For instance, the non-BC related PM_1 shown in **Figure 7-4**e was calculated by subtracting BC-coating species

from the HR-AMS derived species. Further information on the treatment of HR-AMS data can be found in Chen et al. (2018).

7.5 Results

7.5.1 Overview of characteristics and variations of BC-containing particles

The campaign period was characterized by relatively cold and stagnant conditions with an average (±1σ) temperature of 9.2±5.1°C and average wind speed of 0.54±0.32 m/s (**Figure 7-4**a, b, Table S1). The relative humidity (RH) varied significantly on a diurnal basis with values regularly reaching above 90% at night and dipping below 50% on some days (**Figure 7-4**b). However, the water vapor concentration (WV, **Figure 7-4**b) was lower during the middle of the campaign and significantly higher at the beginning and end of the campaign. The concentrations of individual species in BC-containing particles varied diurnally and were typically characterized by high concentrations of rBC and organics at night (**Figure 7-4**c). The average (± 1σ) concentration of rBC was 1.05 (±0.76) μg/m^3 during this study (Table S1), similar to the average BC values observed at other urban locations during wintertime such as London (1.3 μg/m^3) (Liu et al., 2014) and Las Vegas (1.8 μg/m^3) (Brown et al., 2016) and in Fresno during the winter of 2013 (1.5±0.93 μg/m^3) (Zhang et al., 2016). The average concentration of inorganic and organic components internally mixed with rBC was 2.37 (±1.47) μg/m^3, yielding an average value of $R_{coat/rBC}$=2.3. Compared with previous field observations, where aged rBC-containing particles have been observed with $R_{coat/rBC}$ values up to 20 or greater (Cappa et al., 2012; Massoli et al., 2015), the rBC particles in wintertime Fresno were relatively thinly coated. Compared to the total PM_1 mass measured using the HR-AMS and SP2 instruments, 17% of the total mass was associated with rBC-containing particles (**Figure 7-5**a). In other words, a majority (83%) of PM_1 mass (**Figure 7-4**e) in Fresno during winter contained no detectable black carbon.

The average concentration of organics internally mixed with BC was 1.48±1.04 μg/m^3, making it the largest contributor (43%) to the total mass of rBC-containing particles (**Figure 7-4**c). The rBC-containing particles tend to have less inorganic material compared to the bulk and a similar fractional contribution of organics (**Figure 7-4**e, **Figure 7-5**b). The calculated material density of rBC-containing particles varied between 1.22 – 1.54 g/cm^3 with an average value of 1.44 g/cm^3 (**Figure 7-4**c). For rBC-containing particles, organics and rBC displayed highly variable temporal behavior with large concentration enhancements at night (**Figure 7-4**c) likely due to strong primary emissions, especially RWB, coupled with lower boundary layer heights. The non-rBC particle fraction displayed similar variation but with larger contributions from inorganics (**Figure 7-4**e).

Previous studies in Fresno have determined that a large mass fraction of ambient aerosol during wintertime is primary, especially at night, with RWB, cooking, and vehicles as the main sources (Chow et al., 2007; Ge et al., 2012a; Young et al., 2016). Indeed, the rBC concentration has good correlation with the concentrations of ion $C_2H_4O_2^+$ (*m/z*=60, r^2=0.66, **Figure 7-6**a), which is a marker for biomass burning (BB) (Aiken et al., 2010; Cubison et al., 2011; Lee et al., 2010), and with $C_4H_9^+$ (*m/z*=57, r^2=0.59, **Figure 7-6**b), which is a marker of vehicle emissions (Canagaratna

et al., 2004; Collier et al., 2015; Zhang et al., 2005a). Potassium (K^+, *m/z*=39), a marker for RWB (Chow et al., 2007; Corbin et al., 2015; Parworth et al., 2017), also displays a high correlation with rBC (r^2=0.83, **Figure 7-6**c). Relationships with the $C_5H_8O^+$, $C_6H_{10}O^+$, and $C_7H_{12}O^+$ are shown in **Figure 7-7**.

The $C_2H_3O^+$ ion (*m/z*=43) is an important component in both secondary organic aerosol (SOA) (Ng et al., 2010) and BB organic aerosol (BBOA). Indeed, it correlates strongly with $C_2H_4O_2^+$ (a BB marker ion) and K^+ (r^2=0.89 and 0.78, respectively, **Figure 7-8**) during the middle of the campaign when it was cold and RWB was significantly enhanced (period designated as low fog in **Figure 7-4**). However, toward the end of the campaign when it was warmer and foggy (high fog period), it has a relatively large increase in concentration (**Figure 7-6**d) and a significant decrease in correlations with $C_2H_4O_2^+$ and K^+ (r^2=0.40 and 0.48, respectively), indicating that secondary aerosol formation of this ion through either aqueous phase processing or daytime photochemical activity was likely important. More discussions on the low fog (LF) and high fog (HF) periods are provided in Section 4.3.

The high resolution mass spectrum, averaged for the duration of the campaign, is dominated by the ions at *m/z*=43 (68% $C_2H_3O^+$, 29% $C_3H_7^+$) and displays a relatively large peak at *m/z*=60 ($C_2H_4O_2^+$, **Figure 7-9**a). The organic fraction of BC-containing particles has an average O/C=0.38 (**Figure 7-9**b) with an average calculated density of 1.09 g/cm^3. The bulk composition does not appear to vary significantly, as the histogram of O/C shows a relatively tight distribution and only 11% of the data points have O/C values greater than 0.5 (**Figure 7-9**b). However, some processing is evident when examining the triangle plots in **Figure 7-9**d-e. Triangle plots, which display the fractional contribution of one m/z component vs. another (at unit mass resolution), are commonly used to assess chemical oxidation or mixing of aerosols from different sources (Cubison et al., 2011; Mohr et al., 2012; Morgan et al., 2010; Ng et al., 2010). The fractional contribution of the signals at *m/z*=43-to-total organic mass (f_{43}) varies significantly and appears to increase with increasing $R_{coat/rBC}$ (**Figure 7-9**d). This result suggests that conditions that lead to different amounts of coating also affect the organic coating composition. Finally, the fractional contribution of the components at *m/z*=60 (dominated by the $C_2H_4O_2^+$ ion, f_{60}) tends to be higher when $R_{coat/rBC}$ is low (e.g., $R_{coat/rBC} < 2$ at $f_{60} > 0.02$; **Figure 7-9**e), suggesting that rBC-containing particles emitted from BB tend to be thinly coated. Interestingly, the fractional contribution of the ions at *m/z*=44 (dominated by the CO_2^+ ion, f_{44}) is relatively constant, which suggests that all rBC-containing aerosol are likely fresh since observations of an increasing f_{44} are often taken as a signature of aging of organics (Ng et al., 2010). However, the CO_2^+ ion might not be a strong indicator for processed organic aerosol in the SP-AMS given that fragmentation of molecular ions in the SP-AMS is less extensive compared to the traditional AMS (Canagaratna et al., 2015b).

Overall, it appears that primary combustion emissions are the main sources of the organic matter on rBC-containing particles although some secondary processes likely also contribute to the organic coating. The relative contribution of different organic mass spectral markers and coating amount during the two major meteorological regimes identified during this campaign are discussed further in Sections 4.3-4.4.

The average concentrations of nitrate, ammonium, sulfate, and chloride in BC-containing particles are 0.61±0.52, 0.22±0.16, 0.04±0.03, and 0.02±0.02 μg/m^3 respectively. Their time-dependent concentrations behave differently than those of organics and rBC and appear to be influenced by meteorology (**Figure 7-4**d). It is likely that the inorganic species and some secondary organic species became internally mixed with rBC either by gas-to-particle partitioning, coagulation and/or aqueous-phase processing. The mass fraction of inorganics coating BC-containing particles (~26%) is smaller than the mass fraction found in PM_1 (~51%, Figure S4b).

The mass-based size distribution of each species is averaged over the entire campaign and reported in vacuum aerodynamic diameter (D_{va}, **Figure 7-9**f). Note that the measured PToF size includes both the rBC component and the coating material and is not a direct measurement of the rBC core size, but rather a measurement of the particle as a whole. Three main modes are identified: a broad mode centered at 250 nm but likely composed of multiple modes, a mode at 500 nm and a small fraction of particles >600 nm. The left side of the 250 nm size mode which starts at 60 nm appears to have the least amount of coating and has a higher influence from the tracer for vehicle emissions, *m/z*=57 (mainly composed of $C_4H_9^+$, **Figure 7-9**g). Between 250 and 400 nm, the organic fraction becomes more important and in particular the tracer for BB, *m/z*=60 (dominated by $C_2H_4O_2^+$), has a larger influence. As noted earlier, we corrected the ensemble mass measurements for morphological differences in CE based on $R_{coat/rBC}$ ratios, rather than particle size. Thus, the size-dependent concentrations of small BC particles, which are likely thinly coated, fractal BC particles, could be underestimated compared to larger, thickly coated ones due to particle beam divergence resulting in lower detection efficiency. At sizes greater than 400 nm and peaking at 500 nm, the organic fraction has a higher contribution than rBC. At the size mode peaking at ~600 nm, rBC-containing particles appear to be internally mixed with organics and inorganics, although the extent to which these coating materials exist in the same particles (internally mixed) or in distinct BC particles (externally mixed) cannot be discerned from this dataset. The size distributions of nitrate and sulfate are similar, narrower than those of rBC and organics, and primarily in the D_{va} >600 nm mode. These observations further suggest that secondary processes have influenced the mixing state of rBC-containing particles. The size distribution of *m/z*=43 overlaps with inorganics in the >600 nm mode but appears to have a contribution in the lower size mode, corroborating the earlier assertion that it is related to both primary emissions and secondary processes (i.e. condensation / coagulation or aqueous phase reaction).

These aerosol characteristics likely dominate under different conditions. For instance, the larger particles with greater secondary influence are likely more dominant during photochemically active periods or those dominated by aqueous phase processing. The smaller particles are dominated by rBC and primary tracers and are more abundant at night when shallower boundary layer conditions are coupled with higher burning activity. Indeed, as shown in **Figure 7-9**h, the diurnal patterns for rBC and $R_{coat/rBC}$ indicate that at night the rBC concentration tends to be higher and BC-containing particles are relatively more thinly coated. However, the overall diurnal

variability is small for the campaign average; when the different meteorological regimes are examined independently, greater diurnal variations in $R_{coat/rBC}$ are observed.

7.5.2 Characteristics of BC coating as a function of the mass ratio of coating-to-rBC ($R_{coat/rBC}$)

In this section, we examine the relationship between the coating material and rBC in more detail by showing various aerosol parameters as a function of $R_{coat/rBC}$. In previous field observations, aged rBC-containing particles have been observed with $R_{coat/rBC}$ values up to 20 or greater (Cappa et al., 2012; Massoli et al., 2015). In this study the 90th percentile $R_{coat/rBC}$ is approximately 3.5, and $R_{coat/rBC}$=2 is used as a separator between the more thinly coated particles dominated by higher rBC and primary tracers and more thickly coated particles containing secondary tracers (**Figure 7-10**a, refer to section 4.4 and **Figure 7-12**f). Organic mass tends to be larger for particles that have lower $R_{coat/rBC}$ (**Figure 7-10**b). Nitrate has a relatively low and constant mass concentration with respect to $R_{coat/rBC}$ during the first three weeks of the campaign; however, its concentration is strikingly higher later in the campaign (**Figure 7-10**c) and coincides with higher $R_{coat/rBC}$. The $fC_2H_4O_2^+$ has a larger value in thinly-coated rBC particles ($R_{coat/rBC} < 2$) and it decreases in more thickly-coated particles ($R_{coat/rBC} > 2$) (**Figure 7-10**d). The marker for vehicle emissions ($fC_4H_9^+$, **Figure 7-10**e) also decreases with $R_{coat/rBC}$, although to a lesser extent. In contrast, the tracers for oxidized organics ($fC_2H_3O^+$ and fCO_2^+: **Figure 7-10**f, g) increase with increasing $R_{coat/rBC}$, especially $fC_2H_3O^+$. Furthermore, the mass ratio of organic matter-to-rBC in BC-containing particles ($R_{Org/rBC}$) also increases with $R_{coat/rBC}$ (**Figure 7-10**h). The O/C increases with $R_{coat/rBC}$, which is consistent with trends observed for SOA tracers and suggests that more coated rBC may be more aged or have undergone more atmospheric processing (**Figure 7-10**i).

Together, these results suggest that some portion of coating is added to BC through secondary formation, atmospheric aging, coagulation or aqueous phase processing. However, some differences were noted between the LF and HF periods for a given $R_{coat/rBC}$. Parameters which were enhanced significantly during the HF period relative to the other periods for a given $R_{coat/rBC}$ include rBC, organics, nitrate, and $fC_2H_3O^+$, whereas parameters that decrease include $fC_2H_4O_2^+$ and $R_{Org/rBC}$. Since temperatures were overall warmer during the HF period, the decrease in $fC_2H_4O_2^+$ and $R_{Org/rBC}$ may be the result of reduced RWB and lower BB emissions.

Binning the chemically-resolved size distribution profiles by coating amount yields results that are consistent with the relationship observed between rBC and $R_{coat/rBC}$ discussed above. Thinly coated BC-containing particles tend to be smaller with sizes maximizing at 200 nm whereas more thickly coated particles peak around 400-600 nm (**Figure 7-10**j-l). The thinly coated BC-containing particles appear to be dominated by rBC and organics (**Figure 7-10**j, k) whereas particles coated more thickly by nitrate tend to accumulate in the 500 nm size mode. Nitrate apparently does not contribute significantly to smaller BC-containing particles, again indicating that within this urban center, more thinly coated BC particles are likely from fresh and primary emissions and more thickly coated particles tend to be larger and have coatings composed of secondary components.

7.5.3 Diurnal variations of rBC-containing particles during low fog and high fog periods

As shown in **Figure 7-4** and discussed briefly in prior sections, two contrasting meteorological regimes were observed which had large differences in humidity, WV and fog frequency: the low fog period (LF) and the high fog period (HF) (**Figure 7-4**c). The LF consists of a particularly cold period in the middle of the campaign (average T=5.0±4.2 °C, Table S1) and is associated with stronger variations in the measured concentrations of rBC and organics suggesting it is dominated by higher emissions from RWB. The HF is a relatively warmer period (average T = 12.0±3.1 °C, Table S1) toward the end of the campaign characterized by visible nighttime and morning fog events with higher average RH values (RH=84% vs 79%, Table S1) and higher WV. It is important to note that ground-level radiation fogs occur primarily during night and dissipate in the morning.

The wind speed in the city of Fresno is similar for the two periods and conditions are generally stagnant throughout the entire campaign (**Figure 7-11**a). The solar radiation flux is reduced during the HF and delayed due to early morning fog events (**Figure 7-11**b), and the RH remains high later into the day. Temperature is consistently higher during the HF with on average 6-9 °C difference relative to LF (**Figure 7-11**c). Generally speaking, stagnant conditions in this region lead to a shallow boundary layer which, in turn, trap primary emissions, especially at night, leading to very high concentrations of primary pollutants (Young et al., 2016). The colder evening conditions during the LF drive a higher rate of residential burning and this, coupled to strong temperature inversions, may explain the larger variation in measured rBC between daytime and evening hours (**Figure 7-11**d, e). Similar diurnal profiles have been observed for aerosol absorption in Fresno (Zhang et al., 2016) and for BC in Las Vegas (Brown et al., 2016) during wintertime. A morning increase of rBC is also observed, which may be due to morning rush hour. By contrast, the HF is warmer, likely altering burning behavior leading to lower BB emissions. The rBC concentrations are indeed lower at night relative to the LF but remain higher during the day; thus, rBC overall displays less diurnal variation and higher daytime concentrations during HF periods, suggesting more stagnant conditions (**Figure 7-11**d, e). Additionally, a delay in the morning peak was observed for rBC (**Figure 7-11**d) and other species measured here. The higher daytime concentrations during the HF may be due to shallower boundary layer conditions and the delay in the morning peaks may be due to a combination of delayed traffic due to poor visibility, confirmed by similar delays in gas-phase concentrations of primary tracers CO and NO (**Figure 7-11**f, g), and delay in morning break-up of the boundary layer. Both phenomena could be explained by the presence of dense fog. Indeed, the delayed increase in solar radiation during HF suggests dense fog prevented ground level heating of the atmosphere which would delay mixing down of aloft layers as well as deepening of the boundary layer. Furthermore it has been observed that fog episodes can lead to a delay in the morning break-up of the boundary layer (Dupont et al., 2016), which may lead to a stronger accumulation effect keeping rBC concentrations high during HF daytime. Measurements of boundary or mixed-layer height are not available for this campaign; however, calculations of mixed-layer height were performed and model results suggest it was shallower on foggy days (Chen et al., 2018).

It is important to note that although the diurnal profiles for rBC_{TD} (**Figure 7-11**e) and ambient rBC (**Figure 7-11**d) show similar behavior, the ambient rBC during the HF appears to be slightly more enhanced during the middle of the day after the morning rush hour increase. This appears to occur only for the midday HF period and corresponds to both highly oxidized and coated particles. This is likely due to issues with rBC quantification using a coating-dependent CE. See the Appendix for a detailed discussion.

During the LF, $R_{coat/rBC}$ is low at night when primary emissions are high and the boundary layer is shallow but increases significantly during the day, with the early morning increase possibly due to mixing in of aloft residual layers containing aged rBC particles and the midday increase likely due to photochemical activity leading to increased coating by secondary species (**Figure 7-11**i). During the HF, $R_{coat/rBC}$ is similar during the daytime as the LF, but it remains high at night. This observation, together with the increases of nitrate and oxidized organic species on rBC containing particles (**Figure 7-11**k, 4o) could be due to increased nighttime chemistry, e.g., aqueous phase processing, repartitioning of semivolatile material or coagulation of rBC-containing particles with fog droplets which result in residual particles containing both rBC and secondary materials upon droplet evaporation. Additionally, primary emissions were reduced during HF nighttime thus thinly coated particles were less abundant. These together result in a higher frequency of rBC particulates with $R_{coat/rBC}>2$ during the HF. The diurnal behavior of the organic loading is similar to that of rBC (**Figure 7-11**j). Nitrate has a relatively constant concentration during the LF and enhanced concentration during the HF (**Figure 7-11**k). The higher WV content and temperature may be contributing to this dramatic enhancement and promoting gas-to-particle partitioning and aqueous phase processing. **Figure 7-11**l-o shows the diurnal profiles of the tracers for BB, vehicle POA and SOA. Both K^+ and $C_2H_4O_2^+$ have a clear enhancement at night during the LF with very dramatic decreases in concentration in the middle of the day and a slight increase in the morning. During the HF these BB tracers are still enhanced at night relative to daytime but to a lesser extent, following the general behavior exhibited by rBC. The vehicle tracer, $C_4H_9^+$, has a clear morning traffic peak and nighttime traffic enhancement during the LF and a delayed morning peak during the HF. As discussed earlier, $C_2H_3O^+$ appears to be emitted along with BB which is implied from its high correlation with rBC and organics during the LF. However, there is a marked enhancement during the HF and a clear enhancement during the middle of the day suggestive of photochemical production, despite the reduced solar radiation of this period. There is also a significant enhancement of this marker at night, which may be evidence of nighttime BB emission or a combination of secondary production and primary emission.

There also appears to be overall lower concentration of primary components in rBC coating at night during the HF compared to the LF with a marked increase in secondary components in rBC-containing particles. The diurnal profiles are shown normalized to rBC in **Figure 7-11**p-u which helps account for dilution due to boundary layer behavior. On a per-rBC-mass basis, organic displays a small daytime enhancement during the LF, suggesting that some secondary organic coating is produced although it contributes less to overall rBC-coating compared to primary species (**Figure 7-11**p). Nitrate is enhanced during the day on a per-rBC-mass basis due to

secondary formation in both LF and HF and is enhanced overall during the HF (**Figure 7-11**q). The BB tracers (K^+ and $C_2H_4O_2^+$) have a larger contribution on a per-rBC-mass basis during the LF (**Figure 7-11**r and **Figure 7-11**s) particularly at night suggesting emissions are indeed lower during the HF. $C_2H_4O_2^+$ has been shown to degrade under more humid conditions (Arangio et al., 2015). The diurnal profile of the ratio of $C_2H_4O_2^+$ to K^+ shows a decrease when comparing the HF to the LF (Figure S7). Since K^+ is not expected to degrade under humid conditions, this result suggests the reduction in emissions of BB tracers may also be coupled with a higher rate of levoglucosan degradation due to aqueous phase processing.

$C_4H_9^+$/rBC shows very little change between the two periods except for the shift in the morning traffic peak (**Figure 7-11**t), suggesting that vehicle emissions are not significantly affected by these two different meteorological conditions. The increased absolute levels of $C_4H_9^+$ (**Figure 7-11**n) during the daytime HF compared to daytime LF are likely caused by boundary layer dynamics, where HF boundary layer heights may have remained low throughout the day. The SOA tracer ($C_2H_3O^+$) is enhanced on a per-rBC-mass basis during the LF daytime relative to nighttime, likely due to photochemical enhancement (**Figure 7-11**u). However, the ratio of $C_2H_3O^+$/rBC is relatively flat throughout the diurnal cycle during the HF, suggesting that there is some enhanced SOA production at night, likely attributable to aqueous phase processing or enhanced gas-to-particle partitioning.

7.5.4 Influence of aqueous-phase processing on BC-containing particles

Dramatic differences in the concentration, composition, coating amount and size of rBC-containing particles were observed between LF and HF periods. Compared to the LF period, the HF period was associated with less diurnal variation in rBC and organics and substantially higher contributions from inorganic components. The average mass concentration of the rBC-containing aerosol is higher during the HF than during the LF and this change correlates largely with the addition of secondary ammonium nitrate coating where the nitrate contribution increases from 10% to 25% between LF and HF, respectively (**Figure 7-4** and **Figure 7-12**a, b). The organic portion becomes slightly more oxidized during the HF and the average organic mass spectra of the two periods are clearly different, including an increase of $C_2H_3O^+$ (*m/z* 43) during the HF and overall decrease of the contribution of primary tracers ($C_xH_y^+$ and $C_2H_4O_2^+$ at *m/z* 60) (**Figure 7-12**c, d). During the LF period, rBC-containing particulates are dominated by a 300 nm size mode with a minor larger size mode containing organic and nitrate (**Figure 7-12**e). By contrast, during the HF rBC appears to have both a small mode (~180 nm) and a more dominant large size mode (400 nm) while nitrate, organic and rBC reside in a droplet accumulation mode centered around 600 nm (**Figure 7-12**g). When examining the size distributions of total rBC-containing PM_1 (red curve, **Figure 7-12**e, g) this shift in size is apparent. This dramatic shift during the HF in mass-based rBC size mode is indicative of aqueous phase processing, which may enhance secondary aerosol formation as well as particle coagulation (Ge et al., 2012b). In addition to increasing NR-PM associated with rBC (Liu et al., 2013), aqueous phase processing may lead to restructuring of rBC thus increasing sphericity (Pagels et al., 2009). In previous Fresno studies, similar changes in aerosol size modes were noted when comparing drier periods to foggy periods, such that POA and

inorganic aerosol components were found to reside in the droplet accumulation mode centered at 400-500 nm during foggy periods (Ge et al., 2012b). This suggests that fresher primary particles at this location can be processed by fog water leading to a shift in size that results in an aerosol population that appears more internally mixed and displays a narrower size distribution.

To further elucidate how particulate composition is affected by the different meteorological conditions, compositional information was binned by $R_{coat/rBC}$ for the two distinct periods. The most notable difference between the LF and HF periods is that almost all of the particles have an $R_{coat/rBC}>2$ during the HF period whereas during the LF period a significant fraction of particles appear more thinly coated with $R_{coat/rBC}<2$ (**Figure 7-12**f, **Figure 7-13**). In addition, during the HF period, the rBC coating contains a high fraction of both nitrate and organics (**Figure 7-12**h, Figure S8) for all $R_{coat/rBC}$. By contrast, the LF period contains rBC coating dominated by organics at the low $R_{coat/rBC}$ end. However, a small fraction of thickly coated particles in the LF have a similar composition as their analogs during the HF (**Figure 7-12**h). High humidity (close to 100%) at night was observed throughout the campaign and led to the occurrence of fog, but less frequent and shorter duration fog events were observed during LF compared to HF and this may have led to limited aqueous phase processing. Additionally, and as shown in **Figure 7-11**q and **Figure 7-11**u, photochemical processing during the middle of the day may have contributed to thickly coated rBC particles during the LF. It has been demonstrated previously that hygroscopic growth or cloud/fog activation of BC-containing particles can depend on BC particle size (Schroder et al., 2015) or on coating composition (Liu et al., 2013) such that not all BC-containing particles experience hygroscopic growth. During LF, results suggest only a small fraction of rBC particles had increased coatings of secondary species, however during HF the higher WV content (**Figure 7-4**b) resulted in most rBC particles experiencing hygroscopic growth and enhanced gas-to-particle partitioning.

7.6 Conclusions

Real-time characterization of the concentration, composition, particle size and optical properties of absorbing aerosols were performed in Fresno, CA during winter. Here we have focused on the results from a soot particle aerosol mass spectrometer with the tungsten vaporizer removed, thus enabling the characterization of refractory black carbon-containing particles and their associated coatings. During the sampling campaign two distinct periods were captured with a colder and dryer period discussed as the low fog period and a warmer and wetter period called the high fog period.

The main characteristics of rBC-containing particles in Fresno include: 1) dominance of fresh and thinly coated rBC particles that appear to be influenced by biomass burning and vehicle emissions and with particle sizes below 400 nm (D_{va}), 2) a small fraction of more thickly coated rBC particles that tend to be internally mixed with secondary inorganic and organic components, and 3) strong diurnal variations due to boundary layer dynamics coupled with anthropogenic emissions in the early morning and evening times. Additionally, there is evidence that the different sources and processes contributing to rBC affected characteristics such as size and coating amount.

These characteristics can vary to a large extent under different meteorological conditions. Previous studies have shown that fog can delay breakup of the boundary layer and create stable conditions (Dupont et al., 2016) due to reduced surface heating or other factors. Here fog appears to suppress boundary layer break-up and lead to shallower boundary layer depths overall. This leads to pollution concentrations remaining more constant throughout the day. Furthermore, the warmer weather during the HF may have led to decreased residential wood burning emissions which is consistent with the observation of reduced K^+ concentration. However, the reduction in BB emissions did not significantly decrease overall rBC particle concentration during the HF and it appeared to be balanced by accumulation due to lower boundary layer height and delayed rising of the mixed layer. There is strong evidence for aqueous SOA formation on rBC particles during the HF since the tracer for fresher SOA increased dramatically despite an overall decrease in solar radiation with many of these enhancements occurring at night. Furthermore, a portion of rBC particles shifted in size to a typical droplet accumulation mode size during the HF. The dramatic differences in rBC particle behavior, coating chemistry, and size distribution may result in different radiative effects and/or atmospheric lifetimes. Future studies will include parameterizing these characteristics and quantifying how these changes affect the radiative properties of absorbing aerosol in the region.

7.7 Acknowledgments, Samples, and Data

This work was funded by the California Agricultural Experiment Station (Project CA-D-ETX-2102-H), the US Department of Energy (DOE) Atmospheric System Research (ASR) program (DE-SC0014620), and California Air Resources Board (CARB) (Agreement number: 13-330). Development of the SP-AMS was funded in part by the US DOE SBIR Program (DE-FG02-07ER84890). The authors acknowledge J. Liu and N. Williams for assistance in setting up and running the measurement site. Data presented in this manuscript will be available in the AMS Global Database: https://sites.google.com/site/amsglobaldatabase/.

7.8 Appendix A: Determination of SP-AMS collection efficiency as a function of coating-thickness

Collection efficiency (CE) of rBC in the SP-AMS has been found to be dependent on particle morphology (Massoli et al., 2015; Willis et al., 2014). The particle beam has a larger diameter than the laser beam where they overlap in the detection region. The overlap can decrease because non-spherical particles tend to experience higher dispersion in the PToF region (Huffman et al. 2009). The particle beam is thus less focused and the overlap with the intracavity laser is reduced. Particles of similar mass and size but with more compact shape will disperse less, leading to a more focused beam and thus higher CE (Onasch et al. 2012). Coating material can affect rBC morphology and tends to increase CE in the SP-AMS (Willis et al., 2014). Since rBC mass measured by the SP2 is not affected by morphology, it was used to investigate changes in SP-AMS sensitivity to rBC due to morphological changes.

The comparison between SP-AMS and SP2 ambient rBC is shown in **Figure 7-14**a. The scatter between rBC from the SP-AMS ($rBC_{SP\text{-}AMS}$) assuming CE=1 and that of the SP2 (rBC_{SP2}) shows

a slope of 0.37 and a Pearson's r correlation of 0.78 for the ambient data (**Figure 7-14**a). The same scatter under thermodenuder conditions, i.e., after removal of coating material, shows a higher correlation (r=0.82) but a lower slope (0.24, **Figure 7-14**b). Similar results are observed when comparing $rBC_{SP\text{-}AMS}$ to total optical absorption (**Figure 7-14**c, d). The tighter correlations for the thermodenuder data are likely because most rBC coating is evaporated leading to more constant CE. The ratio between $rBC_{SP\text{-}AMS}$ and rBC_{SP2} for ambient data, which can be defined as an apparent CE, appears to vary depending on $R_{coat/rBC}$ (**Figure 7-15**a). Assuming coating thickness affects morphology and hence SP-AMS CE, an $R_{coat/rBC}$-dependent CE correction was derived (Figure S10) by fitting a sigmoid function through the ambient $rBC_{SP\text{-}AMS}/rBC_{SP2}$ vs $R_{coat/rBC}$ relationship (Willis et al. (2014);Massoli et al. (2015), **Figure 7-15**a). The final sigmoid equation is shown below:

$$CE = 0.34 + \left\{ \frac{0.16}{\left[1 + exp\left(\frac{2.5 - R_{BC}}{0.19}\right)\right]} \right\} \quad \text{Eq. A1}$$

The CE for each bypass data point is shown in **Figure 7-16**. For the TD data, a constant value of CE was applied based on the slope found in **Figure 7-14**b. This correction method had the overall effect of increasing the correlation between $rBC_{SP\text{-}AMS}$ and rBC_{SP2} as well as the agreement between ambient by-pass and thermodenuder $rBC_{SP\text{-}AMS}$ (**Figure 7-15**b, c).

As discussed in Section 7.3, this method appeared to overestimate rBC, in particular during the midday foggy period (HF). In this section we explore the possible reasons for this overestimation in order to shed light on quantification issues still remaining for the SP-AMS. By using the sigmoid correction, we make the assumption that coating-to-rBC ratio ($R_{coat/rBC}$) is a proxy for morphology where more coating leads to more spherical particles which would result in a more focused particle beam. However, this assumption may not hold in all cases. As shown in **Figure 7-15**a, the apparent CE ($rBC_{SP\text{-}AMS}/rBC_{SP2}$) values can vary considerably, particularly at $R_{coat/rBC}$>2.5. This variation may not depend exclusively on $R_{coat/rBC}$ and may be induced by varying morphology dependence on other factors, such as coating composition, geometry or phase-state.

We found that the overestimation of rBC, i.e., underestimation of CE using the sigmoid method, occurred during the HF. As shown in **Figure 7-17**, the correlation between uncorrected $rBC_{SP\text{-}AMS}$ and rBC_{SP2}, which here represents variation in apparent CE, is very high during the LF (r^2=0.95) but degrades significantly during the HF (r^2=0.5). **Figure 7-18**a-b shows $rBC_{SP\text{-}AMS}/rBC_{SP2}$ vs $R_{coat/rBC}$ for the HF only with the sigmoid and box plots from **Figure 7-15**a. The data points corresponding to the overestimation periods are well above the sigmoid line, suggesting that this fraction of the particle population is more spherical and forms a more focused particle beam. Nitrate concentration appeared to have a strong correlation with CE for a given $R_{coat/rBC}$ value (**Figure 7-18**b). Other factors such as O/C and fractional contribution of organic tracers were examined as well but nitrate displayed the strongest correlation. This suggests that condensational processes and aqueous-phase processing during the HF modify the morphology such that particles become more spherical and hence display higher CE. These results suggest that the applicability of using $R_{coat/rBC}$ to account for CE change may be influenced by ambient conditions.

Previously published work using the SP-AMS has shown a relatively good correlation between $rBC_{SP\text{-}AMS}$ and rBC from collocated instruments allowing for a constant CE to be applied (Dallmann et al., 2014; Fortner et al., 2012), or have found that CE generally increased with increasing $R_{coat/rBC}$ (Massoli et al., 2015) while many other studies have not sought to quantify rBC or examine effects of coating on CE. In the current study, we have identified a unique situation. However, an exact explanation for why inorganic nitrate coating under foggy conditions increases CE is still unknown. Given these factors, it is not possible to perform additional corrections using a generalized method to increase the correlation between corrected ambient $rBC_{SP\text{-}AMS}$ and rBC_{SP2}. Nevertheless, the aforementioned artifact affects a small portion of the whole data set and does not affect the observations or conclusions discussed in the main manuscript.

7.9 References

Adachi, K., Zaizen, Y., Kajino, M., & Igarashi, Y. (2014). Mixing state of regionally transported soot particles and the coating effect on their size and shape at a mountain site in Japan. *Journal of Geophysical Research: Atmospheres, 119*(9), 5386-5396. doi:10.1002/2013JD020880

Aiken, A., Foy, B. d., Wiedinmyer, C., DeCarlo, P., Ulbrich, I. M., Wehrli, M., . . . Wacker, L. (2010). Mexico city aerosol analysis during MILAGRO using high resolution aerosol mass spectrometry at the urban supersite (T0)–Part 2: Analysis of the biomass burning contribution and the non-fossil carbon fraction. *Atmospheric Chemistry and Physics, 10*(12), 5315-5341.

Aiken, A. C., DeCarlo, P. F., & Jimenez, J. L. (2007). Elemental Analysis of Organic Species with Electron Ionization High-Resolution Mass Spectrometry. *Analytical Chemistry, 79*(21), 8350-8358. doi:10.1021/ac071150w

Allan, J. D., Alice E. Delia, Huge Coe, Keith N. Bower, M. Rami Alfarra, Jose L. Jimenez, . . . Worsnop, D. R. (2004). Technical Note: A generalised method for the extraction of chemically resolved mass spectra from Aerodyne aerosol mass spectrometer data. *Journal of Aerosol Science, 35*, 909-922. doi:10.1016/j.jaerosci.2004.02.007

Allan, J. D., Jimenez, J. L., Williams, P. I., Alfarra, M. R., Bower, K. N., Jayne, J. T., . . . Worsnop, D. R. (2003). Quantitative sampling using an Aerodyne aerosol mass spectrometer 1. Techniques of data interpretation and error analysis. *Journal of Geophysical Research: Atmospheres, 108*(D3).

Antoine, C. (1888). Tensions des vapeurs; nouvelle relation entre les tensions et les températures [Vapor Pressure: a new relationship between pressure and temperature]. *Comptes Rendus des Séances de l'Académie des Sciences (in French), 107*, 681–684, 778–780, 836–837.

Arangio, A. M., Slade, J. H., Berkemeier, T., Pöschl, U., Knopf, D. A., & Shiraiwa, M. (2015). Multiphase Chemical Kinetics of OH Radical Uptake by Molecular Organic Markers of Biomass Burning Aerosols: Humidity and Temperature Dependence, Surface Reaction, and Bulk Diffusion. *The Journal of Physical Chemistry A, 119*(19), 4533-4544. doi:10.1021/jp510489z

Betha, R., Russell, L. M., Chen, C.-L., Liu, J., Price, D. J., Sanchez, K. J., . . . Cappa, C. D. (2018). Larger submicron particles and thicker coatings on black carbon containing particles for emissions with residential burning (in wintertime San Joaquin Valley) than for vehicle combustion (in summertime South Coast Air Basin). *Journal of Geophysical Research: Atmospheres, Submitted*.

Bond, T. C., Doherty, S. J., Fahey, D. W., Forster, P. M., Berntsen, T., DeAngelo, B. J., . . . Zender, C. S. (2013). Bounding the role of black carbon in the climate system: A scientific

assessment. *Journal of Geophysical Research: Atmospheres, 118*(11), 5380-5552. doi:10.1002/jgrd.50171

Bond, T. C., Habib, G., & Bergstrom, R. W. (2006). Limitations in the enhancement of visible light absorption due to mixing state. *Journal of Geophysical Research: Atmospheres (1984–2012), 111*(D20).

Brown, S. G., Hyslop, N. P., Roberts, P. T., McCarthy, M. C., & Lurmann, F. W. (2006). Wintertime Vertical Variations in Particulate Matter (PM) and Precursor Concentrations in the San Joaquin Valley during the California Regional Coarse PM/Fine PM Air Quality Study. *Journal of the Air & Waste Management Association, 56*(9), 1267-1277. doi:10.1080/10473289.2006.10464583

Brown, S. G., Lee, T., Roberts, P. T., & Collett, J. L. (2016). Wintertime Residential Biomass Burning in Las Vegas, Nevada; Marker Components and Apportionment Methods. *Atmosphere, 7*(4), 58.

Buffaloe, G. M., Lack, D. A., Williams, E. J., Coffman, D., Hayden, K. L., Lerner, B. M., . . . Cappa, C. D. (2014). Black carbon emissions from in-use ships: a California regional assessment. *Atmos. Chem. Phys., 14*(4), 1881-1896. doi:10.5194/acp-14-1881-2014

Canagaratna, M., Jayne, J., Jimenez, J., Allan, J., Alfarra, M., Zhang, Q., . . . Middlebrook, A. (2007). Chemical and microphysical characterization of ambient aerosols with the aerodyne aerosol mass spectrometer. *Mass Spectrometry Reviews, 26*(2), 185-222.

Canagaratna, M. R., Jayne, J. T., Ghertner, D. A., Herndon, S., Shi, Q., Jimenez, J. L., . . . Worsnop, D. R. (2004). Chase studies of particulate emissions from in-use New York city vehicles. *Aerosol Science & Technology, 38*, 555-573, 510.1080/02786820490465504.

Canagaratna, M. R., Jimenez, J. L., Kroll, J. H., Chen, Q., Kessler, S. H., Massoli, P., . . . Worsnop, D. R. (2015a). Elemental ratio measurements of organic compounds using aerosol mass spectrometry: characterization, improved calibration, and implications. *Atmos. Chem. Phys., 15*(1), 253-272. doi:10.5194/acp-15-253-2015

Canagaratna, M. R., Massoli, P., Browne, E. C., Franklin, J. P., Wilson, K. R., Onasch, T. B., . . . Worsnop, D. R. (2015b). Chemical Compositions of Black Carbon Particle Cores and Coatings via Soot Particle Aerosol Mass Spectrometry with Photoionization and Electron Ionization. *The Journal of Physical Chemistry A, 119*(19), 4589-4599. doi:10.1021/jp510711u

Cappa, C. D., Onasch, T. B., Massoli, P., Worsnop, D. R., Bates, T. S., Cross, E. S., . . . Zaveri, R. A. (2012). Radiative absorption enhancements due to the mixing state of atmospheric black carbon. *Science, 337*(6098), 1078-1081. doi:10.1126/science.1223447

Carbone, S., Onasch, T., Saarikoski, S., Timonen, H., Saarnio, K., Sueper, D., . . . Hillamo, R. (2015). Characterization of trace metals on soot aerosol particles with the SP-AMS: detection and quantification. *Atmos. Meas. Tech., 8*(11), 4803-4815. doi:10.5194/amt-8-4803-2015

Chen, C.-L., Chen, S., Russell, L. M., Liu, J., Price, D. J., Betha, R., . . . Cappa, C. D. (2018). Organic aerosol particle chemical properties associated with residential burning and fog in wintertime San Joaquin Valley (Fresno) and with vehicle and firework emissions in summertime South Coast Air Basin (Fontana) *Journal of Geophysical Research: Atmospheres, Submitted*.

China, S., Salvadori, N., & Mazzoleni, C. (2014). Effect of Traffic and Driving Characteristics on Morphology of Atmospheric Soot Particles at Freeway On-Ramps. *Environmental Science & Technology, 48*(6), 3128-3135. doi:10.1021/es405178n

China, S., Scarnato, B., Owen, R. C., Zhang, B., Ampadu, M. T., Kumar, S., . . . Mazzoleni, C. (2015). Morphology and mixing state of aged soot particles at a remote marine free troposphere

site: Implications for optical properties. *Geophysical Research Letters, 42*(4), 1243-1250. doi:10.1002/2014GL062404

Chow, J., Watson, J., Lowenthal, D., Chen, L., Zielinska, B., Mazzoleni, L., & Magliano, K. (2007). Evaluation of organic markers for chemical mass balance source apportionment at the Fresno Supersite. *Atmospheric Chemistry and Physics, 7*(7), 1741-1754.

Chow, J. C., Chen, L. W. A., Watson, J. G., Lowenthal, D. H., Magliano, K. A., Turkiewicz, K., & Lehrman, D. E. (2008). PM2.5 chemical composition and spatiotemporal variability during the California Regional PM10/PM2.5 Air Quality Study (CRPAQS). *Journal of Geophysical Research-Atmospheres, 111*(D10), D10S04. doi:10.1029/2005jd006457

Collett, J. L., Herckes, P., Youngster, S., & Lee, T. (2008). Processing of atmospheric organic matter by California radiation fogs. *Atmospheric Research, 87*(3-4), 232-241. doi:DOI 10.1016/j.atmosres.2007.11.005

Collier, S., Zhou, S., Kuwayama, T., Forestieri, S., Brady, J., Zhang, M., . . . Zhang, Q. (2015). Organic PM Emissions from Vehicles: Composition, O/C Ratio, and Dependence on PM Concentration. *Aerosol Science and Technology, 49*(2), 86-97. doi:10.1080/02786826.2014.1003364

Corbin, J. C., Lohmann, U., Sierau, B., Keller, A., Burtscher, H., & Mensah, A. A. (2015). Black carbon surface oxidation and organic composition of beech-wood soot aerosols. *Atmos. Chem. Phys., 15*(20), 11885-11907. doi:10.5194/acp-15-11885-2015

Corbin, J. C., Sierau, B., Gysel, M., Laborde, M., Keller, A., Kim, J., . . . Mensah, A. A. (2014). Mass spectrometry of refractory black carbon particles from six sources: carbon-cluster and oxygenated ions. *Atmos. Chem. Phys., 14*(5), 2591-2603. doi:10.5194/acp-14-2591-2014

Cross, E. S., Onasch, T. B., Ahern, A., Wrobel, W., Slowik, J. G., Olfert, J., . . . Davidovits, P. (2010). Soot Particle Studies—Instrument Inter-Comparison—Project Overview. *Aerosol Science and Technology, 44*(8), 592-611. doi:10.1080/02786826.2010.482113

Cubison, M. J., Ortega, A. M., Hayes, P. L., Farmer, D. K., Day, D., Lechner, M. J., . . . Jimenez, J. L. (2011). Effects of aging on organic aerosol from open biomass burning smoke in aircraft and laboratory studies. *Atmos. Chem. Phys., 11*(23), 12049-12064. doi:10.5194/acp-11-12049-2011

Dallmann, T. R., Onasch, T. B., Kirchstetter, T. W., Worton, D. R., Fortner, E. C., Herndon, S. C., . . . Harley, R. A. (2014). Characterization of particulate matter emissions from on-road gasoline and diesel vehicles using a soot particle aerosol mass spectrometer. *Atmos. Chem. Phys., 14*(14), 7585-7599. doi:10.5194/acp-14-7585-2014

Decesari, S., Allan, J., Plass-Duelmer, C., Williams, B. J., Paglione, M., Facchini, M. C., . . . Dall'Osto, M. (2014). Measurements of the aerosol chemical composition and mixing state in the Po Valley using multiple spectroscopic techniques. *Atmos. Chem. Phys., 14*(22), 12109-12132. doi:10.5194/acp-14-12109-2014

Ding, A. J., Huang, X., Nie, W., Sun, J. N., Kerminen, V. M., Petäjä, T., . . . Fu, C. B. (2016). Black carbon enhances haze pollution in megacities in China. *Geophysical Research Letters*, n/a-n/a. doi:10.1002/2016GL067745

Drewnick, F., Hings, S. S., Curtius, J., Eerdekens, G., & Williams, J. (2006). Measurement of fine particulate and gas-phase species during the New Year's fireworks 2005 in Mainz, Germany. *Atmospheric Environment, 40*(23), 4316-4327.

Dupont, J. C., Haeffelin, M., Badosa, J., Elias, T., Favez, O., Petit, J. E., . . . Bonne, J. L. (2016). Role of the boundary layer dynamics effects on an extreme air pollution event in Paris. *Atmospheric Environment, 141*, 571-579. doi:10.1016/j.atmosenv.2016.06.061

Dusek, U., Reischl, G. P., & Hitzenberger, R. (2006). CCN Activation of Pure and Coated Carbon Black Particles. *Environmental Science & Technology, 40*(4), 1223-1230. doi:10.1021/es0503478

Fortner, E. C., Brooks, W. A., Onasch, T. B., Canagaratna, M. R., Massoli, P., Jayne, J. T., . . . Herndon, S. C. (2012). Particulate Emissions Measured During the TCEQ Comprehensive Flare Emission Study. *Industrial & Engineering Chemistry Research, 51*(39), 12586-12592. doi:10.1021/ie202692y

Fuller, K. A., Malm, W. C., & Kreidenweis, S. M. (1999). Effects of mixing on extinction by carbonaceous particles. *Journal of Geophysical Research: Atmospheres, 104*(D13), 15941-15954. doi:10.1029/1998JD100069

Ge, X., Setyan, A., Sun, Y., & Zhang, Q. (2012a). Primary and secondary organic aerosols in Fresno, California during wintertime: Results from high resolution aerosol mass spectrometry. *Journal of Geophysical Research: Atmospheres, 117*(D19). doi:10.1029/2012JD018026

Ge, X., Zhang, Q., Sun, Y., Ruehl, C. R., & Setyan, A. (2012b). Effect of aqueous-phase processing on aerosol chemistry and size distributions in Fresno, California, during wintertime. *Environ. Chem., 9*(3), 221-235. doi:10.1071/EN11168

Gong, X., Zhang, C., Chen, H., Nizkorodov, S. A., Chen, J., & Yang, X. (2016). Size distribution and mixing state of black carbon particles during a heavy air pollution episode in Shanghai. *Atmos. Chem. Phys., 16*(8), 5399-5411. doi:10.5194/acp-16-5399-2016

Hayes, P. L., Ortega, A. M., Cubison, M. J., Froyd, K. D., Zhao, Y., Cliff, S. S., . . . Jimenez, J. L. (2013). Organic aerosol composition and sources in Pasadena, California, during the 2010 CalNex campaign. *Journal of Geophysical Research-Atmospheres, 118*(16), 9233-9257. doi:10.1002/jgrd.50530

Healy, R. M., Wang, J. M., Jeong, C. H., Lee, A. K. Y., Willis, M. D., Jaroudi, E., . . . Evans, G. J. (2015). Light-absorbing properties of ambient black carbon and brown carbon from fossil fuel and biomass burning sources. *Journal of Geophysical Research: Atmospheres, 120*(13), 6619-6633. doi:10.1002/2015JD023382

Herckes, P., Chang, H., Lee, T., & Collett, J. L. (2007). Air pollution processing by radiation fogs. *Water Air and Soil Pollution, 181*(1-4), 65-75. doi:10.1007/s11270-006-9276-x

Herckes, P., Lee, T., Trenary, L., Kang, G. G., Chang, H., & Collett, J. L. (2002). Organic matter in Central California radiation fogs. *Environmental Science & Technology, 36*(22), 4777-4782. doi:Doi 10.1021/Es025889t

Jimenez, J. L., Canagaratna, M. R., Drewnick, F., Allan, J. D., Alfarra, M. R., Middlebrook, A. M., . . . Worsnop, D. R. (2016). Comment on "The effects of molecular weight and thermal decomposition on the sensitivity of a thermal desorption aerosol mass spectrometer". *Aerosol Science and Technology, 50*(9), i-xv. doi:10.1080/02786826.2016.1205728

Jimenez, J. L., Jayne, J. T., Shi, Q., Kolb, C. E., Worsnop, D. R., Yourshaw, I., . . . Davidovits, P. (2003). Ambient aerosol sampling using the Aerodyne Aerosol Mass Spectrometer. *Journal of Geophysical Research: Atmospheres, 108*(D7), 8425. doi:10.1029/2001JD001213

Kuwata, M., Zorn, S. R., & Martin, S. T. (2011). Using Elemental Ratios to Predict the Density of Organic Material Composed of Carbon, Hydrogen, and Oxygen. *Environmental Science & Technology, 46*(2), 787-794. doi:10.1021/es202525q

Lambe, A. T., Ahern, A. T., Wright, J. P., Croasdale, D. R., Davidovits, P., & Onasch, T. B. (2015). Oxidative aging and cloud condensation nuclei activation of laboratory combustion soot. *Journal of Aerosol Science, 79*, 31-39. doi:10.1016/j.jaerosci.2014.10.001

Lee, A. K. Y., Willis, M. D., Healy, R. M., Onasch, T. B., & Abbatt, J. P. D. (2015). Mixing state of carbonaceous aerosol in an urban environment: single particle characterization using the soot particle aerosol mass spectrometer (SP-AMS). *Atmos. Chem. Phys., 15*(4), 1823-1841. doi:10.5194/acp-15-1823-2015

Lee, T., Sullivan, A. P., Mack, L., Jimenez, J. L., Kreidenweis, S. M., Onasch, T. B., . . . Collett, J. L. (2010). Chemical Smoke Marker Emissions During Flaming and Smoldering Phases of Laboratory Open Burning of Wildland Fuels. *Aerosol Science and Technology, 44*(9), i-v. doi:10.1080/02786826.2010.499884

Liu, D., Allan, J., Whitehead, J., Young, D., Flynn, M., Coe, H., . . . Bandy, B. (2013). Ambient black carbon particle hygroscopic properties controlled by mixing state and composition. *Atmos. Chem. Phys., 13*(4), 2015-2029. doi:10.5194/acp-13-2015-2013

Liu, D., Allan, J. D., Young, D. E., Coe, H., Beddows, D., Fleming, Z. L., . . . Zotter, P. (2014). Size distribution, mixing state and source apportionment of black carbon aerosol in London during wintertime. *Atmos. Chem. Phys., 14*(18), 10061-10084. doi:10.5194/acp-14-10061-2014

Liu, D., Whitehead, J., Alfarra, M. R., Reyes-Villegas, E., Spracklen, D. V., Reddington, C. L., . . . Allan, J. D. (2017). Black-carbon absorption enhancement in the atmosphere determined by particle mixing state. *Nature Geosci, 10*(3), 184-188. doi:10.1038/ngeo2901

Liu, S., Aiken, A. C., Gorkowski, K., Dubey, M. K., Cappa, C. D., Williams, L. R., . . . Prevot, A. S. H. (2015). Enhanced light absorption by mixed source black and brown carbon particles in UK winter. *Nat Commun, 6*. doi:10.1038/ncomms9435

Martin, M., Tritscher, T., Jurányi, Z., Heringa, M. F., Sierau, B., Weingartner, E., . . . Lohmann, U. (2013). Hygroscopic properties of fresh and aged wood burning particles. *Journal of Aerosol Science, 56*, 15-29. doi:10.1016/j.jaerosci.2012.08.006

Massoli, P., Onasch, T. B., Cappa, C. D., Nuamaan, I., Hakala, J., Hayden, K., . . . Worsnop, D. R. (2015). Characterization of black carbon-containing particles from soot particle aerosol mass spectrometer (SP-AMS) measurements on the R/V Atlantis during CalNex 2010. *Journal of Geophysical Research: Atmospheres*, 2575-2593. doi:10.1002/2014JD022834

Matsui, H., Koike, M., Kondo, Y., Moteki, N., Fast, J. D., & Zaveri, R. A. (2013). Development and validation of a black carbon mixing state resolved three-dimensional model: Aging processes and radiative impact. *Journal of Geophysical Research: Atmospheres, 118*(5), 2304-2326. doi:10.1029/2012JD018446

Mohr, C., DeCarlo, P., Heringa, M., Chirico, R., Slowik, J., Richter, R., . . . Seco, R. (2012). Identification and quantification of organic aerosol from cooking and other sources in Barcelona using aerosol mass spectrometer data. *Atmospheric Chemistry and Physics, 12*(4), 1649-1665.

Morgan, W., Allan, J., Bower, K., Highwood, E. J., Liu, D., McMeeking, G., . . . Coe, H. (2010). Airborne measurements of the spatial distribution of aerosol chemical composition across Europe and evolution of the organic fraction. *Atmospheric Chemistry and Physics, 10*(8), 4065-4083.

Murphy, D. M. (2016). The effects of molecular weight and thermal decomposition on the sensitivity of a thermal desorption aerosol mass spectrometer. *Aerosol Science and Technology, 50*(2), 118-125. doi:10.1080/02786826.2015.1136403

Nakayama, T., Ikeda, Y., Sawada, Y., Setoguchi, Y., Ogawa, S., Kawana, K., . . . Matsumi, Y. (2014). Properties of light-absorbing aerosols in the Nagoya urban area, Japan, in August 2011 and January 2012: Contributions of brown carbon and lensing effect. *Journal of Geophysical Research: Atmospheres, 119*(22), 12,721-712,739. doi:10.1002/2014JD021744

Ng, N. L., Canagaratna, M. R., Zhang, Q., Jimenez, J. L., Tian, J., Ulbrich, I. M., . . . Worsnop, D. R. (2010). Organic aerosol components observed in Northern Hemispheric datasets from Aerosol Mass Spectrometry. *Atmos. Chem. Phys., 10*, 4625-4641.

Onasch, T. B., Fortner, E. C., Trimborn, A. M., Lambe, A. T., Tiwari, A. J., Marr, L. C., . . . Worsnop, D. R. (2015). Investigations of SP-AMS Carbon Ion Distributions as a Function of Refractory Black Carbon Particle Type. *Aerosol Science and Technology, 49*(6), 409-422. doi:10.1080/02786826.2015.1039959

Onasch, T. B., Trimborn, A., Fortner, E. C., Jayne, J. T., Kok, G. L., Williams, L. R., . . . Worsnop, D. R. (2012). Soot particle aerosol mass spectrometer: Development, validation, and initial application. *Aerosol Science and Technology, 46*(7), 804-817. doi:10.1080/02786826.2012.663948

Ortega, A. M., Day, D. A., Cubison, M. J., Brune, W. H., Bon, D., de Gouw, J. A., & Jimenez, J. L. (2013). Secondary organic aerosol formation and primary organic aerosol oxidation from biomass-burning smoke in a flow reactor during FLAME-3. *Atmos. Chem. Phys., 13*(22), 11551-11571. doi:10.5194/acp-13-11551-2013

Pagels, J., Khalizov, A. F., McMurry, P. H., & Zhang, R. Y. (2009). Processing of soot by controlled sulphuric acid and water condensation—mass and mobility relationship. *Aerosol Science and Technology, 43*(7), 629-640.

Parworth, C. L., Young, D. E., Kim, H., Zhang, X., Cappa, C. D., Collier, S., & Zhang, Q. (2017). Wintertime water-soluble aerosol composition and particle water content in Fresno, California. *Journal of Geophysical Research: Atmospheres*.

Petzold, A., Ogren, J. A., Fiebig, M., Laj, P., Li, S. M., Baltensperger, U., . . . Zhang, X. Y. (2013). Recommendations for reporting "black carbon" measurements. *Atmospheric Chemistry and Physics, 13*(16), 8365-8379. doi:10.5194/acp-13-8365-2013

Pusede, S. E., Duffey, K. C., Shusterman, A. A., Saleh, A., Laughner, J. L., Wooldridge, P. J., . . . Cohen, R. C. (2016). On the effectiveness of nitrogen oxide reductions as a control over ammonium nitrate aerosol. *Atmos. Chem. Phys., 16*(4), 2575-2596. doi:10.5194/acp-16-2575-2016

Salcedo, D., Laskin, A., Shutthanandan, V., & Jimenez, J. L. (2012). Feasibility of the Detection of Trace Elements in Particulate Matter Using Online High-Resolution Aerosol Mass Spectrometry. *Aerosol Science and Technology, 46*(11), 1187-1200. doi:10.1080/02786826.2012.701354

Schroder, J. C., Hanna, S. J., Modini, R. L., Corrigan, A. L., Kreidenweis, S. M., Macdonald, A. M., . . . Bertram, A. K. (2015). Size-resolved observations of refractory black carbon particles in cloud droplets at a marine boundary layer site. *Atmos. Chem. Phys., 15*(3), 1367-1383. doi:10.5194/acp-15-1367-2015

Schwarz, J. P., Gao, R. S., Spackman, J. R., Watts, L. A., Thomson, D. S., Fahey, D. W., . . . Del Negro, L. A. (2008). Measurement of the mixing state, mass, and optical size of individual black carbon particles in urban and biomass burning emissions. *Geophysical Research Letters, 35*(13), n/a-n/a. doi:10.1029/2008GL033968

Shiraiwa, M., Kondo, Y., Iwamoto, T., & Kita, K. (2010). Amplification of Light Absorption of Black Carbon by Organic Coating. *Aerosol Science and Technology, 44*(1), 46-54. doi:10.1080/02786820903357686

Taylor, J. W., Allan, J. D., Allen, G., Coe, H., Williams, P. I., Flynn, M. J., . . . Palmer, P. I. (2014). Size-dependent wet removal of black carbon in Canadian biomass burning plumes. *Atmos. Chem. Phys., 14*(24), 13755-13771. doi:10.5194/acp-14-13755-2014

Tumolva, L., Park, J.-Y., Kim, J.-s., Miller, A. L., Chow, J. C., Watson, J. G., & Park, K. (2010). Morphological and Elemental Classification of Freshly Emitted Soot Particles and Atmospheric Ultrafine Particles using the TEM/EDS. *Aerosol Science and Technology, 44*(3), 202-215. doi:10.1080/02786820903518907

Wang, J., Ge, X., Chen, Y., Shen, Y., Zhang, Q., Sun, Y., . . . Chen, M. (2016a). Highly time-resolved urban aerosol characteristics during springtime in Yangtze River Delta, China: insights from soot particle aerosol mass spectrometry. *Atmos. Chem. Phys., 16*(14), 9109-9127. doi:10.5194/acp-16-9109-2016

Wang, J., Onasch, T. B., Ge, X., Collier, S., Zhang, Q., Sun, Y., . . . Worsnop, D. R. (2016b). Observation of Fullerene Soot in Eastern China. *Environmental Science & Technology Letters, 3*(4), 121-126. doi:10.1021/acs.estlett.6b00044

Willis, M. D., Healy, R. M., Riemer, N., West, M., Wang, J. M., Jeong, C. H., . . . Lee, A. K. Y. (2016). Quantification of black carbon mixing state from traffic: implications for aerosol optical properties. *Atmos. Chem. Phys., 16*(7), 4693-4706. doi:10.5194/acp-16-4693-2016

Willis, M. D., Lee, A. K. Y., Onasch, T. B., Fortner, E. C., Williams, L. R., Lambe, A. T., . . . Abbatt, J. P. D. (2014). Collection efficiency of the Soot-Particle Aerosol Mass Spectrometer (SP-AMS) for internally mixed particulate black carbon. *Atmos. Meas. Tech., 7*(5), 4507-4516. doi:10.5194/amt-7-4507-2014

Young, D. E., Kim, H., Parworth, C., Zhou, S., Zhang, X., Cappa, C. D., . . . Zhang, Q. (2016). Influences of emission sources and meteorology on aerosol chemistry in a polluted urban environment: results from DISCOVER-AQ California. *Atmos. Chem. Phys., 16*(8), 5427-5451. doi:10.5194/acp-16-5427-2016

Zhang, Q., Alfarra, M. R., Worsnop, D. R., Allan, J. D., Coe, H., Canagaratna, M. R., & Jimenez, J. L. (2005a). Deconvolution and Quantification of Hydrocarbon-like and Oxygenated Organic Aerosols Based on Aerosol Mass Spectrometry. *Environmental Science & Technology, 39*(13), 4938-4952.

Zhang, Q., Canagaratna, M. R., Jayne, J. T., Worsnop, D. R., & Jimenez, J. L. (2005b). Time- and size-resolved chemical composition of submicron particles in Pittsburgh: Implications for aerosol sources and processes. *Journal of Geophysical Research: Atmospheres, 110*(D7).

Zhang, X., Kim, H., Parworth, C. L., Young, D. E., Zhang, Q., Metcalf, A. R., & Cappa, C. D. (2016). Optical Properties of Wintertime Aerosols from Residential Wood Burning in Fresno, CA: Results from DISCOVER-AQ 2013. *Environmental Science & Technology, 50*(4), 1681-1690. doi:10.1021/acs.est.5b04134

7.10 Figures

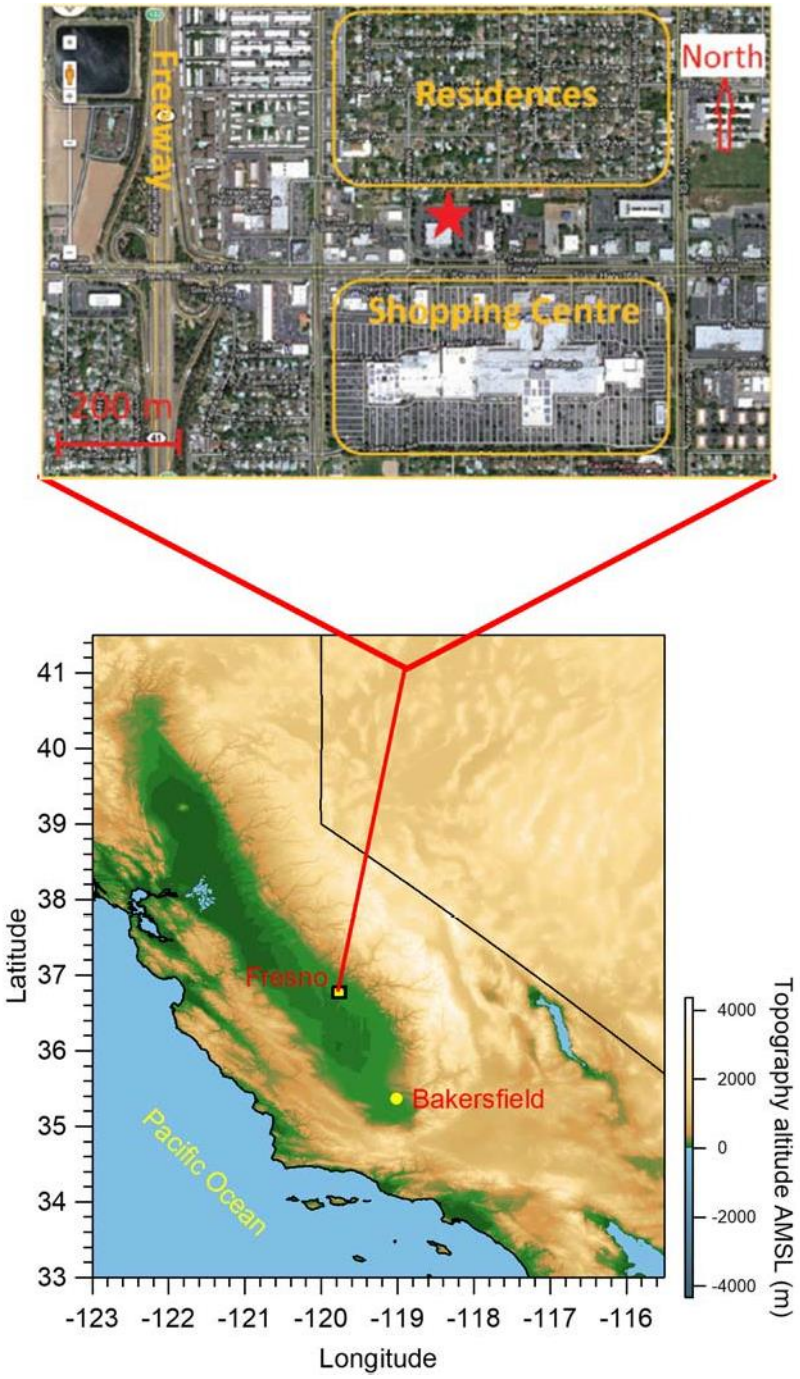

Figure 7-1. Description of sampling location. Top figure reprinted with permission from Ge, et al.

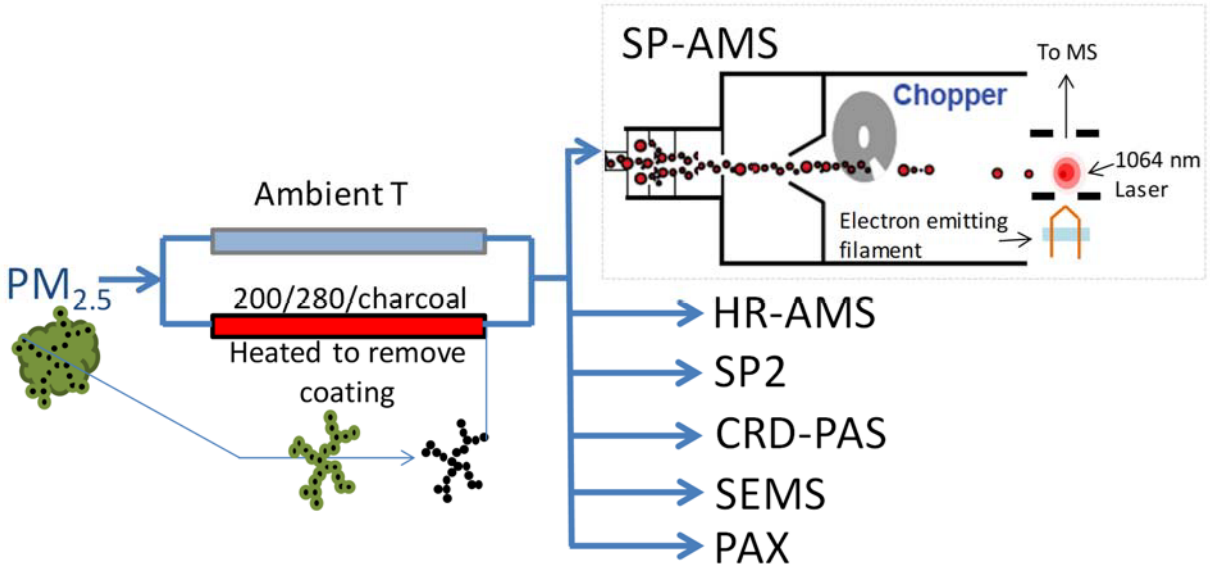

Figure 7-2. Schematic of experimental setup. A cyclone with a 2.5 µm size cutoff preceded a switching thermodenuder (TD) with an ambient bypass line and a heated line. Downstream of the TD, particles were sampled by an Aerodyne soot particle aerosol mass spectrometer (SP- AMS) for the measurement of particles containing rBC, an Aerodyne high resolution aerosol mass spectrometer (HR-AMS) for the measurement of non-refractory fine particulate matter, a Droplet Measurement Technologies single particle soot photometer (SP2) for the measurement of refractory black carbon mass and size, a cavity ringdown photoacoustic spectrometer (CRD- PAS) and a photoacoustic extinctiometer (PAX) for the measurement of optical properties of fine particulate matter, and a scanning electrical mobility sizer (SEMS) for measurement of the size distribution of fine particulate matter.

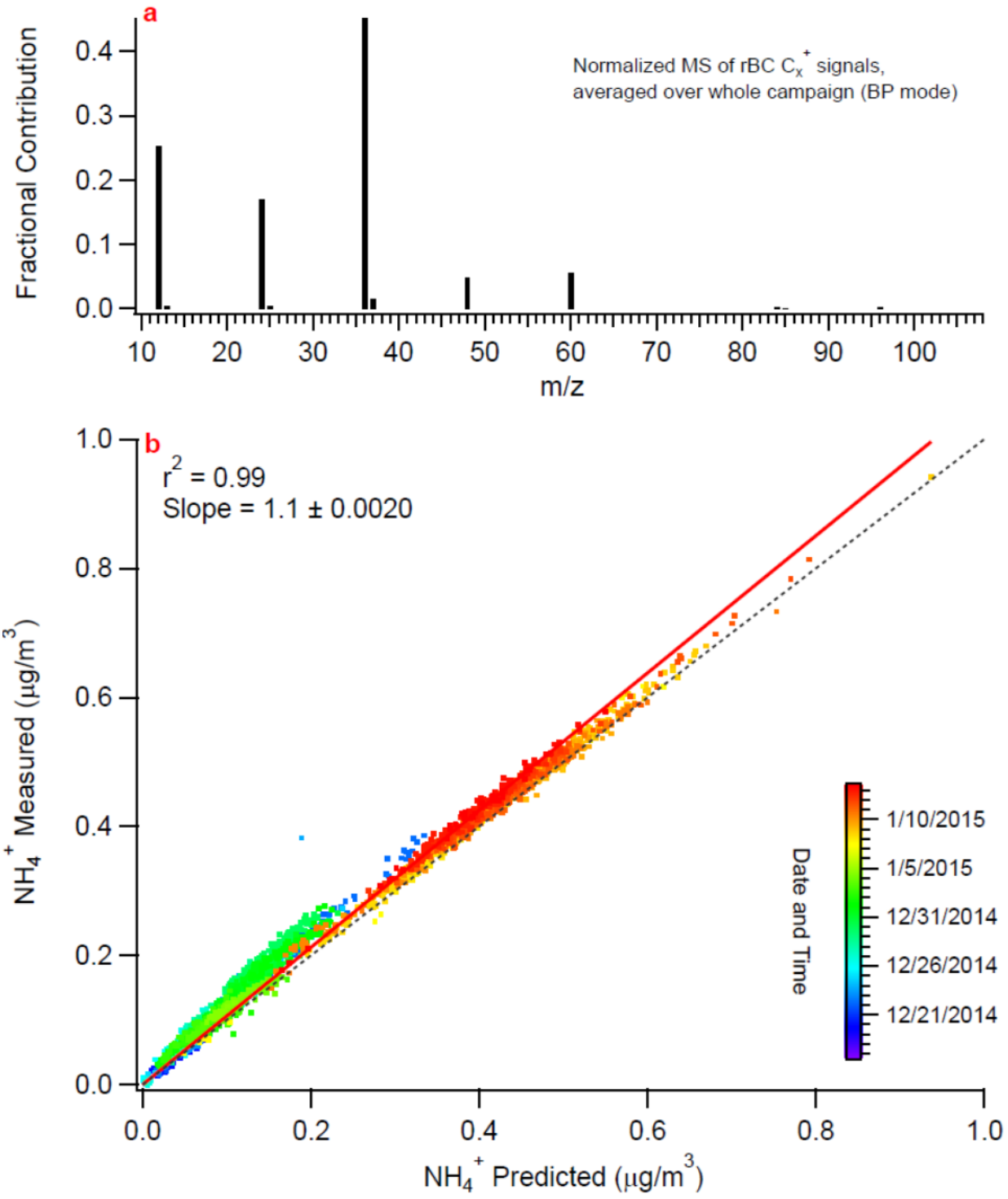

Figure 7-3. a) Normalized mass spectrum of rBC Cx+ ion signals, averaged over whole campaign in bypass mode. b) Scatter plot of measured ammonium derived from high resolution mass spectral analysis versus predicted ammonium, based on sum of cations and where data points are colored by time. Relative ionization efficiency of ammonia is set to 5.2.

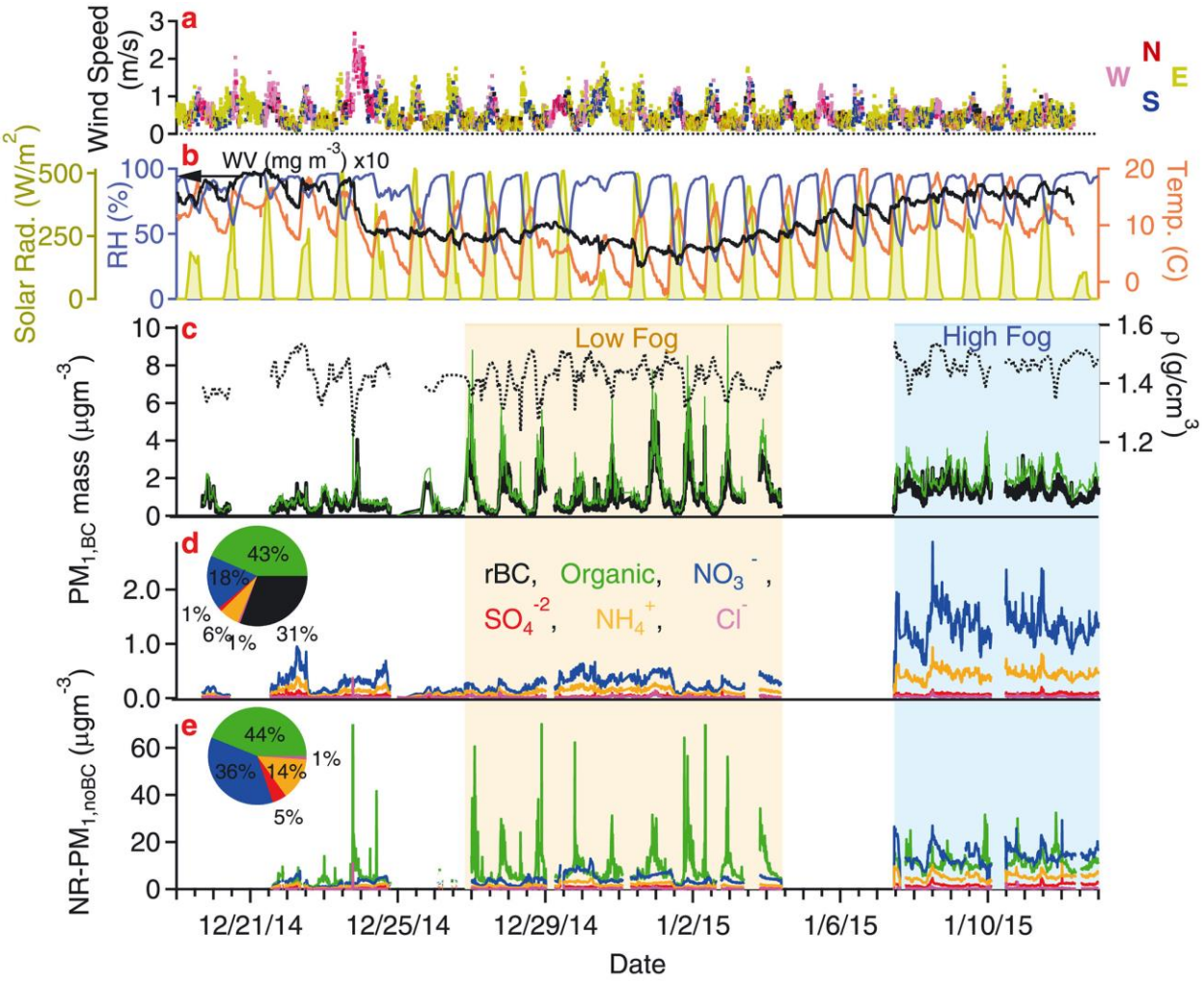

Figure 7-4. Time series of a) wind speed (WS) and direction, b) solar radiation, relative humidity (RH), water vapor content (x10 mg/m^3) and temperature (T), c) organic and rBC mass concentrations (left axis) and the particle density of rBC-containing particles (right axis), d) mass concentrations of inorganic components on rBC-containing particles, and e) mass concentrations of PM_1 not containing rBC ($NR\text{-}PM_{1,noBC} = NR\text{-}PM_1 - PM_{1,BC}$). The average mass fractional contribution of species in rBC-containing particles and non-rBC containing particles are shown in the pies of panels d) and e) where average mass of $PM_{1,BC}$ =3.4 µg/m^3 and $NR\text{-}PM_{1,noBC}$ =19.4 µg/m^3.

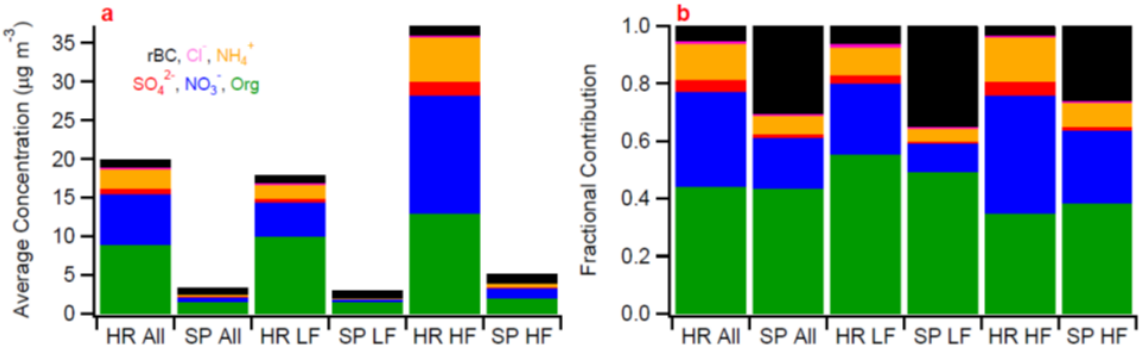

Figure 7-5. Panels a) and b) show the concentration and fractional contribution of the species for the collocated high resolution aerosol mass spectrometer (HR) and the soot-particle aerosol mass spectrometer (SP) divided by campaign-wide average (All), low fog period (LF) and high fog period (HF). For the HR instrument, the rBC concentrations reported are from the collocated SP2 instrument.

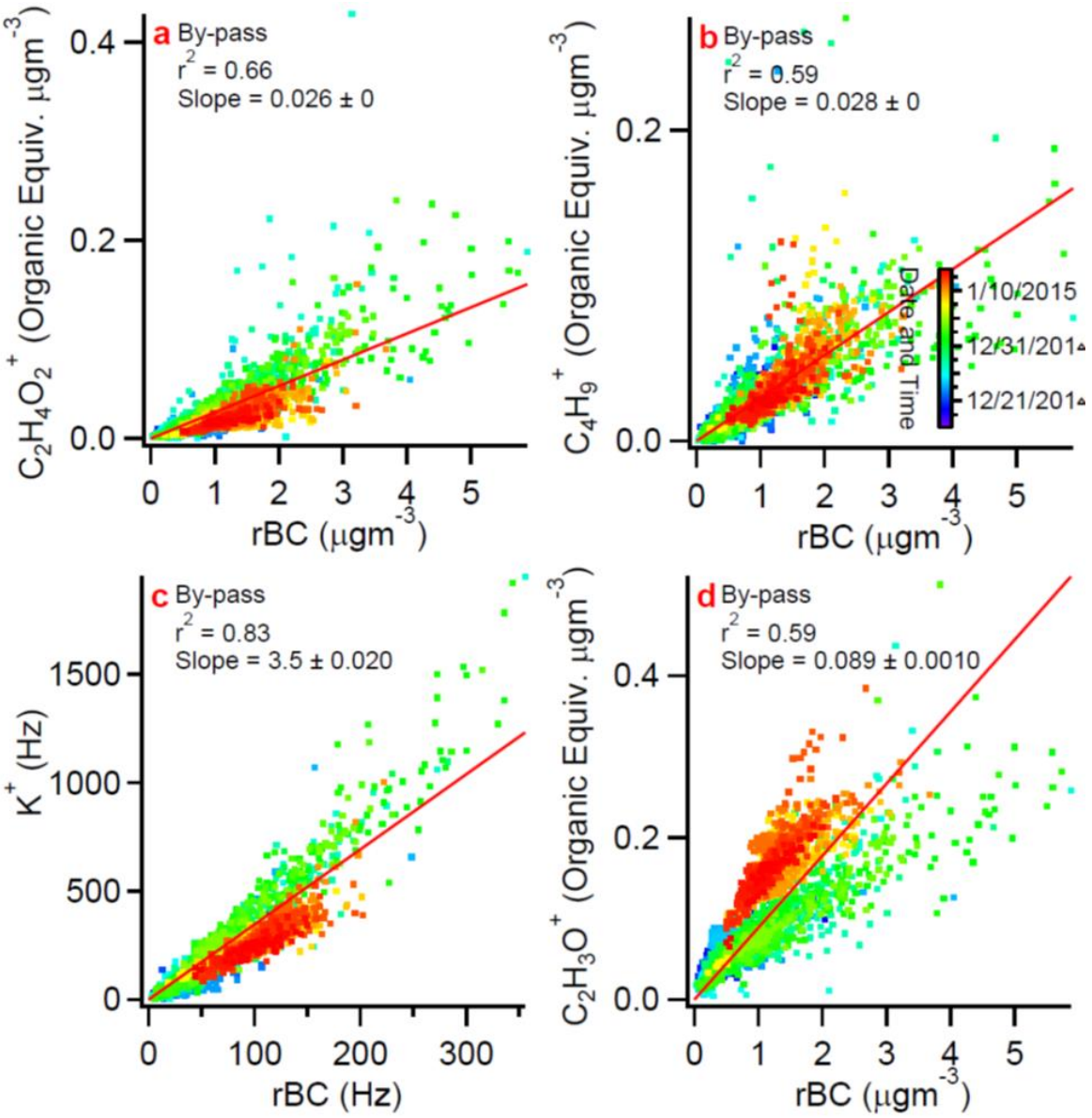

Figure 7-6. Scatter plot of the organic equivalent mass of a) C2H4O2+ (*m/z* = 60, biomass burning tracer) and b) C4H9+ (*m/z* = 57, vehicle tracer), d) the ion signal strength in Hz of K+ (*m/z* = 39, biomass burning tracer) and the organic equivalent mass of d) C2H3O+ (*m/z* = 43, tracer for semi-volatile organic aerosol) vs rBC mass. All markers are colored by date.

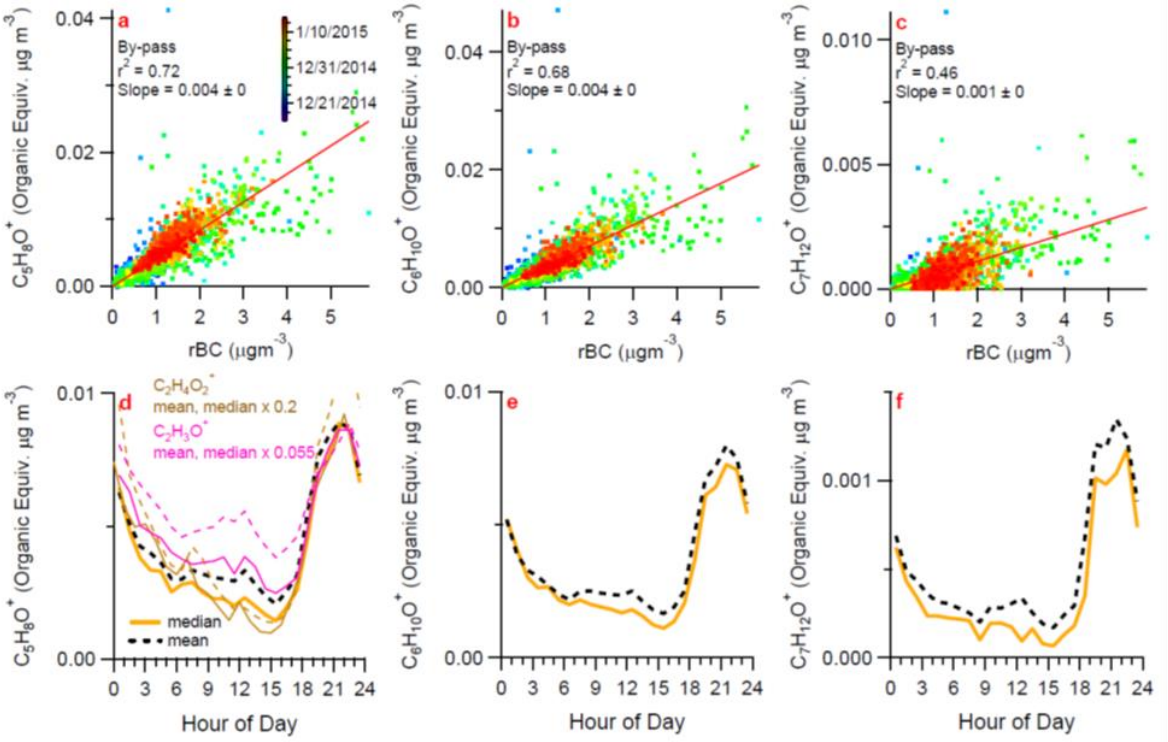

Figure 7-7. : Scatter plot of the organic equivalent mass of a) C5H8O+ (m/z = 84), b) C6H10O+ (m/z= 98) and c) C7H12O+ (m/z = 112) vs rBC mass. Diurnal plots of the median and mean concentrations of the organic equivalent mass of d) C5H8O+, e) C6H10O+ and f) C7H12O+. Panel d) also has the mean and median diurnal values for C2H4O2+ (m/z = 60, BB tracer) multiplied by a factor of 0.2 and the mean and median values of C2H3O+ (m/z = 43) multiplied by a factor of 0.055. Food cooking was found to be a significant source of primary organic aerosol (POA) in Fresno in previous studies and the diurnal patterns of cooking organic aerosol (COA) tend to show noontime peaks suggestive of lunch-related activity 2-4. However, in this current campaign COA was not resolved in the PMF analysis of the NR-PM1 spectra 5 and cooking activities did not appear to significantly affect rBC-containing particles (Figure S6). Here, tracer ions for COA determined previously, e.g., C5H8O+, C6H10O+ and C7H12O+ 6, were examined to evaluate the possible influence of COA on rBC-containing particles at this location. C5H8O+, C6H10O+ and C7H12O+ were found to have moderate to tight correlations with rBC (r2 = 0.72, 0.68, 0.46, respectively, Figure S6) and their diurnal patterns show a slight increase around noon as observed for COA in previous studies 2, 3. However, organic-equivalent concentrations of the COA tracer ions are very low and in the diurnal profiles the noontime peaks are weak compared to larger nighttime peaks that behave more like the BB tracers. In addition, C5H8O+, C6H10O+ and C7H12O+ have moderate correlations with the BB tracers C2H4O2+ (r2 = 0.56, 0.59, and 0.44, respectively) and K+ (r2 = 0.58, 0.60, and 0.43, respectively) and slightly higher correlations with the fossil fuel combustion tracer C4H9+ (r2 = 0.73, 0.72, and 0.52, respectively), suggesting that these ions are associated with BB and vehicle emissions as well. Overall, it appears that cooking activities do not significantly affect rBC-containing particles in this study.

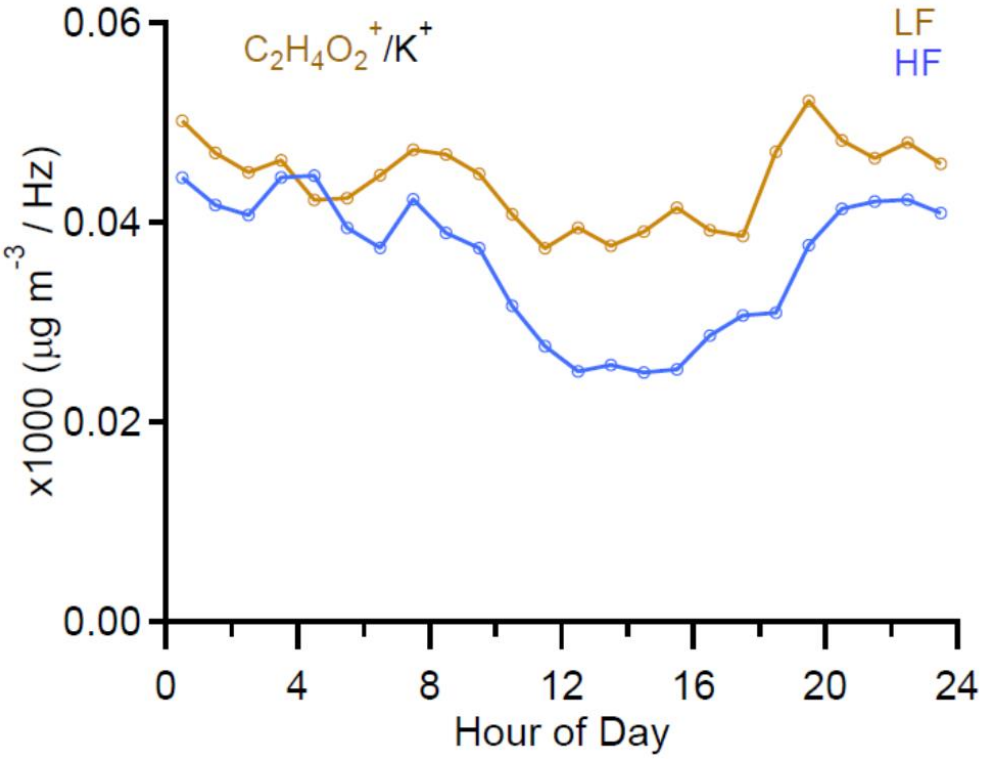

Figure 7-8. Diurnal profile of the ratio of C2H4O2+ (x1000 in organic equivalent µg m-3) to K+ (in Hz) for the LF and HF periods.

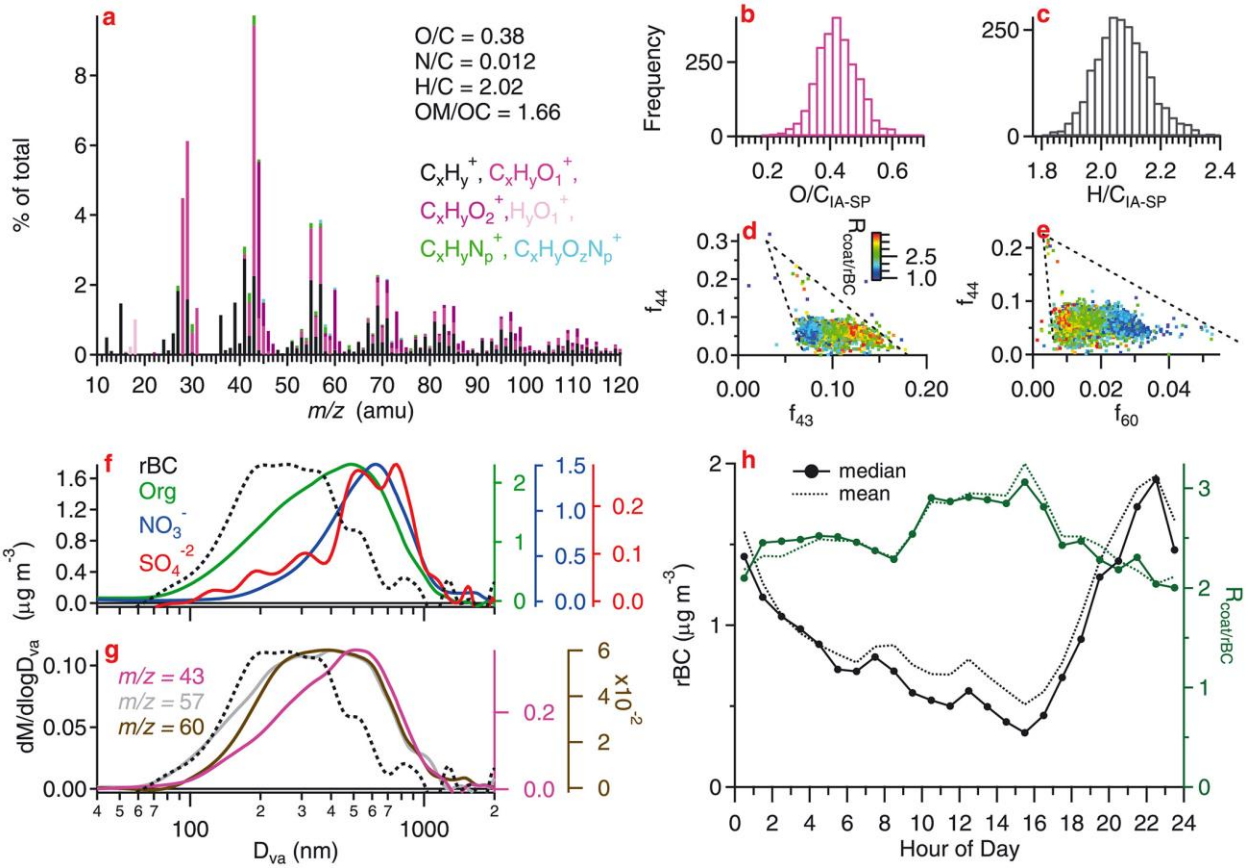

Figure 7-9. a) Campaign averaged mass spectrum of the organic material internally mixed with rBC shown in unit mass resolution where colors represent ion family. Averaged elemental ratios and ion family color scheme are shown in legend. Panels b) and c) show the histograms of the O/C and H/C values, respectively. Panel d) shows the scatter plot of f_{44} vs. f_{43} where dashed lines represent triangle plot boundaries from Ng et al. (2010). Panel e) shows the scatter plot of f_{44} vs. f_{60} where dashed lines represent triangle plot boundaries for BBOA from Ortega et al. (2013). Average chemically resolved size distribution for f) rBC, organic, nitrate and sulfate and g) ion tracers for vehicle emissions (*m/z*=57), biomass burning (*m/z*=60) and oxidized organics (*m/z*=43), and rBC (broken line). Panel h) shows the campaign average diurnal profiles for rBC and $R_{coat/rBC}$.

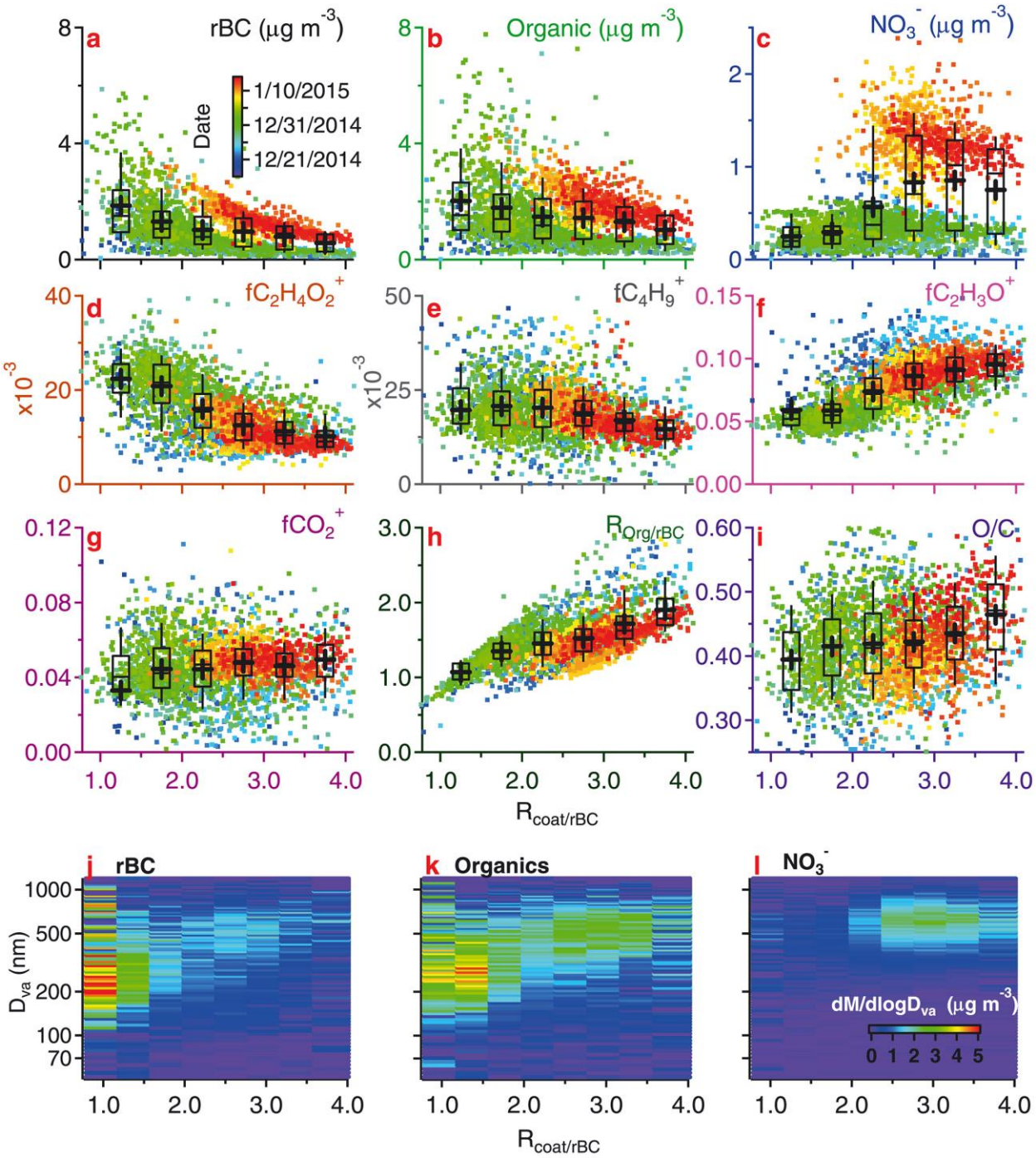

Figure 7-10. Panels a-i show the concentration or fractional contribution of major chemical components as a function of $R_{coat/rBC}$, with raw data points colored by time and box plots summarizing bulk properties in discreet $R_{coat/rBC}$ bins. Panel a) shows the total rBC, b) the total organic mass, c) the total inorganic nitrate mass, d)–f) the fractional contribution of $C_2H_4O_2^+$, $C_4H_9^+$, $C_2H_3O^+$, and CO_2^+ to total organic mass, respectively, h) the ratio of organic-to-rBC and i) the bulk O/C ratio of the organic fraction. In the bottom panels, size distributions are binned by $R_{coat/rBC}$ for j) rBC, k) organics and l) nitrate.

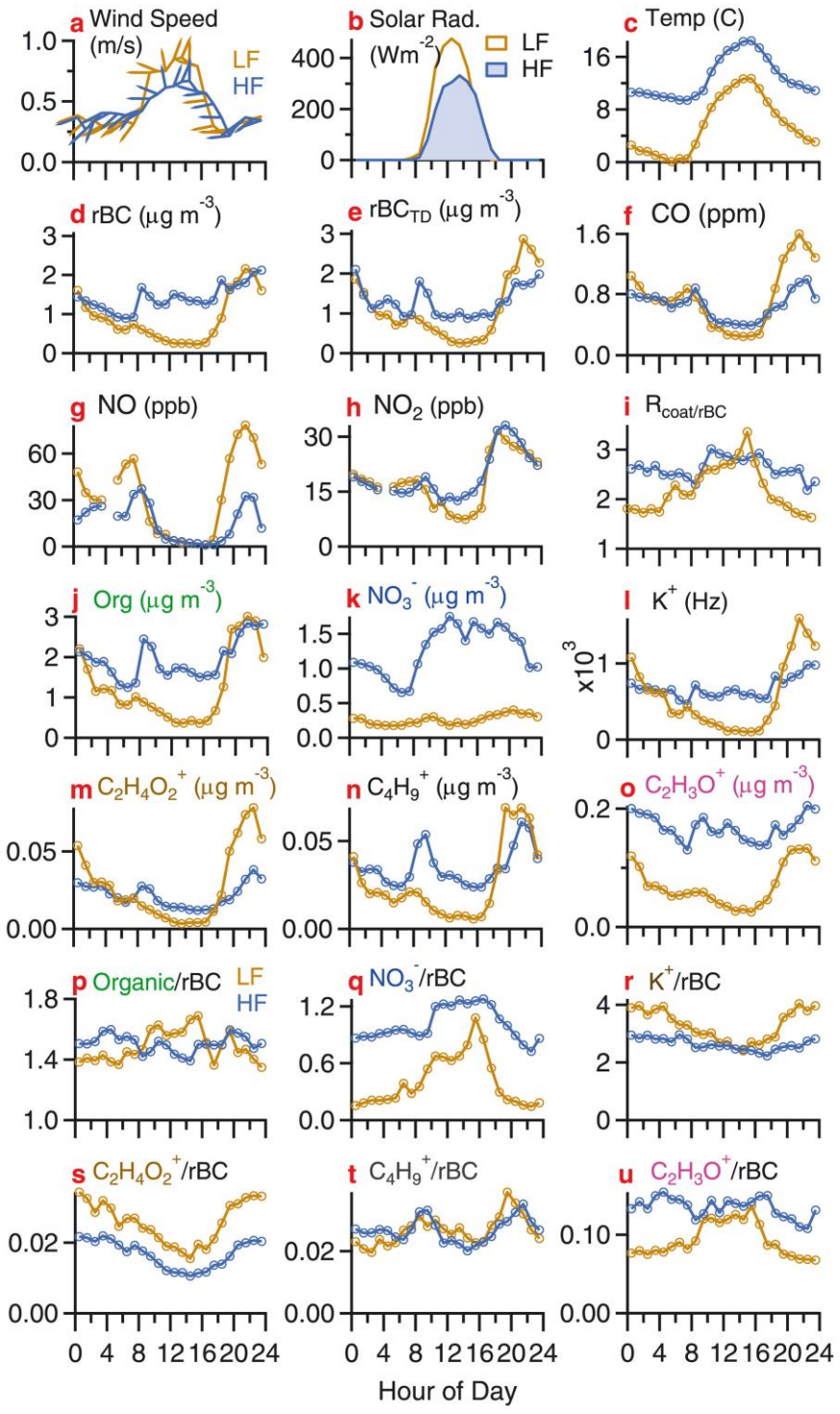

Figure 7-11. Diurnal plots for low fog (brown) and high fog (blue) periods of a) wind speed with arrows showing wind direction, b) solar radiation, c) temperature, d) rBC, e) thermodenuder rBC, f) CO concentration, g) NO concentration, h) NO_2 concentration, i) $R_{coat/rBC}$, j) organic, k) nitrate, l) potassium (K^+), m) $C_2H_4O_2^+$, n) $C_4H_9^+$ and o) $C_2H_3O^+$. Panels m-o are in organic equivalent µg/m^3. Concentrations normalized by rBC are shown in panels p-u for p) total organics, q) nitrate, r) K^+, s) $C_2H_4O_2^+$, t) $C_4H_9^+$ and u) $C_2H_3O^+$.

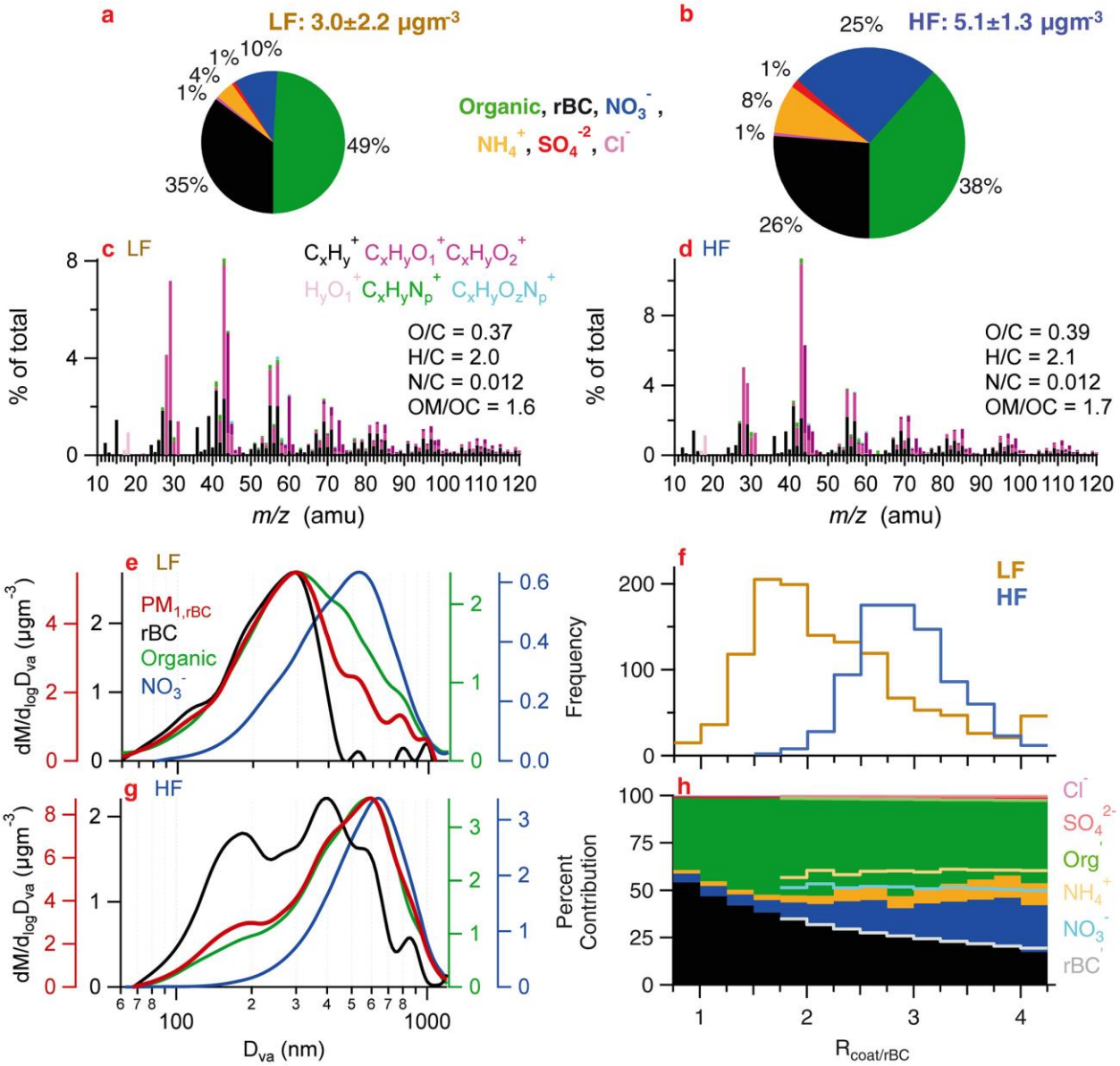

Figure 7-12. Panels a) and b) show the fractional contribution of species in rBC-containing particles averaged over the low fog (LF) and high fog (HF) periods, respectively. Panels c) and d) show the average high resolution mass spectra of the organic fraction by ion family type for the LF and HF periods, respectively. Panels e) and g) show the mass-based size distributions of rBC, organic coating, nitrate coating and total rBC-particle ($PM_{1,rBC}$) for the LF and HF respectively. Panel f) shows the histogram of data point frequency of $R_{coat/rBC}$ for each period. Panel h) shows the fractional contribution of species as a function of $R_{coat/rBC}$ in solid fill for LF and in lighter colored lines for HF.

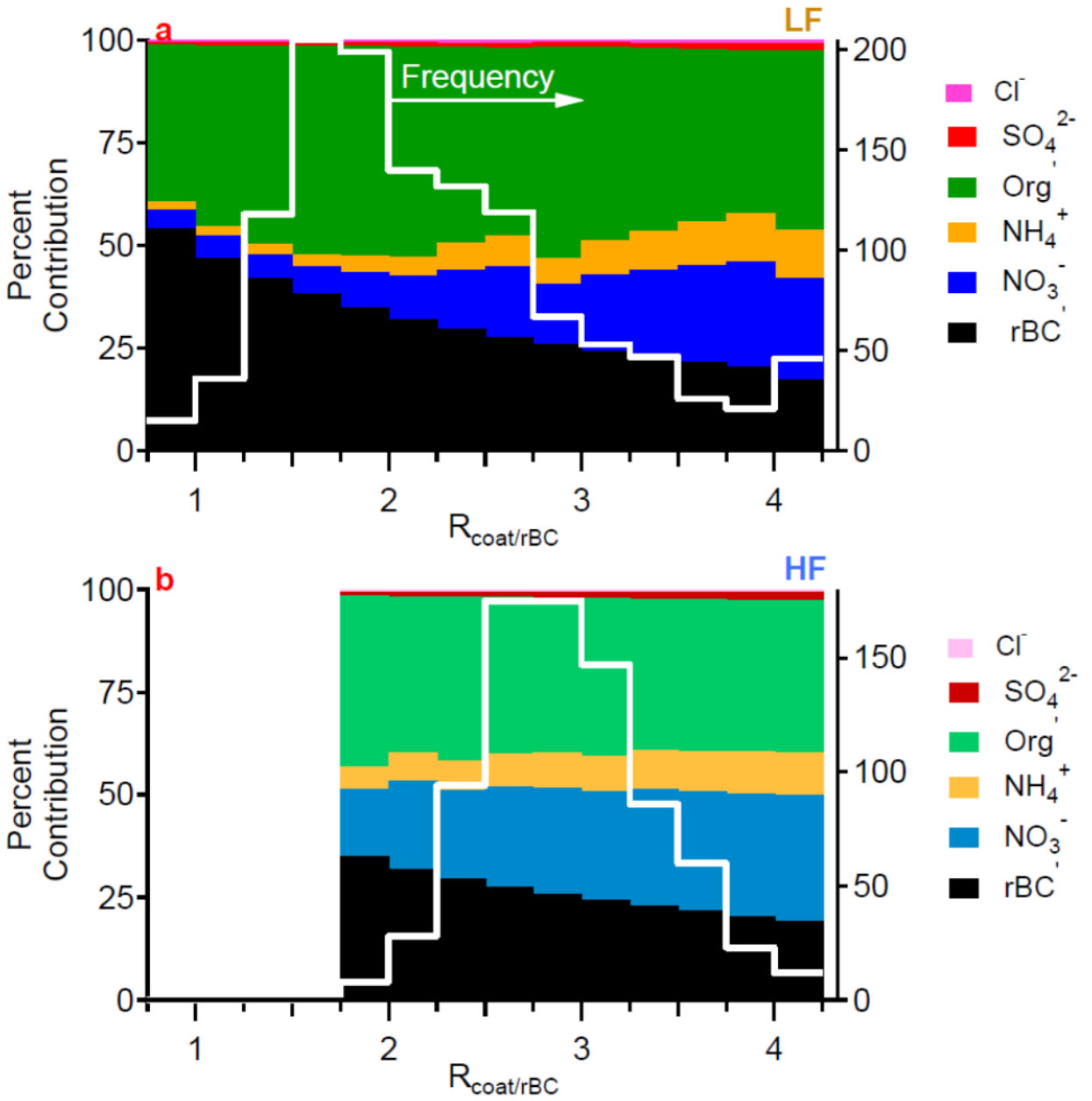

Figure 7-13. The fractional contribution of species as a function R_{coat}/rBC in solid fill for the a) LF and b) for the HF. The histogram of data point frequency of R_{coat}/rBC during the two periods is shown in white. This information is also shown in Figure 5f and 5h in the main manuscript.

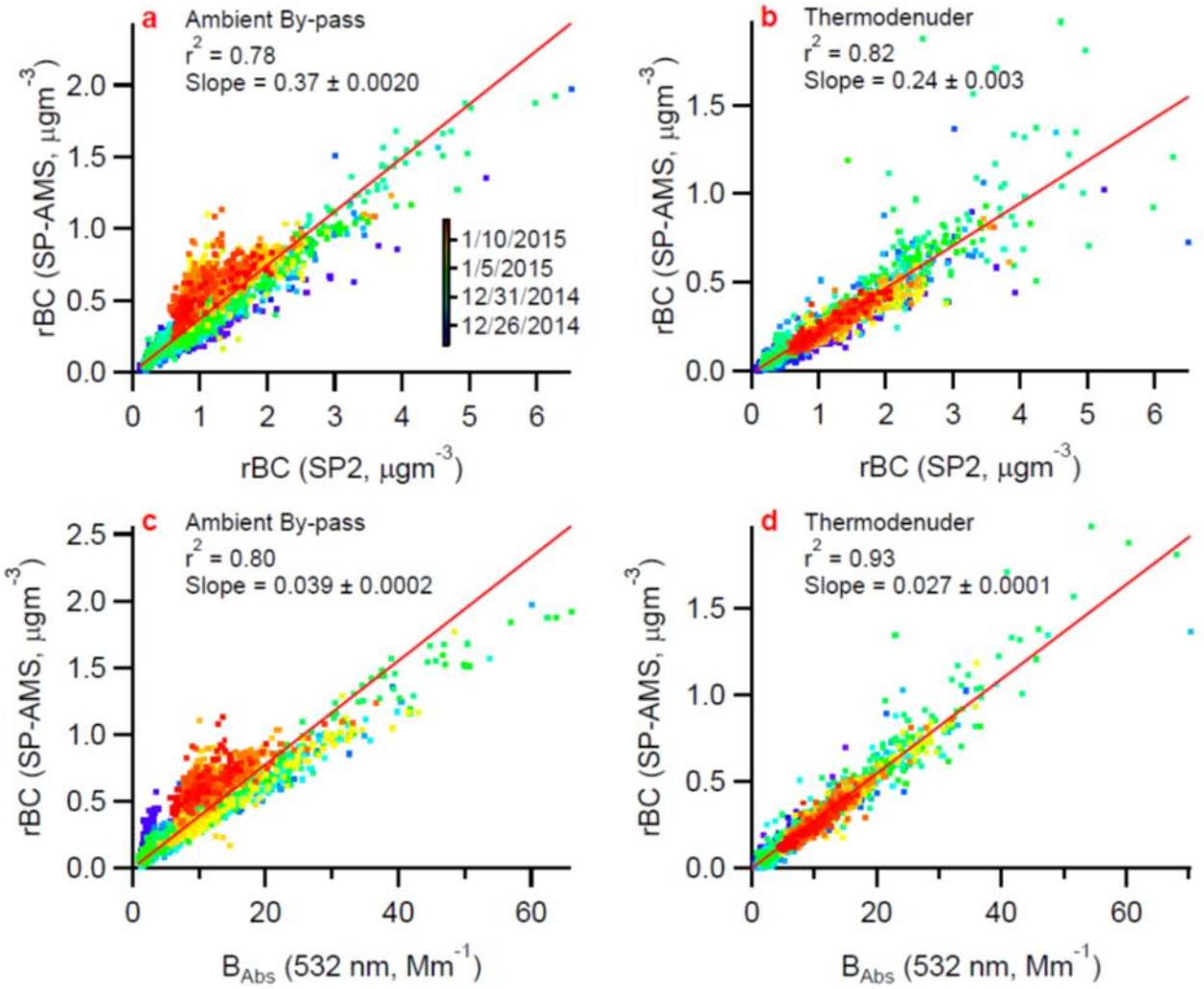

Figure 7-14. Scatter plots between rBC from SP-AMS instrument (uncorrected for CE) and rBC from SP2 for entire campaign for a) ambient by-pass and b) thermodenuder modes. Scatter plots between rBC from SP-AMS and optical absorption for c) ambient by-pass and b) thermodenuder modes.

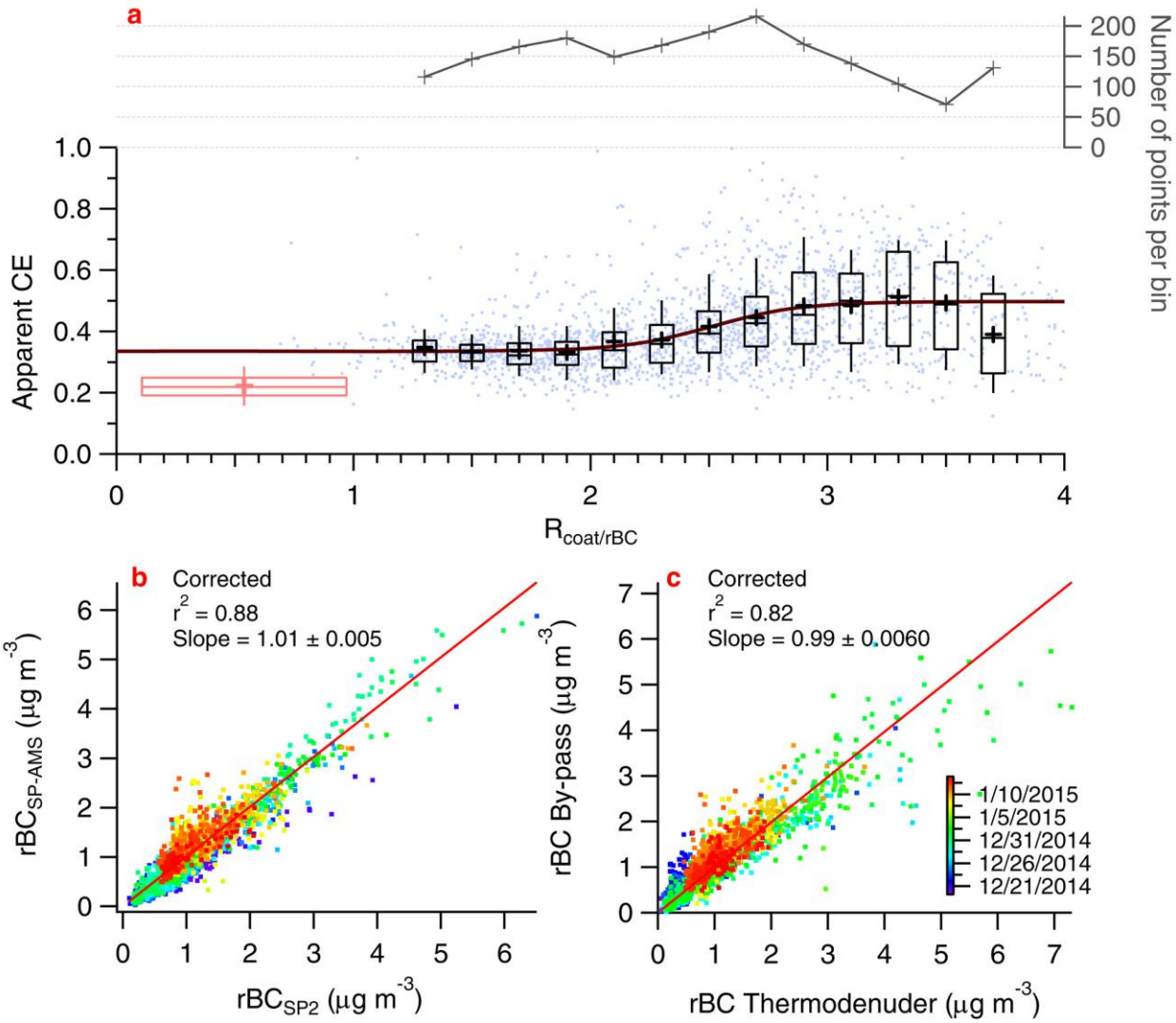

Figure 7-15. Panel (a) shows the apparent collection efficiency (CE) of rBC for the SP-AMS bypass data as a function of $R_{coat/rBC}$. Box plots represent the distribution of rBC_{SP-AMS}/rBC_{SP2} binned by $R_{coat/rBC}$ with crosses representing the mean, lines the median, top and bottom of boxes representing 75th and 25th percentiles, respectively, and top and bottom whiskers representing 90th and 10th percentiles respectively. The total number of data points in each bin is plotted on the right axis. A sigmoid function fit through all bypass data is used to calculate the $R_{coat/rBC}$-dependent correction. The single red box plot represents the distribution of TD data points with the box centered on the median of $R_{coat/rBC}$ for the TD data and the width is the standard deviation of $R_{coat/rBC}$ for TD data. Panels (b) and (c) show the scatter plots between rBC_{SP-AMS} and rBC_{SP2} and BP and TD rBC_{SP-AMS}, respectively, after the $R_{coat/rBC}$-dependent correction was applied. TD data corrected for TD losses. Points are colored by time.

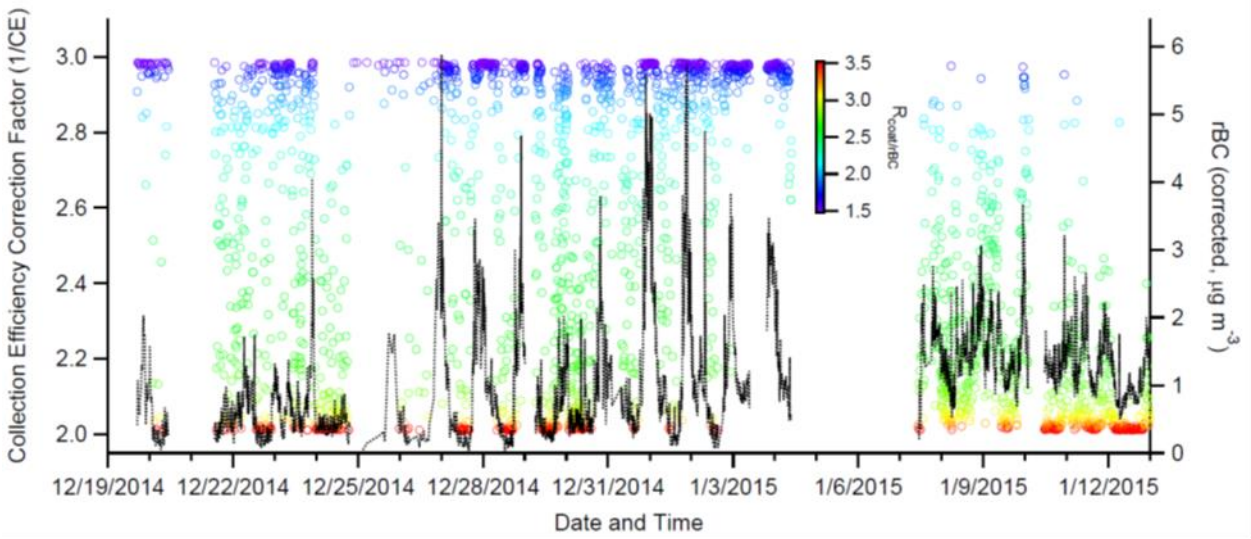

Figure 7-16. Collection efficiency correction factor (1/CE) for individual data points throughout campaign period where ambient data is represented by open circles and are colored by Rcoat/rBC. Corrected rBC concentration is shown in black dashed line and plotted on the right axis for reference.

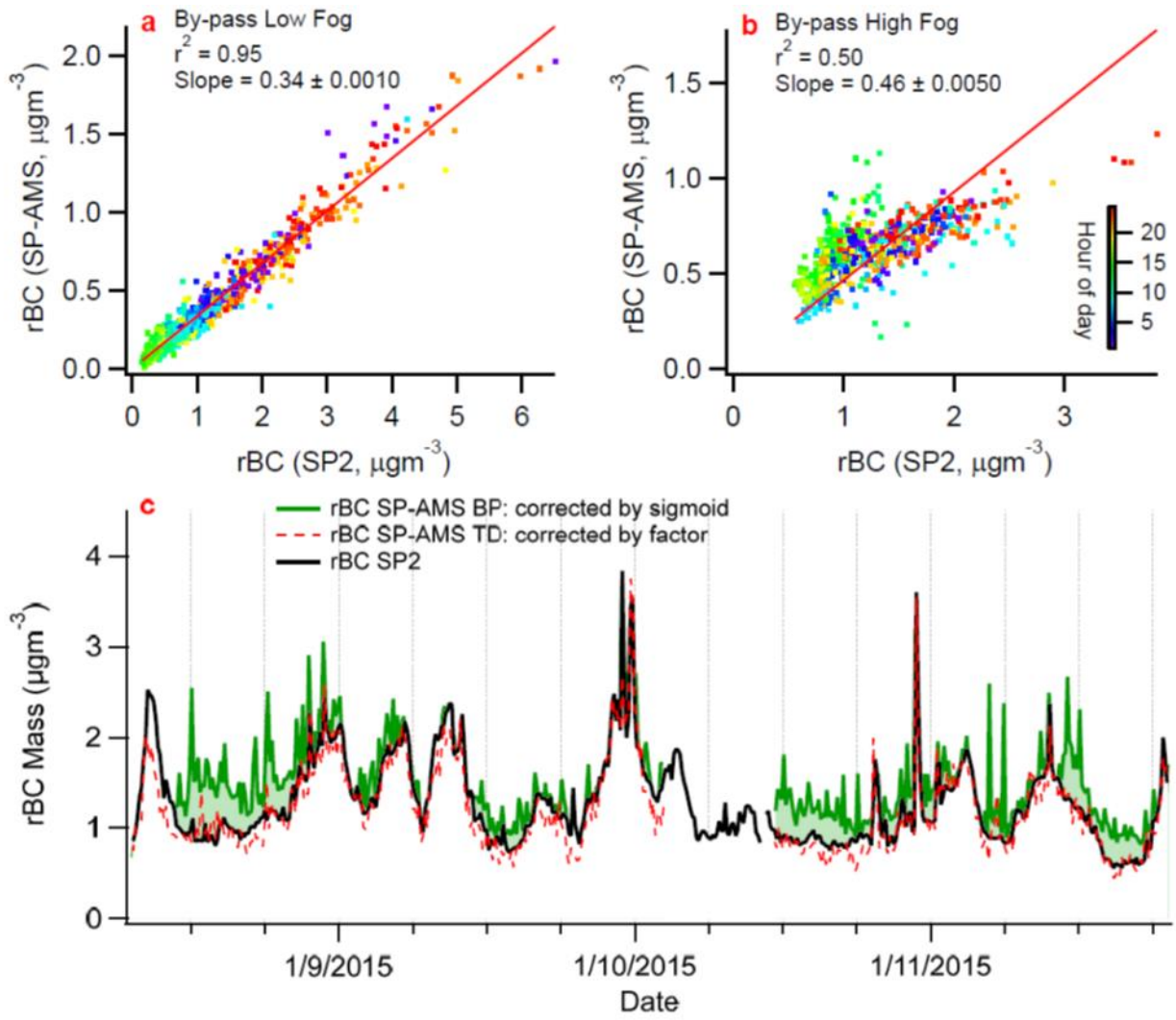

Figure 7-17. The scatter plot between uncorrected rBCSP-AMS and rBCSP2 for (a) the LF and (b) HF periods. (c) The time-dependent concentrations of rBCSP-AMS (corrected using sigmoid a function of Rcoat/rBC), rBCSP2 and thermodenuded rBCSP-AMS for several days during the FP. Periods where rBCSP-AMS corrected by sigmoid function are significantly larger than rBCSP2 are highlighted by green filled areas.

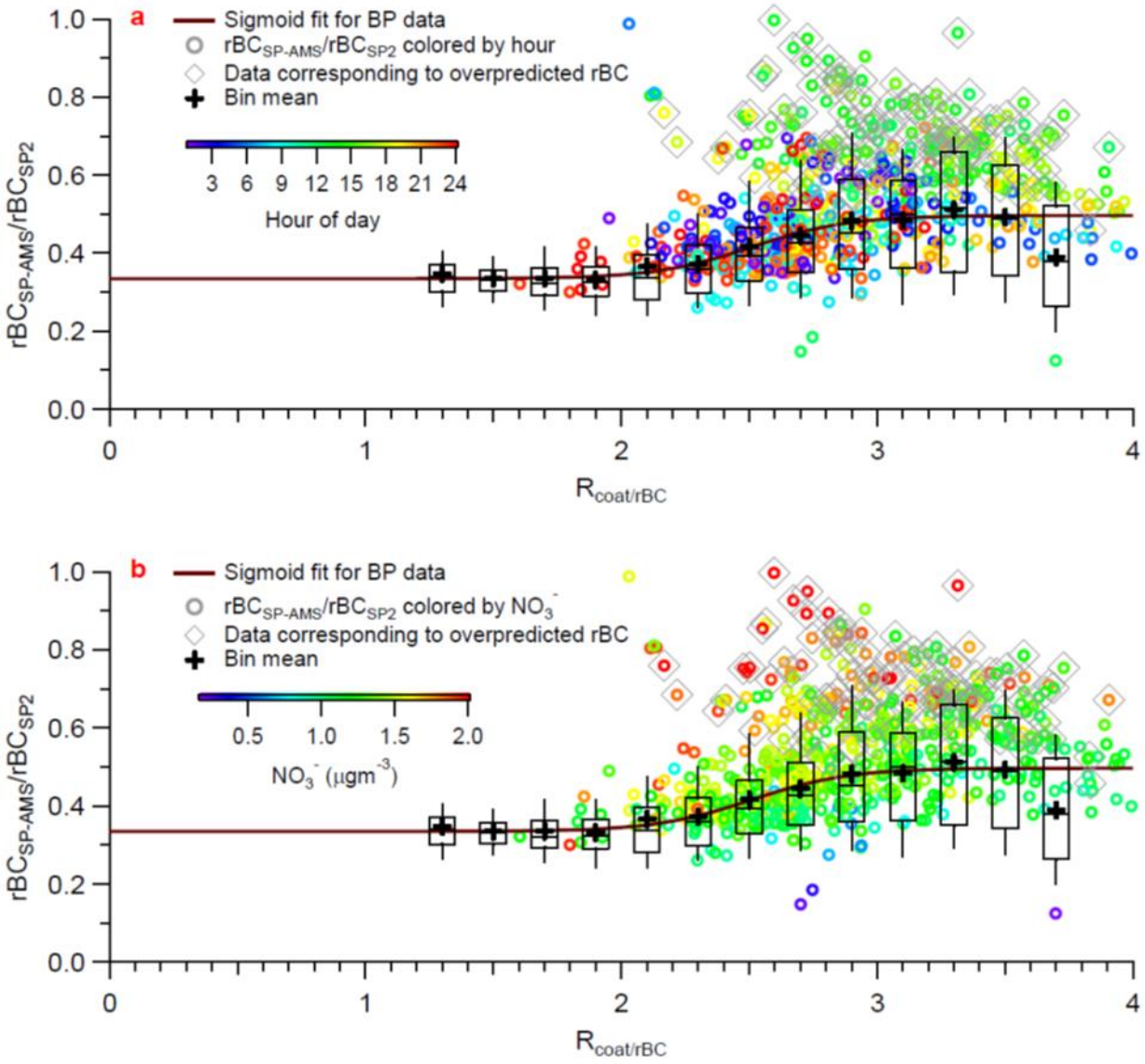

Figure 7-18. Panels (a) and (b) show a recreation of Figure A1a in the main text but with data from the HF only. The original sigmoid fit and binned means and medians for all ambient data is shown for reference. Individual data points are colored by hour of day in (a) and total nitrate concentration in (b). Data points corresponding to periods where sigmoid corrected rBCSP-AMS was enhanced relative to rBCSP2 (see Figure S9) are highlighted by the grey diamonds.

8 Formation of secondary organic aerosol coating on black carbon particles near vehicular emissions

8.1 Abstract.

Black carbon (BC) emitted from incomplete combustion can result in significant impacts on air quality and climate. Understanding the mixing state of ambient BC and the chemical characteristics of its associated coatings are particularly important to evaluate BC fate and environmental impacts. In this study, we investigate the formation of organic coatings on BC particles in an urban environment (Fontana, California) under hot and dry conditions using a Soot-Particle Aerosol Mass Spectrometer (SP-AMS). The SP-AMS was operated in a configuration that can detect refractory BC (rBC) particles and their coatings exclusively. Using the $-\log(NO_x/NO_y)$ ratio as a proxy for photochemical age of air masses, substantial formation of secondary organic aerosol (SOA) coatings on rBC particles was observed due to active photochemistry in the afternoon, whereas primary organic aerosol (POA) components were strongly associated with rBC from fresh vehicular emissions in the morning rush hours. There is also evidence that cooking related organic aerosols were externally mixed from rBC. Positive matrix factorization and elemental analysis illustrate that most of the observed SOA coatings were freshly formed, providing an opportunity to examine SOA coating formation on rBC near vehicular emissions. Approximately 7-20 wt% of secondary organic and inorganic species were estimated to be internally mixed with rBC on average, implying that rBC is unlikely a major condensation sink of SOA in this study. Comparison of our results to a co-located standard high-resolution time-of-flight aerosol mass spectrometer (HR-ToF-AMS) measurement suggests that at least a portion of SOA materials condensed on rBC surface were chemically different from oxygenated organic aerosol (OOA) particles that were externally mixed with rBC, although they could be both generated from local photochemistry.

8.2 Introduction

Black carbon (BC) emitted from incomplete combustion of fossil fuel and biomass has profound impacts on air quality and climate. BC is the dominant absorber of visible solar radiation in the atmosphere, introducing significant contributions to positive radiative forcing on both regional and global scales (Ramanathan and Carmichael, 2008;Bond et al., 2013). Organic coatings can be formed on BC through condensation and/or coagulation of co-emitted primary organic aerosol (POA) and secondary organic aerosol (SOA) produced via photochemical processing. The hydrophilic nature of SOA coating has been shown to modify hygroscopicity of ambient BC for cloud droplet activation (Kuwata et al., 2009;McMeeking et al., 2011;Laborde et al., 2013;Liu et al., 2013). Increasing coating thickness may enhance light absorption of BC due to a "lensing effect" depending on the degree of particle aging (Jacobson, 2001;Cappa et al., 2012;Peng et al., 2016;Liu et al., 2017), and alter BC morphology from highly fractal to compact structures and thus their aerodynamic properties (Moffet and Prather, 2009;Schnitzler et al., 2014;Guo et al., 2016;Peng et al., 2016). Understanding the mixing state of ambient BC and the chemical characteristics of its associated coatings is therefore particularly important to evaluate their fate and environmental impacts.

In typical urban environments, traffic emission is one of the major sources of BC particles. A complex mixture of gas-phase organic compounds with a wide range of volatility and molecular structure are co-emitted with BC from vehicles, contributing prominently to the

urban SOA burden (Gentner et al., 2017 and references therein). Although it is not straightforward to identify the role of individual SOA precursors, previous studies have shown that organic coating thickness of BC particles and their degree of oxygenation increased with photochemical age or oxidant levels in the atmosphere (Cappa et al., 2012;Liu et al., 2015;Wang et al., 2017). Of particular concern is the timescale that is required for sufficient SOA condensation to modify the physical, chemical and optical properties of BC near emission sources. Peng et al. (2016) recently performed on-site chamber experiments to examine coating formation on size-selected BC seeds using SOA precursors from particle-free ambient air, demonstrating that only a few hours of photochemical aging can lead to complete particle morphology modification and light absorption enhancement of BC in polluted urban regions. Moffet and Prather (2009) also provided field evidence that fresh BC can quickly evolve in terms of particle morphology in a photochemically active urban environment by developing coatings of secondary species over a timescale of several hours, highlighting the importance of local SOA chemistry on BC aging mechanisms.

While most previous studies focused on determining potential effects of SOA coatings to the BC properties, there is still a lack of laboratory and field investigations to examine effectiveness and selectivity of BC seed particles for condensation of SOA materials especially in the presence of other existing seed particles. Recent field observations reported that SOA condensed on BC only accounted for 35% and 41% of total SOA mass near traffic emission sources and in a polluted offshore environment, respectively (Massoli et al., 2012;2015). Metcalf et al. (2013) conducted a series of smog chamber experiments to investigate photooxidation of naphthalene and α-pinene in the presence of both BC and ammonium sulfate seed particles with comparable surface area of each particle type. Although their observations indicated that the use of BC as a seed is not expected to alter the overall basic chemistry of SOA formation, whether the SOA condensed on BC particles is chemically different from those condensed on ammonium sulfate particles or formed through homogeneous nucleation remains unclear.

Real-time and mass-based chemical compositions of organic coatings on ambient BC particles were seldom reported until the recent development of an Aerodyne Soot-Particle Aerosol Mass Spectrometer (SP-AMS) (Cappa et al., 2012;Massoli et al., 2012;2015;Onasch et al., 2012;Liu et al., 2015;Lee et al., 2016;Willis et al., 2016). In this study, we investigate formation of organic coatings on BC particles by deploying a SP-AMS in Fontana, California, which is located in the broader South Coast Air Basin and includes the greater Los Angeles area. The sampling site was located in an urban environment with strong influences of vehicular emissions. The SP-AMS was operated in a configuration that can detect refractory BC (rBC) and their coating materials exclusively. The term of rBC is operationally defined (Onasch et al., 2012) and will be used throughout the rest of this paper. The repeated diurnal patterns of inorganic species, POA and SOA that are internally mixed with rBC reported here provides a unique opportunity to investigate the chemical characteristics and formation of POA and SOA coatings on rBC particles near traffic emissions. A co-located Aerodyne High resolution Time-of-Flight Aerosol Mass Spectrometer (HR-ToF-AMS) was operated simultaneously to quantify the total amounts of non-refractory organic and inorganic specices in PM_1 (Chen et al., 2017). The results provide insights into the effectiveness of rBC particles as a condensation sink of

fresh SOA near traffic emissions and the chemical characteristics of SOA coatings compared to SOA that were externally mixed with rBC.

8.3 Experiment

8.3.1 Sampling location and instrumentations

The sampling site in Fontana, managed by South Coast Air Quality Management District (SCAQM), was located behind the fire station at 14360 Arrow Highway (34.100 N, 117.490 W). Surrounded by the I-15 freeway to the west (4.3 km), I-10 freeway to the east (3.9 km), and an auto speedway to the south, the sampling site was strongly influenced by vehicular emissions, as well as the broader urban plume. Aerosol particle instruments housed in a sampling van with a custom isokinetic inlet were deployed. Air pulled through the inlet was dried using diffusion driers and subsequently distributed to different real-time particle instruments. This study focuses on the results from a soot-particle aerosol mass spectrometer (SP-AMS, Aerodyne Research) that was configured to detect rBC-containing particles and their coating materials exclusively (See Sections 2.2 and 2.3 for the descriptions of SP-AMS and the calibration approach, respectively). The details of other particle instruments, including a high-resolution time-of-flight aerosol mass spectrometer (HR-ToF-AMS, Aerodyne Research), a single-particle soot photometer (SP2, Droplet Measurement Technologies), and a scanning electrical mobility spectrometer (SEMS, Brechtel) have been reported in Chen et al. (2017) and Betha et al. (2017). Two nitrogen oxide analyzers (Model 42i and 42i NO_y, Thermo Fisher Scientific) were used to measure mixing ratios of NO_x and NO_y for determining photochemical age (PCA) of air masses. The heated molybdenum converter in the 42i nitrogen oxide analyzer was replaced by an UV-LED photolytic NO_2 converter (Air Quality Design) for NO_x measurement. Hourly average ozone data was obtained from the co-located SCAQM air monitoring station.

Measurements were performed from 5 to 28 July 2015 with ambient temperature varying from 14.9 to 35.9 °C. Companion studies have shown that aerosol compositions were strongly influenced by fireworks from 4 to 8 July 2015 (Chen et al., 2017; Betha et al., 2017). There were few clouds and little precipitation with the exception of a short storm with high rainfall and winds on 18–19 July (two-day precipitation = 3.6 cm and maximum wind speed = 10 ms^{-1}). Sampling days with the maximum daily temperature above 30 °C (11–17 and 20–28 July) and lower than 27 °C (9–10 July) were classified as "hot" and "cooler" days, respectively (Chen et al., 2017). The identified hot days were dry with the average hourly relative humidity (RH) varied between 30 and 50% during the daytime. The Hybrid Single-Particle Lagrangian Integrated Trajectory (HYSPLIT) model with input from NOAA Air Resource Laboratory Archived Eta Data Assimilation System was used (http://www.arl.noaa.gov/HYSPLIT_info.php) to evaluate whether particular upwind source regions affected the aerosol measured at the sampling site. Air mass back trajectories were consistently westerly from the coast within the entire sampling period except for the storm days (Chen et al., 2017). Classification of sampling periods based on meteorological conditions and pollutant characteristics is shown in **Figure 8-4**.

8.3.2 Soot particle aerosol mass spectrometer (SP-AMS)

The working principle of SP-AMS has been reported in detail previously (Onasch et al., 2012). In brief, rBC-containing particles are vaporized at ~4000 K by a 1064 nm continuous wave intracavity infrared laser similar to that of the SP2 instrument (Onasch et al., 2012). The resulting vapour is ionized via 70 eV electron impact and then detected by a high-resolution time-of-flight mass spectrometer operated in V-mode, which provides a mass resolving power of ~2000 at m/z 28 (DeCarlo et al., 2006;Canagaratna et al., 2007). Note that BC particles detected by SP-AMS are operationally defined as refractory black carbon (rBC). A resistively heated tungsten vaporizer was removed from our instrument so that only rBC and its coating materials were detected (Massoli et al., 2012;2015;Lee et al., 2016;Willis et al., 2016). An efficient particle time-of-flight system (ePToF, multi-slit chopper with 50% aerosol throughput) was used for measuring aerosol size distributions. The SP-AMS was operated alternating between ensemble mode (i.e., 1-min average of bulk mass spectrum and PToF size distribution) and event trigger mode (i.e., single particle mass spectrum with PToF size).

The SP-AMS was operated from 6 to 28 July 2015 and only the ensemble measurements are reported in this paper. The ensemble data were processed using the AMS data analysis software (Squirrel, version 1.56D for unit mass resolution data and Pika, version 1.15D for high resolution data from http://cires1.colorado.edu/jimenez-group/ToFAMSResources/ToFSoftware/) with the corrected air fragment column of the standard fragmentation table (Allan et al., 2004;DeCarlo et al., 2006). In particular, the average contribution of gas-phase CO_2 to CO_2^+ organic fragment in particle phase was determined (i.e., CO_2–to-N_2 ratio) based on the measurements of particle-free ambient air (i.e., at least 10 min per day) throughout the sampling period. Positive matrix factorization (PMF) was performed to investigate the potential sources and characteristics of rBC and organic aerosol components. Signals of C_x^+ fragments from rBC were included in the PMF analysis so that mass fraction of rBC and organic components can be calculated for each PMF factor (Lee et al., 2015; 2016;Willis et al., 2016). The bilinear model was solved using the PMF2 algorithm in robust mode (Paatero and Tapper, 1994) and a final solution was selected using the PMF Evaluation Tool (PET) version 2.06 according to the method described previously (Ulbrich et al., 2009;Zhang et al., 2011). A four-factor solution, including two POA factors from traffic emissions and two SOA factors due to local photochemistry, was selected by examining the solutions for up to eight PMF factors, with details of the PMF analysis shown in **Figure 8-1**, **Figure 8-2**, and **Figure 8-3**. Elemental analysis (i.e., oxygen- and hydrogen-to-carbon ratios, O/C and H/C) was performed based on the improved ambient method (Canagaratna et al., 2015a).

8.3.3 SP-AMS calibration

A water suspension of Regal Black (Regal 400R Pigment Black, Cabot Corp., a calibration standard recommended by Onasch et al., 2012), was atomized using a constant output atomizer (TSI Inc., Model 3076) for generating standard rBC particles. Dried 300 nm Regal Black particles were used to determine mass-based ionization efficiency of rBC (mIE_{rBC}). Signals for Regal Black particles were quantified by the sum of carbon ion clusters (C_x^+, i.e. C_1^+-C_9^+) using high-resolution mass spectral data. The average C_1^+ to C_3^+ ratio of 0.478 obtained from Regal Black calibration was used to correct the interference in C_1^+ from non-refractory organics in ambient aerosol. The product of material density and the Jayne shape factor (also defined as

effective density, ρ_{eff}) of the dried 300 nm Regal Black particles was 0.86±0.02 g/cm^3, which can be derived from the ratio of the vacuum aerodynamic diameter (d_{va}) measured by the SP-AMS to the mobility diameter (d_m) selected by a differential mobility analyzer (DMA) as follow:

$$\rho_{eff} = \rho_m S = (d_{va} / d_m) \rho_0 \quad \text{(Eq.1)}$$

where ρ_m and S are the material density and Jayne shape factor, respectively, and ρ_0 is the unit density (DeCarlo et al., 2004). The average effective density of 0.86 and d_m were used to further calculate the mass of individual dried 300 nm Regal Black particles (DeCarlo et al., 2004) which was approximately 12.2 fg. The average mIE_{rBC} value was 255±50 ions/pg of Regal Black particle based on three independent calibrations performed throughout the study.

Direct calibration of the ionization efficiency for nitrate (IE_{NO3}) is not possible without the tungsten vaporizer. Before removal of the tungsten vaporizer from the SP-AMS, dried 300 nm pure ammonium nitrate (NH_4NO_3) and Regal Black particles were generated for determining mass-based ionization efficiency of nitrate (mIE_{NO3}) and mIE_{rBC}, respectively. Note that the mIE_{NO3} was determined without operating the laser vaporizer. The relative ionization of rBC ($RIE_{rBC} = mIE_{rBC}/mIE_{NO3}$) was 0.26. Assuming that RIE_{rBC} remains unchanged after removing the tungsten vaporizer, mIE_{NO3} and IE_{NO3} were calculated based on measured values of mIE_{rBC}. The calculated IE_{NO3} was then used with recommended RIE values (Jimenez et al. (2003), i.e., nitrate = 1.1, sulfate = 1.2, chloride = 1.3, organics = 1.4 and ammonium = 4) to quantify non-refractory aerosol species associated with rBC (referred to as NR-PM_{rBC}). Note that our previous studies have shown that this calibration approach likely yields the calculated IE_{NO3} values as a lower limit, leading to over quantification of the NR-PM_{rBC} mass loadings in ambient aerosol (Willis et al., 2014;Lee et al., 2015).

The collection efficiency (CE) for rBC particles that is governed by the degree of overlap between particle and laser beams was determined using beam width probe (BWP) measurements described previously (Willis et al., 2014). Ambient rBC-containing particles had an average beam width (σ) = 0.45±0.04 mm based on three sets of BWP measurements performed throughout the study. The measured particle beam width suggests a condition of incomplete beam overlap, arising from non-spherical rBC particles, and hence a CE of 0.6 was applied for absolute quantification of rBC and NR-PM_{rBC} (Willis et al., 2014). All BWP measurements were performed around the morning rush hours. Fresh rBC-containing particles from vehicular emissions in the morning had thinner coatings compared to those rBC-containing particles observed in the afternoon that were more photochemically aged (see discussion in Section 3). It has been demonstrated that CE for rBC particles increases (or rBC particle beam width decreases) with coating thickness (Willis et al., 2014). The applied CE may be therefore less relevant for the time with high ambient SOA loading (i.e., high NR-PM_{rBC}/rBC mass ratio, or R_{BC}), leading to over quantification of the SOA components in NR-PM_{rBC} by at most 40% due to this uncertainty. Furthermore, a wider particle beam than the laser beam implies that some rBC-containing particles may undergo incomplete vaporization at the edges of the laser vaporizer, which would in turn bias the measurement towards the coatings rather than the rBC cores (see unpublished data from, http://cires.colorado.edu/jimenezgroup/UsrMtgs/UsersMtg16/JDASPAMSfocusing.pdf). Since the CE of 0.6 was primarily determined for rBC, this phenomenon may further increase the degree of over

quantification of NR-PM_{rBC}. Overall, the values of NR-PM_{rBC} reported in this work likely represent their upper limits.

8.4 Results and Discussion

Figure 8-4 shows the time series of meteorological data (temperature, relative humidity (RH), wind direction and wind speed), mixing ratios of ozone and NO_x, NO_x/NO_y ratio, and chemical compositions of rBC-containing particles (i.e., rBC and NR-PM_{rBC}) from 5 to 28 July 2015. **Figure 8-5** shows the time series for the four PMF factors. The whole sampling period can be divided into four categories as previously reported (Chen et al., 2017; Betha et al., 2017). In brief, fireworks had strong impacts on aerosol compositions from 5 to 8 July, and significant enhancements of inorganic aerosol components were observed in rBC-containing particles (**Figure 8-4**f). After the firework period, mass loadings of rBC-containing particles remained low from 9 to 10 July without clear diurnal patterns (indicated as cooler days in **Figure 8-4**). A storm cleaned up the atmosphere from 18 to 19 July, leading to very low levels of all aerosol components within the two days. The SP-AMS was under maintenance from 20 July 18:00 to 21 July 12:00. The weather was relatively hot and dry for the rest of sampling days (indicated as hot days in **Figure 8-4**). Repeated diurnal patterns of Org/rBC ratio (or R_{BC}) with peak values in the afternoon were observed over the hot period (**Figure 8-4**e), indicating a unique opportunity to examine POA and SOA formation on rBC near vehicular emissions via daytime chemistry. The observations during the hot period will be the focus of the following discussion.

8.4.1 Chemical characteristics of rBC coating materials (NR-PM_{rBC})

Figure 8-6a shows the average diurnal cycles of rBC and NR-PM_{rBC} during the hot period. Mass loadings of rBC increased continuously in the morning rush hours and peaked at ~8:00–9:00, and they were strongly correlated with the NO_x mixing ratio (r = 0.82), consistent with local traffic emissions as a major source (**Figure 8-4**d). Boundary layer break up led to the decrease of rBC and NO_x concentrations (i.e., dilution as air from residual layer mixed down to the surface). These diurnal patterns indicate that there were minimal influences of other combustion sources such as biomass burning and industrial emissions to the observed rBC concentrations. Nitrate and ammonium concentrations correlated well with each other (r = 0.97). Their mass loadings increased slowly over the night and reached the maximum levels at ~10:00–11:00 in the morning (**Figure 8-6**a). While NO_2 reacts with ozone to generate N_2O_5 at night, OH radicals oxidation of NO_2 during daytime produce nitric acid that can be neutralized by ammonia, forming particulate NH_4NO_3. A recent tunnel study has observed such NH_4NO_3 formation chemistry in aged traffic emissions (Tkacik et al., 2014). The decrease of particulate nitrate and ammonium (i.e., NH_4NO_3) concentrations could be the combined effects of boundary layer break up and evaporative loss at the increasing temperature during the day. Sulfate remained in low concentrations with a relatively modest pattern (see also **Figure 8-10**d) potentially caused by the transport of regional pollution into the area during the day. Chloride was also associated with traffic (see also **Figure 8-10**e) and was likely due to condensation of HCl vapor that was subsequently neutralized by ammonia (i.e., formation of NH_4Cl).

Organic aerosol (OA) was the dominant component of NR-PM_{rBC} during the hot period as illustrated in **Figure 8-6**a. Mass loadings of organic coating increased with rBC concentrations in the morning rush hours. PMF results show that two primary emission factors, referred to as hydrocarbon-like OA-rich (HOA-rich) and rBC-rich factors hereafter, were the major

contributors to the total OA mass during the morning rush hours (**Figure 8-7**e and f). (For comparison, results from the two-factor solution are shown in **Figure 8-8**.) The mass concentration of the rBC-rich factor was slightly lower than the HOA-rich factor. Mass spectra of HOA- and rBC-rich factors indicate that rBC accounted for 14.2 and 44.4 wt% of the two primary aerosol factors, respectively. The fragmentation pattern of rBC was similar to those previously reported in urban environments near traffic emissions and engine exhausts (Massoli et al., 2012;Lee et al., 2015;Enroth et al., 2016;Willis et al., 2016;Saarikoski et al., 2017). With the support of single particle measurement, Willis et al. (2016) also separated traffic-related OA into HOA- and rBC-rich factors in the roadside environment using a SP-AMS with a tungsten vaporizer being removed and estimated that approximately 90% of rBC mass emitted from vehicle resided in rBC-rich particles. By following the calculation procedure described in Willis et al. (2016), rBC-rich factor contributed about 82 wt% of the freshly emitted rBC from traffic. Note that rBC-rich particles were composed of more oxygenated organic fragments compared to the HOA-rich factor (**Figure 8-7**a and b), likely due to the presence of refractory ion fragments (i.e., CO^+ and CO_2^+) that originated from oxygenated functionalities on the soot surface and in the soot nanostructure (Corbin et al., 2014;Malmborg et al., 2017).

Using $-\log (NO_x/NO_y)$ as a proxy for PCA of air masses and Org/rBC ratio (or R_{BC}) as an indicator for SOA formation, production of fresh SOA coating materials on rBC particles was observed due to active photochemistry in the afternoon (**Figure 8-6**b). The secondary nature of organic coatings observed in the afternoon peak was supported by the diurnal cycles of O/C, H/C and average carbon oxidation state ($OS_c \approx 2O/C - H/C$, Kroll et al. (2011)) of total OA (**Figure 8-6**d). Higher values of O/C and OS_c were observed in the afternoon compared to in the morning rush hours, consistent with the expectation that the O/C ratio of SOA is greater than POA. The PMF analysis identified two types of oxygenated OA (OOA), referred to as OOA-1 and OOA-2 hereafter, both of which are likely SOA coatings. Mass spectra of both OOA factors were dominated by an oxygen-containing organic fragment at m/z 43 (i.e., $C_2H_3O^+$, **Figure 8-7**c and d), similar to those previously observed by Massoli et al. (2015). OOA-1 represented less oxygenated SOA components (O/C = 0.53) with 13.4 wt% of rBC content, and its concentration started increasing in the morning coincident with nitrate and ammonium (i.e., peaks at ~10:00-11:00, **Figure 8-6**a and **Figure 8-7**g) and sustained at relatively constant levels until ~15:00–16:00. This suggests a possibility that OOA-1 represented a fresher portion of SOA coating materials generated by photochemistry of anthropogenic gas-phase precursors from vehicular emissions. OOA-2 represented a more oxygenated fraction of SOA coating (O/C = 0.62) with the maximum mass loadings observed at ~15:00-16:00 and its diurnal pattern matched well with Org/rBC ratios (**Figure 8-6**b and **Figure 8-7**h). The diurnal pattern of OOA-2 indicates the importance of local photochemistry for OOA-2 production in the afternoon but the contribution of regional transport to OOA-2 cannot be completely ruled out. Given that rBC accounted for only 0.5 wt% of OOA-2 (i.e. much lower than other PMF factors), OOA-2 could represent SOA materials generated through local photochemistry and/or formed regionally under conditions with relatively low rBC particle concentrations.

8.4.2 Chemical characteristics of OA as a function of R_{BC}

Figure 8-9a illustrates that R_{BC} increased continuously as a function of –log (NO_x/NO_y) within the hot period. Assuming ambient daytime OH radical concentration was ~4×10^6 molecules cm^{-3} (Takegawa et al., 2006;Slowik et al., 2011) and the major NO_x loss product was HNO_3, the estimated PCA values (i.e., PCA ≈ –ln ($[NO_x]/[NO_y]$) / k_{rxn} [OH]) were about 5-7 h in the afternoon given that the rate constant between OH radicals and NO_x for HNO_3 formation (k_{rxn}) is equal to 7.9×10^{-12} cm^3 $molecules^{-1}$ s^{-1} (Brown et al., 1999;Cappa et al., 2012). Such estimation further supports our hypothesis that OOA-1 and OOA-2 were fresh SOA produced in the local atmosphere. Furthermore, OA components became more oxygenated as the PCA and R_{BC} increased (i.e., solid circles with the coloured scale of OS in **Figure 8-9**a). **Figure 8-9**c illustrates that ~85-90 wt% of total NR-PM_{rBC} was organic regardless of the values of R_{BC}. POA from traffic emissions (i.e., rBC- and HOA-rich factors) accounted for ~50–70 wt% of total NR-PM_{rBC} when R_{BC} is smaller than 4 whereas the contributions of SOA components (i.e., OOA-1 and OOA-2 factors) increased with R_{BC}, reaching a plateau at about 70–75% of total NR-PM_{rBC} when R_{BC} is larger than 8.

Figure 8-9b shows that R_{BC} decreased continuously with higher rBC loadings, highlighting the fact that most of the rBC mass observed within the hot period was associated with POA materials. Based on the mass fraction of rBC signals in the mass spectra of each PMF factor, it can be estimated that over 80 wt% of rBC mass was associated with traffic-related POA (i.e., about 60 and 20 wt% from rBC-rich and HOA-rich factors, respectively) when R_{BC} is smaller than 4 (**Figure 8-9**d). An increasing contribution of OOA factors to rBC mass was observed for particles with thicker OA coating. OOA-1 factor contributed up to ~60 wt% of rBC mass when R_{BC} is larger than 10 while OOA-2 factor was only a minor contributor to rBC mass for the whole range of R_{BC} values. The small contribution of OOA-2 particles to the rBC burden occurred despite the substantial contribution of OOA-2 to the total NR-PM_{rBC} mass. This is because rBC accounted for only 0.5 wt% of the OOA-2 factor, implying that such OOA materials co-existed with small rBC inclusions. Willis et al. (2014) reported that SP-AMS could accurately measure the mass fraction of rBC, at least down to 0.05 (5 wt%), in laboratory-generated organically coated Regal Black particles. Vaporization efficiency of an individual particle with a tiny rBC core diameter (e.g., < 5 wt%) and its uncertainties to mass quantification remain unclear (e.g., insufficient volatilization may lead to an underestimate of mass in the factor).

8.4.3 Comparisons of NR-PM_{rBC} and NR-PM components

To understand the mixing state of OA and rBC particles, the SP-AMS measurements (NR-PM_{rBC}) were compared to the co-located HR-ToF-AMS measurements (NR-PM) as presented in **Figure 8-10** and **Figure 8-11**. Mass loadings of secondary species in NR-PM_{rBC} were lower than their corresponding NR-PM components based on the CE and IE_{NO3} values used in this work, suggesting that significant fractions of secondary aerosol species were externally mixed with rBC. Specifically, diurnal cycles of nitrate, ammonium and chloride were strongly correlated ($r > 0.96$) between the two measurements but only about 8-20 wt% (or NR-PM_{rBC}/NR-PM = 0.08-0.2) of their masses were coated on rBC. The fraction of sulfate that was internally mixed with rBC was small, on average (NR-PM_{rBC}/NR-PM = 0.07). The relative abundance of HOA and OOA (i.e., comparing OA mass loadings in the morning and afternoon

peaks in **Figure 8-10**a) suggests that a larger fraction of OOA was externally mixed with rBC compared to HOA from traffic emissions, discussed further below. In general, OOA and sulfate tend to be concentrated in the accumulation mode peaking between 400-600 nm in d_{va} (Zhang et al., 2011), and hence the above argument also explains the larger difference of OA and sulfate mass with d_{va} larger than 300 nm between the two measurements (**Figure 8-10**i).

Chen et al. (2017) identified four PMF factors, namely HOA, cooking OA (COA), nitrate-related OOA (NOOA) and very OOA (VOOA), to describe the potential sources of OA measured by the HR-ToF-AMS (Figure S6) in this field campaign. The HOA and COA factors are assumed primary and the NOOA and VOOA factors are assumed secondary in origin. First, HOA exhibited a strong peak in the morning rush hours, and its diurnal cycle and mass loading was very similar to the sum of rBC- and HOA-rich factors in terms of both shape and the absolute concentrations (**Figure 8-10**f). HOA accounted for 9 wt% of total OA in NR-PM. **Figure 8-11** further demonstrates that the average ratio of NR-PM_{rBC}/NR-PM for HOA components (i.e., ([HOA-rich] + [rBC-rich]) / [HOA]) is about 1.32, implying that HOA materials were largely internally mixed with rBC but their concentrations in NR-PM_{rBC} might be over quantified by 32% on average based on our CE correction and IE calibration approach. Note that the mass loadings of rBC contributing to the HOA-rich and rBC-rich factors (estimated from the C_n^+ ions) were subtracted in the calculation of NR-PM_{rBC}/NR-PM. Nevertheless, the presence of refractory oxygenated organic fragments in the mass spectra of the rBC-rich factor could introduce positive biases to such estimation. The average ratio drops to about 1.05 if the three major oxygenated organic fragments, including CO^+, CO_2^+ and $C_2H_3O^+$, are also excluded in the calculation. Using the same measurement approach and R_{BC}-dependent CE, Massoli et al. (2012; 2015) reported that 81 and 87 % of HOA were associated with rBC particles near vehicular emissions and in a polluted offshore environment.

COA was another POA that contributed to 14 wt% of total OA in NR-PM. However, COA was not identified in the PMF analysis of SP-AMS data. The comparison suggests that COA was unlikely co-emitted with rBC from modern kitchens, and the mixing of rBC and COA through particle coalescence was insignificant near the sampling location. Similar observations have been reported in previous studies in downtown Toronto. Willis et al. (2016) could not identify COA by measuring rBC-containing particles exclusively whereas Lee et al. (2015) could separate a COA factor from other OA components by deploying a SP-AMS equipped with dual vaporizers (i.e., laser and tungsten vaporizers). Comparing the results obtained from two different operational modes (i.e., switching laser vaporizer on and off), Lee et al. (2015) provided indirect evidence that COA was largely externally mixed with rBC in the urban atmosphere.

SOA was the most abundant OA component. VOOA and NOOA accounted for 60 and 17 wt% of total OA in NR-PM, respectively. Diurnal variations of NOOA were minimal, whereas VOOA mass concentrations increased continuously from ~8:00 and peaked at ~18:00 (**Figure 8-10**g and S6). Although PMF analysis identified two SOA factors for both AMS measurements, the total SOA concentrations were calculated to provide overall comparisons of SOA mass loadings in NR-PM and NR-PM_{rBC} regardless their sources. Specifically, SOA_{NR-PM} = NOOA + VOOA for HR-ToF-AMS and SOA_{rBC} = OOA-1 and OOA-2 for SP-AMS. The average SOA_{rBC}/SOA_{NR-PM} is equal to 0.2, indicating that approximately 20 wt% of OOA components were internally mixed with rBC on average during the hot period (**Figure 8-11**).

It is worth noting that SOA_{rBC} increased at a faster rate in the morning compared to $SOA_{NR\text{-}PM}$, suggesting that SOA_{rBC} and $SOA_{NR\text{-}PM}$ could be produced or transported from different sources, at least to some extent. Furthermore, $SOA_{NR\text{-}PM}$ mass concentrations started dropping substantially at ~18:00-19:00, which was about 1-2 hours delay compared to SOA_{rBC} (**Figure 8-10**g). This observable delay corresponded to the time of increasing sulfate levels in NR-PM, implying potential sources and formation pathways of VOOA (i.e., the major component of $SOA_{NR\text{-}PM}$ within that period) that might be related to the regional transport of aged particles. This possible explanation is consistent with the observation that VOOA represented more oxidized OOA materials (i.e. more aged) and that the strongest average wind speed was observed at around 18:00-19:00 (**Figure 8-6**c). Single particle measurements using the light scattering module of the HR-ToF-AMS also suggests internal mixing of sulfate and highly oxidized OOA materials in NR-PM (Chen et al., 2017). Nevertheless, VOOA could also be produced through local photochemistry as 1) it was unlikely that all the locally formed SOA materials were condensed on rBC particles exclusively during the day and 2) the HR-ToF-AMS should be able to detect OOA-1 and OOA-2 materials as well. The relative contributions of local photochemistry and regional transport to the observed VOOA mass could not be separated by the PMF analysis possibly due to the chemical similarity of those SOA materials.

A key question remaining is whether the OOA materials identified by the SP-AMS and HR-ToF-AMS are the same in terms of AMS mass spectral characteristics. **Figure 8-7** and S6 show that the mass spectra of OOA factors measured by the two instruments were clearly distinct from each other. Specifically, VOOA and NOOA were dominated by an organic fragment of CO_2^+ (i.e. a tracer of organic acids) and $C_2H_3O^+$ followed by CHO^+, respectively whereas $C_2H_3O^+$ was the major fragment of OOA-1 and OOA-2. However, it is particularly important to point out that different aerosol vaporization schemes utilized in SP-AMS and HR-ToF-AMS makes the direct comparison of organic mass spectra not straightforward. It has been demonstrated that thermal vaporization (operated at 600ºC) used in the HR-ToF-AMS produces significant decomposition and dehydration of oxidized organic compounds (Canagaratna et al., 2015a) but the laser vaporization used in SP-AMS can provide soft vaporization of organic coatings on rBC particles at lower temperature, resulting in less molecular fragmentation (Canagaratna et al., 2015b). The OOA-1 and OOA-2 spectra notably have more peaks and with higher intensities at larger m/z (> 60 amu) compared to the NOOA and VOOA spectra. Also, the relative intensity of the peaks at m/z 28 and 29 (CO^+ and CHO^+ respectively) are substantially reduced in the OOA-1 and OOA-2 spectra compared to NOOA and VOOA. Both of these observations are consistent with reduced fragmentation from vaporization in the SP-AMS being a major reason for the differences.

The elemental ratios (O/C and H/C) extracted from the SP-AMS and HR-ToF-AMS mass spectra of oxidized organic species have been shown to be different. Canagaratna et al. (2015b) reported that the SP-AMS O/C and H/C values differ from their corresponding HR-ToF-AMS values by factors of 0.83 and 1.16, respectively, based on the laboratory analysis of chemical standards, including dicarboxylic acids, multifunctional acids and alcohols. These conversion factors are applied to the O/C and H/C ratios of NOOA, VOOA and $SOA_{NR\text{-}PM}$ (i.e., mass-weighted values of NOOA and VOOA) (Chen et al., 2017) in order to perform a more meaningful comparison to our SP-AMS measurements in the Van Krevelen diagram (**Figure 8-12**). The elemental ratios of SOA_{rBC} and $SOA_{NR\text{-}PM}$ are comparable to each other, well within

the measurement uncertainties. Similar observations are obtained between OOA-2 and VOOA. In contrast, the O/C and H/C ratios of OOA-1 are rather different to the adjusted values of NOOA, VOOA and $SOA_{NR\text{-}PM}$, suggesting some chemical difference between OOA-1 and those SOA materials. This is also consistent with the fact that OOA-1 mass concentrations increased faster than other OOA materials in the morning. More field and laboratory data are required to validate and improve the empirical relationships proposed by Canagaratna et al., (2015b) and to understand the extent to which the observed differences are a result of true chemical differences versus explainable by differences in molecular fragmentation due to the different vaporization schemes used in the instruments.

8.5 Conclusions and Atmospheric Implications

The repeated diurnal patterns of inorganic species, POA and SOA reported here provide a unique opportunity to investigate the chemical characteristics and formation of OA coating on rBC particles near traffic emissions. There is no doubt that HOA was internally mixed with rBC significantly as they were largely co-emitted by vehicles. The results of PMF illustrate that rBC- and HOA-rich factors accounted for about 60 and 20 wt% of rBC with thin coating, respectively, and the rBC-rich factor contributed about 82 wt% of the freshly emitted rBC from traffic, similar to previous observation in the roadside environment (Willis et al., 2016). The COA factor is commonly observed in urban areas (Allan et al., 2010;Mohr et al., 2012) but its mixing with ambient rBC is seldom reported. The absence of a COA factor in rBC-containing particles highlights the fact that emissions of rBC from modern kitchens and the mixing of rBC and COA through particle coalescence were negligible in this study. Previous measurements conducted in an urban area also pointed to the same conclusion (Lee et al., 2015;Willis et al., 2016).

Increases in coating thickness were primarily due to substantial formation of fresh SOA through local photochemical processing on the timescale of a few hours. On average, about 7-20 wt% of secondary aerosol species, including both inorganic and OOA species, were condensed on rBC particles, suggesting that rBC was unlikely the major sink for condensation of fresh SOA in this study. During the peak of SOA production, the average mass loadings of rBC and VOOA were about 0.2 and 4 $\mu g/m^3$, respectively, which were a few factors to orders of magnitude lower than those generated in some recent aging experiments of soot particles (Metcalf et al., 2013;Li et al., 2017). Peng et al. (2016) recently showed that the timescale for producing sufficient fresh SOA to completely modify rBC properties strongly depends on pollution levels. Our observations may provide insight into the design of soot aging experiments for investigating the formation rate of fresh SOA coatings (e.g., growth rate of coating thickness) as well as their environmental impacts under a more atmospherically relevant condition.

Our measurement approach leads to a conclusion that at least a fraction of OOA condensed on rBC was chemically distinct from that externally mixed with rBC, although uncertainties of organic fragmentation due to the application of the laser vaporizer still need to be fully established to quantify this difference. The reason for this unique observation remains unclear. One of the possibilities is that SOA_{rBC} formed more locally on shorter timescales (e.g., photo-oxidation of anthropogenic volatile organic compounds (VOCs) near traffic emissions) could preferentially condense onto rBC particles in Aiken mode that can provide a larger overall

surface area to the condensing gases compared to other existing background particles. The more oxidized OOA materials formed regionally on longer timescales (e.g., a fraction of VOOA that were largely externally mixed with rBC) under conditions with relatively low concentrations of (or without) rBC particle could be advected to the sampling region during the day. Furthermore, atmospheric dilution of traffic emissions can modify the chemical compositions and concentrations of SOA precursors and seed particles so that the formation of secondary coatings on rBC might be less efficient and chemically different under diluted conditions (e.g., after boundary layer break up and mixing with air masses from residual layer). This may partially explain the formation of VOOA in $SOA_{NR\text{-}PM}$ through local photochemistry. There may also be a mechanistic preference for material to condense onto certain surfaces because of their chemical nature (e.g., hydrophobic coating (e.g. HOA and soot surface functionality) but future research efforts are required to explore this possibility further.

8.6 Acknowledgements

Lee A. K. Y. would like to acknowledge the support from the NUS Start-up Grant (R-302-000-173-133). Cappa D. C. and Russell L. M. were supported by the California Air Resources Board (Agreement number: 13-330)The authors would also like to thank the Fontana Fire Department and the South Coast Air Quality Management District (SCAQMD) for Fontana site logistics.

8.7 References

Allan, J. D., Delia, A. E., Coe, H., Bower, K. N., Alfarra, M. R., Jimenez, J. L., Middlebrook, A. M., Drewnick, F., Onasch, T. B., Canagaratna, M. R., Jayne, J. T., and Worsnop, D. R.: A generalised method for the extraction of chemically resolved mass spectra from aerodyne aerosol mass spectrometer data, J.Aerosol Sci., 35, 909, 10.1016/j.jaerosci.2004.02.007, 2004.

Allan, J. D., Williams, P. I., Morgan, W. T., Martin, C. L., Flynn, M. J., Lee, J., Nemitz, E., Phillips, G. J., Gallagher, M. W., and Coe, H.: Contributions from transport, solid fuel burning and cooking to primary organic aerosols in two UK cities, Atmospheric Chemistry and Physics, 10, 647-668, 10.5194/acp-10-647-2010, 2010.

Betha, R., Russell, L. M., Chen, C.-L., Liu, J., Price, D. J., Sanchez, K. J., Chen, S., Lee A. K. Y., Collier, S. C., Zhang, Q., Zhang, X., and Cappa, C. D.: Larger submicron particles for emissions with residential burning in wintertime San Joaquin Valley (Fresno) than for vehicle combustion in summertime South Coast Air Basin (Fontana), under review.

Bond, T. C., Doherty, S. J., Fahey, D. W., Forster, P. M., Berntsen, T., DeAngelo, B. J., Flanner, M. G., Ghan, S., Karcher, B., Koch, D., Kinne, S., Kondo, Y., Quinn, P. K., Sarofim, M. C., Schultz, M. G., Schulz, M., Venkataraman, C., Zhang, H., Zhang, S., Bellouin, N., Guttikunda, S. K., Hopke, P. K., Jacobson, M. Z., Kaiser, J. W., Klimont, Z., Lohmann, U., Schwarz, J. P., Shindell, D., Storelvmo, T., Warren, S. G., and Zender, C. S.: Bounding the role of black carbon in the climate system: A scientific assessment, Journal of Geophysical Research-Atmospheres, 118, 5380-5552, 10.1002/jgrd.50171, 2013.

Brown, S. S., Talukdar, R. K., and Ravishankara, A. R.: Rate constants for the reaction OH+NO2+M -> HNO3+M under atmospheric conditions, Chemical Physics Letters, 299, 277-284, 10.1016/s0009-2614(98)01283-4, 1999.

Canagaratna, M. R., Jayne, J. T., Jimenez, J. L., Allan, J. D., Alfarra, M. R., Zhang, Q., Onasch, T. B., Drewnick, F., Coe, H., Middlebrook, A., Delia, A., Williams, L. R., Trimborn, A. M., Northway, M. J., DeCarlo, P. F., Kolb, C. E., Davidovits, P., and Worsnop, D. R.: Chemical and microphysical characterization of ambient aerosols with the aerodyne aerosol mass spectrometer, Mass Spectrometry Reviews, 26, 185-222, 10.1002/mas.20115, 2007.

Canagaratna, M. R., Jimenez, J. L., Kroll, J. H., Chen, Q., Kessler, S. H., Massoli, P., Ruiz, L. H., Fortner, E., Williams, L. R., Wilson, K. R., Surratt, J. D., Donahue, N. M., Jayne, J. T., and Worsnop, D. R.: Elemental ratio measurements of organic compounds using aerosol mass spectrometry: characterization, improved calibration, and implications, Atmospheric Chemistry and Physics, 15, 253, 10.5194/acp-15-253-2015, 2015a.

Canagaratna, M. R., Massoli, P., Browne, E. C., Franklin, J. P., Wilson, K. R., Onasch, T. B., Kirchstetter, T. W., Fortner, E. C., Kolb, C. E., Jayne, J. T., Kroll, J. H., and Worsnop, D. R.: Chemical Compositions of Black Carbon Particle Cores and Coatings via Soot Particle Aerosol Mass Spectrometry with Photoionization and Electron Ionization, Journal of Physical Chemistry A, 119, 4589-4599, 10.1021/jp510711u, 2015b.

Cappa, C. D., Onasch, T. B., Massoli, P., Worsnop, D. R., Bates, T. S., Cross, E. S., Davidovits, P., Hakala, J., Hayden, K. L., Jobson, B. T., Kolesar, K. R., Lack, D. A., Lerner, B. M., Li, S. M., Mellon, D., Nuaaman, I., Olfert, J. S., Petaja, T., Quinn, P. K., Song, C., Subramanian, R., Williams, E. J., and Zaveri, R. A.: Radiative Absorption Enhancements Due to the Mixing State of Atmospheric Black Carbon, Science, 337, 1078-1081, 10.1126/science.1223447, 2012.

Corbin, J. C., Sierau, B., Gysel, M., Laborde, M., Keller, A., Kim, J., Petzold, A., Onasch, T. B., Lohmann, U., and Mensah, A. A.: Mass spectrometry of refractory black carbon particles from six sources: carbon-cluster and oxygenated ions, Atmospheric Chemistry and Physics, 14, 2591-2603, 10.5194/acp-14-2591-2014, 2014.

Chen, C.-L., Chen, S., Russell, L. M., Liu, J., Price, D. J., Betha, R., Sanchez, K. J., Lee A. K. Y., Collier, S. C., Zhang, Q., Kumar, A., Kleeman, M., Zhang, X., and Cappa, C. D.: Organic aerosol particle chemical properties associated with residential burning and fog in wintertime San Joaquin Valley (Fresno) and with vehicle and firework emissions in summertime South Coast Air Basin (Fontana), Under review.

DeCarlo, P. F., Slowik, J. G., Worsnop, D. R., Davidovits, P., and Jimenez, J. L.: Particle morphology and density characterization by combined mobility and aerodynamic diameter measurements. Part 1: Theory, Aerosol Science and Technology, 38, 1185-1205, 10.1080/027868290903907, 2004.

DeCarlo, P. F., Kimmel, J. R., Trimborn, A., Northway, M. J., Jayne, J. T., Aiken, A. C., Gonin, M., Fuhrer, K., Horvath, T., Docherty, K. S., Worsnop, D. R., and Jimenez, J. L.: Field-deployable, high-resolution, time-of-flight aerosol mass spectrometer, Anal.Chem., 78, 8281, 10.1021/ac061249n, 2006.

Enroth, J., Saarikoski, S., Niemi, J., Kousa, A., Jezek, I., Mocnik, G., Carbone, S., Kuuluvainen, H., Ronkko, T., Hillamo, R., and Pirjola, L.: Chemical and physical characterization of traffic particles in four different highway environments in the Helsinki metropolitan area, Atmospheric Chemistry and Physics, 16, 5497-5512, 10.5194/acp-16-5497-2016, 2016.

Gentner, D. R., Jathar, S. H., Gordon, T. D., Bahreini, R., Day, D. A., El Haddad, I., Hayes, P. L., Pieber, S. M., Platt, S. M., de Gouw, J., Goldstein, A. H., Harley, R. A., Jimenez, J. L., Prevot, A. S. H., and Robinson, A. L.: Review of Urban Secondary Organic Aerosol Formation from Gasoline and Diesel Motor Vehicle Emissions, Environmental Science & Technology, 51, 1074-1093, 10.1021/acs.est.6b04509, 2017.

Guo, S., Hu, M., Lin, Y., Gomez-Hernandez, M., Zamora, M. L., Peng, J. F., Collins, D. R., and Zhang, R. Y.: OH-Initiated Oxidation of m-Xylene on Black Carbon Aging, Environmental Science & Technology, 50, 8605-8612, 10.1021/acs.est.6b01272, 2016.

Jacobson, M. Z.: Strong radiative heating due to the mixing state of black carbon in atmospheric aerosols, Nature, 409, 695-697, 10.1038/35055518, 2001.

Jimenez, J. L., Jayne, J. T., Shi, Q., Kolb, C. E., Worsnop, D. R., Yourshaw, I., Seinfeld, J. H., Flagan, R. C., Zhang, X. F., Smith, K. A., Morris, J. W., and Davidovits, P.: Ambient aerosol sampling using the Aerodyne Aerosol Mass Spectrometer, Journal of Geophysical Research-Atmospheres, 108, 10.1029/2001jd001213, 2003.

Kroll, J. H., Donahue, N. M., Jimenez, J. L., Kessler, S. H., Canagaratna, M. R., Wilson, K. R., Altieri, K. E., Mazzoleni, L. R., Wozniak, A. S., Bluhm, H., Mysak, E. R., Smith, J. D., Kolb, C. E., and Worsnop, D. R.: Carbon oxidation state as a metric for describing the chemistry of atmospheric organic aerosol, Nature Chemistry, 3, 133-139, 10.1038/nchem.948, 2011.

Kuwata, M., Kondo, Y., and Takegawa, N.: Critical condensed mass for activation of black carbon as cloud condensation nuclei in Tokyo, Journal of Geophysical Research-Atmospheres, 114, 10.1029/2009jd012086, 2009.

Laborde, M., Crippa, M., Tritscher, T., Juranyi, Z., Decarlo, P. F., Temime-Roussel, B., Marchand, N., Eckhardt, S., Stohl, A., Baltensperger, U., Prevot, A. S. H., Weingartner, E., and Gysel, M.: Black carbon physical properties and mixing state in the European megacity Paris, Atmospheric Chemistry and Physics, 13, 5831-5856, 10.5194/acp-13-5831-2013, 2013.

Lee, A. K. Y., Willis, M. D., Healy, R. M., Onasch, T. B., and Abbatt, J. P. D.: Mixing state of carbonaceous aerosol in an urban environment: single particle characterization using the soot particle aerosol mass spectrometer (SP-AMS), Atmospheric Chemistry and Physics, 15, 1823-1841, 10.5194/acp-15-1823-2015, 2015.

Lee, A. K. Y., Willis, M. D., Healy, R. M., Wang, J. M., Jeong, C. H., Wenger, J. C., Evans, G. J., and Abbatt, J. P. D.: Single-particle characterization of biomass burning organic aerosol (BBOA): evidence for non-uniform mixing of high molecular weight organics and potassium, Atmospheric Chemistry and Physics, 16, 5561-5572, 10.5194/acp-16-5561-2016, 2016.

Li, K. W., Chen, L. H., Han, K., Lv, B. A., Bao, K. J., Wu, X. C., Gao, X., and Cen, K. F.: Smog chamber study on aging of combustion soot in isoprene/SO2/NOx system: Changes of mass, size, effective density, morphology and mixing state, Atmospheric Research, 184, 139-148, 10.1016/j.atmosres.2016.10.011, 2017.

Liu, D., Allan, J., Whitehead, J., Young, D., Flynn, M., Coe, H., McFiggans, G., Fleming, Z. L., and Bandy, B.: Ambient black carbon particle hygroscopic properties controlled by mixing state and composition, Atmospheric Chemistry and Physics, 13, 2015-2029, 10.5194/acp-13-2015-2013, 2013.

Liu, D. T., Whitehead, J., Alfarra, M. R., Reyes-Villegas, E., Spracklen, D. V., Reddington, C. L., Kong, S. F., Williams, P. I., Ting, Y. C., Haslett, S., Taylor, J. W., Flynn, M. J., Morgan,

W. T., McFiggans, G., Coe, H., and Allan, J. D.: Black-carbon absorption enhancement in the atmosphere determined by particle mixing state, Nature Geoscience, 10, 184-U132, 10.1038/ngeo2901, 2017.

Liu, S., Aiken, A. C., Gorkowski, K., Dubey, M. K., Cappa, C. D., Williams, L. R., Herndon, S. C., Massoli, P., Fortner, E. C., Chhabra, P. S., Brooks, W. A., Onasch, T. B., Jayne, J. T., Worsnop, D. R., China, S., Sharma, N., Mazzoleni, C., Xu, L., Ng, N. L., Liu, D., Allan, J. D., Lee, J. D., Fleming, Z. L., Mohr, C., Zotter, P., Szidat, S., and Prevot, A. S. H.: Enhanced light absorption by mixed source black and brown carbon particles in UK winter, Nature Communications, 6, 10.1038/ncomms9435, 2015.

Malmborg, V. B., Eriksson, A. C., Shen, M., Nilsson, P., Gallo, Y., Waldheim, B., Martinsson, J., Andersson, O., and Pagels, J.: Evolution of In-Cylinder Diesel Engine Soot and Emission Characteristics Investigated with Online Aerosol Mass Spectrometry, Environmental Science & Technology, 51, 1876-1885, 10.1021/acs.est.6b03391, 2017.

Massoli, P., Fortner, E. C., Canagaratna, M. R., Williams, L. R., Zhang, Q., Sun, Y., Schwab, J. J., Trimborn, A., Onasch, T. B., Demerjian, K. L., Kolb, C. E., Worsnop, D. R., and Jayne, J. T.: Pollution Gradients and Chemical Characterization of Particulate Matter from Vehicular Traffic near Major Roadways: Results from the 2009 Queens College Air Quality Study in NYC, Aerosol Science and Technology, 46, 1201-1218, 10.1080/02786826.2012.701784, 2012.

Massoli, P., Onasch, T. B., Cappa, C. D., Nuamaan, I., Hakala, J., Hayden, K., Li, S. M., Sueper, D. T., Bates, T. S., Quinn, P. K., Jayne, J. T., and Worsnop, D. R.: Characterization of black carbon-containing particles from soot particle aerosol mass spectrometer measurements on the R/V Atlantis during CalNex 2010, Journal of Geophysical Research-Atmospheres, 120, 2575-2593, 10.1002/2014jd022834, 2015.

McMeeking, G. R., Good, N., Petters, M. D., McFiggans, G., and Coe, H.: Influences on the fraction of hydrophobic and hydrophilic black carbon in the atmosphere, Atmospheric Chemistry and Physics, 11, 5099-5112, 10.5194/acp-11-5099-2011, 2011.

Metcalf, A. R., Loza, C. L., Coggon, M. M., Craven, J. S., Jonsson, H. H., Flagan, R. C., and Seinfeld, J. H.: Secondary Organic Aerosol Coating Formation and Evaporation: Chamber Studies Using Black Carbon Seed Aerosol and the Single-Particle Soot Photometer, Aerosol Science and Technology, 47, 326-347, 10.1080/02786826.2012.750712, 2013.

Moffet, R. C., and Prather, K. A.: In-situ measurements of the mixing state and optical properties of soot with implications for radiative forcing estimates, Proceedings of the National Academy of Sciences of the United States of America, 106, 11872-11877, 10.1073/pnas.0900040106, 2009.

Mohr, C., DeCarlo, P. F., Heringa, M. F., Chirico, R., Slowik, J. G., Richter, R., Reche, C., Alastuey, A., Querol, X., Seco, R., Penuelas, J., Jimenez, J. L., Crippa, M., Zimmermann, R., Baltensperger, U., and Prevot, A. S. H.: Identification and quantification of organic aerosol from cooking and other sources in Barcelona using aerosol mass spectrometer data, Atmospheric Chemistry and Physics, 12, 1649-1665, 10.5194/acp-12-1649-2012, 2012.

Onasch, T. B., Trimborn, A., Fortner, E. C., Jayne, J. T., Kok, G. L., Williams, L. R., Davidovits, P., and Worsnop, D. R.: Soot Particle Aerosol Mass Spectrometer: Development, Validation, and Initial Application, Aerosol Science and Technology, 46, 804-817, 10.1080/02786826.2012.663948, 2012.

Paatero, P., and Tapper, U.: POSITIVE MATRIX FACTORIZATION - A NONNEGATIVE FACTOR MODEL WITH OPTIMAL UTILIZATION OF ERROR-ESTIMATES OF DATA VALUES, Environmetrics, 5, 111-126, 10.1002/env.3170050203, 1994.

Peng, J. F., Hu, M., Guo, S., Du, Z. F., Zheng, J., Shang, D. J., Zamora, M. L., Zeng, L. M., Shao, M., Wu, Y. S., Wang, Y., Glen, C. R., Collins, D. R., Molina, M. J., and Zhang, R. Y.: Markedly enhanced absorption and direct radiative forcing of black carbon under polluted urban environments, Proceedings of the National Academy of Sciences of the United States of America, 113, 4266-4271, 10.1073/pnas.1602310113, 2016.

Ramanathan, V., and Carmichael, G.: Global and regional climate changes due to black carbon, Nature Geoscience, 1, 221-227, 10.1038/ngeo156, 2008.

Saarikoski, S., Timonen, H., Carbone, S., Kuuluvainen, H., Niemi, J. V., Kousa, A., Ronkko, T., Worsnop, D., Hillamo, R., and Pirjola, L.: Investigating the chemical species in submicron particles emitted by city buses, Aerosol Science and Technology, 51, 317-329, 10.1080/02786826.2016.1261992, 2017.

Schnitzler, E. G., Dutt, A., Charbonneau, A. M., Olfert, J. S., and Jager, W.: Soot Aggregate Restructuring Due to Coatings of Secondary Organic Aerosol Derived from Aromatic Precursors, Environmental Science & Technology, 48, 14309-14316, 10.1021/es503699b, 2014.

Slowik, J. G., Brook, J., Chang, R. Y.-W., Evans, G. J., Hayden, K., Jeong, C.-H., Li, S.-M., Liggio, J., Liu, P. S. K., McGuire, M., Mihele, C., Sjostedt, S., Vlasenko, A., and Abbatt, J. P. D.: Photochemical processing of organic aerosol at nearby continental sites: contrast between urban plumes and regional aerosol, Atmos. Chem. Phys., 11, 2991-3006, doi:10.5194/acp-11-2991-2011, 2011.

Takegawa, N., Miyakawa, T., Kondo, Y., Blake, D. R., Kanaya, Y., Koike, M., Fukuda, M., Komazaki, Y., Miyazaki, Y., Shimono, A., and Takeuchi, T.: Evolution of submicron organic aerosol in polluted air exported from Tokyo, Geophysical Research Letters, 33, 10.1029/2006gl025815, 2006.

Tkacik, D. S., Lambe, A. T., Jathar, S., Li, X., Presto, A. A., Zhao, Y. L., Blake, D., Meinardi, S., Jayne, J. T., Croteau, P. L., and Robinson, A. L.: Secondary Organic Aerosol Formation from in-Use Motor Vehicle Emissions Using a Potential Aerosol Mass Reactor, Environmental Science & Technology, 48, 11235-11242, 10.1021/es502239v, 2014.

Ulbrich, I. M., Canagaratna, M. R., Zhang, Q., Worsnop, D. R., and Jimenez, J. L.: Interpretation of organic components from Positive Matrix Factorization of aerosol mass spectrometric data, Atmospheric Chemistry and Physics, 9, 2891-2918, 10.5194/acp-9-2891-2009, 2009.

Wang, Q. Y., Huang, R. J., Zhao, Z. Z., Cao, J. J., Ni, H. Y., Tie, X. X., Zhu, C. S., Shen, Z. X., Wang, M., Dai, W. T., Han, Y. M., Zhang, N. N., and Prevot, A. S. H.: Effects of photochemical oxidation on the mixing state and light absorption of black carbon in the urban atmosphere of China, Environmental Research Letters, 12, 10.1088/1748-9326/aa64ea, 2017.

Willis, M. D., Lee, A. K. Y., Onasch, T. B., Fortner, E. C., Williams, L. R., Lambe, A. T., Worsnop, D. R., and Abbatt, J. P. D.: Collection efficiency of the soot-particle aerosol mass

spectrometer (SP-AMS) for internally mixed particulate black carbon, Atmospheric Measurement Techniques, 7, 4507-4516, 10.5194/amt-7-4507-2014, 2014.

Willis, M. D., Healy, R. M., Riemer, N., West, M., Wang, J. M., Jeong, C. H., Wenger, J. C., Evans, G. J., Abbatt, J. P. D., and Lee, A. K. Y.: Quantification of black carbon mixing state from traffic: implications for aerosol optical properties, Atmospheric Chemistry and Physics, 16, 4693-4706, 10.5194/acp-16-4693-2016, 2016.

Zhang, Q., Jimenez, J. L., Canagaratna, M. R., Ulbrich, I. M., Ng, N. L., Worsnop, D. R., and Sun, Y. L.: Understanding atmospheric organic aerosols via factor analysis of aerosol mass spectrometry: a review, Analytical and Bioanalytical Chemistry, 401, 3045-3067, 10.1007/s00216-011-5355-y, 2011.

8.8 Figures

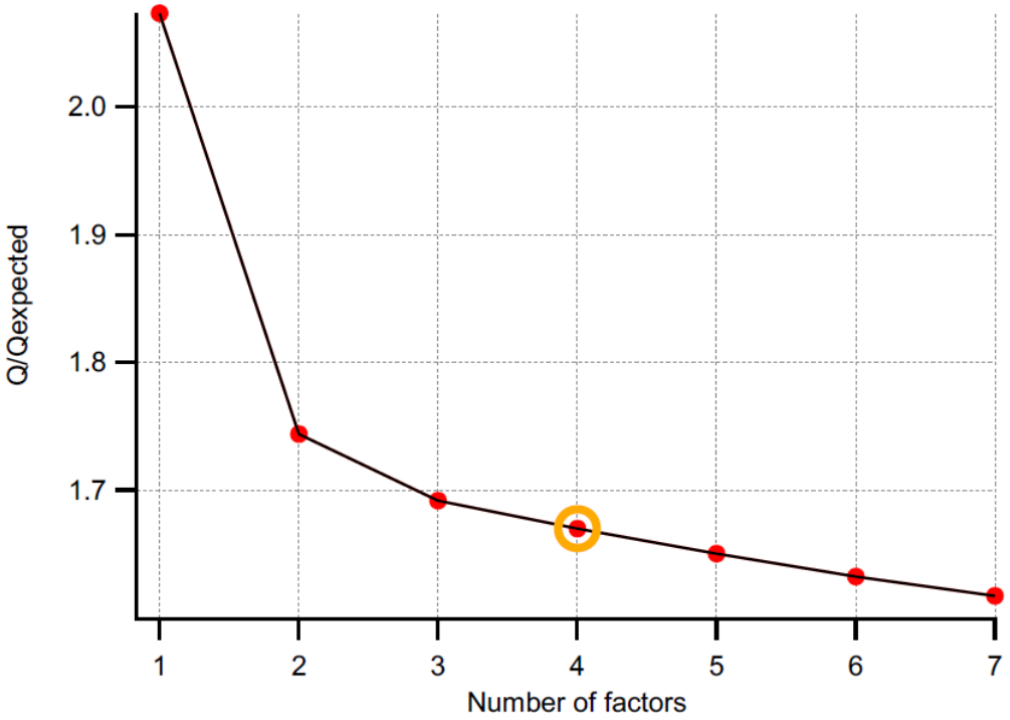

Figure 8-1. $Q/Q_{expected}$ values as a function of number of PMF factors. A 4-factor solution, including two POA factors from traffic emissions and two SOA factors due to local photochemistry, was determined as a final solution.

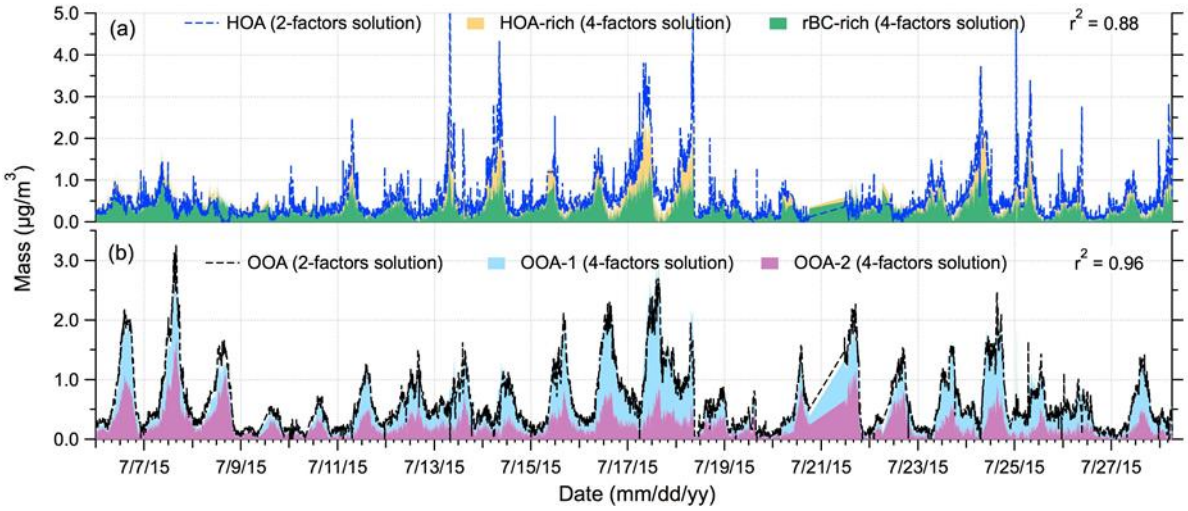

Figure 8-2. Time series of 2-factor solution: (a) HOA and (b) OOA. Increasing the number of PMF factors to four splits HOA into HOA-rich and rBC-rich factors and OOA into OOA-1 and OOA-2 factors. The physical meanings of individual factors are described in the main text (RIE of 0.26 15 and 1.4 were applied for rBC and organic fragments, respectively).

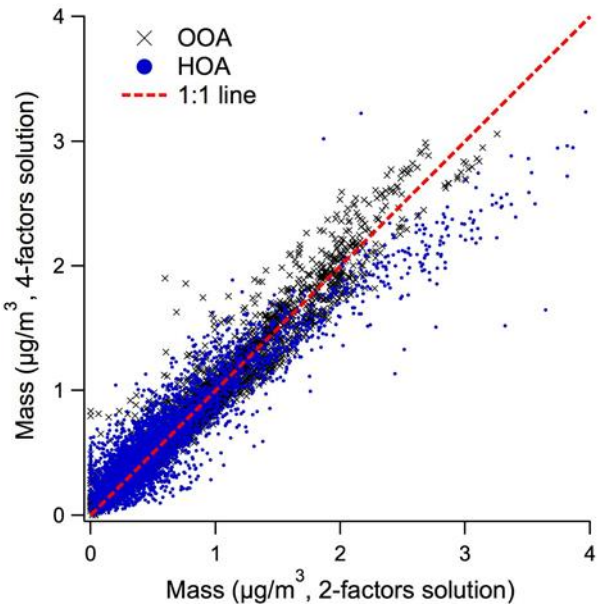

Figure 8-3. Correlations between 4-factor and 2-factor solutions: (HOA-rich + rBC-rich) vs. HOA and (OOA-1 + OOA-2) vs. OOA. (RIE of 0.26 and 1.4 were applied for rBC and organic fragments, respectively).

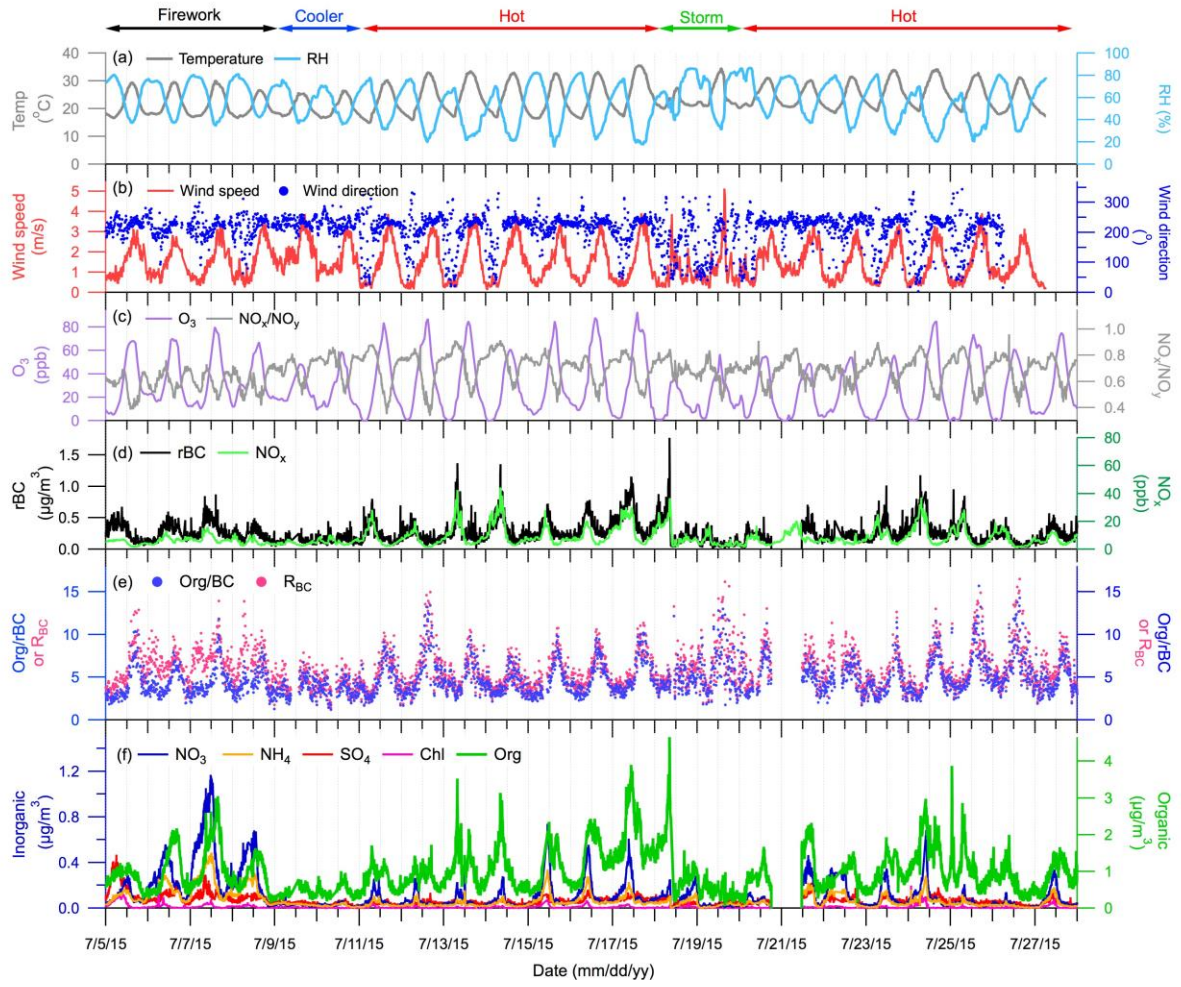

Figure 8-4. Time series of (a) temperature and RH, (b) wind speed and direction, (c) ozone and NO_x/NO_y ratio, (d) rBC and NO_x, (e) Org/rBC ratio and R_{BC}, and (f) NR-PM_{rBC} (NO3 = nitrate, NH4 = ammonium, SO4 = sulfate, Chl = chloride and Org = organic)

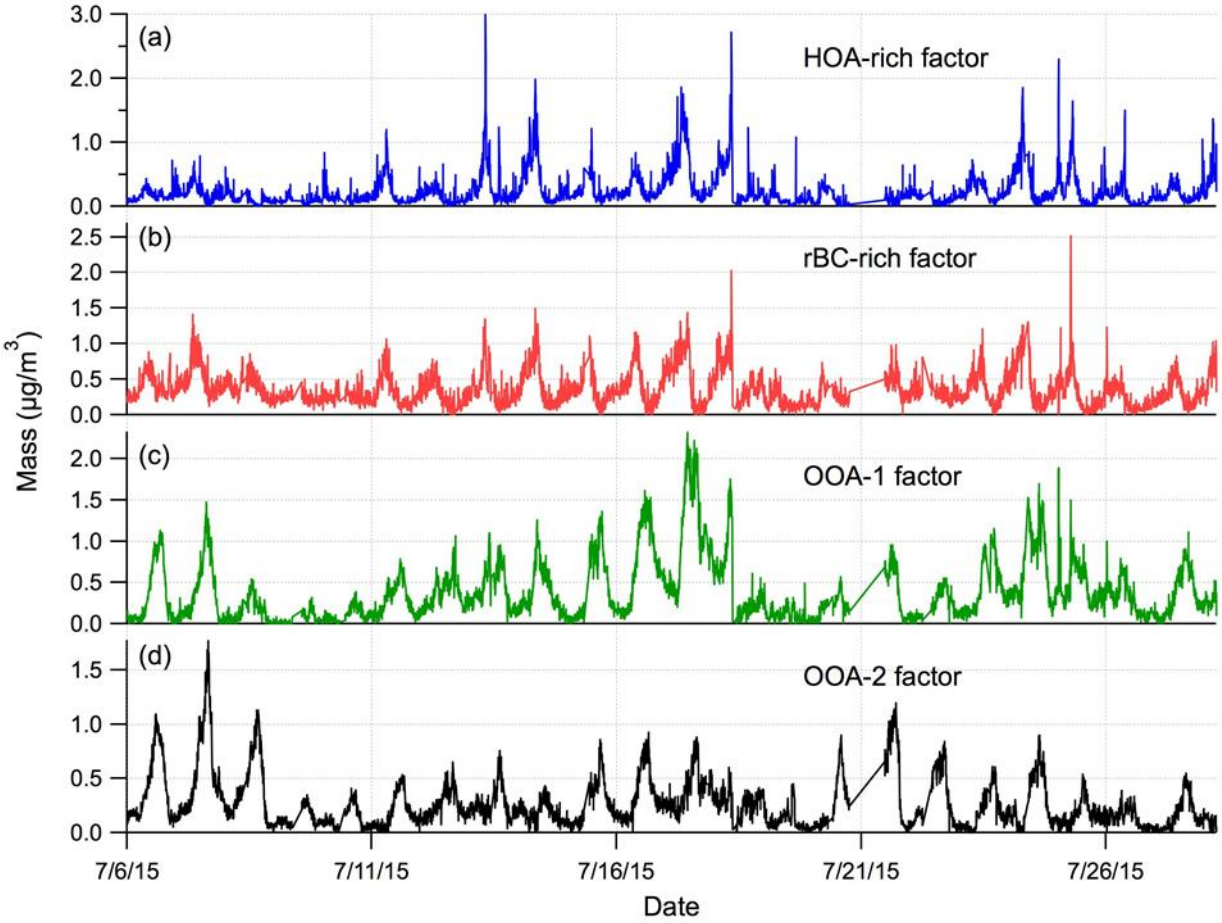

Figure 8-5. Time series of the 4-factor solution: (a) HOA-rich, (b) rBC-rich, (C) OOA-1, and (d) OOA-2 (RIE of 0.26 and 1.4 were applied for rBC and organic fragments, respectively).

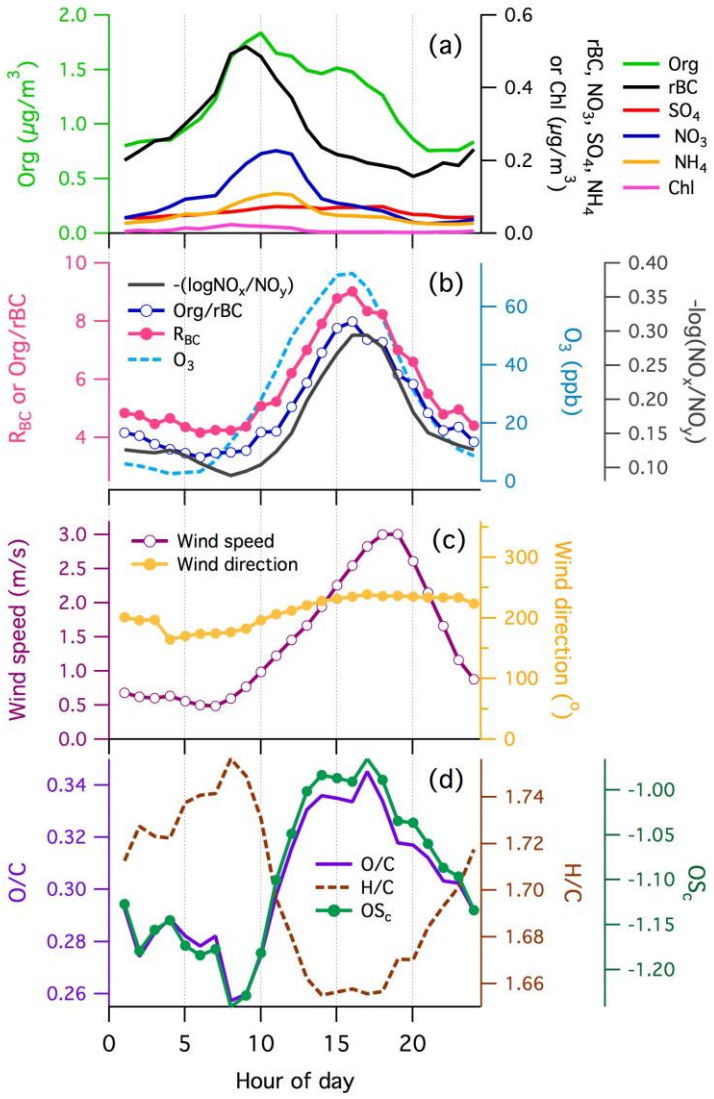

Figure 8-6. Diurnal cycles of (a) rBC and NR-PM_{rBC}, (b) Org/rBC ratio, R_{BC}, ozone and –log (NO_x/NO_y), (c) wind speed and direction, and (d) O/C, H/C and OS within the hot period (See Figure S7 for the uncertainties of data)

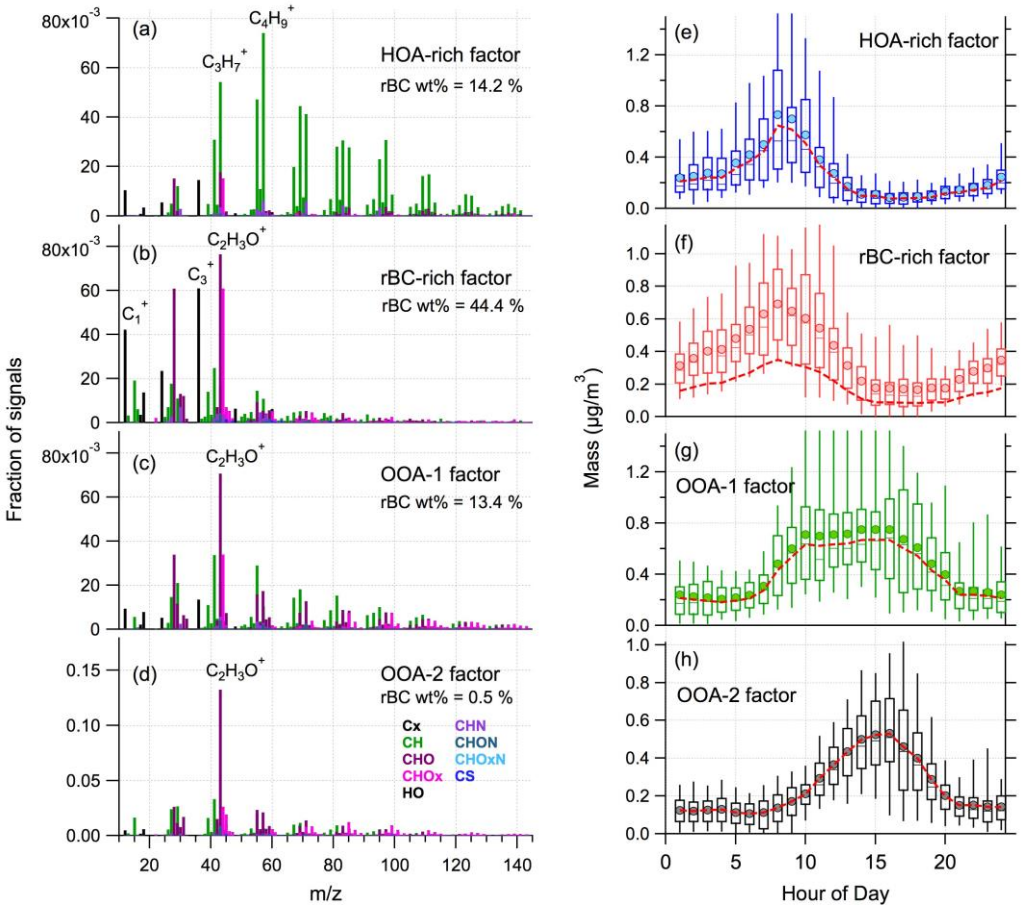

Figure 8-7. Mass spectra (a-d) and diurnal cycles (e-h) of PMF factors from SP-AMS data within the hot period. (Box plots: 5th, 25th, 50th, 75th and 95th percentile, Filled circles: mean values for organic + C_x^+ fragments, Red dashed lines: mean values for organic alone. RIE of 0.26 and 1.4 were applied for rBC and organic fragments, respectively, for the diurnal patterns.)

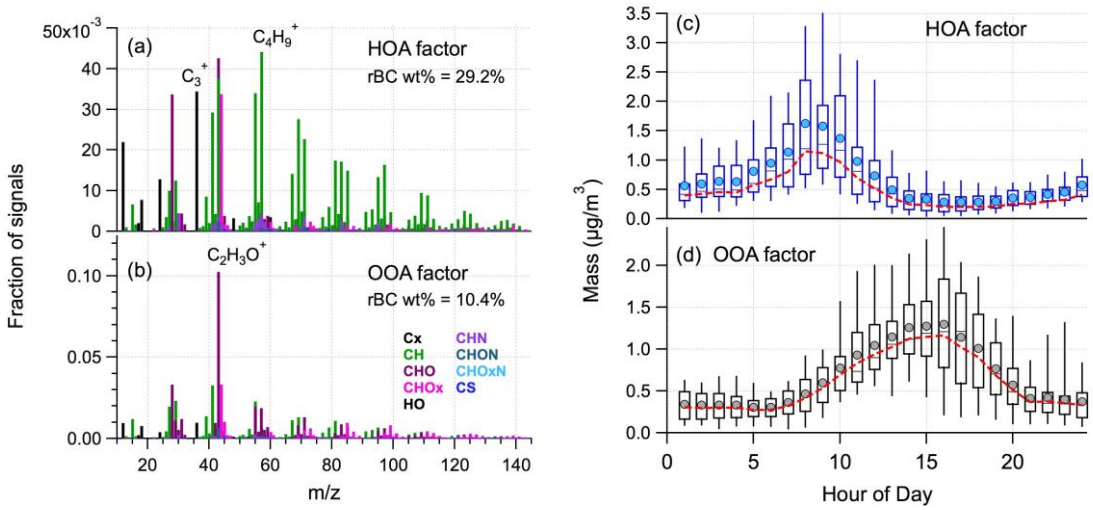

Figure 8-8. Mass spectra (a-b) and diurnal cycles (c-d) of two-factor solution from SP-AMS data within the hot period. (Box plots: 5th, 25th, 50th, 75th and 95th percentile, Filled circles: mean values for organic + C_5^+ fragments, Red dashed lines: mean values for organic alone.

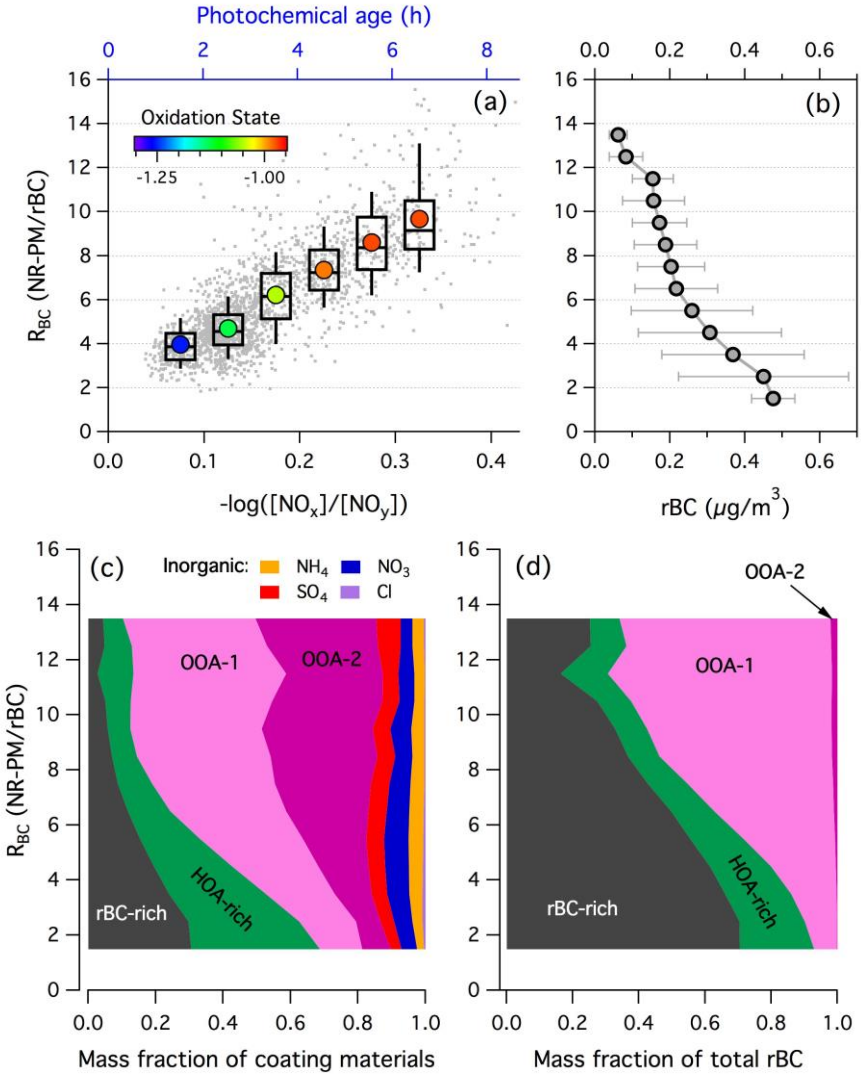

Figure 8-9. Coating thickness (R_{BC}) as a function of (a) photochemical age, (b) rBC mass loadings, (c) chemical compositions of coating, and (d) rBC mass fractions contributed by individual PMF factors within the hot period

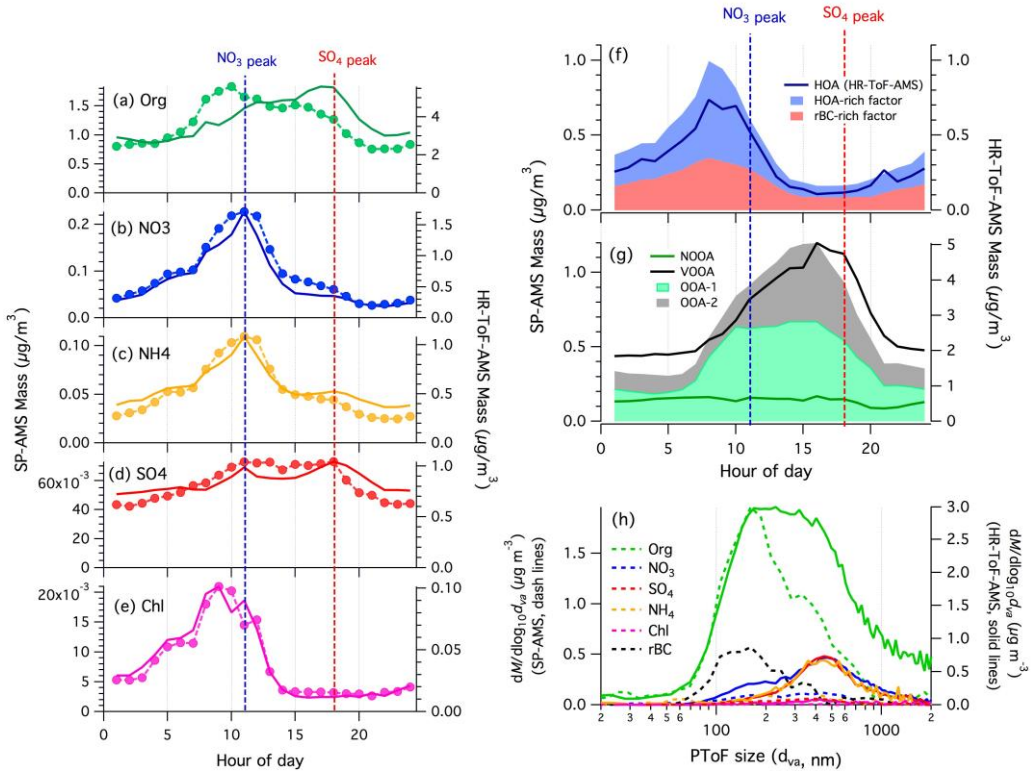

Figure 8-10. (a-e) Diurnal cycles of NR-PM and NR-PM_{rBC} measured by HR-ToF-AMS (solid lines) and SP-AMS (dashed lines with circles), respectively. (f-g) Diurnal cycles of PMF factors from HR-ToF-AMS (solid lines) and SP-AMS (filled areas, organics components only for PMF factors) data. (h) PToF size distribution of rBC, NR-PM (dashed lines) and NR-PM_{rBC} (solid lines).

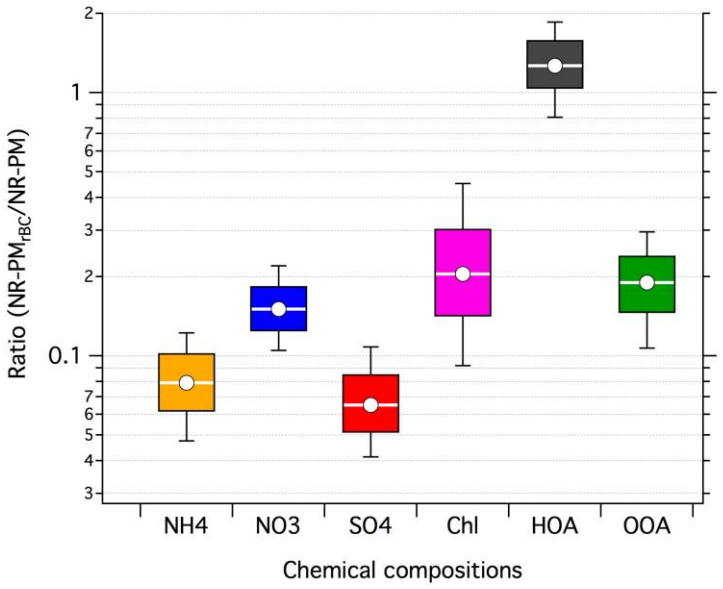

Figure 8-11. NR-PM_{rBC}-to-NR-PM ratios for individual aerosol components and PMF factors (Box plots: 10th, 25th, 50th, 75th and 90th percentile, White circles: mean values, OOA = ([OOA-1] + [OOA-2]) / ([NOOA] + [VOOA]) = SOA_{rBC} / SOA_{NR-PM} and HOA = ([HOA-rich] + [rBC-rich]) / [HOA]). Only organics components for PMF factors measured by SP-AMS were used in this calculation. HOA loadings less than 0.15 μg/m^3 from HR-ToF-AMS were removed for the calculation.

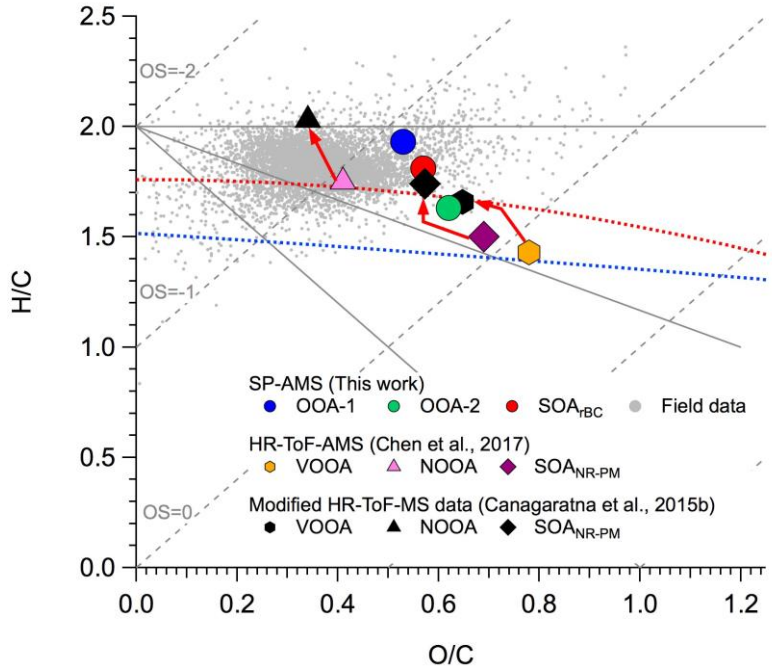

Figure 8-12. Van Krevelen diagram: Red arrows indicate the changes in the elemental ratios of VOOA, NOOA factors and SOA_{NR-PM} measured by the HR-ToF-AMS after applying the correction factors for more oxygenated organic species proposed by Canagaratna et al. (2015b).

9 Optical Properties of Wintertime Aerosols from Residential Wood Burning in Fresno, CA: Results from DISCOVER-AQ 2013

9.1 Abstract

The optical properties, composition and sources of the wintertime aerosols in the San Joaquin Valley (SJV) were characterized through measurements made in Fresno, CA during the 2013 DISCOVER-AQ campaign. $PM_{2.5}$ extinction and absorption coefficients were measured at 405, 532 and 870 nm along with refractory black carbon (rBC) size distributions and concentrations. BC absorption enhancements (E_{abs}) were measured using two methods, a thermodenuder and mass absorption coefficient method, which agreed well. Relatively large diurnal variations in the E_{abs} at 405 nm were observed, likely reflecting substantial nighttime emissions of wood burning organic aerosols (OA) from local residential heating. Comparably small diurnal variations and absolute nighttime values of E_{abs} were observed at the other wavelengths, suggesting limited lensing-driven enhancement. Positive matrix factorization analysis of OA mass spectra from an aerosol mass spectrometer resolved two types of biomass burning OA, which appeared to have different chemical composition and absorptivity. Brown carbon (BrC) absorption was estimated to contribute up to 30% to the total absorption at 405 nm at night but was negligible (<10%) during the day. Quantitative understanding of retrieved BrC optical properties could be improved with more explicit knowledge of the BC mixing state and the distribution of coating thicknesses.

9.2 Introduction

Recent studies in the past decade or so have suggested a substantial positive radiative forcing (i.e. global warming effect) of atmospheric black carbon (BC).[1-3] The most recent scientific assessment estimated BC to be the second largest anthropogenic warming agent, with its direct radiative forcing (DRF) estimated to be 0.71 ± 0.17 W m^{-2}.[1] However, uncertainties in the forcing remain due to limitations in knowledge of the emission, spatial distribution, [2] mixing state,[3] and contribution from non-BC species to observed absorption.[1]

The observable light absorption coefficient for BC, $b_{abs,BC}$, depends on particle mixing state.[4-5] The magnitude of $b_{abs,BC}$ can be enhanced by internal mixing of non-absorbing "coating" materials with BC (sometimes colloquially referred to as the "lensing" effect and here referred to as the mixing effect).[4,6] BC is often co-emitted and mixed with organic compounds, some of which absorb and in which case are collectively referred to as brown carbon (BrC).[7] The specific properties of BrC vary with source and production mechanism,[8-12] yet remain incompletely characterized. The quantification and attribution of the total observable b_{abs} to these different effects and components is critical for accurately estimating the absorption aerosol optical depth (AAOD) and direct radiative forcing (DRF) caused by each aerosol component.

Laboratory studies[13-15] and theoretical calculations[5,16] suggest substantial mixing-related absorption enhancement is possible for typical atmospheric particles, leading some to apply an *ad hoc* factor of 1.5 upward scaling of simulated BC AAOD in models.[1] This scaling, together with the inclusion of BrC, has been shown to reduce, although not eliminate, the model low bias compared to remotely sensed AAOD, a primary constraint for BC DRF.[17] However, recent observations of the absorption enhancement (E_{abs}) for particles undergoing photochemical

aging near urban centers indicated that E_{abs} from mixing can be smaller than expected, even for thickly coated BC particles,[18] although the extent to which this is true around the world and in all environments remains unclear.[19-21] Additionally, the separation of the BC AAOD from the total observed AAOD is subject to considerable uncertainty.[1] The lack of constraints on the apportioned b_{abs} components in both modeled and observed AAOD contributes substantially to uncertainty in the BC DRF (along with emissions and vertical distributions).

One approach to apportion b_{abs} into contributions from BC ($b_{abs,BC}$), mixing ($b_{abs,mixing}$) and BrC ($b_{abs,BrC}$) utilizes the different wavelength (λ) dependencies (i.e., absorption Angström exponents, AAE) of BC and BrC. $b_{abs,BC}$ is typically assumed to vary inversely with λ (AAE of ~ 1), whereas $b_{abs,BrC}$ typically exhibits a stronger λ dependence (AAE > 1) and is assumed to absorb negligibly at longer wavelengths (λ > ~600 nm).[9,22-23] The AAE method is the basis for apportioning remotely sensed AAOD to different absorbing components.[24-25] However, the method cannot characterize the influence of mixing and is confounded by knowledge of the exact AAE for BC,[26] making it only a robust estimation under limited circumstances, i.e. AAE > 1.6.[16] A second approach compares measured mass absorption coefficients (MAC) for atmospheric BC to a reference state (e.g., fresh emitted nascent BC)[27]. The use of absolute MAC values requires accurate measurements of both BC mass concentrations and absorption coefficients, as well as consistency of the operational definitions among the measurements. Unrealistically low or high MAC values have often been found, possibly as a result of inaccurate or inconsistent measurements. A third approach characterizes b_{abs} before and after *in situ* heating in a thermodenuder (TD) to remove BC coatings and externally-mixed BrC.[18,21,28-30] The TD method is independent of instrument calibration or inter-comparison, but complete removal of the coating materials is critical and may not always occur. Ideally, combinations of the above approaches can be used to overcome the complications associated with any individual methodology.

The San Joaquin Valley (SJV) in central California has suffered from severe air pollution problems for decades.[31-32] Previous studies focused on this region have shown that primary emissions, such as vehicles, cooking, residential wood combustion, and agricultural activities,[33-37] are the major sources of particulate matter (PM) during winter. However, few studies have characterized optical properties of the wintertime aerosol. In this work, highly time resolved *in situ* measurements of $PM_{2.5}$ light extinction and absorption made in conjunction with a broad suite of aerosol chemical composition measurements during the DISCOVER-AQ 2013 campaign in Fresno, CA are reported on. The particularly cold and dry winter of 2013 led to high PM concentrations,[38] with major contributions from residential wood burning emissions. The diurnal and episodic variability of the optical properties and their connection with the chemical composition and emissions sources are quantitatively examined to investigate the sources and climate effect of the light-absorbing particles. The key optical properties of residential burning aerosols are calculated and implications for aerosol DRF and emissions control in the SJV and the state of California are discussed.

9.3 Experimental Method

9.3.1 Sampling

During the NASA DISCOVER-AQ 2013 California campaign, a suite of ground

measurements of $PM_{2.5}$ chemical composition and optical properties were carried out from January 13 to February 11, 2013 at the California Air Resources Board (CARB) Fresno-Garland air monitoring facility (36.7854°, -119.7732°). The site is surrounded by residential and commercial areas and is approximately 1500 m to the east of Yosemite FWY-41. Particles were sampled into the building from 1.5 m above the rooftop through 4 m of 1/2 in. diameter stainless steel tubing. The air stream passed through a $PM_{2.5}$ cyclone (URG) at 16.7 lpm and distributed to the various instruments through 1/4 in. or 3/8 in. tubing.

9.3.2 Instrumentation

Table 9-1 summarizes the instruments and measurements made at the Fresno ground site. $PM_{2.5}$ light extinction (b_{ext}) and absorption (b_{abs}) coefficients at 405 and 532 nm were measured for dried particles (relative humidity < 30%) with the UC Davis cavity-ringdown photoacoustic spectrometer (CRD-PAS).[39-41] The PAS was calibrated approximately every five days using gas-phase O_3 by referencing the observed photoacoustic signal to the corresponding b_{ext} measured by the CRD.[39] $PM_{2.5}$ b_{ext} and b_{abs} values were also measured at 870 nm with a PhotoAcoustic eXtinctiometer (PAX; DMT, Boulder, CO, USA). The PAX was calibrated prior to and after the campaign using atomized Aquadag and PSL particles for the absorption and scattering channel, respectively. Instrument zeros were determined using filtered ambient air for 3 min of every 30 min. The 1σ standard deviations in b_{abs} for filtered air at the 2 s sampling time were measured to be approximately 0.8 Mm^{-1} (405 nm), 0.4 Mm^{-1} (532 nm), and < 1 Mm^{-1} (870 nm). The uncertainties in b_{ext} were estimated to be 5% (405 nm, 532 nm and 870 nm) and in b_{abs} were 10% at 532 nm and 20% at 405 nm and 870 nm.

Refractory black carbon (rBC) mass concentrations and size distribution measurements were made with a DMT Single Particle Soot Photometer (SP2),[42] which was calibrated with atomized and size-selected Fullerene soot particles before and after the campaign. Fullerene soot has been shown to provide a similar response in the SP2 per unit mass as diesel and biomass burning derived rBC.[43] The masses of individual rBC particles were measured from which rBC volume equivalent diameters (d_{ve}) were calculated assuming this mass is compacted to a spherical particle with a density of 1.8 g cm^{-3}.[44] The observed 5-min average rBC volume-weighted size distributions (from 100 nm ≤ d_{ve} ≤ 300 nm) were individually fit using a bimodal lognormal distribution. The fits were extrapolated to 20-1000 nm to estimate the "missing" rBC mass outside the measurement range. The overall shape of the rBC size distribution and mode diameter varied throughout the day, indicating variations in the dominant rBC source (vehicles versus wood combustion; **Figure 9-1**a). Consequently, a unique "missing" mass correction was applied for each 5 min period, as opposed to a single campaign-average value. Here, we assume that the "missing" portion follows the same bimodal lognormal distributions as those directly observed. The SP2 rBC concentrations were compared with daily-average elemental carbon (EC) measurements made every 3rd day by CARB. The measured [rBC] was ~30% lower than the [EC], which could indicate a systematic bias in the SP2 (due, perhaps, to deviations in the assumed shape in the missing-mass regions or calibration errors) or in the EC measurements (**Figure 9-2**). The 1σ standard deviation in the rBC mass, characterized during a period when the rBC concentration was relatively stable, is 0.06 μg m^{-3}. The uncertainty in rBC mass is estimated to be at least 50%, considering the uncertainties associated with the instrument operation, external calibration, and the lognormal fits. Further discussion is

provided in Section 9.3.

The mass concentrations of submicron (PM_1) non-refractory (NR) inorganic (NH_4^+, SO_4^{2-}, NO_3^-, Cl^-) and organic aerosols (OA) were determined with an Aerodyne High Resolution Time-of-Flight Aerosol Mass Spectrometer (HR-ToF-AMS).[45] Positive Matrix Factorization (PMF) analysis was performed on the OA mass spectral matrix[46] and six OA components were resolved: two types of biomass burning OA (BBOA-1 and BBOA-2), hydrocarbon-like OA (HOA), semi-volatile oxygenated OA (SV-OOA), low volatility oxygenated OA (LV-OOA), cooking OA (COA). The sum of the two BBOA factors will be referred to as BBOA. *Young et al.*[38] provide detailed information about the HR-ToF-AMS operation and data analysis. Hourly meteorological data (e.g., ambient temperature, relative humidity) and trace gases (e.g., NO_x, CO, SO_2) were routinely measured at the CARB Fresno-Garland monitoring site.

Particle size distributions over the diameter range of 16-685 nm mobility diameter (d_m) were measured with a Scanning Mobility Particle Sizer (SMPS; TSI, Inc.). Particle size distributions from 0.8-2.5 μm aerodynamic diameter (d_a) were determined with an Aerodynamic Particle Sizer (APS; TSI, Inc.). A merged ambient particle size distribution (**Figure 9-3**) was determined from the SMPS and APS distributions after adjusting the APS d_a values to mobility-equivalent values (d_m) using time-dependent particle density values and slip correction factor. The particle density was estimated by comparison of the PM_1 volume concentrations calculated from the size distribution and the AMS-measured bulk PM_1 mass concentrations.

9.3.3 Thermodenuder

The CRD-PAS, PAX, SP2 and SMPS alternatively sampled either ambient particles or particles that passed through a thermodenuder on an automated 5 min cycle. The TD was a 1 in. OD, 36 in. long stainless steel tube with the first 18 in. heated to 175 °C and the second 18 in. to 275 °C. The final 12 in. contained an activated charcoal cloth held around the inner circumference with rolled stainless steel mesh. The residence time in the dual-heating stage of the TD was ~7 s at room temperature. The two-stage heating was utilized to help minimize charring of the sample particles. Ambient (bypass) sampling was done through an unheated stainless steel tube of the same dimensions as the TD. All TD data were corrected for particle losses relative to the bypass using a transmission factor of 0.88, determined from measurements of size-selected Fullerene soot particles.

9.3.4 Absorption Enhancement

Two independent methods were used to characterize and quantify the absorption enhancement (E_{abs}) that results from the (time-varying) combination of internal mixing of rBC particles and BrC absorption. In the first (the TD method), E_{abs} is the ratio between ambient particle ($b_{abs,ambient}$) and TD particle ($b_{abs,TD}$) absorption:[18,21]

$$E_{abs,TD} = \frac{b_{abs,ambient}}{b_{abs,TD}} \quad (1)$$

Heating in the TD induces evaporation of non-refractory PM and leaves behind, ideally, pure rBC particles.

In the second method, E_{abs} was determined from measurements of the mass absorption coefficient (MAC), defined as $MAC = b_{abs,ambient}/m_{rBC}$, where m_{rBC} is the rBC mass

concentration. $E_{abs,MAC}$ can be estimated by normalizing the observed *MAC* by some reference *MAC* that is characteristic of pure rBC, i.e. $E_{abs,MAC} = MAC_{obs}/MAC_{ref}$. The accuracy of the MAC method to determine $E_{abs,MAC}$ is limited by the accuracy of the b_{abs} and m_{rBC} and by knowledge of MAC_{ref}. For this analysis, wavelength-specific MAC_{ref} values are estimated by forcing good agreement between $E_{abs,MAC}$ and the daily minimum in $E_{abs,TD}$ (see Sect. 3.2 and **Figure 9-4**b). (Alternatively, MAC_{ref} could be taken from the literature. However, as we are primarily interested in variations in the *MAC* and since the m_{rBC} are somewhat uncertain, we have adopted this alternative approach.) This definition allows for direct comparison of the temporal variation in E_{abs} between the two methods and makes the derived $E_{abs,MAC}$ values, in particular, their temporal variations, dependent upon the instrument precision, rather than accuracy (further discussed in Sect. 3.2).

9.4 Results and discussion

9.4.1 Overview of DISCOVER-AQ Fresno Measurements.

Figure 9-5 provides an overview of meteorological conditions (temperature and relative humidity (RH)) and of aerosol optical properties and chemical composition observed during the campaign. The average NR-PM_1 mass concentration was more than two times higher (26.4 $\mu g\ m^{-3}$ vs. 11.9 $\mu g\ m^{-3}$) during DISCOVER-AQ than during a previous study in Fresno in winter 2010.[37] The average OA concentration in 2013 was ~1.5 times higher (11.9 $\mu g\ m^{-3}$ vs. 7.9 $\mu g\ m^{-3}$), including a ~3 times higher average BBOA concentration (3.6 $\mu g\ m^{-3}$ vs. 1.24 $\mu g\ m^{-3}$). Two severe air pollution episodes (1/14-1/23 and 1/29-2/5) having $PM_{2.5}$ concentrations exceeding the National Ambient Air Quality Standards (NAAQS, 24-hr average of 35 $\mu g\ m^{-3}$) occurred. These two episodes were separated by a relatively clean period (1/24-1/27) that was identified as being marine influenced with enhanced particulate Cl^- and SO_4^{2-} concentrations.[38] The mass extinction coefficient (MEC), which is the ratio between b_{ext} and [PM_1], was slightly larger during the clean period than the polluted periods (**Figure 9-6**). This is consistent with an increased contribution of coarse-mode particles during the clean period compared to the pollution episodes, when the majority of PM mass was in submicrometer particles ($D_p < 1\mu m$) (**Figure 9-7**).

There is a strong diurnal variation in most of the measured PM properties (**Figure 9-8**). The fraction of BBOA in total PM_1 mass is highest at night, when the temperatures are lowest (T_{amb} often below 0°C), while the fraction of secondary OA components (SV-OOA and LV-OOA) was highest during the daytime (T_{amb} ~ 10-20°C). This leads to a negative correlation between T_{amb} and the ratio of BBOA:OA throughout the study (**Figure 9-9**), which is relatively insensitive to meteorological conditions (i.e. no major shift in the correlation was observed for polluted vs. clean periods). This strongly suggests that the greater contribution of BBOA during the cold winter of 2013 (relative to 2010)[37] is driven primarily by enhanced emissions from residential wood burning for domestic heating.

The campaign average dry $PM_{2.5}$ b_{ext} and b_{abs} at 532 nm were 130.8 and 13.5 Mm^{-1}, respectively, corresponding to a single scatter albedo (*SSA*) of 0.90. $PM_{2.5}$ $b_{ext,532nm}$ was well correlated with the PM_1 mass concentrations ($r^2 = 0.86$) (**Figure 9-6**), with an average MEC of 3.76 m^2g^{-1}. The b_{abs} were highly correlated with rBC mass concentration (405 nm: $r^2 = 0.95$; 532 nm: $r^2 = 0.95$; 870 nm: $r^2 = 0.97$), although rBC only accounts for < 5% of total PM_1 mass.

The b_{abs}, *SSA* and, to a lesser degree, b_{ext} of $PM_{2.5}$ vary diurnally (**Figure 9-8**a). During the day, $b_{abs,532nm}$ was strongly influenced by vehicle emissions, indicated from the peak during morning rush hour that coincides with the peak in HOA (**Figure 9-8**b). At night, $b_{abs,532nm}$ is nearly 5 times higher than daytime while $b_{ext,532nm}$ increases by only a factor of 1.7, leading to a lower nighttime aerosol SSA. The BBOA concentration is also enhanced at night, by a factor of ~5. The clear diurnal variability in chemical composition, driven by variations in the dominating aerosol sources, allows for assessment of the optical properties of aerosol components from different sources.

9.4.2 Absorption Enhancement

The observed wavelength-dependent b_{abs} and E_{abs} include contributions from rBC, internal mixing of rBC with other NR materials, and absorption by BrC. The campaign average $E_{abs,TD}$ at 405, 532 nm and 870 nm were 1.27±0.17, 1.18±0.06 and 1.21±0.09, respectively. The observed E_{abs} exhibit wavelength-specific diurnal dependencies (**Figure 9-4**). At 405 nm and 532 nm, the E_{abs} during nighttime are larger than during daytime, especially at 405 nm, whereas at 870 nm, the E_{abs} is slightly larger during daytime. The $E_{abs,TD}$ and $E_{abs,MAC}$ are relatively similar in magnitude, although the $E_{abs,MAC}$ exhibit a somewhat larger diurnal variation than do the $E_{abs,TD}$. (Recall that MAC_{ref} has been defined here to ensure good agreement with the daily minimum $E_{abs,TD}$.) The similar magnitudes and distributions of the observed E_{abs} at 532 and 870 nm suggest that 1) non-BC particles do not absorb significantly at λ > ~500 nm, and 2) internal mixing of BC with other NR-PM contributes only moderately (~10-20%) to the enhancement of the BC absorption. The limited enhancement observed here is likely due to either limited amounts of coating material existing on the BC or the particles having an internal morphology that differs from the ideal core-shell configuration.[18] The relatively narrow E_{abs} distributions and small day-night differences at 532 nm and 870 nm suggest that the mean particle mixing (i.e. coating) state, or at least the influence of such coatings on BC absorption, does not strongly differ between the major BC sources (i.e. vehicle emissions vs. fresh residential wood combustion). These observations of relatively small E_{abs} due to internal mixing are similar to previous measurements made in the summertime in other urban environments in California,[18] where relatively thickly-coated particles were observed; in Nagoya, Japan,[30] where the particles tended to be relatively thinly coated; and in Toronto, Canada,[20] where local, wildfire-impacted and transboundary (aged) particles were sampled. They are, however, lower than those reported for air masses dominated by freshly emitted particles from the Four Mile Canyon fire in Colorado ($E_{abs,532nm}$~1.4)[21] and for some air masses sampled in Detling, UK (near London).[19]

The comparatively larger average $E_{abs,405nm}$ during nighttime ($E_{abs,TD}$ ~ 1.4; $E_{abs,MAC}$ ~ 1.5) indicates a strong contribution of BrC to the observed $b_{abs,405nm}$, whereas the similarity of $E_{abs,405nm}$ to the other wavelengths and the relatively small values during the day suggests limited BrC contributions during the day (**Figure 9-4**). There is a good correlation between $E_{abs,405nm}$ and the BBOA-to-OA mass concentration ratio (BBOA:OA; **Figure 9-10**a), which together with the observed diurnal behavior clearly implicates nighttime residential wood burning is an important BrC source in this region. The decrease in $E_{abs,405nm}$ during daytime likely results from ventilation, vertical mixing, or particle evaporation.

The two BBOA factors, BBOA-1 and BBOA-2, were identified from the PMF analysis in part based on enhanced signals at ion $C_2H_4O_2^+$ (m/z 60) and $C_3H_5O_2^+$ (m/z 73) in their mass spectra[47-48] (detailed mass spectra information is presented by *Young et al.*[38]). The relative contributions of BBOA-1 and BBOA-2 varied throughout the study, especially between the two PM episodes (**Figure 9-11**a). BBOA-2 has a more pronounced day/night variation compared to BBOA-1 (**Figure 9-11**b). The $E_{abs,405nm}$ exhibited strong, approximately linear relationship with the BBOA-2:OA ratio, but had almost no dependence on the BBOA-1: OA ratio (**Figure 9-10**b and **Figure 9-10**c). This suggests that BBOA-2 may be more absorbing than BBOA-1. BBOA-2 has a higher O:C ratio and a smaller f_{44} : f_{60} ratio,[38] suggesting that the different absorptivity for BBOA-1 and BBOA-2 may be linked to the difference in their chemical compositions. (f_{44} and f_{60} are the fraction of the signal at *m/z* 44 and 60 in the AMS OA mass spectra, respectively). Several laboratory and ambient studies have observed variability in the OA composition and absorptivity under different burning conditions, e.g., combustion temperature, burning load, and fuel type.[21,28,49-50] The seemingly more absorbing BBOA-2 is the dominant BBOA type during the second PM episode when the ambient temperature was higher (**Figure 9-5**), possibly indicating some difference in the typical burn conditions (e.g., burning load/temperature), which can affect BBOA/BC emission ratio.[51]

The $E_{abs,MAC}$ and $E_{abs,TD}$ exhibited similar diurnal peak-to-trough amplitude differences. However, the absolute nighttime average $E_{abs,MAC}$ are slightly larger, and the overall distributions are somewhat wider at all three wavelengths. These relatively minor differences between $E_{abs,TD}$ and $E_{abs,MAC}$ could result from biases or errors in either of the methods. Biases in $E_{abs,TD}$ tend to be negative (i.e. depress E_{abs}) and can potentially result from i) residual BC "coatings" that did not fully evaporate in the TD, ii) residual BrC that did not fully evaporate in the TD, or iii) "browning" of residual OA in the TD. Biases or errors in $E_{abs,MAC}$ result from time-varying biases or errors in the b_{abs} or m_{rBC} measurements, with an underestimate of m_{rBC} leading to an overestimate of MAC, or vice versa. We posit that the biases or errors in the m_{rBC} determined by the SP2 is more likely responsible for the difference between methods in this study because the magnitude of the discrepancy between nighttime $E_{abs,TD}$ and $E_{abs,MAC}$ is similar across all three wavelengths (~10%). The SP2 measurements require correction for rBC outside the detection range and, although this "missing" mass is approximately accounted for through bimodal fitting of SP2 size distributions with high time resolution, the robustness of this correction may vary with time/source. Consider that the MAC_{TD} at all three wavelengths during the daytime are slightly smaller than those during morning and evening rush hours and those around midnight, when the BBOA and rBC concentrations peak (**Figure 9-12**). This could indicate that smaller rBC particles (d_{ve} < 100 nm) from fresh fossil fuel combustion (vehicles) are not fully accounted for by bimodal lognormal fitting.[52] Similarly, fresh rBC particles derived from residential wood combustion may also be underestimated, leading to an overestimate of both MAC_{amb} and MAC_{TD}. Regardless of the exact reason for the small quantitative differences between the methods, the overall general behavior of E_{abs} and interpretation of the observations is method independent.

9.4.3 Optical properties of brown carbon aerosols

Knowledge of the imaginary part (*k*) of the complex refractive index for OA is needed to allow simulation of the climate impacts of absorbing OA particles.[7] Here, time-dependent *k*

values for the total OA (k_{OA}) are determined at 405 nm by performing an optical closure analysis between observed and calculated values of E_{abs} (as opposed to absolute b_{abs} values).[21] The calculations are constrained by the observations of rBC-only (from the SP2) and PM_1 (from the SMPS) size distributions (**Figure 9-13**) and the wavelength-dependent aerosol optical properties. The base case considered uses Mie theory assuming spherical particles with core-shell morphologies.

Information regarding the rBC coating state is required to fully separate contributions from internal mixing and BrC absorption and to elucidate the relationship between the mixing effect and coating amount. Since no direct coating state measurement is available from this study, time-dependent rBC effective coating thicknesses (or effective coating-to-core radius ratios, r_{coat}/r_{core}) are estimated from the $E_{abs,532nm}$ measurements via optical closure under the assumption that non-BC species do not absorb significantly at 532 nm and, thus, that $E_{abs,532nm}$ arises only from the mixing effect.[21] If BrC influences $E_{abs,532nm}$, then this method will overestimate the effective coating thickness and consequently the magnitude of the mixing effect at 405 nm, which will in turn lead to an underestimate of the BrC absorptivity. (The derived effective coating thicknesses may substantially underestimate the actual mean coating amount.[18])

Additional base case assumptions are as follows. The r_{coat}/r_{core} is assumed core-size independent, with effective diameters for the coated rBC particles determined by multiplying the rBC core diameters by r_{coat}/r_{core}. The size distributions for externally mixed PM_1 are determined by subtracting the resulting coated rBC size distributions from the observed total PM_1 size distributions. The complex RI for rBC is assumed to be $1.88 + 0.8i$.[18] All NR-PM_1 components, including OA, are assumed to be internally well mixed with a real RI of 1.50, and all non-OA species are non-absorbing. The k values for the NR-PM_1 material in both BC-containing and BC-free particles are determined from volume mixing rules. Thus, $k_{NR\text{-}PM1} = f_{OA} \cdot k_{OA}$, where f_{OA} is the OA volume fraction. The f_{OA} values are determined from the observed species-specific NR-PM_1 mass concentrations using the densities shown in **Table 9-2**. The time-dependent k_{OA} values are retrieved by forcing optical closure (to within 1%) between the observed and calculated $E_{abs,405nm}$ values. The overall retrieval process is illustrated in **Figure 9-14**.

In addition to the above base case, a variety of alternate cases are considered to assess the sensitivity of the derived k_{OA} values to the model assumptions and measurement uncertainties, with details provided in Appendix A. In brief, the sensitivity to morphology is examined by assuming the BC core is an aggregate of individual (non-interacting) spherules (either 40 or 70 nm) with Rayleigh-Debye-Gans (RDG) theory.[44] The sensitivity to the assumed RI is examined by considering alternate values for BC or for the NR-PM_1 components. The sensitivity to the distribution of the coating material with respect to the BC core size is tested by allowing for size-dependent variation in r_{coat}/r_{core}. The sensitivity to measurement uncertainties in m_{rBC}, f_{OA} and $E_{abs,532nm}$ is examined by perturbing these up or down by constant percentages. Each case is treated independently, and thus cross-sensitivities are not assessed.

The base-case campaign average k_{OA} at 405 nm (from Mie) was 0.0046 ± 0.0055 (1σ), with a pronounced diurnal profile and an average nighttime value of 0.008 (**Figure 9-15**a). The BBOA fraction of OA averaged ~22% at night, corresponding to a campaign-average k_{BBOA} of 0.037 at 405 nm under the assumption that BBOA is the only absorbing non-BC species. The

retrieved nighttime k_{OA} values exhibit the largest sensitivity to uncertainties in m_{rBC}, f_{OA} and $E_{abs,532nm}$, with comparably small sensitivity to assumptions associated with particle morphology, RI or the coating distribution (**Table 9-4** and **Figure 9-16** and **Figure 9-17**). For example, a ±50% change in m_{rBC} corresponds to a ~±37% change in the nighttime k_{OA}, while the alternate morphology or coating distribution cases lead to changes of only a few percent.

Values for the OA-specific *MAC*, referred to as MAC_{OA}, are calculated as the ratio between the calculated OA-specific absorption (sum of internally and externally mixed OA) and the observed OA concentration. The nighttime MAC_{OA} (20:00-6:00) exhibits a reasonably linear relationship with the BBOA:OA ratio (**Figure 9-15**b). Extrapolation of a Deming fit of MAC_{OA} versus BBOA:OA to BBOA:OA = 1 can provide an estimate of the BBOA-specific *MAC* (MAC_{BBOA}) at 405 nm. The extrapolated base-case MAC_{BBOA} = 0.60±0.02 m^2 g^{-1} if the fit is constrained to go through zero and is 0.53±0.01 m^2 g^{-1} if it is unconstrained with an intercept at BBOA:OA = 0 of 0.10 m^2 g^{-1}. The estimated mean MAC_{BBOA} is an order of magnitude smaller than MAC_{BC}. The derived MAC_{BBOA} values exhibit similar sensitivities to the model assumptions as do the k_{OA} values, with, for example, a ±50% change in m_{rBC} yielding a ~±34% change in the MAC_{BBOA}. The MAC_{BBOA} can alternatively be estimated from the ratio between calculated OA absorption and [BBOA]; the mean from this method is similar to the constrained fit (**Figure 9-15**c). The non-zero intercept from the unconstrained fit suggests the non-BBOA organic components (HOA, COA and OOA) are also slightly absorbing, although we suggest that it is more likely that this is simply a limitation of the data set and fitting, and that the *MAC* for these other OA components is close to zero.

The k_{BBOA} and MAC_{BBOA} determined here are compared with literature results from various laboratory and ambient studies in **Table 9-3**.

. The reported absorption characteristics of biomass burning aerosols vary greatly, likely due to differences between measurement techniques, burning conditions or extent of atmospheric processing. The k_{BBOA} and MAC_{BBOA} determined from this study are likely lower-limit values, since some fraction of BBOA may be non-absorbing (**Figure 9-10**). However, this just illustrates the difficulty in clearly defining "brown" carbon, for example whether it should be considered as the total OA or just some fraction of the total OA (or even some sub-fraction of a given OA type).

The contributions from rBC absorption, absorption due to internal mixing (lensing), and direct absorption by BrC to the total observed $b_{abs,405nm}$ were on average 67.3%, 13.9% and 18.8% and at night were 56.3%, 14.2% and 29.5%, respectively (**Figure 9-18**). These values depend on the relative contribution from biomass burning versus fossil fuel combustion, which vary with time of day and between days. Clearly, the fractional contribution of BrC to light absorption in even a single region is highly variable, which underscores the importance of accurate in-situ characterizations of BrC optical properties in multiple locations. Future studies would additionally benefit from direct measurement of the BC coating state and from comparison between optical measurements made using multiple methodologies. Although the BrC contribution was substantial at nighttime, it was overall negligible during the day, suggesting that BrC may not drive surface radiative forcing in Fresno in winter, although the export of this BrC throughout the wider SJV may be of regional importance. However, primary BrC aerosols from biomass burning sources often contain PAHs, nitrogen-containing aromatic

compounds[53-54] and humic-like substances (HULIS),[55-56] which can exert negative effects on human health.[57-58]

9.5 Acknowledgement

We thank the CARB Fresno-Garland monitoring site for providing space and logistical help during the course of the study, and NASA for travel support and coordination of the larger DISCOVER-AQ study. Additional support was provided by the California Air Resources Board, Research Division, under Contract No. 13-330. CDC and XZ thank Gavin McMeeking at DMT for the PAX instrument and Haf Jonsson for facilitating the deployment of the SP2. QZ, HK and CP thank NASA and the California Agricultural Experiment Station (Project CA-D-ETX-2102-H) for supporting the acquisition and analysis of the AMS data. This work has not been formally reviewed by the funding agencies and represents the views of the authors.

9.6 Appendix A: Sensitivity tests of the optical closure analysis:

In addition to the base case, a variety of alternate cases are considered to assess the sensitivity of the derived k_{OA} values to the model assumptions and measurement uncertainties. In one case, the model assumption on the spherical-particle shape has been evaluated by performing closure calculations using Rayleigh-Debye-Gans (RDG) theory, since Mie theory is known to underestimate the absorption of non-spherical BC particles.[1] With RDG, the BC core is assumed to be an aggregate of individual (non-interacting) spherules. The total absorption by each BC aggregate is the sum of the absorption by the individual spherules.[2] Here, spherule sizes ($D_{p,sph}$) of 40 and 70 nm have been considered. For the coated particles, we similarly assume that the total absorption is the sum over individual coated spherules and that the coating thickness is the same for each spherule.[3]

In another set of sensitivity tests, in calculating the effective coating thicknesses, instead of assuming a constant refractory black carbon (rBC) coating-to-core radius ratio (r_{coat}/r_{core}) across all particle sizes, the distribution of the non-refractory (NR) coating materials is assumed to follow a diffusion-controlled growth law:[4]

$$\frac{dD_p}{dt} = \frac{1}{D_p}$$

where D_p is the rBC volume equivalent diameter (d_{ve}). A previous laboratory study[5] on the evolution of rBC coating formation found good agreement between the modeled and measured coating thickness diameters when diffusion controlled growth was assumed. Like the base case (constant r_{coat}/r_{core}), the time-varying, size-dependent distributions of coating thicknesses across the rBC core distribution were obtained by constraining the calculated $E_{abs,532nm}$ due to internal mixing to the observed $E_{abs,532nm}$, i.e. via optical closure.

The influence of the assumed rBC refractive index was tested by comparing rBC absorption coefficients ($b_{asb,BC}$) calculated using spherical-particle Mie theory for five alternate RI values with those calculated from the base case value (1.88-0.8i). The five RI values used are provided in **Table 9-4** and are from *Bond and Bergstrom*.[1] Based on the slopes of the linear fits (**Figure 9-14**), the $b_{asb,BC}$ determined from all five alternate RI values agree with the base case $b_{asb,BC}$ to within 11%. The largest difference from the base case is obtained for the RI = 1.75-0.63i case. Since this case gives the largest deviation in the calculated $b_{abs,BC}$, the difference between the

retrieved k_{OA} value using this case (RI = 1.75-0.63i) versus the base case was assessed (Table 2, **Figure 9-17**).

The sensitivity of the retrieved k_{OA} to the assumed real component of the refractive index (n) of the non-BC components was assessed by using values of 1.45 and 1.55, compared to the base case value of 1.50.

Table 9-4 summarizes the uncertainties associated with measurements of rBC mass, m_{rBC}, volume fraction of organic aerosols, f_{OA}, and absorption enhancement, E_{abs}. In the sensitivity tests on the measurement uncertainties, the measured values of these input parameters were varied up and down by constant percentages (±30% and 50% for m_{rBC}, ±20% for f_{OA} and ±5% for E_{abs}).

9.7 References

1. Bond, T. C. et al. Bounding the role of black carbon in the climate system: A scientific assessment. *J Geophys. Res.* **2013**, *118*(11), 5380-5552; DOI 10.1002/jgrd.50171.

2. Ramanathan V.; Carmichael, G. Global and regional climate changes due to black carbon. *Nat. Geosci*. **2008**, 1, 221–227; DOI 10.1038/ngeo156.

3. Jacobson, M. Z. Global direct radiative forcing due to multicomponent anthropogenic and natural aerosols. *J. Geophys. Res*. **2001**, *106*, 1551–1568; DOI 10.1029/2000JD900514.

4. Fuller, K. A.; Malm, W. C.; Kreidenweis, S. M. Effects of mixing on extinction by carbonaceous particles. *J. Geophys. Res*. **1999**, *104*, 15941–15954; DOI 10.1029/1998JD100069.

5. Bond, T. C.; Habib, G.; Bergstrom, R. W. Limitations in the enhancement of visible light absorption due to mixing state. *J. Geophys. Res*. **2006**, *111*(D20), D20211; DOI 10.1029/2006JD007315.

6. Jacobson, M. Z. A physically based treatment of elemental carbon optics: Implications for global direct forcing of aerosols. *Geophys. Res. Lett.* **2000**, *27*, 217–220; DOI 10.1029/1999GL010968.

7. Andreae, M.; Gelencser, A. Black carbon or brown carbon? The nature of light absorbing carbonaceous aerosols. *Atmos. Chem. Phys*. **2006**, *6*, 3131-3148; DOI 10.5194/acp-6-3131-2006.

8. Barnard, J. C.; Volkamer, R.; Kassianov, E. I. Estimation of the mass absorption cross section of the organic carbon component of aerosols in the Mexico City Metropolitan Area. *Atmos. Chem. Phys.* **2009**, *8*, 6665–6679; DOI 10.5194/acp-8-6665-2008.

9. Kirchstetter, T. W.; Novakov, T.; Hobbs, P. V. Evidence that the spectral dependence of light absorption by aerosols is affected by organic carbon. *J. Geophys. Res*. **2004**, *109*(D21), D21208; DOI 10.1029/2004JD004999.

10. Updyke, K. M.; Nguyen, T. B.; Nizkorodov, S. A. Formation of brown carbon via reactions of ammonia with secondary organic aerosols from biogenic and anthropogenic precursors. *Atmos. Environ*. **2012**, *63*, 22-31; DOI 10.1016/j.atmosenv.2012.09.012.

11. Yang, M.; Howell, S. G.; Zhuang, J.; Huebert, B. J. Attribution of aerosol light absorption to black carbon, brown carbon, and dust in China - Interpretations of atmospheric measurements during EAST-AIRE. *Atmos. Chem. Phys*. **2009**, *9*, 2035-2050; DOI 10.5194/acp-9-2035-2009.

12. Zhang, X.; Lin, Y.-H.; Surratt, J. D.; Zotter, P.; Prévôt, A. H. S.; Weber, R. J. Light-absorbing soluble organic aerosol in Los Angeles and Atlanta: A contrast in secondary organic aerosol. *Geophys. Res. Lett.* **2011**, *38*, L21810; DOI 10.1029/2011GL049385.

13. Cross, E. S. et al. Soot particle studies-Instrument inter-comparison-Project overview. *Aerosol Sci. Technol*. **2010**, *44*, 592-611; DOI 10.1080/02786826.2010.482113.

14. Metcalf, A. R.; Loza, C. L.; Coggon, M. M.; Craven, J. S.; Jonsson, H. H.; Flagan, R. C.; Seinfeld, J. H. Secondary Organic Aerosol Coating Formation and Evaporation: Chamber Studies Using Black Carbon Seed Aerosol and the Single-Particle Soot Photometer. *Aerosol Sci. Technol*. **2013**, *47*(3), 326–347; DOI 10.1080/02786826.2012.750712.

15. Zhang, R.; Khalizov, A. F.; Pagels, J.; Zhang, D.; Xue, H.; McMurry, P. H. Variability in morphology, hygroscopicity, and optical properties of soot aerosols during atmospheric processing. *Proc. Natl. Acad. Sci.* **2008**, *105*, 10291-10296; DOI 10.1073/pnas.0804860105.

16. Lack, D. A.; Cappa, C. D. Impact of brown and clear carbon on light absorption enhancement, single scatter albedo and absorption wavelength dependence of black carbon. *Atmos. Chem. Phys.* **2010**, *10*(9), 4207-4220; DOI 10.5194/acp-10-4207-2010.

17. Wang, X.; Heald, C. L.; Ridley, D. A.; Schwarz, J. P.; Spackman, J. R.; Perring, A. E.; Coe, H.; Liu, D.; Clarke, A. D. Exploiting simultaneous observational constraints on mass and absorption to estimate the global direct radiative forcing of black carbon and brown carbon. *Atmos. Chem. Phys*. **2014**, *14*, 10989-11010; DOI 10.5194/acp-14-10989-2014.

18. Cappa, C. D. et al. Radiative absorption enhancements due to the mixing state of atmospheric black carbon. *Science* **2012**, *337*, 1078–1081; DOI 10.1126/science.1223447.

19. Liu, S.; Aiken, A. C.; Gorkowski, K.; Dubey, M. K.; Cappa, C. D.; WIlliams, L. R.; Herndon, S. C.; Massoli, P.; Fortner, E. C.; Chhabra, P. S.; Brooks, W. A.; Onasch, T. B.; Worsnop, D. R.; China, S.; Sharma, N.; Mazzoleni, C.; Xu, L.; Ng. N. L.; Liu, D.; Allan,J. D.; Lee, J. D.; Fleming, Z. L.; Mohr, C.; Zotter, P.; Szidat, S.; Prevot, A. S. H. Enhanced light absorption by mixed source black and brown carbon particles in UK winter. *Nat. Commun.* **2015**, *6*:8435; DOI:10.1038/ncomms9435.

20. Healy, R. M.; Wang, J. M.; Jeong, C.-H.; Lee, A. K. Y.; Willis, M. D.; Jaroudi, E.; Zimmerman, N.; Hilker, N.; Murphy, M.; Eckhardt, S.; Stohl, A.; Abbatt, J. P. D.; Wenger, J. C.; Evans, G. J. Light-absorbing properties of ambient black carbon and brown carbon from fossil fuel and biomass burning sources. *J. Geophys. Res*. **2015**, *120*, 6619-6633; DOI 10.1002/2015JD023382.

21. Lack, D. A.; Langridge, J. M.; Bahreini, R.; Cappa, C. D.; Middlebrook, A. M.; Schwarz, J. P. Brown carbon and internal mixing in biomass burning particles. *Proc. Natl. Acad. Sci.* **2012**, *109*, 14802-14807; DOI 10.1073/pnas.1206575109.

22. Bergstrom, R. W.; Pilewskie, P.; Russell, P. B.; Redemann, J.; Bond, T. C.; Quinn, P. K.; Sierau, B. Spectral absorption properties of atmospheric aerosols *Atmos. Chem. Phys.* **2007**, *7*(23), 5937-5943; DOI 10.5194/acp-7-5937-2007.

23. Kirchstetter, T. W.; Thatcher, T. L. Contribution of organic carbon to wood smoke particulate matter absorption of solar radiation. *Atmos. Chem. Phys.* **2012**, *12*(14), 6067-6072; DOI 10.5194/acp-12-6067-2012.

24. Bahadur, R.; Praveen, P. S.; Xu, Y.; Ramanathan, V. Solar absorption by elemental and brown carbon determined from spectral observations. *Proc. Natl. Acad. Sci.* **2012**, *109*(43), 17366-17371; DOI 10.1073/pnas.1205910109.

25. Chung, C. E.; Ramanathan, V.; Decremer, D. Observationally constrained estimates of carbonaceous aerosol radiative forcing. *Proc. Natl. Acad. Sci.* **2012**, *109*(29), 11624-11629; DOI 10.1073/pnas.1203707109.

26. Gyawali, M.; Arnott, W. P.; Lewis, K.; Moosmüller, H. In situ aerosol optics in Reno, NV, USA during and after the summer 2008 California wildfires and the influence of absorbing and non-absorbing organic coatings on spectral light absorption. *Atmos. Chem. Phys.* **2009**, *9*(20), 8007-8015; DOI 10.5194/acp-9-8007-2009.

27. Knox, A.; Evans, G. J.; Brook, J. R.; Yao, X.; Jeong, C. H.; Godri, K. J.; Sabaliauskas, K.; Slowik, J. G. Mass Absorption Cross-Section of Ambient Black Carbon Aerosol in Relation to Chemical Age. *Aerosol Sci. Technol.* **2009**, *43*(6), 522-532; DOI 10.1080/02786820902777207.

28. Saleh, R.; Hennigan, C. J.; McMeeking, G. R.; Chuang, W. K.; Robinson, E. S.; Coe, H.; Donahue, N. M.; Robinson, A. L. Absorptivity of brown carbon in fresh and photo-chemically aged biomass-burning emissions. *Atmos. Chem. Phys*. **2013**, *13*, 7683–7693; DOI 10.5194/acp-13-7683-2013.

29. McMeeking, G.; Fortner, E.; Onasch, T. B.; Taylor, J.; Flynn, M.; Coe, H.; Kreidenweis, S. M. Impacts of non-refractory material on light absorption by aerosols emitted from biomass burning. *J. Geophys. Res*. **2014**, *119*, D021750; DOI 10.1002/2014JD021750.

30. Nakayama, T.; Ikeda, Y.; Sawada, Y.; Setoguchi, Y.; Ogawa, S.; Kawana, K.; Mochida, M.; Ikemori, F.; Matsumoto, K.; Matsumi, Y. Properties of light-absorbing aerosols in the Nagoya urban area, Japan, in August 2011 and January 2012: Contributions of brown carbon and lensing effect. *J. Geophys. Res*. **2014**, *119*, 12721-12739; DOI 10.1002/2014JD021744.

31. Cox, P.; Delao, A.; Komorniczak, A. The California almanac of emissions and air quality, *California Air Resource Board* **2013**, Sacramento, CA.

32. Ngo, M. et al. Airborne particles in the San Joaquin Valley may affect human health, *Calif. Agric*. **2010**, *64*(1), 12–16; DOI 10.3733/ca.v064n01p12.

33. Chow, J. C.; Chen, L. W. A.; Watson, J. G.; Lowenthal, D. H.; Magliano, K. A.; Turkiewicz, K.; Lehrman, D. E. PM2.5 chemical composition and spatiotemporal variability during the California Regional PM10/PM2.5 Air Quality Study (CRPAQS). *J. Geophys. Res.* **2006**, *111*, D10S04; DOI 10.1029/2005JD006457.

34. Chow, J. C.; Watson, J. G.; Lowenthal, D. H.; Chen, L. W. A.; Zielinska, B.; Mazzoleni, L. R.; Magliano, K. L. Evaluation of organic markers for chemical mass balance source apportionment at the Fresno Supersite. *Atmos. Chem. Phys*. **2007**, *7*(7), 1741–1754; DOI 10.5194/acp-7-1741-2007.

35. Chen, L. W. A.; Watson, J. G.; Chow, J. C.; Magliano, K. L. Quantifying PM2.5 source contributions for the San Joaquin Valley with multivariate receptor models. *Environ. Sci. Technol*. **2007**, *41*(8), 2818–2826; DOI 10.1021/es0525105.

36. Magliano, K. L.; Hughes, V. M.; Chinkin, L. R.; Coe, D. L.; Haste, T. L.; Kumar, N.; Lurmann, F. W. Spatial and temporal variations in PM10 and PM2.5 source contributions and comparison to emissions during the 1995 integrated monitoring study. *Atmos. Environ.* **1999**, *33*(29), 4757–4773; DOI 10.1016/S1352-2310(99)00265-4.

37. Ge, X.; Setyan, A.; Sun, Y.; Zhang, Q. Primary and secondary organic aerosols in Fresno, California during wintertime: Results from high resolution aerosol mass spectrometry. *J. Geophys. Res.* **2012**, *117*(D19), D19301; DOI 10.1029/2012JD018026.

38. Young, D. E.; Kim, H.; Parworth, C.; Zhou, S.; Zhang, X.; Cappa, C. D.; Seco, R.; Kim, S.; Zhang, Q. Influences of emission sources and meteorology on aerosol chemistry in a polluted urban environment: results from DISCOVER-AQ California. *Atmos. Chem. Phys. Discuss.* **2015**, *15*, 35057-35115; DOI 10.5194/acpd-15-35057-2015.

39. Cappa, C. D.; Che, D. L.; Kessler, S. H.; Kroll, J. H.; Wilson, K. R. Variations in organic aerosol optical and hygroscopic properties upon heterogeneous OH oxidation. *J. Geophys. Res.* **2011**, *116*, D15204; DOI 10.1029/2011jd015918.

40. Langridge, J. M.; Richardson, M. S.; Lack, D.; Law, D.; Murphy, D. M. Aircraft instrument for comprehensive characterization of aerosol optical properties, Part I: Wavelength-dependent optical extinction and its relative humidity dependence measured using cavity ringdown spectroscopy. *Aerosol Sci. Technol.* **2011**, *45*, 1305-1318; DOI 10.1080/02786826.2011.592745.

41. Lack, D. A.; Richardson, M. S.; Law, D.; Langridge, J. M.; Cappa, C. D.; McLaughlin, R. J.; Murphy, D. M. Aircraft instrument for comprehensive characterization of aerosol optical properties, Part 2: Black and brown Carbon absorption and absorption Enhancement measured with photo acoustic spectroscopy. *Aerosol Sci. Technol.* **2012**, *46*, 555-568; DOI 10.1080/02786826.2011.645955.

42. Schwarz, J. P.; Gao, R. S.; Fahey, D. W.; Thomson, D. S.; Watts, L. A.; Wilson, J. C.; Reeves, J. M.; Darbeheshti, M.; Baumgardner, D. G.; Kok, G. L.; Chung, S. H.; Schulz, M.; Hendricks, J.; Lauer, A.; Karcher, B.; Slowik, J. G.; Rosenlof, K. H.; Thompson, T. L.; Langford, A. O.; Loewenstein, M.; Aikin, K. C. Single-particle measurements of midlatitude black carbon and light-scattering aerosols from the boundary layer to the lower stratosphere. *J. Geophys. Res.* **2006**, *111*, D16207; DOI 10.1029/2006JD007076.

43. Laborde, M.; Mertes, P.; Zieger, P.; Dommen, J.; Baltensperger, U.; Gysel, M. Sensitivity of the Single Particle Soot Photometer to different black carbon types. *Atmos. Meas. Technol.* **2012**, *5*, 1031-1043; DOI 10.5194/amt-5-1031-2012.

44. Bond, T. C.; Bergstrom R. W. Light absorption by carbonaceous particles: an investigative review. *Aerosol Sci. Technol.* **2006**, *40*, 27–67; DOI 10.1080/02786820500421521.

45. Canagaratna, M.; Jayne, J.; Jimenez, J. L.; Allan, J. A.; Alfarra, R.; Zhang, Q.; Onasch, T.; Drewnick, F.; Coe, H.; Middlebrook, A.; Delia, A.; Williams, L.; Trimborn, A.; Northway, M.; DeCarlo, P.; Kolb, C.; Davidovits, P.; Worsnop, D. Chemical and microphysical characterization of ambient aerosols with the aerodyne aerosol mass spectrometer. *Mass Spectrom. Rev.* **2007**, *26*, 185-222; DOI 10.1002/mas.20115.

46. Zhang, Q.; Jimenez, J. L.; Canagaratna, M.; Ng, N. L.; Ulbrich, I.; Worsnop, D.; Sun, Y. L. Understanding organic aerosols via factor analysis of aerosol mass spectrometry: A review. *Anal. Bioanal. Chem.* **2011**, *401*, 3045-3067; DOI 10.1007/s00216-011-5355-y.

47. Schneider, J.; Weimer, S.; Drewnick, F.; Borrmann, S.; Helas, G.; Gwaze, P.; Schmid, O.; Andreae, M. O.; Kirchner, U. Mass spectrometric analysis and aerodynamic properties of various types of combustion-related aerosol particles. *Int. J. Mass. Spec.* **2006**, *258*, 37–49; DOI 10.1016/ j.ijms.2006.07.008.

48. Alfarra, M. R.; Prévôt, A. H. S.; Szidat, S.; Sandradewi, J.; Weimer, S.; Lanz, V. A.; Schreiber, D.; Mohr, M.; Baltensperger, U. Identification of the mass spectral signature of organic aerosols from wood burning emissions. *Environ. Sci. Technol.* **2007**, *41*(16), 5770–5777; DOI 10.1021/es062289b.

49. Chen, Y.; Bond, T. C. Light absorption by organic carbon from wood combustion. *Atmos. Chem. Phys*. **2010**, *10*, 1773–1787; DOI 10.5194/acp-10-1773-2010.

50. Bruns, E. A.; Krapf, M.; Orasche, J.; Huang, Y.; Zimmermann, R.; Drinovec, L.; Mocnik, G.; El-Haddad, I.; Slowik, J. G.; Dommen, J.; Baltensperger, U.; Prévôt, A. H. S. Characterization of primary and secondary wood combustion products generated under different burner loads. *Atmos. Chem. Phys.* **2015**, *15*, 2825-2841; DOI 10.5194/acp-15-2825-2015.

51. U.S.EPA. Report to congress on black carbon. **2012**, Agency, U.S.E.P.A., Washington DC. http://www.epa.gov/blackcarbon/.

52. Buffaloe, G. M.; Lack, D. A.; Williams, E. J.; Coffman, D.; Hayden, K. L.; Lerner, B. M.; Li, S-M.; Nuaaman I.; Massoli, P.; Onasch, T. B.; Quinn, P. K.; Cappa, C. D. Black carbon emissions from in-use ships: a California regional assessment. *Atmos. Chem. Phys*. **2014**, *14*, 1881-1896; DOI 10.5194/acp-14-1881-2014.

53. Mohr, C.; Lopez-Hilfiker, F. D.; Zotter, P.; Prévôt, A. S. H.; Xu, L.; Ng, N. L.; Herndon, S. C.; Williams, L. R.; Franklin, J. P.; Zahniser, M. S.; Worsnop, D. R.; Knighton, W. B.; Aiken, A. C.; Gorkowski, K. J.; Dubey, M. K.; Allan, J. D.; Thornton, J. A. Contribution of Nitrated Phenols to Wood Burning Brown Carbon Light Absorption in Detling, United Kingdom during Winter Time. *Environ. Sci. Technol*. **2013**, *47* (12), 6316–6324; DOI 10.1021/es400683v.

54. Desyaterik, Y.; Sun, Y.; Shen, X.; Lee, T.; Wang, X.; Wang T.; Collett Jr., J. L. Speciation of "Brown" Carbon in Cloud Water Impacted by Agricultural Biomass Burning in Eastern China. *J. Geophys. Res.* **2013**, *118*, 7389-7399; DOI 10.1002/jgrd.50561.

55. Hoffer, A.; Gelencser, A.; Guyon, P.; Kiss, G.; Schmid, O.; Frank, G. P.; Artaxo, P.; Andreae, M. O. Optical properties of humic-like substances (HULIS) in biomass-burning aerosols. *Atmos. Chem. Phys*. **2006**, *6*, 3563-3570; DOI 10.5194/acp-6-3563-2006.

56. Lukacs, H.; Gelencser, A.; Hammer, S.; Puzbaum, H.; Pio, C.; Legrand, M.; Kasper-Giebl, A.; Handler, M.; Limbeck, A.; Simpson, D.; Preunkert, S. Seasonal trends and possible sources of brown carbon based on 2-year aerosol measurements at six sites in Europe. *J. Geophys. Res*. **2007**, *112*, D23S18; DOI 10.1029/2006JD008151.

57. Huang, Q. G.; Wang, L. S.; Han, S. K. The genotoxicity of substituted nitrobenzenes and the quantitative structure-activity relationship studies. *Chemosphere* **1995**, *30*(5), 915−923; DOI 10.1016/0045-6535(94)00450-9.

58. Verma, V.; Rico-Martinez, R.; Kotra, N.; King, L.; Liu, J.; Snell, T. W.; Weber, R. J. Contribution of water-soluble and insoluble components and their hydrophobic/hydrophilic subfractions to the reactive oxygen species-generating potential of fine ambient aerosols. *Environ. Sci. Technol*. **2012**, *46*, 11384-11392; DOI 10.1021/es302484r.

59. Chakrabarty, R. K.; Moosmüller, H.; Chen, L.-W. A.; Lewis, K.; Arnott, W. P.; Mazzoleni, C.; Dubey, M. K.; Wold, C. E.; Hao, W. M.; Kreidenweis, S. M. Brown carbon in tar balls from smoldering biomass combustion. *Atmos. Chem. Phys*. **2010**, *10*, 6363–6370; DOI 10.5194/acp-10-6363-2010.

60. Wandinger, U.; Müller, D.; Bockmann, C.; Althausen, D.; Matthias,V.; Bösenberg, J.; Weiss, V.; Fiebig, M.; Wendisch, M.; Stohl, A.; Ansmann, A. Optical and micro10 physical characterization of biomass-burning and industrial-pollution aerosols from multiwavelength lidar and aircraft measurements. *J. Geophys. Res.* **2002**, *107*(D21), 8125; DOI 10.1029/2000JD000202.

61. Adler, G.; Flores, J. M.; Abo Riziq, A.; Borrmann, S.; Rudich, Y. Chemical, physical, and optical evolution of biomass burning aerosols: a case study. *Atmos. Chem. Phys*. **2011**, *11*, 1491–1503; DOI 10.5194/acp-11-1491-2011.

9.8 Tables

Table 9-1. Summary of the instrumentation, size cut and the measurements made at the Fresno ground site during DISCOVER-AQ.

Instrumentation	Size cut	Measurement
Cavity ringdown Spectrometer (**CRD**)	$PM_{2.5}$	Dry particle light extinction (b_{ext}) at 405 and 532 nm
Photoacoustic Spectrometer (**PAS**)	$PM_{2.5}$	Dry particle light absorption (b_{abs}) at 405 and 532 nm
Photoacoustic Extinctiometer (**PAX**)	$PM_{2.5}$	Dry particle light extinction (b_{ext}) and absorption (b_{abs}) at 870 nm
Single Particle Soot Photometer (**SP2**)	$PM_{2.5}$	Refractory black carbon (rBC) mass and number size distributions at size range of [100,300nm] (extrapolated to [20,1000nm] in the post analysis)
High Resolution Time-of-Flight Aerosol Mass Spectrometer (**HR-ToF-AMS**)	PM_1	Non refractory submicron particle (NR-PM_1) mass and chemical composition
Scanning Mobility Particle Sizer (**SMPS**)	PM_1	Particle number size distribution (16 - 685 nm)
Aerodynamic Particle Sizer (**APS**)	$PM_{2.5}$	Particle number size distribution (0.8 -2.5 μm)
Thermodenuder (**TD**)	$PM_{2.5}$	Absorption Enhancement (E_{abs}) at 405, 532 and 870 nm

Table 9-2. Density values of the PM_1 components used in the optical closure calculation.

Component	Density, g cm^{-3}
NH_4NO_3	1.72[a]
$(NH_4)_2SO_4$	1.77[a]
NaCl	2.16[a]
BC	1.80[b]
Organics	[c]

[a]from "Properties of the Elements and Inorganic Compounds", in CRC Handbook of Chemistry and Physics, Internet Version 2005, David R. Lide, ed., <http://www.hbcpnetbase.com>, CRC Press, Boca Raton, FL, 2005.
[b]adopted from Bond and Bergstrom[1]
[c]determined from the ratio of organic aerosol mass and the difference between the total aerosol volume determined with an SMPS and the sum of the volumes of the individual inorganic components.

Table 9-3. Published values of the imaginary part of the complex refractive index (k_{BBOA}) and the mass absorption cross-section (MAC_{BBOA}) of the OA components of wood burning aerosols, excluding BC contributions.

	λ , nm	k_{BBOA}	MAC_{BBOA} $m^2\ g^{-1}$	Optical Measurement	Aerosol type sampled	Sampling Location	Literature
Laboratory	550	0.02-0.06		Aethalometer	Oak burning POA	-	[28]
	550	0.015-0.04		Aethalometer	Pocosin Pine burning POA	-	[28]
	550	0.0055-0.022		Aethalometer	Galberry burning POA	-	[28]
	400	0.038	1.1	UV/Vis (filter methanol extracts)	Pine/Oak wood burning	-	[49]
	405	0.015		Photo-Acoustic Spectrometer	Tar balls from Ponderosa Pine Duff burning	-	[59]
	405	0.0076		Photo-Acoustic Spectrometer	Tar balls from Alaskan Duff burning	-	[59]
Ambient	404	0.01	1.0-1.1	Photo-Acoustic Spectrometer	Wild fire, near-source emission	Four Mile Canyon, Colorado	[21]
	470		1.01	Aethalometer	Biomass burning influenced	Beijing, China	[11]
	400	0.112	2.9	Light transmission (filter)	Wood burning and biomass smoke aerosols	Savanna	[9]
	532	0.0016-0.0019	0.029-0.031	Photo-Acoustic Spectrometer	HULIS from biomass burning aerosols	Amazon basin	[55]
	Broadband	0.05-0.07		Airborne lidar	Upwind of forest fires	Northern Canada	[60]
	Broadband	0.07±0.03/ 0.04±0.01		White light optical particle counter	Open fire/ Smoldering phase	Urban Rehovot, Israel	[61]
This study	405	0.037	0.53 or 0.60	Photo-Acoustic Spectrometer	Biomass burning influenced	Fresno, CA	-

Table 9-4. Uncertainty (% change) in the retrieved k_{OA} resulted from the model assumptions (spherical particle shape, refractive indices of black carbon (BC) and non-BC particles) and measurement uncertainties associated with refractory BC mass, organic aerosol volume fraction and absorption enhancement.

Assumption/Parameter	Base case	Alternate case	% change in k_{OA}*
Spherical Particle Shape	Mie	RDG (40 nm)	-2.2%
		RDG (70 nm)	+5.9%
Coating Distribution	Constant r_{coat}/r_{core}	Diffusion-controlled growth of the coating materials on rBC core	-2.8%
RI (n, k) for BC	1.88-0.8i	1.75-0.63i	-12.4%
RI (n) of non-BC particles	1.50	+0.05	-5.4%
		-0.05	+3.8%
rBC mass concentration (m_{rBC})	as measured	+30%	+19.1%
		-30%	-24.0%
		+50%	+35.8%
		-50%	-37.6%
Organic aerosol volume fraction (f_{OA})	as measured	+20%	-17.5%
		-20%	+13.6%
Absorption Enhancement at 405 and 532 nm (E_{abs})	as measured	+5%	-4.6%
		-5%	1.1%

* Percentage (%) change in the campaign-average k_{OA} value averaged between 23:00 and 2:00 relative to that derived from the base case

9.9 Figures

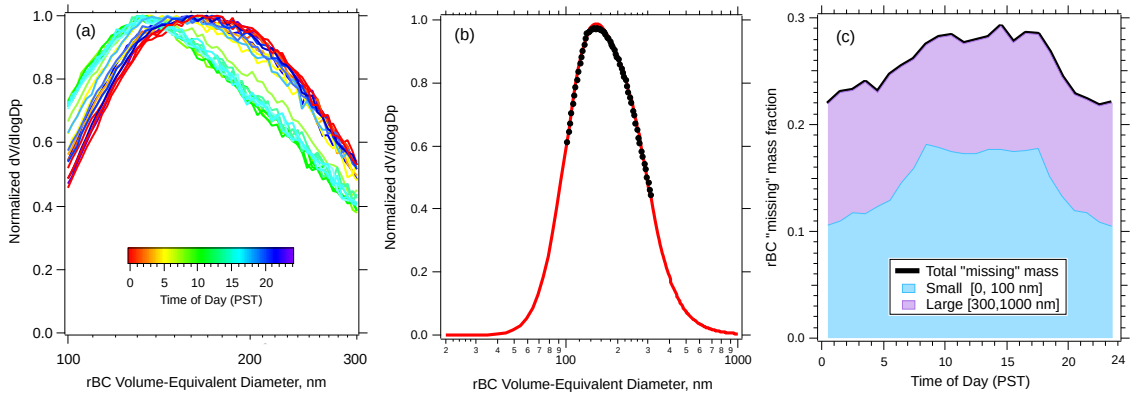

Figure 9-1. (a) Volume-weighted size distribution for refractory black carbon (rBC) determined from the SP2 measurements, averaged and colored by hour of day, (b) campaign-average rBC volume-weighted size distribution (black markers) during DISCOVER-AQ; the red dashed solid line represents the bimodal log-normal fit to the observation for the volume-equivalent diameter (d_{ve}) range of 20 to 1000 nm, and (c) the diurnal profile of the mass fraction of the rBC "missing" mass, calculated as the ratio between the rBC mass that is outside the SP2 detection window (100-300 nm) and the rBC mass determined from the lognormal fit (solid red line in **Figure 9-1**b). The fractions of the total rBC mass that are attributable to "missing" mass from the smaller rBC particles (20 nm < d_{ve} < 100 nm) and from the bigger rBC particles (300 nm < d_{ve} < 1000 nm) are shown separately in the figure. The "missing" mass correction increases the total rBC mass by ~26% on average, with larger corrections during the daytime than at nighttime.

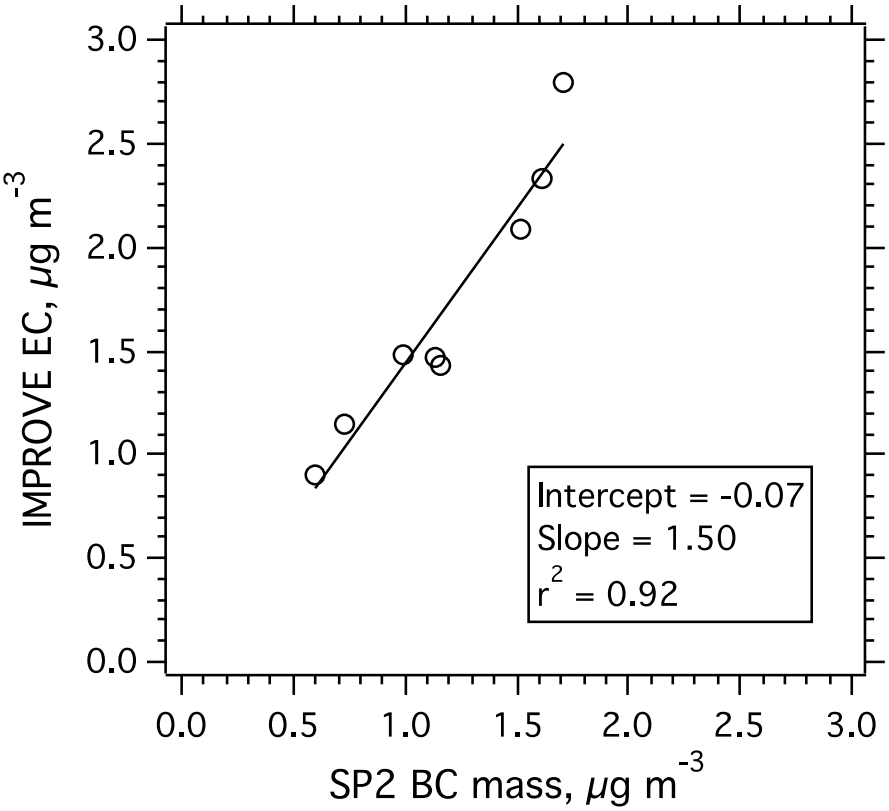

Figure 9-2. Scatter plot of the IMPROVE elemental carbon (EC) mass concentrations versus the daily-average SP2 refractory black carbon (BC) mass concentrations for the days that EC data were available during DISCOVER-AQ.

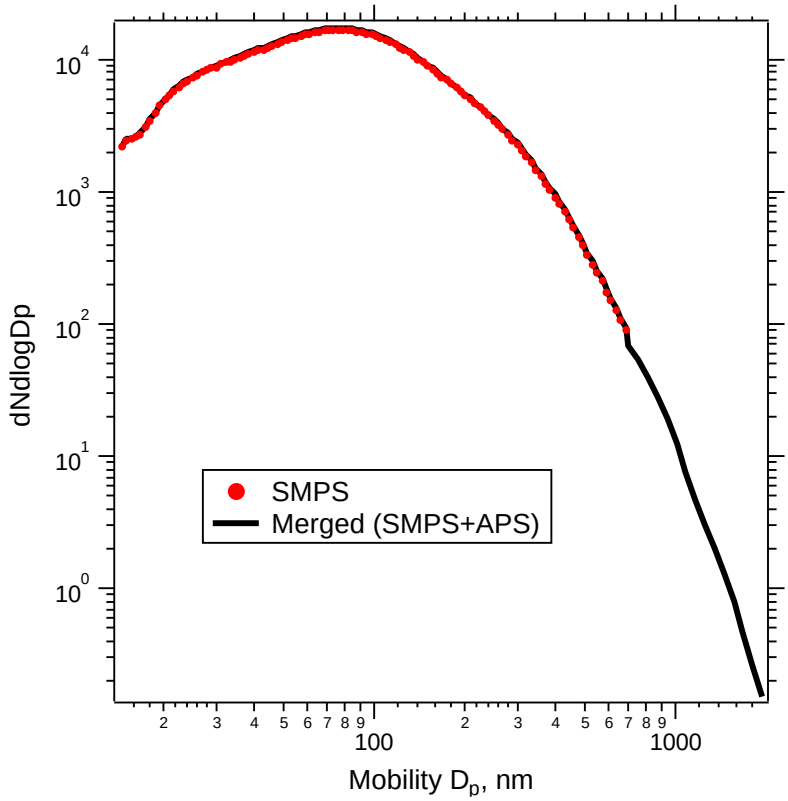

Figure 9-3. Campaign-average size distributions of ambient $PM_{2.5}$ from the scanning mobility particle sizer (SMPS) (red marker) and merged SMPS + aerodynamic particle sizer (APS) (black line) measurements.

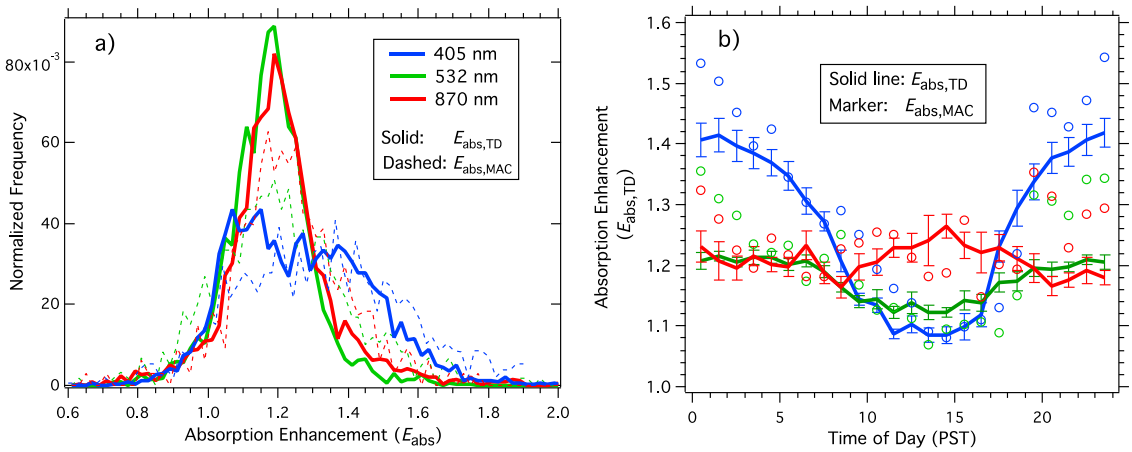

Figure 9-4. Normalized frequency distributions (a) and diurnal trends (b) of the measured $PM_{2.5}$ absorption enhancements using the TD method ($E_{abs,TD}$) and using the mass absorption cross-section method ($E_{abs,MAC}$) at 405, 532 and 870 nm during DISCOVER-AQ. The $E_{abs,MAC}$ values were determined by normalizing the *MAC* of the ambient particles (MAC_{amb}) to the average *MAC* of the thermo-denuded particles (MAC_{TD}) during the period between 13:00 and 16:00 (PST). Error bars shown for the $E_{abs,TD}$ in (b) are 1 standard error of the mean (SEM).

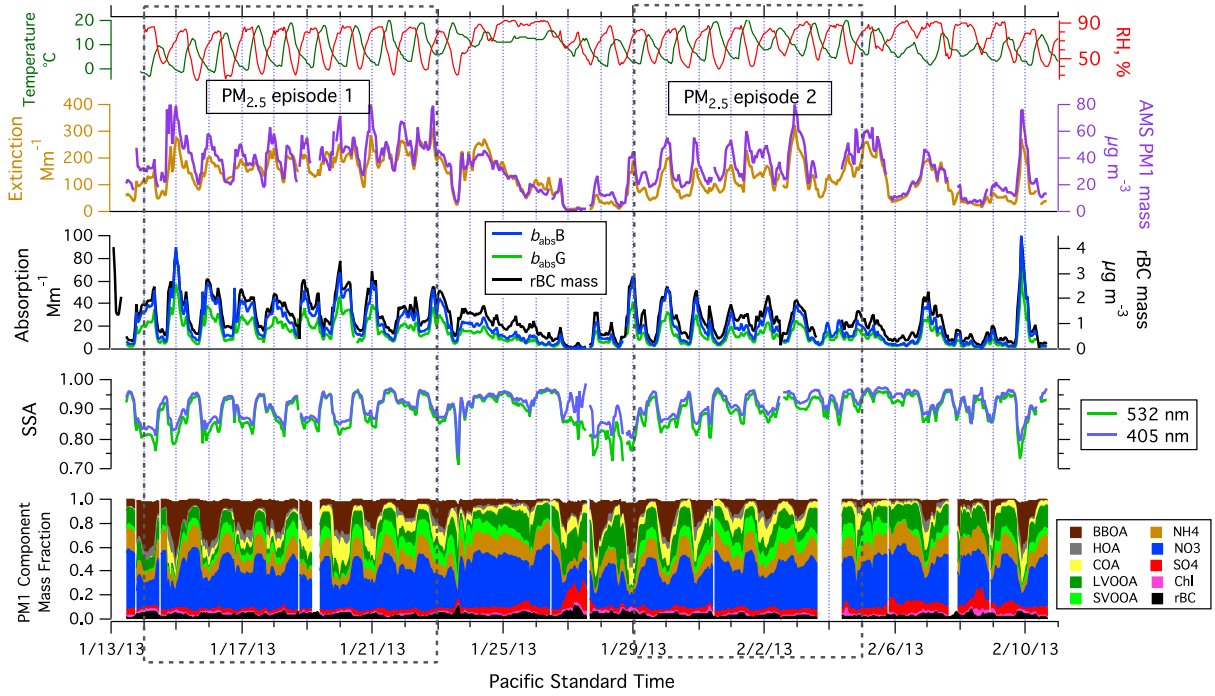

Figure 9-5. Time series of ambient temperature and relative humidity (RH), dry $PM_{2.5}$ light extinction coefficients at 532 nm, total PM_1 mass, dry $PM_{2.5}$ light absorption coefficients at 405 nm ($b_{abs}B$) and 532 nm ($b_{abs}G$), SP2 refractory black carbon (rBC) mass, single scattering albedo (SSA) at 405 and 532 nm, and the fractional composition of AMS PM_1 components during the DISCOVER-AQ 2013 California campaign in Fresno. Two $PM_{2.5}$ episodes with substantially elevated ground $PM_{2.5}$ concentrations, 1/14 – 1/23 and 1/29 – 2/5, are identified and labeled in the time series plot.

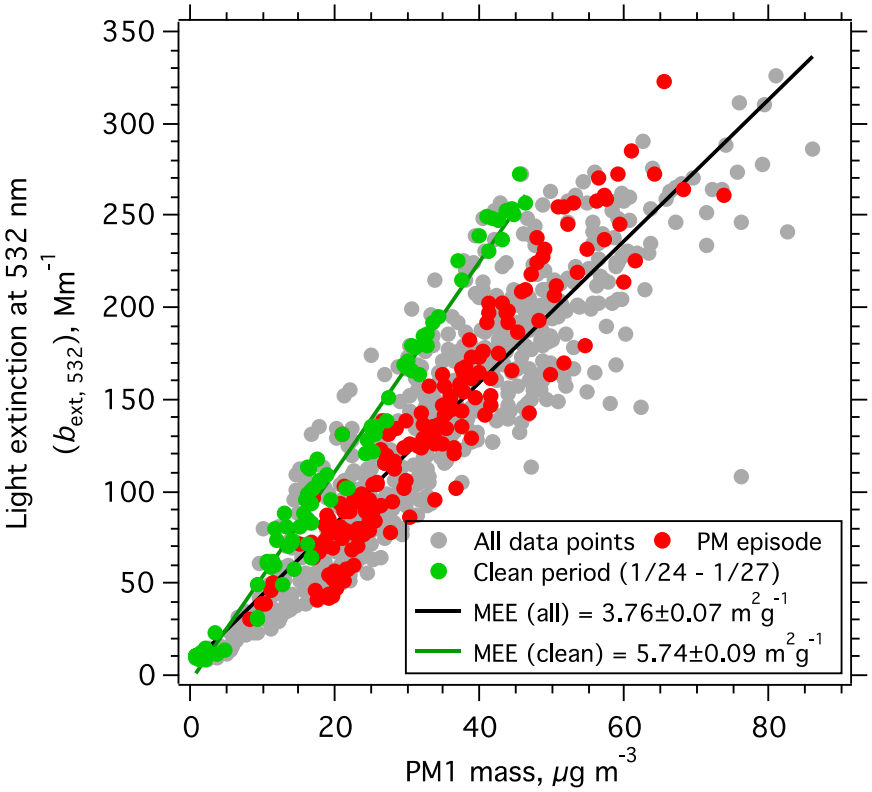

Figure 9-6. Scatter plot of $PM_{2.5}$ light extinction coefficients at 532 nm versus the PM_1 mass concentrations. The gray, red and green markers represent all data, data during the two PM episodes, and data during a clean period (1/24-1/27). The slopes of the Deming regression fits of the data yield the $PM_{2.5}$ mass extinction coefficient (MEC) (±1 standard deviation).

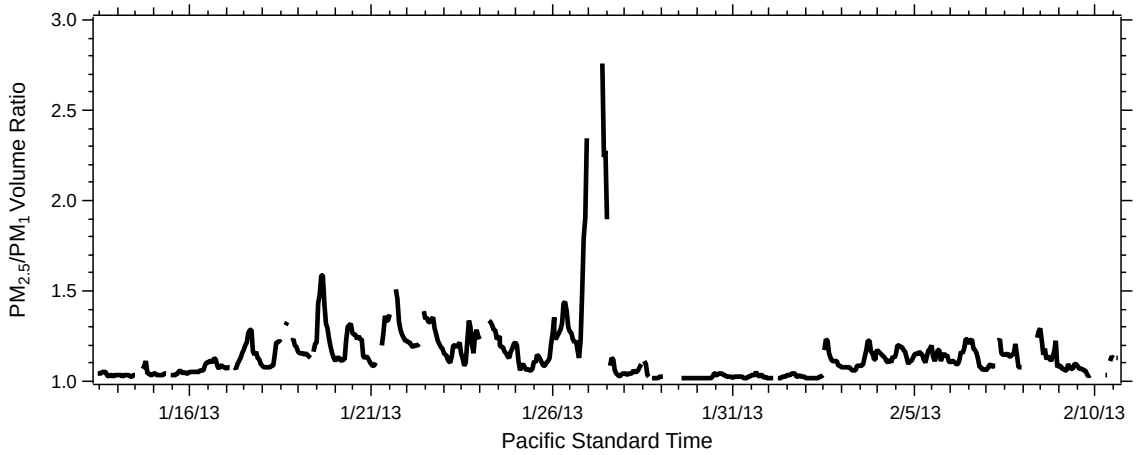

Figure 9-7. Time series of the $PM_{2.5}/PM_1$ volume ratio. Values >>1 correspond to periods with substantial contributions from supermicron particles to the total $PM_{2.5}$ volume concentration, with particularly large supermicron contributions observed on 27 January during the "clean" period. PM_1 volume is determined from the ambient SMPS size distribution measurements, while $PM_{2.5}$ volume is determined from the merged ambient SMPS+APS size distribution measurements. The gaps in the data are due to instrumentation issues.

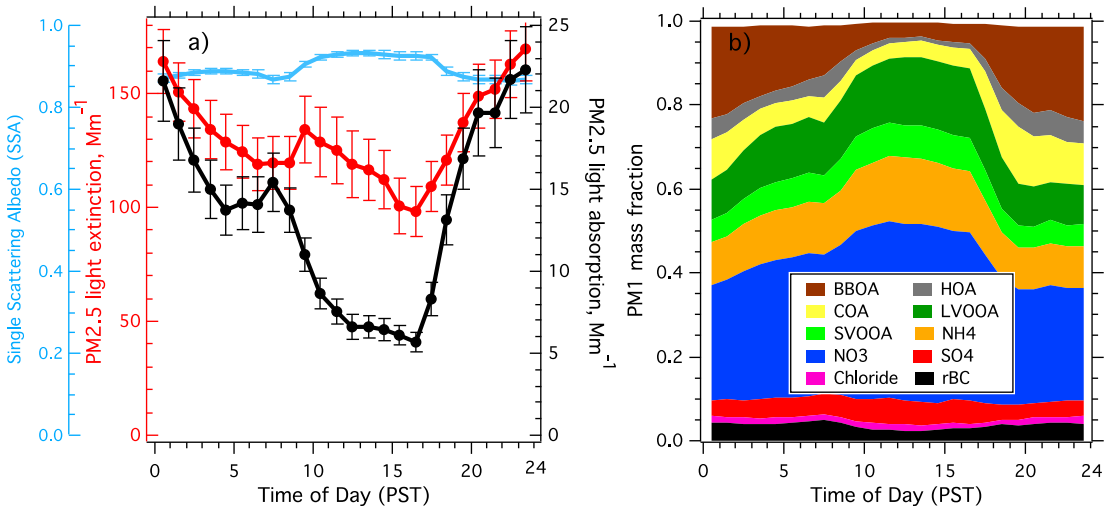

Figure 9-8. Campaign-average diurnal profiles of (a) $PM_{2.5}$ light extinction (b_{ext}), absorption coefficients (b_{abs}) and single scattering albedo (SSA) at 532nm determined from CRD-PAS measurements and (b) the fractional contribution of PM_1 inorganic and organic aerosols determined from AMS measurements. The organic factors, i.e. biomass burning organic aerosol (BBOA), hydrocarbon-like organic aerosol (HOA), cooking organic aerosol (COA), low-volatility oxygenated organic aerosol (LVOOA) and semi-volatile oxygenated organic aerosol (SVOOA), are determined from the Positive Matrix Factorization (PMF) analysis on the organic aerosol mass spectral matrix.

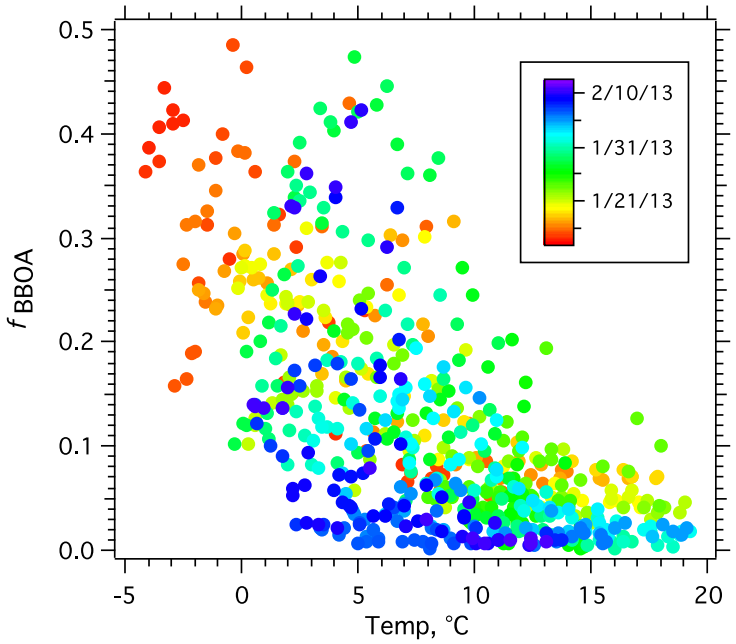

Figure 9-9. Correlation of the 1-hr average mass fraction of the AMS biomass burning organic aerosol component (f_{BBOA}) in the total PM_1 with the 1-hr average ambient temperature (Temp) during DISCOVER-AQ. The data are color-coded by the sampling date.

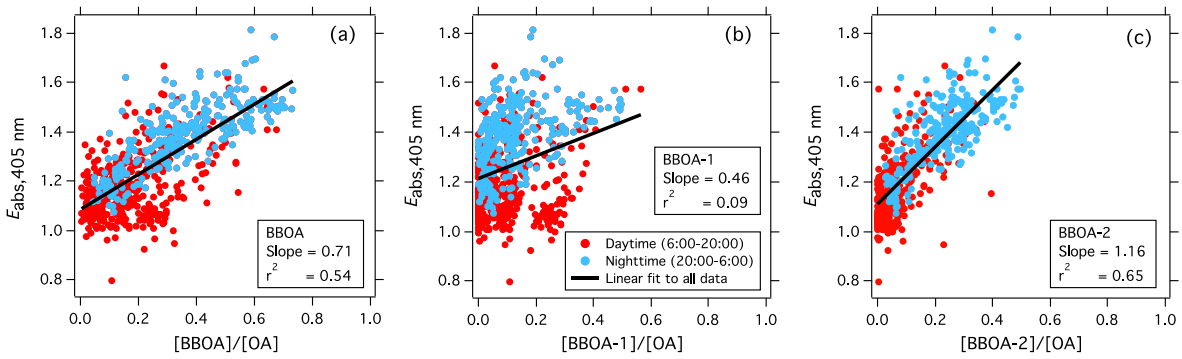

Figure 9-10. Scatter plots of the measured $PM_{2.5}$ absorption enhancement at 405 nm ($E_{abs,405nm}$) versus the AMS BBOA:OA ratio (a), $E_{abs,405nm}$ versus BBOA-1:OA ratio (b), and $E_{abs,405nm}$ versus BBOA-2:OA ratio (c). Data were split into daytime (6:00-20:00, red) and nighttime (20:00-6:00, blue). The slopes given in the scatter plots are determined from a one-sided linear regression of the data in each panel (daytime + nighttime data).

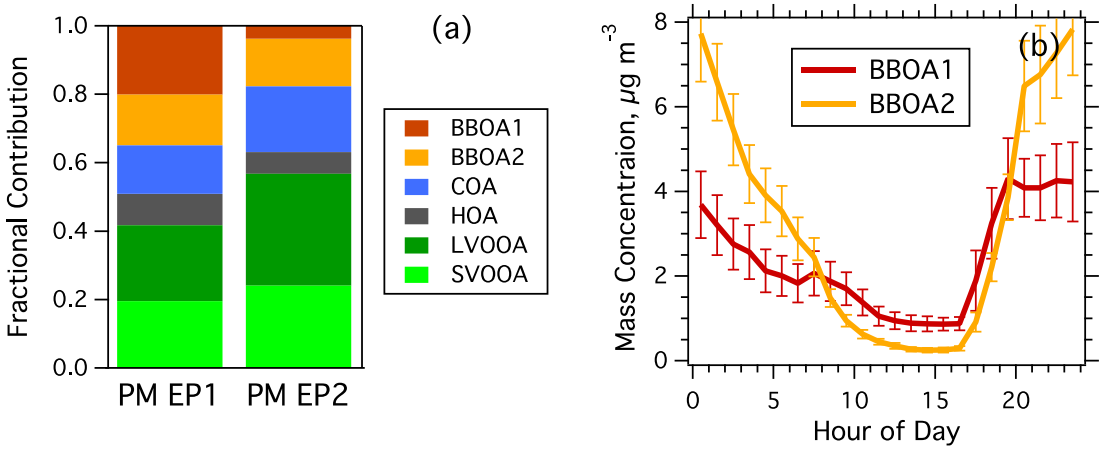

Figure 9-11. (a) Average fractional contribution of AMS organic aerosol (OA) factors, i.e., two types of biomass burning OA (BBOA-1 and BBOA-2), cooking OA (COA), hydrocarbon-like OA (HOA), low volatility oxygenated OA (LV-OOA) and semi-volatile oxygenated OA (SV-OOA), to total AMS OA mass for the two $PM_{2.5}$ episodes (1/14 – 1/23 and 1/29 – 2/5). (b) Diurnal plots of the mass concentrations of BBOA-1 and BBOA-2. The error bars are 1 sigma standard deviation of the diurnal averages.

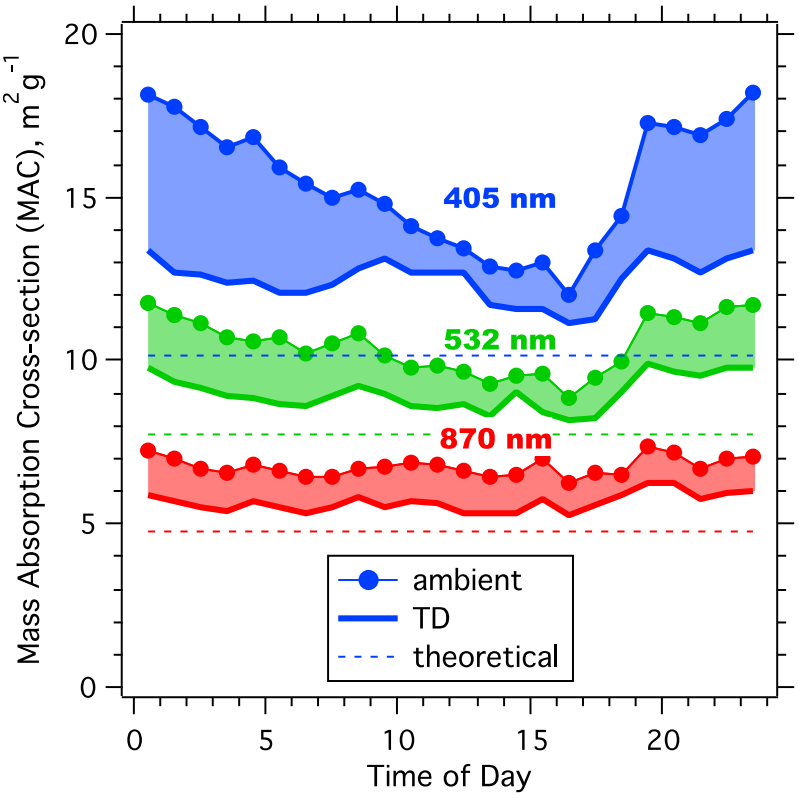

Figure 9-12. Diurnal profiles of the Mass Absorption Cross-section (*MAC*) of the ambient (lines with markers) and thermo-denuded (TD) (solid lines) $PM_{2.5}$ at 405, 532, and 870 nm. The dashed lines represent the *MAC* values recommended by *Bond and Bergstrom*[1] for freshly emitted black carbon particles at the corresponding wavelengths.

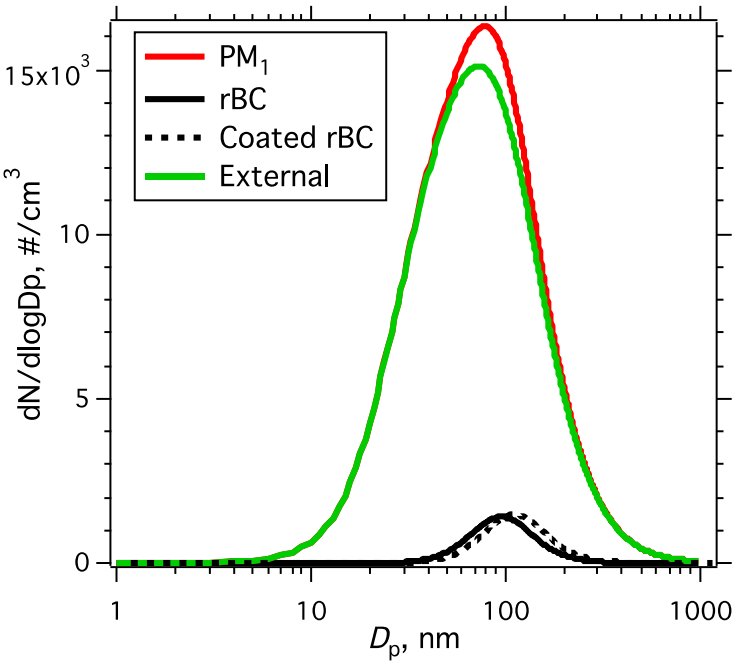

Figure 9-13. Campaign-average number-weighted size distributions ($dN/dlogD_p$) used as inputs to the Mie and RDG calculations. The refractory black carbon (rBC) size distribution was determined from the SP2 measurements, and the total PM_1 size distribution was determined from the SMPS measurements. The coated BC size distribution was constructed based on the estimated rBC equivalent coating thickness (or coating-to-core radius ratio, or r_{coat}/r_{core}). The externally mixed particle number size distribution ("External") was the difference between the total PM_1 and the coated BC number size distributions.

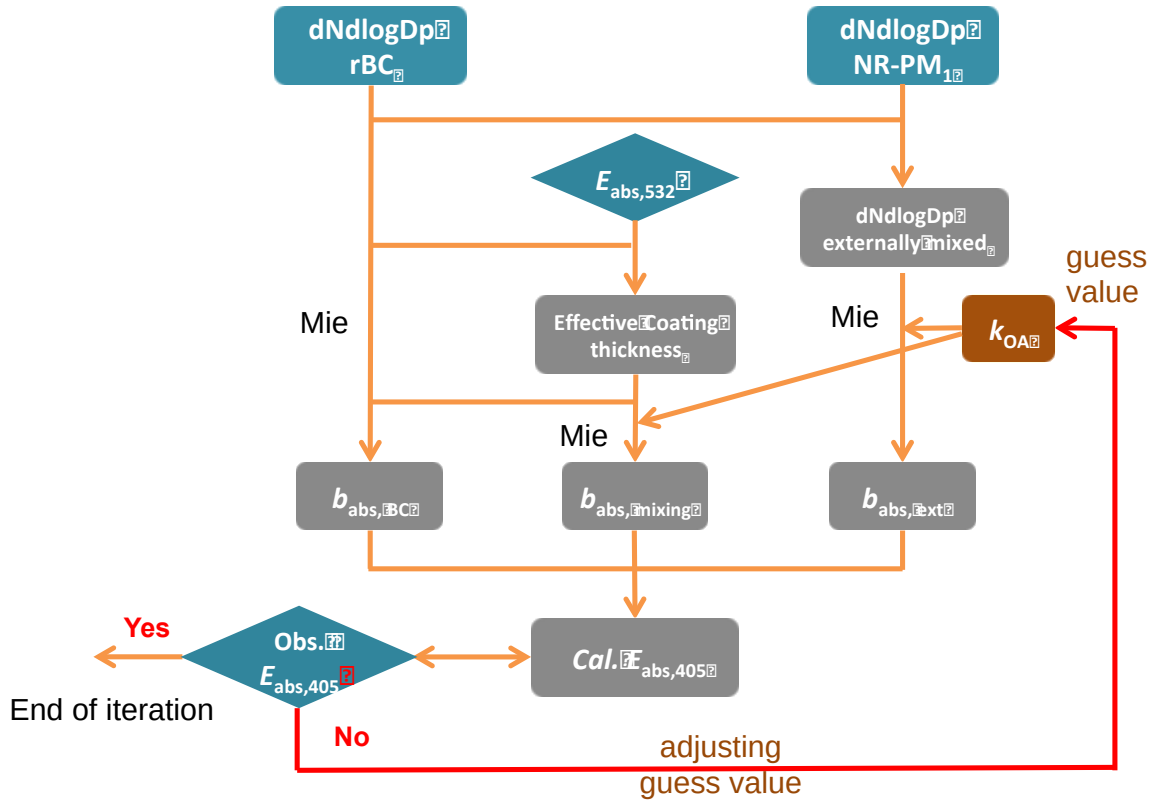

Figure 9-14. Schematic illustrating the retrieval process of the imaginary refractive index of the organic aerosols (k_{OA}) using optical closure analysis. The size distributions (dNdlogDp) of refractory black carbon (rBC) and non-refractory (NR) PM_1 were measured with a Single Particle Soot Photometer (SP2) and a Scanning Mobility Particle Sizer (SMPS), respectively. Observed absorption enhancement at 532 nm ($E_{abs,532}$) and 405 nm ($E_{abs,405}$) were determined with thermo-denuder (TD)-coupled absorption measurements using a Photo-Acoustic Spectrometer (PAS).

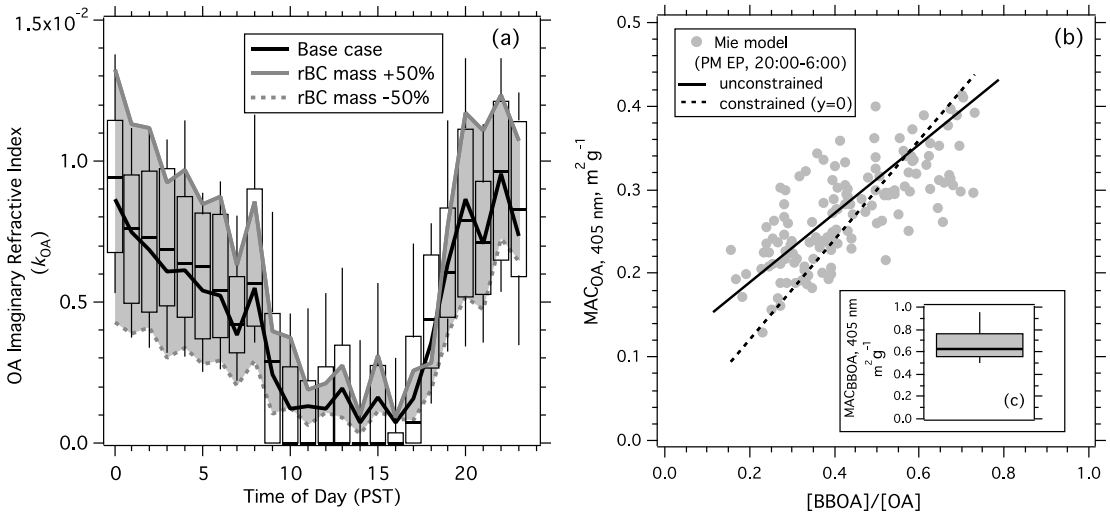

Figure 9-15. (a) Diurnal variation of the retrieved imaginary refractive index for organic aerosols (k_{OA}) (Mie model base case) (solid black line). The median value (thick horizontal bar), 25th and 75th percentiles (lower and upper box bounds, respectively), and 10th and 90th percentiles (lower and upper whiskers, respectively) of the k_{OA} are shown in the box and whisker plot. The uncertainty in the retrieved k_{OA} is assessed through sensitivity tests. Shown here as the upper and lower bounds of the shaded grey areas are the uncertainties in k_{OA} associated with ± 50% measurement uncertainty in the rBC mass. (b) Scatter plot of the mass absorption cross-section of the organic aerosol (MAC_{OA}) at 405 nm versus the AMS biomass burning organic aerosol (BBOA)-to-OA mass ratio. Only the nighttime (20:00-6:00) data during the two PM episodes are included. The lines show Deming regression fits to the data where the fit has been constrained to go through the origin (dashed) or unconstrained (solid). (c, inset) Box and whisker plot showing the variation in the MAC_{BBOA} values derived by taking the ratio of MAC_{OA} and [BBOA]:[OA].

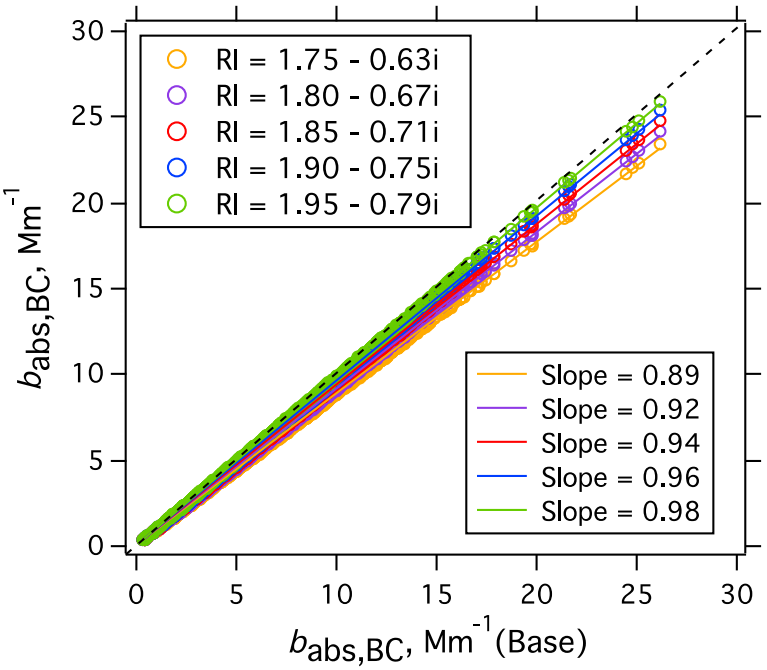

Figure 9-16. Sensitivity test on the calculated black carbon (BC) light absorption ($b_{abs,BC}$) at 532 nm using the base case Mie model with various refractive indices (RI) for BC as input. The RI values tested here are those listed in **Table 9-4** and are from Bond and Bergstrom.[1] The base case RI (x-axis) is 1.88 -0.8*i*. The slopes are derived from the linear fits of $b_{abs,BC}$ calculated with the alternate RI values versus the base case.

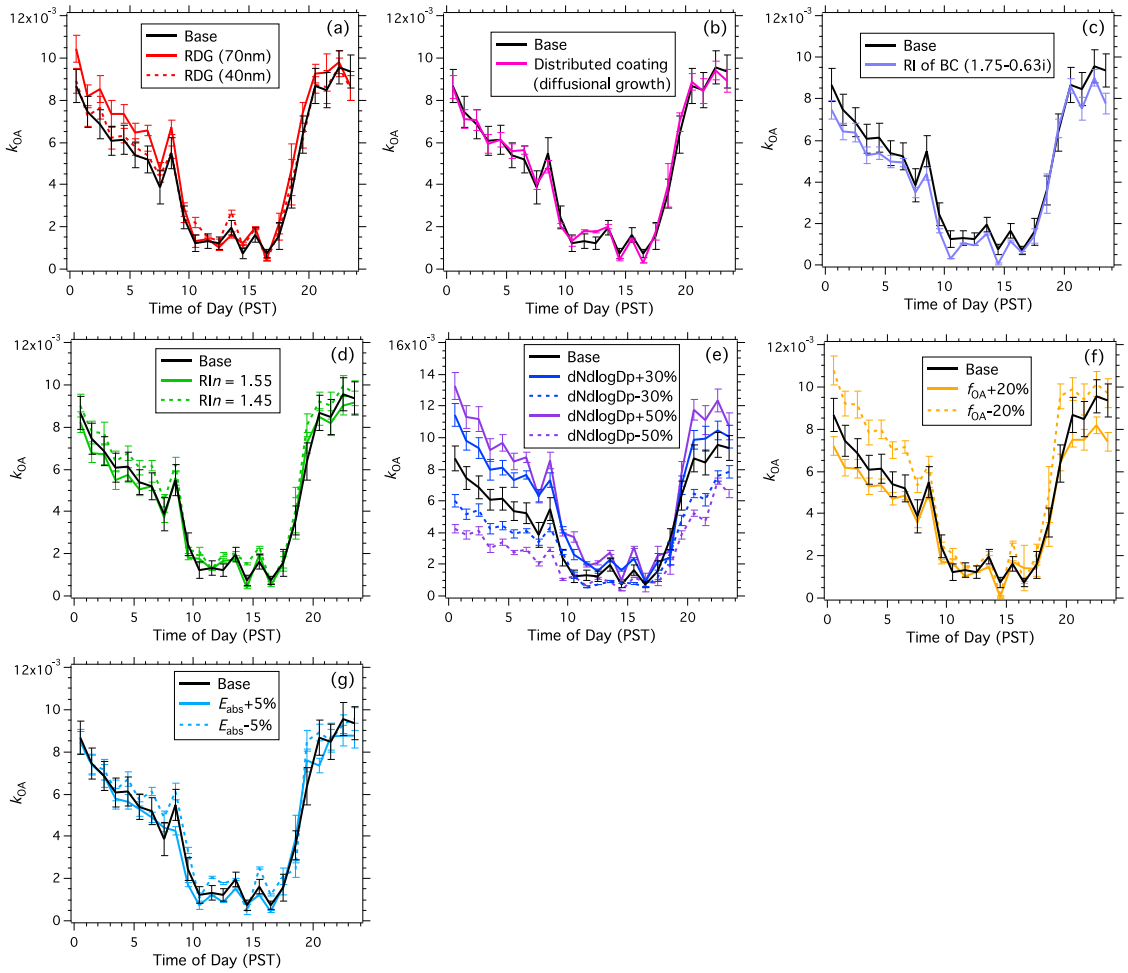

Figure 9-17. Diurnal plots of the refractive index of the organic component (k_{OA}) derived from the optical closure for the different sensitivity tests listed in **Table 9-4**. The result from the base case is shown as a solid black line in each panel and the results from the sensitivity tests as colored solid and dashed lines.

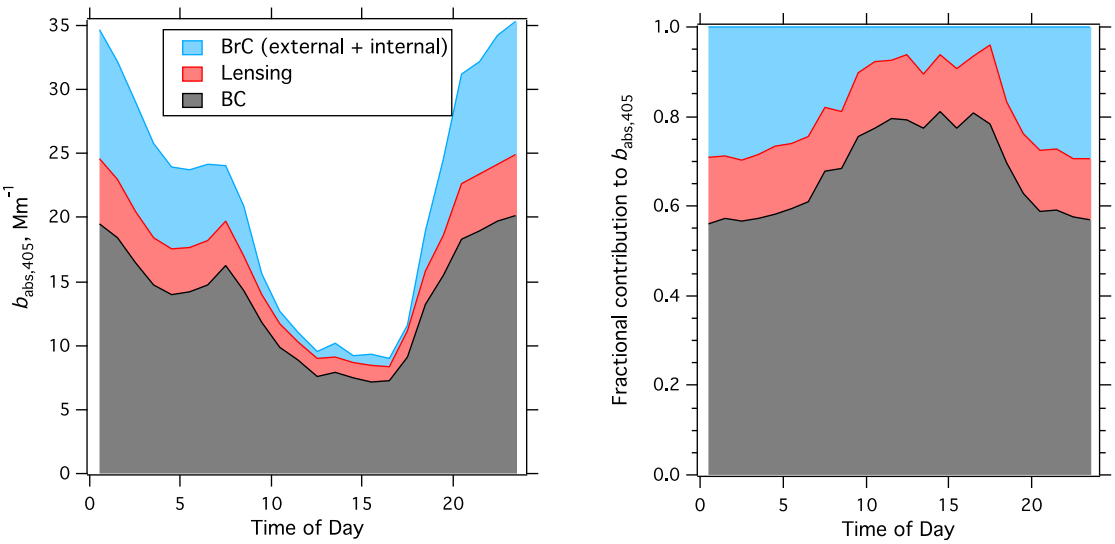

Figure 9-18. Apportionment of the $PM_{2.5}$ light absorption at 405 nm ($b_{abs,405}$): absolute values (left) and fractional contributions (right).

10 Modeling Source Contributions to Regional Impacts of Brown Carbon on California Climate

10.1 Introduction

The most recent report by the Intergovernmental Panel on Climate Change (IPCC) notes that global surface temperatures have already increased by 1.0 ± 0.2 ºC compared to pre-industrial levels [1]. The IPCC report authors conclude that immediate action is required to prevent global mean surface temperatures from increasing beyond 1.5 ºC because temperature increase beyond this level will result in even more severe negative consequences from global climate change. The most immediate path to mitigating climate change is to reduce emissions of Green House Gases (GHGs) such as CO_2, but reductions in Short-Lived Climate Forcers (SLCFs) such as black carbon (BC) and brown carbon (BrC) contained in airborne particles can also help to mitigate the effects of global warming [1].

Black carbon (BC) in the atmosphere refers to a collection of low-volatility compounds contained in airborne particles that were formed as products of incomplete combustion. BC absorbs solar radiation efficiently at wavelengths across the UV-visible-IR bands. Brown carbon (BrC) [2] in the atmosphere refers to carbonaceous material contained in airborne particles that absorbs preferentially at near-UV and visible wavelengths [3-8]. Biomass combustion is a major source of atmospheric BrC across the world [9], but BrC can also be formed by atmospheric chemical reactions [10, 11]. Global models have estimated that the direct radiative effects (DRE) of BrC range from +0.03 to +0.6 W m^{-2} [12-18] which is significant compared to the +1.33 to +2.03 W m^{-2} associated with CO_2. Therefore, BrC is an important component of the atmospheric radiation budget and it may be possible to partially mitigate climate change by reducing emissions of primary BrC or BrC precursors.

California is leading the efforts to mitigate climate change in the United States through a comprehensive set of science-based policies that seek to reduced GHG emissions by 80% relative to 1990 levels by the year 2050 (Executive Order S-3-05). Many of these policies will have immediate co-benefits via improved air quality [19] but the regional climate benefits of targeted BrC control programs in California have not been previously published. Multiple studies have analyzed the effects of BrC on climate change at the global scale, but these calculations have necessarily used simplified aerosol chemistry to represent the complex interactions between aerosols, clouds, and radiation. The global studies have also been forced to simplify their representation of emissions control programs which can distort important regional details in the air quality analysis [19, 20] and possibly the regional climate analysis.

The purpose of this study is to examine the effects of BrC on regional climate over California using a coupled Weather Research & Forecast model with Chemistry (WRF/Chem) that includes a detailed representation of particle mixing state combined with a highly resolved emissions inventory. Particles in model calculations are tracked in source-oriented categories so that their optical properties can be accurately calculated for use in radiative transfer calculations. Emissions to the model are based on a detailed library of measured particle size and composition profiles maintained by the University of California at Davis (UCD) combined with the emissions inventory maintained by the California Air Resources Board (CARB). WRF/Chem simulations were carried out for a one year period from Aug, 2014 to July, 2015

to examine the effect of BrC over an annual cycle. Predictions are compared to routine measurements of particle-phase and gas-phase pollutants across California and compared to detailed measurements made with an Aerodyne Aerosol Mass Spectrometer (AMS) and Fourier Transform Infrared spectroscopy (FTIR) during two intensive field campaigns in summer and winter. The effects of BrC absorption on temperature, humidity, precipitation, cloud cover, and concentrations of air pollutants are quantified over the simulated annual cycle. Conclusions are then drawn about the possible direct benefits to climate in California from the control of biomass combustion emissions that contain BrC.

10.2 Model Description

The Weather Research and Forecast model developed by the National Center for Atmospheric Research (NCAR) and the National Oceanic and Atmospheric Administration (NOAA) is widely used for meteorological simulations across the world. The Weather Research & Forecasting (WRF) model with chemistry (WRF/Chem) [21] allows for coupled simulations of atmospheric chemistry and meteorology so that feedbacks can be considered. WRF/Chem is developed and supported by an active user-community with over 700 peer-reviewed articles published using WRF/Chem calculations to date.

The standard WRF/Chem model simulates the combined direct, indirect, and semi-direct effects of aerosols on climate [21-23]. The source-oriented WRF/Chem model [24-26] enhances the base calculations by adopting a more sophisticated representation of airborne particles and hydrometers. The source-oriented WRF/Chem model tracks airborne particles emitted from different emissions sources separately through the atmosphere as they are modified by photochemical aging (condensation / evaporation of semi-volatile material). The source-oriented particles evolve in the atmosphere based on predicted rates of chemical reaction and gas-particle conversion. The operators used in the source-oriented WRF/Chem model are identical to those employed in the UCD/CIT source-oriented regional chemical transport model. Numerous previous studies have used the source-orientated representation of the particles for regional air quality simulations using off-line meteorology to understand how different sources contribute to air pollution in California [27-33]. The source-oriented WRF/Chem model combines the benefits of this approach with online meteorological feedbacks inherent in the standard WRF/Chem model.

In the present study, source-oriented calculations were added to WRF/Chem version 3.6 enabling the model to track 5-dimension (X, Z, Y, Source Types and Species) gas-phase variables and 6-dimensional (X, Z, Y, Size Bins, Source Types and Species) particle-phase and cloud-phase variables in each model grid cell. Aerosol activation was calculated at each time step based on the critical super-saturation for each source-oriented particle. Water uptake by aerosols and cloud droplets was treated as a dynamic process limited by the rate of diffusion of water vapor towards the condensing surface. Particle mass and number are conserved in all grid cells with and without clouds. Cloud droplets interact with other hydrometeors including ice, rain, snow, and graupel. Ice and wet cloud droplets can evaporate to release source-oriented particles under drying conditions. Rain, snow, and graupel can also partially evaporate but the source-oriented particles contained in these hydrometers are combined into an agglomerated particle under these conditions. Further details of the cloud microphysics are

described by Morrison, et al. [34] as modified by Lee, Chen, Kleeman, Zhang, DeNero and Joe [25].

Particle and hydrometer (cloud droplets, rain, cloud ice, snow, and graupel) chemical composition in the source-oriented WRF/Chem model was represented using 38 chemical species including BC, BrC, other organic matter, inorganic acids / bases, metals, SOA species, crustal material, and water. The aerosol size distribution was represented using eight particle size bins spanning the range from 0.01 – 10 μm (initial bin radii are 0.0275, 0.055, 0.1105, 0.221, 0.4415, 0.8835, 1.767 and 3.3535 μm). Moving sectional particle size bins were used during gas-particle conversion to conserve particle radius, mass, and number concentrations throughout all atmospheric processes. Cloud droplets and ice crystals were also represented with separate eight moving sectional bins initialized to the size of the aerosols at the time they activated. Cloud droplets grew to the size dictated by the condensation of water using a modified version of the Morrison microphysics scheme [34].

Model calculations were configured to separately track particles emitted from different sources if they had different initial hygroscopic properties. Coagulation combines particles over time and atmospheric chemical reactions transform particles such that the degree of internal mixing increases with age, but these processes are tracked over time rather than instantaneously combining particles into an internal mixture. The source-oriented approach avoids artificially mixing light absorbing black and brown carbon particles with materials such as sulfate that would encourage the formation of additional coatings. In the present study, particles emitted from diesel engines (high in BC), biomass combustion (high in BrC), and processes that burned fuel with high sulfur content (high in sulfate) were all treated as separate source-oriented categories. All other particle emissions were grouped into a fourth source-oriented category.

Gas-phase chemical reactions were represented using the SAPRC11 chemical mechanism [35]. The vapor pressures of acids and bases (HNO_3, HCl, H_2SO_4 and NH_3) above particles were predicted using the ISORROPIA thermodynamic solver [36]. Secondary organic aerosol (SOA) formation was calculated using the approach implemented in CMAQ version 4.7 [37]. More sophisticated representations of SOA formation were also explored following the work of Jathar et al. [38-40] but these methods did not yield realistic SOA predictions when applied to the emissions inventories prepared for 2014-15. Several mechanisms that could produce nitrogen-containing organic aerosol (NOOA) during fog events were investigated in the current study, but none of the investigated formation pathways produced significant concentrations under realistic ambient conditions. NOOA was therefore not included in the current simulations.

All gas-to-particle conversion processes were treated dynamically rather than assuming instantaneous equilibrium [41]. Transfer of inorganic acids and bases followed the ACPD method [42]. Further details of gas-particle partitioning, coagulation, advection, vertical mixing and deposition used in the model are provided by Zhang, DeNero, Joe, Lee, Chen, Michalakes and Kleeman [26].

The pollutant concentrations predicted by the source-oriented WRF/Chem model feed back into the radiative transfer calculations using the Goddard Space Flight Center (GSFC) shortwave [43] radiation module and a comparable GSFC longwave [43, 44] radiation module. The refractive index of each source-oriented particle was calculated using the volume averaging method [45] applied with a core and shell model [46]. A Mie routine was used to calculate the

combined optical properties of all particles, cloud droplets, and other hydrometers for use with radiative transfer calculations.

Particle phase components that absorb solar radiation in the current study included BC and BrC. All of the BrC was emitted by biomass combustion from routine sources such as residential wood combustion, agricultural burning, or other waste burning described in the emissions inventories provided by CARB. Additional BrC was contained in biomass burning from wildfires with emissions obtained from the Global Fire Emissions Database (GFED) [47]. Wildfire emissions were assigned the same particle size and composition distribution as routine biomass combustion. "Tar balls" (soot coated with organics found in wildfires) [48-50] were not included in source-oriented WRF/Chem model calculations. SOA species were assumed to have the same optical properties as primary organic aerosol (POA) from sources other than wood smoke with no absorbance of solar radiation. The nitrogen-containing organic aerosol (NOOA) that was observed in field measurements was not included in simulations because the formation mechanism for this material is unknown.

The optical properties of BrC in source-oriented WRF/Chem calculations were based on measurements from the field campaign described in the current report. Figure 10-1 illustrates the imaginary component of the BrC refractive index while Table 10-1 summarizes both the real and imaginary components of the BrC refractive index for the different wavelengths used in radiative transfer calculations. The imaginary component of BrC is less than 0.055 at all wavelengths between 0.2 to 62.5 μm, with the greatest absorbance at smaller wavelengths. The measurements on which the optical properties are based were made at 405 nm, 532 nm, and 870 nm. Imaginary refractive indices (k) below, between, and above these wavelengths were determined by extrapolation based on the observed wavelength dependence (w) using the measurements at 405 nm as the reference wavelength. The wavelength-dependent k are therefore: $k_\lambda = k_{405nm} \cdot 10^{(-w \cdot \lambda/405)}$, where $k_{405nm} = 0.03$ and $w = 0.82$. This extrapolation into the UV and near-UV is likely reasonable, based on measurements of water-soluble and water-insoluble BrC at shorter wavelengths (Zhang et al., 2013). Above 2 microns the k values are likely underestimated by this extrapolation, as organic compounds have absorption features in the infrared. However, absorption by aerosols in the infrared has negligible influence on radiative forcing owing to the long wavelength of light. Thus, this likely underestimation at infrared wavelengths will have no significant impact on the results presented here.

10.3 Model Application

Two regional simulations were conducted from August 2014 to July, 2015 to quantify the effect of BrC over California. The first simulation (**with BrC**) considered the absorbance of BrC using the imaginary component of the refractive index illustrated in Figure 10-1 (based on measurements described in Chapters 3, 4, and 5), while the second simulation (**without BrC**) removed the absorbance of the BrC emissions by setting the imaginary component of the refractive index to zero. The difference between the results predicted in these simulations quantifies the effects of BrC on regional climate in California. The emissions, boundary conditions, and chemical mechanisms were identical in both simulations.

10.3.1 Domain Configuration

The source-oriented WRF/Chem model was configured using double-nested domains with the first domain divided into 38 × 38 grid cells with 36-km horizontal resolution and the second domain divided into 64 × 73 grid cells with 12-km resolution. A third domain with 40 × 40 grid cells and 4-km resolution was used for one month over Fresno (Dec, 2014-Jan, 2015) and one month over Fontana (Jul, 2015) to enable a more detailed comparison with measurements made during the intensive field campaign carried out during these two months. Thirty one vertical layers from ground level to the top pressure of 100 hPa were used for all domains.

10.3.2 Meteorological Initial and Boundary Conditions

Meteorological initial and boundary conditions were obtained from the National Centers for Environmental Prediction (NCEP) Final (FNL) Operational Global Analysis dataset, which has a spatial resolution of 1° × 1° and a temporal resolution of 6h. Simulations were directed without data assimilation or nudging to minimize the artificial forcing so that the effects of BrC could be more clearly observed.

10.3.3 Emissions

Biogenic emissions were generated using MEGAN 2.1 [51] and wildfire emissions were generated using the Global Fire Emissions Database (GFED) [47]. Anthropogenic emissions were generated based on the emission inventory supplied by California Air Resources Board (CARB). Biomass combustion emissions from GFED (wildfires) and CARB (residential wood combustion and waste burning) both contained BrC. Initial and boundary conditions for gas-phase and particle-phase pollutants were obtained from MOZART simulations [52]. The organic carbon supplied by the boundary conditions was assumed to not contain BrC in order to focus the model simulations on the effects of BrC emitted in California.

Figure 10-2 illustrates annual-average particulate matter emissions over California for non-wildfire sources in the current study. Emissions of elemental carbon (BC) follow patterns of traffic density due to the dominance of diesel engines and off-road diesel equipment (associated with road maintenance) for this species. Emissions of organic carbon (OC) follow patterns of population density due to the influence of food cooking emissions.

Figure 10-2 shows that BC and BrC have significantly different emissions patterns. The highest BrC emissions occur in northern California associated with waste burning (possibly related to fire suppression activities) and residential wood combustion for winter heating. Emissions of BrC in the San Joaquin Valley cities of Modesto, Fresno, and Bakersfield are greatly reduced relative to their levels in the year 2000 due to the limits on residential wood combustion adopted after the year 2003. The regional ratio of BrC/OC emissions is ~15% but this value varies strongly with location and season. In contrast to BrC, the highest BC emissions occur in Los Angeles and the San Francisco Bay Area with less intense peaks observed in smaller cities including Sacramento, Fresno, Bakersfield, and San Diego. BC emissions are also apparent along major transportation corridors. The chemical speciation profile used for biomass combustion in the current study [53, 54] contains only minor amounts of BC and so biomass combustion emissions do not dominate BC. Diesel particle filters have greatly reduced particulate matter emissions from on-road diesel vehicles after 2007, but diesel

engines still made the largest contribution to BC emissions during the current study period (2014-15).

Figure 10-3 shows wildfire EC and BrC emissions over California averaged from Sept 13 – Oct 9, 2014 when the King wildfire burned 395 km^2 of vegetation in El Dorado County. EC and BrC emissions rates during this single extreme event were 5-7 orders of magnitude higher than routine emissions rates shown in Figure 10-2. A total of 25 wildfires burned 1,946 km^2 of vegetation in Northern California and central California from July 1 – December 31, 2014. The average fire size was 83 km^2 and the average duration was 22 days. Even accounting for the smaller emissions area and time duration associated with wildfires vs. residential wood combustion, wildfires dominated total BrC emissions in California in 2014-15.

10.4 Results and Discussion

10.4.1 Comparison to Measurements

Figures 10-4 and 10-5 show the predicted and measured time series of daily $PM_{1.0}$ mass concentration at Fontana (July 3-27, 2015) and Fresno (Dec 18, 2014 – Jan 13, 2015) for the model configured with BrC. Model predictions for this comparison are based on results using a 4-km nest over the study site. Predicted $PM_{1.0}$ mass concentrations are in reasonable agreement with measurements at Fontana (Figure 10-4) with the exception that the emissions inventories do not represent the increase in activity during the July 4 holiday. Predicted $PM_{1.0}$ mass concentrations are in good agreement with measurements at the start of the winter intensive sampling period at Fresno (Figure 10-5), but the model does not accurately predict day to day variation during fog events (low fog days 25 Dec, 2014 to 5 Jan, 2015) and high fog days (7 Jan to 13 Jan, 2015). This difficulty capturing day-to-day variability in fog events is consistent with past studies using WRF/Chem [55]. Neither comparison site was affected by wildfires.

Figure 10-6 illustrates the contribution from BrC to $PM_{1.0}$ at Fresno averaged from Dec 18, 2014 – Jan 13, 2015. Figure 10-6a illustrates the biomass burning contributions to $PM_{1.0}$ mass calculated using Positive Matrix Factorization (PMF) analysis of FTIR measurements (Chapter 3). Figure 10-6b shows the source-oriented WRF/Chem model prediction for the biomass burning source contribution to $PM_{1.0}$. Figure 10-6c illustrates the BrC contributions to $PM_{1.0}$ organic aerosol (OA) calculated using PMF analysis of AMS measurements (Chapter 3). Figure 10-6d shows the source-oriented WRF/Chem model prediction for BrC contributions to OA. In both the upper and lower panels of Figure10- 6, the source-oriented WRF/Chem predictions are in reasonable agreement with the measured features of the airborne particulate matter. BrC contributes approximately 10-17% to total $PM_{1.0}$ mass and 25-26% to $PM_{1.0}$ organic aerosol during the winter measurements at Fresno. BrC concentrations at Fontana during the summer were both measured and predicted to be very low (not shown). These results point to the importance of biomass burning as a source of BrC and suggest that the type of SOA that forms in the region surrounding Los Angeles during the summer does not contain significant amounts of BrC.

10.4.2 Surface Concentrations

Figure 10-7 shows the annual-average surface concentration of different $PM_{2.5}$ species predicted using the source-oriented WRF/Chem model with BrC absorption included. Surface

$PM_{2.5}$ mass concentrations are predicted to be highest in Los Angeles and San Diego with maximum annual-average concentrations of approximately 6 μg m^{-3}. This concentration falls slightly below the typical measured value in the region (~10 μg m^{-3}) primarily because the WRF/Chem model was operated without data assimilation or nudging towards measured wind speed. Even when surface observations are assimilated, WRF and WRF/Chem over-predict wind speed during stagnation events which leads to a systematic bias of lower concentrations during pollution episodes [31]. The usual remedy for this problem is a 50% enhancement of the friction velocity (u*) causing a reduction in wind velocity [31]. These techniques were not employed in the current study in order to study the maximum unconstrained feedbacks between BrC and local meteorology. Enhanced mixing caused by higher wind speeds in the surface layer should not greatly bias the column-averaged concentration of BrC and EC that drives radiative feedback effects.

The use of 12-km grid resolution for annual-average simulations may be an additional factor that lowered predicted $PM_{2.5}$ mass concentrations. Larger grid cells increase the effects of artificial dilution for emissions in smaller cities with size comparable to the grid cell dimensions. Typical surface air quality analysis in California is carried out using 4-km resolution, while climate studies typically use coarser resolution. The 12-km resolution used for annual-average simulations in the current study is well suited for regional climate analysis even though it may not be optimal for surface air quality modeling.

Figure 10-7 shows that primary $PM_{2.5}$ EC, OC, and BrC all make significant contributions to $PM_{2.5}$ mass with spatial patterns that follow the emissions trends illustrated in Figures 10-2 and 10-3. $PM_{2.5}$ EC and OC concentrations are predicted to be highest in Southern California, while BrC concentrations peak in the region with highest concentrations in Northern California. Nitrate (NO_3^-) is highest in Los Angeles due to the formation of sodium nitrate ($NaNO_3$) from the conversion of fresh sea salt (NaCl). Additional nitrate forms in the San Joaquin Valley (SJV) as ammonium nitrate (NH_4NO_3). Nitrate concentrations are lower than the values typically measured in the SJV because NOx concentrations are under-predicted. Recent studies suggest the possibility of NOx emissions from soils [56] but the scientific debate around this topic continues. Soil NOx emissions were not included in the current study. Maximum ammonium (NH^+) concentrations occur at the location of maximum sulfate (SO_4^{2-}) associated with a point source between San Francisco and Sacramento, California.

10.4.3 Column Totals

Figure 10-8 shows the predicted column-total (surface to ~16 km) of elemental carbon (EC), organic carbon (OC), organic brown carbon (BrC), and cloud fraction (Cldfra) averaged from August 2014 – July 2015. Column total EC and BrC concentrations are dominated by the King wildfire that occurred in Placer County in September and October, 2014. Column-total OC concentrations are dominated by routine urban and regional sources generally following the pattern of urban development in California. Urban signatures for EC and POM are also present over Los Angeles with more muted values in smaller cities, but these concentrations are overwhelmed by the effects of the large King wildfire. Cloud fractions are highest over the ocean and over the Sierra Nevada Mountains.

Figure 10-9 shows column-total aerosol extinction associated with absorption and scattering averaged from August, 2014 – July, 2015. Absorption contributions to

approximately 39% of the total extinction at 475nm and 36% of extinction at 525nm. Maximum absorption occurs in the smoke plume of the King Wildfire (see Figure 10-3 for location), but values of absorption in the San Joaquin Valley and Los Angeles are close to this regional maximum. Scattering contributions to extinction are highest in Northern California with peak values once again occurring over the King Wildfire.

10.4.4 Source Contributions to Absorption

Figure 10-10 shows source contributions to column-total scattering and absorption at 475 nm and 525 nm averaged from August 2014-July 2015. The results shown in panels (a-h) of Figure 10-10 shows that diesel engines dominate regional column-total absorption at both 475nm and 525nm. Wood smoke contributions to column-total absorption through the effects of BrC are an order of magnitude smaller than diesel engine contributions through the effects of EC. Wildfires dominate the wood smoke absorption but the relatively short duration of wildfire events make them less consequential than routine emissions from diesel engines.

Figure 10-11 shows the meridionally-averaged elemental carbon (EC) and organic brown carbon (BrC) from July 2014 – August 2015, and meridionally-averaged BrC from September 13 – October 9, 2014. The latter results correspond to the time period when the King Fire was active in Placer County. Annual-average EC concentrations are highest at ground level due to emissions from anthropogenic sources. Annual-average BrC concentrations are highest in the upper atmosphere due to wildfire contributions that are orders of magnitude larger than surface contributions from residential wood combustion. Wildfire plumes were injected at the top of the model domain at a height of approximately 15 km in the current simulations. Typical wildfire plumes rise to 6-10 km in the atmosphere depending on the intensity of the fire and the local meteorological conditions [57]. Simulations are being revised to inject wildfire emissions at a height of 5km in the calculation, but the overall radiative effect on surface meteorology should not change strongly due to this update. BrC concentrations in the upper atmosphere are an order of magnitude higher during the 27-day wildfire event.

10.4.5 BrC Climate Impact

Figure 10-12 illustrates differences (from with BrC absorption to without BrC absorption) for meteorological variables and ozone concentrations averaged from August 2014 – July 2015. Temperature at 2-m (T-2m) and at 20-m increased by ~0.005 K due to the influence of BrC. The maximum surface temperature increase occurs over northern California where BrC concentrations are highest. The increase in T-2m is higher (0.006 K) over land in comparison to ocean (0.003). Surface temperature is mainly influenced by BrC in the lower levels of the atmosphere, with smaller effects of BrC in the upper atmosphere. It is possible that BrC from wildfires could interact with clouds to cause heating and evaporation of cloud droplets, but wildfire events typically occur in hot, dry, and windy conditions that do not have typically have significant cloud cover.

Figure 10-12 shows that top of atmosphere (TOA) forcing increased by ~0.277 (W m^{-2}) due to BrC absorption. Both outgoing short wave flux (+0.228 W m^{-2}) and long wave flux (+0.049 W m^{-2}) increased at the top of the atmosphere due to BrC absorption. The short wave flux responds more strongly to BrC in comparison to long wave flux because the refractive indices of BrC are higher at shorter wavelengths (Table 10-1).

Figure 10-12 also shows the net short wave flux (GSW) and downward long wave flux (GLW) at the ground. GSW (+0.188 W m^{-2}) increased while GLW (-0.008 W m^{-2}) decreased due to the effects of BrC. Cloud fraction over land (cldfra), water mixing ratio (Qvapor), and total precipitation increased slightly due to BrC absorption. Cloud water mixing ratio (Qcloud) decreases in response to the increased precipitation. The reduction in cloud water mixing ratio increased net short wave flux by 0.278 W m^{-2} over ocean and 0.132 W m^{-2} over land. Similarly, TOA increased by 0.329 W m^{-2} and 0.244 W m^{-2} over ocean and land respectively.

Figure 10-12 shows BrC absorption slightly decreases regional average ozone (O_3) concentrations, but O_3 slightly increases over Northern California where temperature increases.

Figures 10-13 and 10-14 show the difference (with – without BrC absorption) of temperature (T), Qvapor, relative humidity and O_3 averaged zonally and meridionally for the first 4km of the atmosphere. The results shown in Figures 10-13 and 10-14 show that air temperature warms near the surface due to BrC absorption. Water vapor content and RH are higher in most of the locations between 0.5 to 1.5 km altitude due to the water evaporated from clouds due to the effects of warmer temperatures caused by BrC absorption. Ozone increases slightly in regions where NOx and VOC concentrations favor increased ozone formation rates at increased temperature [58].

10.5 Conclusions

A source-oriented WRF/Chem model was used to simulate the effects of BrC over California from August 2014 – July 2015. An evaluation of model performance shows that the source-oriented WRF/Chem predictions are in reasonable agreement with surface measurements. Comparisons to the results from BrC measurements during intensive field campaigns also show satisfactory model performance, although some forms of nitrogen-containing BrC formed during fog events could not be predicted because the mechanisms are not known.

Total BrC emissions were dominated by wildfires in Northern California during the study period, with more minor BrC contributions from residential wood combustion during the winter season. Wildfire BrC dominated total column BrC absorption with the majority of the wildfire BrC located in the upper atmosphere above an elevation of 5km. Concentrations of residential wood combustion BrC were highest near the surface.

Total-column aerosol absorption over California was dominated by elemental carbon emitted from diesel engines. The combined effects of diesel engines and wildfires produced a maximum total column absorption over Placer County in Northern California, but regional absorption from diesel engines was also significant over the entire San Joaquin Valley and Los Angeles.

Absorption by BrC in California (including the effect of wildfires) results in a net regional forcing at the top of the atmosphere of +0.28 W m^{-2}. This value is consistent with previous estimates of BrC radiative forcing in global studies. The total effect of absorption by BrC in California (including the effect of wildfires) results in a temperature increase of approximately +0.005 K.

10.6 References

1. IPCC *Climate Change 2014: Synthesis Report. Contribution of Working Groups I, II and III to the Fifth Assessment Report of the Intergovernmental Panel on Climate Change*; IPCC: Geneva, Switzerland, 2014.
2. Laskin, A.; Laskin, J.; Nizkorodov, S. A., Chemistry of Atmospheric Brown Carbon. *Chemical Reviews* **2015,** *115*, (10), 4335-4382.
3. Kirchstetter, T. W.; Novakov, T.; Hobbs, P. V., Evidence that the spectral dependence of light absorption by aerosols is affected by organic carbon. *Journal of Geophysical Research-Atmospheres* **2004,** *109*, (D21).
4. Kirchstetter, T. W.; Thatcher, T. L., Contribution of organic carbon to wood smoke particulate matter absorption of solar radiation. *Atmospheric Chemistry and Physics* **2012,** *12*, (14), 6067-6072.
5. Alexander, D. T. L.; Crozier, P. A.; Anderson, J. R., Brown carbon spheres in East Asian outflow and their optical properties. *Science* **2008,** *321*, (5890), 833-836.
6. Yang, M.; Howell, S. G.; Zhuang, J.; Huebert, B. J., Attribution of aerosol light absorption to black carbon, brown carbon, and dust in China - interpretations of atmospheric measurements during EAST-AIRE. *Atmospheric Chemistry and Physics* **2009,** *9*, (6), 2035-2050.
7. Hecobian, A.; Zhang, X.; Zheng, M.; Frank, N.; Edgerton, E. S.; Weber, R. J., Water-Soluble Organic Aerosol material and the light-absorption characteristics of aqueous extracts measured over the Southeastern United States. *Atmospheric Chemistry and Physics* **2010,** *10*, (13), 5965-5977.
8. Arola, A.; Schuster, G.; Myhre, G.; Kazadzis, S.; Dey, S.; Tripathi, S. N., Inferring absorbing organic carbon content from AERONET data. *Atmospheric Chemistry and Physics* **2011,** *11*, (1), 215-225.
9. Ramanathan, V.; Li, F.; Ramana, M. V.; Praveen, P. S.; Kim, D.; Corrigan, C. E.; Nguyen, H.; Stone, E. A.; Schauer, J. J.; Carmichael, G. R.; Adhikary, B.; Yoon, S. C., Atmospheric brown clouds: Hemispherical and regional variations in long-range transport, absorption, and radiative forcing. *Journal of Geophysical Research-Atmospheres* **2007,** *112*, (D22).
10. Nguyen, T. B.; Lee, P. B.; Updyke, K. M.; Bones, D. L.; Laskin, J.; Laskin, A.; Nizkorodov, S. A., Formation of nitrogen- and sulfur-containing light-absorbing compounds accelerated by evaporation of water from secondary organic aerosols. *Journal of Geophysical Research-Atmospheres* **2012,** *117*.
11. Updyke, K. M.; Nguyen, T. B.; Nizkorodov, S. A., Formation of brown carbon via reactions of ammonia with secondary organic aerosols from biogenic and anthropogenic precursors. *Atmospheric Environment* **2012,** *63*, 22-31.
12. Jo, D. S.; Park, R. J.; Lee, S.; Kim, S.-W.; Zhang, X., A global simulation of brown carbon: implications for photochemistry and direct radiative effect. *Atmospheric Chemistry and Physics* **2016,** *16*, (5), 3413-3432.
13. Park, R. J.; Kim, M. J.; Jeong, J. I.; Youn, D.; Kim, S., A contribution of brown carbon aerosol to the aerosol light absorption and its radiative forcing in East Asia. *Atmospheric Environment* **2010,** *44*, (11), 1414-1421.
14. Feng, Y.; Ramanathan, V.; Kotamarthi, V. R., Brown carbon: a significant atmospheric absorber of solar radiation? *Atmospheric Chemistry and Physics* **2013,** *13*, (17), 8607-8621.
15. Lin, G.; Penner, J. E.; Flanner, M. G.; Sillman, S.; Xu, L.; Zhou, C., Radiative forcing of organic aerosol in the atmosphere and on snow: Effects of SOA and brown carbon. *Journal of Geophysical Research-Atmospheres* **2014,** *119*, (12), 7453-7476.
16. Saleh, R.; Marks, M.; Heo, J.; Adams, P. J.; Donahue, N. M.; Robinson, A. L., Contribution of brown carbon and lensing to the direct radiative effect of carbonaceous aerosols

from biomass and biofuel burning emissions. *Journal of Geophysical Research-Atmospheres* **2015,** *120*, (19), 10285-10296.
17. Wang, X.; Heald, C. L.; Liu, J.; Weber, R. J.; Campuzano-Jost, P.; Jimenez, J. L.; Schwarz, J. P.; Perring, A. E., Exploring the observational constraints on the simulation of brown carbon. *Atmospheric Chemistry and Physics* **2018,** *18*, (2), 635-653.
18. Wang, X.; Heald, C. L.; Ridley, D. A.; Schwarz, J. P.; Spackman, J. R.; Perring, A. E.; Coe, H.; Liu, D.; Clarke, A. D., Exploiting simultaneous observational constraints on mass and absorption to estimate the global direct radiative forcing of black carbon and brown carbon. *Atmospheric Chemistry and Physics* **2014,** *14*, (20), 10989-11010.
19. Zapata, C. B.; Yang, C.; Yeh, S.; Ogden, J.; Kleeman, M. J., Low-carbon energy generates public health savings in California. *Atmospheric Chemistry and Physics* **2018,** *18*, (7), 4817-4830.
20. Zapata, C.; Yang, C.; Ogden, J.; Kleeman, M., Estimating Criteria Pollutant Emissions Using the California Regional Multisector Air Quality Emissions (CA-REMARQUE) Model version 1.0. *Geoscientific Model Development* **2017,** *in review*.
21. Grell, G. A.; Peckham, S. E.; Schmitz, R.; McKeen, S. A.; Frost, G.; Skamarock, W. C.; Eder, B., Fully coupled "online" chemistry within the WRF model. *Atmospheric Environment* **2005,** *39*, (37), 6957-6975.
22. Chapman, E. G.; Gustafson, W. I., Jr.; Easter, R. C.; Barnard, J. C.; Ghan, S. J.; Pekour, M. S.; Fast, J. D., Coupling aerosol-cloud-radiative processes in the WRF-Chem model: Investigating the radiative impact of elevated point sources. *Atmospheric Chemistry and Physics* **2009,** *9*, (3), 945-964.
23. Fast, J. D.; Gustafson, W. I., Jr.; Easter, R. C.; Zaveri, R. A.; Barnard, J. C.; Chapman, E. G.; Grell, G. A.; Peckham, S. E., Evolution of ozone, particulates, and aerosol direct radiative forcing in the vicinity of Houston using a fully coupled meteorology-chemistry-aerosol model. *Journal of Geophysical Research-Atmospheres* **2006,** *111*, (D21).
24. Joe, D. K.; Zhang, H.; DeNero, S. P.; Lee, H.-H.; Chen, S.-H.; McDonald, B. C.; Harley, R. A.; Kleeman, M. J., Implementation of a high-resolution Source-Oriented WRF/Chem model at the Port of Oakland. *Atmospheric Environment* **2014,** *82*, 351-363.
25. Lee, H.-H.; Chen, S.-H.; Kleeman, M. J.; Zhang, H.; DeNero, S. P.; Joe, D. K., Implementation of warm-cloud processes in a source- oriented WRF/Chem model to study the effect of aerosol mixing state on fog formation in the Central Valley of California. *Atmospheric Chemistry and Physics* **2016,** *16*, (13), 8353-8374.
26. Zhang, H.; DeNero, S. P.; Joe, D. K.; Lee, H. H.; Chen, S. H.; Michalakes, J.; Kleeman, M. J., Development of a source oriented version of the WRF/Chem model and its application to the California regional PM10/PM2.5 air quality study. *Atmospheric Chemistry and Physics* **2014,** *14*, (1), 485-503.
27. Kleeman, M. J.; Cass, G. R., A 3D Eulerian Source-Oriented Model for an Externally Mixed Aerosol. *Environmental Science & Technology* **2001,** *35*, (24), 4834-4848.
28. Mahmud, A.; Hixson, M.; Hu, J.; Zhao, Z.; Chen, S. H.; Kleeman, M. J., Climate impact on airborne particulate matter concentrations in California using seven year analysis periods. *Atmospheric Chemistry and Physics* **2010,** *10*, (22), 11097-11114.
29. Ying, Q.; Fraser, M. P.; Griffin, R. J.; Chen, J.; Kleeman, M. J., Verification of a source-oriented externally mixed air quality model during a severe photochemical smog episode. *Atmospheric Environment* **2007,** *41*, (7), 1521-1538.
30. Hu, J.; Zhang, H.; Chen, S.; Ying, Q.; Wiedinmyer, C.; Vandenberghe, F.; Kleeman, M. J., Identifying PM2.5 and PM0.1 Sources for Epidemiological Studies in California. *Environmental Science & Technology* **2014,** *48*, (9), 4980-4990.

31. Hu, J.; Zhang, H.; Chen, S.-H.; Wiedinmyer, C.; Vandenberghe, F.; Ying, Q.; Kleeman, M. J., Predicting Primary PM2.5 and PM0.1 Trace Composition for Epidemiological Studies in California. *Environmental Science & Technology* **2014,** *48*, (9), 4971-4979.
32. Hu, J.; Zhang, H.; Ying, Q.; Chen, S. H.; Vandenberghe, F.; Kleeman, M. J., Long-term particulate matter modeling for health effect studies in California - Part 1: Model performance on temporal and spatial variations. *Atmospheric Chemistry and Physics* **2015,** *15*, (6), 3445-3461.
33. Hu, J. L.; Jathar, S.; Zhang, H. L.; Ying, Q.; Chen, S. H.; Cappa, C. D.; Kleeman, M. J., Long-term particulate matter modeling for health effect studies in California - Part 2: Concentrations and sources of ultrafine organic aerosols. *Atmospheric Chemistry and Physics* **2017,** *17*, (8), 5379-5391.
34. Morrison, H.; Thompson, G.; Tatarskii, V., Impact of Cloud Microphysics on the Development of Trailing Stratiform Precipitation in a Simulated Squall Line: Comparison of One- and Two-Moment Schemes. *Monthly Weather Review* **2009,** *137*, (3), 991-1007.
35. Carter, W. P. L.; Heo, G., Development of revised SAPRC aromatics mechanisms. *Atmospheric Environment* **2013,** *77*, 404-414.
36. Nenes, A.; Pandis, S. N.; Pilinis, C., ISORROPIA: A new thermodynamic equilibrium model for multiphase multicomponent inorganic aerosols. *Aquatic Geochemistry* **1998,** *4*, (1), 123-152.
37. Carlton, A. G.; Bhave, P. V.; Napelenok, S. L.; Edney, E. D.; Sarwar, G.; Pinder, R. W.; Pouliot, G. A.; Houyoux, M., Model Representation of Secondary Organic Aerosol in CMAQv4.7. *Environmental Science & Technology* **2010,** *44*, (22), 8553-8560.
38. Cappa, C. D.; Jathar, S. H.; Kleeman, M. J.; Docherty, K. S.; Jimenez, J. L.; Seinfeld, J. H.; Wexler, A. S., Simulating secondary organic aerosol in a regional air quality model using the statistical oxidation model - Part 2: Assessing the influence of vapor wall losses. *Atmospheric Chemistry and Physics* **2016,** *16*, (5), 3041-3059.
39. Jathar, S. H.; Cappa, C. D.; Wexler, A. S.; Seinfeld, J. H.; Kleeman, M. J., Simulating secondary organic aerosol in a regional air quality model using the statistical oxidation model - Part 1: Assessing the influence of constrained multi-generational ageing. *Atmospheric Chemistry and Physics* **2016,** *16*, (4), 2309-2322.
40. Jathar, S. H.; Cappa, C. D.; Wexler, A. S.; Seinfeld, J. H.; Kleeman, M. J., Multi-generational oxidation model to simulate secondary organic aerosol in a 3-D air quality model. *Geoscientific Model Development* **2015,** *8*, (8), 2553-2567.
41. Wexler, A. S.; Seinfeld, J. H., THE DISTRIBUTION OF AMMONIUM-SALTS AMONG A SIZE AND COMPOSITION DISPERSED AEROSOL. *Atmospheric Environment Part a-General Topics* **1990,** *24*, (5), 1231-1246.
42. Jacobson, M. Z., A solution to the problem of nonequilibrium acid/base gas-particle transfer at long time step. *Aerosol Sci. Technol.* **2005,** *39*, (2), 92-103.
43. Chou, M. D.; Suarez, M. J. *An efficient thermal infrared radiation parameterization for use in general circulation models.*; NASA, Laboratory for Atmospheres, NASA/Goddard Space Flight Center, Greenbelt, MD 1994.
44. Chen, S.-H.; Wang, S.-H.; Waylonis, M., Modification of Saharan air layer and environmental shear over the eastern Atlantic Ocean by dust-radiation effects. *Journal of Geophysical Research-Atmospheres* **2010,** *115*.
45. Stelson, A. W., URBAN AEROSOL REFRACTIVE-INDEX PREDICTION BY PARTIAL MOLAR REFRACTION APPROACH. *Environmental Science & Technology* **1990,** *24*, (11), 1676-1679.
46. Toon, O. B.; Ackerman, T. P., ALGORITHMS FOR THE CALCULATION OF SCATTERING BY STRATIFIED SPHERES. *Applied Optics* **1981,** *20*, (20), 3657-3660.
47. Global Fire Emissions Database. https://www.globalfiredata.org/

48. Li, J.; Posfai, M.; Hobbs, P. V.; Buseck, P. R., Individual aerosol particles from biomass burning in southern Africa: 2, Compositions and aging of inorganic particles. *Journal of Geophysical Research-Atmospheres* **2003,** *108*, (D13).
49. Posfai, M.; Gelencser, A.; Simonics, R.; Arato, K.; Li, J.; Hobbs, P. V.; Buseck, P. R., Atmospheric tar balls: Particles from biomass and biofuel burning. *Journal of Geophysical Research-Atmospheres* **2004,** *109*, (D6).
50. Posfai, M.; Simonics, R.; Li, J.; Hobbs, P. V.; Buseck, P. R., Individual aerosol particles from biomass burning in southern Africa: 1. Compositions and size distributions of carbonaceous particles. *Journal of Geophysical Research-Atmospheres* **2003,** *108*, (D13).
51. Guenther, A. B.; Jiang, X.; Heald, C. L.; Sakulyanontvittaya, T.; Duhl, T.; Emmons, L. K.; Wang, X., The Model of Emissions of Gases and Aerosols from Nature version 2.1 (MEGAN2.1): an extended and updated framework for modeling biogenic emissions. *Geoscientific Model Development* **2012,** *5*, (6), 1471-1492.
52. Hauglustaine, D. A.; Brasseur, G. P.; Walters, S.; Rasch, P. J.; Muller, J. F.; Emmons, L. K.; Carroll, C. A., MOZART, a global chemical transport model for ozone and related chemical tracers 2. Model results and evaluation. *Journal of Geophysical Research-Atmospheres* **1998,** *103*, (D21), 28291-28335.
53. Hays, M. D.; Fine, P. M.; Geron, C. D.; Kleeman, M. J.; Gullett, B. K., Open burning of agricultural biomass: Physical and chemical properties of particle-phase emissions. *Atmospheric Environment* **2005,** *39*, (36), 6747-6764.
54. Kleeman, M. J.; Robert, M. A.; Riddle, S. G.; Fine, P. M.; Hays, M. D.; Schauer, J. J.; Hannigan, M. P., Size distribution of trace organic species emitted from biomass combustion and meat charbroiling. *Atmospheric Environment* **2008,** *42*, (13), 3059-3075.
55. Chen, C. L.; Chen, S.; Russell, L. M.; Liu, J.; Price, D. J.; Betha, R.; Zhang, Q., Organic aerosol particle chemical properties associated with residential burning and fog in wintertime San Joaquin Valley (Fresno) and with vehicle and firework emissions in summertime South Coast Air Basin (Fontana). *Journal of Geophysical Research: Atmospheres* **2018,** *In Press*.
56. Almaraz, M.; Bai, E.; Wang, C.; Trousdell, J.; Conley, S.; Faloona, I.; Houlton, B. Z., Agriculture is a major source of NOx pollution in California. *Science Advances* **2018,** *4*, (1).
57. Paugam, R.; Wooster, M.; Freitas, S.; Martin, M. V., A review of approaches to estimate wildfire plume injection height within large-scale atmospheric chemical transport models. *Atmospheric Chemistry and Physics* **2016,** *16*, (2), 907-925.
58. Rasmussen, D. J.; Hu, J.; Mahmud, A.; Kleeman, M. J., The Ozone-Climate Penalty: Past, Present, and Future. *Environmental Science & Technology* **2013,** *47*, (24), 14258-14266.

10.7 Tables

Table 10-1. Spectral refractive indices of organic brown carbon used in the study.

Wavelength (μm)	Organic brown carbon	
	Real	Imag
0.2000	1.5	0.0535
0.2350	1.5	0.0469
0.2525	1.5	0.0442
0.2875	1.5	0.0397
0.3025	1.5	0.0381
0.3150	1.5	0.0369
0.3625	1.5	0.0329
0.5500	1.5	0.0233
0.9600	1.5	0.0148
1.7450	1.5	0.0091
4.0820	1.5	0.0045
6.1350	1.5	0.0032
6.3290	1.5	0.0031
7.6920	1.5	0.0027
8.6580	1.5	0.0024
9.6150	1.5	0.0022
11.2360	1.5	0.0020
14.7060	1.5	0.0016
17.2410	1.5	0.0014
22.7270	1.5	0.0011
62.5000	1.5	0.0005

10.8 Figures

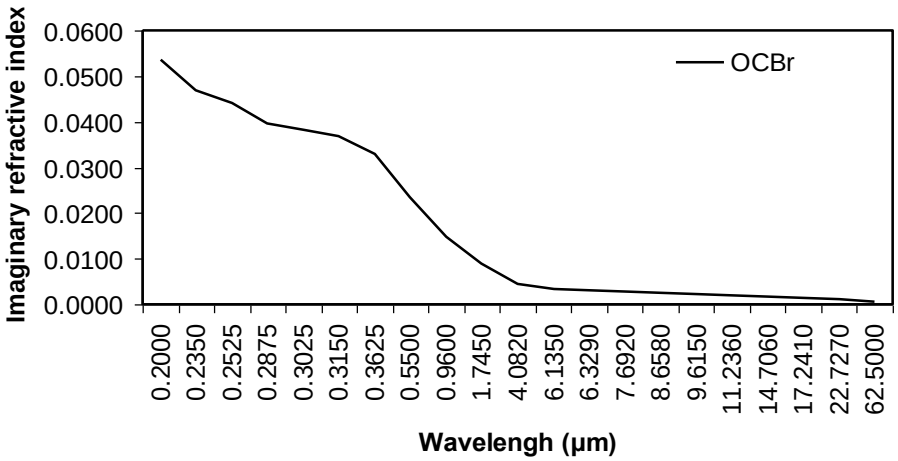

Figure 10-1. Imaginary refractive indices organic brown carbon (BrC) based on field measurements at Fresno. Values below 0.405 µm and above 0.87 µm are extrapolated.

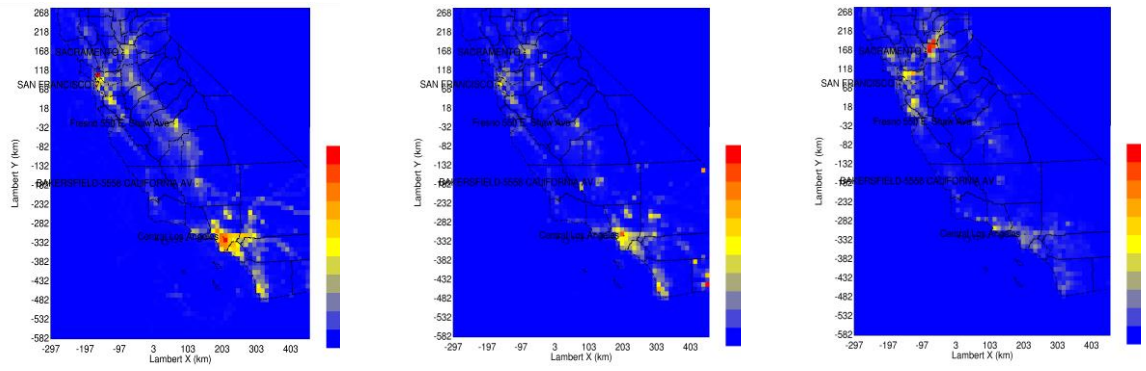

(a) EC (µg/m^2/s) (5.97E-04) (b) OC (µg/m^2/s) (1.93E-03) (c) BrC (µg/m^2/s) (2.82E-04)

Figure 10-2. Annual average emissions of PM_{10} elemental carbon (EC), organic carbon (OC) and organic brown carbon (BrC) from non-wildfire sources. May include waste burning associated with fire suppression activities. Values in parenthesis are the regional average over land. Units are µg m^{-2} min^{-1}.

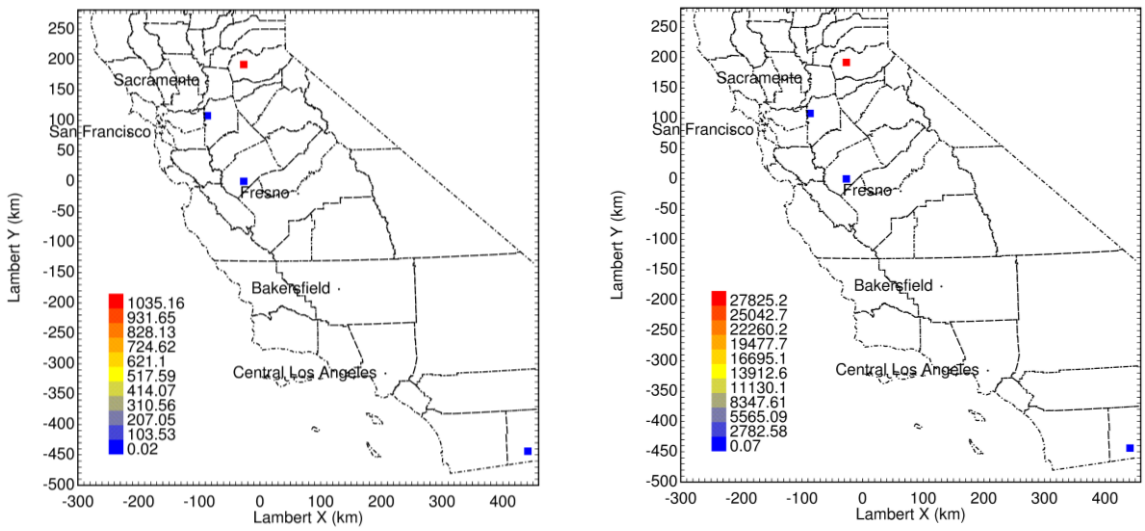

(a) Wildfire EC (µg m^{-2}) (258.9)

(b) Wildfire BrC (µg m^{-2}) (6956)

Figure 10-3. Emissions of PM_{10} elemental carbon (EC) and organic brown carbon (BrC) from wildfire sources from Sept 13 – Oct 9, 2014. Color is present for the grid cells that have wildfire emissions. The wildfires are sparse and so only a few grid cells have color. Values in parenthesis are the regional average over land. Units are µg m^{-2} min^{-1}.

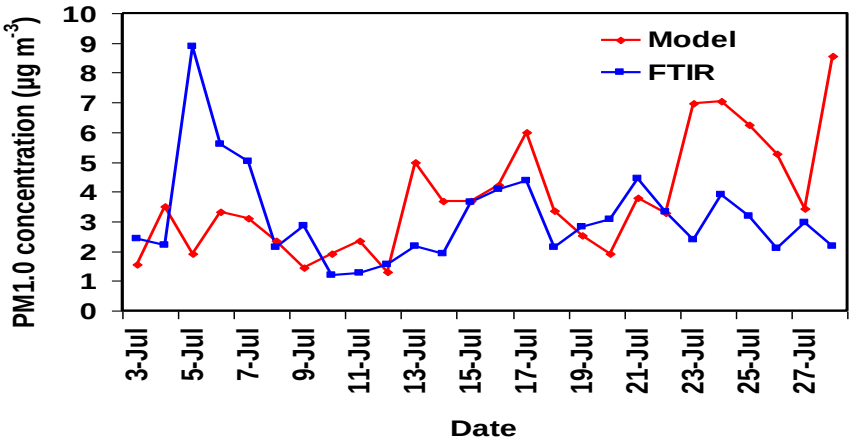

Figure 10-4. Time series comparison of $PM_{1.0}$ mass predicted by source-oriented WRF/Chem calculations (red line) and measured using a FTIR (blue line) at Fontana from July 3 – 27, 2015. BrC absorption included in model results.

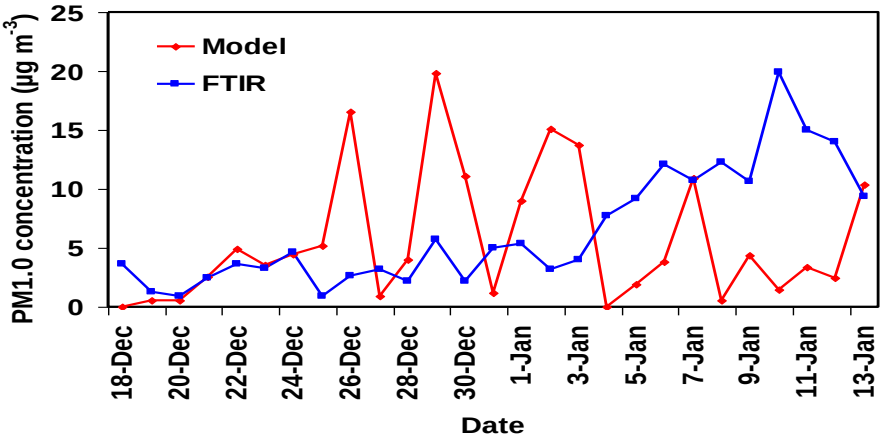

Figure 10-5. Time series comparison of $PM_{1.0}$ mass predicted by source-oriented WRF/Chem calculations (red line) and measured using a FTIR at Fresno from Dec 18, 2014 to Jan 13, 2015. BrC absorption included in model results.

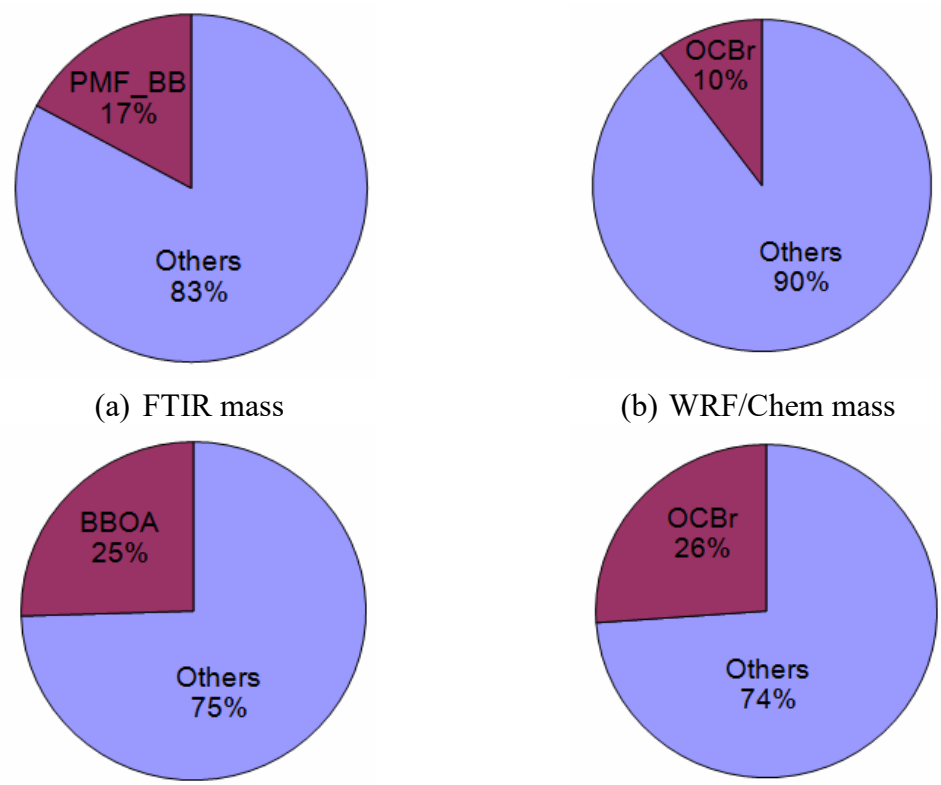

(a) FTIR mass (b) WRF/Chem mass

(c) AMS OA (d) WRF/Chem OA

Figure 10-6. Comparison of biomass burning contribution to total $PM_{1.0}$ (a) measured by FTIR and (b) predicted by source-oriented WRF/Chem calculations. Comparison of biomass burning contribution to organic aerosols (c) measured by AMS and (d) predicted by source-oriented WRF/Chem. All comparisons from Dec 18, 2014 – Jan 13, 2015 at Fresno.

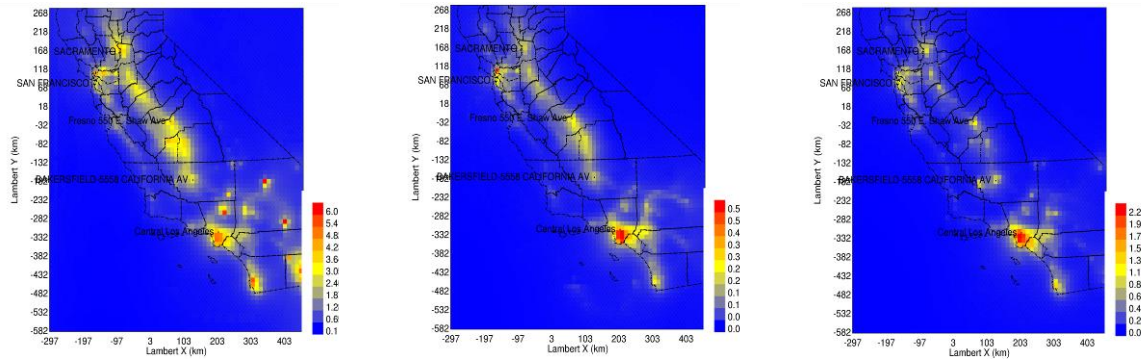

(a) $PM_{2.5}$ (0.5145, ld=0.7084, oc=0.2038)

(b) EC (0.0290, ld=0.0401, oc=0.0113)

(c) OC (0.0859, ld=0.1191, oc=0.0326)

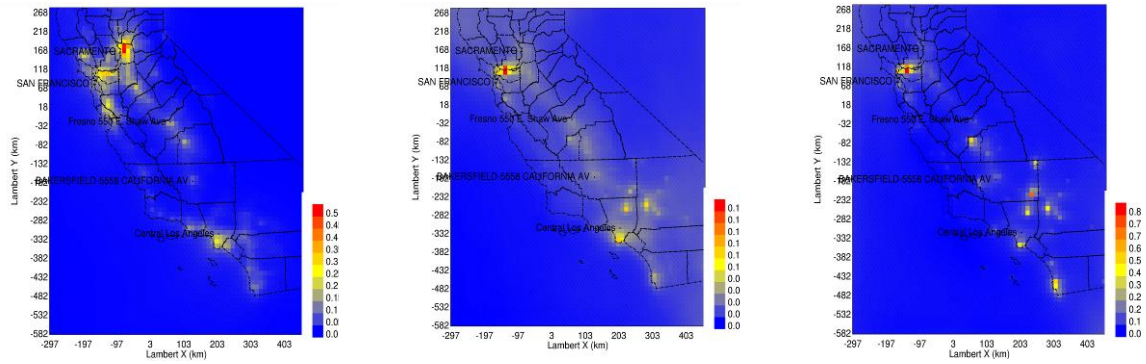

(d) BrC (0.0142, ld=0.0193, oc=0.0326)

(e) NH_4^+ (0.0174, ld=0.0230, oc=0.0083)

(f) SO_4^{2-} (0.0572, ld=0.0643, oc=0.0459)

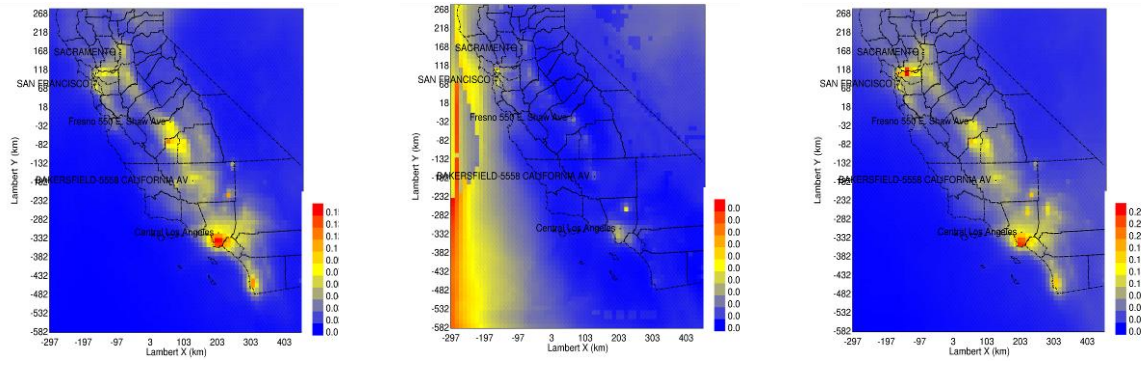

(g) NO_3^- (0.0126, ld=0.0183, oc=0.0034)

(h) Cl^- (0.0046, ld=0.0026, oc=0.0079)

(i) NH_4NO_3 (0.03, ld=0.0413, oc=0.0117)

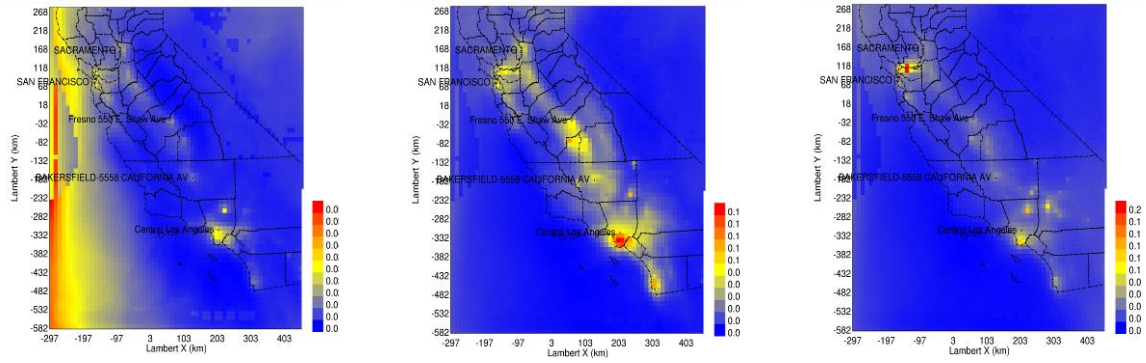

(j) NaCl (0.0102, ld=0.0067, oc=0.0157)

(k) $NaNO_3$ (0.018, ld=0.0224, oc=0.0112)

(l) NH_4Cl (0.0220, ld=0.0256, oc=0.0162)

Figure 10-7. Predicted surface $PM_{2.5}$ (a) mass, (b) elemental carbon (EC), (c) organic carbon (OC), (d) organic brown carbon (BrC), (e) NH_4^+, (f) SO_4^{2-}, (g) NO_3^-, (h) Cl^-, (i) NH_4NO_3, (j) NaCl, (k) $NaNO_3$ and (l) NH_4Cl averaged from August 2014 to July 2015. BrC absorption included. All units $\mu g\ m^{-3}$.

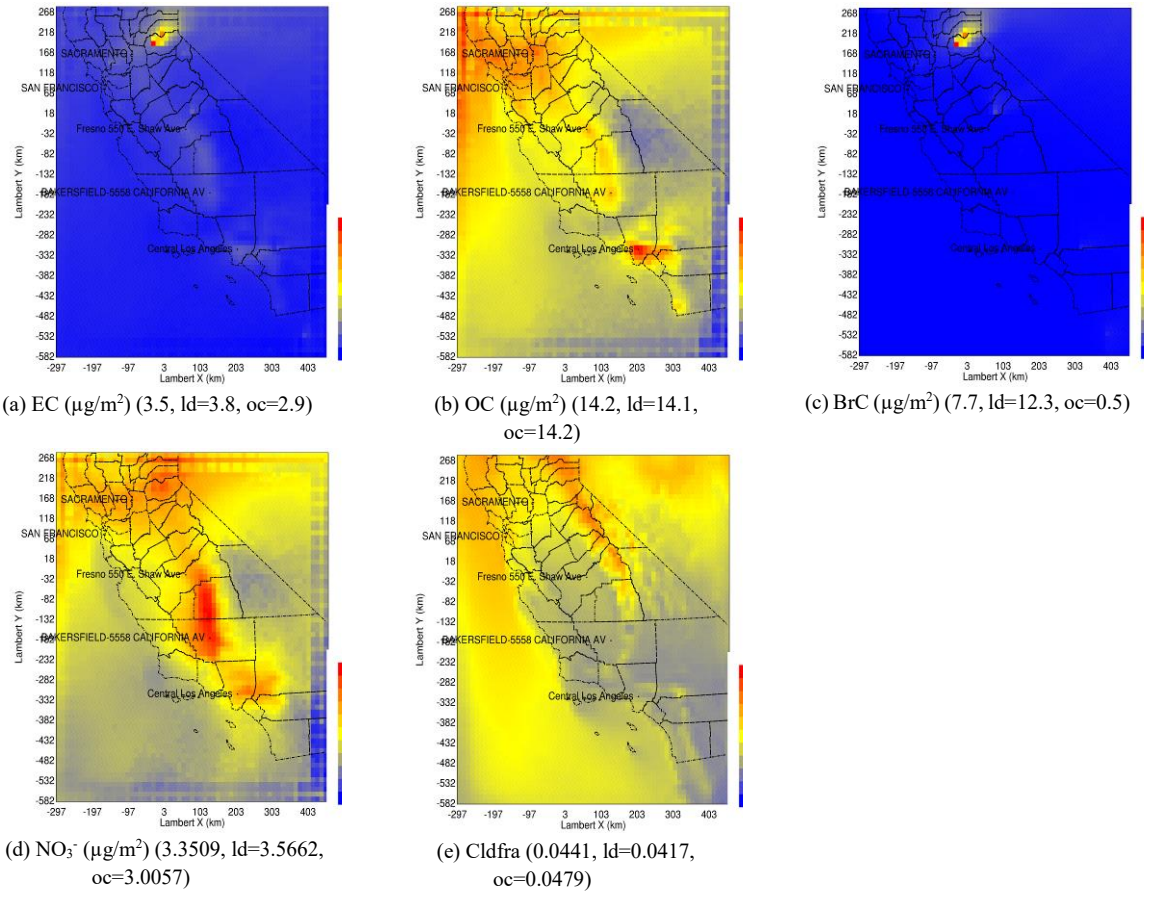

(a) EC (µg/m^2) (3.5, ld=3.8, oc=2.9)

(b) OC (µg/m^2) (14.2, ld=14.1, oc=14.2)

(c) BrC (µg/m^2) (7.7, ld=12.3, oc=0.5)

(d) NO_3^- (µg/m^2) (3.3509, ld=3.5662, oc=3.0057)

(e) Cldfra (0.0441, ld=0.0417, oc=0.0479)

Figure 10-8. Predicted column total (a) elemental carbon (EC), (b) organic carbon (OC), (c) organic brown carbon (BrC), (d) nitrate (NO_3^-), (e) cloud fraction (Cldfra) averaged from August 2014 – July 2015.

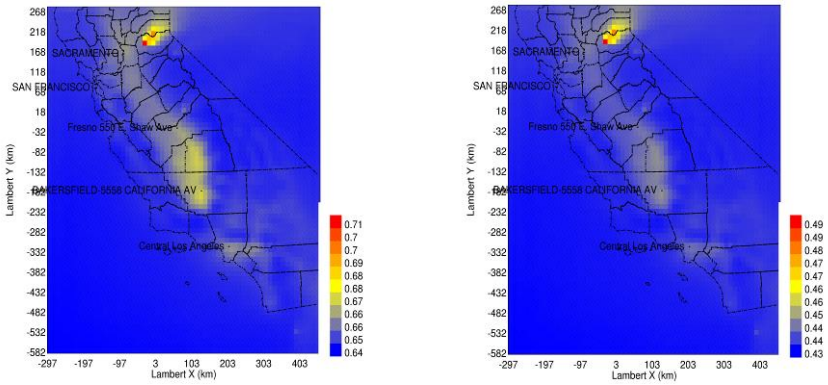

(a) Babs@475 nm (0.6482, ld=0.6500, oc=0.6453)

(b) Babs @525 nm (0.4353, ld=0.4366, oc=0.4332)

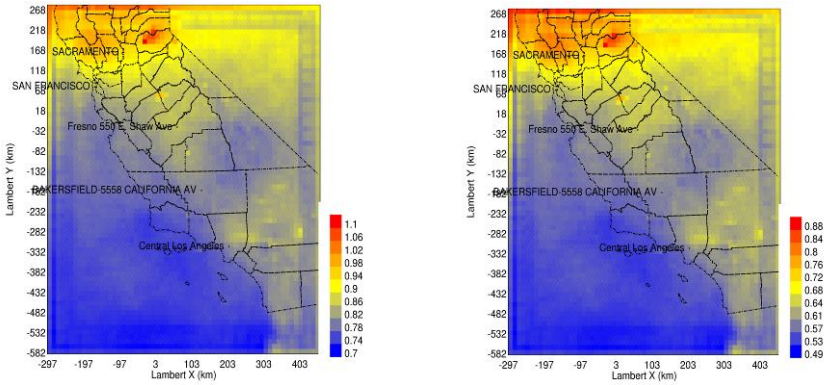

(c) Bscat@475 nm (0.84044, ld=0.8357, oc=0.7542)

(d) Bscat@525 nm (0.5964, ld=0.6306, oc=0.5415)

Figure 10-9. Predicted column total aerosol (a) Babs coefficient at 475 nm, (b) Babs coefficient at 525 nm, (c) Bscat coefficient at 475 nm, (d) Bscat coefficient at 525 nm averaged from August 2014 – July 2015. Units are km^{-1} multiplied by 1000. Note that blue corresponds to all values between zero and the displayed minimum value in the concentration key. Cloud effects not shown.

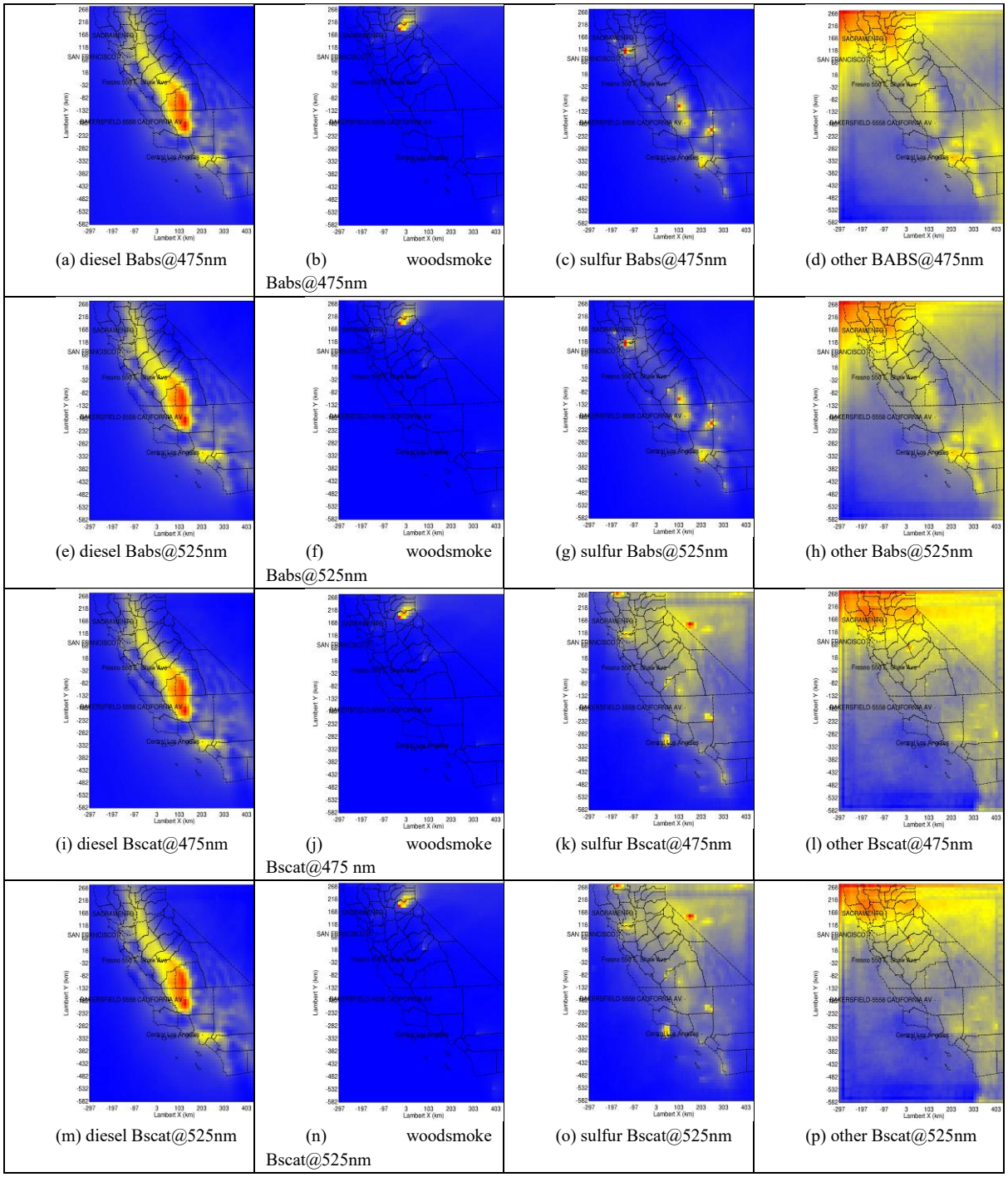

(a) diesel Babs@475nm | (b) woodsmoke Babs@475nm | (c) sulfur Babs@475nm | (d) other BABS@475nm

(e) diesel Babs@525nm | (f) woodsmoke Babs@525nm | (g) sulfur Babs@525nm | (h) other Babs@525nm

(i) diesel Bscat@475nm | (j) woodsmoke Bscat@475 nm | (k) sulfur Bscat@475nm | (l) other Bscat@475nm

(m) diesel Bscat@525nm | (n) woodsmoke Bscat@525nm | (o) sulfur Bscat@525nm | (p) other Bscat@525nm

Figure 10-10. Predicted source contributions to column total aerosol Babs and Bscat from diesel engines (a,e,i,m), wood smoke (b,f,j,n), combustion of high sulfur fuel (c,g,k,o), and other sources (d,h,l,p) averaged from August 2015 – July 2015. Units are km^{-1} multiplied by 1000. Note that blue corresponds to all values between zero and the displayed minimum value in the concentration key. Cloud effects not shown.

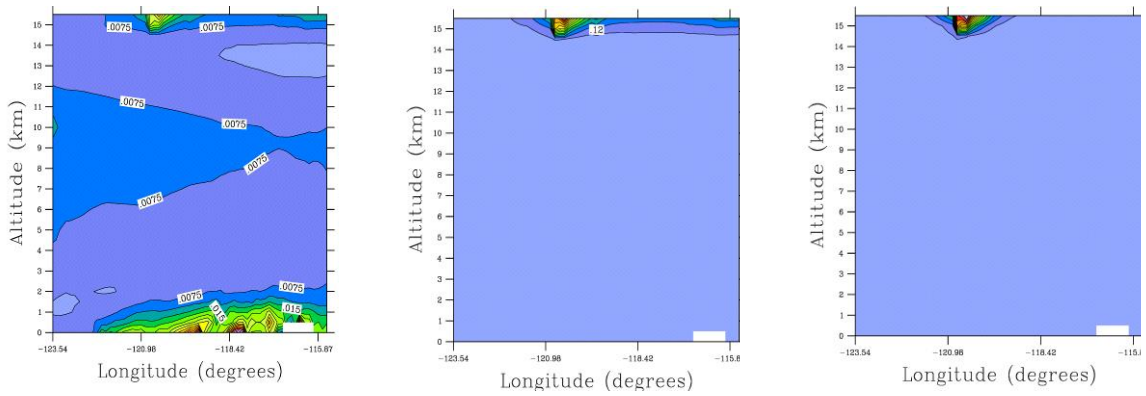

(a) EC **(b)** BrC **(c)** BrC

Figure 10-11. Meridionally-averaged (a) elemental carbon (EC), and (b) organic brown carbon (BrC) averaged from August 2015 – July 2015. Meridionally-averaged (c) organic brown carbon (BrC) averaged from Sept 13 – Oct 9, 2014. Viewer is facing north. Units are $\mu g\ m^{-3}$.

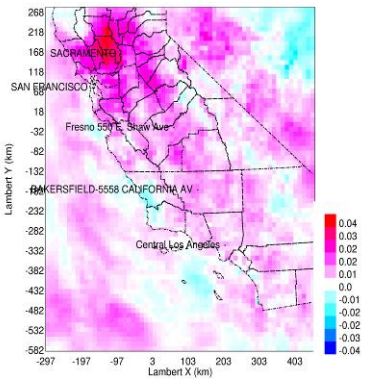

(a) Δ 2-mT (K) (+0.005, ld=+0.006, oc=+0.003)

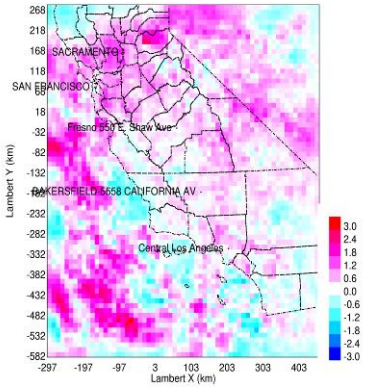

(b) Δ TOA (W/m^2) (+0.277, ld=+0.244, oc=+0.329)

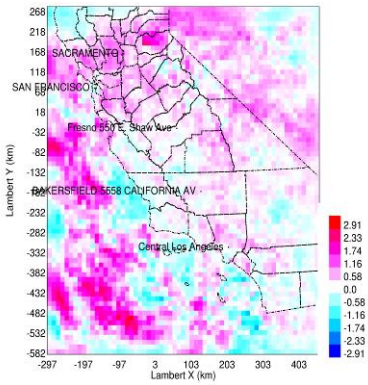

(c) Δ RSWTOA (W/m^2) (+0.228, ld=+0.188, oc=+0.291)

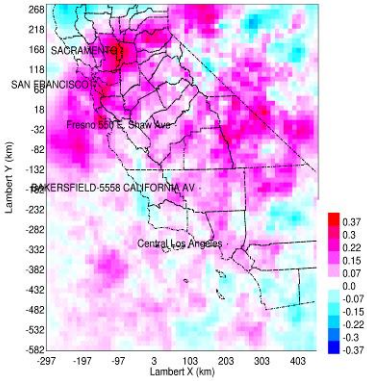

(d) Δ RLWTOA (W/m^2) (+0.049, ld=+0.057, oc=+0.038)

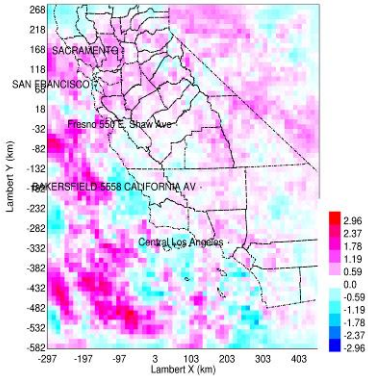

(e) Δ GSW (W/m^2) (+0.188, ld=+0.132, oc=+0.278)

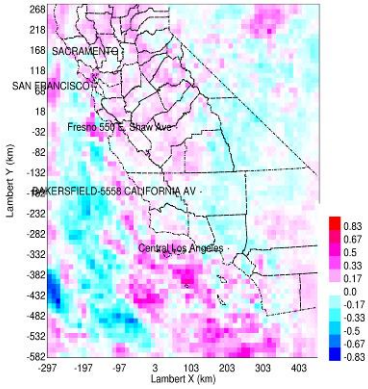

(f) Δ GLW (W/m^2) (-0.008, ld=-0.004, oc=-0.014)

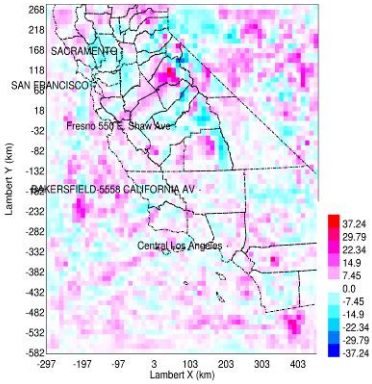

(g) Δ Rain (mm/day) (+0.517, ld=+0.246, oc=+0.951)

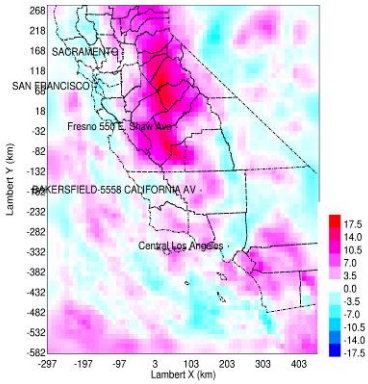

(h) Δ Qvapor (mg/kg) (+1.17, ld=+1.68, oc=+0.35)

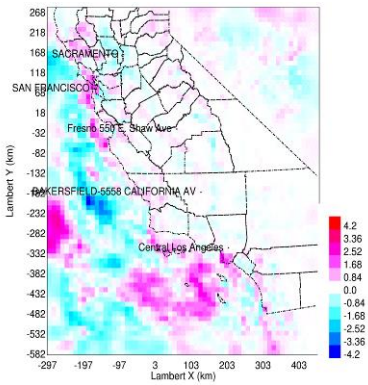

(i) Δ Qcloud (mg/kg) (-0.08, ld=-0.01, oc=-0.19)

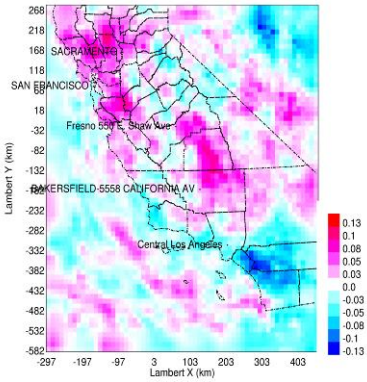

(j) Δ O3 (ppb) (-0.003, ld=-0.001, oc=-0.006)

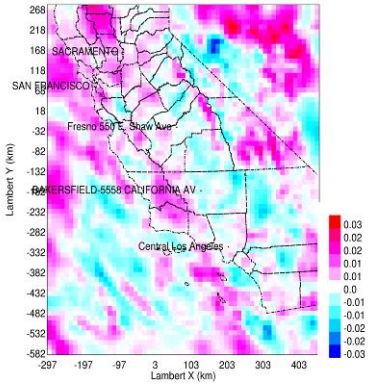

(k) Δ U10 (m/s) (+0.001, ld=+0.002, oc=+0.001)

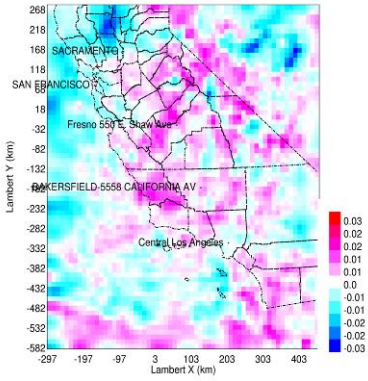

(l) Δ V10 (m/s) (-0.001, ld=+0.00004, oc=-0.002)

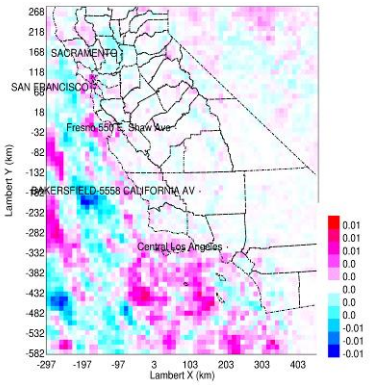

(m) Δ Cldfra (+1.42E-06, ld=-4.15E-05, oc=+7.02E-05)

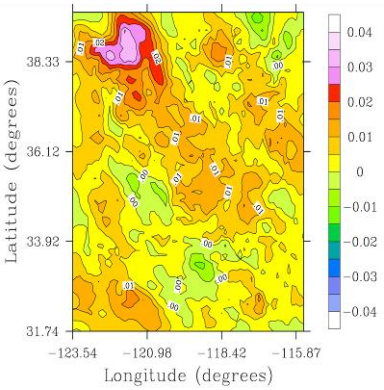

(n) Δ ~20-m T (K) (+0.006, ld=+0.007, oc=+0.004)

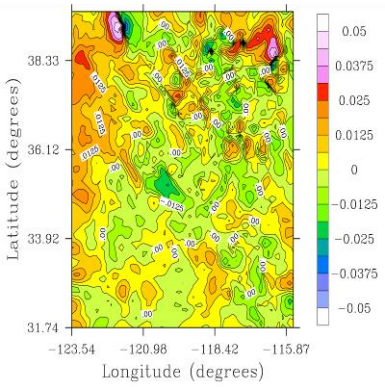

(o) Δ ~20-m wspd (m/s) (+0.002, ld=+0.001, oc=+0.004)

Figure 10-12. Difference (with - without BrC absorption) of (a) T 2-m, (b) top of atmosphere (TOA) radiation, (c) RSWTOA, (d) RLWTOA, (e) GSW, (f) GLW, (g) rain, (h) water mixing ratio (Qvapor), (i) cloud water mixing ratio (Qcloud), (j) ozone (O3), (k) U10, (l) V10, (m) cloud fraction (Cldfra), (n) T ~20-m, (o) wind speed (wspd) ~20-m, (p) BABS coefficient at 475 and (q) BABS coefficient at 525 nm.

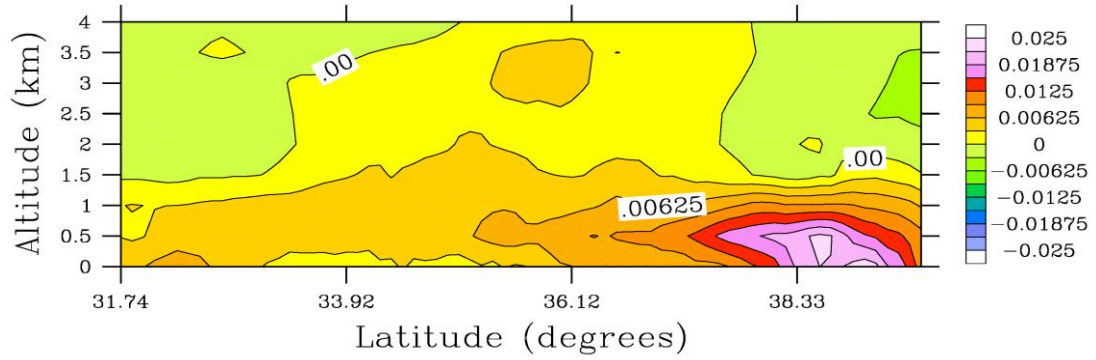

(a) Δ zonal T (K) w-w/o BrC absorption

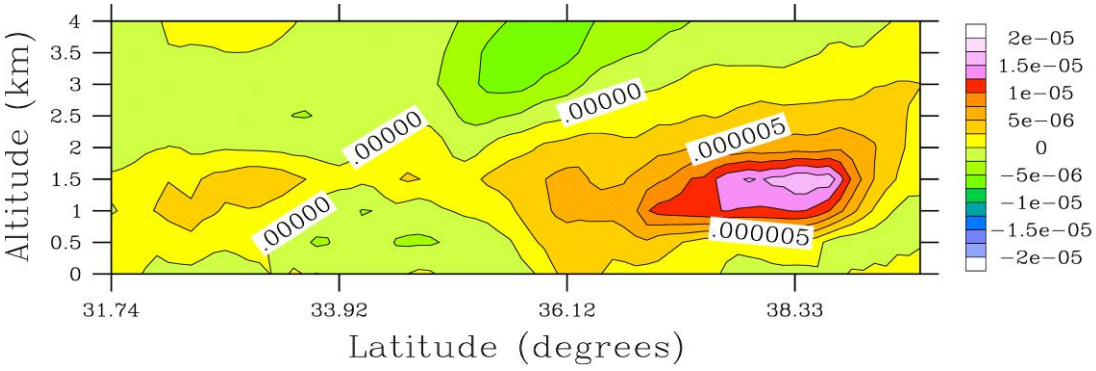

(b) Δ zonal Qvapor (kg/kg) w-w/o BrC absorption

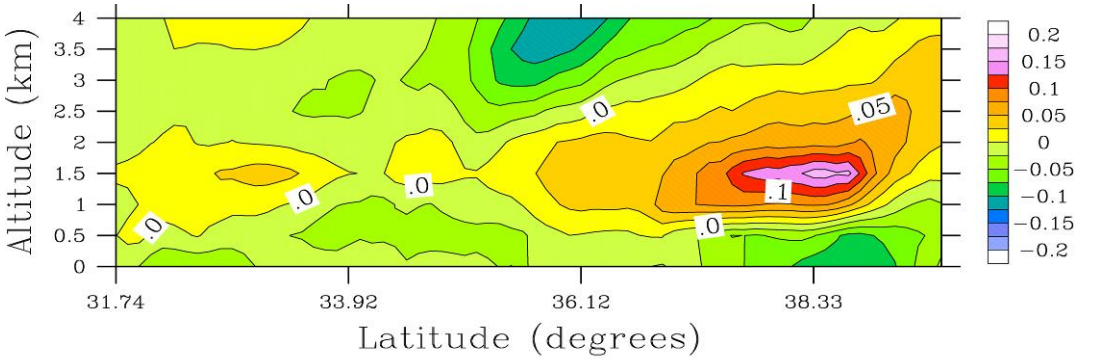

(c) Δ zonal RH (%) w-w/o BrC absorption

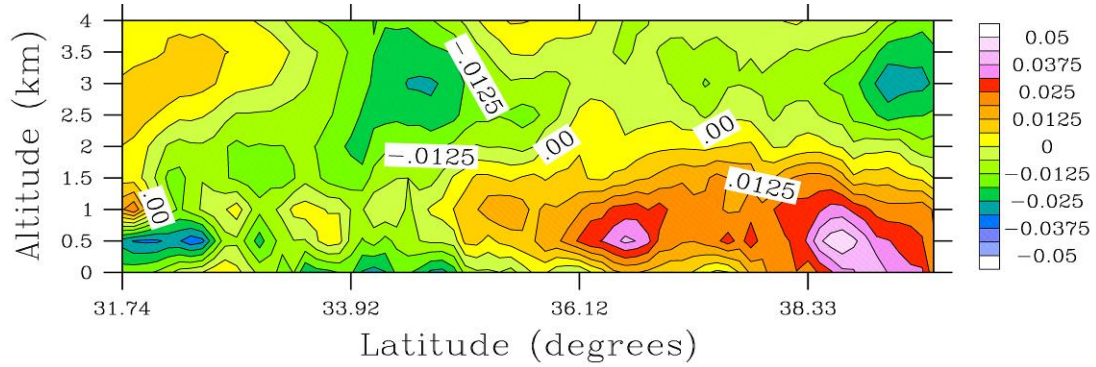

(d) Δ zonal O3 (ppb) w-w/o BrC absorption

Figure 10-13. Zonally averaged differences of (a) T, (b) Qvapor, (c) relative humidity (RH) and (d) O3. Viewer is facing west.

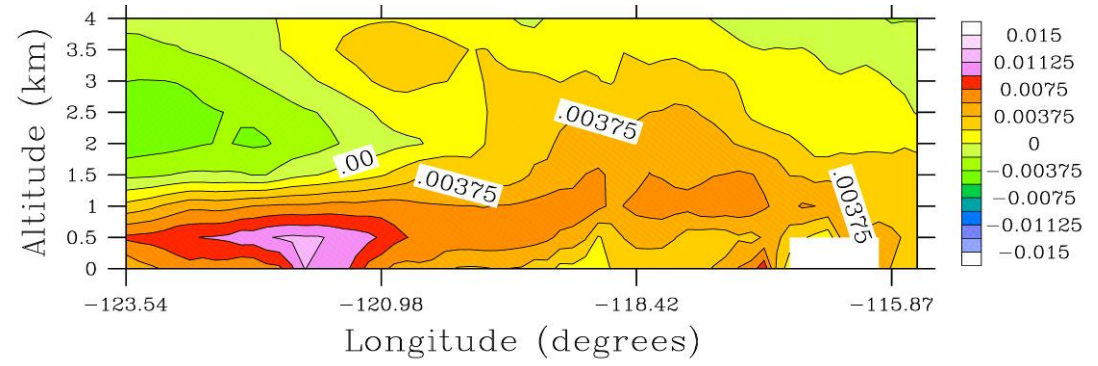

(a) Δ meridionally T (K) w-w/o BrC absorption

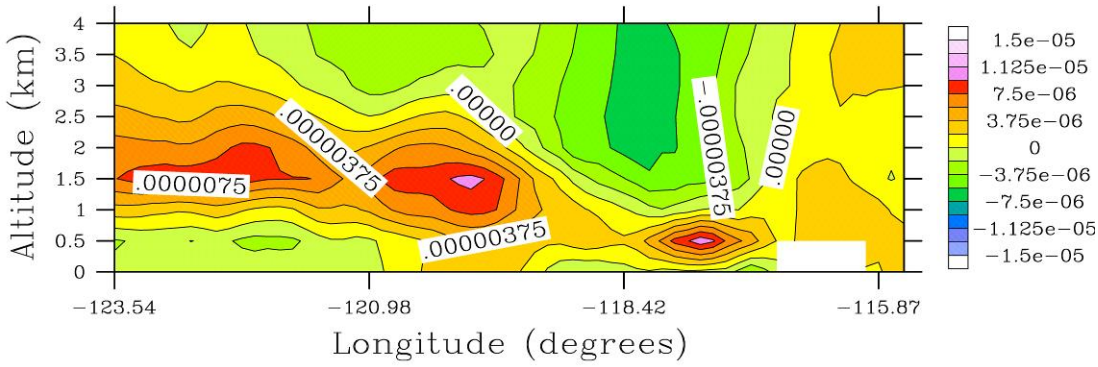

(b) Δ meridionally Qvapor (kg/kg) w-w/o BrC absorption

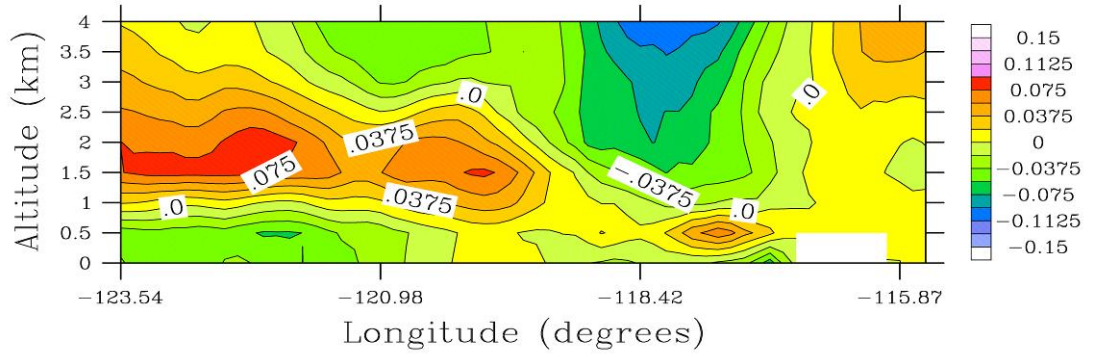

(c) Δ meridionally RH (%) w-w/o BrC absorption

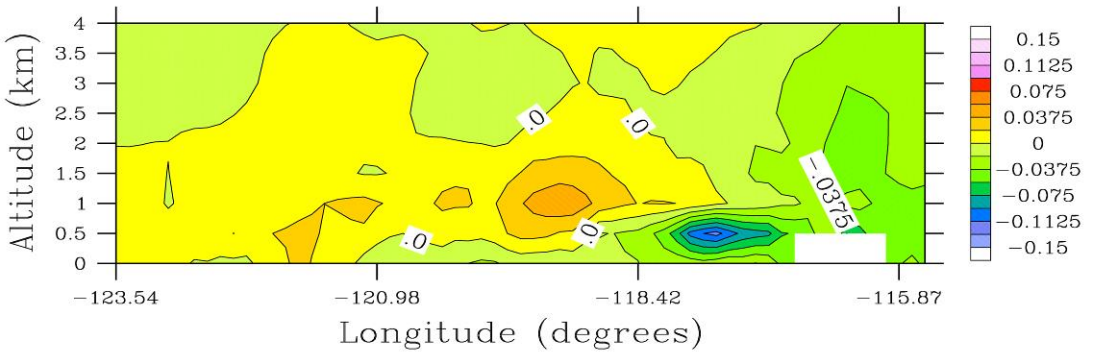

(d) Δ meridionally O3 (ppb) w-w/o BrC absorption

Figure 10-14. Meridionally averaged differences of (a) T, (b) Qvapor, (c) relative humidity (RH) and (d) O3. Viewer is facing north.

11 Modeling Global through Regional Impacts of Brown and Black Carbon on California Climate

11.1 Introduction

The purpose of this study is to examine the short-term (1-year) impacts of brown carbon (BrC) and black carbon (BC) on California climate using a contemporary (2014-2015) highly resolved in space, time, and composition emission inventory. The two major steps in the study are the development of an hour-by-hour gas and particle emission inventory for a year and the global-through-local nested simulation of the impacts of brown and black carbon on California climate. Development of the emissions inventory is summarized in Chapter 10 while simulations using this inventory along with a global simulation are discussed in the current Chapter. Nested global-through-California simulations were carried out here with the GATOR-GCMOM global-through-local air pollution-weather-climate model, described in Section 11.2. Section 11.3 describes the simulations, and Section 11.4 discusses the results of this study.

11.2 Description of GATOR-GCMOM

The model used for this study is the global-through-urban nested air pollution-weather-climate model, GATOR-GCMOM (Gas, Aerosol, Transport, Radiation, General Circulation, Mesoscale, and Ocean Model) [*Jacobson*, 2001a,b, 2012, 2014; *Jacobson et al*., 2007; *Jacobson and Ten Hoeve*, 2012]. GATOR-GCMOM simulates feedbacks among meteorology, solar and thermal-infrared radiation, gases, aerosol particles, cloud particles, oceans, sea ice, snow, roads, rooftops, soil, and vegetation without data assimilation or nudging. The model treats brown and black carbon inclusions within and between cloud and precipitation particles, within snow grains, and within aerosol particles. Model predictions have been compared with data in 19 peer-reviewed studies and have taken part in 11 multi-model inter-comparisons. Below, the model is briefly described.

11.2.1 Meteorological, Transport, Gas, and Surface Processes

On the global scale, the momentum equation is solved with the potential enstrophy, vorticity, energy, and mass-conserving scheme of Arakawa and Lamb [1981]. On regional scales, it is solved with an enstrophy-, mass-, and kinetic-energy-conserving scheme [Lu and Turco, 1995]. Two-dimensional ocean mixed-layer dynamics conserve potential enstrophy, vorticity, energy, and mass while providing mixed-layer velocities, heights, and energy transport [Ketefian and Jacobson, 2009]. GATOR-GCMOM solves 3-D ocean energy and chemistry diffusion, 3-D ocean equilibrium chemistry, and ocean-atmosphere exchange with mass conserving and unconditionally stable schemes among 10 ocean layers [Jacobson, 2005]. The dynamical time step (for predicting meteorology) is 30 s on the global scale and 15 s on the regional scale.

Horizontal and vertical atmospheric advection of gases and size- and composition-resolved aerosol particles are solved with the mass-conserving, peak-preserving, mixing ratio bounded scheme of Walcek [2000]. Eddy diffusion coefficients, used in a second-order local closure diffusion scheme for gases and particles, are calculated with the Mellor and Yamada [1982] level 2.5 parameterization. Gas processes include emissions, photochemistry, gas-to-particle

conversion, gas-to-cloud conversion, gas-cloud exchange, gas-ocean exchange, advection, convection, molecular diffusion, turbulent diffusion, and dry deposition. Gas photochemistry is solved with SMVGEAR II for 161 gases and 404 tropospheric and stratospheric kinetic, heterogeneous, and photolysis reactions.

In each land surface grid cell, the model treats water and energy transport through 10 subsurface soil layers for each of up to 13 subgrid soil types. It also treats energy transfer through roads or vegetation overlying soil; rooftop material; snow over roads, rooftops, vegetation, and soil; water bodies; sea ice over water; and snow over sea ice over water [Jacobson, 2001a; Jacobson and Ten Hoeve, 2012]. The model further solves for the depth, aging, compaction, and horizontal transport of sea ice, conserving mass [Jacobson and Ten Hoeve, 2012; Jacobson et al., 2015].

Roads are assumed to consist of 5-cm-thick asphalt, impermeable to water and with asphalt properties, overlying soil. In terms of the 10-layer subsurface module, the top five layers are assumed to be asphalt, and the rest are assumed to be a soil-air-water mixture, Snow and liquid water can accumulate on the asphalt as an additional (11th) layer in the subsurface module. Roofs are assumed to consist of five layers of roofing material on top of five layers of air [Jacobson, 2001a; Jacobson and Ten Hoeve, 2012]. Dew that collects on the roof can evaporate.

During each 15 s subsurface module time step, surface and subsurface temperatures and moisture, sensible heat fluxes, latent heat fluxes, water vapor fluxes, friction wind speeds, Monin-Obhukov lengths, Richardson numbers, snow depths, ice thicknesses, sublimation rates, runoff, foliage temperatures, leaf stomata specific humidities, foliage air temperatures, foliage specific humidities, and water/snow stored on leaves, roads, and roofs are calculated for each surface class in each grid cell from the column subsurface module. Surface temperatures, sensible heat fluxes, latent heat fluxes, and water vapor fluxes are then weighted by the fractional surface type in the cell to give an effective value for the whole cell. Jacobson [2001a, Figure 3 and 2001b, Figure 3] compare modeled temperatures from this method with hourly data over four days at two-dozen locations, including in cities.

The surface albedo of each grid cell at each wavelength is the area-weighted sum of the albedos of each surface class in the cell. The albedos of roads and roofs are assumed to be those of asphalt. Solar albedos of paved asphalt range from 0.04 (new) to 0.17 (aged), averaging 0.12 [Pomerantz et al., 2000]. Albedos of all other surfaces are from 0.05o resolution MODIS combined Terra plus Aqua satellite data in seven spectral bands [MODIS/USGS, 2007; Schaaf et al., 2010]. These solar albedos are interpolated spatially and spectrally to each of 86 solar wavelengths below 800 nm and 232 solar-IR wavelengths/probability intervals from 800-10,000 nm.

11.2.2 Aerosol Processes

Aerosol processes include anthropogenic and natural emissions, binary and ternary homogeneous nucleation, condensation, dissolution, internal-particle chemical equilibrium, aerosol-aerosol coagulation, aerosol-hydrometeor coagulation, sedimentation, dry deposition, and transport [Jacobson, 2002, 2003, 2012]. The model treats any number of discrete aerosol size distributions, each with any number of size bins and chemicals per bin. Particle number and mole concentrations of each chemical are tracked in each size bin. The components within each size bin of each aerosol size distribution are internally mixed in the bin but externally

mixed from other bins and other size distributions. For this study, one aerosol size distribution with 14 size bins ranging from 2 nm to 50 □m diameter, and with 47 liquid, ionic, and solid chemical components in each size bin, is used in each grid cell of each domain. Aerosol components in each size bin include black carbon (BC), tarballs, other primary organic matter, nitrocresol, other secondary organic matter, H2O(aq), H2SO4(aq), HSO4-, SO42-, HNO3(aq), NO3-, Cl-, OH-, CO2(aq), HCO3-, CO32-, H+, NH3(aq), NH4+, Na+, K+, Ca2+, Mg2+, soil dust, pollen/spores/bacteria, SiO2(s), Fe2O3(s), NH4NO3(s), NH4Cl(s), NH4HSO4(s), (NH4)2SO4(s), (NH4)3H(SO4)2(s), NaNO3(s), NaCl(s), NaHSO4(s), Na2SO4(s), Na2CO3(s), KNO3(s), KHSO4(s), K2SO4(s), K2CO3(s), CaCl2(s), CaSO4-2H2O(s), CaCO3(s), MgSO4(s), MgCO3(s), and other PM. Each aerosol component in each size bin is tracked and transported in the model. Tarballs originate only from biomass and biofuel burning. Nitrocresol aerosol is a surrogate group for all secondary organic aerosol components that condense from nitrated aromatic gases (including nitrocresol, nitrophenol, organic nitrate, C2 dinitrate group, peroxybenzoyl nitrate, and dinitrate of isoprene).

11.2.3 Convective Cloud, Stratiform Cloud, Aerosol-Cloud Processes

For each simulation, a global and a nested California domain are used. For both domains, convective clouds are treated at the subgrid scale (with multiple sub-grid cloud clouds per column) and stratus clouds are treated at the grid scale. Size- and composition-resolved aerosols and gases are transported vertically within each sub-grid cloud. Size- and composition-resolved liquid and ice cloud particles then form on top of the discrete aerosol size distribution in the cloudy portion of each grid cell. The liquid and ice particles take part in multiple physical processes and either remain as clouds or form precipitation by the collision/coalescence or Bergeron process. Cloud and precipitation particles retain their aerosol inclusions and coalesce with other aerosol particles by coagulation. The explicit size- and composition-resolved microphysical evolution of clouds and precipitation from size-and composition resolved aerosol particles is described in Jacobson [2003; 2012] and Jacobson et al. [2007]. On all scales, the model treats three hydrometeor size distributions (liquid, ice, graupel), each with 30 size bins (0.5 □m to 8 mm in diameter), and tracks concentrations of all aerosol component inclusions in each size bin of each hydrometeor distribution.

11.2.4 Radiative Processes

For radiative calculations, each model column is divided into clear- and cloudy-sky columns, and separate calculations are performed for each. Radiative transfer is solved simultaneously through multiple layers of air and one snow, sea ice, or ocean water layer at the bottom to calculate, rather than prescribe, spectral albedos over these surfaces. For vegetated or bare land surfaces, no such layer is added. The 2-stream radiative code [Toon et al., 1989] solves the atmospheric radiative transfer equation for radiances, irradiances, photosynthetically active radiation (PAR), actinic fluxes, and atmospheric heating rates through each model layer in each column, over each of 694 wavelengths/probability intervals in the ultraviolet, visible, solar-infrared, and thermal-infrared spectra, accounting for gas and size- and composition-dependent aerosol, cloud, and precipitation optical properties [Jacobson, 2012]. The intervals include 86 ultraviolet and visible wave intervals from 170 to 800 nm, 232 visible, solar-infrared, and thermal-infrared probability intervals from 800 nm to 10 μm, and 376 thermal-

infrared probability intervals from 10 μm to 1000 μm. Solar radiation calculations span from 170 nm to 10 μm.

The model accounts for atmospheric scattering and absorption by gases and size- and composition-resolved aerosol and hydrometeor particles. Since the model treats the time-dependent evolution of the size and composition of aerosol particles and clouds and the feedbacks of aerosol particles to atmospheric stability and winds, it accounts for the first indirect effect, second indirect effect, and the semi-direct effect of aerosol particles on clouds.

Aerosol and cloud optical properties are calculated by integrating spectral optical properties over each size bin of each aerosol and hydrometeor particle size distribution. Aerosol spectral optical properties of a given size are determined by assuming that black carbon, if present, is a core surrounded by a mixed shell and that the aerosol liquid water content is a function of the ambient relative humidity and aerosol composition. Cloud spectral optical properties of a given size are determined accounting for scattering by aerosol particles between cloud particles, where aerosol particle liquid water content is determined at the relative humidity of the cloud. Cloud drop, ice crystal, and graupel optical properties are determined accounting for the time-dependent evolution of black carbon, brown carbon, and soil dust inclusions within the drops, crystals, and graupel. Ice crystal and graupel optical properties also account for the nonsphericity of these particles. As such, the model accounts for cloud absorption effects I and II, which are the heating of a cloud due to solar absorption by absorbing inclusions in cloud drops and by swollen absorbing aerosol particles interstitially between cloud drops, respectively [Jacobson, 2012]. Table 11-1 and Figure 11-1 provide the refractive indices of black carbon and the different types of organic matter used in the present simulations.

Since the model tracks BC, tarballs, soil dust, and all other aerosol inclusions within precipitation particles that fall onto snow and sea ice, the radiative transfer calculation then also accounts for the optics of BC, tarballs, soil dust within and between snow and sea ice grains [Jacobson, 2012].

11.2.5 Emissions

For the global domain, the anthropogenic emission inventory used is the Fifth Assessment Report (AR5) inventory for 2005 assuming the Representative Concentration Pathway (RCP) 4.5 trajectory [Clarke et al., 2007]. This inventory is at 0.5-degree horizontal resolution. Emitted pollutants include CO, CH4, acids, alcohols, benzene, butanes, chlorinated hydrocarbons, esters, ethane, ethene, ethers, ethyne, formaldehyde, hexanes and higher alkanes, ketones, other volatile organic compounds (VOCs), other alkanals, other alkenes, other aromatics, pentanes, propane, propene, terpenes, toluene, trimethylbenzenes, xylene, NO, NO2, NH3, SO2, SO3, BC, and primary organic carbon (POC). The EDGAR 2005 inventory [European Commission, 2014] was used for emissions of CO2, N2O, CFCs, and HFCs. Emissions from open biomass and biofuel burning are obtained as in Jacobson [2014] as are heat and moisture fluxes from fossil fuel, biomass, and biofuel combustion.

Natural emissions from lightning (NO, NO2, HONO, HNO3, N2O, H2O2, HO2, CO), soils (dust, bacteria, NO, N2O, H2, CH4, H2S, DMS, OCS, CS), oceans (bacteria, sea spray, DMS, N2O, H2, CH4, CH3Cl), and vegetation (pollen, spores, isoprene, monoterpenes, methanol, other VOCs) are calculated as a function of modeled meteorology as in Jacobson and Streets [2009].

Anthropogenic gas and size- and composition-resolved aerosol emission inventories are developed for California for each hour of a full year (July 1, 2014 to June 30, 2015) starting with raw emission inventories from U.C. Davis. The raw inventories were originally in the Lambert Conformal coordinate system, were interpolated here to the spherical (geographic) coordinate system for use in GATOR-GCMOM. A total of 365 daily files, each containing 24 hours of emission data for California, were prepared in this manner. GATOR-GCMOM was then modified to process the emissions.

Gases in the California anthropogenic inventory include CO, NO, NO2, NH3, SO2, H2SO4 and the following explicit or carbon-bond-group organics: CH3OH, C2H5OH, C2H4, HCHO, CH3CHO, PAR, TOL, OLE, XYL, and ISOP. Aerosol particle components included black carbon (BC), primary organic carbon (POC), Na+, NH4+, S(VI), Cl-, NO3-, metals, Cu(I), Cu(II), Mn(II), Mn(III), Fe(II), Fe(III), and S(IV). The California domain also includes gas and particle emissions from natural sources, calculated as a function of modeled meteorology, as described for the global domain.

11.3 Model Application

For this study, the model was run for one year in nested mode with two domains, a global and California domain. The global domain horizontal resolution was 5º west-east by 4º south-north, with 68 vertical layers between the ground and 0.219 hPa (≈60 km), 15 layers in the bottom 1 km, and 500-m resolution from 1-21 km. The California domain included 95 west-east grid cells of 0.15º (12.4-14.4 km) resolution by 60 south-north cells of 0.20º (22.2 km) resolution. The center of the southwest grid cell was at 129º W, 30º N.

The nested domain included 55 layers from the surface to 47.3 hPa, matching exactly the bottom 55 sigma-pressure levels of the 68-layer global domain. Emissions entered both domains, and all gas, aerosol, radiative, dynamical, and surface processes were solved in all domains. Gases and particles were transported one way from the global domain to the California domain, allowing for long-range transport of pollutants into the California domain. Clouds were not transported from the global to California domains, but the liquid and ice water from clouds in the global domain was evaporated and transported to the California domain, where it could reform clouds in the finer domain.

Simulations were run for one year from July 1, 2014 at 1200 GMT to July 1, 2015 at 1200 GMT. Meteorological fields in all domains were initialized with Global Forecast System 0.5ºx0.5º reanalysis fields for July 1, 2014 [*GFS*, 2018].

Four simulations were run. Emissions and all results for the global domain were exactly the same in all four simulations.

Simulation 1: The first simulation was a baseline that included all processes.

Simulation 2: The second simulation was one in which the imaginary refractive indices of all types of organic carbon in the model (tarballs, other primary organic carbon, nitrocresol, and other secondary organic carbon) were set to zero for all solar and thermal-infrared wavelengths for all aerosol optical property calculations in the California domain.

Simulation 3: The third simulation was the same as the second (no organic carbon absorption) but in addition, the imaginary refractive indices of black carbon incorporated within liquid, ice, and graupel cloud particles were set to zero for all solar and thermal-infrared wavelengths in the California domain. Absorption by black carbon aerosol particles

between cloud particles and in the clear sky was still treated (thus BC refractive indices were not set to zero for those particles).

Simulation 4: The fourth simulation was the same as the second (no brown carbon absorption) except that black carbon imaginary refractive indices were set to zero in all aerosol particles and in all cloud particles for all solar and thermal-infrared wavelengths. Thus, neither BC nor BrC absorbed at all in this simulation in the California domain.

In all simulations, whenever imaginary indices of refraction of BrC or BC were set to zero, the particles also did not absorb when they precipitated onto snow.

The four main types of absorption accounted for here in the baseline simulation (Simulation 1) were (a) clear-sky aerosol absorption, (b) absorption by cloud and precipitation particles containing aerosol inclusions (Cloud Absorption Effect I), (c) absorption by swollen aerosol particles in between cloud and precipitation particles at the relative humidity of the cloud (Cloud Absorption Effect II) [*Jacobson*, 2012], and absorption by precipitation and dry-deposited aerosol particles within snow and sea ice [*Jacobson*, 2004]. The difference between Simulations 1 and 2 gives the impacts of all four absorption types for organic carbon on California climate. The difference between Simulations 1 and 3 gives the impact of absorption by black carbon inclusions within cloud and precipitation particles (Cloud Absorption Effect I), but not between cloud particles or in the clear sky (Cloud Absorption Effect II), and all organic carbon on California climate. The difference between Simulations 1 and 4 gives the impact of all four absorption types for both organic and black carbon on California climate. The difference between Simulations 3 and 4 gives the impacts of clear-sky aerosol absorption and cloud absorption effect II for BC on California climate.

11.4 Results and Discussion

Figures 11-2 through 11-6 summarize the main results among the different simulations. Figure 11-2 shows baseline near-surface, annually averaged concentrations of many aerosol particle constituents. Figure 11-3 shows baseline column annually averaged concentrations of some aerosol constituents and baseline annually averaged aerosol optical depth, aerosol absorption optical depth, cloud optical depth, cloud absorption optical depth, and cloud fraction. Figure 11-4 shows near-surface, annually averaged changes in many parameters between Simulations 1 and the other three simulations. Figure 11-5 shows zonally and annually averaged changes (averaged over all longitudes in the California domain for each latitude and altitude in the bottom 4 km). Figure 11-6 shows meridionally and annually averaged changes (averaged over all latitudes in the California domain for each longitude and altitude in the bottom 4 km).

11.4.1 Results for Brown Carbon Alone

Figure 11-4 (left column) indicates that absorption by BrC in aerosol particles and BrC inclusions within clouds increased domain-averaged near-surface air temperatures in the California domain (which includes parts of Nevada) by ~0.018 K over the full year of simulation. Whereas the BrC alone slightly cooled air over land by -0.005 K, strong absorption over the oceans, particularly within low-lying stratus clouds, warmed the air there by ~+0.033 K. Vertically, BrC stabilized the air, warming it appreciably up to around 2-3 km relative to the ground (Figure 11-5).

Slight overall warming due to BrC can be explained as follows. BrC increased domain average 550-nm aerosol absorption optical depth by ~33% (versus no BrC absorption) and 650-nm cloud absorption optical depth by ~9%. BrC absorption alone (Figure 11-4, left column), decreased cloud optical depth over the ocean by ~0.054 and over land by ~0.028. This resulted in a decrease in cloud fraction over the ocean of -0.0066 (-1.5%) and over land of -0.00021 (-0.12%). The reduction in cloudiness reduced precipitation over the total domain by ~0.8%, increasing near-surface dry $PM_{2.5}$ concentrations by ~0.16% and PM_{10} concentrations ~0.19%.

The reduction in cloudiness over ocean and land along with clear-sky aerosol absorption by BrC caused BrC to increase solar plus thermal-infrared (TIR) net down minus up irradiance over the entire domain by +1.07 W/m^2, with an increase in solar net down minus up irradiance of +1.03 W/m^2 and thermal infrared of ~+0.04 W/m^2. The increase in solar+TIR net downward irradiance was +1.26 W/m^2 over the ocean and +0.89 W/m^2 over land. The larger increase over the ocean was due to the fact that BrC burned off stratus clouds, allowing more solar irradiance to penetrate downward (+1.3 W/m^2) but more of the Earth's TIR to penetrate upward (-0.05 W/m^2).

Meanwhile, BrC reduced downward UV radiation by ~4.4% averaged over the domain, with similar reductions over both land and water. The UV reductions reduced near-surface ozone a ~0.11 ppbv over the entire domain, or ~0.55% over land and ~0.024% over the ocean.

11.4.2 Results for Black Carbon Plus Brown Carbon

Figure 11-4 (right column) indicates that absorption by BrC plus BC in aerosol particles and clouds increased domain-averaged near-surface temperatures by ~0.17 K. Considering that the near-surface warming due to BrC alone was ~0.018K, the warming to BC alone (in aerosol particles and clouds) was ~0.15 K. Based on results from Figure 11-4, middle column, ~0.01 K of the BC warming (~7%) was due to absorption by black carbon inclusions within cloud and precipitation particles and the rest was due to black carbon absorption interstitially between cloud particles at the relative humidity of the cloud plus absorption by black carbon in clear-sky aerosol particles. The substantial stratus cloudiness over oceans and coastal areas of California created an environment where black carbon interstitially between cloud particles had a strong warming effect on clouds, dissipating some of them.

In particular, BC+BrC absorption together (Figure 11-4, right column) decreased cloud optical depth over the ocean by ~0.56 and over land by ~0.25 and cloud fraction over the ocean by ~5.4% and over land by ~0.12%, primarily due to BC-containing aerosol particles interstitially between marine stratus cloud particles and in the clear sky. The decreases in cloud optical depth and fraction were due both to direct absorption and stabilization of the air by BC and BrC. Figures 11-5 and 11-6, for example, show that BrC+BC warmed the air aloft and stabilized the lowest part of the atmosphere by increasing the air temperature at ~0.5 km altitude more than at the surface.

The water evaporated from clouds contributed to higher water vapor contents in most locations, near the surface and aloft, and an increase in the relative humidity in some locations (Figures 11-5 and 11-6).

The reduction in cloudiness increased net downward top-of-the-atmosphere (TOA) solar irradiance over the ocean by ~9.4 W/m^2 and net downward (down minus up) TOA solar plus thermal-infrared (TIR) irradiance over the ocean by ~8.7 W/m^2.

BrC absorption alone (Figure 11-4, left column), decreased cloud optical depth over the ocean and land by lesser amounts, ~0.054 and ~0.028, respectively, than did BC+BrC. BrC absorption alone similarly decreased cloud fraction over the ocean and land by lesser amounds, ~0.66% and ~0.22%, respectively, than did BC+BrC. Such reductions due to BrC alone still contributed to an increase in net downward TOA solar and solar plus TIR irradiance over the ocean, but by lesser amounts of ~1.3 W/m^2 and 1.26 W/m^2, respectively.

The net irradiance change due to BC is 5.1 W m^{-2} overall (1.6 W m^{-2} over land and 7.4 W m^{-2} over water). These values are calculated by subtracting the irradiance change in the BrC full case from that in the BC+BrC full case (Figure 11-4, 3rd column minus 1st column for Delta TAO net solar+TIR).

The reduction in cloudiness due to BC+BrC absorption increased net downward surface solar irradiance by 7.2 W/m^2 over the ocean but decreased it by 1.9 W/m^2 over land, resulting in a domain-averaged increase of 3.6 W/m^2. The decrease over land was likely due to the fact that BC+BrC itself absorbed solar radiation, preventing it from reaching the surface more than the slight decrease in cloud fraction over land increased surface solar irradiance.

BC+BrC absorption decreased downward ultraviolet (UV) irradiance to the ground both over land (0.56 W/m^2) and over the ocean (0.23 W/m^2), for a domain average of 0.36 W/m^2 (Figure 11-4, right column). The decrease in UV irradiance to the ground, despite the increase in total solar irradiance to the ground, is likely due to the fact that BrC strongly preferentially absorbs UV radiation. BC also preferentially absorbs UV over longer wavelengths, but the variation of its absorption with wavelength is much smaller. So, even though both BC and BrC reduce cloudiness, increasing solar penetration to the ground, the UV otherwise scattered by clouds is now absorbed primarily by BrC and BC within aerosol particles. This UV reduction seems to be due mostly to BrC, as Figure 11-4 (left column), shows that BrC absorption alone decreased downward UV irradiance 0.46 W/m^2 over land, 0.45 W/m^2 over the ocean, and 0.46 W/m^2 overall, thus by an overall similar magnitude as BC+BrC absorption.

The reduction in UV radiation due to preferential absorption by BrC reduced ozone and PAN near the surface and aloft (Figures 11-4 through 11-6), a result similarly found in *Jacobson* [1999], who found that preferential UV and short-visible absorption by nitrated and aromatic aerosol particles and nitrated aromatic gases not only reduced UV radiation much more than total solar radiation in the Los Angeles Basin but also decreased ozone.

11.5 Conclusions

Nested global-through-regional simulations were run to estimate the transient impacts of brown carbon and black carbon absorption on California climate with a realistic, contemporary (2014-2015) highly resolved in space, time, and composition emission inventory.

Results suggest that, averaged over a single year, absorption by brown carbon in aerosol particles and clouds increased domain-averaged near-surface air temperatures by ~0.018 K, whereas absorption by organic matter plus black carbon increased it by ~0.17 K, suggesting a warming by black carbon of ~0.15 K. Of that, ~0.01 K warming (~7%) was due to absorption by black carbon inclusions within cloud and precipitation particles and the rest was due to black carbon absorption interstitially between cloud particles at the relative humidity of the cloud plus absorption by black carbon in clear-sky aerosol particles. The substantial stratus

cloudiness over oceans and coastal areas of California created an environment where black carbon interstitially between cloud particles had a strong warming effect on clouds.

Absorption increased temperatures aloft more than near the surface, stabilizing the air. It also increased top-of-the-atmosphere (TOA) net downward solar and solar plus thermal-infrared-irradiance, thus creating a net positive overall radiative forcing. Atmospheric heating and increased atmospheric stability due to aerosol absorption decreased cloud fraction and cloud optical depth, primarily over the ocean. Such decreases increased total surface solar radiation reaching the surface. However, preferential absorption of UV radiation by BrC in particular but also BC decreased UV radiation to the surface. Such UV reductions due to BrC absorption contributed to lower ozone and PAN levels, a result consistent with a previous study. The water evaporated from clouds contributed to higher water vapor contents in most locations and an increase in the relative humidity in some locations.

11.6 References

Alexander, D.T.L., P.A. Crozier, and J.R. Anderson (2008), Brown carbon spheres in East Asian outflow and their optical properties, *Science, 321,* 833-836.

Arakawa, A., and V. R. Lamb (1981), A potential enstrophy and energy conserving scheme for the shallow water equations, *Mon. Wea. Rev., 109,* 18-36.

Cappa, C. D., Zhang, X., Russell, L. M., Collier, S., Lee, A. K. Y., Chen, C.-L., Betha, R., Chen, S., Liu, J., Price, D. J., Sanchez, K. J., McMeeking, G., Williams, L. R., Onasch, T. B., Worsnop, D. R., Abbatt, J., and Zhang, Q.: Black carbon mixing state and absorption by ambient black and brown carbon, in review.

Clarke, L., J. Edmonds, H. Jacoby, H. Pitcher, J. Reilly, and R. Richels (2007), Scenarios of Greenhouse Gas Emissions and Atmospheric Concentrations, Sub-report 2.1A of Synthesis and Assessment Product 2.1 by the U.S. Climate Change Science Program and the Subcommittee on Global Change Research, 154 pp., Department of Energy, Office of Biological & Environmental Research, Washington, D. C., USA, http://tntcat.iiasa.ac.at:8787/RcpDb/dsd?Action=htmlpage&page=compare (accessed April 1, 2018).

European Commission Joint Research Centre (JRC)/Netherlands Environmental Assessment Agency (PBL) (2014), Emission Database for Global Atmospheric Research (EDGAR), http://edgar.jrc.ec.europa.eu (accessed April 1, 2018).

Foster, V.G. (1992), Determination of the refractive index dispersion of liquid nitrobenzene in the visible and ultraviolet, *J. Phys. D: Applied Phys*., *25*, 525-529.

GFS (Global Forecast System) (2018), 1° x 1° reanalysis fields, http://nomads.ncdc.noaa.gov/data/gfs-avn-hi/ (accessed April 1, 2018).

Hoffer, A., A. Toth, M. Posfai, C.E. Chung, and A. Gelencser (2017), Brown carbon absorption in the red and near-infrared spectral region, *Atmos. Meas. Tech., 10*, 2353-2359.

Jacobson, M. Z. (1999), Isolating nitrated and aromatic aerosols and nitrated aromatic gases as sources of ultraviolet light absorption, *J. Geophys. Res., 104*, 3527-3542.

Jacobson M. Z. (2001a), GATOR-GCMM: A global through urban scale air pollution and weather forecast model. 1. Model design and treatment of subgrid soil, vegetation, roads, rooftops, water, sea ice, and snow, *J. Geophys. Res*., *106*, 5385-5402.

Jacobson, M. Z. (2001b), GATOR-GCMM: 2. A study of day- and nighttime ozone layers aloft, ozone in national parks, and weather during the SARMAP Field Campaign, *J. Geophys. Res., 106*, 5403-5420.

Jacobson, M. Z. (2002), Analysis of aerosol interactions with numerical techniques for solving coagulation, nucleation, condensation, dissolution, and reversible chemistry among multiple size distributions, *J. Geophys. Res*., *107* (D19), 4366, doi:10.1029/ 2001JD002044.

Jacobson, M. Z. (2003), Development of mixed-phase clouds from multiple aerosol size distributions and the effect of the clouds on aerosol removal, *J. Geophys. Res., 108* (D8), 4245, doi:10.1029/2002JD002691.

Jacobson, M.Z. (2004), The climate response of fossil-fuel and biofuel soot, accounting for soot's feedback to snow and sea ice albedo and emissivity, *J. Geophys. Res., 109*, D21201, doi:10.1029/2004JD004945.

Jacobson, M. Z. (2005), Studying ocean acidification with conservative, stable numerical schemes for nonequilibrium air-ocean exchange and ocean equilibrium chemistry, *J. Geophys. Res., 110,* D07302, doi:10.1029/2004JD005220.

Jacobson, M. Z. (2008), The causal link between carbon dioxide and air pollution mortality, *Geophysical Res. Lett., 35,* L03809, doi:10.1029/2007GL031101.

Jacobson, M. Z. (2012), Investigating cloud absorption effects: Global absorption properties of black carbon, tar balls, and soil dust in clouds and aerosols, *J. Geophys. Res*., *117*, D06205, doi:10.1029/2011JD017218.

Jacobson, M.Z. (2014), Effects of biomass burning on climate, accounting for heat and moisture fluxes, black and brown carbon, and cloud absorption effects, *J. Geophys. Res.*, *119*, 8980-9002, doi:10.1002/2014JD021861.

Jacobson, M. Z., Y. J. Kaufmann, and Y. Rudich (2007), Examining feedbacks of aerosols to urban climate with a model that treats 3-D clouds with aerosol inclusions, *J. Geophys. Res.*, *112*, D24205, doi:10.1029/2007JD008922.

Jacobson, M. Z., and D. G. Streets (2009), The influence of future anthropogenic emissions on climate, natural emissions, and air quality, *J. Geophys. Res.*, 114, D08118, doi:10.1029/2008JD011476.

Jacobson, M. Z., and J. E. Ten Hoeve (2012), Effects of urban surfaces and white roofs on global and regional climate, *J. Climate*, *25*, 1028-1044, doi:10.1175/JCLI-D-11-00032.1.

Jauregui, E. and E. Romales (1996), Urban effects on convective precipitation in Mexico City, *Atmos. Environ., 30*, 3383-3389.

Ketefian, G. S., and M. Z. Jacobson (2009), A mass, energy, vorticity, and potential enstrophy conserving boundary treatment scheme for the shallow water equations, *J. Comp. Phys.*, *228*, 1-32, doi:10.1016/j.jcp.2008.08.009.

Kirchstetter, T.W., and T. Novakov (2004), Evidence that the spectral dependence of light absorption by aerosols is affected by organic carbon, *J. Geophys. Res., 109*, D21208, doi:10.1029/2004JD004999.

Krekov, G.M. (1993), Models of atmospheric aerosols. In *Aerosol Effects on Climate*, S.G. Jennings, Ed., U. Arizona Press, 9-72.

Lu, R., and R. P. Turco (1995), Air pollutant transport in a coastal environment, II, Three-dimensional simulations over Los Angeles basin, *Atmos. Environ.*, *29*, 1499-1518.

Mellor, G. L., and T. Yamada (1982), Development of a turbulence closure model for geophysical fluid problems, *Rev. Geophys. Space Phys.*, *20*, 851-873.

MODIS/USGS Terra plus Aqua Combined Albedo 16-Day L3 Global 0.05˚ CMG V4 data, https://lpdaac.usgs.gov/about/news_archive/modisterra_land_cover_types_yearly_l3_global_005deg_cmg_mod12c1 (accessed April 1, 2018).

Pomerantz, M., B. Pon, H. Akbari, and S.-C. Chang (2000) The effect of pavements's temperatures on air temperatures in large cities, LBNL-43442, https://buildings.lbl.gov/sites/default/files/2000_pomerantz_et_al_effect_of_pavement_temp_on_air_temp_in_large_cities.pdf (accessed April 1, 2018).

Schaaf, C. et al. (2002) First Operational BRDF, albedo nadir reflectance products from MODIS, *Remote. Sens. Environ.*, *83*, 135-148.

Toon, O. B., C. P. McKay, T. P. Ackerman, and K. Santhanam (1989), Rapid calculation of radiative heating rates and photodissociation rates in inhomogeneous multiple scattering atmospheres, *J. Geophys. Res.*, *94,* 16,287-16,301.

Twitty, J.T., and J.A. Weinman (1971), Radiative properties of carbonaceous aerosols, J. Appl. Meteorol., 10, 725-731.

Walcek, C. J. (2000), Minor flux adjustment near mixing ratio extremes for simplified yet highly accurate monotonic calculation of tracer advection, *J. Geophys. Res.*, 105 (D7), 9335-9348.

11.7 Tables

Table 11-1. Spectral refractive indices of black carbon, primary organic matter aside from tarballs, tarballs, secondary organic matter aside from nitrocresol, and nitrocresol used in the study.

Wavelength (μm)	Black carbon[a]		Primary organic matter[b]		Tarballs[c]		Secondary organic matter[d]		Nitrocresol[e]	
	Real	Imag	Real	Imag	Real	Imag	Real	Imag	Real	Imag
0.170	1.80	0.740	1.85	0.408	1.35	0.288	1.85	0.408	1.70	0.300
0.180	1.80	0.740	1.85	0.408	1.35	0.288	1.85	0.408	1.70	0.300
0.185	1.80	0.740	1.85	0.408	1.35	0.288	1.85	0.408	1.70	0.300
0.190	1.80	0.740	1.85	0.408	1.35	0.288	1.85	0.408	1.70	0.300
0.195	1.80	0.740	1.85	0.408	1.35	0.288	1.85	0.408	1.70	0.300
0.200	1.80	0.740	1.85	0.402	1.35	0.289	1.85	0.402	1.70	0.300
0.205	1.80	0.740	1.82	0.357	1.35	0.293	1.82	0.357	1.70	0.300
0.210	1.80	0.740	1.79	0.311	1.36	0.298	1.79	0.311	1.70	0.300
0.215	1.80	0.740	1.76	0.291	1.37	0.302	1.76	0.291	1.70	0.300
0.220	1.80	0.740	1.73	0.268	1.38	0.307	1.73	0.268	1.70	0.300
0.225	1.80	0.740	1.73	0.207	1.39	0.312	1.73	0.207	1.70	0.300
0.230	1.80	0.740	1.73	0.150	1.39	0.317	1.73	0.150	1.70	0.300
0.235	1.80	0.740	1.76	0.161	1.40	0.322	1.76	0.161	1.70	0.300
0.240	1.80	0.740	1.80	0.185	1.41	0.327	1.80	0.185	1.70	0.300
0.245	1.80	0.740	1.80	0.218	1.42	0.331	1.80	0.218	1.70	0.300
0.250	1.80	0.740	1.80	0.252	1.42	0.336	1.80	0.252	1.70	0.300
0.255	1.80	0.740	1.80	0.287	1.43	0.341	1.80	0.287	1.70	0.300
0.260	1.80	0.740	1.79	0.322	1.44	0.346	1.79	0.322	1.70	0.300
0.265	1.80	0.740	1.77	0.356	1.45	0.351	1.77	0.356	1.70	0.300
0.270	1.80	0.740	1.74	0.387	1.46	0.355	1.74	0.387	1.70	0.300
0.275	1.80	0.740	1.72	0.393	1.46	0.360	1.72	0.393	1.70	0.300
0.280	1.80	0.740	1.70	0.393	1.47	0.364	1.70	0.393	1.70	0.303
0.285	1.80	0.740	1.68	0.378	1.48	0.364	1.68	0.378	1.68	0.325
0.290	1.80	0.740	1.66	0.362	1.48	0.362	1.66	0.362	1.66	0.350
0.295	1.80	0.740	1.65	0.343	1.49	0.361	1.65	0.343	1.65	0.375
0.300	1.80	0.740	1.64	0.325	1.49	0.359	1.64	0.326	1.64	0.399
0.304	1.80	0.740	1.64	0.313	1.50	0.358	1.64	0.318	1.63	0.418
0.306	1.80	0.740	1.64	0.305	1.50	0.357	1.64	0.314	1.62	0.430
0.308	1.80	0.740	1.64	0.299	1.50	0.357	1.64	0.311	1.61	0.440
0.310	1.80	0.740	1.64	0.293	1.50	0.356	1.64	0.307	1.60	0.451
0.312	1.80	0.740	1.64	0.287	1.50	0.356	1.64	0.304	1.59	0.470
0.314	1.80	0.740	1.63	0.280	1.51	0.355	1.63	0.300	1.58	0.490
0.316	1.80	0.740	1.63	0.273	1.51	0.354	1.63	0.297	1.57	0.512
0.320	1.80	0.740	1.63	0.262	1.51	0.353	1.63	0.290	1.55	0.531
0.325	1.80	0.740	1.63	0.246	1.52	0.352	1.63	0.282	1.55	0.509
0.330	1.80	0.740	1.63	0.230	1.52	0.350	1.63	0.274	1.55	0.483
0.335	1.80	0.740	1.63	0.215	1.53	0.349	1.63	0.265	1.55	0.457
0.340	1.80	0.740	1.62	0.199	1.53	0.348	1.62	0.257	1.55	0.430
0.345	1.80	0.740	1.62	0.184	1.54	0.346	1.62	0.248	1.55	0.405
0.350	1.80	0.740	1.62	0.168	1.54	0.345	1.62	0.240	1.55	0.379
0.355	1.80	0.740	1.61	0.154	1.55	0.343	1.62	0.231	1.55	0.345
0.360	1.80	0.740	1.59	0.141	1.55	0.342	1.61	0.223	1.55	0.310

Wavelength (μm)	Black carbon[a]		Primary organic matter[b]		Tarballs[c]		Secondary organic matter[d]		Nitrocresol[e]	
0.365	1.80	0.740	1.58	0.127	1.56	0.340	1.61	0.214	1.55	0.275
0.370	1.80	0.740	1.56	0.114	1.56	0.339	1.61	0.205	1.55	0.241
0.375	1.80	0.740	1.55	0.100	1.57	0.337	1.61	0.196	1.55	0.213
0.380	1.80	0.740	1.54	0.0880	1.58	0.336	1.60	0.188	1.55	0.204
0.385	1.80	0.740	1.53	0.0760	1.58	0.334	1.60	0.179	1.55	0.198
0.390	1.80	0.740	1.52	0.0640	1.59	0.333	1.60	0.162	1.55	0.184
0.395	1.80	0.740	1.51	0.0520	1.59	0.331	1.60	0.0950	1.55	0.121
0.400	1.80	0.740	1.50	0.0403	1.60	0.330	1.59	0.0284	1.55	0.0584
0.405	1.80	0.740	1.50	0.0312	1.62	0.331	1.51	0.0130	1.55	0.0460
0.410	1.80	0.740	1.50	0.0298	1.64	0.331	1.50	0.0117	1.55	0.0420
0.415	1.80	0.740	1.50	0.0295	1.66	0.332	1.50	0.0114	1.55	0.0380
0.420	1.80	0.740	1.50	0.0293	1.67	0.333	1.50	0.0111	1.55	0.0340
0.425	1.80	0.740	1.50	0.0291	1.69	0.334	1.50	0.0107	1.55	0.0300
0.430	1.81	0.740	1.50	0.0288	1.72	0.335	1.50	0.0103	1.55	0.0250
0.440	1.81	0.740	1.50	0.0283	1.75	0.336	1.50	0.00980	1.55	0.0180
0.450	1.81	0.740	1.50	0.0279	1.79	0.337	1.50	0.00917	1.55	0.0109
0.460	1.81	0.740	1.50	0.0274	1.83	0.339	1.50	0.00854	1.56	0.00900
0.470	1.81	0.740	1.50	0.0269	1.86	0.337	1.50	0.00791	1.57	0.00800
0.480	1.82	0.740	1.50	0.0265	1.86	0.326	1.50	0.00728	1.58	0.00700
0.490	1.82	0.740	1.50	0.0260	1.86	0.315	1.50	0.00665	1.59	0.00600
0.500	1.82	0.740	1.50	0.0255	1.86	0.304	1.50	0.00602	1.59	0.00511
0.510	1.82	0.740	1.50	0.0250	1.86	0.293	1.50	0.00539	1.55	0.00490
0.520	1.83	0.740	1.50	0.0246	1.86	0.283	1.50	0.00476	1.50	0.00480
0.530	1.83	0.740	1.50	0.0241	1.86	0.272	1.50	0.00415	1.46	0.00468
0.540	1.83	0.740	1.50	0.0236	1.86	0.261	1.50	0.00393	1.45	0.00446
0.550	1.83	0.740	1.50	0.0232	1.86	0.250	1.50	0.00384	1.45	0.00421
0.560	1.83	0.740	1.50	0.0227	1.85	0.243	1.50	0.00375	1.45	0.00397
0.570	1.84	0.740	1.50	0.0223	1.84	0.236	1.50	0.00366	1.45	0.00373
0.580	1.84	0.740	1.50	0.0218	1.83	0.229	1.50	0.00357	1.45	0.00349
0.590	1.84	0.740	1.50	0.0214	1.82	0.223	1.50	0.00349	1.45	0.00324
0.600	1.84	0.740	1.50	0.0209	1.82	0.216	1.50	0.00340	1.45	0.00302
0.610	1.84	0.738	1.50	0.0204	1.81	0.209	1.50	0.00331	1.45	0.00290
0.620	1.84	0.736	1.50	0.0200	1.80	0.202	1.50	0.00322	1.45	0.00280
0.630	1.84	0.733	1.50	0.0195	1.79	0.195	1.50	0.00313	1.45	0.00270
0.640	1.84	0.731	1.50	0.0191	1.78	0.188	1.50	0.00304	1.45	0.00260
0.650	1.85	0.729	1.50	0.0186	1.77	0.182	1.50	0.00295	1.45	0.00250
0.660	1.85	0.727	1.50	0.0182	1.77	0.177	1.50	0.00286	1.45	0.00240
0.680	1.85	0.722	1.50	0.0173	1.75	0.170	1.50	0.00269	1.45	0.00220
0.700	1.85	0.718	1.50	0.0163	1.74	0.163	1.50	0.00251	1.45	0.00200
0.720	1.85	0.715	1.50	0.0155	1.73	0.157	1.50	0.00235	1.45	0.00182
0.740	1.85	0.711	1.50	0.0145	1.72	0.149	1.50	0.00215	1.45	0.00160
0.760	1.86	0.707	1.50	0.0136	1.71	0.142	1.50	0.00198	1.45	0.00140
0.780	1.86	0.704	1.50	0.0127	1.70	0.135	1.50	0.00180	1.45	0.00120
0.800	1.86	0.700	1.50	0.0119	1.69	0.129	1.50	0.00164	1.45	0.00103
0.813	1.86	0.698	1.50	0.0112	1.68	0.124	1.50	0.00151	1.45	0.00100
0.835	1.87	0.694	1.50	0.0102	1.67	0.116	1.50	0.00131	1.46	0.00100
0.875	1.87	0.690	1.49	0.00770	1.64	0.103	1.49	0.00104	1.46	0.00100

Wavelength (μm)	Black carbon[a]		Primary organic matter[b]		Tarballs[c]		Secondary organic matter[d]		Nitrocresol[e]	
0.925	1.88	0.688	1.46	0.00469	1.62	0.0936	1.46	0.00100	1.46	0.00100
0.975	1.89	0.685	1.46	0.00406	1.61	0.0900	1.46	0.00100	1.46	0.00100
1.02	1.90	0.682	1.47	0.00344	1.61	0.0900	1.47	0.00100	1.47	0.00100
1.08	1.91	0.680	1.47	0.00278	1.61	0.0900	1.47	0.00100	1.47	0.00100
1.12	1.91	0.680	1.47	0.00207	1.61	0.0900	1.47	0.00100	1.47	0.00100
1.17	1.92	0.680	1.47	0.00136	1.61	0.0900	1.47	0.00100	1.47	0.00100
1.30	1.93	0.680	1.47	0.00100	1.61	0.0900	1.47	0.00100	1.47	0.00100
1.50	1.95	0.680	1.48	0.00100	1.70	0.0700	1.48	0.00100	1.48	0.00100
1.70	1.97	0.680	1.49	0.00100	1.78	0.0250	1.49	0.00100	1.49	0.00100
1.90	2.00	0.680	1.50	0.00100	1.79	0.01000	1.50	0.00100	1.50	0.00100
2.25	2.05	0.706	1.50	0.00270	1.79	0.0103	1.50	0.00270	1.50	0.00270
2.75	2.09	0.720	1.46	0.0121	1.79	0.0121	1.46	0.0121	1.46	0.0121
3.25	2.12	0.720	1.54	0.224	1.78	0.224	1.54	0.224	1.54	0.224
3.75	2.16	0.732	1.65	0.0912	1.78	0.0912	1.65	0.0912	1.65	0.0912
4.25	2.21	0.755	1.57	0.0105	1.78	0.0105	1.57	0.0105	1.57	0.0105
4.75	2.24	0.770	1.50	0.00445	1.78	0.00445	1.50	0.00445	1.50	0.00445
5.25	2.27	0.760	1.45	0.00805	1.78	0.00805	1.45	0.00805	1.45	0.00805
5.75	2.30	0.725	1.30	0.0235	1.78	0.0235	1.30	0.0235	1.30	0.0235
6.25	2.35	0.705	1.30	0.0445	1.78	0.0445	1.30	0.0445	1.30	0.0445
6.75	2.37	0.715	1.69	0.326	1.78	0.326	1.69	0.326	1.69	0.326
7.25	2.37	0.740	1.92	0.371	1.78	0.371	1.92	0.371	1.92	0.371
7.75	2.38	0.740	1.78	0.0794	1.78	0.0794	1.78	0.0794	1.78	0.0794
8.25	2.34	0.725	1.62	0.0909	1.78	0.0909	1.62	0.0909	1.62	0.0909
8.75	2.33	0.775	1.51	0.183	1.78	0.183	1.51	0.183	1.51	0.183
9.25	2.35	0.835	1.47	0.284	1.78	0.284	1.47	0.284	1.47	0.284
9.75	2.38	0.925	1.63	0.247	1.78	0.247	1.63	0.247	1.63	0.247
10.2	2.41	1.01	1.71	0.0940	1.78	0.0940	1.71	0.0940	1.71	0.0940
10.7	2.43	1.02	1.59	0.105	1.78	0.105	1.59	0.105	1.59	0.105
11.2	2.44	1.04	1.52	0.231	1.78	0.231	1.52	0.231	1.52	0.231
11.7	2.47	1.04	1.69	0.183	1.78	0.183	1.69	0.183	1.69	0.183
12.2	2.55	1.05	1.77	0.0268	1.78	0.0268	1.77	0.0268	1.77	0.0268
12.7	2.63	1.06	1.64	0.0268	1.78	0.0268	1.64	0.0268	1.64	0.0268
13.2	2.65	1.06	1.58	0.0545	1.78	0.0545	1.58	0.0545	1.58	0.0545
13.7	2.63	1.07	1.50	0.0865	1.78	0.0865	1.50	0.0865	1.50	0.0865
14.2	2.61	1.07	1.65	0.390	1.81	0.390	1.65	0.390	1.65	0.390
14.7	2.60	1.08	1.83	0.672	1.83	0.672	1.83	0.672	1.83	0.672
15.2	2.60	1.08	1.83	0.672	1.83	0.672	1.83	0.672	1.83	0.672
15.7	2.60	1.08	1.83	0.672	1.83	0.672	1.83	0.672	1.83	0.672
16.2	2.60	1.08	1.83	0.672	1.83	0.672	1.83	0.672	1.83	0.672
16.7	2.60	1.08	1.83	0.672	1.83	0.672	1.83	0.672	1.83	0.672
17.2	2.60	1.08	1.83	0.672	1.83	0.672	1.83	0.672	1.83	0.672
17.7	2.60	1.08	1.83	0.672	1.83	0.672	1.83	0.672	1.83	0.672
18.2	2.60	1.08	1.83	0.672	1.83	0.672	1.83	0.672	1.83	0.672
18.7	2.60	1.08	1.83	0.672	1.83	0.672	1.83	0.672	1.83	0.672
19.2	2.60	1.08	1.83	0.672	1.83	0.672	1.83	0.672	1.83	0.672
19.8	2.60	1.08	1.83	0.672	1.83	0.672	1.83	0.672	1.83	0.672
21.0	2.60	1.08	1.83	0.672	1.83	0.672	1.83	0.672	1.83	0.672

Wavelength (μm)	Black carbon[a]		Primary organic matter[b]		Tarballs[c]		Secondary organic matter[d]		Nitrocresol[e]	
23.5	2.60	1.08	1.83	0.672	1.83	0.672	1.83	0.672	1.83	0.672
27.5	2.60	1.08	1.83	0.672	1.83	0.672	1.83	0.672	1.83	0.672
32.5	2.60	1.08	1.83	0.672	1.83	0.672	1.83	0.672	1.70	0.672
37.5	2.60	1.08	1.83	0.672	1.83	0.672	1.83	0.672	1.70	0.672
45.0	2.60	1.08	1.83	0.672	1.83	0.672	1.83	0.672	1.70	0.672
60.0	2.60	1.08	1.83	0.672	1.83	0.672	1.83	0.672	1.70	0.672
85.0	2.60	1.08	1.83	0.672	1.83	0.672	1.83	0.672	1.70	0.672
150	2.60	1.08	1.83	0.672	1.83	0.672	1.83	0.672	1.70	0.672
250	2.60	1.08	1.83	0.672	1.83	0.672	1.83	0.672	1.70	0.672
400	2.60	1.08	1.83	0.672	1.83	0.672	1.83	0.672	1.70	0.672
600	2.60	1.08	1.83	0.672	1.83	0.672	1.83	0.672	1.70	0.672
850	2.60	1.08	1.83	0.672	1.83	0.672	1.83	0.672	1.70	0.672

[a]Krekov (1993) from 300-14,500 nm. Values above and below held to first and last values, respectively.

[b]Real and imaginary 200-300 nm from Foster et al. (1992) for nitrobenzene; imaginary at 350 nm from Kirchstetter et al. (2004); Cappa et al. (2018) for BBOA from Fresno for 405-870 nm for imaginary; imaginary interpolated between 300-350 and between 350-405 nm; real values 400-870 nm held constant at 1.5; real values 300-400 nm interpolated; real values 870 nm to 14,500 nm and imaginary values from 1,200 to 14,500 from Krekov (1993); imaginary values interpolated from 870 to 1,200 nm; real and imaginary values above 14,500 nm equal values at 14,500 nm from Krekov (1993).

[c]Alexander et al. (2008) from 200-400 nm; Values below 200 nm assumed the same as at 200 nm; real and imaginary from 467-950 nm from Hoffer et al. (2017); real and imaginary interpolated between 400 and 467 nm and held constant with 950 nm values between 950 nm and 1400 nm; real extrapolated from Alexander et al. (2008) value at 1,200 nm to 1,600 nm. Real part interpolated 1,400-1,600 nm and 1,600-2,500 nm. Imaginary part decreased from 1,600-1,800 nm then held constant 1,800-2,500 nm. Same imaginary as Primary Organic Matter 2,500-14,500 nm and real held constant 2,500-14,500 nm. Same real and imaginary parts as Primary Organic Matter above 14,500 nm.

[d]Same real and imaginary as Primary Organic Matter below 300 nm and above 1,300 nm; same real as Primary Organic Matter from 410-1,300 nm. Cappa et al. (2018) for OOA2 from Fresno 405-870 nm for imaginary; other wavelengths interpolated.

[e]Real 280-310, from Foster et al. (1992) for nitrobenzene; real 310-450 nm uses 310-nm value for 3-methoxybenzaldehyde from Jacobson (1999); real at 500 nm uses 500-nm value for nitrobenzene from Foster et al. (1992); Real 530-14,500 nm from Krekov (1993). Real 14,500-30,000 nm the same as for Primary Organic Matter. Real above 30,000 nm held constant. Imaginary at 319 nm from Jacobson (1999) for nitrocresol and scaled between 280 and 400 nm using profile from Foster et al. (1992) for nitrobenzene. Imaginary 400-800 nm from Jacobson (1999) extrapolating slope past 450 nm for 4-nitrophenol. Imaginary 800-2,000 nm from Krekov (1993); imaginary above 2,000 nm the same as for Primary Organic Matter. Real and imaginary below 280 nm held constant to values at 280 nm.

11.8 Figures

Figure 11-1. Real (left) and imaginary (right) refractive indices below 1 micrometer wavelength for BC and organics used in this study. Table 11-1 gives the values for all wavelengths.

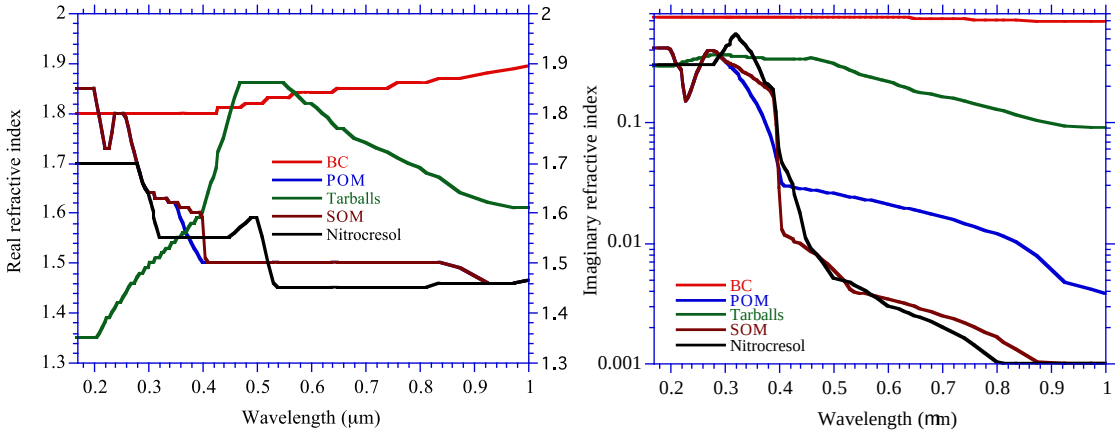

Figure 11-2. Modeled baseline annually averaged, near-surface (15 m) dry $PM_{2.5}$, total (wet) $PM_{2.5}$, and all sizes of black carbon (BC), primary organic matter (POM) aside from tarballs, tarballs, secondary organic matter (SOM) aside from nitrocresol, NH_4^+, S(VI)=H_2SO_4(aq)+HSO_4^-+SO_4^{2-}, HNO3(aq)+NO_3^-, Cl^-, NH_4NO_3, NaCl(s), $NaNO_3$(s), NH_4Cl(s), and soildust concentrations.

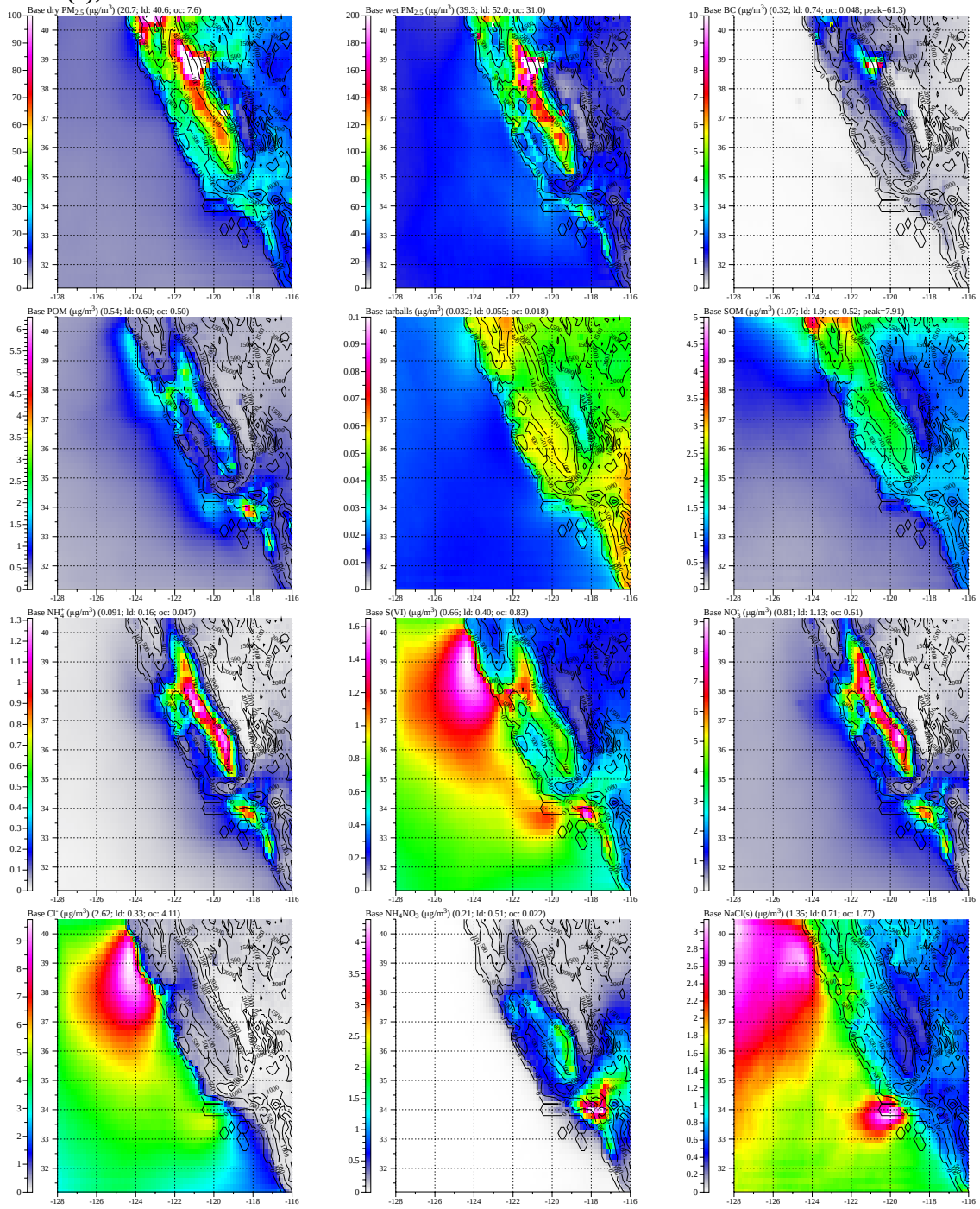

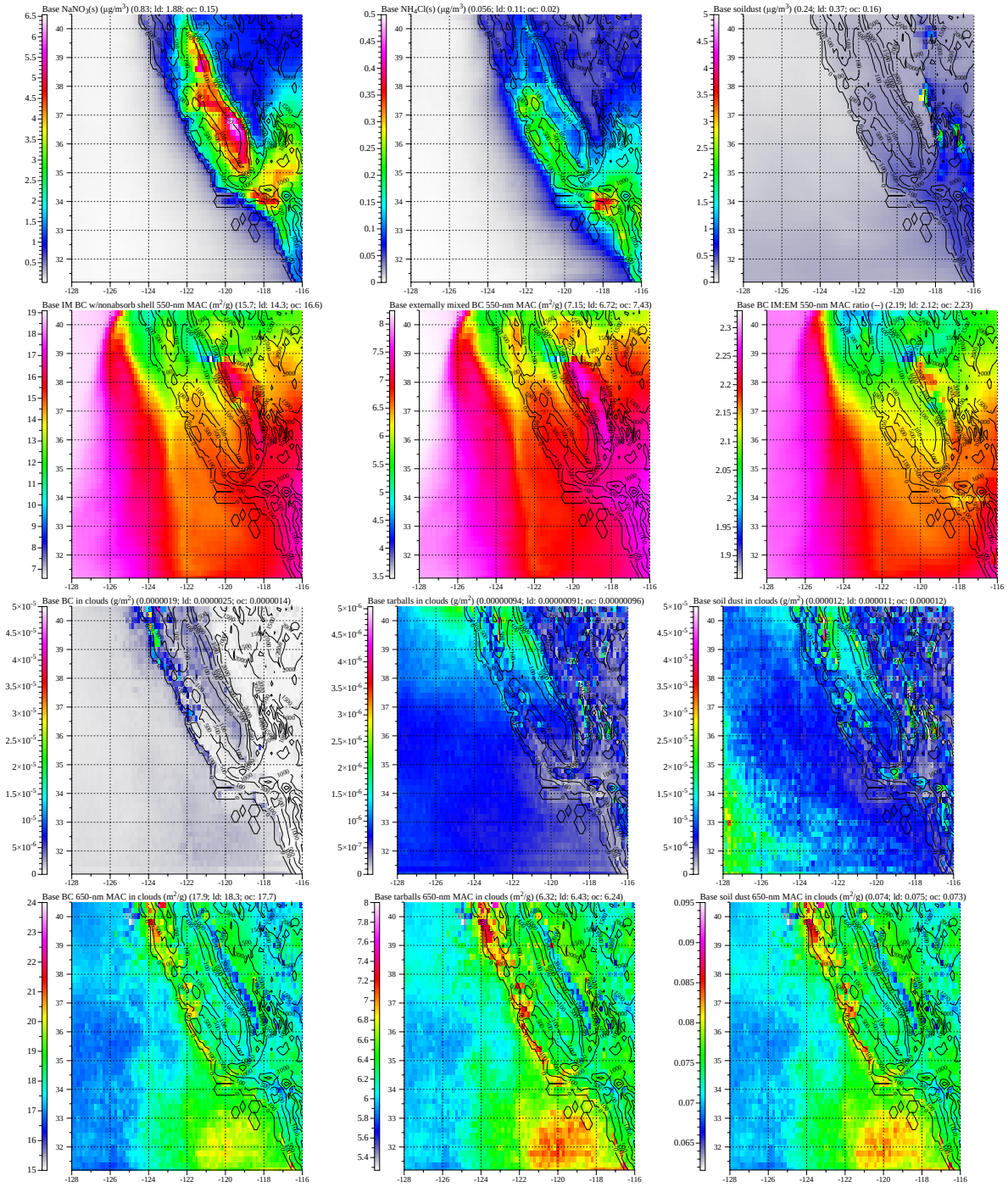
Base $NaNO_3$(s) (μg/m^3) (0.83; ld: 1.88; oc: 0.15)
Base NH_4Cl(s) (μg/m^3) (0.056; ld: 0.11; oc: 0.02)
Base soildust (μg/m^3) (0.24; ld: 0.37; oc: 0.16)
Base IM BC w/nonabsorb shell 550-nm MAC (m^2/g) (15.7; ld: 14.3; oc: 16.6)
Base externally mixed BC 550-nm MAC (m^2/g) (7.15; ld: 6.72; oc: 7.43)
Base BC IM:EM 550-nm MAC ratio (--) (2.19; ld: 2.12; oc: 2.23)
Base BC in clouds (g/m^2) (0.0000019; ld: 0.0000025; oc: 0.0000014)
Base tarballs in clouds (g/m^2) (0.00000094; ld: 0.00000091; oc: 0.00000096)
Base soil dust in clouds (g/m^2) (0.000012; ld: 0.000011; oc: 0.000012)
Base BC 650-nm MAC in clouds (m^2/g) (17.9; ld: 18.3; oc: 17.7)
Base tarballs 650-nm MAC in clouds (m^2/g) (6.32; ld: 6.43; oc: 6.24)
Base soil dust 650-nm MAC in clouds (m^2/g) (0.074; ld: 0.075; oc: 0.073)

Figure 11-3. Modeled annually averaged, column all-sized black carbon (BC), column all-sized primary organic matter (POM) aside from tarballs, column all-sized tarballs, column all-sized secondary organic matter (SOM) aside from nitrocresol, aerosol optical depth (AOD), aerosol absorption optical depth (AAOD), cloud optical depth (COD), cloud absorption optical depth (CAOD), and cloud fraction. For comparison, the annually averaged column nitrocresol concentration was around 60% of the POM concentration.

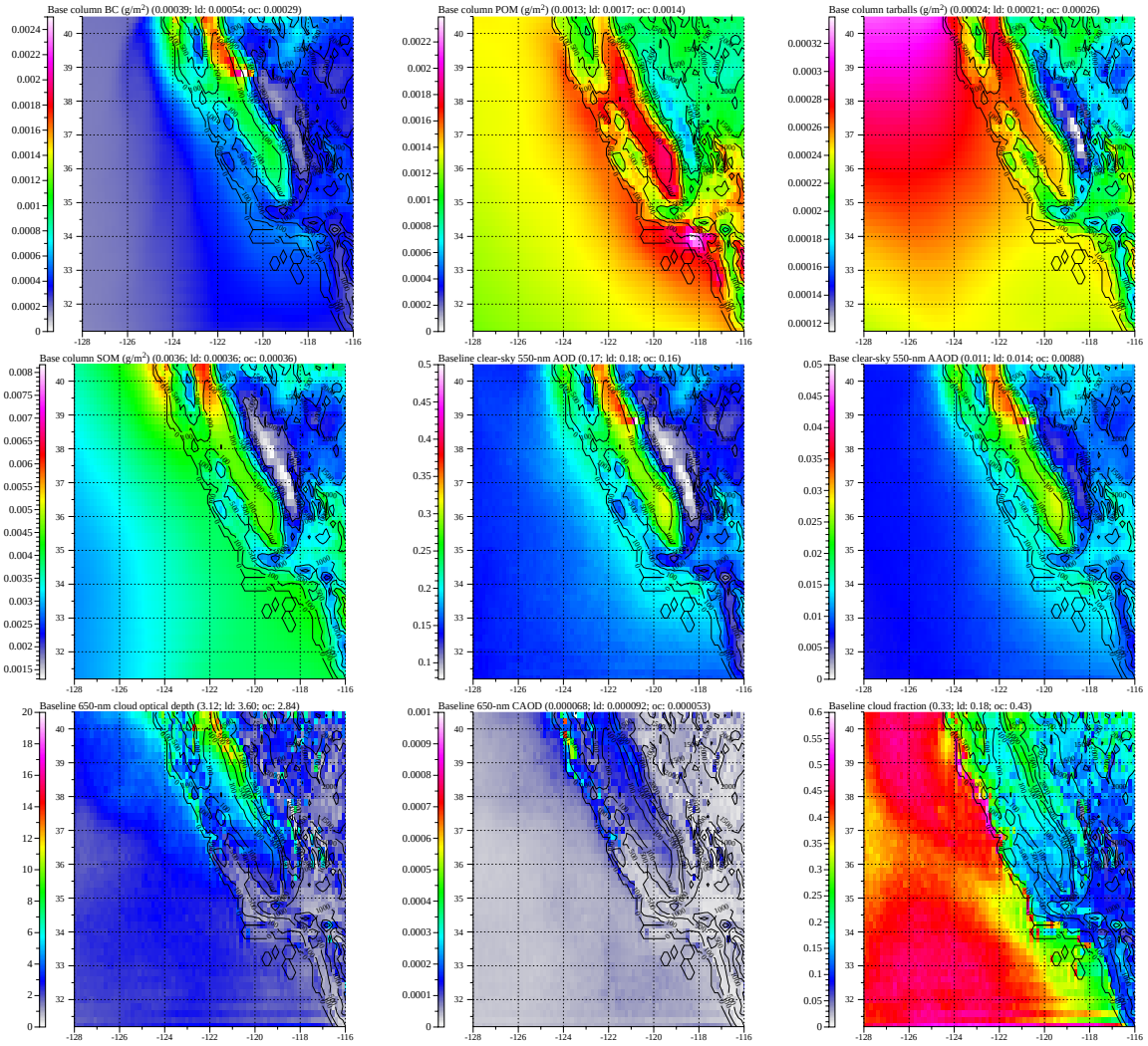

Figure 11-4. Horizontal annually averaged difference plots between Simulation 1 (baseline simulation) and (left) Simulation 2 (the simulation with zero aerosol or cloud absorption by BrC in solar or thermal-infrared wavelengths, (middle) Simulation 3 (no BC absorption within cloud or precipitation particles and no BrC absorption but absorption by BC aerosol particles between cloud particles and in the clear sky was still treated), and (right) Simulation 4 (no BrC or BC absorption in aerosol particles, cloud or precipitation particles, or in aerosol particles interstitially between cloud or precipitation particles. OM=organic matter; BC=black carbon; AAOD=aerosol absorption optical depth; CAOD=cloud absorption optical depth; COD=cloud optical depth; TOA=top-of-atmosphere; TIR=net downward minus upward thermal-infrared irradiance; sol=net downward minus upward solar irradiance; down surface UV=downward only ultraviolet irradiance reaching the surface.

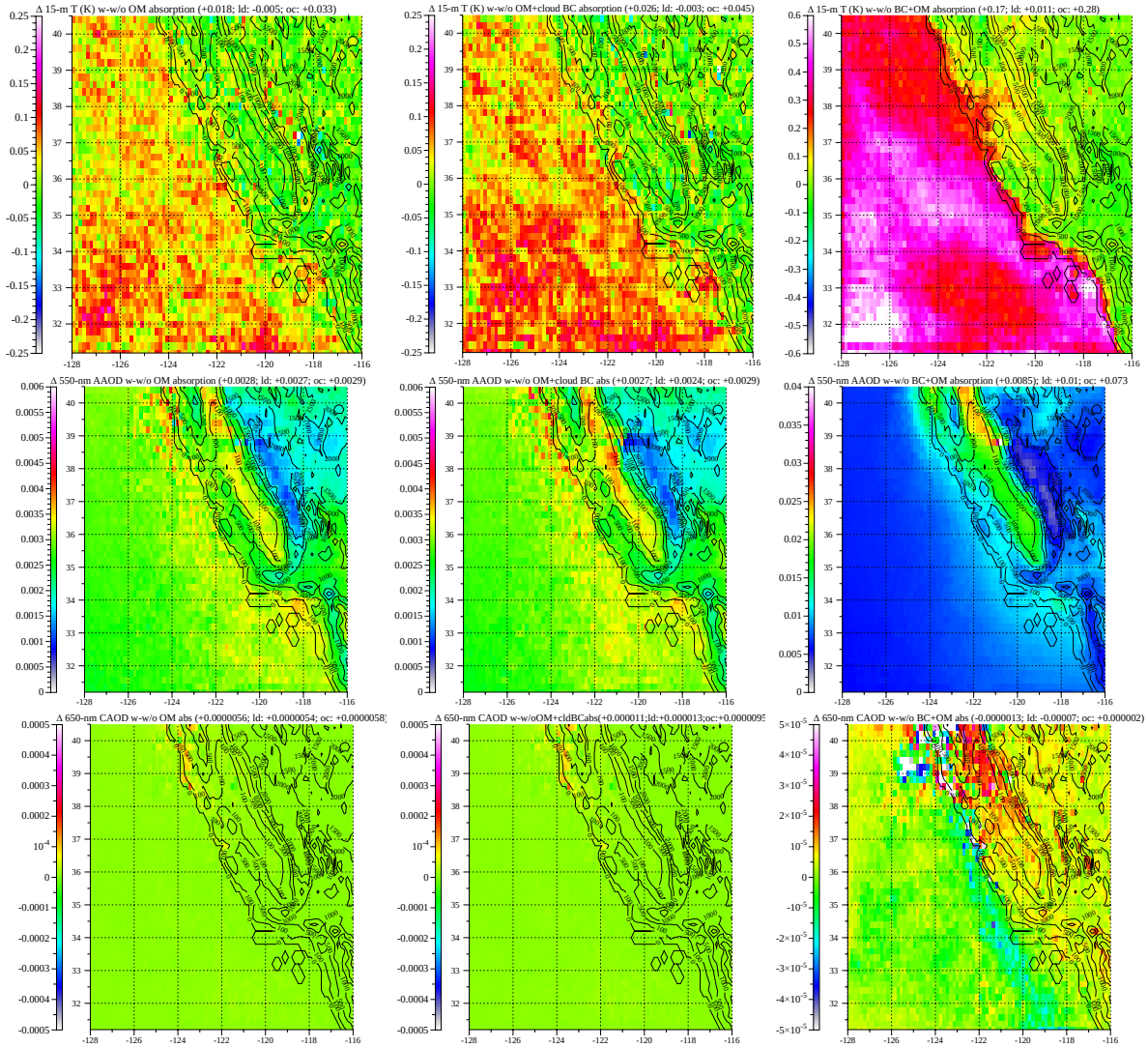

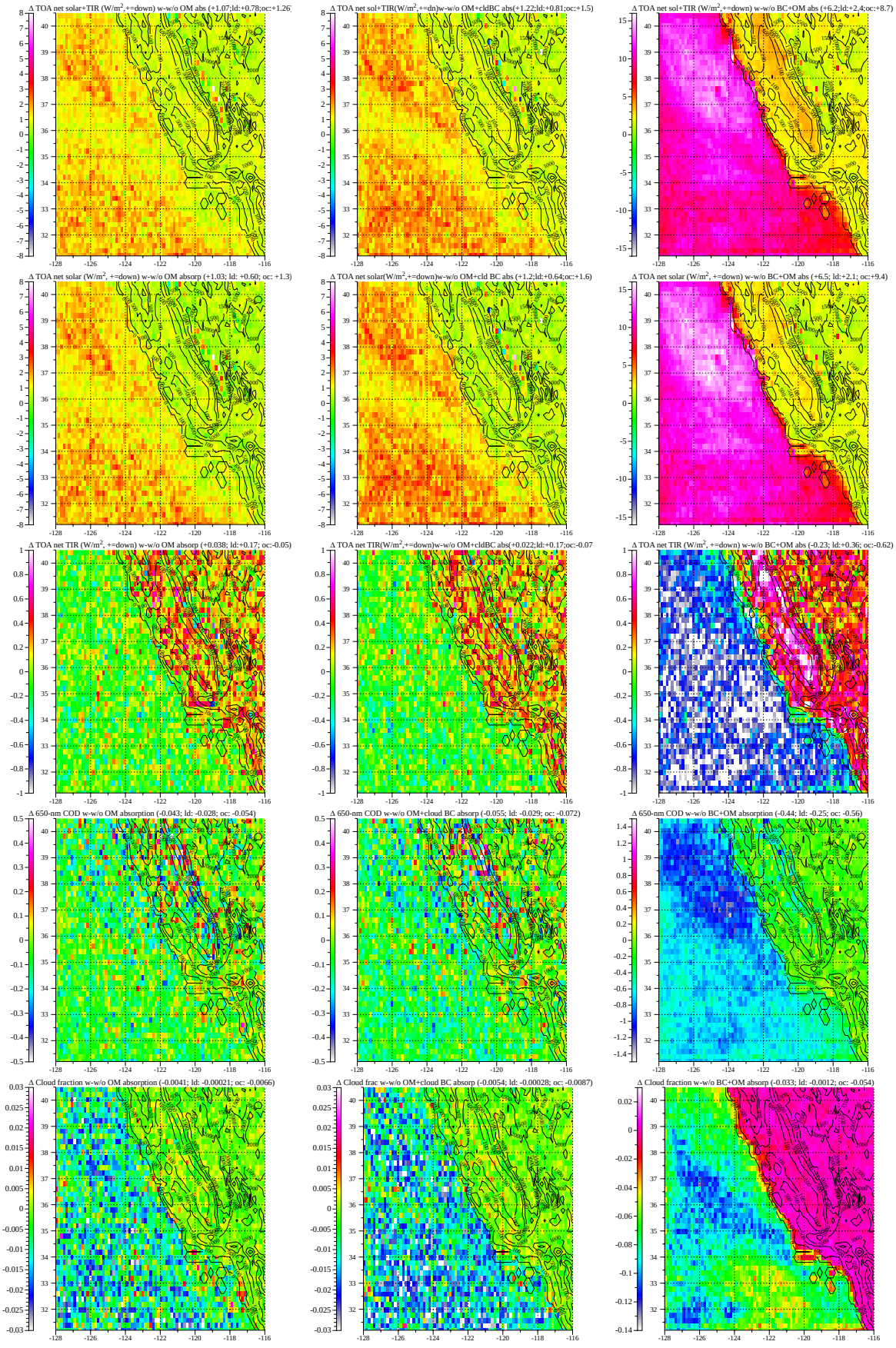
Δ TOA net solar+TIR (W/m2,+=down) w-w/o OM abs (+1.07;ld:+0.78;oc:+1.26
Δ TOA net sol+TIR(W/m2,+=dn)w-w/o OM+cldBC abs(+1.22;ld:+0.81;oc:+1.5)
Δ TOA net sol+TIR (W/m2,+=down) w-w/o BC+OM abs (+6.2;ld:+2.4;oc:+8.7)
Δ TOA net solar (W/m2, +=down) w-w/o OM absorp (+1.03; ld: +0.60; oc: +1.3)
Δ TOA net solar(W/m2,+=down)w-w/o OM+cld BC abs (+1.2;ld:+0.64;oc:+1.6)
Δ TOA net solar (W/m2, +=down) w-w/o BC+OM abs (+6.5; ld:+2.1; oc:+9.4)
Δ TOA net TIR (W/m2, +=down) w-w/o OM absorp (+0.038; ld:+0.17; oc:-0.05)
Δ TOA net TIR(W/m2,+=down)w-w/o OM+cldBC abs(+0.022;ld:+0.17;oc:-0.07
Δ TOA net TIR (W/m2, +=down) w-w/o BC+OM abs (-0.23; ld:+0.36; oc:-0.62)
Δ 650-nm COD w-w/o OM absorption (-0.043; ld: -0.028; oc: -0.054)
Δ 650-nm COD w-w/o OM+cloud BC absorp (-0.055; ld: -0.029; oc: -0.072)
Δ 650-nm COD w-w/o BC+OM absorption (-0.44; ld: -0.25; oc: -0.56)
Δ Cloud fraction w-w/o OM absorption (-0.0041; ld: -0.00021; oc: -0.0066)
Δ Cloud frac w-w/o OM+cloud BC absorp (-0.0054; ld: -0.00028; oc: -0.0087)
Δ Cloud fraction w-w/o BC+OM absorp (-0.033; ld: -0.0012; oc: -0.054)

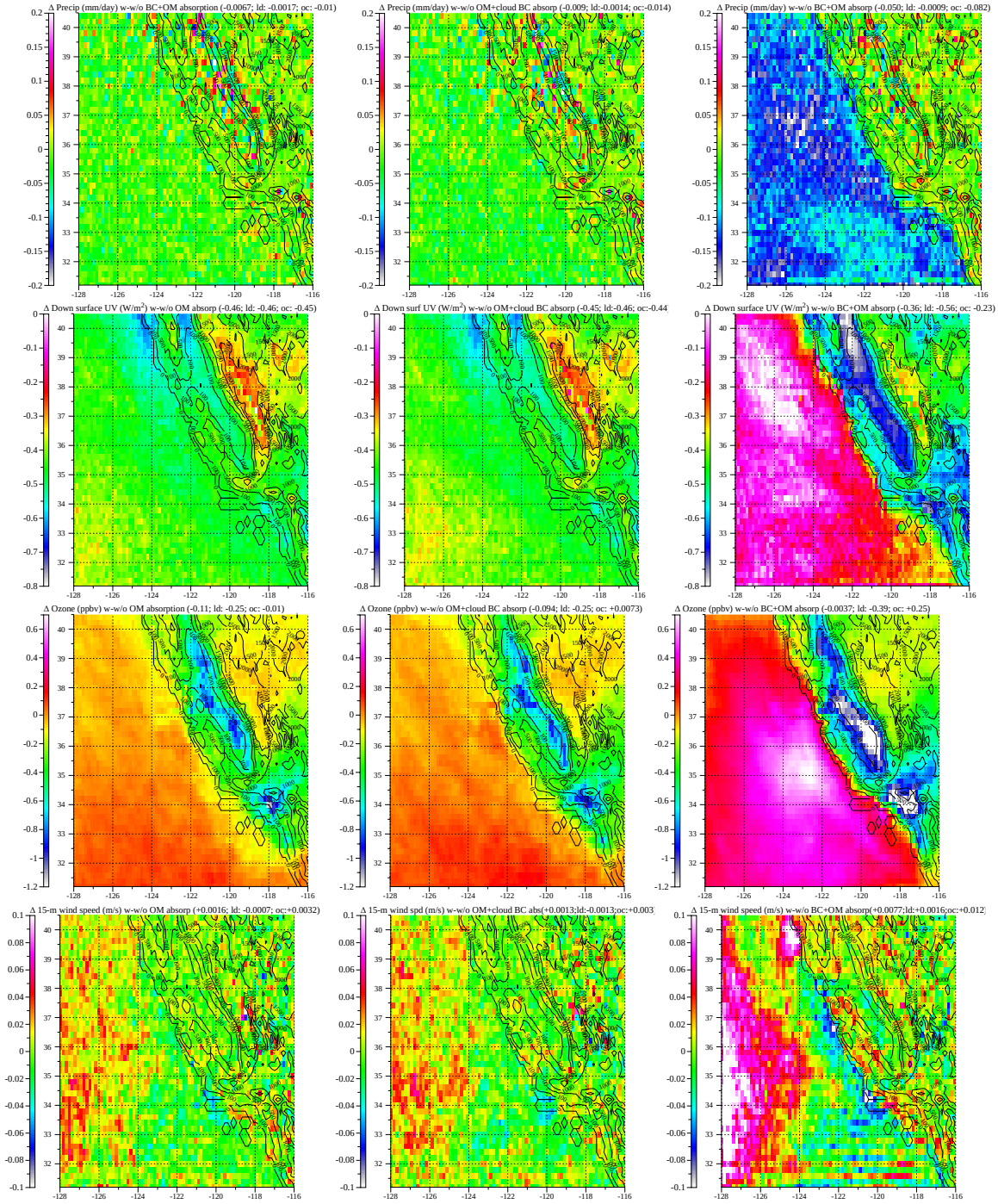
Δ Precip (mm/day) w-w/o BC+OM absorption (-0.0067; ld: -0.0017; oc: -0.01)
Δ Precip (mm/day) w-w/o OM+cloud BC absorp (-0.009; ld:-0.0014; oc:-0.014)
Δ Precip (mm/day) w-w/o BC+OM absorp (-0.050; ld: -0.0009; oc: -0.082)
Δ Down surface UV (W/m2) w-w/o OM absorp (-0.46; ld: -0.46; oc: -0.45)
Δ Down surf UV (W/m2) w-w/o OM+cloud BC absorp (-0.45; ld:-0.46; oc:-0.44
Δ Down surface UV (W/m2) w-w/o BC+OM absorp (-0.36; ld: -0.56; oc: -0.23)
Δ Ozone (ppbv) w-w/o OM absorption (-0.11; ld: -0.25; oc: -0.01)
Δ Ozone (ppbv) w-w/o OM+cloud BC absorp (-0.094; ld: -0.25; oc: +0.0073)
Δ Ozone (ppbv) w-w/o BC+OM absorp (-0.0037; ld: -0.39; oc: +0.25)
Δ 15-m wind speed (m/s) w-w/o OM absorp (+0.0016; ld: -0.0007; oc:+0.0032)
Δ 15-m wind spd (m/s) w-w/o OM+cloud BC abs(+0.0013;ld:-0.0013;oc:+0.003
Δ 15-m wind speed (m/s) w-w/o BC+OM absorp(+0.0077;ld:+0.0016;oc:+0.012

Figure 11-5. Same as Figure 11-4, but for zonally averaged differences.

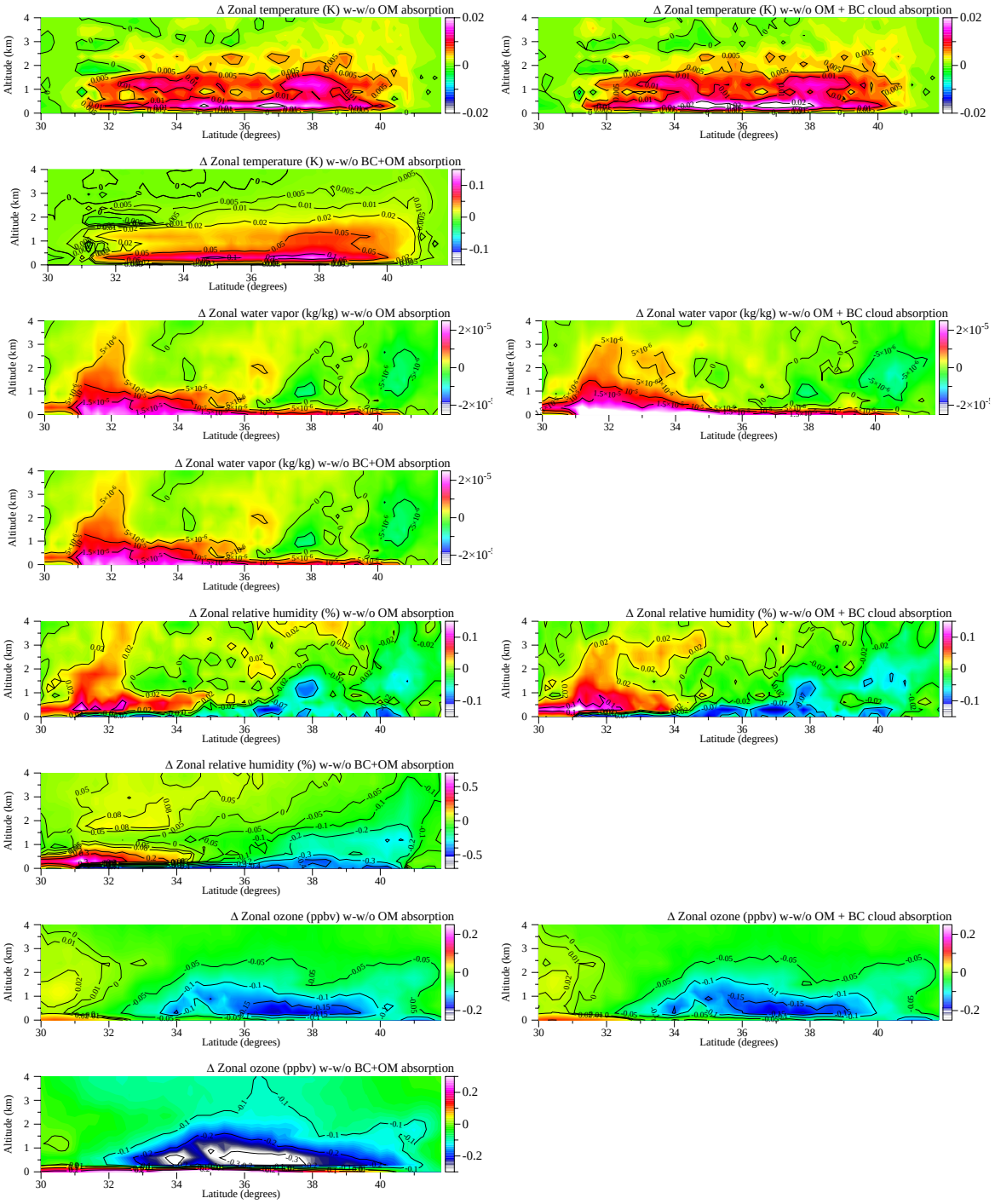

Figure 11-6. Same as Figure 11-4, but for meridionally averaged differences.

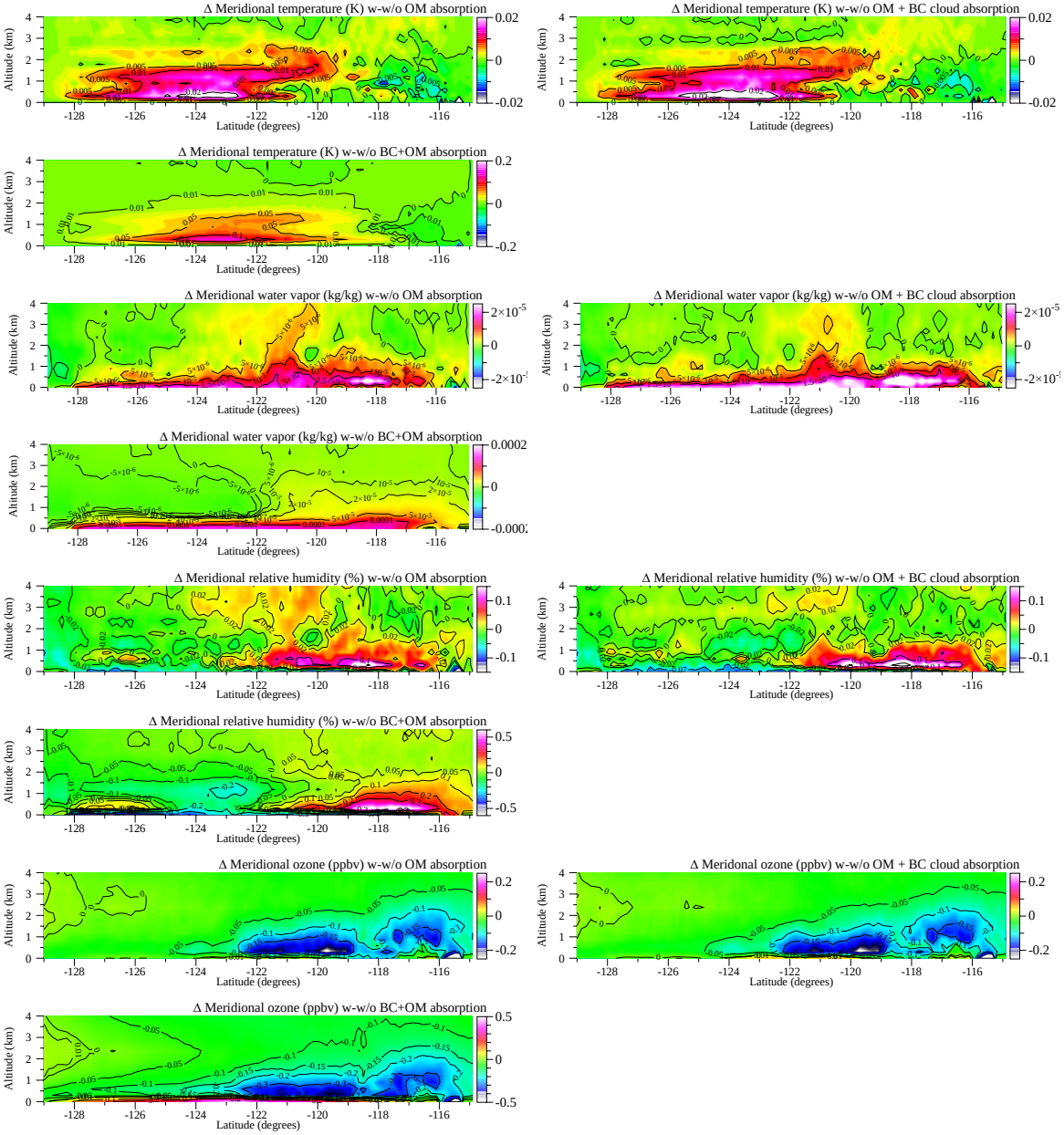

12 Conclusions

12.1 Tasks 1 and 2

The major conclusions of Tasks 1 and 2 funded by Agreement Number 13-330 are summarized below.

12.1.1 Aerosol Organic Composition and Sources

PM1 components were measured using AMS-PMF analysis, LS cluster analysis, and FTIR-PMF analysis at Fresno and Fontana. The AMS-VOOA factor with oxidized organic components and the AMS-BBOA factor from residential burning activities constitute the majority of organic mass (OM) on low-fog days, while the nitrate-related AMS-NOOA component constitutes the majority of the OM during the Fresno high-fog days in winter.

The AMS-NOOA factor (47% of OM) is associated with enhanced nitrate concentration (35%) during Fresno high-fog days. SOA formation at Fresno is strongly affected by persistent fog stagnation and high humidity impacts on particles leading to enhanced organic aerosol concentration. The increased amine, and organosulfate fragments were likely related to aqueous phase reaction at Fresno on high-fog days, which provides some preliminary evidence for aqueous reactions forming nitrate-containing, nitrogen-containing, and sulfate-containing organic component particles. Similarly, a previous study in SJV found that a large number of organic nitrogen compounds (including amines, nitrate esters, peptides, and nitroso compounds) were present in fog water [Herckes et al., 2007]. The lack of association of the products to a specific type of particle suggests that the reactions did not depend on particle components other than water.

AMS-VOOA contributes 58-69% of OM and increases in the afternoon in summertime Fontana, consistent with the expectation that SOA formation from vehicle and other VOC emissions is a significant PM1 source in summer at Fontana. Unusual trace organic fragments (m/z 27, 46, and 63) and increased nitrate, ammonium, sulfate, and alcohol group submicron mass at Fontana measured for more than five days after 4th of July fireworks provided a unique aerosol signature and extended air quality impacts. These results mean that firework contributions have a chemical signature that could be used to estimate their contributions in other areas. Also the persistence of these tracers in SoCAB for multiple days suggests that the contribution of fireworks to air quality degradation in stagnant conditions may be underestimated. Amine fragments (27% CHN+) and organosulfate fragments (32% CH3SO+) were higher on Fontana firework days than on non-firework days. The amine (CH4N+) fragment was an interesting difference between wintertime Fresno and summertime Fontana, consistent with the expected differences in amine precursor sources, likely more from vehicle and other fossil fuel related emissions in summertime at Fontana while more from agriculture, residential burning, and animal husbandry operations in wintertime at Fresno.

Two sets of PMF factors from AMS and FTIR as well as LS single-particle clustering with and without inorganic fragments provided comparable source-related OM contributions and single-particle types. Particularly, nitrate-related OM (NOOA) contributes 36% of particles at Fresno, while very-oxygenated OM (VOOA) makes up 60% of particles at Fontana. In addition, at Fontana there is clear evidence from the correlation of the FTIR-DDS factor to

AMS-VOOA and AMS-NOOA for SOA contributing organic components to refractory dust particles.

The moderate or strong correlations of LS-BBOA with AMS-BBOA, LS-HOA with AMS-HOA, and LS-NOOA with AMS-NOOA at Fresno indicated that BBOA, HOA, and NOOA were largely on separate particle types, in contrast to Fontana where the lack of evidence for external mixing was likely the result of the longer time for and larger mass contribution of photochemically oxidized components in SoCAB in summer. The association of amine fragments with LS-BBOA particles from residential burning emissions on low-fog days at Fresno but with LS-NOOA particles on high-fog days suggests that the formation pathway was changed in high-fog conditions, likely to one involving aqueous processes.

12.1.2 Aerosol Sizes and Processing

Given that different aerosol sources have different characteristic sizes and compositions, their size and composition are not independent [*Ge et al.*, 2012a; *Laborde et al.*, 2013]. During winter in Fresno and summer in Fontana, the size-resolved number, mass, and composition of aerosol particles and organic aerosol sources showed that Fresno had single-mode distributions with D_{N_mode}, D_{V_mode}, D_{M_mode}, and D_{VED_mode} (and low number-to-volume ratio of 285-2000 μm^{-3}) that varied between 6% and 200% larger than in Fontana, which had a large fraction of smaller (<100 nm) aerosol particles (and higher number-to-volume ratios of 800-4750 μm^{-3}). In Fontana particle number distribution had a maximum number concentration between 30 and 50 nm on non-firework days but in Fresno the maximum number concentration was between 70 and 80 nm in the evening and at night. Similarly, rBC mass distributions had mode peaks at volume equivalent diameter between 100 and 120 nm in Fontana and between 130 and 180 nm in Fresno. In Fontana, organic mass distributions had D_{M_mode} between 130 and 140 nm (often with a lower-concentration mode at 275 nm) and between 260 and 370 nm in Fresno. The differences in particle mode diameters between Fresno and Fontana are consistent with the different sources in the two regions: in Fresno larger particles are at high concentrations in the evening and at night, likely due to residential wood burning activities; in Fontana smaller particles are prevalent during most of the day, likely associated with vehicular traffic emissions [*Fujita et al.*, 2007; *Ge et al.*, 2012a].

In addition to sources, different atmospheric processes in Fresno and Fontana affected particle sizes: The ratios of organic mass-to-particle mass and m/z 44-to-particle mass were nearly constant with size in Fresno and were decreasing with size in Fontana. The lack of size dependence is consistent with volume-limited growth (or aqueous phase reactions) of particles larger than 200 nm diameter in Fresno. Similarly the decrease in fraction of organic and oxidized markers with size could result from surface-limited (or mass-transfer limited) processes for aerosol particles in Fontana. In Fresno the narrowing of size distributions on high-fog days, a characteristic of aqueous processing of activated particles, increased D_{M_mode} and D_{V_mode}. In Fontana formation of organic components from mass-transfer limited processes resulted in the growth of smaller mode aerosol particles.

12.1.3 Aerosol Absorbing Components

The observations for two field campaigns in distinctly different urban environments (wintertime Fresno, CA versus summertime Fontana, CA) here demonstrate that the magnitude

of the mixing-induced absorption enhancement for BC (i.e. the "lensing" effect) is small for the ensemble-average absorption. Additionally, the absorption enhancement shows limited dependence on the ensemble-average coating-to-BC core ratio. These observations, considered with others (*Cappa et al.*, 2012; *Healy et al.*, 2015; *Liu et al.*, 2015c; *McMeeking et al.*, 2014), demonstrate that spherical core-shell Mie theory calculations will not reliably give good agreement with observations when ensemble-average properties are considered, which is what is done in most climate models. This is the case because most models that consider internal mixing of BC assume that all components are internally mixed, and do not account for only a small fraction of the NR-PM material being internally mixed with BC. For these two studies, only around 10-20% of NR-PM is internally mixed with BC. Thus, the amount of "coating" material is likely to be overestimated by models, and the mixing-induced absorption enhancement would be overestimated to an even greater extent. Instead, it is suggested that accounting for BC mixing-state diversity (i.e. differences in the composition between BC-containing particles, beyond whether a particle simply contains BC or not), such as has been done by *Fierce et al.* (2016), will be necessary to allow for accurate simulation of absorption by BC. While an empirical relationship between the mixing-induced E_{abs} for BC and $R_{coat\text{-}rBC}$ could be determined from the current observations, such a relationship is unlikely to be robust or generalizable, given differences observed around the world (*Cappa et al.*, 2012; *Healy et al.*, 2015; *Liu et al.*, 2015c; *McMeeking et al.*, 2014).

For the Fresno observations, two types of brown carbon were identified and characterized: BBOA and NOOA. The BBOA, derived from residential wood combustion, was highly absorbing at 405 nm (MAC_{BBOA} = 0.84 m^2 g^{-1}) and the absorptivity persisted out to 870 nm (MAC_{BBOA} = 0.085 m^2 g^{-1}). The NOOA was less absorbing, with MAC_{NOOA} = 0.52 m^2 g^{-1} at 405 nm and absorption that was indistinguishable from zero at 870 nm. The NOOA was associated with the occurrence of heavy, early-morning fog and with an increased prevalence of particulate nitrate. The NOOA likely results from nitrate radical oxidation, coupled with aqueous processing. In the Fresno wintertime environment, the BBOA contribution (and associated absorption) was limited primarily to the nighttime, when surface emissions were high and the nocturnal boundary layer was low. Consequently, the local and regional radiative impacts of BBOA from residential wood combustion (and the co-emitted BC) are likely small because these are highly diluted into the daytime mixed boundary layer. In contrast, the NOOA concentration (and associated absorption) is greatest during the day. Thus, the NOOA may impact local and regional radiative forcing by increasing the daytime absorption of solar radiation. Also, since it seems likely that the NOOA is formed to a large extent by nocturnal chemical processing in the residual layer, the NOOA might exist above the ground-level fogs and could contribute to stabilization of the atmosphere and to fog persistence. In contrast to Fresno, there was little evidence of a notable contribution from brown carbon in summertime Fontana.

12.2 Task 3

The major conclusions of Task 3 funded by Agreement Number 13-330 are summarized below.

12.2.1 Comparison of Surface and Column Absorption by BrC

After comparing BC and BrC absorption from AERONET and surface measurements at wintertime Fresno, California, we found greater similarities in 2014 than in 2013, although both years had more BC (67% to 89%) than BrC (11% to 33%). In 2014, BC and BrC absorption calculated from AERONET (72% BC and 28% BrC) were quite similar to those of surface measurements (68% BC and 32% BrC). Surface absorption scaled to BLH moderately correlated ($R^2 = 0.60$) to column AERONET AAOD. Similarly, surface BC absorption scaled to BLH moderately correlated ($R^2 = 0.49$) to the BC fraction of AERONET AAOD. In contrast, in 2013, the AERONET AAOD from BC (67%) and BrC (33%) weakly correlated, showing a greater difference from surface-based BC (89%) and BrC (11%).

However, the comparisons between AERONET and surface measurements are only appropriate under limited conditions. Limitations included assuming that 1) the aerosol is well-mixed throughout the boundary layer, and 2) AOD and AAOD values in the boundary layer account for most of extinction and absorption in the air column. For example, in 2013, 36% of the clear-sky measurements were made when the BLH was lower than 200 m but in 2014, only 9% of measurements were made when the BLH was below 200 m. This combination of local meteorological patterns and timing of clear-sky conditions was largely the reason that surface measurements scaled by BLH correlate strongly or moderately with AERONET measurements at wintertime Fresno in 2014 but not in 2013. By removing measurements with BLH lower than 200 m, the average ratio of AERONET measurements to the surface-based estimates was actually closer to unity in 2013 than in 2014, even though the correlations in 2013 remained only moderate.

This work demonstrates that additional research using both AERONET and surface-based measurements is needed to assess the extent to which the AERONET-AAE method could be used to provide estimates of BC and BrC absorption across the nearly global AERONET network. Because AERONET retrievals are necessarily biased toward high aerosol loadings in current AERONET products, the fraction of overlapping AERONET times and surface measurements during almost 60 days of measurements is less than 5%. The small number of overlapping AERONET and surface measurements limit the representativeness of the comparisons of surface and column measurements. This limitation might be addressed by employing retrieval algorithms that are more accurate for low aerosol absorption measurements or not limited by clear-sky conditions.

12.2.2 Regional BrC Contributions to Total Absorption in California

Simulations for California carried out at 12km spatial resolution from August 2014 – July 2015 predict that regional BrC absorption causes 0.28 W m^{-2} of forcing at the top of the atmosphere and +0.005K temperature increase at the surface. Regional BrC in this context is defined as BrC that was emitted in California, which neglects BrC that may be transported to California from other locations. The majority of the regional BrC absorption was associated with wildfires rather than with residential wood combustion or waste burning. Each of these sources contains BrC, but the magnitude of the emissions from wildfires dominate over the other sources. Wildfire plumes generally rise above 5km in the atmosphere and so ground-based measurements are largely unable to detect these effects. Total-column regional

absorption in California was dominated by diesel engine particles which are concentrated at ground level, but this forcing is associated with BC, not BrC.

12.2.3 Global Plus Regional BrC Contributions to Total Absorption in California

Global through regional simulations carried out at 13km x 22 km spatial resolution over California from July 1, 2014 – July 1, 2015 predict that total BrC absorption causes +1.07 W m^{-2} of net downward irradiance change at the top of the atmosphere and +0.018K air temperature increase at the surface. Total BrC in this context is defined as BrC that was emitted in California and BrC that was transported to California from outside the regional domain. Given this assumption of BrC sources, the results from the global plus regional modeling are consistent with the results from the regional-only modeling summarized in Section 12.2.2. Both sets of calculations predict that the warming effects of BrC in California are relatively minor. The effects of total BC+BrC were more pronounced, with 5.1 W m^{-2} of net downward irradiance change at the top of the atmosphere and +0.17K of surface warming attributed to these combined species in the global-regional simulations. Again, these results are consistent with the source apportionment results summarized in Section 12.2, which find that diesel engine contributions are more significant than biomass burning contributions to total-column absorption in California.

12.2.4 Regional vs. Global Results

The regional and global calculations bound the range of reasonable assumptions related to atmospheric BrC. Regional BrC in Chapter 10 was defined as BrC emitted in California. Global plus regional BrC in Chapter 11 was defined as BrC emitted in California plus BrC transported to California from outside the domain. The background BrC in the global simulations is significant, accounting for approximately 40% of the column-total BrC over California. The regional calculations assumed that food cooking OC and SOA was not absorbing based on measurements of fresh or 2-3 day equivalent aged aerosols. The global calculations assumed that all OC was absorbing given sufficiently long time scales in the atmosphere. In summary, global calculations assumed that all atmospheric OC was absorbing, while regional calculations assumed that only biomass combustion OC was absorbing. Despite the factor of three differences in calculated irradiance change and surface temperature change, both calculations are in agreement that BrC changes surface temperature by less than 0.02K which is a very small perturbation.

12.2.5 Uncertainty in Model Results

The regional and global simulations performed in the study bound the regional parameter space describing BrC in the atmosphere. The regional calculations made relatively conservative assumptions about OC absorption while the global calculations made relatively aggressive assumptions about OC absorption. The fact that both of these independent calculations predict temperature change less than 0.02K in response to BrC in the atmosphere is therefore a robust conclusion. Further model perturbations would fall between the current estimates of 0.005K and 0.018K.

12.3 Synthesis of Conclusions

This project has provided accurate chemical and optical characterization of particles in diverse but much polluted regions of the state. These results have shown that BrC is important for surface-level absorption in wintertime Fresno, although BC is still the largest fraction of surface-level absorption. In summertime Fontana, BC is the major surface-level absorber with relatively small contributions from BrC. These surface measurements provide an important comparison to remote sensing measurements, reflecting local surface conditions with hourly time and source type resolution. Using these measurements to constrain regional and global simulations provides an accurate simulation of BC and BrC absorption for California, showing that BrC results in very little warming (less than 0.02K) and that diesel emissions of BC are the major contributor of that aerosol warming.

12.4 Appendix: Results From Long-Term Global Simulations

Stanford University has performed numerical simulations of the impacts of brown carbon on global climate. Simulations were carried out with the GATOR-GCMOM global-through-local air pollution-weather-climate model. For this application, the model was run on the global scale at a horizontal resolution of 4^{o}x5^{o}, with 68 vertical layers between the ground and 0.219 hPa (≈60 km), 15 layers in the bottom 1 km, and 500-m resolution from 1-21 km. The dynamical time step (for predicting meteorology) was 30 s.

Several simulations were set up and run up to 25 years. These include (A) a baseline simulation with all natural and anthropogenic gas and particle emissions and urban surfaces; (B) a simulation the same as A but with no anthropogenic greenhouse gas (AGHG) emissions, anthropogenic aerosol particle (AAP) or precursor gas emissions, or urban heat island (UHI) effects; (C) a simulation the same as A, but with no emissions of fossil fuel soot (FS), biofuel soot or gases (BSG), or biomass burning (BB) gases or particles; (D) a simulation the same as A, but with no absorption by brown carbon (BrC) or any other organic aerosol from FS, BSG, or BB sources; (E) a simulation the same as A but with no FS or BSG; and (F) a simulation the same as A but with no BB. Fossil fuel soot (FS) contains black carbon (BC), BrC, sulfate, and associated water. BSG and BB contain these and additional particle components plus all the major pollutant and greenhouse gases associated with those sources. AGHGs include all greenhouse gases, including carbon dioxide, methane, nitrous oxide, ozone, CFCs, CO, etc. AAPs include air pollutant gases as well as particles.

Figure 12-1 compares the modeled impact of all anthropogenic emissions plus the UHI effect on global near-surface air temperatures with surface air temperature anomaly data. The transient (14-year) climate response of all emissions is ~1.3 K globally-averaged warming (**Figure 12-1**a). This is for all emissions since preindustrial times. **Figure 12-1**b indicates that the observed global warming since between the 2016 and 1901-1930 average has also been ~1.3 K. The warming since preindustrial times is likely to be even larger because anthropogenic emissions began to build up in the 1700s. However, the modeled temperature change will also likely increase as the simulation continues. **Figure 12-1**a and **Figure 12-1**b show similar regional trends as each other. Namely, they both show strong high-latitude warming, stronger Northern than Southern Hemisphere warming, stronger continental than ocean warming, modest southeast U.S. warming and strong North Atlantic cooling.

Given that model temperature changes are driven solely by AGHGs, AAPs, and the UHI, the model result (**Figure 12-1**a) demonstrates by cause and effect what the data (**Figure 12-1**b) show by correlation, namely that only humans cause virtually all observed global warming.

Figure 12-2 examines the different components of the warming in **Figure 12-1**a. **Figure 12-2**a indicates that a large portion of the modeled all-cause anthropogenic warming in Figure 1a can be explained by FS, BSG, and BB. Note that BB includes CO_2 and CH_4 from biomass combustion. Separate simulations of the impacts of FS+BSG (**Figure 12-2**c) indicate that it is responsible for ~43% of the impacts of FS+BSG+BB global warming; BB is responsible for ~26%. The sum of these two 100%, indicating the non-linear nature of the impacts of different sources on climate.

Finally, **Figure 12-2**b indicates absorption by BrC and other organic aerosol from all sources was responsible for ~70% of the warming due to FS+BSG+BB; most of this is due to the brown carbon from BSG+BB.

12.5 Figures

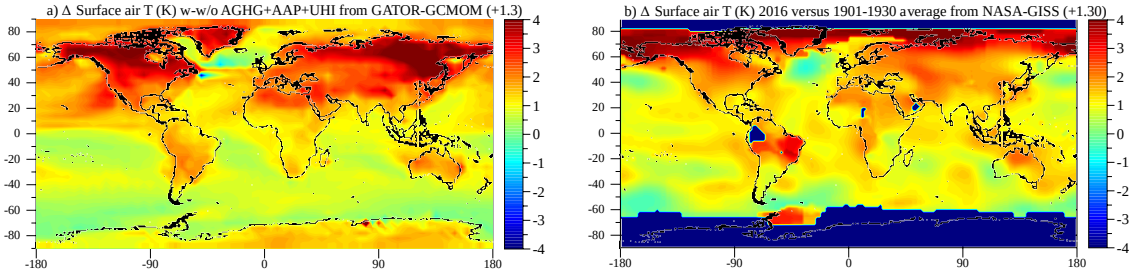

Figure 12-1. Comparison of (a) modeled impacts of all anthropogenic greenhouse gases (AGHGs) , anthropogenic aerosol particles (AAPs), and the urban heat island (UHI) effect on global temperatures with (b) NASA-GISS global temperature anomaly data 2016 minus the 1901-1930 mean (http://data.giss.nasa.gov/gistemp/). The model used was GATOR-GCMOM. Two simulations were run: one with AGHG+AAP+UHI plus all natural emissions (Simulation A) and the other without (Simulation B), both for 14 years. Simulation-average differences were then taken. Dark areas in (b) indicate no data available.

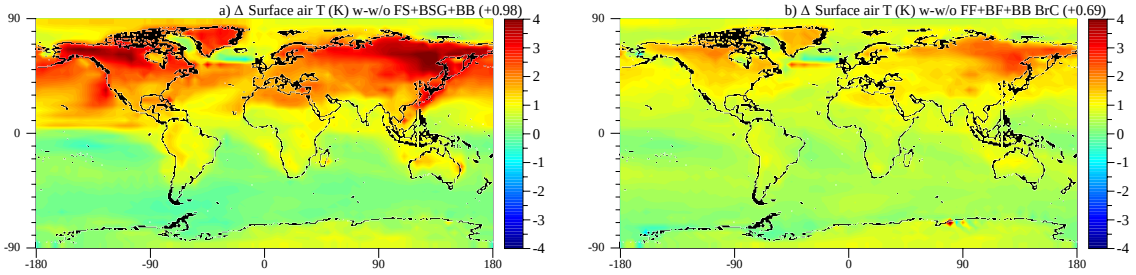

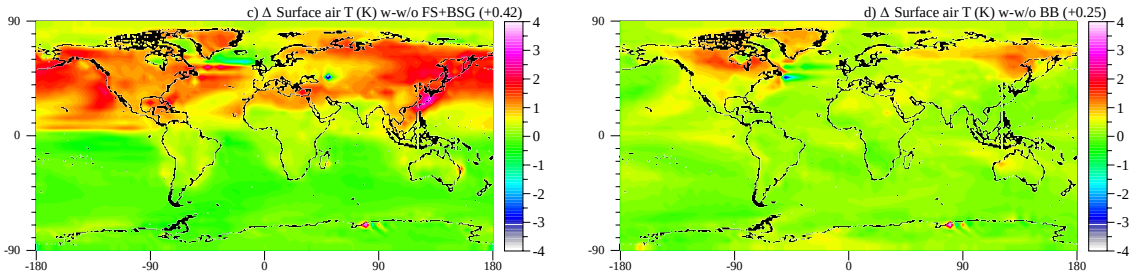

Figure 12-2. Modeled impacts of (a) all FS+BSG+BB components on global climate, from the difference between Simulations A and C over 25 years; (b) absorption in isolation by BrC and other organic aerosol components from FS+BSG+BB on global climate, from the difference between Simulations A and D over 25 years; (c) all FS+BSG components on global climate, from the difference between Simulations A and E over 25 years; and (d) all BB components on global climate, from the difference between Simulations A and F over 19 years.